UQAC
Université du Québec
à Chicoutimi

Développement de la chimie de l'apatite en tant qu'indicateur pétrogénétique et de provenance : implications pour l'exploration minérale

Par

Marie Kieffer

Sous la direction de Sarah Dare

Thèse présentée à l'Université du Québec à Chicoutimi en vue de l'obtention du grade de Doctorat (Ph.D.) en Sciences de la Terre et de l'atmosphère

Québec, Canada

RÉSUMÉ

La précipitation d'un minéral à partir d'un liquide est causée par des changements dans les variables intensives de pression, température, composition du liquide et fugacité d'oxygène (fO_2). Ces changements sont provoqués par des processus tels que le transfert du magma dans la croûte (changements de pression), le refroidissement du liquide (changements de température), la cristallisation fractionnée, l'ajout d'un autre liquide ou la contamination crustale (changements de composition), ou le démixage d'un seul liquide en deux liquides distincts (immiscibilité). Les éléments majeurs d'un minéral sont essentiels à sa formation, et ne peuvent donc varier que d'une façon limitée, tandis que son contenu en éléments traces peut varier de plusieurs ordres de grandeur. Les concentrations d'un grand nombre d'éléments traces sont suffisamment élevées dans l'apatite pour pouvoir être quantifiées. De plus, l'apatite est retrouvée dans la plupart des roches crustales, ce qui reflète le fait qu'elle peut précipiter à partir d'une grande variété de liquides et selon un grand nombre de conditions différentes. Cette thèse documente le contenu en éléments traces d'apatites provenant d'intrusions mafiques litées et de granites afin d'investiguer si ces éléments peuvent être utilisés pour déduire les conditions dans lesquelles les apatites se sont formées. Comme les intrusions mafiques litées et les granites (types I, S et A) sont hôtes de différents types de minéralisations, les résultats seront ensuite appliqués à l'utilisation de l'apatite en tant qu'outil pour l'exploration minérale.

Les buts principaux de cette thèse sont: 1) d'identifier quels processus sont enregistrés par les apatites dans les intrusions mafiques litées, et développer des proxys géochimiques pour tracer ces processus; et 2) de développer et d'améliorer la discrimination des apatites provenant des intrusions mafiques et des granites de type I, S et A, ce qui pourra être employé par les études de provenance et l'exploration minérale. Ces buts sont atteints via l'identification des éléments et ratios clefs sur un diagramme multiélément nouvellement conçu et en suivant une approche pétrogénétique.

L'exemple bien caractérisé de la Suite Intrusive de Sept-Iles (Québec, Canada) permet de démontrer que l'évolution des apatites cumulus correspond à celle du magma (*liquid line of descent*), et enregistre donc la cristallisation fractionnée depuis un magma mafique vers un magma feslique. L'apatite cumulus montre un enrichissement en ETR+Y, Th, U, K, Pb et Rb, et un appauvrissement en Sr, Ba, V et Mg durant la cristallisation fractionnée. Les apatites cumulus peuvent aussi tracer la cristallisation de plagioclase, ainsi qu'une recharge et un mélange avec un magma plus primitif. Il est également démontré que la composition des apatites cumulus des niveaux riches et pauvres en Fe-Ti-P de la Zone Critique minéralisée est le résultat de l'immiscibilité de liquides silicatés. La signature de l'apatite permet d'identifier les parties les plus primitives ou évoluées d'une intrusion mafique. En effet, l'apatite intercumulus cristallise à partir du liquide piégé et est enrichie en éléments incompatibles (Lu, Th et Cl), ainsi qu'en éléments compatibles (V), car elle se forme dans la partie la plus primitive de l'intrusion.

L'analyse et la comparaison des apatites cumulus de plusieurs intrusions mafiques permet d'investiguer l'effet de plusieurs paramètres additionnels sur la composition des apatites. Pour la première fois, il est démontré que l'apatite cumulus peut enregistrer la contamination crustale de son magma parent. Cela se traduit par des valeurs plus élevés en $(La/Nd)_N$, Th, U, Pb et As dans les intrusions les plus contaminées (e.g., Complexe du Bushveld, Complexe Igné de Sudbury), et est confirmé par des ratios $(^{87}Sr/^{86}Sr)_{initial}$ plus élevés dans l'apatite. La profondeur de fusion partielle du magma parent (i.e., la présence ou l'absence de grenat dans la source) est également tracée via le ratio $(Gd/Yb)_N$ de l'apatite cumulus.

Enfin, ces travaux proposent un nouveau schéma de classification pour identifier les apatites provenant d'intrusions mafiques et de différents types d'intrusions felsiques (i.e., granites de type I, S et A). Premièrement, le diagramme Sr/Y vs. ETR légers existant permet d'identifier les apatites d'origine mafique et felsique des autres types de roches. Deuxièmement, les apatites des intrusions felsiques sont séparées de celles des intrusions mafiques en utilisant 2 diagrammes ternaires (ETR+Y, Sr/Y et Eu/Eu*; et As, $(Gd/Yb)_N$ et Pb+Th+U). Troisièmement, le diagramme $\log(La/Yb)_N$ vs. Yb_N diagram existant distingue les apatites des intrusions archéennes et post-archéennes. Enfin, les apatites post-archéennes sont identifiées comme provenant de granites de type I, S ou en A selon

Mn, V et le ratio $(La/Nd)_N$. Les apatites des intrusions felsiques reflètent la présence des minéraux accessoires plutôt que la composition du magma.

Les résultats de cette thèse démontrent que l'apatite reflète effectivement son environnement de formation, et peut donc être utilisée en tant qu'indicateur pétrogénétique robuste. De plus, pouvoir identifier la roche source d'une apatite détritique dans un terrain inexploré et recouvert de sédiments (e.g., glaciaires) peut se révéler un outil additionnel pour aider à l'évaluation de la prospectivité d'une large zone.

ABSTRACT

Precipitation of a mineral from a liquid is brought about by changes in the intensive variables pressure, temperature, composition of the liquid and oxygen fugacity (fO_2). These changes are caused by processes such as magma transfer in the crust (changing pressure), cooling of the liquid (changing temperature), fractionational crystallisation, addition of another liquid or crustal contamination (changes in composition), or unmixing of a single liquid into separate liquids (immiscibility). The major elements in a mineral are essential to the formation of the mineral, and thus can only vary by a limited amount, whereas the variations in trace elements can vary by orders of magnitude. The concentrations of a wide variety of trace elements are sufficiently high in apatite for them to be quantified by laser ablation ICP-MS. In addition, apatite is found in most crustal rocks, reflecting the fact that it can precipitate from a wide variety of liquids and under a number of different conditions. This thesis will document the trace element contents of apatite from mafic layered intrusions and granites to investigate whether these can be used to deduce the conditions under which the apatite formed. As mafic layered intrusions and granites (i.e., I-, S- or A-type) are hosts to different types of mineralisations (Fe-Ti-V, Fe-Ti-P or Ni-Cu-PGE-Cr, and porphyry Cu-Mo, W-Sn skarns or hydrothermal veins, respectively), the results will then be applied to the use of apatite as a tool for mineral exploration.

The main aims of this thesis are: 1) to identify which processes are recorded by apatite within mafic layered intrusions and develop petrogenetic geochemical proxies to trace those processes; and 2) to develop and improve the discrimination of apatite from mafic intrusions and from I-, S- and A-type granites, that will prove useful for provenance and mineral exploration studies. These aims are achieved using a petrogenetic approach, through the use of a newly designed multielement diagram that allows to identify key trace elements and ratios.

Using the example of the well-characterised Sept-Iles Intrusive Suite (Quebec, Canada), it is demonstrated that the evolution of cumulus apatite matches that of the evolving magma (liquid line of descent) and thus records fractional crystallisation from mafic to felsic melts. Cumulus apatite records an increase in REE + Y, Th, U, K, Pb and Rb, and a decrease in Sr, Ba, V and Mg with fractional crystallisation. It can also fingerprint extensive crystallisation of plagioclase, as well as replenishment and mixing with a more primitive magma. In addition, it is demonstrated that the distinct composition of cumulus apatite from Fe-Ti-P-rich and -poor layers within the mineralised Critical Zone of Sept Iles is the result of silicate liquid immiscibility. Apatite signature also allows to clearly identify the more primitive or evolved parts of a mafic intrusion. Intercumulus apatite that crystallised from trapped liquid is enriched in incompatible elements (Lu, Th and Cl) as well as in compatible elements (V), as it forms in the more primitive part of the intrusion.

The analysis and comparison of cumulus apatite from various mafic intrusions allows us to investigate the effect of the following additional parameters on apatite chemistry. For the first time, it is shown that cumulus apatite can record crustal contamination of its parental melt. This results in higher $(La/Nd)_N$, Th, U, Pb and As in apatite from the most contaminated intrusions (e.g., Bushveld Complex, Sudbury Igneous Complex), and is confirmed by higher $(^{87}Sr/^{86}Sr)_{initial}$ in apatite. The depth of partial melting of the parental magma (i.e., the presence or absence of garnet in the mantle source) is also fingerprinted by the $(Gd/Yb)_N$ ratio of cumulus apatite.

Lastly, this study proposes a novel classification scheme to identify apatite originating from mafic and the different types of felsic intrusions (i.e., I-. S- and A-type granites). First, the existing Sr/Y vs. LREE diagram identifies apatite of mafic and felsic origin from other types of rocks. Second, apatite from felsic intrusions are more precisely identified from mafic intrusions using 2 ternary diagrams (REE+Y, Sr/Y and Eu/Eu*; and As, $(Gd/Yb)_N$ and Pb+Th+U). Third, apatite from felsic intrusions can be identified as Archean or post-Archean based on the existing $\log(La/Yb)_N$ vs. Yb_N diagram. Finally, post-Archean apatite is identified as originating from I-, S- or A-type granites using Mn, V and $(La/Nd)_N$ ratio. Apatite from felsic intrusions reflects the presence of REE-bearing accessory minerals rather than melt composition.

The results of this thesis demonstrates that apatite does reflect its magmatic environment of formation and can therefore be used as a powerful petrogenetic indicator. Furthermore, being able to

fingerprint the host rock of detrital apatite in unexplored, covered terrains (e.g., with glacial sediments) could provide an additional tool to help evaluate the prospectivity of a larger area.

TABLE DES MATIÈRES

LISTE DES FIGURES

CHAPITRE 1

CHAPITRE 2

CHAPITRE 3

LISTE DES TABLEAUX

CHAPITRE 1

CHAPITRE 2

CHAPITRE 3

CHAPITRE 4

LISTE DES ANNEXES

CHAPITRE 1

CHAPITRE 2

CHAPITRE 3

CHAPITRE 4

REMERCIEMENTS

Tout a commencé par un après-midi d'hiver 2019. Par un concours de circonstances dans lequel les diagrammes de phases de 'Principes de géochimie' n'y sont pas pour rien, celle qui deviendra ma directrice m'a proposé un projet de thèse. Sarah, merci du fond du cœur pour ces 4 années que je n'ai pas vues passer, et durant lesquelles tu m'as énormément appris. Merci pour ta confiance, et pour m'avoir permis d'enseigner et de m'impliquer dans le SEG en parallèle du doctorat, car ces opportunités ont été très enrichissantes. Merci surtout pour ta bonne humeur, ton support et ton encadrement exceptionnel. J'espère avoir été à la hauteur de tes espérances!

Merci Olivier Namur, pour m'avoir permis de travailler sur tes échantillons de la Suite Intrusive de Sept-Iles que tu connais si bien. Ton expertise et nos discussions ont apporté beaucoup à cette thèse. Merci également à Eduardo Mansur, pour avoir contribué aux discussions et effectué les analyses des isotopes de Sr dans les apatites.

Le workshop Wager & Brown III à Sept-Iles durant l'été 2022 a été l'occasion de voir les roches et affleurements typiques de la Suite Intrusive de Sept-Iles. Merci Michael Higgins d'avoir organisé et dirigé cette 1ère excursion internationale post-confinements, car grâce à toi j'ai pu voir les roches autrement qu'au travers d'un microscope et rencontrer une équipe de géologues enthousiastes.

Je voudrais également remercier les professeurs Renée-Luce, Pape et Dominique pour leur soutien et leurs conseils au long de mon parcours, mais également pour m'avoir permis de sortir du laboratoire pour accompagner plusieurs camps de terrain. Ces diversions ont été très appréciées et m'ont permis de prendre l'air pour mieux me replonger dans la rédaction. Merci à Audrey et Dany, au LabMaTer, pour leur aide lors des analyses LA-ICP-MS.

Merci Nils pour avoir pris de ton temps afin de m'aider à organiser l'excursion métallogénique du SEG au Chili, bien que tu ne puisses pas nous y accompagner, ainsi qu'à Laura-Pier pour t'être autant investie. Sans vous deux, cette 4e et dernière session d'hiver de mon doctorat aurait été encore plus compliquée qu'elle ne l'a été, et l'excursion n'aurait pas été un succès !

Le groupe de Chicoutimi : Pierre, Jen, Maxime, Sidonie, Mike, Sophie, Adrien et Julien, toujours présents pour les innombrables barbecues, feux de camp improvisés en toute saison, les randonnées qui finissent parfois en expédition, les sorties raquettes, le ski (juste Max), les soirées jeux, les séances de bureau des plaintes et les journées de bûcheronnage. Grâce à vous, j'aurais appris que si je décidais d'abandonner la recherche, je pourrais toujours ouvrir une boulangerie-pâtisserie spécialisée dans le lembas.

La bande de non géologues de Perros restés en Bretagne - sauf Marine (et Régis) à Québec - mais aussi Marion, Gaëtan, Francis, Victoria et Étienne, toujours fidèles au poste malgré la distance. Et toute la troupe de feu le RÉDiST (Nils, Théo, Esther, Arnaud, Rémi, Charles, Foulques, Hélène et Jonathan) pour les débats et discussions parfois inutiles, mais toujours animés, qui m'ont motivée (même si j'en dis le contraire) à passer au moins une journée par semaine à l'université.

Merci à toute ma famille, et particulièrement à mes parents, qui m'ont toujours encouragée même si cela m'amène à l'autre bout du monde. Sincères remerciements à mes 2 petits (mais grands) frères. À force de m'appeler petite sœur, vous aurez réussi à me faire terminer mes études après vous (de peu, ça ne s'est pas joué à grand-chose) ! Mais ne l'oubliez pas : vous dépendrez toujours de mes roches pour construire vos avions et téléphériques …

Enfin, je voudrais remercier Julien pour son soutien sans faille et ses encouragements tout au long du projet, car me supporter durant ces 4 années supplémentaires (et surtout, pendant la rédaction) n'a pas dû être une mince affaire. J'aurais eu du mal à terminer ce projet sans toi !

'*At the time of writing, we were fast asleep*
At the time of writing, we were in too deep
At the time of writing…'
(Midnight Oil, 2022)

Merci à Erebus, toujours présent pour superviser les séances de rédaction (ou y mettre fin).

Ces 4 années n'auront pas été de tout repos, mais elles auront certainement été très formatrices. Il est maintenant temps de débuter un nouveau chapitre et de clore celui-ci sur le mot de la fin : ice cream !

FINANCEMENT

Ces travaux ont principalement été supportés par une bourse de recherche du CRSNG (RGPIN-2015-05924) et la Chaire de recherche du Canada en géochimie appliquée aux gisements métalliques (CRC-2017-0286) de Sarah Dare.

J'ai également obtenu une bourse d'excellence pour étudiants étrangers (PBEEE) du Fonds de Recherche du Québec – Nature and technologies (319772).

CHAPITRE 1

INTRODUCTION

1.1 Introduction

Les éléments traces dans les minéraux sont sensibles aux variations liées à l'environnement géologique dans lequel ils se forment et sont donc communément utilisés en tant qu'indicateurs pétrogénétique et/ou de provenance (e.g., zircon, Henrique-Pinto *et al.* 2015; chromite, Arai *et al.* 2006; Barnes *et al.* 2022; magnétite, Dare *et al.* 2014; apatite, Belousova *et al.* 2002; Bruand *et al.* 2014; O'Sullivan *et al.* 2020; Pedersen *et al.* 2021). Un indicateur pétrogénétique est un minéral dont la composition renseigne sur la nature, la source et l'évolution du magma ou du fluide à partir duquel il cristallise. Un minéral indicateur est préservé dans l'environnement secondaire (e.g., sédiments fluvio-glaciaires), et sa présence en abondance est souvent suffisante pour être considéré en tant que tel (e.g.,Kelley *et al.* 2011). En revanche, le développement des techniques analytiques, et en particulier l'ablation laser (*laser ablation inductively coupled plasma mass spectrometer*; LA-ICP-MS), permet de mesurer un grand nombre d'éléments traces dans les minéraux et ainsi de développer leur utilisation en tant que minéraux indicateurs pour l'exploration (e.g., Caraballo *et al.* 2022; Miranda *et al.* in press).

Les minéraux indicateurs sont d'un grand intérêt pour les études de provenance sédimentaires et pour l'exploration minérale. En effet, l'étude de minéraux indicateurs dans une roche ou un gisement permet de mieux comprendre sa formation, tandis que l'exploration en environnement secondaire est critique pour trouver de nouveaux gisements dans des régions couvertes par des sédiments glaciaires ou alluviaux. Des travaux récents ont notamment montré que la signature de la magnétite (Dupuis et Beaudouin 2011; Dare *et al.* 2014; Nadoll *et al.* 2014), de la pyrite (Genna et Gaboury 2015; Duran *et al.* 2019), de la chalcopyrite (Caraballo *et al.* 2022) et de la scheelite (Miranda *et al.* in press) varie en fonction de son origine (e.g., magmatique, hydrothermale, ou type de gisement).

Les roches intrusives sont hôtes de divers types de minéralisations. Par exemple, les roches intrusives felsiques peuvent être associées à des minéralisations de type porphyre à Cu-Mo, des skarns à Sn, W, Pb ou Zn, des greisens à W-Sn, ou encore à des veines hydrothermales (Blevin et Chappell 1995; Bouzari *et al.* 2018; Li *et al.* 2018; Liu *et al.* 2020). Les intrusions mafiques sont plutôt hôtes de minéralisations en Fe-Ti-P, Fe-Ti-V, et Ni-Cu-EGP-Cr (Boudreau et Kruger 1990; Warner *et al.* 1998; Ma *et al.* 2003; Charlier *et al.* 2011; Chen *et al.* 2013). Dans ces intrusions, les processus

magmatiques (e.g., différenciation) ainsi que leur contrôle sur les éléments traces (e.g., coefficients de partage) sont connus et bien contraints. Dans ces intrusions, mafiques et felsiques, la composition des minéraux indicateurs renseigne non seulement sur le type de minéralisation, mais également sur le type de magma et son évolution.

Plusieurs études ont montré que l'apatite a un fort potentiel pour être utilisée en tant qu'indicateur pétrogénétique dans les intrusions mafiques (e.g., Tollari *et al.* 2008, Chen *et al.* 2013; Pedersen *et al.* 2021) et felsiques (e.g., Hsieh *et al.* 2008; Chu *et al.* 2009; Bruand *et al.* 2014; Qu *et al.* 2019), dont les gisements de type porphyre (e.g., Bouzari *et al.* 2018; Cao *et al.* 2023), ainsi que pour les études de provenance sédimentaire (e.g., O'Sullivan *et al.* 2020), et l'exploration minérale (e.g., discrimination de différents types de gisements; Mao *et al.* 2016; Zhou *et al.* 2023). Les sections suivantes illustrent l'état des connaissances sur l'apatite et son utilisation en tant que minéral indicateur. Cela permettra de souligner des lacunes que ce projet de doctorat a pour objectif de combler.

1.2 Structure de l'apatite et variations de sa chimie

L'apatite est un minéral accessoire commun dans la majorité des roches crustales (< 1% vol. ; Piccoli et Candela 2002 ; Webster et Piccoli 2015) et dans de nombreux types de gisements (e.g., porphyre, épithermal, skarn; Mao *et al.* 2016). L'apatite est un phosphate de calcium dont la composition est donnée par la formule générale suivante :

[1] $M_{10}(ZO_4)_6X_2$

où le site M (métal) est formé de 4 cellules unitaires M1 et 6 cellules unitaires M2, respectivement en coordination IX et VII, qui sont habituellement occupées par le calcium (Ca2+). Le site Z est occupé par le tétraèdre PO_4^{3-}, et le site X par des composés volatiles tels que OH-, F- et Cl- en proportions variables (Pan et Fleet 2002 ; Hughes et Rakovan 2015).

Le groupe de l'apatite recense plus de 29 espèces minérales, ce qui indique que de nombreux éléments peuvent se substituer au Ca, P et OH, F, Cl dans les sites M, Z et X respectivement (Pan et Fleet 2002). Les éléments qui peuvent théoriquement s'y substituer ont été suggérés en appliquant les règles de Goldschmidt (Figure 1.1) : 1) leur rayon ionique doit différer de moins de 15 %, mais la

substitution reste possible, bien que partielle, jusqu'à 30 % ; et 2) leur charge ionique doit être similaire. Toutefois, un élément de charge différente peut se substituer à un autre par le biais d'une substitution couplée, qui rétablit la balance des charges. Les éléments de terres rares (ETR) de valence 3+ peuvent par exemple se substituer au Ca^{2+} du site M selon les équations suivantes (Pan et Fleet 2002):

[2] $ETR^{3+} + OH^{2-} = Ca^{2+} + F^{-}$

[3] $ETR^{3+} + Na^{+} = 2Ca^{2+}$

[4] $ETR^{3+} + SiO_4^{4-} = Ca^{2+} + PO_4^{3-}$

Les techniques d'analyse actuelles montrent que l'apatite ignée peut incorporer au moins 65 éléments différents dans sa structure, et/ou sous forme de micro- ou nano-inclusions (Figure 1.1). En particulier, l'étude de Desormiers (2015) montre qu'il est possible de détecter au moins 34 éléments traces à l'aide du LA-ICP-MS dans les apatites magmatiques (carbonatites, nelsonites, anorthosites) et hydrothermales (*iron oxide-apatite* (IOA) : Durango) analysées.

De façon générale, la composition chimique et la texture (cathodoluminescence) des apatites est affectée par son environnement géologique de formation. Ainsi, sa signature est différente selon le type de roche hôte (Figure 1.2a; Belousova *et al.* 2002; O'Sullivan *et al.* 2020), et peut changer, de même que sa texture, suite à la circulation de fluides hydrothermaux (Harlov *et al.* 2005; Xing et Wang 2017). Dans le cas des granites, il semble y avoir des différences entre les apatites des granites de type I et S (Sha et Chappell 1999), et des granites de type I et A (Wang *et al.* 2018). La composition des apatites varie également selon le type de minéralisation (Figure 1.2b; Mao *et al.* 2016; Qiu *et al.* in press), et quelques exemples à l'échelle d'un district (e.g., porphyre, skarn) montrent que l'apatite peut aussi indiquer si elle provient d'une intrusion stérile, fertile ou minéralisée (e.g., Bouzari *et al.* 2018; Jia *et al.* 2020; Zafar *et al.* 2020).

La signature chimique de l'apatite peut aussi être modifiée au sein d'une même intrusion ou d'un gisement, pendant ou après sa cristallisation (Figure 1.3). Ces variations peuvent être causées par la différenciation magmatique et la cristallisation fractionnée de minéraux (Chen *et al.* 2013; Tollari *et al.* 2008; Zhang *et al.* 2020), ou des changements de la fugacité d'oxygène (She *et al.* 2016). Ainsi,

les variations chimiques de l'apatite entre différents types de roches et de gisements, mais aussi sein d'une même intrusion, suggèrent que ce minéral pourrait être utilisé comme minéral indicateur pour les études de provenance et l'exploration minérale, mais aussi en tant qu'indicateur pétrogénétique, au même titre que des minéraux comme le zircon, la magnétite, la pyrite, la chalcopyrite ou la scheelite.

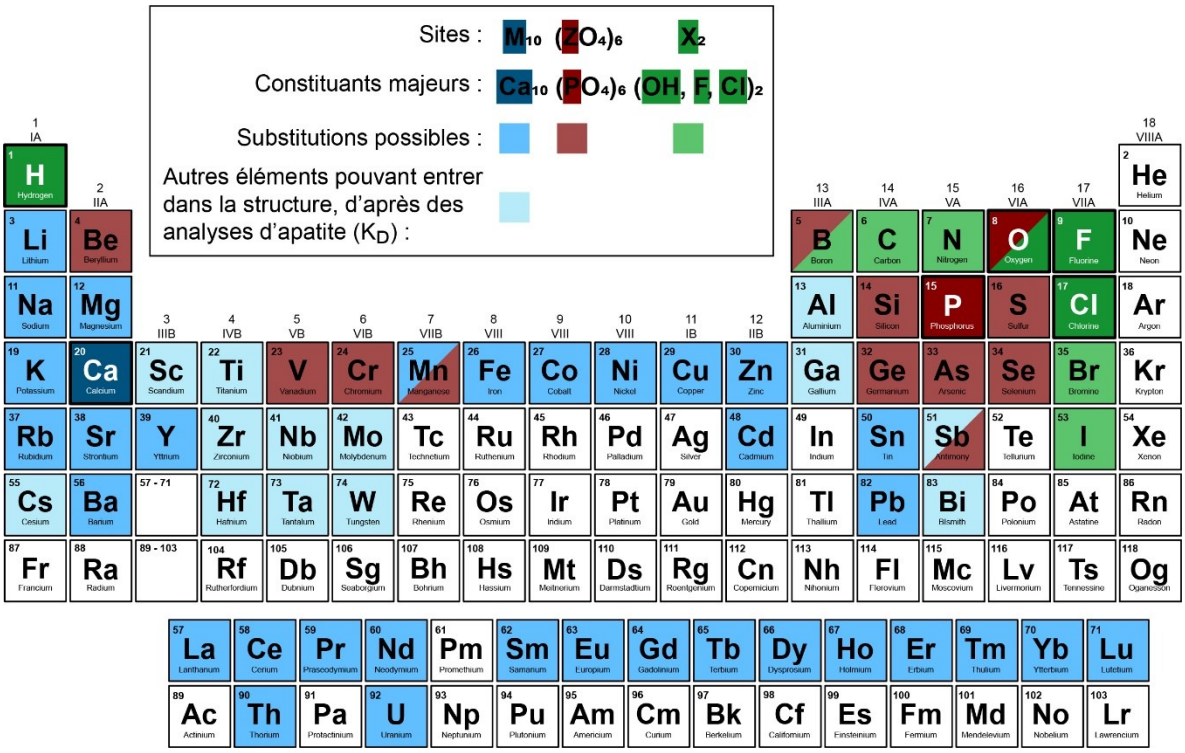

Figure 1.1 – Résumé des substitutions possibles pour chacun des sites de l'apatite provenant d'une grande diversité de roches, basé sur les règles de substitutions de Goldschmidt et une compilation d'analyses à la microsonde et LA-ICP-MS (Belousova *et al.* 2002 ; Piccoli et Candela 2002 ; Watts 2014 ; Desormiers 2015 ; Mao *et al.* 2016 ; She *et al.* 2016)

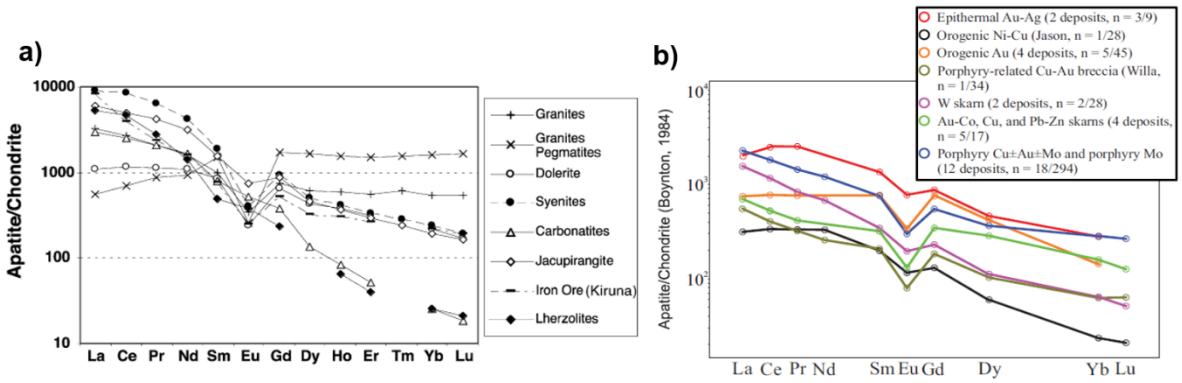

Figure 1.2 – a) Contenu en ETR d'apatites issues de différents types de roches (modifié d'après Belousova *et al.* 2002); b) Contenu en ETR d'apatites issues de différents types de gisements (modifié d'après Mao *et al.* 2016)

1.3 L'apatite en tant que minéral indicateur pour les études de provenance et l'exploration

L'apatite est résistante à l'altération dans l'environnement secondaire (O'Sullivan *et al.* 2020, et les références qui y figurent) et sensible à l'environnement géologique dans lequel elle se forme (Belousova *et al.* 2002; Abdullin *et al.* 2016; O'Sullivan *et al.* 2020). Ces caractéristiques font qu'elle est de plus en plus utilisée pour les études de provenance sédimentaire, où la signature des apatites détritiques permet d'identifier la roche hôte (Morton et Yaxley 2007; Hu *et al.* 2019; O'Sullivan *et al.* 2020). L'utilisation de l'apatite en tant que minéral indicateur pour l'exploration est également en développement. Les travaux de Mao *et al.* (2016) indiquent que la composition chimique de l'apatite varie selon les types de gisements. À l'échelle d'un district, il est également possible d'identifier la fertilité des intrusions felsiques associées à des porphyres ou des skarns (e.g., Azabakht *et al.* 2018; Bouzari *et al.* 2018; Qian *et al.* 2019; Gao *et al.* 2020; Zafar *et al.* 2020). L'exploration pour les gisements de type porphyre à partir de la présence d'apatite dans les sédiments glaciaires (Kelley *et al.* 2011), mais aussi de sa chimie (Rukhlov *et al.* 2016), ont donné des résultats concluants. Plus récemment, les travaux de Tan *et al.* (2023) et de Qiu *et al.* (in press), utilisant respectivement les statistiques multivariées et l'apprentissage automatique (*machine learning*) sur un large éventail de données, confirment qu'il est possible de séparer les apatites selon le type de gisement dusquel elles proviennent.

Il ressort de cette revue de littérature qu'aucun des travaux cités ci-dessus n'inclut les apatites des intrusions mafiques litées ni des massifs anorthositiques, qui peuvent pourtant être hôtes de minéralisations (Fe-Ti-P, Fe-Ti-V, Ni-Cu-EGP-Cr; Boudreau et Kruger 1990, Warner *et al.* 1998, Ma *et al.* 2003, Charlier *et al.* 2011; et Fe-Ti-P, Chen *et al.* 2013), que ce soit dans le cas des études de provenance sédimentaire ou pour l'exploration. De la même manière, bien que les granites puissent être classifiés en différents types (i.e., I, S et A) pouvant chacun être associé à des minéralisations différentes, les diagrammes de discrimination regroupent les granites en une seule catégorie (e.g., Belousova *et al.* 2002; Tan *et al.* 2023). Pourtant, des études individuelles sur les apatites des granites de type I, S et A montrent que leur composition est différente. La plupart des travaux existants se concentrent sur des apatites provenant de 2 types de granites à la fois (e.g., types I et S: Sha et Chappell 1999, Laurent *et al.* 2017; types I et A, Wang *et al.* 2018), seuls les travaux de Richard (2019) prenant en compte des apatites provenant des 3 types de granites. Or, ces derniers se concentrent sur une zone et un nombre d'éléments traces restreints. L'ensemble des diagrammes de discrimination actuellement proposés pourrait donc ne pas être applicable à une plus grande échelle et en utilisant un jeu de données global.

1.4 L'apatite en tant qu'indicateur pétrogénétique

Plusieurs processus intervenant pendant et après la cristallisation de l'apatite (syn-cristallisation et post-cumulus respectivement), puis durant la solidification de la roche (subsolidus), influencent le contenu en éléments traces de l'apatite dans les systèmes mafiques (Figure 1.3). Il est important de noter que dans les systèmes mafiques, le contenu en ETR des apatites reflète la composition du magma, car aucun minéral accessoire porteur d'ETR ne cristallise avant ou avec l'apatite (Charlier *et al.* 2005; Tollari *et al.* 2008). Dans les systèmes felsiques, la composition de l'apatite ne reflète probablement pas toujours celle du magma à cause de la compétition entre l'apatite et des minéraux accessoires porteurs d'ETR (e.g., Hine *et al.* 1978; Sha et Chappell 1999).

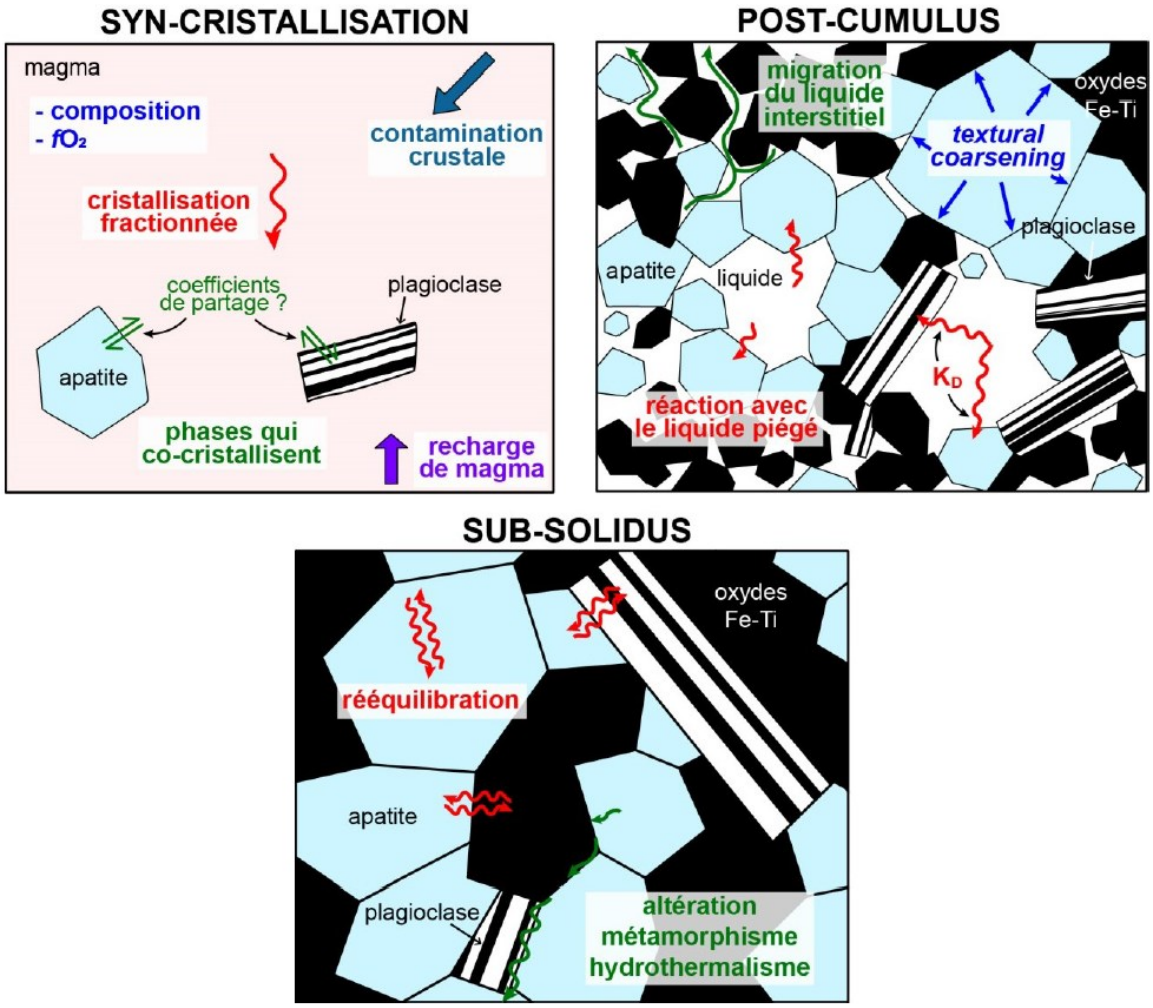

Figure 1.3 – Schémas conceptuels des différents processus influençant la chimie des apatites dans les systèmes ignés mafiques

Processus syn-cristallisation: la composition du magma a un impact majeur sur la chimie des apatites. Par exemple, un magma avec des concentrations élevées en ETR (e.g., magma felsique, polymérisé) résultera en une concentration élevée de ces éléments dans l'apatite (Figure 1.4). Les conditions d'oxydo-réduction (fO_2) du magma peuvent aussi influencer la répartition de certains éléments à plusieurs états d'oxydation dans l'apatite (Bromiley 2021). Dans un magma réduit, l'apatite qui cristallise présenterait une anomalie négative en Eu et positive en Ce, car elle accepte préférentiellement Eu^{2+} que Eu^{3+} (She *et al.* 2016), et Ce^{3+} que Ce^{4+} (Prowatke et Klemme 2006), dans sa structure cristalline. En revanche, l'apatite cristallisant à partir d'un magma oxydé contiendrait plus d'As et ou de Sb, car As^{5+} et Sb^{5+} sont compatibles dans l'apatite au détriment des formes

réduites, trivalentes (Maciag et Brenan 2020). Bien qu'initialement considéré comme indicateur de la fO_2 (Miles *et al.* 2014), l'augmentation de la concentration en Mn dans les apatites est plutôt liée au degré de polymérisation du magma (Stokes *et al.* 2019; Bromiley 2021). Il a aussi été montré que la cristallisation fractionnée a un impact majeur sur la chimie des apatites, puisqu'elle cause un enrichissement en ETR et certains éléments traces (e.g., Y, Na, Mn, Ba ou Pb) et parfois un appauvrissement en Sr (Belousova *et al.* 2002 ; Charlier *et al.* 2008 ; Cawthorn 2013 ; Xing *et al.* 2014 ; Zafar *et al.* 2020).

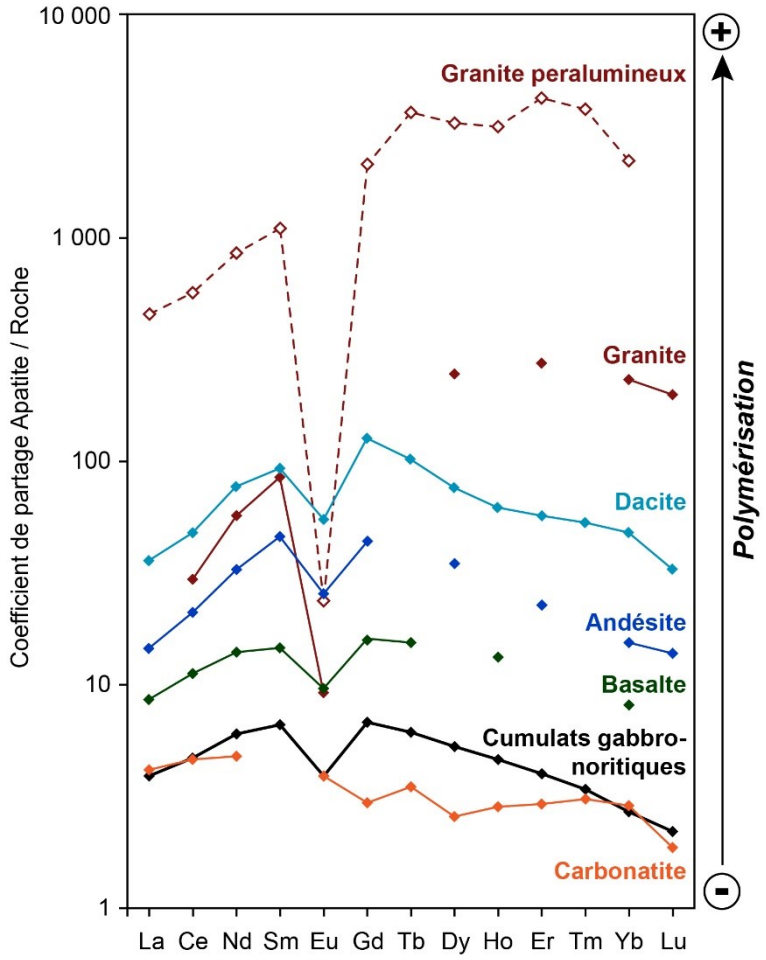

Figure 1.4 – Coefficients de partage pour les ETR entre l'apatite et différentes roches peu à très polymérisées (données compilées d'après la base de données des coefficients de partage GERM)

Les phases qui co-cristallisent avec l'apatite peuvent aussi impacter sa chimie, dépendamment de la compétition pour un élément entre les phases qui co-cristallisent. Ceci peut être illustré par les coefficients de partage (D) pour un élément entre les différents minéraux et le magma. Par exemple, la cristallisation d'un important volume de plagioclase avant ou pendant la cristallisation d'apatite diminuera la quantité de Eu et Sr qui pourrait être incorporée dans cette dernière (Belousova *et al.* 2002; Xing *et al.* 2014; She *et al.* 2016). La cristallisation de biotite et/ou l'amphibole enrichit les apatites en Cl, car ces minéraux incorporent du F au détriment du Cl (Boudreau et Kruger 1990; Meurer et Boudreau 1996). En revanche, la suppression de la cristallisation du plagioclase (enrichissement en Sr et Eu) et la cristallisation d'amphibole (appauvrissement en Y) dans des magmas hydratés en contexte d'arc conduit à une augmentation du ratio Sr/Y et à une diminution de l'anomalie négative en Eu dans les apatites (Nathwani *et al.* 2020; Zhou *et al.* 2022). Dans les granites, la cristallisation de minéraux enrichis en ETR légers (monazite, allanite, épidote, feldspaths potassiques) conduit à un appauvrissement des apatites en ETR légers (Chu et al. 2009), tandis que la cristallisation de titanite ou de zircon causera plutôt un appauvrissement en ETR lourds, Zr et Hf (Fujimaki 1986; Padilla et Gualda 2016). Le *timing* de cristallisation de l'apatite (e.g., avant ou pendant/après la cristallisation) de ces minéraux aura donc aussi un effet sur sa composition chimique. De même, les magmas granitiques cristallisent différents minéraux accessoires suivant leur composition (e.g., monazite dans les types S, Sha et Chappell 1999; titanite dans les types I, Chappell et White 1992), ce qui va influencer la signature des apatites.

Les paramètres qui régissent la chimie des apatites décrits ci-dessus pourraient être modifiés par une recharge de magma et/ou l'assimilation de roches encaissantes (e.g., contamination crustale), que cela soit dans les systèmes mafiques ou felsiques. Quelques études proposent qu'une recharge de magma affecterait le contenu en ETR et en volatiles des apatites (Miles *et al.* 2014; Xing *et al.* 2014; Zhang *et al.* 2020). La contamination crustale peut être tracée grâce à l'enrichissement de la roche en éléments incompatibles concentrés dans la croûte (e.g., La, Th, U, ou Pb; DePaolo 1981), ou via une augmentation du ratio $(^{87}Sr/^{86}Sr)_{initial}$ dans la roche ou les plagioclases (DePaolo et Wasserburg 1979). Dans les systèmes mafiques, une récente étude corrèle les isotopes du Sr dans les apatites avec la contamination crustale (Tang *et al.* 2023). En revanche, aucune étude ne corrèle

la chimie des apatites avec la contamination crustale, bien qu'elle incorpore ces éléments incompatibles (voir Figure 1.1).

Processus post-cumulus: dans les intrusions mafiques, ces processus interviennent lorsque l'apatite a cristallisé mais qu'il reste encore du liquide interstitiel, qui peut être piégé ou non (Figure 1.3). La composition de l'apatite peut être modifiée lorsqu'elle réagit avec le liquide piégé (*trapped liquid shift effect*; Cawthorn 1994). Plus la proportion de liquide est grande et celle d'apatite est faible (< 2%), plus la composition de l'apatite sera impactée (Cawthorn 1994, 2013). Le liquide interstitiel peut également migrer, par compaction ou dégazage durant la cristallisation. Ce processus n'est documenté que pour les éléments volatiles, Cl et OH étant plus mobiles que F (Boudreau et Kruger 1990). Ainsi, ces fluides peuvent former des apatites intercumulus riches en Cl vers la base de certaines intrusions mafiques, et moins riches en Cl à cause du dégazage vers leur sommet (e.g., Stillwater; Boudreau et McCallum 1989). Enfin, le processus de grossissement des grains (*textural coarsening*) vise à réduire l'énergie totale des cristaux grâce à la réaction des petits grains avec le liquide interstitiel pour former des grains plus grands (Higgins 2011). Bien que connu pour les plagioclases et les olivines (Higgins 2011), ce processus a aussi été suggéré pour des apatites (Grant 2020), mais son effet sur la chimie des apatites reste à ce jour inconnu.

Processus subsolidus: les processus subsolidus interviennent durant le refroidissement de la roche, qui peut être perturbé par un/des épisode(s) de métamorphisme (modification des conditions thermiques). Les travaux de Tacker et Stormer (1989) montrent que l'apatite est peu sensible à une rééquilibration par diffusion à basse température. Ceci est confirmé par des études plus récentes (Cherniak 2000, 2005; Cherniak *et al.* 1991; Cherniak et Ryerson 1993), qui montrent que la diffusion des éléments (ETR, Mn, Pb, Sr, volatiles) dans et hors de l'apatite ne peut se produire qu'à température moyenne/élevée (600 / 1000 °C ; Figure 1.5a) et que la rééquilibration des zonations est plus rapide dans les petits que dans les gros grains (Figure 1.5b). La diffusion de certains éléments, notamment He, peut aussi être influencée par le degré de dommages radioactifs causé à l'apatite par la désintégration de U-Th (Flowers *et al.* 2009; Chew et Spikings 2015). La rééquilibration des apatites peut donc se produire durant le refroidissement de la roche et/ou à la faveur d'événements thermiques (métamorphisme), mais à une température supérieure à 600 °C pour la plupart des

éléments, certains ayant une température plus basse (350-550 °C, Chew et Spikings 2015; Pb: 350 °C, Cochrane *et al.* 2014). Il est probable que, comme pour les oxydes de Fe-Ti (Frost *et al.* 1988), l'influence et l'importance de la rééquilibration dépende aussi de: 1) la nature des minéraux en contact avec l'apatite ; 2) leurs proportions respectives; et 3) la durée de refroidissement de l'intrusion. Bien que leurs effets soient peu documentés, les fluides métamorphiques et hydrothermaux peuvent aussi lessiver, respectivement, le Cl, Na, P et ETR légers (Warner et al. 1998), et les ETR (Xing et Wang 2017) le long de fractures et à la bordure des grains d'apatite, que cela soit dans les systèmes mafiques ou felsiques. L'altération de l'apatite par des fluides (magmatiques, hydrothermaux), contemporains ou non, forme également des textures de dissolution/reprécipitation identifiables via la cathodoluminescence (Xing et Wang 2017). Ces textures sont particulièrement intéressantes dans les systèmes porphyriques, car elles peuvent être indicatrices de minéralisation (Bouzari *et al.* 2016, 2018).

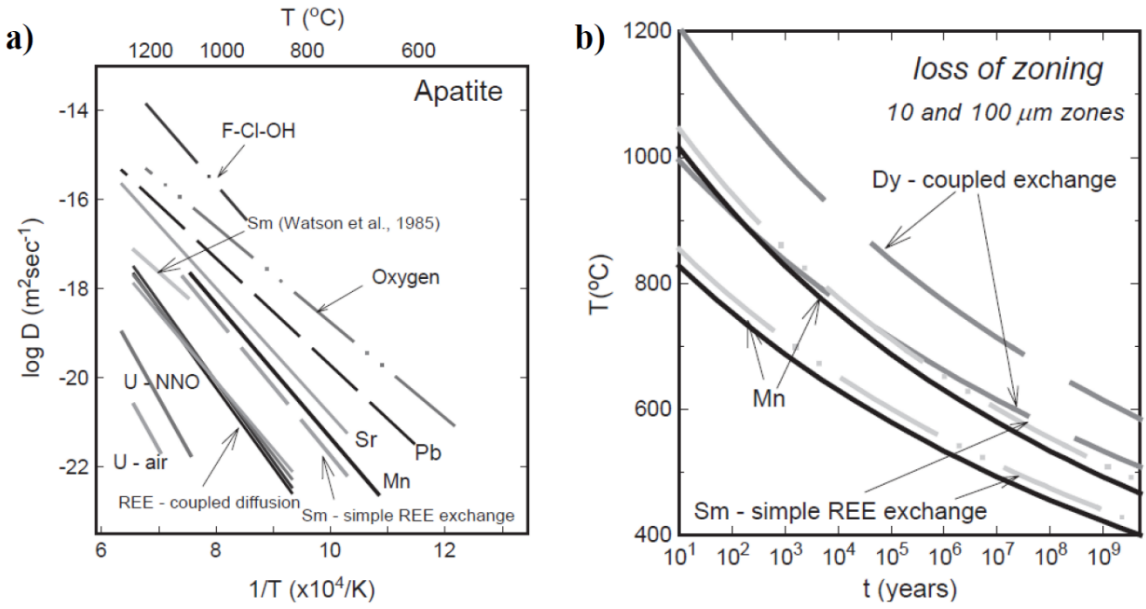

Figure 1.5 – a) résumé des données de diffusion pour des cations et anions dans l'apatite (Cherniak 2005); b) préservation des zonations en Mn et en ETR : ETR-ETR, sans compensation de charge (exemple du Sm); avec compensation de charge : $REE^{3+} + Si^{4+} \rightarrow Ca^{2+} + P^{5+}$ (exemple de Dy) (Cherniak 2005). Les courbes représentent les conditions temps-température maximales pour lesquelles les zonations sont préservées (au-dessus = perte des zonations). Pour chaque cas, les courbes les plus basses correspondent aux grains de 10 µm (hautes : 100 µm)

1.5 Problème et objectifs

La revue de la littérature a fait ressortir que les apatites présentent un fort potentiel pour être utilisées en tant qu'indicateur pétrogénétique et comme indicateur de provenance pour les études sédimentaires et l'exploration, mais que ce potentiel est sous-exploité pour les raisons suivantes:

- Il est nécessaire d'identifier et de comprendre les causes des variations chimiques de l'apatite avant de pouvoir l'utiliser comme indicateur pétrogénétique, puis pour les études de provenance et l'exploration minérale. Les intrusions mafiques litées représentent un laboratoire naturel pour comprendre ces variations, car leur organisation stratigraphique permet de contraindre les processus (e.g., degré de différenciation) étudiés, ce qui n'est pas le cas de massifs anorthositiques;
- Les apatites des intrusions mafiques ne sont pas intégrées dans les diagrammes de discrimination existants, bien que ces dernières puissent être hôtes de minéralisations;
- Dans les diagrammes de discrimination, les granites sont regroupés dans un champ distinct. Séparer les granites selon leur type, chacun associé à un type de minéralisation (e.g., type I et porphyres), permettrait d'améliorer les diagrammes pour les études de provenance et l'exploration minérale en milieu secondaire;
- Enfin, la plupart des études se concentrent sur un territoire ou un jeu de données restreint, ce qui ne permet pas de généraliser l'application des diagrammes.

Cette thèse se concentre donc sur le test des hypothèses générales suivantes : 1) la composition de l'apatite est influencée par les processus syn-cristallisation, et peut être modifiée par les processus post-cumulus et subsolidus; et 2) la signature de l'apatite varie selon le type de roche de laquelle elle provient. Les objectifs visant à tester ces hypothèses sont les suivants :

1) Dans une même intrusion mafique litée, où les processus magmatiques sont contraints, comprendre si et comment la composition de l'apatite est influencée par les processus syn-cristallisation, et si elle est modifiée par les processus post-cumulus et subsolidus.
    - Mesurer les variations de la concentration en éléments traces dans l'apatite en fonction de la hauteur stratigraphique, afin de voir si la différenciation l'impacte;

- Déterminer quels processus sont enregistrés par la composition des apatites;
- Déterminer si les apatites cumulus et intercumulus ont un contenu en éléments traces distinct;
- Déterminer si la signature des apatites provenant de zones minéralisées et Fe-Ti-P est différente de celles des portions non minéralisées.

2) Lier les variations chimiques des apatites de différentes intrusions mafiques litées à des processus magmatiques.
    - Caractériser la signature des apatites de plusieurs intrusions mafiques litées ayant des caractéristiques différentes (e.g., contamination crustale, *timing* de saturation en apatite, profondeur de fusion partielle du magma parent), grâce à de nouvelles analyses et une compilation de la littérature;
    - Déterminer l'impact de ces caractéristiques sur la composition des apatites (e.g., si la signature des apatites est modifiée, et/ou si elle reflète ces caractéristiques).
3) Identifier les apatites provenant de différents types de granites grâce à leur signature.
    - Compiler des analyses d'apatites de granites de type I, S et A;
    - Compléter cette compilation avec de nouvelles analyses d'apatites couvrant le spectre d'éléments traces;
    - Déterminer quels éléments permettent d'identifier les apatites de 3 types de granites, et établir des diagrammes de discrimination.
4) Discriminer différents types de roches et de gisements grâce à la signature des apatites.
    - Avec les toutes les analyses d'apatites utilisées précédemment, tester les diagrammes de discrimination existants;
    - Identifier les points forts et les lacunes de ces diagrammes afin de les améliorer et/ou d'en proposer de nouveaux;
    - Établir une suite de diagrammes permettant d'identifier les apatites provenant d'intrusions mafiques et de différents types de granites, afin d'améliorer l'utilisation de l'apatite en tant qu'indicateur pétrogénétique et comme indicateur de provenance pour les études sédimentaires et l'exploration.

Cette thèse veut s'intègre dans un contexte global, en apportant des informations sur la nature des roches dans le cas des études de provenance ou pour l'exploration à partir de grains d'apatite détritiques. Elle vise également à fournir un cadre pour l'étude d'intrusions où les silicates ne sont pas présents (e.g., minéralisation en Fe-Ti-P des massifs anorthositiques) ou trop altérés pour renseigner sur le degré d'évolution du magma ou la contamination crustale.

1.6 Méthodologie

Cette section présente une synthèse des méthodes utilisées pour investiguer les hypothèses mentionnées ci-dessus et atteindre les objectifs établis. Le détail des procédures analytiques est fourni dans les sections consacrées à la méthodologie de chaque contribution.

1.6.1 Choix de l'approche

Plusieurs approches peuvent être utilisées afin de répondre aux objectifs présentés ci-dessus : 1) une approche statistique, 2) une approche pétrogénétique, ou 3) une combinaison des deux approches précédentes. L'approche statistique consiste à corréler des éléments en fonction de classes définies d'apatites (e.g., de différents types de gisements) à partir d'un grand jeu de données. Chaque classe doit être représentée équitablement afin d'éviter les biais, et contenir la même suite d'éléments traces. Cette approche inclut notamment les statistiques multivariées (Mao *et al.* 2016; Tan *et al.* 2023) et l'apprentissage automatique (Qiu *et al.* in press). Bien que cette approche permette de faire ressortir des liens entre les classes et des éléments traces, les données ne sont pas facilement visualisables, l'interprétation des diagrammes n'est pas toujours intuitive, et les informations liées à chaque jeu de données sont sous-exploités (e.g., quels sont les liens entre des éléments qui covarient et des processus géologiques ?). Par contraste, l'approche pétrogénétique consiste à choisir des échantillons spécifiques, où l'interprétation des analyses d'apatite est supportée par d'autres informations tirées du contexte de chaque échantillon (e.g., minéralogie de l'échantillon). Dans ce cas, la visualisation des éléments traces sur un diagramme multiélément permet de mettre en évidence des combinaisons d'éléments clefs et de définir des ratios qui seront utilisés pour produire des diagrammes de discrimination binaires ou ternaires (e.g., Dare *et al.* 2014). La combinaison des approches statistiques et pétrogénétique serait idéale, comme montré par les travaux de Caraballo *et al.* (2022) sur la chalcopyrite.

Dans le cadre de cette thèse de doctorat, l'approche choisie est l'approche pétrogénétique pour les raisons suivantes : 1) cela permet d'étudier en détails les variations chimiques de l'apatite au sein d'une même intrusion; 2) cette approche permet de comparer visuellement les données et de faire des liens entre composition et processus; et 3) pour utiliser une approche statistique, il faudrait un jeu de données homogène pour chaque classe, ce qui n'est pas le cas dans la littérature (e.g., granites de type I suréchantillonnés par rapport à ceux de type S et A).

1.6.2 Choix des échantillons

La Suite Intrusive de Sept-Iles a été sélectionnée car il s'agit d'une intrusion mafique litée pour laquelle les processus magmatiques sont bien contraints par les travaux de Higgins (2005), Namur *et al.* (2010, 2011a, 2011b, 2012), et Charlier *et al.* (2011) et qui contient des apatites intercumulus et cumulus dans la totalité de la séquence. Le sommet de la partie mafique de l'intrusion contient un niveau minéralisé en Fe-Ti-P (Paiement *et al.* 2013) qui serait lié à un processus d'immiscibilité (Charlier *et al.* 2011; Namur *et al.* 2012), et est surmontée d'une partie felsique, représentant le produit final de la cristallisation fractionnée du magma parent ferrobasaltique (Namur *et al.* 2011a). La contamination crustale est négligeable et le métamorphisme absent. Cela permet de contraindre les variations chimiques qui pourraient être observées dans l'apatite et de les corréler à des processus magmatiques, telles que la différenciation, l'immiscibilité ou la recharge de magma. Les intrusions mafiques du Complexe du Bushveld et du Complexe Igné de Sudbury ont été sélectionnées car elles ont subi de la contamination crustale en proportion variable, ce qui devrait affecter la signature de l'apatite. Des analyses d'apatites provenant d'autres intrusions mafiques ont été compilées depuis la littérature afin d'agrandir le champ de variations (e.g., différents degrés de contamination crustale ou de saturation en apatite, profondeur de fusion partielle variable). Aucune des intrusions étudiées n'a été sujette au métamorphisme, à l'exception du Complexe Igné de Sudbury (faciès des schistes verts supérieur à amphibolite inférieur; Thomson *et al.* 1985). Des analyses d'apatites provenant de massifs anorthositiques ont également été compilées afin de vérifier la signature 'mafique' des apatites.

Les échantillons d'apatites provenant de granites ont été classés suivant la classification de Chappell et White (1974), basée sur l'environnement tectonique (granites de type I, S et A). Les

échantillons de granites couvrent donc les types I, S et A, à la fois via de nouvelles analyses et via une compilation de la littérature. Malgré le soin apporté au choix des échantillons dans la littérature, les apatites des granites de type I sont sur-représentées par rapport à celles des types S et A, et aucune analyse d'apatite de granite de type A peralcalin n'a été trouvée. Cela est dû à l'intérêt porté aux granites de type I, qui est hôte de minéralisations de type porphyre, au détriment des granites de type S et A qui sont moins échantillonnés. Cette dichotomie est également observée dans la compilation d'analyses de la littérature. Celle-ci recense la grande majorité des publications disponibles contenant des analyses d'apatites provenant de granites de type I, S et A, et constitue la base de données la plus complète à notre connaissance.

1.6.3 Étude pétrographique

La description pétrographique générale de la majorité des échantillons a été publiée dans des études antérieures. L'analyse pétrographique au microscope optique a permis d'identifier les apatites (phase intercumulus ou cumulus), leur taille et leur proportion. Les observations ont également permis d'identifier les autres phases minéralogiques, dont les phases accessoires (e.g., zircon, titanite). Elles ont permis de sélectionner les grains qui ont été analysés à la microsonde et au LA-ICP-MS.

1.6.4 Cathodoluminescence

La cathodoluminescence utilisée à l'UQAC a permis de vérifier l'absence de zonations dans les grains d'apatite, ainsi que les grains n'ont pas été altérés par des fluides. La présence de zonations pourrait indiquer une réaction de l'apatite avec le liquide piégé, comme discuté au chapitre 2.

1.6.5 Éléments majeurs et volatiles: microsonde électronique

Les éléments majeurs (Ca, P) et les éléments volatiles (F, Cl) ont été déterminés à la microsonde électronique du Laboratoire de Microanalyse de l'Université Laval (Québec, Canada) à l'aide d'un micro-analyseur à électron Cameca SX1000 couplé à 5 spectromètres à dispersion de longueur d'onde (WDS). Le F peut migrer lors des analyses, et ainsi causer une fausse mesure de sa concentration (Stormer *et al.* 1993). Les conditions analytiques ont donc été optimisées afin de limiter cette migration tout en assurant une détermination correcte de F, Cl et Ca. Suivant ce nouveau protocole, les analyses ont été réalisées à 15 kV, avec un courant de faisceau de 10 nA et un faisceau défocalisé de 10 µm.

1.6.6 Éléments traces: LA-ICP-MS

Une suite de 31 éléments traces (ETR+Y, Pb, Rb, K, Ba, Sr, Na, Th, U, Mn, Mg, Zr, Sc, Nb, Ti, V et As) a été déterminée dans les apatites (et dans certains cas, dans des plagioclases) par ablation laser et spectrométrie de masse (LA-ICP-MS) au LabMaTer (UQAC), en utilisant un laser Excimer 193 nm Resonetics Resolution M-50 couplé à un spectromètre de masse Agilent 7900. Des lignes ont été ablatées depuis le cœur vers la bordure des grains avec un faisceau variant entre 15 et 55 µm, selon la taille des grains, une fréquence laser de 15 Hz, une puissance de 5 J/cm^2 et une vitesse de déplacement de 10 µm/s, afin d'évaluer la présence de zonations chimiques. La calibration a été réalisée avec le matériel de référence certifié NIST610 tandis que les matériaux de référence secondaires NIST612, GSD et UQAC-APA ont été utilisés pour monitorer la qualité des données. Le Ca, préalablement déterminé à la microsonde, est utilisé comme standard interne pour la quantification des résultats pour les apatites. La réduction des données a été faite en utilisant le logiciel Iolite (Paton *et al.* 2011). Les résultats obtenus ont été représentés sur un diagramme multi-élément spécialement conçu pour l'apatite, où les éléments sont ordonnés selon leur compatibilité (les détails sont rapportés au chapitre 2). En permettant de visualiser l'ensemble des données, ce diagramme aide à identifier les éléments clefs et les ratios à l'origine des interprétations et des diagrammes de discrimination proposés.

1.6.7 Isotopes du Sr: LA-MC-ICP-MS

Les analyses *in situ* des isotopes du Sr ont été réalisées au Laboratoire Norvégien pour la Caractérisation des Minéraux et Matériaux (MiMaC), à la Commission Géologique de Norvège (NGU). Le matériel utilisé est un Photon Machine Analyte excite, couplé avec un laser Excimer 193 nm et 3 collecteurs Nu Plasma (LA-MC-ICP-MS). Les détails du protocole analytique sont fournis au chapitre 3.

1.7 Format de la thèse

Cette thèse de doctorat en Sciences de la Terre et de l'Atmosphère est organisée sous forme d'un recueil de trois articles de recherche qui sont publiés, acceptés ou soumis (en cours de revue) à des journaux internationaux au moment de la soumission finale. Chaque article, rédigé en anglais, est inséré dans la thèse sous la forme d'un chapitre distinct.

Le premier article a été publié dans la revue *Geochimica et Cosmochimica Acta* en février 2023. Il s'insitule '*The use of trace elements in apatite to trace differentiation of a ferrobasaltic melt in the Sept-Iles Intrusive Suite, Quebec, Canada: Implications for provenance discrimination*' et constitue le chapitre 2 de la thèse. L'article étudie les variations chimiques de l'apatite cumulus et intercumulus dans la MCU II de l'intrusion mafique litée de Sept-Iles, et les compare avec la composition des apatites de la partie felsique de l'intrusion. Cette étude montre que la composition des apatites cumulus suit la *liquid line of descent* définie pour Sept-Iles et enregistre la cristallisation fractionnée. Elle permet de confirmer que la formation des niveaux riches et pauvres en oxydes de Fe-Ti et apatite est due à des épisodes répétés d'immiscibilité. Les travaux proposent également des diagrammes de discrimination afin d'identifier les apatites de la partie felsique et de celles de la partie mafique, qui peuvent cristalliser en phase cumulus ou intercumulus avec une signature chimique distincte, ce qui participe au développement de l'apatite en tant que minéral indicateur pour l'exploration.

Le deuxième article a été accepté pour publication dans la revue *Journal of Petrology* en juillet 2023, sous réserve de révisions. La version intégrée dans la thèse correspond au manuscrit révisé. Il s'intitule '*Apatite chemistry as a petrogenetic indicator for mafic layered intrusions*' et constitue le chapitre 3 de la thèse. Le manuscrit compare la composition chimique d'apatites provenant de différentes intrusions mafiques litées afin de démontrer la fiabilité de l'apatite en tant qu'indicateur pétrogénétique. Les travaux établissent que la signature de l'apatite permet de tracer les processus de contamination crustale et de recharge de magma, ainsi que la profondeur de fusion partielle du magma parent. Le manuscrit montre également que les conclusions établies dans l'article présenté au chapitre 2 sont généralisables aux autres intrusions mafiques litées.

Le manuscrit du troisième article a été soumis à la revue *Chemical Geology* le 19 septembre 2023. Il s'intitule '*Discrimination of apatite from I-, S- and A-type granites using trace elements: implications for mineral exploration and provenance studies'* et correspond au chapitre 4 de la thèse. Ce manuscrit établit un schéma pour identifier la signature des apatites des granites de type I, S et A de celle d'autres types de roches grâce à de nouveaux diagrammes de discrimination. Les diagrammes proposés permettent d'identifier la roche source des apatites dans un environnement secondaire non

exploré, pouvant couvert de sédiments glaciaires ou alluviaux, et fournissent donc outil supplémentaire pour l'évaluation de la prospectivité d'un territoire.

Le chapitre 5 consiste en une synthèse des principales découvertes présentées dans la thèse, ayant permis de développer l'apatite en tant qu'indicateur pétrogénétique et comme minéral indicateur pour les études de provenance et l'exploration.

1.8 Déclaration de contribution originale

Chaque manuscrit a été soumis à des revues spécialisées pour publication originale. Les données présentées dans les 3 manuscrits ont été acquises durant ce projet et ont été supplémentées par une compilation d'analyses d'apatites de la littérature, réalisée durant ce projet.

Les apatites cumulus de la MCU II de la Suite Intrusive de Sept-Iles (Zone Critique, minéralisée en Fe-Ti-P) ont été précédemment étudiées par Nabil (2003) et Tollari *et al.* (2008). En revanche, cette thèse de doctorat est la première étude des apatites dans l'intégralité de la Suite Intrusive de Sept-Iles. À notre connaissance, il s'agit de la première étude synthétisant et comparant les signatures chimiques d'apatites provenant de 7 intrusions mafiques litées différentes, et n'étant pas exclusivement centrée sur les éléments volatiles. Il s'agit également de la première étude analysant et compilant un grand nombre d'analyses d'apatites de différents types de granites pour proposer un schéma de discrimination complet, étant basé sur une approche pétrogénétique plutôt que statistique.

1.9 Contribution des co-auteurs

L'auteure de cette thèse est le l'auteure principale de chacun des trois articles/manuscrits constituant les chapitres 2, 3 et 4. Pour chaque contribution, l'auteure principale est responsable de la collecte des données (analyses en laboratoire), de leur interprétation, de la production des figures et de la rédaction.

Sarah A.S. Dare a initialisé l'idée originale et a supervisé cette thèse, prodiguant conseils, enseignement et support tout au long de sa réalisation, et a apporté le financement de cette étude doctorale. Elle a révisé chacun des manuscrits et a contribué à les améliorer avant leur soumission.

Olivier Namur a fourni les lames minces de la Suite Intrusive de Sept-Iles, et a contribué aux réflexions ayant mené à l'aboutissement des contributions présentées aux chapitres 2 et 3, ainsi qu'à leur révision et à leur amélioration avant soumission.

Eduardo T. Mansur a réalisé les analyses des isotopes du Sr utilisées dans le chapitre 3. Il a traité les données et rédigé la partie de la section méthodologie correspondante. Il a également contribué à la révision et à l'amélioration du manuscrit avant sa soumission.

Marylou Gendron a sélectionné des apatites sur 16 lames minces de granites de type I, S, et A et les a préparées pour les analyses à la microsonde électronique, puis au LA-ICP-MS par Marie A. Kieffer, et a contribué au traitement, à la visualisation et à une interprétation préliminaire des données. Elle a été co-supervisée par Sarah A.S. Dare et Marie A. Kieffer pour son projet de fin d'études au baccalauréat à la session d'hiver 2021, intitulé 'Les éléments traces dans l'apatite des granites de type I, S et A: implications pour l'exploration minérale' (44p.). Les données ont été incorporées dans le chapitre 4.

1.10 Communications (conférences)

Le Tableau 1.1 ci-dessous résume les communications réalisées sous forme d'affiches et/ou de présentations orales lors de conférences nationales et internationales. L'ensemble des résumés est présenté en annexe. Le Tableau 1.2 résume les distinctions obtenues lors de la thèse.

Table 1.1 – Résumé des participations aux conférences et congrès

Date	Congrès	Type de communication	Résumé
2021			
8-11 mars	PDAC-SEG Student Mineral Colloquium (Toronto, Canada)	Affiche + présentation orale (virtuel)[1]	Annexe 1
4-9 juillet	Goldschmidt (Lyon, France)	Présentation orale (virtuel)	Annexe 2
2022			
28-31 mars	16th biennial meeting SGA 2022 (Rotorua, Nouvelle-Zélande)	Présentation orale (virtuel)	Annexe 3
11-16 juillet	Wager & Brown Layered Intrusions Workshop III (Sept-Iles, Canada)	Présentation orale (présentiel)	–
21-24 novembre	Québec Mines+Énergie 2022, Défi de la recherche en géosciences (Québec, Canada)	Affiche + présentation orale (présentiel)[2]	Annexe 4
2023			
24-27 mai	GAC-MAC Sudbury 2023 (Sudbury, Canada)	Présentation orale, délivrée par Sarah Dare	Annexe 5
30 juin-2 juillet	Wager & Brown Layered Intrusions Workshop IV (Cardiff, Royaume-Uni)	Présentation orale (présentiel)	Annexe 6
4-7 juin	14th International Platinum Symposium (Cardiff, Royaume-Uni)	Affiche (présentiel)[3] Présentation orale (présentiel)[3]	Annexe 7 Annexe 8
20-23 novembre	Québec Mines+Énergie 2023, Défi de la recherche en géosciences (Québec, Canada)	Affiche + présentation orale (présentiel)[4]	Annexe 9

[1] obtention du 3ème prix au doctorat; [2] obtention du 1er prix au doctorat; [3] obtention du 1er prix au doctorat; [4] obtention du 2ème prix au doctorat

Table 1.2 – Résumé des distinctions et bourses obtenues lors de la thèse de doctorat

Année	Distinction	Montant
2021	3ème prix au doctorat (affiche et présentation orale) au PDAC-SEG Student Mineral Colloquium (Toronto, Canada)	300 $
	Inscription au Tableau d'honneur de l'UQAC 2020-2021	–
	Bourse d'Excellence Denis W. Roy (UQAC)	8 000 $
	Une des 4 finalistes pour l'obtention de la médaille du Gouverneur général du Canada (or), décernée par l'Université du Québec à Chicoutimi	–
2022	Bourse d'excellence du Fonds de la Fonds de Recherche du Québec – Nature and Technologies, Programme de Bourses d'Excellence pour Étudiants Étrangers (PBEEE), bourse 319772	16 667 $
	1er prix au doctorat (affiche et présentation orale) au Défi de la recherche en géosciences lors du congrès Québec Mines+Énergie 2022, (Québec, Canada)	2 000 $
2023	Inscription au Tableau d'honneur de l'UQAC 2022-2023	–
	Une des 4 finalistes pour l'obtention de la médaille du Gouverneur général du Canada (or), décernée par l'Université du Québec à Chicoutimi	–
	1er prix au doctorat (affiche et présentation orale) au 14th International Platinum Symposium (Cardiff, Royaume-Uni)	200 £
	Bourse de voyage de l'Association minéralogique du Canada, pour participer au 14th International Platinum Symposium (Cardiff, Royaume-Uni)	1 000 $
	2ème prix au doctorat (affiche et présentation orale) au Défi de la recherche en géosciences lors du congrès Québec Mines+Énergie 2023, (Québec, Canada)	700 $

Références

Abdullin, F., Solé, J., Solari, L., Shchepetilnikova, V., Meneses-Rocha, J.J., Pavlinova, N., et Rodríguez-Trejo, A. 2016. Single-grain apatite geochemistry of Permian–Triassic granitoids and Mesozoic and Eocene sandstones from Chiapas, southeast Mexico: implications for sediment provenance. International Geology Review **58**(9): 1132-1157. doi: 10.1080/00206814.2016.1150212.

Arai, S., Kadoshima, K., et Morishita, T. 2006. Widespread arc-related melting in the mantle section of the northern Oman ophiolite as inferred from detrital chromian spinels. Journal of the Geological Societey, London **163**: 869-879. doi: 10.1144/0016-76492005-057.

Azadbakht, Z., Lentz, D.R., et McFarlane, C.R.M. 2018. Apatite Chemical Compositions from Acadian-Related Granitoids of New Brunswick, Canada: Implications for Petrogenesis and Metallogenesis. Minerals **8**: 598. doi: 10.3390/min8120598.

Barnes, S.-J., Mansur, E.T., Maier, W.D., et Prevec, S.A. 2022. A comparison of trace element concentrations in chromite from komatiites, picrites, and layered intrusions: implications for the formation of massive chromite layers. Canadian Journal of Earth Sciences **60**(2): 97-132. doi: 10.1139/cjes-2022-0064.

Belousova, E.A., Griffin, W.L., O'Reilly, S.Y., et Fischer, N.I. 2002. Apatite as an indicator mineral for mineral exploration: trace-element compositions and their relationship to host rock type. Journal of Geochemical Exploration **76**: 45-69. doi: 10.1016/S0375-6742(02)00204-2.

Blevin, P.L., et Chappell, B.W. 1995. Chemistry, Origin, and Evolution of Mineralized Granites in the Lachlan Fold Belt, Australia: The Metallogeny of I- and S-Type Granites. Economic Geology **90**: 1604-1619. doi: 10.2113/gsecongeo.90.6.1604.

Boudreau, A.E., et Kruger, F.J. 1990. Variation in the Composition of Apatite through the Merensky Cyclic Unit in the Western Bushveld Complex. Economic Geology **85**: 737-745. doi: 10.2113/gsecongeo.85.4.737.

Boudreau, A.F., et McCallum, I.S. 1989. Investigations of the Stillwater Complex: Part V. Apatites as indicators of evolving fluid composition. Contributions to Mineralogy and Petrology **102**: 138-153.

Bouzari, F., Hart, C.J.R., Bissig, T., et Barker, S. 2016. Hydrothermal Alteration Revealed by Apatite Luminescence and Chemistry: A Potential Indicator Mineral for Exploring Covered Porphyry Copper Deposits. Economic Geology **111**: 1397-1410. doi: 10.2113/econgeo.111.6.1397.

Bouzari, F., Hart, C.J.R., Bissig, T., et Lesage, G. 2018. Mineralogical and Geochemical Characteristics of Porphyry-Fertile Plutons: Guichon Creek, Takomkane and Granite Mountain Batholiths, south-central British Columbia (NTS 092I, P, 093A, B). Geoscience BC Report 2018-17 **412**: 36p.

Bromiley, G.D. 2021. Do concentrations of Mn, Eu and Ce in apatite reliably record oxygen fugacity in magmas ? Lithos **384-385**: 105900. doi: 10.1016/j.lithos.2020.105900.

Bruand, E., Storey, C.D., et Fowler, M. 2016. Accessory Mineral Chemistry of High Ba-Sr Granites from Northern Scotland: Constraints on Petrogenesis and Records of Whole-rock Signature. Journal of Petrology **55**(8): 1619-1651. doi: 10.1093/petrology/egu037.

Cao, C., Wu, S., Shen, P., Wang, S., Guo, Z., Xiu, D., Li, C., et Feng, H. 2023. Geochemical characteristics of apatite and amphibole within the granitic intrusions from the Suyunhe Mo deposit, Xinjiang province, NW China: Insights into petrogenesis and mineralization potential. Ore Geology Reviews **152**: 105232. doi: 10.1016/j.oregeorev.2022.105232.

Caraballo, E., Dare, S.A.S., et Beaudouin, G. 2022. Variation of trace elements in chalcopyrite from worldwide Ni-Cu sulfide and Reef-type PGE deposits: implications for mineral exploration. Mineralium Deposita **57**(8): 1-29. doi: 10.1007/s00126-021-01091-y.

Cawthorn, R.G. 1994. Formation of chlor- and fluor-apatite in layered intrusions. Mineralogical Magazine **58**: 299-306. doi: 10.1180/minmag.1994.058.391.12.

Cawthorn, R.G. 2013. Rare earth element abundances in apatite in the Bushveld Complex—A consequence of the trapped liquid shift effect. Geology **41**(5): 603-606. doi: 10.1130/G34026.1.

Chappell, B.W., et White, A.J.R. 1974. Two Contrasting Granite Types. Pacific Geology **8**: 173-174.

Chappell, B.W., et White, A.J.R. 1992. I- and S-type granites in the Lachlan Fold Belt. Transactions of the Royal Society of Edinburgh: Earth Sciences **83**: 1-26. doi: 10.1017/S0263593300007720.

Charlier, B., Vander Auwera, J., et Duchesne, J.-C. 2005. Geochemistry of cumulates from the Bjerkreim–Sokndal layered intrusion (S. Norway) Part II. REE and the trapped liquid fraction. Lithos **83**: 255-276. doi: 10.1016/j.lithos.2005.03.005.

Charlier, B., Sakoma, E., Sauvé, M., Stanaway, K., Vander Auwera, J., et Duchesne, J.-C. 2008. The Grader layered intrusion (Havre-Saint-Pierre Anorthosite, Quebec) and genesis of nelsonite and other Fe–Ti–P ores. Lithos **101**(3-4): 359-378. doi: 10.1016/j.lithos.2007.08.004.

Charlier, B., Namur, O., Toplis, M.J., Schiano, P., Cluzel, N., Higgins, M.D., et Auwera, J.V. 2011. Large-scale silicate liquid immiscibility during differentiation of tholeiitic basalt to granite and the origin of the Daly gap. Geology **39**(10): 907-910. doi: 10.1130/g32091.1.

Chen, W.T., Zhou, M.-F., et Zhao, T.-P. 2013. Differentiation of nelsonitic magmas in the formation of the ~1.74 Ga Damiao Fe–Ti–P ore deposit, North China. Contributions to Mineralogy and Petrology **165**(6): 1341-1362. doi: 10.1007/s00410-013-0861-x.

Cherniak, D.J. 2000. Rare earth element diffusion in apatite. Geochemica et Cosmochemica Acta **64**(22): 3871-3885. doi: 10.1016/S0016-7037(00)00467-1.

Cherniak, D.J. 2005. Uranium and manganese diffusion in apatite. Chemical Geology **219**(1-4): 297-308. doi: 10.1016/j.chemgeo.2005.02.014.

Cherniak, D.J., Lanford, W.A., et Ryerson, F.J. 1991. Lead diffusion in apatite and zircon using ion implantatio and Rutherford Backscattering techniques. Geochemica et Cosmochemica Acta **55**: 1663-1673. doi: 10.1016/0016-7037(91)90137-T.

Cherniak, D.J., et Ryerson, F.J. 1993. A study of strontium diffusion in apatite using Rutherford backscattering spectroscopy and ion implantation. Geochemica et Cosmochemica Acta **57**: 4653-4662. doi: 10.1016/0016-7037(93)90190-8.

Chew, D., M., et Spikings, R.A. 2015. Geochronology and thermochronology using apatite: time and temperature, lower crust to surface. Elements **11**(3): 189-194. doi: 10.2113/gselements.11.3.189.

Chu, M.-F., Wang, K.-L., Griffin, W.L., Chung, S.-L., O'Reilly, S.Y., Pearson, N.J., et Iizuka, Y. 2009. Apatite Composition: Tracing Petrogenetic Processes in Transhimalayan Granitoids. Journal of Petrology **50**(10): 1829-1855. doi: 10.1093/petrology/egp054.

Cochrane, R., Spinkings, R.A., Chew, D., Wotzlaw, J.-F., Chiaradia, M., Tyrrell, S., Schaltegger, U., et Van der Lelij, R. 2014. High temperature (> 350 °C) thermochronology and mechanisms of Pb loss in apatite. Geochimica et Corsmochimica Acta **127**: 39-56. https://doi.org/10.1016/j.gca.2013.11.028.

Dare, S.A.S., Barnes, S.-J., Beaudoin, G., Méric, J., Boutroy, E., et Potvin-Doucet, C. 2014. Trace elements in magnetite as petrogenetic indicators. Mineralium Deposita **49**(7): 785-796. doi: 10.1007/s00126-014-0529-0.

DePaolo, D.J. 1981. Trace element and isotopic effects of combined wallrock assimilation and fractional crystallization. Earth and Planetary Science Letters **53**: 189-202. doi: 10.1016/0012-821X(81)90153-9.

DePaolo, D.J., et Wasserburg, G.J. 1979. Petrogenetic mixing models and Nd^Sr isotopic patterns. Geochimica et Cosmichimica Acta **43**: 615-625. doi: 10.1016/0016-7037(79)90169-8.

Desormiers, M. 2015. In-situ determination of volatile and trace elements in apatite [Ca5(PO4)3(F, Cl, OH)] from Fe-Ti-P deposits by electron microprobe and laser ablation ICP-MS. Mémoire de maîtrise en sciences de la Terre, University of Ottawa, Ottawa, Ontario, 40p.

Dupuis, C., et Beaudoin, G. 2011. Discriminant diagrams for iron oxide trace element fingerprinting of mineral deposit types. Mineralium Deposita **46**(4): 319-335. doi: 10.1007/s00126-011-0334-y.

Duran, C.J., Dubé-Loubert, H., Pagé, P., Barnes, S.-J., Roy, M., Savard, D., Cave, B.J., Arguin, J.-P., et Mansur, E.T. 2019. Applications of trace element chemistry of pyrite and chalcopyrite in glacial sediments to mineral exploration targeting: Example from the Churchill Province, northern Quebec, Canada. Journal of Geochemical Exploration **196**: 105-130. doi: 10.106/j.gexplo.2018.10.006.

Flowers, R.M., Ketcham, R.A., Shuster, D.L., et Farley, K.A. 2009. Apatite (U–Th)/He thermochronometry using a radiation damage accumulation and annealing model. Geochimica et Cosmochimica Acta **73**(8): 2347-2365. doi: 10.1016/j.gca.2009.01.015.

Frost, B.R., Lindsley, D.H., et Andersen, D.J. 1988. Fe-Ti oxide-silicate equilibria: Assemblages with fayalitic olivine. American Mineralogist **73**: 727-740.

Fujimaki, H. 1986. Partition coefficients of Hf, Zr, and REE between zircon, apatite, and liquid. Contributions to Mineralogy and Petrology **94**: 42-45. doi: 10.1007/BF00371224.

Gao, X., Yang, L., Wang, C., He, W., Bao, X., et Zhang, S. 2020. Halogens and trace elements of apatite from Late Mesozoic and Cenozoic porphyry Cu-Mo-Au deposits in SE Tibet, China: Constraints on magmatic fertility and granitoid petrogenesis. Journal of Asian Earth Sciences **203**: 104552. doi: 10.1016/j.jseaes.2020.104552.

Gendron, M. 2021. Les éléments traces dans l'apatite des granites de type I, S et A : implication pour l'exploration minérale, Université du Québec à Chicoutimi, Chicoutimi, Quebec, 44p.

Genna, D., et Gaboury, D. 2015. Deciphering the Hydrothermal Evolution of a VMS System by LA-ICP-MS Using Trace Elements in Pyrite: An Example from the Bracemac-McLeod Deposits, Abitibi, Canada, and Implications for Exploration. Economic Geology **110**: 2087-2108. doi: 10.2113/econgeo.110.8.2087.

Grant, M. 2020. Formation of magmatic Fe-Ti-V-P deposits within the Lac St. Jean area Saguenay, Québec, Canada: Insights from trace element composition of Fe-oxides and apatite, Department of Earth Sciences, University of Ottawa, Ottawa, 359p.

Harlov, D.E., Richard, W., et F., H.-J. 2005. An experimental study of dissolution-reprecipitation in fluorapatite: fluid infiltration and the formation of monazite. Contributions to Mineralogy and Petrology **150**(3): 268-286. doi: 10.1007/s00410-005-0017-8.

Henrique-Pinto, R., Janasi, V.A., Vasconcellos, A.C.B.C., Sawyer, E.W., Barnes, S.J., Basei, M.A.S., et Tassinari, C.C.G. 2015. Zircon provenance in meta-sandstones of the São Roque Domain: Implications for the Proterozoic evolution of the Ribeira Belt, SE Brazil. Precambrian Research **256**: 271-288. doi: 10.1016/j.precamres.2014.11.014.

Higgins, M.D. 2005. A new interpretation of the structure of the Sept Iles Intrusive suite, Canada. Lithos **83**(3-4): 199-213. doi: 10.1016/j.lithos.2005.03.002.

Higgins, M.D. 2011. Textural coarsening in igneous rocks. International Geology Review **53**(3-4): 354-376. doi: 10.1080/00206814.2010.496177.

Hine, E., Williams, I.S., Chappell, B.W., et White, A.J.R. 1978. Contrasts between I- and S-type granitoids of the Kosciusko Batholith. Journal of the Geological Society of Australia **25**: 219-234. doi: 10.1080/00167617808729029.

Hsieh, P.-S., Chen, C.-H., Yang, H.-J., et Lee, C.-Y. 2008. Petrogenesis of the Nanling Mountains granites from South China: Constraints from systematic apatite geochemistry and whole-rock geochemical and Sr–Nd isotope compositions. Journal of Asian Earth Sciences **33**: 428-451. doi: 10.1016/j.jseaes.2008.02.002.

Hu, S., Zeng, Z., Fang, X., Qi, H., Yin, X., Chen, Z., Li, X., et Zhu, B. 2019. Geochemical Study of Detrital Apatite in Sediment from the Southern Okinawa Trough: New Insights into Sediment Provenance. Minerals **9**(10). doi: 10.3390/min9100619.

Hughes, J.M., et Rakovan, J.F. 2015. Structurally Robust, Chemically Diverse: Apatite and Apatite Supergroup Minerals. Elements **11**(3): 165-170. doi: 10.2113/gselements.11.3.165.

Jia, F., Zhang, C., Liu, H., Meng, X., et Kong, Z. 2020. In situ major and trace element compositions of apatite from the Yangla skarn Cu deposit, southwest China: Implications for petrogenesis and mineralization. Ore Geology Reviews **127**: 103360. doi: 10.1016/j.oregeorev.2020.103360.

Kelley, K.D., Eppinger, R.G., Lang, J., Smith, M.D., et Fey, D.L. 2011. Porphyry Cu indicator minerals in till as an exploration tool: example from the giant Pebble porphyry Cu-Au-Mo deposit, Alaska, USA. Geochemistry: Exploration, Environment, Analysis **11**: 321-334. doi: 10.1144/1467-7873/10-IM-041.

Laurent, O., Zeh, A., Gerdes, A., Villaros, A., Gros, K., et Słaby, E. 2017. How do granitoid magmas mix with each other? Insights from textures, trace element and Sr–Nd isotopic composition of apatite and titanite from the Matok pluton (South Africa). Contributions to Mineralogy and Petrology **172**: 80. doi: 10.1007/s00410-017-1398-1.

Li, H., Palinkaš, L.A., Watanabe, K., et Xi, X.-S. 2018. Petrogenesis of Jurassic A-type granites associated with Cu-Mo and W-Sn deposits in the central Nanling region, South China: Relation to mantle upwelling and intra-continental extension. Ore Geology Reviews **92**: 449-462. doi: 10.1016/j.oregeorev.2017.11.029.

Liu, L., Hu, R.-Z., Zhong, H., Yang, J.-H., Kang, L.-F., Zhang, X.-C., Fu, Y.-Z., Mao, W., et Tang, Y.-W. 2020. Petrogenesis of multistage S-type granites from the Malay Peninsula in the Southeast Asian tin belt and their relationship to Tethyan evolution. Gondwana Research **84**: 20-37. doi: 10.1016/j.gr.2020.02.013.

Ma, Y., Ji, X.T., Li, J.C., Huang, M., et Kan, Z.Z. 2003. Mineral Resources of the Panzhihua Region. Sichuan Science and Technology Press, Chengdu.

Maciag, B.J., et Brenan, J.M. 2020. Speciation of arsenic and antimony in basaltic magmas. Geochimica et Cosmochimica Acta **276**: 198-218. doi: 10.1016/j.gca.2020.02.022.

Mao, M., Rukhlov, A.S., Rowins, S.M., Spence, J., et Coogan, L.A. 2016. Apatite Trace Element Compositions: A Robust New Tool for Mineral Exploration. Economic Geology **111**(5): 1187-1222. doi: 10.2113/econgeo.111.5.1187.

Meurer, W.P., et Boudreau, A.E. 1996. An evaluation of models of apatite compositional variability using apatite from the Middle Banded series of the Stillwater Complex, Montana. Contributions to Mineralogy and Petrology **125**: 225-236. doi: 10.1007/s004100050218.

Miles, A.J., Graham, C.M., Hawkesworth, C.J., Gillespie, M.R., Hinton, R.W., et Bromiley, G.D. 2014. Apatite: A new redox proxy for silicic magmas? Geochimica et Cosmochimica Acta 132: 101-119. doi: 10.1016/j.gca.2014.01.040.

Miranda, A.C.R., Beaudoin, G., Rottier, B., Pasava, J., Bohdalek, P., et Malec, J. in press. Trace Element Signatures in Scheelite Associated with Various Deposit Types: A Tool for Mineral Targeting. Journal of Geochemical Exploration. doi: 10.2139/ssrn.4470997.

Morton, A., et Yaxley, G. 2007. Detrital apatite geochemistry and its application in provenance studies. Dans Sedimentary Provenance and Petrogenesis: Perspectives from Petrography and Geochemistry. Sous la direction de J. Arribas et S. Critelli et M.J. Johnsson. Geological Society of America Special Paper **420**. pp. 319-344.

Nabil, H. 2003. Genèse des dépôts de Fe-Ti-P associés aux intrusions litées (exemples: l'intrusion mafique de sept-Îles, au Québec; Complexe de Duluth aux Etats-Unis). Thèse de doctorat en ressources minérales, Université du Québec à Chicoutimi, Chicoutimi, Québec.

Nadoll, P., Angerer, T., Mauk, J.L., French, D., et Walshe, J. 2014. The chemistry of hydrothermal magnetite: A review. Ore Geology Reviews **61**: 1-32. doi: 10.1016/j.oregeorev.2013.12.013.

Namur, O., Charlier, B., Toplis, M.J., Higgins, M.D., Liégeois, J.-P., et Vander Auwera, J. 2010. Crystallization Sequence and Magma Chamber Processes in the Ferrobasaltic Sept Iles Layered Intrusion, Canada. Journal of Petrology **51**(6): 1203-1236. doi: 10.1093/petrology/egq016.

Namur, O., Charlier, B., Pirard, C., Hermann, J., Liégeois, J.-P., et Vander Auwera, J. 2011. Anorthosite formation by plagioclase flotation in ferrobasalt and implications for the lunar crust. Geochimica et Cosmochimica Acta **75**(17): 4998-5018. doi: 10.1016/j.gca.2011.06.013.

Namur, O., Charlier, B., Toplis, M.J., Higgins, M.D., Hounsell, V., Liegeois, J.P., et Vander Auwera, J. 2011. Differentiation of Tholeiitic Basalt to A-Type Granite in the Sept Iles Layered Intrusion, Canada. Journal of Petrology **52**(3): 487-539. doi: 10.1093/petrology/egq088.

Namur, O., Charlier, B., et Holness, M.B. 2012. Dual origin of Fe–Ti–P gabbros by immiscibility and fractional crystallization of evolved tholeiitic basalts in the Sept Iles layered intrusion. Lithos **154**: 100-114. doi: 10.1016/j.lithos.2012.06.034.

Nathwani, C.L., Loader, M.A., Wilkinson, J.J., Buret, Y., Sievwright, R.H., et Hollings, P. 2020. Multi-stage arc magma evolution recorded by apatite in volcanic rocks. Geology 48(4): 323-327. doi: 10.1130/G46998.1.

O'Sullivan, G., Chew, D., Kenny, G., Henrichs, I., et Mulligan, D. 2020. The trace element composition of apatite and its application to detrital provenance studies. Earth-Science Reviews **201**: 103044. doi: 10.1016/j.earscirev.2019.103044.

Padilla, A.J., et Gualda, G.A.R. 2016. Crystal-melt elemental partitioning in silicic magmatic systems: An example from the Peach Spring Tuff high-silica rhyolite, Southwest USA. Chemical Geology **440**(15): 326-344. doi: 10.1016/j.chemgeo.2016.07.004.

Paiement, J.-P., Gagne, J., Duplessis, C., Rousseau, G., Gagnon, G., et M., D. 2013. Pre-Feasability Study Mine Arnaud Inc. Sept-Iles Deposit, Québec; Final Report, Technical Report NI 43-101. 377.

Pan, Y., et Fleet, M.E. 2002. Compositions of the Apatite-Group Minerals: Substitution Mechanisms and Controlling Factors. Reviews in Mineralogy and Geochemistry **48**(1): 13-49. doi: 10.2138/rmg.2002.48.2.

Paton, C., Hellstrom, J.C., Paul, B., Woodhead, J., et Hergt, J. 2011. Iolite: freeware for the visualisation and processing of mass spectrometric data. Journal of Analytical Atomic Spectrometry **26**: 2508-2518. doi: 10.1039/C1JA10172B.

Pedersen, J.M., Ulrich, T., Whitehouse, M.J., Kent, A.J.R., et Tegner, C. 2021. The volatile and trace element composition of apatite in the Skaergaard intrusion, East Greenland. Contributions to Mineralogy and Petrology **176**: 102. doi: 10.1007/s00410-021-01861-x.

Piccoli, P.M., et Candela, P.A. 2002. Apatite in Igneous Systems. Reviews in Mineralogy and Geochemistry **48**(1): 255-292. doi: 10.2138/rmg.2002.48.6.

Prowatke, S., et Klemme, S. 2006. Trace element partitioning between apatite and silicate melts. Geochimica et Cosmichimica Acta **70**: 4513-4527. doi: 10.1016/j.gca.2006.06.162.

Qian, L., Wang, Y., Xie, J., et Sun, W. 2019. The Late Mesozoic granodiorite and polymetallic mineralization in southern Anhui Province, China: A perspective from apatite geochemistry. Solid Earth Sciences **4**: 178-189. doi: 10.1016/j.sesci.2019.11.006.

Qiu, K.-F., Zhou, T., Chew, D., Hou, Z.-L., Müller, A., Yu, H.-C., Lee, R.G., Chen, H., et Deng, J. in press. Apatite trace element composition as an indicator of ore deposit types: a machine learning approach. American Mineralogist. doi: 10.2138/am-2022-8805.

Qu, P., Li, N.-B., Niu, H.-C., Yang, W.-B., Shan, Q., et Zhang, Z.-Y. 2019. Zircon and apatite as tools to monitor the evolution of fractionated I-type granites from the central Great Xing'an Range, NE China. Lithos **348-349**: 105207. doi: 10.1016/j.lithos.2019.105207.

Richard, B.J. 2019. Tracing magmatic processes in plutonic environments: Insinght from apatite and rift-related granites. M.Sc. , Department of Geology and Environmental Earth Science, Faculty of Miami University, Miami, 79p.

Rukhlov, A.S., Plouffe, A., Ferbey, T., Mao, M., et Spence, J. 2016. Application of trace-element compositions of detrital apatite to explore for porphyry deposits in central British Columbia. *Dans* Geological Fieldwork 2015, British Columbia Geological Survey Paper 2016-1. *Sous la direction de* British Columbia Ministry of Energy and Mines. pp. 145-179.

Sha, L.-K., et Chappell, B.W. 1999. Apatite chemical composition, determined by electron microprobe and laser-ablation inductively coupled plasma mass spectrometry, as a probe into granite petrogenesis. Geochimica et Cosmichimica Acta **63**(22): 3861-3881. doi: 10.1016/S0016-7037(99)00210-0.

She, Y.-W., Song, X.-Y., Yu, S.-Y., Chen, L.-M., et Zheng, W.-Q. 2016. Apatite geochemistry of the Taihe layered intrusion, SW China: Implications for the magmatic differentiation and the origin of apatite-rich Fe-Ti oxide ores. Ore Geology Reviews **78**: 151-165. doi: 10.1016/j.oregeorev.2016.04.004.

Stokes, T.N., Bromiley, G.D., Potts, N.J., Saunders, K.E., et Miles, A.J. 2019. The effect of melt composition and oxygen fugacity on manganese partitioning between apatite and silicate melt. Chemical Geology **506**: 162-174. doi: 10.1016/j.chemgeo.2018.12.015.

Stormer, J.C., Pierson, M.L., et Tacker, R.C. 1993. Variation of F and Cl X-ray intensity due to anisotropic diffusion in apatite during electron microprobe analysis. American Mineralogist **78**(5-6): 641-648.

Tacker, R.C., et Stormer Jr., J.C. 1989. A thermodynamic model for apatite solid solutions, applicable to high-temperature geologic problems. American Mineralogist **74**: 877-888.

Tan, H.M.R., Huang, X.-W., Meng, Y.-M., Xie, H., et Qi, L. 2023. Multivariate statistical analysis of trace elements in apatite: Discrimination of apatite with different origins. Ore Geology Reviews **153**: 105269. doi: 10.1016/j.oregeorev.2022.105269.

Tang, Q., Chusi, L., Liu, C., Xue, S., Xu, S., Zhang, Y., Li, Z., Bao, J., et Song, H. 2023. Contrasting magmatic controls on the genesis of Fe-Ti-V oxide deposits in the Emeishan large igneous province using apatite Sr-Nd isotopes and apatite-zircon trace elements. Mineralium Deposita **58**: 1279-1296. doi: 10.1007/s00126-023-01180-0.

Thomson, M.L., Barnett, R.L., Fleet, M.E., et Kerrich, R. 1985. Metamorphic assemblages in the South-Range norite and footwall mafic rocks near the Kirkwood Mine, Sudbury, Ontario The Canadian Mineralogist **23**(2): 173-186.

Tollari, N., Barnes, S., Cox, R., et Nabil, H. 2008. Trace element concentrations in apatites from the Sept-Îles Intrusive Suite, Canada — Implications for the genesis of nelsonites. Chemical Geology **252**(3-4): 180-190. doi: 10.1016/j.chemgeo.2008.02.016.

Wang, K., Wang, C.Y., et Ren, Z.-Y. 2018. Apatite-hosted melt inclusions from the Panzhihua gabbroic-layered intrusion associated with a giant Fe–Ti oxide deposit in SW China: insights for magma unmixing within a crystal mush. Contributions to Mineralogy and Petrology **173**: 59. doi: 10.1007/s00410-018-1484-z.

Warner, S., Martin, R.F., Abdel-Rahman, A.-F.M., et Doig, R. 1998. Apatite as a monitor of fractionation, degassing, and metamorphism in the Sudbury Igneous Complex, Ontario. The Canadian Mineralogist 36: 981-999.

Watts, K.M. 2014. A melt inclusion study of the Sudbury Igneous Complex (Ontario, Canada): Evidence for two-liquid immiscibility and constraints on trace elements distribution. Mémoire de maîtrise en Sciences Appliquées, Saint Mary's University, Halifax, Nouvelle-Ecosse, 129p.

Webster, J.D., et Piccoli, P.M. 2015. Magmatic Apatite: A Powerful, Yet Deceptive, Mineral. Elements **11**(3): 177-182. doi: 10.2113/gselements.11.3.177.

Xing, C.-M., Wang, C.Y., et Li, C. 2014. Trace element compositions of apatite from the middle zone of the Panzhihua layered intrusion, SW China: Insights into the differentiation of a P- and Si-rich melt. Lithos **204**: 188-202. doi: 10.1016/j.lithos.2014.02.009.

Xing, C.-M., et Wang, C.Y. 2017. Cathodoluminescence images and trace element compositions of fluorapatite from the Hongge layered intrusion in SW China: A record of prolonged crystallization and overprinted fluid metasomatism. American Mineralogist **102**: 1390-1401. doi: 10.2138/am-2017-6028.

Zafar, T., Rehman, H.U., Mahar, M.A., Alam, M., Oyebamiji, A., Rehman, S.U., et Leng, C.-B. 2020. A critical review on petrogenetic, metallogenic and geodynamic implications of granitic rocks exposed in north and east China: New insights from apatite geochemistry. Journal of Geodynamics **136**: 101723. doi: 10.1016/j.jog.2020.101723.

Zhang, X., Guo, F., Zhang, B., Zhao, L., Wu, Y., Wang, G., et Alemayehu, M. 2020. Magmatic evolution and post-crystallization hydrothermal activity in the early Cretaceous Pingtan intrusive complex, SE China: records from apatite geochemistry. Contributions to Mineralogy and Petrology **175**: 35. doi: 10.1007/s00410-020-1675-2.

Zhou, R.-J., Wen, G., Li, J.-W., Cao, K., Wei, K.-T., Cai, H.-A., Shang, S.-C., Sun, Y.L., Fan, L., Li, B.-C., et Dai, X.-K. 2022. Petrogenesis and metal fertility of Yinzu pluton in the Daye district, eastern China: Insights from whole-rock and mineral (zircon, apatite and amphibolite) geochemistry. Lithos **432-433**: 106898. doi: 10.1016/j.lithos.2022.106898.

Zhou, T., Cai, Y.-W., An, M.-G., Zhou, F., Zhi, C.-L., Sun, X.-C., et Tamer, M. 2023. Visual Interpretation of Machine Learning: Genetical Classification of Apatite from Various Ore Sources. Minerals **13**(4): 491. doi: 10.3390/min13040491.

CHAPITRE 2

THE USE OF TRACE ELEMENTS IN APATITE TO TRACE DIFFERENTIATION OF A FERROBASALTIC MELT IN THE SEPT-ILES INTRUSIVE SUITE, QUEBEC, CANADA: IMPLICATIONS FOR PROVENANCE DISCRIMINATION

Marie A. Kieffer[1], Sarah A.S. Dare[1]*, Olivier Namur[2]

[1]Department of Applied Sciences, University of Quebec in Chicoutimi (UQAC), 555 Boulevard de l'Université, Chicoutimi G7H 2B1, QC, Canada

[2]Department of Earth and Environmental Sciences, KU Leuven, 3000 Leuven, Belgium

*Canada Research Chair in Geochemistry Applied to Ore Deposits

Geochimica et Cosmochimica Acta (2023)

DOI: 10.1016/j.gca.2022.12.016

Résumé

La Suite Intrusive de Sept-Iles (Québec, Canada) contient l'une des plus volumineuses intrusions mafiques litées au monde. Il s'agit d'un laboratoire naturel afin d'étudier les processus de différenciation d'un liquide ferrobasaltique dont la cristallisation fractionnée extrême produit un magma résiduel felsique. De plus, l'immiscibilité de liquides est impliquée dans la formation de la minéralisation en Fe–Ti–P (oxydes de Fe-Ti et apatite) de la Zone Critique, riche en apatite, et située au sommet de la séquence mafique. Dans cette étude, nous explorons et développons l'utilisation des éléments traces dans l'apatite en tant qu'indicateur pétrogénétique de ces processus magmatiques. Une suite de 31 éléments traces a été analysée au LA-ICP-MS et à la microsonde dans les apatites de la Série Litée mafique, ainsi que dans la Série Supérieure felsique, de la Suite Intrusive de Sept-Iles. Nous montrons que le contenu em éléments traces des apatites enregistre les changements compositionnels lors du fractionnement du liquide ferrobasaltique, depuis les roches mafiques jusqu'aux roches felsiques (augmentation des ETR+Y, Th, U, K, Pb et Rb, et diminution de Sr, Ba, V et Mg dans l'apatite), ce qui concorde avec l'évolution de la *liquid line of descent* de Sept-Iles. Dans la Zone Critique, minéralisée, les variations chimiques causées par le fractionnement se surimposent aux différences compositionnelles des apatites et plagioclases normalement observées dans la succession de niveaux riches et pauvres en Fe–Ti–P. Ceci est en partie attribué à la répartition des éléments traces entre les liquides silicatés immiscibles riches en Fe et en Si, mais aussi aux différentes proportions cotectiques d'apatite qui peuvent cristalliser à partir de ces liquides, calculées respectivement à 5 à 8% et à 1% pour les liquides riches et pauvre en Fe–Ti–P. Puis, la chute des cristaux et leur accumulation est responsable des fortes proportions d'apatite (7 à 36 vol%) observées dans les niveaux riches en Fe–Ti–P. Une série de nouveaux diagrammes de discrimination basée sur la chimie des apatites est proposée afin d'aider à l'identification de la provenance des roches. À Sept-Iles, les ETR+Y, Sr et l'anomalie en Eu permettent de distinguer les apatite des roches mafiques et felsiques. Les apatites intercumulus, qui cristallisent à partir du liquide interstitiel, sont facilement différenciables des apatites cumulus grâce à leur enrichissement en éléments incompatibles (ratios Cl/F et Th/Lu plus élevés). Cela suggère que l'apatite, et notamment

l’apatite détritique, pourrait être utilisée en tant que minéral indicateur pour l’exploration de minéralisations en Fe–Ti–P dans les intrusions mafiques litées.

Mots-clefs : apatite; intrusion litée de Sept-Iles; LA-ICP-MS; minéralisation en Fe–Ti–P; volatils

Abstract

The Sept Iles Intrusive Suite, Quebec, Canada, comprises one of the world's largest mafic layered intrusions. It is a natural laboratory to study differentiation processes of a ferrobasaltic melt whereby extreme fractional crystallisation of the mafic melt resulted in residual, felsic magma. Furthermore, liquid immiscibility played a role in forming Fe–Ti–P mineralisation (Fe-Ti oxides and apatite) in the apatite-bearing Critical Zone near the top of the mafic sequence. In this study, we explore and develop the use of trace elements in apatite as a petrogenetic indicator of these magmatic processes. A full suite of 31 trace elements was determined in apatite by LA-ICP-MS and electron microprobe from the mafic Layered Series and felsic Upper Series of the Sept-Iles Intrusive Suite. We show that the trace element content of cumulus apatite records the changing melt composition of the fractionating ferrobasalt from the mafic to the felsic rocks (increase in REE + Y, Th, U, K, Pb and Rb, and decrease in Sr, Ba, V and Mg of apatite), in accordance with the evolution of Sept-Iles liquid line of descent. In the mineralised Critical Zone, the fractionation trend overprints systematic chemical differences in apatite and plagioclase composition between alternating Fe–Ti–P-rich and -poor layers. This is attributed in part to partitioning behaviour of trace elements between immiscible Fe-rich and Si-rich silicate melts and the different cotectic proportions of apatite crystallising from these melts, which was calculated to be 5 to 8 % and 1 % for the Fe–Ti–P-rich and -poor, respectively. Crystal settling and accumulation is then responsible for the elevated proportion of apatite (7 to 36 vol%) observed in Fe–Ti–P-rich layers. Furthermore, a series of new discrimination diagrams is proposed to help identify the provenance of igneous rocks using apatite chemistry. At Sept-Iles, apatite from mafic rocks is distinguished from the felsic rocks using REE + Y, Sr and the Eu anomaly. Intercumulus apatite, which crystallised from the interstitial liquid, is readily distinguishable from cumulus apatite by enrichment in highly incompatible elements (higher Cl/F and Th/Lu ratios). This suggests that apatite could be used as an indicator mineral for the exploration of Fe–Ti–P mineralisation in mafic layered intrusions using detrital apatite.

Keywords: Apatite; Fe-Ti-P mineralisation; LA-ICP-MS; Sept-Iles layered intrusion; Volatiles

2.1 Introduction

Apatite is a weathering-resistant and widespread accessory mineral that can be found in most crustal rocks (Piccoli and Candela, 2002; Webster and Piccoli, 2015) and in a wide number of ore deposits (e.g., Mao et al., 2016; Mercer et al., 2020). Though its general formula is $Ca_5(PO_4)_3(OH,F,Cl)$, apatite may also concentrate an elevated amount of various trace elements (e.g. REE, Sr, Th, V, Mg, etc.) by means of substitutions to its major constituents (Pan and Fleet, 2002). The trace element content of apatite is controlled by several parameters including the trace element partitioning between the melt and apatite (e.g., competition with other minerals; Fujimaki, 1986; Chu et al., 2009; She et al., 2016), the changing magma or fluid composition and its oxygen fugacity (fO2; Prowatke and Klemme, 2006; Konecke et al., 2019; Sadove et al., 2019; Maciag and Brenan, 2020). As the trace element composition of apatite is closely related to its geological environment of formation, there is growing interest to develop apatite chemistry as a provenance tool, in particular as an indicator mineral for exploration for hydrothermal ore deposits using detrital apatite grains (Morton and Yaxley, 2007; Mao et al., 2016; Hu et al., 2019; O'Sullivan et al., 2020). Moreover, apatite can be used as a petrogenetic indicator (Belousova et al., 2002) because its trace element content may record igneous processes, such as fractional crystallisation in mafic layered intrusions (Tollari et al., 2008; Pedersen et al., 2021), anorthosites (Chen et al., 2013), granites (Zhang et al., 2020), or carbonatites (Andersson et al., 2019). For example, apatite can record modifications to the magma composition by a new magma injection (Xing et al., 2014) or by the assimilation of country rocks (Miles et al., 2013). However, several processes may have an impact on the primary composition of apatite after its crystallisation, such as post-cumulus reaction with trapped liquid (Cawthorn, 1994, 2013), hydrothermal fluid circulation (Xing and Wang, 2017), subsolidus re-equilibration with surrounding minerals (Boudreau and McCallum, 1989; Schisa et al., 2015) and metamorphism (Warner et al., 1998). The effect of these later-stage processes on the trace element composition of apatite are not yet fully demonstrated or understood.

The study of apatite from mafic layered intrusions offers a natural laboratory to evaluate the processes controlling the variation of trace elements in apatite during differentiation processes (fractional crystallisation, magma mixing, contamination and liquid immiscibility) so that it may be

used as a petrogenetic indicator to improve our understanding of processes that took place during crystallisation of the magma chamber. Apatite is ubiquitous in mafic (basaltic) layered intrusions. It mostly crystallises in low proportions as an intercumulus phase (i.e., interstitial) from the trapped liquid (Boudreau et al., 1986; Cawthorn, 1994). However, it becomes a modally important phase in the late crystallisation history of the layered intrusion, when it becomes a cumulus phase crystallising from an evolved melt together with Fe-Ti oxides (Brown and Peckett, 1977; Eales and Cawthorn, 1996; Cimon, 1998). As apatite crystallisation exerts an important control on many trace elements in mafic systems (e.g., REE, Sr, Th; Toplis and Dingwell, 1996; Tollari et al., 2008), it records trace element fractionation during magma differentiation in the upper part of mafic layered intrusions and thus provide insights on the latestage melt evolution. Moreover, cumulus apatite can be associated with Fe–Ti oxides in variable proportions (e.g., Panzhihua, Zhou et al., 2005; Bushveld Upper and Upper Main Zone, Fischer and Yuan, 2016), and sometimes in a sufficient amount to be considered as Fe–Ti–P mineralisation (e.g., Sept-Iles Critical Zone, Tollari et al., 2008; Paiement et al., 2013). Intercumulus apatite can also be associated with Ni-Cu-PGE mineralisation in the lower parts of some mafic layered intrusions (e.g., Bushveld, Stillwater, Cawthorn, 1994; Skaergaard, Nielsen et al., 2015).

However, there are a limited number of trace element studies on apatite from mafic layered intrusions. The majority focus on volatile trace elements, determined by electron probe micro-analyzer (EMPA; Boudreau et al., 1986; Boudreau and McCallum, 1989; Boudreau and Kruger, 1990; Meurer and Boudreau, 1996; Ripley et al., 1998), or often report REE and only a few other trace elements, e.g. Th, U, Sr, determined by Laser Ablation Inductively Coupled Plasma Mass Spectrometry (LA-ICP-MS; Sept Iles, Tollari et al., 2008; Bushveld Complex, Van Tongeren and Mathez, 2012; Taihe, She, et al., 2016; Hongge, Xing and Wang, 2017). Furthermore, variations within the apatite chemistry could also be useful to distinguish intercumulus and cumulus apatite, which can be associated with two different types of mineralisation: Ni–Cu–PGE, typically associated with more primitive magmas in the lower parts of intrusions, and Fe–Ti ± P,V, associated with more evolved magmas in the upper parts of mafic intrusions. This chemical information is useful to develop

apatite as a provenance indicator (i.e., Mao et al., 2016) using detrital grains from till or river sediments (i.e., O'Sullivan et al., 2020).

The Sept-Iles Intrusive Suite, Quebec, Canada, hosts the third largest mafic layered intrusion in the world (Loncarevic et al., 1990; Namur et al., 2010), including Fe–Ti–P mineralisation (482 Mt at 4.18 % P_2O_5; Paiement et al., 2013) in its Critical Zone near the top of the mafic sequence. It is an ideal case study to develop apatite as a petrogenetic and provenance indicator for the following reasons. The crystallisation history of the Sept-Iles Intrusive Suite has been well constrained through whole rock, mineral,and isotope analyses (Higgins and van Breemen, 1998; Higgins, 2005; Namur et al., 2010, 2011a, 2011b, 2012, 2015, and references therein). It records the evolution from a mafic (ferrobasaltic) to felsic magma (i.e., type A granite; Namur et al., 2011a), with the mafic part of the intrusion resulting from multiple magma injections and magma mixing. However, only one study has been performed on apatite from the Critical Zone (Tollari et al., 2008), showing that the composition of apatite records magma fractionation, using a limited range of trace elements (i.e., REE, Sr, Th and U). The intrusion in unmetamorphosed (Higgins, 2005) and the amount of crustal contamination is negligible (<2 %; Namur et al., 2010). Magma mixing and immiscibility between Fe-rich and Si-rich silicate melts is recorded in the Fe–Ti–P mineralised Critical Zone as compositionally bimodal melt inclusions in apatite (Charlier et al., 2011; Namur et al., 2012). Though it remains debated, evidence also points to an immiscibility process involving conjugate Fe- and Si- rich melts in several mafic layered intrusions such as Bushveld (Fischer et al., 2016), Skaergaard (Jakobsen et al., 2005) or Panzhihua (Wang et al., 2018), which might also be responsible for the formation of apatite-rich mineralisation.

In this study, we apply in situ analytical methods (EPMA and LA-ICP-MS) to systematically determine a full suite of major and trace elements in apatite from the mafic and felsic portions of the Sept-Iles layered intrusion. We show that the effect of subsolidus re-equilibration is negligible and that cumulus apatite can thus be robustly used to trace different magmatic processes. Apatite records late-stage fractionation of a mafic, ferrobasaltic magma to form felsic rocks and places constraints on the immiscibility process occurring in the mineralised Critical Zone. In addition, we propose new discrimination diagrams to compositionally separate apatite from the felsic and mafic rocks and

apatite associated with mineralisation in the Layered Series, which seeks to set a framework for the exploration of magmatic mineralisation associated with mafic layered intrusions.

2.2 Geological background

The Sept-Iles Intrusive Suite is located on the north shore of the St Lawrence River at about 500 km to the north-east of Quebec City (Fig. 2.1). The intrusive suite has a dinner plate-like shape with a diameter of ca. 80 km, a maximum thickness of ca. 6 km, and an estimated volume of 20 000 km3 (Loncarevic et al., 1990). Most of the Sept-Iles Intrusive Suite lies beneath the St Lawrence River, but the northern part outcrops on the Sept-Iles peninsula and on the islands of the Sept-Iles archipelago (Fig. 2.1). The intrusion was emplaced into the high-grade gneisses of the Grenville Province (Davidson, 1995; Rivers, 2008) at 564 ± 4 Ma (U-Pb on zircons; Higgins and van Breemen, 1998). This age is contemporaneous with a widespread magmatic phase attributed to the formation of the St Lawrence rift system, and corresponding to the initial stages of opening of the Iapetus Ocean (Kumarapeli and Saull, 1966; Higgins and van Breemen, 1998). According to Higgins (2005), the igneous activity at Sept-Iles started with the eruption of flood basalts, which are now completely eroded. The Sept-Iles layered intrusion was emplaced at the unconformity between those basalts and the Grenville basement (Higgins 2005). The Sr isotopic composition of the Sept-Iles layered intrusion implies a mantle source (Higgins and Doig, 1981), which is in agreement with the activity of a mantle plume (Hill et al., 1992) or with a lithospheric reorganisation process related to the opening of the Iapetus Ocean (Namur et al., 2010).

The Sept-Iles Intrusive Suite is composed of three different series of rocks: the Layered Series (mafic layered intrusion), the Upper Border Series (anorthositic), and the Upper Series (felsic). It also includes other intrusive components, namely the composite Pointe du Criard sill (mafic and felsic), and several dolerite dykes that belong to the Late Gabbro intrusion (Fig. 2.1; Cimon, 1998; Higgins, 2005; Namur et al., 2011a). The Layered Series is surrounded by a > 20 m thick Border Zone made of massive, fine-grained, mafic rocks (dolerite) corresponding to a ‘chilled’ margin separating the intrusion from the Grenvillian country rocks (Fig. 2.1; Namur et al., 2011). Based upon the Border Zone whole rock compositions, calculations with MELTS thermodynamic calculator and by analogies

with other layered intrusions, Namur et al. (2010) proposed that the Sept-Iles parent magma corresponds to an Fe–rich tholeiitic basalt (ferrobasalt).

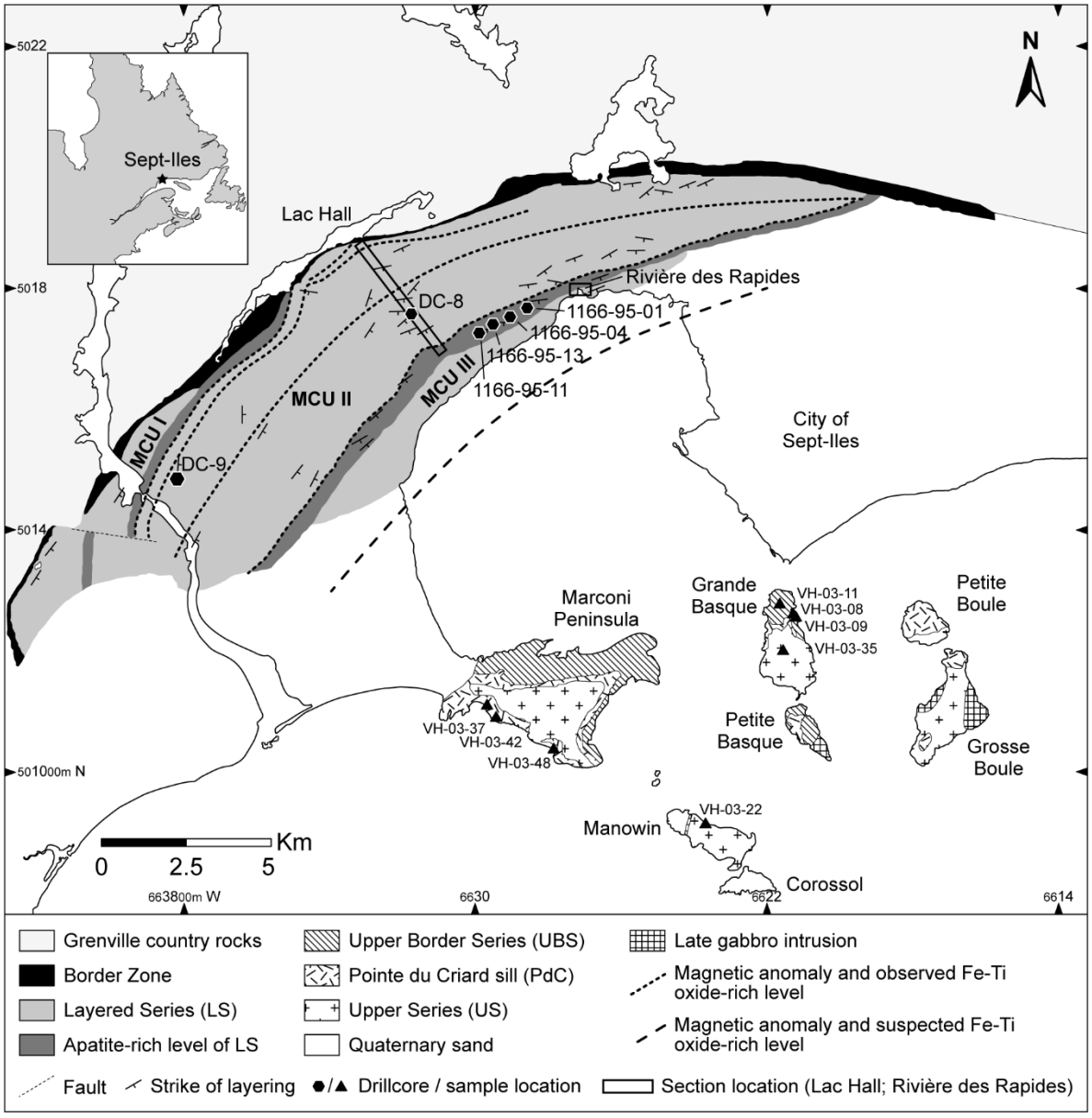

Figure 2.1 – Geological map of the Sept-Iles Intrusive Suite adapted from Higgins (2005), with subdivision of the Layered Series into 3 megacyclic units (MCU) (modified from Namur et al., 2011). The Critical Zone corresponds to the apatite-rich level at the top of MCU II. Location of drill cores and the sections where surface samples were collected are indicated.

The ca. 4.7 km-thick Layered Series represents the largest component of the Sept-Iles Intrusive Suite (Fig. 2.2). It is composed of 3 megacyclic units (MCU) containing the following succession of cumulus assemblages, as defined by Namur et al. (2010), following the classification of Irvine (1982): 1) troctolite (plagioclase + olivine; po-C), 2) Fe–Ti oxide-bearing troctolite (plagioclase + olivine + magnetite + ilmenite; pomi-C) indicating that saturation of oxides was relatively early, 3) layered gabbro (plagioclase + magnetite + ilmenite + clinopyroxene ± olivine; pomic-C, pmic-C), and 4) Fe–Ti oxide-apatite-bearing gabbro (plagioclase + olivine + magnetite + ilmenite + clinopyroxene + apatite; pomica-C). The saturation of apatite occurred at the very top of both MCU I and MCU II from the most evolved magma. However, only the top of MCU II is mineralised in Fe–Ti oxides and apatite (termed the Critical Zone; Cimon, 1998). It has been named the Critical Zone (Cimon, 1998) due to its potential economic value for P (measured + indicated resources estimated at 482 Mt at 4.18 % P_2O_5; Paiement et al., 2013).

Each MCU corresponds to the crystallisation of a new influx of ferrobasaltic parent magma marked by a compositional reversal to more primitive mineral compositions at the base (see Namur et al., 2010 for details). MCU I crystallised from a single injection of mafic melt. However, at least six minor magma replenishments occurred during the crystallisation of MCU II (Fig. 2.2; Namur et al., 2010, 2011a). Namur et al. (2010) estimated that the Layered Series mostly crystallised under oxygen fugacity (fO_2) close to the FMQ (Fayalite–Magnetite–Quartz) buffer.

The ca. 200 m thick unit of leucocratic apatite-bearing gabbroic rocks topping MCU I is homogeneous and contains 3–4 vol% apatite and 15–20 vol% Fe–Ti oxides. In contrast, the ca. 250 m thick apatite-bearing gabbroic unit of MCU II is heterogeneous, with the proportion of oxide and apatite decreasing overall from base to top (Fig. 2.2). In detail, a 10 m thick layer of massive nelsonite (up to ca. 30 vol% of apatite and 70 vol% of Fe-Ti oxides) defines the base of the Critical Zone. In certain places it is underlain by a < 50 m thick layer of massive Fe–Ti oxides, visible in only 3 drillcores (1166–95-04, 1166–95-01, and 1166–95-11; Nabil, 2003; Tollari et al., 2008). The massive oxides/nelsonites are overlain by ~240 m of nelsonitic troctolite/gabbro and troctolite/gabbro with a matrix of nelsonite (Nabil, 2003; Tollari et al., 2008; Charlier et al., 2011). Superimposed on this overall decrease of the nelsonite component up sequence, there exists a 1–20 m scale alternance

between Fe–Ti–P-rich, melanocratic gabbroic layers (>4 vol% up to 36 vol% apatite and >15 up to 70 vol% Fe–Ti oxides) alternating with Fe–Ti–P-poor, leucocratic gabbroic layers (<5 vol% apatite and <10 vol% Fe–Ti oxides; Tollari et al., 2008; Namur et al., 2010; Charlier et al., 2011; Namur et al., 2012). This bimodality is clearly shown in the fluctuating P_2O_5 content (Fig. 2.2c) and density, which is directly correlated with apatite and Fe–Ti oxides abundance in the layers (Charlier et al., 2011; Namur et al., 2012; Fig. 2.2d, e). Rocks forming the Fe–Ti–P-poor layers contain 0.3 to ~2 wt% P_2O_5 and have a density of 3.0 to 3.2 g/cm^2, while those from the Fe–Ti–P-rich layers contain more P_2O_5 (3 to ~14 wt%) and are denser (3.6 to 3.8 g/cm2). The P_2O_5 content of Fe–Ti–P-poor layers remains globally constant throughout the Critical Zone (Fig. 2.2c). However, the Fe–Ti–P-rich rocks at the base of the Critical Zone (i.e., nelsonites) contain the highest P_2O_5 concentration (10 to 15 wt% P_2O_5), which then decreases to 3–5 wt% towards the top (Fig. 2.2c). As a comparison, the P_2O_5 content of the rocks containing intercumulus apatite (i.e., in MCU II, below the base of the Critical Zone; < 0.01 vol% apatite) is distinctly lower, with an average of 0.04 wt% P_2O_5 and varies from 0.01 to 0.29 wt% P_2O_5 (Namur et al., 2010). It is proposed that the difference between homogeneous apatite-bearing gabbroic rocks of MCU I and the alternation of Fe–Ti–P-rich and -poor gabbroic rocks of MCU II is due to the development of immiscibility of Fe-rich and Si-rich melts during the late-stage differentiation of MCU II, which was absent for MCU I (Charlier et al., 2011; Namur et al., 2012; Keevil et al., 2020).

The ca. 100–500 m thick Upper Border Series is composed of anorthosite with minor leucotroctolite and leucogabbro (Higgins, 1991). This unit was formed upon the accumulation of buoyant plagioclase, at the roof of the magma chamber, by flotation (Higgins 2005) from an Fe-Ti oxide undersaturated melt (Namur et al., 2011b).

The felsic rocks of the Upper Series form small, separated cupolas topping the central part of the intrusion and likely represents <10 % of the total intrusion (Namur et al., 2010; 2011a). This unit is composed of ferroan, metaluminous syenite and granite with minor monzonite (Higgins and Doig, 1986; Namuret al., 2011a). It has been demonstrated that these A-type granites represent the evolved, residual liquids remaining after extensive fractionation of the mafic cumulates (Layered

Series and the Upper Border Series) from the Sept-Iles ferrobasaltic parent magma (Namur et al., 2011a).

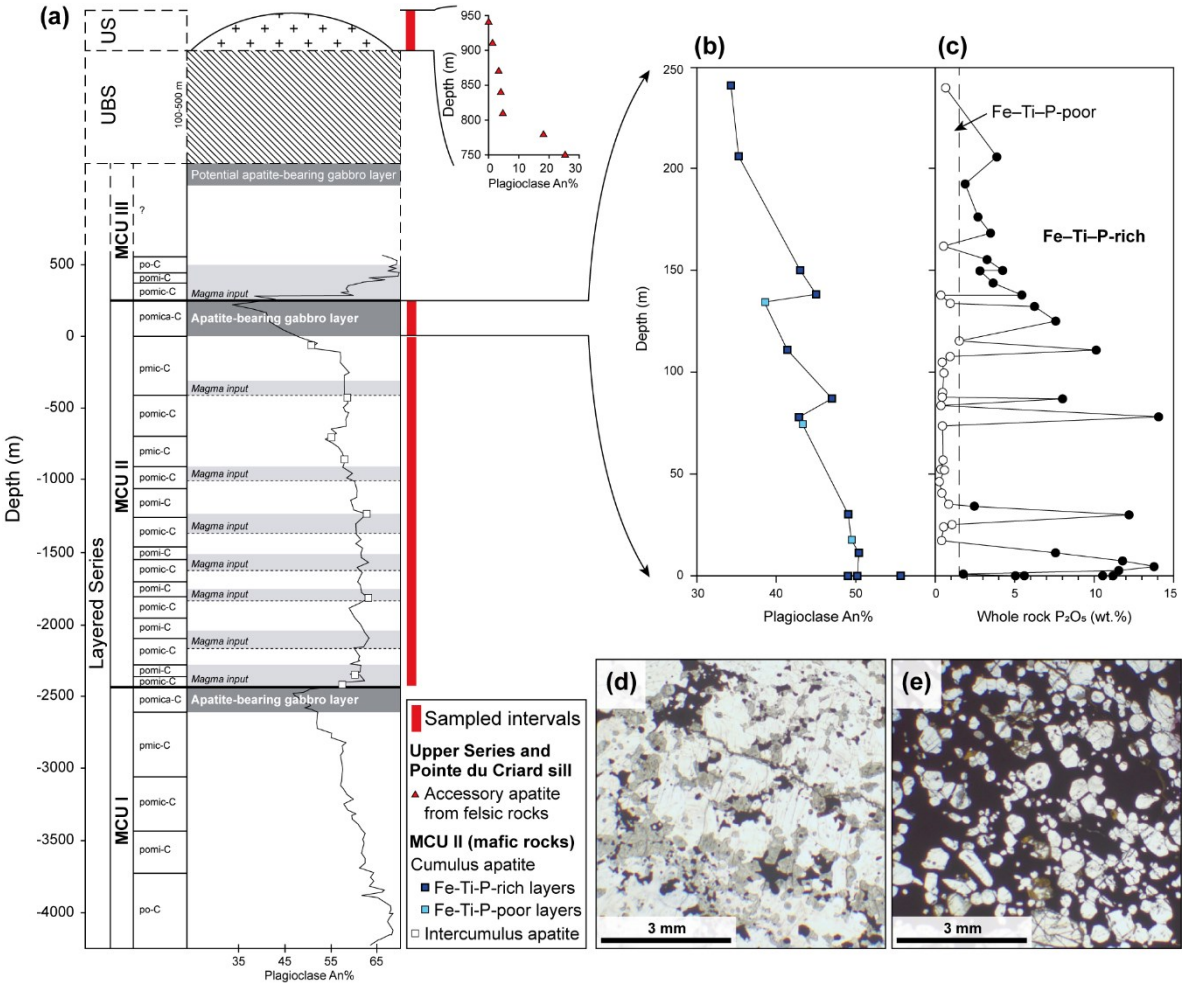

Figure 2.2 – (a) Schematic stratigraphic column of the Sept-Iles layered intrusion with evolution of the anorthite content (An%) of plagioclase within the Layered Series (modified from Namur et al., 2010, 2011a). Light grey bands in MCU II and at the base of MCU III represent mixing zones between residual liquid and new magma inputs. Inset graph represent the stratigraphic position and anorthite content of the selected samples within the Upper Series and Pointe du Criard sill. Arbitrary depth was assigned to the surface samples of felsic rocks from the Upper Series and Pointe du Criard sill according to decreasing anorthite content of plagioclase. (b) Stratigraphic position and anorthite content of the selected samples within the apatite-bearing Critical Zone (CZ) of MCU II. Anorthite content of plagioclase from the Layered Series is from Nabil (2003) and Namur et al. (2010), and values for the felsic rocks are from the Namur et al. (2011). (c) Stratigraphic variation of P_2O_5 (wt.%) content throughout the Critical Zone (data from Nabil 2003; Namur et al., 2010, 2012). Representative microphotographs of Fe–Ti–P-poor (d) and Fe–Ti–P-rich (e) layers within the Critical Zone.

The Upper Border Series and Upper Series are cross-cut by the 50 m thick Pointe du Criard composite sill. It outcrops on the Sept-Iles peninsula and archipelago (Fig. 2.1). The margins of the dykes are made of dolerite, which grades into leucogabbro, then into the silicic rocks (syenite, granite) representing the bulk of the sill (Higgins, 1990).

2.3 Sample selection

Eighty-four mafic samples from the MCU II of Sept-Iles layered intrusion were examined in thin section for the occurrence of cumulus or intercumulus apatite (see Annexe 10): 55 samples from the entire stratigraphy of MCU II characterised by Namur et al. (2010) and an additional 29 samples from the Critical Zone from the work of Nabil (2003) and Tollari et al., 2008). It corresponds to 61 samples investigated for the occurrence of cumulus apatite, and 23 samples that could contain intercumulus apatite. Furthermore, 7 samples from the Upper Series and 4 samples from the Pointe du Criard sill were examined from the studies of Hounsell (2008) and Namur et al. (2011a). All of these samples were thoroughly characterised by Namur et al. (2010, 2011a), Nabil (2003), Hounsell (2008), and Tollari et al. (2008), including whole rock and mineral (plagioclase, olivine, pyroxene, oxides) composition analyses. Previous work on apatite is limited to 12 samples from Fe–Ti–P-rich melanocratic layers of the Critical Zone by Tollari et al. (2008). These analyses consisted of 11 elements determined by LA-ICP-MS (REE, Sr, Ba, Th and U). Therefore, some of these samples were re-analysed with a full suite of trace elements in this study for completion.

A set of 31 samples was subsequently selected to perform detailed apatite chemical analysis (Annexe 10). The selection was made to provide a complete coverage of the stratigraphy and is based upon the presence of apatite (minimum 2 crystals per thin section) and its purity (i.e., as few fractures, mineral and melt inclusions as possible; Fig. 2.2; Table 2.1). Only apatite in samples with grains >20 lm was selected to ensure the reliability of analyses (i.e., to avoid mixed signal).

All samples containing 2 or more grains of intercumulus apatite were selected below the Critical Zone, thus covering the lower part of the MCU II (from –46 to –2411 m). However, due to the scarcity of intercumulus apatite, only 8 samples were selected from the 23 investigated samples. Fifteen samples containing cumulus apatite were selected regularly throughout the whole Critical Zone,

covering the upper part of the MCU II (i.e., between 0 and 240 m). They include 4 pairs of samples of closely related Fe–Ti–P-poor and Fe–Ti–P-rich -rich layers in order to resolve the potential chemical variation in minerals associated with apatite abundance. In 7 of these 15 samples, apatite fully enclosed in different host phases (e.g., plagioclase, olivine, clinopyroxene, or Fe–Ti oxides) were selected in order to test if the nature of the host might cause a compositional difference in apatite chemistry. In order to characterise apatite from the felsic units of Sept-Iles layered intrusion, 5 samples from the Upper Series and 3 samples from the Pointe du Criard sill were selected (Fig. 2.2; Table 2.1).

2.4 Apatite petrography

In the lower part of the MCU II, between 0 and – 2411 m below the base of the Critical Zone, intercumulus apatite is scarce, with generally no more than a few grains per thin section, but its size can considerably vary within the same sample (from ~40 µm to 500 µm). Interstitial apatite (20 to 150 µm) is subhedral to anhedral, as it fills the spaces between plagioclase crystals, and generally presents fractures (Fig. 2.3a). Apatite can also be associated with trapped melt pockets containing Fe–Ti oxides and small clinopyroxene crystals. In this case, apatite is subhedral to euhedral, with a size ranging from 40 µm to 200 µm, and often contains Fe–Ti oxides, melt, or fluid inclusions (Fig. 2.3b). Identical textures of interstitial apatite were observed in gabbros from the Skaergaard intrusion (Holness et al., 2013).

Cumulus apatite, along with Fe-Ti-oxides, is heterogeneously distributed in the Critical Zone at the top of MCU II. At the base, apatite is abundant (up to 36 vol%; Table 2.1) and large (200 µm to 2 mm; Fig. 2.3c). Apatite crystals are euhedral in shape and can be found in close association with all the other cumulus minerals. Light and dark rounded inclusions have been recognised in some apatite crystals (Fig. 2.3c). They may correspond to, respectively, Si–rich and Fe–rich immiscible melts, as identified by Charlier et al. (2011) and Namur et al. (2012). Apatite abundance in these Fe–Ti–P-rich, melanocratic layers, decreases to ~7 vol% towards the top of the Critical Zone (Table 2.1) along with its size (50 µm to 700 µm). Apatites are still euhedral and associated with all the other cumulus phases (Fig. 2.3d). However, fewer melt inclusions have been observed. In Fe–Ti–P-poor, leucocratic layers, apatite is smaller (50 to 200 µm) and its abundance does not exceed ~1 vol% (Fig. 2.3e), regardless

of its position in the stratigraphy. In this case, apatite is euhedral and located within or close to melt pockets containing Fe–Ti oxides ± clinopyroxene, or is euhedral to subeuhedral and interstitial to the other cumulus phases. A few small melt inclusions (<5 μm), most of them being light, have been observed in apatite from Fe–Ti–P-poor layers.

Apatite is an accessory mineral in the felsic rocks of the Upper Series and Pointe du Criard sill, typically forming long needles (<10 to 60 lm in length), included within plagioclase, too thin (<2 to 5 μm) for analysis by LA-ICP-MS. Slightly bigger apatite crystals (60 to 400 μm in length, 20 to 30 μm in diameter), suitable for analysis, are generally found at the rim of Fe–Ti oxide pockets and/or within amphibole and biotite crystals (Fig. 3f).

2.5 Analytical methods

2.5.1 EMPA

Major (P, Ca), minor (Si, Ti, Fe, La, Ce, Pr, Nd, S) and volatile (F, Cl) elements in apatite were determined using a Cameca SX100 electron micro-analyser (EMPA), fitted with 5 WDS (wavelength-dispersive) spectrometers, at the Laboratoire de Microanalyse, Université Laval, Canada. Detail of the analytical protocol is given in Annexe 11 to 13. Four of the analysed elements are used for this study: Ca as the internal standard for LA-ICP-MS analyses, and Si, F and Cl as they are best determined by EMPA than by LA-ICP-MS. The other elements are used to monitor the purity of the apatite analyses. However, F and Cl can be subject to migration during beam exposure when measured by EMPA, as described by Stormer et al. (1993). Goldoff et al. (2012) recommend analytical conditions of 10 kV acceleration voltage, 4 nA beam current and a defocused 10 μm diameter beam. This protocol optimises F and Cl measurements but results in high detection limits for the other elements due to the low beam current. By testing several analytical protocols on an in-house apatite reference material, we determined a new protocol which allows optimal F and Cl measurement, as well as the acceptable determination of the other elements (see Annexe 11). Thus, the analytical conditions were set to a 15 kV acceleration voltage, a 10 nA beam current (to optimise detection limits), and a defocused beam of 10 μm diameter (to limit diffusion of volatiles). Analysis of Durango apatite reference material showed that F and Cl were accurate and precise to within 3.8 and

20.1 % (based on relative difference with certified value) and 5.5 and 7.5 % (based on relative standard deviation), respectively, using the defocused beam. However, using a focused beam of 2 µm leads to significant volatile loss (27.7 % relative difference) and loss in precision (8.5 % relative standard deviation). In the mafic samples from MCU II, there is no significant F and Cl difference between analyses of basal and longitudinal sections of apatite within the same sample, indicating that the selected protocol limits halogen migration. In the felsic samples, higher F values were obtained on the basal sections (n = 3; 4.23 to 4.77 wt% F) due to their smaller size. The other analyses were performed on longitudinal sections (n = 17; 3.66 to 4.32 wt%) in order to avoid halogen migration (see Annexe 14). A Durango apatite reference material was used for Ca, P, F and Cl. Average detection limits are ~450 ppm for F, ~120 ppm for Cl, ~150 ppm for P and Ca, ~110 ppm for Si, and 450–850 ppm for Fe, Ti, La, Ce, Pr and Nd. The analytical accuracy and precision were determined by repeated analyses of the Durango apatite (Annexe 13). Analytical accuracy is 4 % for F, < 20 % for Cl, 1.2 % for CaO, and <30 % for SiO_2. Analytical precision is ~5.5 % for F, < 8 % for Cl, < 0.6 for CaO, and <15 % for SiO_2. Even though the purity of apatite was checked before analyses, analyses were discarded if the electron beam hit fractures, inclusions, or produced mixed signal between apatite and the surrounding mineral (i.e., apatite grain too thin or too small). F, Cl, and OH mole fractions were calculated using the method of Piccoli and Candela (2002). A correction was applied when the calculated F moles fraction was >1 and/or OH mole fraction was < 0, due to a high F wt.% content of apatite (see Annexe 14 for details). Results of the analyses are given in Annexe 14 and Table 2.1.

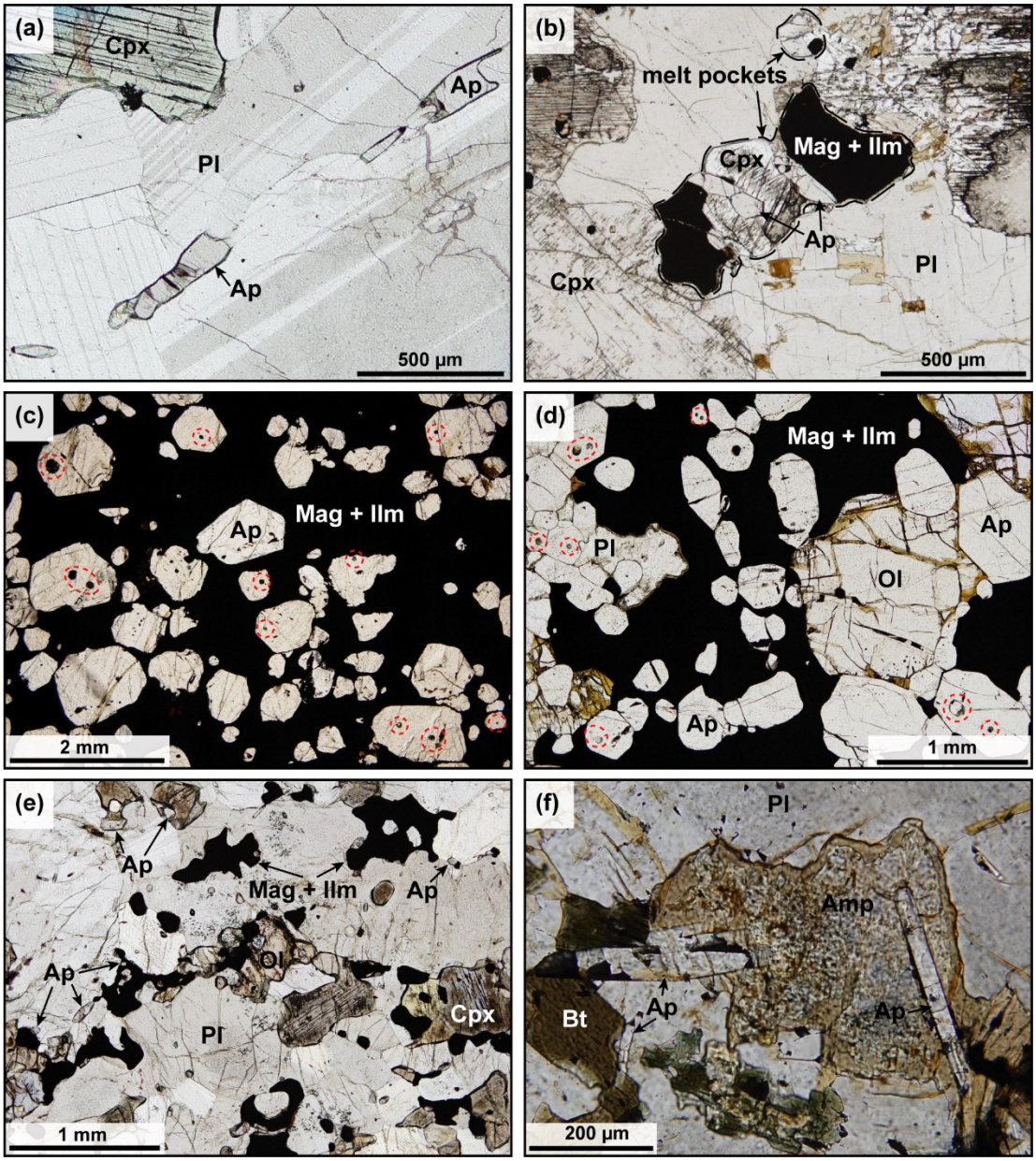

Figure 2.3 – Microphotographs of apatite from the Sept-Iles layered intrusion. (a) intercumulus apatite (subhedral to anhedral) of MCU II, interstitial to plagioclase grains (sample 8–5.5); (b) intercumulus apatite (euhedral) of MCU II, associated with clinopyroxene and Fe–Ti oxides in melt pocket (sample 8–195); (c) cumulus apatite in massive nelsonite, at the base of the Critical Zone, are the largest and most abundant (sample HN-99–46); (d) cumulus apatite in a melanocratic gabbro layer, located higher (11.3 m) in the Critical Zone, are smaller and less abundant (sample S9-214.8); (e) cumulus apatite in a leucocratic gabbro layer, located higher (17.3 m) in the Critical Zone, are small and scarce (<1 vol%) and mostly associated with Fe–Ti oxides in pockets (sample S9-208.8); (f) accessory apatite from the felsic rocks of the Upper Series crystallised as small needles (sample VH-03–42). Dashed red circles in (c) and (d) highlight the presence of rounded Fe– and Si– rich melt inclusions (dark and light, respectively) in apatite as characterised by Charlier et al. (2011). Ap apatite, Bt biotite, Cpx clinopyroxene, Ilm ilmenite, Mag magnetite, Ol olivine, Pl plagioclase. (For interpretation of the references to colour in this figure legend, the reader is referred to the web version of this article.)

Table 2.1 – Average major, volatile and trace element composition of apatite from Sept-Iles Intrusive Suite.

		Felsic part of Sept-Iles Intrusive Suite					
Unit		US	US	PdC	US	PdC	PdC
Rock type / Cumulus assemblage[1]		Granite	Granite	Granite	Granite	Syenite	Granite
Ap (%)		Accessory	Accessory	Accessory	Accessory	Accessory	Accessory
An content[2]		0	0	1.4	3.4	4.2	4.9
Height (m)		940	940	910	870	840	810
Fe–Ti–P[3]							
Location		Manowin	Gde Basque	Gde Basque	Marconi	Gde Basque	Gde Basque
Sample		**VH-03-22**	**VH-03-35**	**VH-03-11**	**VH-03-37**	**VH-03-08**	**VH-03-09**
EMPA (wt.%)	*D.L.*			*n=2*		*n=6*	*n=1*
P_2O_5	0.033	–	–	40.57	–	40.75	38.41
CaO	0.021	–	–	53.07	–	52.57	51.11
SiO_2	0.023	–	–	0.83	–	1.02	1.84
F	0.041	–	–	3.92	–	4.20	3.66
Cl	0.012	–	–	0.01	–	0.01	0.01
Cl/F		–	–	0.003	–	0.004	0.001
$X_{F\ Ap}$		–	–	1.00	–	1.00	0.97
$X_{Cl\ Ap}$		–	–	0.00	–	0.00	0.00
$X_{OH\ Ap}$		–	–	0.00	–	0.00	0.03
LA-ICP-MS[4]	*D.L.*	*n=2*	*n=1*	*n=4*	*n=3*	*n=1*	*n=4*
^{208}Pb	0.010	14.49	29.81	8.56	3.98	7.49	8.56
^{85}Rb	0.420	2.03	7.00	6.04	7.72	1.95	6.16
^{39}K	7.088	37.88	574.98	515.84	257.60	23.46	848.66
^{137}Ba	0.005	3.64	16.89	5.16	3.53	1.94	26.01
^{88}Sr	0.005	332.20	1019.52	197.62	103.25	270.25	206.01
^{23}Na	0.808	1297.60	3037.41	1115.69	648.15	886.11	1875.98
^{139}La	0.001	2549.85	3724.29	3297.11	1100.60	3921.43	3314.94
^{140}Ce	0.001	5725.14	10460.04	7937.95	2943.78	9386.26	8056.97
^{141}Pr	0.001	732.85	1594.72	1081.84	418.20	1248.62	1087.97
^{146}Nd	0.002	3150.12	7137.52	4664.13	2076.05	5285.04	4614.07
^{147}Sm	0.003	668.62	1695.40	1076.01	458.90	1096.64	1046.30
^{153}Eu	0.002	60.93	173.30	76.52	31.50	112.16	81.79
^{157}Gd	0.003	641.70	1587.68	1039.83	449.79	1031.99	1017.62
^{159}Tb	0.000	75.17	216.79	138.25	53.52	133.99	134.27
^{163}Dy	0.001	398.41	1269.39	776.9	290.66	783.00	750.23
^{89}Y	0.002	1927.04	5230.85	3646.83	1408.54	3755.10	3550.10
^{165}Ho	0.000	70.55	219.17	139.85	52.26	136.85	131.66
^{166}Er	0.001	181.53	532.02	337.78	129.53	353.30	333.85
^{169}Tm	0.001	19.49	57.41	38.92	13.19	38.23	39.11
^{172}Yb	0.001	98.19	255.25	186.71	67.65	198.26	194.09
^{175}Lu	0.000	11.55	22.64	20.83	7.38	20.59	21.60
^{232}Th	0.001	24.20	66.09	38.76	4.70	41.66	77.63
^{238}U	0.000	7.38	7.17	7.2	1.71	8.38	10.03
^{55}Mn	0.185	474.51	862.08	417.56	338.06	521.37	516.21
^{25}Mg	0.140	23.44	605.43	34.34	24.25	43.54	283.09
^{90}Zr	0.002	2.17	11.37	4.92	0.45	5.83	2.45
^{45}Sc	0.073	1.85	3.45	1.1	1.29	0.75	2.01
^{93}Nb	0.001	0.17	13.39	4.2	0.04	1.38	2.17
^{49}Ti	0.201	5.47	233.83	134.46	4.05	9.69	12.66
^{51}V	0.029	0.61	1.59	0.72	0.68	0.18	0.24
^{75}As	0.061	24.49	29.27	37.29	10.71	19.62	33.22
∑REE+Y		16311.12	34176.46	24459.46	9501.56	27501.45	24374.57
Eu/Eu*		0.28	0.32	0.22	0.21	0.32	0.24
Sr/Y		0.17	0.19	0.05	0.07	0.07	0.06
Th/Lu		2.10	2.92	1.86	0.64	2.02	3.59

Table 2.1 – (continued)

Mafic part of Sept-Iles Intrusive Suite							
US Syenite	US Monzonite	MCU II pomica-C	MCU II pomica-C	MCU II pomica-C	MCU II pomica-C	MCU II pomica-C	MCU II pomica-C
Accessory	Accessory	1.3	6.7	7.6	19.4	0.1	24.2
18.3	25.5	34.3	35.3	43	45	38.6	41.4
780	750	240	206	150	138	134	111
–	–	-poor layer	**-rich layer**	**-rich layer**	**-rich layer**	-poor layer	**-rich layer**
Marconi	Marconi	RS	RS	1166-95-04	1166-95-04	RS	RS
VH-03-48	**VH-03-42**	**ON-07-120**	**ON-07-125**	**HN-99-01**	**HN-99-04**	**ON-05-53**	**ON-05-07**
n=7	*n=4*	*n=6*	*n=6*	*n=17*	*n=20*	–	–
40.89	41.09	40.71	40.77	41.45	42.49	–	–
53.29	54.44	54.57	54.08	54.95	55.12	–	–
0.88	0.68	0.37	0.21	0.17	0.16	–	–
4.02	3.81	2.92	3.22	3.17	3.46	–	–
0.13	0.03	0.12	0.12	0.12	0.14	–	–
0.032	0.009	0.042	0.038	0.039	0.042	–	–
0.98	0.99	0.77	0.86	0.84	0.92	–	–
0.02	0.01	0.02	0.02	0.02	0.02	–	–
0	0	0.21	0.13	0.14	0.06	–	–
n=6	*n=6*	*n=5*	*n=9*	*n=21*	*n=20*	*n=4*	*n=4*
3.42	5.94	2.07	6.42	1.74	1.88	5.64	5.72
10.83	2.22	1.67	0.09	0.48	1.6	–	–
231.68	178.23	30.49	5.77	9.08	17.74	–	–
5.47	1.51	1.51	3.27	6.64	8.33	4.53	7.67
139.6	192.69	479.39	511.68	607.38	588.78	660.41	772.98
1154.9	529.43	382.12	430.02	212.84	242.6	–	–
1645.72	1284.52	906.59	776.45	444.3	506.39	662.93	471.37
4454.94	3439.9	2424.89	1997.41	1215.94	1298.38	1842.37	1290.13
654.9	492.88	375.76	287.09	185.21	184.1	268.81	187.65
3206.07	2246.33	1808.46	1373.74	932.36	895.97	1308.2	907.97
746.53	508.37	411.05	288.4	225.47	199.46	285.98	201.57
40.69	58.14	56.81	47.52	48.72	41.77	49.15	54.29
730.85	503.89	387.89	271.24	227.82	193.05	280.73	199.1
102.61	62.57	48.55	32.5	26.49	23.37	33.96	23.74
600.77	337.27	266.6	164.52	135.2	128.19	183.59	126.58
3041.78	1721.65	1196.93	734.33	571.35	559.44	820.9	585.71
110.84	62.99	48.07	28.07	22.87	22.35	31.07	21.63
292.41	162.12	120.44	64.57	52.63	54.54	70.16	50.53
33.52	20.06	13.03	6.91	5.76	6.13	6.81	5.3
169.13	109.52	66.11	35.74	32.21	34.56	34.18	27.32
21.06	13.44	8.91	4.6	4.45	4.53	4.45	3.44
14.01	37.15	11.4	19.24	11.31	9.09	10.68	6.9
18.47	19.47	3.64	5.18	4.81	3.65	3.64	1.99
419.99	334.99	419.97	427.92	284.31	254.88	–	–
360.93	33.79	82.87	168.89	249.18	298.48	–	–
1.45	1.88	3.38	2.68	5.63	6.3	–	–
2.37	2.03	1.24	0.77	1.51	0.6	–	–
2.48	0.07	0.01	0.11	0.05	0.01	–	–
60.21	9.64	1.55	75.54	57.92	15.44	–	–
1.83	0.26	0.45	0.54	0.57	1.28	–	–
12.59	18.74	8.44	3.12	8.12	4.05	–	–
15851.83	11023.65	8140.1	6113.11	4130.79	4152.24	5883.3	4156.32
0.17	0.35	0.43	0.51	0.65	0.64	0.52	0.82
0.05	0.11	0.4	0.7	1.06	1.05	0.8	1.32
0.67	2.76	1.28	4.18	2.54	2	2.4	2.01

Table 2.1 – (continued)

MCU II pomica-C	MCU II pomica-C	MCU II pomica-C	MCU II pomica-C	MCU II pomica-C	MCU II pomica-C	MCU II pomica-C	MCU II pomica-C
17.7	16.4	0.9	21.8	0.14	23.99	32	32.2
47	42.9	43.3	49	49.5	50.4	49	50.2
87	78.1	73.7	30	17.3	11.3	0	0
-rich layer	**-rich layer**	-poor layer	**-rich layer**	-poor layer	**-rich layer**	**-rich layer**	**-rich layer**
1166-95-04	DC-9	DC-9	1166-95-04	DC-9	DC-9	1166-95-13	1166-95-11
HN-99-14	**S9-148**	**S9-152,4**	**HN-25**	**S9-208,8**	**S9-214,8**	**HN-99-50**	**HN-99-53**
n=16	*n=6*	*n=5*	*n=12*	*n=6*	*n=6*	*n=21*	*n=13*
43.06	40.44	41.18	42.59	40.9	40.73	42.43	41.44
54.89	53.65	54.57	55.15	53.84	53.92	55.09	55.08
0.16	0.12	0.14	0.14	0.26	0.12	0.1	0.11
3.35	3.33	3.3	3.26	3.69	3.19	3.1	3.03
0.13	0.09	0.1	0.1	0.05	0.08	0.13	0.11
0.04	0.026	0.031	0.031	0.014	0.024	0.043	0.036
0.89	0.88	0.88	0.86	0.98	0.85	0.82	0.81
0.02	0.01	0.01	0.01	0.01	0.01	0.02	0.02
0.09	0.1	0.11	0.12	0.01	0.14	0.16	0.18
n=14	*n=9*	*n=6*	*n=11*	*n=6*	*n=6*	*n=20*	*n=17*
1.37	3.99	1.86	0.7	0.96	1.01	1.53	1.13
2.28	0.43	4.45	0.9	3.5	0.27	1.23	0.43
22.12	17.64	66	12.2	69.98	13.09	18.47	16.42
5.85	4.73	4.62	6.84	6.16	8.25	5.82	7.01
624.78	731.98	506.58	630.31	439.21	776.39	610.57	622.21
189.9	292.7	240.57	173.48	468.65	175.63	162.4	184.28
373.88	492.33	486.51	321.14	1045.43	328.59	225.97	225.42
980.21	1307.82	1298.66	850.71	2620.46	896.56	630.54	628.25
142.96	191.06	185.2	125.12	361.86	143.61	96.68	98.3
723.48	899.07	861.97	640.4	1661.21	734.69	520.12	517.34
166.51	197.23	189.31	146.84	341.3	175.5	125.61	129.17
41.38	45.65	31.26	39.88	37.56	57.38	42.75	43.35
164.71	188.49	186.72	145.24	306.83	176.29	128.64	135.9
19.93	22.78	22.43	17.43	38.07	21.22	14.97	15.61
108.17	121.33	122.25	95.02	201.04	108.21	78.66	79.4
473.41	547.16	602.63	414.16	987.68	456.64	339.68	348.64
18.76	21.17	21.85	16.57	34.79	18.53	13.23	13.36
45.21	49.44	54.19	38.94	84.42	42.76	31.07	30.53
5	5.39	5.78	4.23	8.96	4.4	3.23	3.33
27.39	27.94	29.54	22.43	45.8	22.3	17.36	17.43
3.53	3.73	4	2.92	6	2.94	2.23	2.28
6.21	7.12	11.1	3.14	6.74	3.39	6.1	2.46
2.3	2.21	3.69	1.02	1.56	1.1	1.78	0.86
256.98	271.04	265.46	260.38	302.23	320.57	375.97	299.13
382.24	495.33	324.43	453.4	256.38	508.42	586.11	597.15
4.87	10.32	5.29	3.98	6.34	5.67	7.17	4.89
0.7	1.05	1.34	0.83	1.42	1.12	1.42	2.45
0	0	0.02	0	0.03	0	0	0.01
15.75	16.38	2.01	3.51	2.06	11.62	5.31	54.02
3.84	9.31	9.02	8.74	3.1	10.24	6.53	7.43
3.2	4.29	7.1	3.16	12.33	3.47	2.05	5.5
3294.53	4120.59	4102.28	2881.04	7781.4	3189.62	2270.75	2288.33
0.75	0.71	0.5	0.82	0.35	0.98	1.02	0.99
1.32	1.34	0.84	1.52	0.44	1.7	1.8	1.78
1.76	1.91	2.78	1.07	1.12	1.15	2.73	1.08

Table 2.1 – (continued)

MCU II pomica-C	MCU II pmic-C	MCU II pomic-C	MCU II pmic-C	MCU II pmic-C	MCU II pomi-C	MCU II pomi-C	MCU II pomic-C	MCU II pomic-C
36.2	0.01	0.01	0.01	0.01	0.01	0.01	0.01	0.01
55.7	50.7	58.5	53.8	57.9	62.5	62.9	60.2	57.4
0	-46	-423	-690	-845	-1210	-1795	-2338	-2411
-rich layer	--	--	--	--	–	–	–	–
1166-95-01	LHS	LHS	DC-8	DC-8	DC-8	DC-8	LHS	DC-9
HN-99-46	**ON-07-157**	**ON-07-149**	**8-5,5**	**8-195**	**8-640,5**	**8-1355**	**ON-07-41**	**9-337**
n=22	*n=6*	*n=3*	*n=6*	*n=6*	*n=2*	*n=6*	*n=2*	*n=4*
42.33	41.53	41.06	40.28	41.31	40.6	39.86	41.04	43.12
55.13	55.73	55.28	54.76	55.83	55.19	54.6	54.86	55.85
0.1	0.15	0.12	0.13	0.14	0.15	0.12	0.15	0.12
3.05	3.68	2.02	2.68	2.2	1.97	2.42	2.45	3.21
0.1	0.22	0.69	0.42	0.48	0.43	0.22	0.32	0.26
0.034	0.061	0.343	0.156	0.216	0.219	0.091	0.129	0.081
0.81	0.97	0.54	0.71	0.58	0.52	0.64	0.65	0.85
0.02	0.03	0.1	0.06	0.07	0.06	0.03	0.05	0.04
0.18	0	0.36	0.23	0.35	0.41	0.33	0.3	0.11
n=29	*n=6*	*n=3*	*n=6*	*n=4*	*n=1*	*n=6*	*n=2*	*n=4*
0.57	2.3	2.59	1.08	6.48	2.43	1.08	1.83	0.72
1.55	0.09	1.7	2.17	1.12	2.05	1.88	0.81	0.13
20.1	5	30.14	28.98	299.61	23.45	25.02	17.29	15.07
6.41	1.28	5.61	7.64	10.48	2.38	2.36	6.99	11.35
488.13	588.05	534.31	645.68	497.66	522.12	471.83	566.18	739.41
161.66	243.23	215.45	144.74	18610.91	137.9	181.48	225.1	111.2
253.95	516.4	297.41	325.79	241.55	238.43	215.17	305.68	246.63
699.25	1285.39	870.08	823.96	722.99	724	654.52	854.98	685.77
105.66	175.79	134.94	120.54	113.09	114.77	105.82	134.04	107.99
555.86	772.24	675.91	592.39	576.64	588.53	559.55	661.01	565.01
132.47	175.51	161.2	134.4	130.64	138.61	138.4	150.27	131.38
39.02	33.56	29.22	36.34	28.14	27.9	22.32	35.89	39.28
135.32	177.88	157.44	130.49	129.76	138.08	142.79	146.46	136.78
15.98	23.45	19.65	15.08	14.2	15.71	17.01	17.41	15.14
84.84	123.73	99.63	77.33	65.32	82.02	91.52	85.47	75.28
374.48	620.95	452.61	351.13	324.15	422.78	439.77	386.62	326.64
14.47	22.32	17.24	13.1	10.92	15.06	15.67	15.04	12.66
33.48	53.66	40.69	29.32	23.59	38.48	36.8	35.15	28.09
3.39	5.92	4.16	2.99	2.28	3.95	3.94	3.68	2.66
17.61	29.63	20.74	15.56	10.79	20.74	19.48	18.39	13.93
2.18	3.74	2.65	2.01	1.45	2.11	2.61	2.43	1.72
2.82	18.78	39.94	17.97	12.11	33.29	13.07	17.44	10.97
0.77	6.14	7.57	3.52	2.64	8.51	3.44	4.58	2.7
267.96	349.39	406.38	378.99	243.53	98.59	291.97	387.86	258.49
546.51	343.97	440.01	489.23	4995.1	206.95	187.17	682.36	686.53
3.6	1.94	5.36	4.43	9.09	5.65	8.89	7.05	4.82
1.02	0.75	1.12	1.11	2.05	0.96	0.89	0.75	0.96
0.01	0.01	0.01	0.01	0.14	0	0.01	0	0.04
4.91	1.98	1.21	0.99	66.57	0.6	1.1	0.78	132.05
7.06	5.88	37.31	15.9	21.73	31.67	23.83	27.34	23.32
2.25	2.62	3.76	4.84	6.27	6.63	4.47	2.84	1.46
2467.97	4020.18	2983.56	2670.45	2395.5	2571.18	2465.39	2852.52	2388.95
0.88	0.57	0.55	0.83	0.65	0.61	0.48	0.73	0.89
1.3	0.95	1.18	1.84	1.54	1.23	1.07	1.46	2.26
1.3	5.02	15.07	8.94	8.36	15.78	5.01	7.16	6.38

Ap apatite; *D.L.* detection limit; *RS* Rivière des Rapides section.

[1]Cumulus assemblages as defined by Namur et al. (2010) and following the classification of Irvine (1982): po-C plagioclase + olivine (troctolite); pomi-C plagioclase + olivine + Fe–Ti oxide minerals (Fe–Ti oxide-bearing troctolite); pomic-C, pmic-C, pomica-C plagioclase + Fe–Ti oxide minerals + clinopyroxene ± olivine ± apatite (layered gabbro).
[2]Anorthite content of plagioclases (An%). The values for the felsic rocks are from Namur et al. (2011) and values for the mafic rocks of MCUII are from Nabil (2003) and Namur et al. (2010).
[3]Fe–Ti–P-rich and -poor layers of the Critical Zone. Those written in bold correspond to couples of Fe-Ti-P-rich and -poor layers stratigraphically close where apatite compositions are compared.
[4]Values are in ppm. Elements are ordered according to the proposed new multielement diagram (see text for details) and only include elements used in this study; the full suite of trace elements, ordered by isotopic mass, is given in Annexe 22.
[5]The LA-ICP-MS detection limits correspond to the average of the detection limits obtained for this element for all analyses of the project. determined on the apatite standard UQAC-APA with a 55 µm beam by the method of Longerich et al. (1996). See details in Annexe 20.

2.5.2 LA-ICP-MS

Fifty-two trace element concentrations were determined in apatite by LA-ICP-MS at LabMaTer, Université du Québec à Chicoutimi. The system is a Resonetics Resolution M-50 193 nm Excimer laser coupled with an Agilent 7900 ICP-MS. Details of the analytical protocol is given in Annexe 15 to 19. Lines were ablated across each apatite grain (i.e., through core and rims) using a beam size ranging from 15 µm to 55 µm, depending on the apatite size, with an ablation rate of 15 Hz, a fluence set to 5 J/cm^2, and a dwell time of 10 µm/s. Analyses begin with a 30 s gas blank (i.e., background) followed by 60 to 100 s of signal, and a minimal flushing out time of 90 s between each analysis. The Ca content, as determined by EMPA for each apatite grain, was used as the internal standard for quantification of the LA-ICP-MS results. The certified reference material NIST610 was used for calibration (using a 55 µm beam), and secondary reference materials (NIST612, GSD, and in-house apatite UQAC-APA) were used for monitoring data quality. The in-house apatite reference material is a pressed powder made of natural, igneous apatite from Lac à Paul Ti–P deposit, Lac St Jean (Quebec). Repeated analyses of these reference materials indicate that most trace elements are determined with accuracy better than ± 4 % when using a 55 µm beam, and better than ± 10 % when using a 15 µm beam, compared to certified/working values (Annexe 15 to 20). The precision is also better than 5 % for all elements except Cl and K. Data processing was performed using the Iolite 4 software (Paton et al., 2011). Thirty-one elements, of the 52 analysed, are commonly above detection limit, i.e., Na, Mg, K, Sc, Ti, V, Mn, As, Rb, Sr, Zr, Nb, Ba, REE + Y, Pb, Th and U. A value below the limit of detection is replaced by the value of the limit of detection given for the analysis. Elements that are mostly below detection limits (Li, B, S, Cl, Cr, Co, Ni, Cu, Mo, Sn, Sb, W, and Bi) are not used in this study. Al, Na, K, Si, Mg, Fe, Ti, Mn and Ce are used to monitor for inclusions. Most analyses

were performed at LabMaTer (UQAC), and 4 samples (ON-07-125, ON- 05-53, ON-05-07 and S9-148) were analysed at the Research School of Earth Sciences (RSES; The Australian National University) using the same analytical protocol. Results are given as supplementary information in Annexe 21 and summarised in Table 2.1.

Following the same analytical protocol, LA-ICP-MS analyses were also performed on plagioclase grains from 3 couples of stratigraphically close Fe–Ti–P-poor and -rich samples in order to check if they crystallised from a trapped liquid. In both type of layer, lines were ablated across big (0.5 – 2 mm) plagioclase grains, which are likely to record core to rim trace element zonation as an effect of crystallisation from an interstitial, trapped liquid (i.e., trace elements-enriched plagioclase overgrowth). Lines were also ablated across smaller plagioclase grains (<0.3 mm), which could have entirely crystallised from, or reacted with, the trapped liquid. Results are given as supplementary information in Annexe 22 and summarised in Table 2.2.

2.5.3 A new multi-element diagram specific to apatite

To date, most apatite studies focused on REE + Y and a few trace elements, some of which being usually not displayed on multielement diagrams (e.g., Tollari et al., 2008; Van Tongeren and Mathez, 2012; Xing et al., 2014; She et al., 2016; Jia et al., 2020; Mercer et al., 2020; Pedersen et al., 2021; and others). Belousova et al. (2002) proposed a multi-element diagram where REE + Y and 9 other trace elements are ordered by decreasing ionic radius. However, our apatite dataset includes over 30 trace elements and requires the creation of a new diagram in order to display the full dataset.

Our new multi-element diagram has been designed specifically for a full suite of trace elements in apatite (31 elements analysed by LA-ICP-MS, and F, Cl and Si analysed by EMPA), which are ordered from left to right as follows (Fig. 2.8): (1) volatile elements in the X-site, as determined by EMPA; (2) Large Ion Lithophile Elements, then High Field Strength Elements, mainly substituting to Ca in the Ca1 site (Pan and Fleet, 2002; Hughes and Rakovan, 2015) and ordered by decreasing ionic radius. Pb is however placed before Rb (instead of between Ba and Sr) to smooth the pattern, and Th and U are placed after the REE; and (3) High Field Strength Elements substituting for P in the Z-site (Pan and Fleet, 2002; Hughes and Rakovan, 2015), ordered by decreasing ionic radius, and including Si determined by EMPA. The values of ionic radii used for the construction of this diagram

are given in coordination IX, and in coordination VIII (Mn^{2+}, Mg^{2+} and Sc^{3+}) or VI (Nb^{3+}) when values for coordination IX were not available (Shannon, 1976). Data are normalised to the C1 chondrite of McDonough and Sun (1995).

This new order places the analysed elements according to their expected compatibility into apatite. The choice has been made to consider substitutions in the Ca1 (coordination IX) site, because Ca2 site is in coordination VII and less elements can substitute (Pan and Fleet, 2002). Elements can more easily substitute to Ca^{2+} in the Ca1 site if their ionic radius is ±15 % of this of Ca^{2+} in coordination IX, i.e., between 1.00 and 1.36 Å (Goldschmidt's rule). Thus, the elements are ordered by increasing (Pb to MREE), then decreasing (MREE to Si) compatibility into apatite, the elements between Sr and U, as well as Pb, being the most compatible (Fig. 2.8; Watson and Green, 1981; Prowatke and Klemme, 2006).

Table 2.2 – Average trace element composition of plagioclase from the Sept-Iles Intrusive Suite

		Mafic part of intrusion					
Unit		MCU II	MCU II	MCU II	MCU II	MCU II	MCU II
Cumulus assemblage[1]		pomica-C	pomica-C	pomica-C	pomica-C	pomica-C	pomica-C
Ap (%)		1.3	6.7	16.4	0.9	0.14	23.99
An content[2]		34.3	35.3	42.9	43.3	49.5	50.4
Height (m)		240	206	78.1	73.7	17.3	11.3
Fe–Ti–P[3]		-poor layer	**-rich layer**	**-rich layer**	-poor layer	-poor layer	**-rich layer**
Location		RS	RS	DC-9	DC-9	DC-9	DC-9
Sample		**ON-07-120**	**ON-07-125**	**S9-148**	**S9-152.4**	**S9-208.8**	**S9-214.8**
LA-ICP-MS[4]	*D.L.*	*n=8*	*n=6*	*n=5*	*n=9*	*n=7*	*n=7*
^{208}Pb	0.010	6.26	9.86	6.13	3.83	5.36	1.17
^{85}Rb	0.420	2.96	2.36	0.47	0.34	2.80	0.39
^{39}K	7.088	7574.77	4704.29	1871.02	3707.64	14050.51	834.16
^{137}Ba	0.005	1406.48	1031.87	484.01	516.95	2502.63	519.46
^{88}Sr	0.005	1185.56	996.78	1110.26	1150.46	1185.68	1521.39
^{23}Na	0.808	51286.49	49147.89	43349.59	38941.65	53325.89	40841.01
^{139}La	0.001	12.26	6.60	6.71	7.36	16.38	3.44
^{140}Ce	0.001	18.28	10.78	10.31	11.56	21.89	5.72
^{141}Pr	0.001	1.72	1.06	0.97	1.12	1.87	0.60
^{146}Nd	0.002	5.48	3.59	3.17	3.61	5.53	2.24
^{147}Sm	0.003	0.66	0.50	0.33	0.40	0.57	0.29
^{153}Eu	0.002	11.39	7.25	2.99	3.01	6.69	2.63
^{157}Gd	0.003	0.41	0.35	0.22	0.26	0.62	0.17
^{159}Tb	0.000	0.05	0.04	0.02	0.02	0.03	0.02
^{163}Dy	0.001	0.23	0.19	0.08	0.11	0.21	0.15
^{89}Y	0.002	1.01	0.88	0.32	0.38	0.43	0.27
^{165}Ho	0.000	0.04	0.03	0.01	0.01	0.04	0.02
^{166}Er	0.001	0.10	0.08	0.03	0.02	0.08	0.05
^{169}Tm	0.001	0.01	0.01	0.00	0.00	0.06	0.01
^{172}Yb	0.001	0.09	0.06	0.02	0.02	0.02	0.10
^{175}Lu	0.000	0.00	0.00	0.00	0.00	0.06	0.12
^{232}Th	0.001	0.09	0.03	0.00	0.00	0.10	0.03
^{238}U	0.000	0.01	0.01	0.01	0.00	0.06	0.08
^{55}Mn	0.185	65.46	88.57	731.23	69.11	13.42	103.05
^{25}Mg	0.140	751.74	1093.24	6019.38	1360.79	383.56	1989.91
^{90}Zr	0.002	14.22	0.95	0.10	0.08	1.01	0.28
^{45}Sc	0.073	4.14	3.55	3.05	2.56	3.80	3.02
^{93}Nb	0.001	0.11	0.24	0.02	0.01	0.16	0.06
^{49}Ti	0.201	259.82	406.47	318.91	257.40	389.48	404.16
^{51}V	0.029	0.59	0.65	0.76	0.59	6.52	2.37
^{75}As	0.061	0.15	0.10	0.25	0.23	2.97	1.35
∑REE+Y	–	51.72	31.42	25.18	27.88	54.49	15.84
Eu/Eu*	–	61.90	50.45	31.89	26.49	34.01	33.05

Ap apatite; *D.L.* detection limit; *RS* Rivière des Rapides section.

[1] Cumulus assemblages. as defined by Namur et al. (2010) and following the classification of Irvine (1982): pomica-C plagioclase + Fe–Ti oxide minerals + clinopyroxene + olivine + apatite (layered gabbro).

[2] Anorthite content of plagioclases (An%). The values for the felsic rocks are from Namur et al. (2011) and values for the mafic rocks of MCUII are from Nabil (2003) and Namur et al. (2010).

[3] Fe–Ti–P-rich and -poor layers of the Critical Zone. Those written in bold correspond to couples of Fe-Ti-P-rich and -poor layers stratigraphically close where apatite compositions are compared.

[4] Values are in ppm. Elements are ordered according to the proposed new multielement diagram (see text for details) and only include elements used in this study; the full suite of trace elements ordered by isotopic mass is given in Annexe 22.

[5] The LA-ICP-MS detection limits correspond to the average of the detection limits obtained for this element for all analyses of the project determined on the apatite standard UQAC-APA with a 55 µm beam by the method of Longerich et al. (1996). See details in Annexe 20.

2.6 Results

2.6.1 Volatile composition of apatite

The volatile composition of apatite was determined on 211 individual apatite grains from 26 samples covering the whole MCUII, as well as the felsic rocks of the Upper Series and Pointe du Criard sill (Fig. 2.2). All the apatites analysed in this study are fluorapatite with F > 2 wt%, as is typical of apatite from the evolved part of mafic layered intrusions (Boudreau et al., 1995). However, their Cl content significantly varies according to rock type (Fig. 2.4; average composition is given in Table 2.1).

Cumulus and intercumulus apatite define two different fields in the F-Cl-OH ternary space (Fig. 2.4). Cumulus apatite contains >75 % mole fraction of F and <5 % and 25 % mole fractions of Cl and OH, respectively. In contrast, intercumulus apatite generally contains less F and more OH (50–75 and 20–45 % mole fractions, respectively) than cumulus apatite, with the most discriminating feature being significantly higher Cl mole fractions (5 to 15 %). Apatite from the felsic rocks contained high F wt.% values, some of them that needed correcting when converted to mole fraction (see Section 2.5.1). Notwithstanding, the apatite from the felsic rocks are centered on the F-pole, with <5 % mole fractions of Cl and OH (Fig. 2.4).

The variation in the concentration of volatile composition of intercumulus, cumulus, and felsic apatite with stratigraphic position in Sept Iles layered intrusion is shown in Fig. 2.5 (Table 2.1). Overall, intercumulus apatite has the highest Cl and lowest F (0.2 to 0.8 wt% Cl, and ~1.9 to 3.3 wt% F, respectively). Two intercumulus samples, located at the bottom of MCU II (sample 9–337; ~2411 m) and just below the base of the Critical Zone (sample ON-07–157; ~46 m), have a F content typical of cumulus apatite with ~3.4 wt% F (Fig. 2.5a). They also display Cl content lower than the average for intercumulus apatite (i.e., from 0.1 up to 0.4 wt%; Fig. 2.5b). Despite a relatively large within-sample variation, intercumulus apatite displays no clear variation of F with height (Fig. 2.5a), but Cl seems to increase from the bottom of MCU II towards the base of the overlying Critical Zone (~0.2 to 0.7 wt%; Fig. 2.5b). Cumulus apatite has higher F (2.8 to 4.0 wt%) and lower Cl (0.05 to 0.2 wt %) contents than intercumulus apatite (Fig. 2.5). There is a slight increase (~3.1 to 3.5 wt%) then

decrease of F (~3.5 to 2.9 wt%) towards the top of the Critical Zone (Fig. 2.5a) whereas Cl content is increasing very slightly (~0.10 to 0.12 wt%; (Fig. 2.5b). Tollari et al. (2008) also showed that the Cl content in apatite, as well as in whole rock, slightly increases upwards in the Critical Zone cumulate pile. Apatite from the felsic samples have the highest F (~3.7 to 4.2 wt%) and lowest Cl (<0.012 to ~0.13 wt%) concentrations of all samples, which are constant (Fig. 2.5).

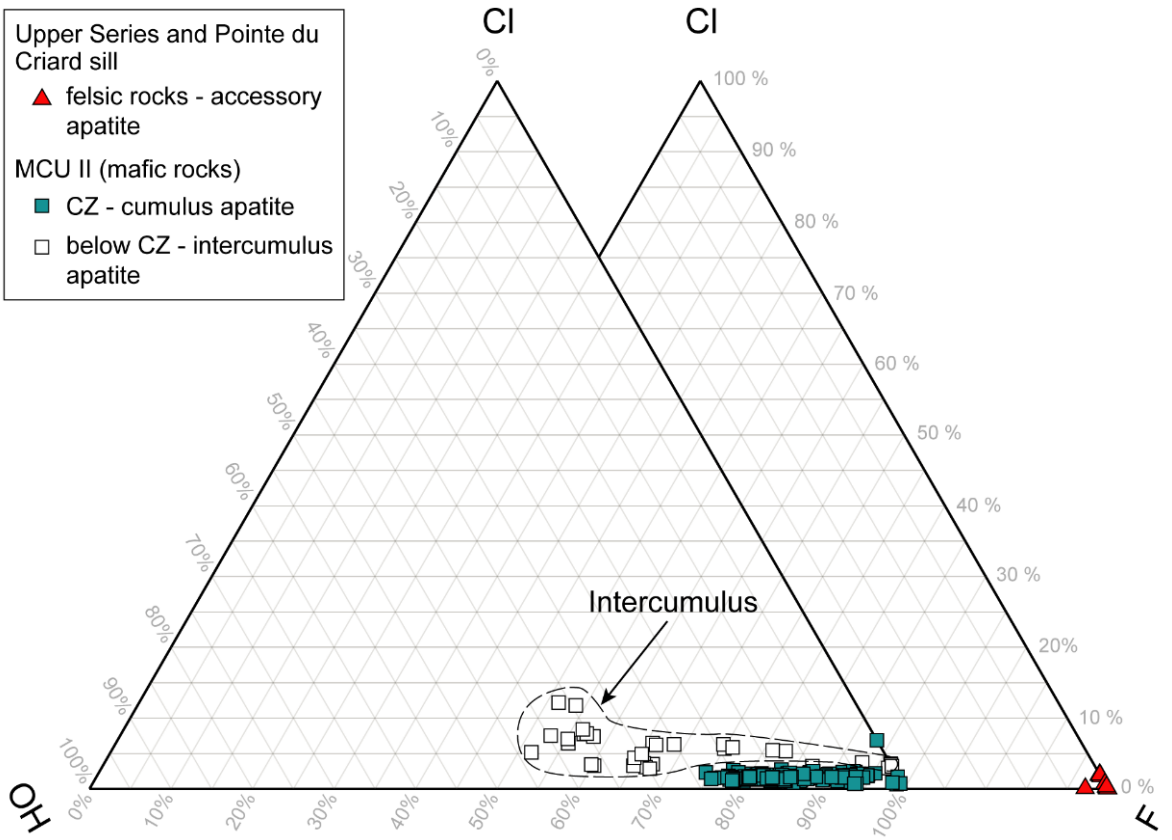

Figure 2.4 – Variations of F-Cl-OH mole fraction in apatite as a function of apatite type in the Sept-Iles layered intrusion. Stoichiometric F, Cl and OH fractions were calculated according to the approach of Piccoli and Candela (2002). Intercumulus apatite is richer in Cl and OH compared to cumulus apatite. Apatite from the felsic rocks have a more homogeneous composition and are the most enriched in F. CZ Critical Zone.

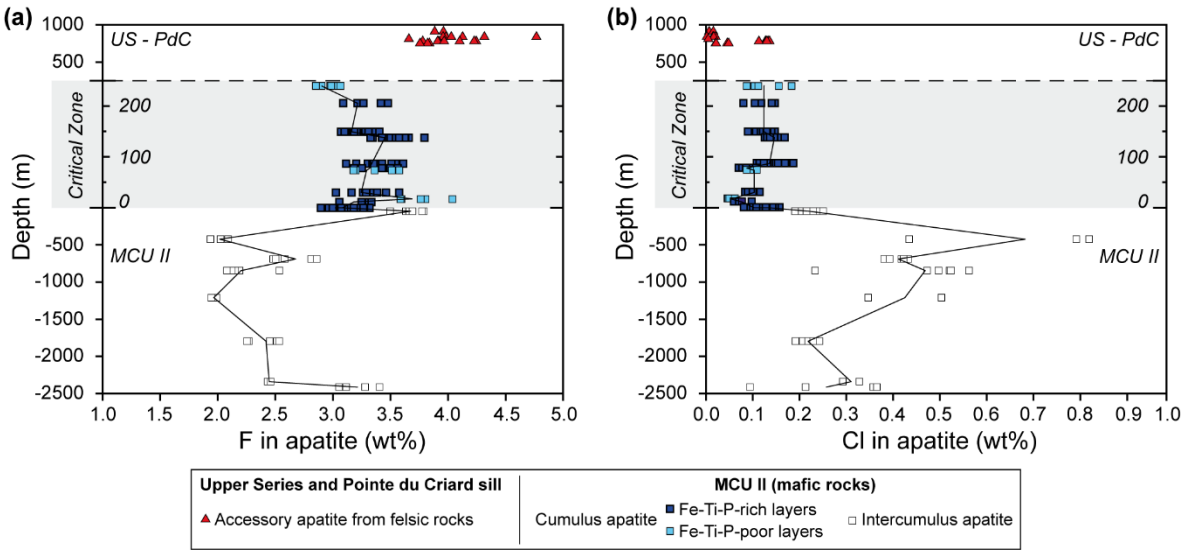

Figure 2.5 – The volatile composition of F (a) and Cl (b) of apatite (individual grains) plotted against stratigraphic depth within the Sept-Iles layered intrusion. Legend as in Fig. 2.4. Black lines link the average F and Cl composition of each sample. Scale within the Critical Zone (containing cumulus apatite) has been enlarged for clarity. Note the clear difference in volatile content between the 3 groups of apatite. As no depth value was available for the felsic samples (PdC Pointe du Criard sill; US Upper Series) they were ordered by decreasing anorthite content towards the top. Detection limit for Cl is 0.012 wt%.

2.6.2 Trace element composition of apatite

2.6.2.1 Within sample variation

Before presenting inter-sample variation of trace elements in detail, 7 samples from the Critical Zone were analysed in greater detail to assess if within-sample chemical variations (i.e., heterogeneity) within apatite is important. To ascertain if apatite composition is influenced by its surrounding minerals, the following types of apatite were analysed for each sample (Fig. 2.6): 1) apatite fully enclosed within different host phases (e.g., plagioclase, olivine, magnetite, etc.), 2) apatite at the interface between 2 phases (e.g., magnetite and ilmenite), and 3) apatite at the interface of multiple phases (i.e., in visible contact with ≥2 grains of ≥2 different minerals). However, even if an apatite appears to be in a single mineral grain in a thin section, the view is in 2 dimensions and it remains possible that another mineral lies below or above the apatite grain. In each thin section, 3 to 4 apatite grains of different sizes were analysed in each type of enclosing mineral. It led to the analysis of 11 to 29 apatite grains per thin section, depending of the occurrence of apatite within the different kinds of mineral phases.

At the sample-scale, there is no significant and systematic variation of any of the 31 elements, analysed by LA-ICP-MS, according to the type of encasing mineral(s) or apatite grain size (Fig. 2.6a). This indicates that subsolidus equilibration through apatite and adjacent minerals is likely to be negligible; i.e., there was no gradient of chemical potential for any element. In addition, no significant chemical zonation has been observed in all the analysed apatite crystals. As a result, for the other samples, on average between 4 and 8 grains per thins section were analysed and deemed to be representative of the sample.

The same exercise was made for apatite grains from the felsic rocks of Sept-Iles layered intrusion. Thirty-three apatite grains were analysed on 8 thin sections. Here, we observe large within-sample variations which do not appear to be systematic and there is no apparent correlation between the enriched element and the nature of the host mineral (Fig. 2.6b). We therefore consider that these variations are likely not caused by subsolidus reequilibration. Instead, heterogeneity could be due to crystallisation of apatite grains from a range of late-stage melt compositions.

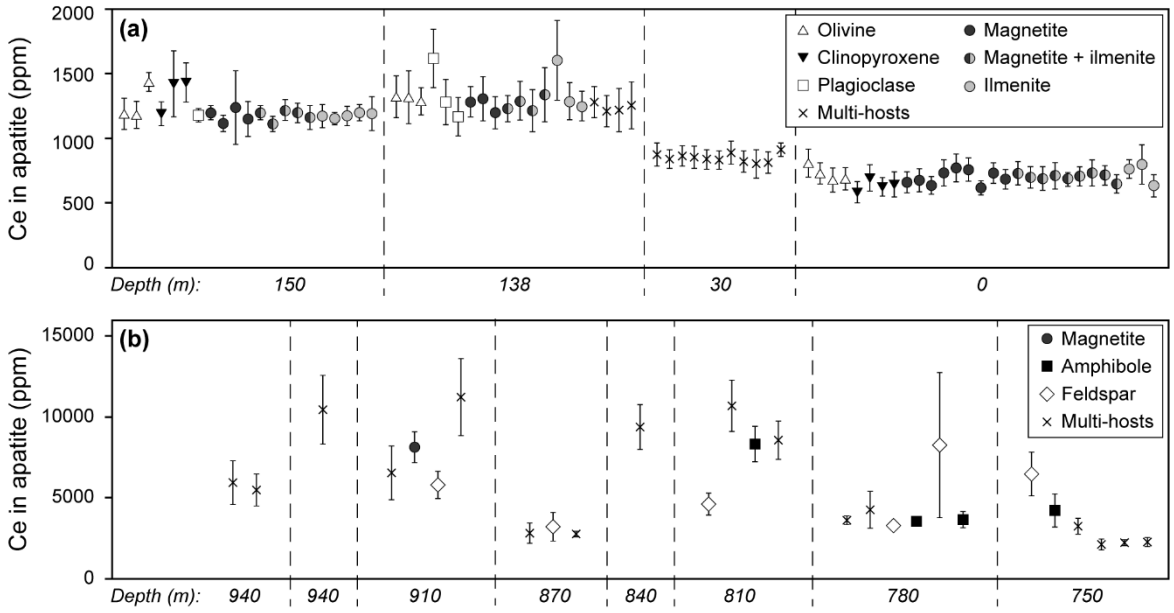

Figure 2.6 – Ce concentration of apatite analysed by LA-ICP-MS in (a) 4 representative samples from Sept-Iles Critical Zone and (b) the felsic samples from the Upper Series and Pointe du Criard sill. Note that there is no systematic and significant variation between apatite included in different host phases within the same sample, indicating that there is negligible subsolidus re-equilibration. Multi-hosts apatite analyses (x) indicate apatite included in, or in contact with, >2 mineral phases. Analytical error bars are 2σ.

2.6.2.2 Variation with stratigraphy and between intercumulus and cumulus apatite

The trace element content of apatite was determined in 31 samples on 240 individual apatite grains (Fig. 2.2; Table 2.1; Annexe 21). The variation of 6 representative trace elements (REE + Y, Th, Eu/Eu*, Sr, V, and Mg) with stratigraphic position in the Sept-Iles layered intrusion is shown in Fig. 2.7 to illustrate the different behaviours of trace elements during fractional crystallisation (see Annexe 23 for chemicostratigraphic variations of the other trace elements). Those elements have been chosen because they are commonly used to track fractionation using whole rock analyses, and most display marked variations with stratigraphic depth.

Elements that increase up sequence/behave incompatibly (REE + Y, Na, As, Pb, Th, U ± K, Rb, Nb, Sc, Ti, Mn): The REE + Y content of intercumulus apatite remains constant or slightly increases throughout the MCU II, with an average value of 2500 ppm (Fig. 2.7a). Cumulus apatite at the bottom of the Critical Zone has REE + Y concentrations close to those of intercumulus apatite (i.e., ~2400 ppm). There is then an overall increase of REE + Y, including Eu, in cumulus apatite towards the top of the Critical Zone (<7800 ppm) and apatite from the felsic rocks (Upper Series and Pointe du Criard sill) display the highest REE + Y concentrations, with ~7200 to ~31000 ppm (Fig. 2.7a). This large-scale upwards increase in concentration, at least in the Critical Zone, also applies to Na, As, Pb, Th and U (Table 2.1; Annexe 23). The increase of REE + Y, Th and U from the base towards the top of the Critical Zone is in agreement with the previous results of Tollari et al. (2008). Elements such as Th (Fig. 2.7b) and U show a slightly different behaviour than REE + Y. Although they continuously increase in concentration in the Critical Zone and towards the felsic rocks, their concentrations are higher in intercumulus apatites than in cumulus apatites from the Critical Zone (averages of ~18 ppm and 7 ppm respectively). A similar behaviour was observed in rocks from Skaergaard layered intrusion (Namur and Humphreys, 2018). An extra level of complexity is observed in the Critical Zone, with meter-scale heterogeneity between Fe–Ti–P-rich and Fe–Ti–P-poor layers; apatite from the Fe–Ti–P-rich layers contains less REE + Y and As, and more Pb, than apatite from Fe–Ti–P-poor layers. However, there is no clear difference in Na, U and Th between apatite crystals from the two types of layers (Fig. 2.7a; Table 2.1; Annexe 23).

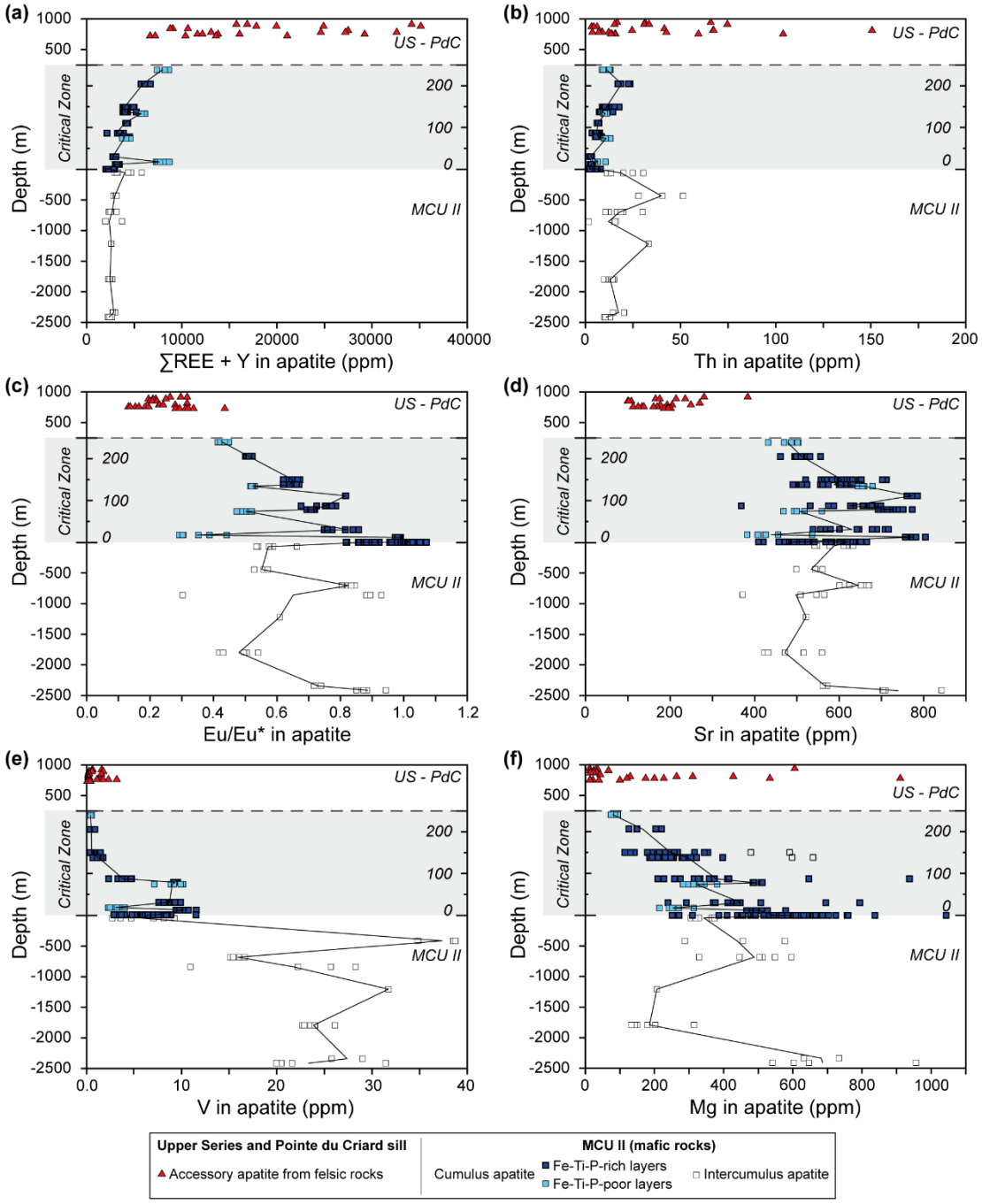

Figure 2.7 – Variation of selected trace elements in apatite with stratigraphic depth within the Sept-Iles layered intrusion: (a) total rare earth elements (∑REE) + Y, (b) Th, (c) Europium anomaly ($Eu/Eu^* = (2Eu/Eu_N)/[(Sm/Sm_N + Gd/Gd_N)]$), (d) Sr, (e) V, and (f) Mg in apatites from the mafic rocks of the MCUII (white squares - intercumulus apatite; blue squares - cumulus apatite) and from the felsic rocks of the Upper Series and Pointe du Criard sill (red triangles). Each data point corresponds to an apatite analyse. Black lines link the average composition of each sample. Note that an increase in ∑REE + Y and a decrease in Eu/Eu*, Sr and V is observed within the cumulus apatite from the Critical Zone towards the felsic rocks. The higher V content of intercumulus apatite distinguishes them from cumulus apatite. PdC Pointe du Criard sill; US Upper Series. (For interpretation of the references to colour in this figure legend, the reader is referred to the web version of this article.)

The Eu anomaly (Eu/Eu*, expressed as $2Eu_N/(Gd_N + Sm_N)$, N being chondrite-normalised) of apatite (Fig. 2.7c) is mostly negative and shows large variations for both intercumulus (~0.4 to 0.95) and cumulus apatite (0.3 to 1.1). However, cumulus apatite has an overall increasingly negative Eu anomaly from the base towards the top of the Critical Zone (~1 to ~0.4), which is correlated with increasing REE + Y content of apatite (Fig. 2.7a and 7c). This has also been observed in the previous study from Tollari et al. (2008). Apatite from the felsic rocks have the strongest negative anomalies, with Eu/Eu* values of 0.35 to ~0.1 (Fig. 2.7c), correlating with the highest REE + Y contents (Fig. 2.7a). The decreasing Eu/Eu* up sequence is thus deemed an artifact of the REE (i.e., Sm and Gd) increasing up sequence (~200 ppm difference between base and top of the Critical Zone), while Eu only shows a slight increase (~15 ppm difference between base and top). Again, there are marked differences between apatite from Fe–Ti–P-rich (melanocratic) and Fe–Ti–P-poor (leucocratic) layers: apatite from the Fe–Ti–P-poor layers have more pronounced negative Eu anomalies (0.3 to 0.5) than the Fe–Ti–P-rich, melanocratic layers (0.5 to 1.1).

There is no clear variation of K, Rb, Nb, Sc with stratigraphic position in the mafic portion of Sept Iles layered intrusion, but these elements are enriched in the apatite crystals from the overlying felsic rocks compared to those from the MCU II (K: ~346 vs ~26 ppm; Rb: ~6 vs ~1.3 ppm; Nb: ~2.1 vs ~0.02 ppm; and Sc: ~1.9 vs ~1.2 ppm, respectively). The concentrations of Ti and Mn are similar for apatite throughout the stratigraphy, with average values of ~25 ppm and ~315 ppm respectively. Only Mn concentration increases to ~400 ppm in apatite at the very top of the Critical Zone (see Table 2.1; Annexe 23). This is consistent with the increase in Mn measured by Méric (2011) in magnetite and ilmenite.

Elements that decrease up sequence/behave compatibly (Sr, V, Mg, Zr, Ba): Sr in intercumulus apatite is largely scattered (~575 ± 100 ppm) throughout the lower part of MCU II. There is also a wide scatter of Sr values in cumulus apatites, with a clear decrease only observed in the last 3 samples towards the top of the Critical Zone (from ~600 to ~480 ppm) (Fig. 2.7d). The lowest Sr values are measured in the felsic rocks (~220 ppm) at the top of the intrusion (Fig. 2.7a). The trend observed for Sr also applies to Zr and Ba, with the exception of Ba concentration of apatite from the felsic rocks being similar to those of cumulus apatite at the top of the Critical Zone (see Table 2.1;

Annexe 23). Apatite from the Fe–Ti–P-rich layers is enriched in Sr and Ba compared to apatite from the Fe–Ti–P-poor layers. There is however no significant difference in Zr abundance.

There is a marked difference in V concentration between intercumulus and cumulus apatite (Fig. 2.7e). Intercumulus apatite has a V content > 12 ppm, with the exception of the sample located just below the base of the Critical Zone. This sample has V values similar to cumulus apatite, where V content is systematically < 12 ppm (Fig. 2.7e). In the Critical Zone, V decreases from ~8 ppm to almost ~0.5 ppm from the base to the top. Apatite from the Fe–Ti–P-poor layers display lower V concentrations than apatite from Fe–Ti–P-rich layers, the difference being more pronounced towards the base of the Critical Zone. Apatite from the felsic rocks is also V-poor (average of 0.8 ppm).

The Mg content of apatite (Fig. 2.7f) continually decreases from the bottom of the MCU II to the base of the Critical Zone (intercumulus apatite, from ~690 to ~345 ppm Mg), then from the base towards the top of the Critical Zone (cumulus apatite, from ~570 to ~83 ppm Mg) and the felsic rocks (Mg in apatite ~25 ppm, plus some scattered values of ~100 to ~600 ppm). Apatite crystals from the Fe–Ti–P-poor layers have systematically lower Mg concentrations (by 100 to 250 ppm) than apatite from Fe–Ti–P-rich layers.

2.6.2.3 Multi-element diagram

Chondrite-normalised multi-element diagrams reveal clear differences between the different portions of the Sept-Iles Intrusive Suite (i.e., felsic vs mafic, cumulus vs intercumulus in the mafic portion) for a full suite of trace elements (Fig. 2.8; Annexe 24 to 26). In addition to higher Cl and lower F contents, intercumulus apatite has overall less REE + Y and more Th, U, V and Si than cumulus apatite (Fig. 2.8). The REE + Y slope (e.g., $(La/Lu)_N$) is steeper and the ratio Th/Lu higher than those of cumulus apatite. Intercumulus apatite also have slightly less HREE than cumulus apatite, that may be due to the presence of accessory phases (e.g., zircon, amphibole) retaining these elements. Apatite from the felsic rocks have higher total abundance of REE + Y and a more pronounced negative Eu anomaly than apatite from the mafic cumulates of MCU II. They are also enriched in F, Nb and As, and depleted in Cl, compared to cumulus apatite (Fig. 2.8).

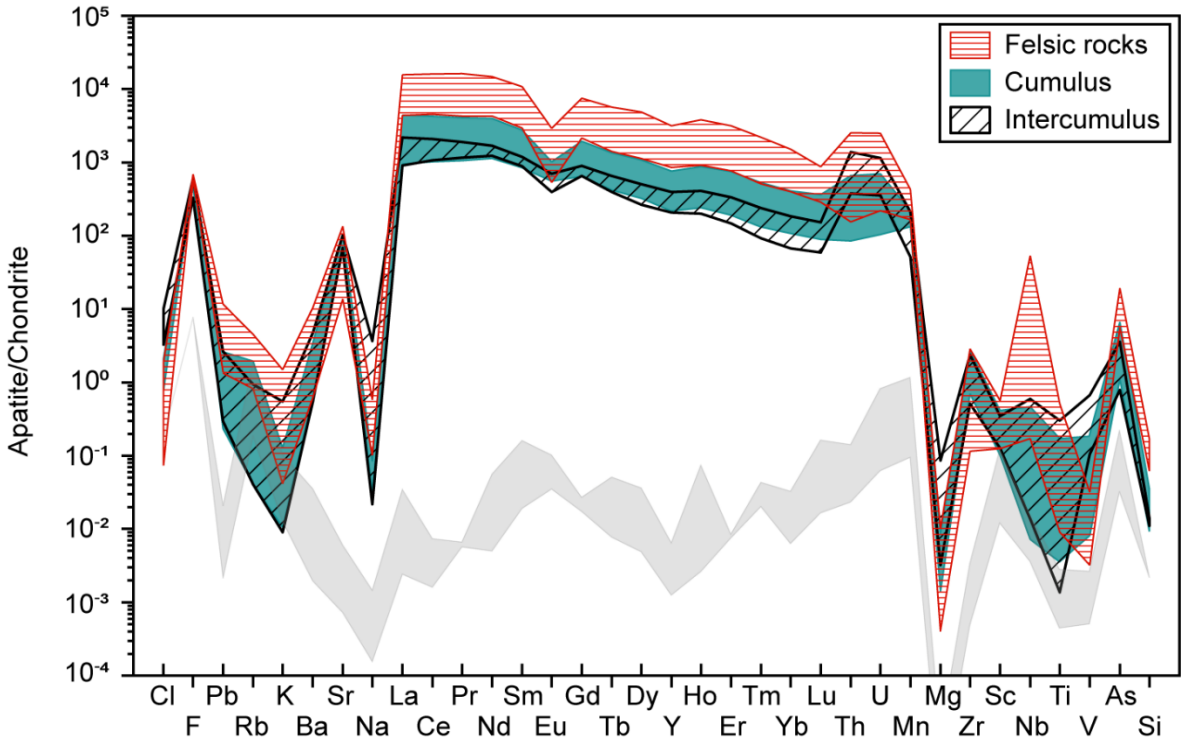

Figure 2.8 – Chondrite-normalised multielement patterns of intercumulus and cumulus apatite from the mafic rocks of MCU II compared to accessory apatite from the felsic rocks of the Upper Series and Pointe du Criard sill (chondrite values for normalisation are from McDonough and Sun, 1995). All elements are determined by LA-ICP-MS except for Cl,F and Si which are determined by EMPA. Elements are ordered by decreasing ionic radius (see text for details). The grey field corresponds to lower limits of detection determined with a 15 µm beam (top line) and 55 µm beam (bottom line) on the apatite reference material (UQAC-APA). Cl, F and Si detection limits are from electron microprobe analyses.

2.6.3 Trace element composition of plagioclase

The trace element composition of plagioclase was determined on 3 pairs of spatially associated Fe–Ti–P-rich and Fe–Ti–P-poor layers on 42 individual plagioclase grains (Table 2.2; Annexe 22). At the sample-scale, there is no compositional variation between small (<0.3 mm) and big (0.5 to 2 mm) plagioclase grains. Likewise, no significant chemical variation is detected between the core and the rim of any plagioclase grains, all variations being comprised within the 2σ analytical error (see details in Annexe 22). Similar to apatite, plagioclase from the two types of layers also display distinct trace element compositions: plagioclase from Fe–Ti–P-poor layers have higher REE + Y, Rb, K, Th and As concentrations, and lower Sr, Pb, Eu, Mn, Mg, and Nb contents than plagioclase from Fe–Ti–P-rich layers (Table 2.2; Annexe 27).

2.7 Discussion

The Sept-Iles Intrusive Suite is a natural laboratory to develop apatite as a petrogenetic indicator, using a full suite of trace elements, by investigating how magmatic processes have affected the trace element content of apatite during differentiation. The mafic and felsic magmas of Sept-Iles layered intrusion are cogenetic and define a liquid line of descent of a ferrobasalt (Namur et al., 2011a). In addition, the mineralised Critical Zone at the top of MCUII records immiscibility between Fe-rich and Si-rich silicate melts (Charlier et al., 2011; Namur et al., 2012). Given that apatite underwent no subsolidus re-equilibration, the trace element composition of apatite reflects the original magmatic composition.

In this section, we discuss how the trace elements of apatite can record late-stage fractionation of a ferrobasalt and model fractional crystallization to constrain the cotectic proportions of apatite in the mineralised Critical Zone. We investigate several processes that might be responsible for the distinct apatite and plagioclase compositions in Fe–Ti–P-poor and Fe–Ti–P-rich layers, and propose a new model to explain the origin of layering and the Fe–Ti–P enrichment of the Critical Zone. Finally, we establish new discrimination diagrams to help identify prospective rocks for Fe–Ti–P exploration in mafic layered intrusions.

2.7.1 Tracing late-stage fractionation of ferrobasalt using trace elements in apatite

We show that a wider variety of trace elements in cumulus apatite than previously thought records the changing melt composition of the fractionating ferrobasalt from the mafic Critical Zone to the felsic Upper Series at Sept-Iles. The apatite data are plotted against the anorthite content of co-existing plagioclase, which is used as a proxy for the degree of fractional crystallisation of the melt (Fig. 2.9). However, intercumulus apatite cannot be used to trace differentiation, as it has been demonstrated that the concentration of trace elements (i.e., REE) in interstitial apatite from the Skaergaard layered intrusion depends on the relative proportions of trapped liquid and cumulus phases (Pedersen et al., 2021). Indeed, intercumulus apatite does not always plot on the same trend defined by cumulus apatite in Fig. 2.9 and Annexe 28, such as Th, U or Zr. In order to constrain which elements in cumulus apatite reflect changing melt composition, and those that are affected by other factors (i.e., co-crystallising minerals, melt polymerisation, or coupled substitutions), we compare the behaviour of

trace elements in apatite with that of the liquid line of descent of Sept-Iles, which was determined from the mafic chilled margin and dykes and the felsic intrusions (Namur et al., 2011a; Annexe 28). The behaviour of most trace elements in apatite matches well the evolution of the liquid line of descent of Sept-Iles (Table 2.3). As observed in other layered intrusions and felsic rocks, apatite records an increase in REE + Y (Fig. 9a, 9b), Th, U and decrease in Sr with progressive fractionation (Belousova et al., 2002; Charlier et al., 2008; Cawthorn, 2013; Xing et al., 2014; Zafar et al., 2020). Our study also allows us to identify additional trace elements which vary with fractional crystallisation. Other incompatible elements that increase in apatite are K, Pb and Rb. Zirconium first increases and then decreases upon crystallisation of zircon in the felsic melt. Finally, compatible elements, such as V (Fig. 2.9c, 2.9d) and Mg continuously decrease. The evolution of these elements matches that of the Sept-Iles liquid line of descent, confirming the idea that the felsic rocks are related to the mafic Layered Series by differentiation (Namur et al., 2011a). However, some elements, such as Mn (Fig. 2.9e, 2.9f) or Na, do not behave similarly as the liquid line of descent after 60 wt% SiO_2 (i.e., crystallisation of the felsic rocks). Several processes may explain this, namely the effect of co-crystallising phases, the changing Si content of the melt and its subsequent affect on partition coefficients (i.e., partitions coefficients are higher in more polymerised, felsic melts), or coupled substitutions in apatite, as discussed below.

The mineral phases that crystallise together with apatite, and control the bulk partition coefficient, affects apatite composition for certain elements. For example, extensive plagioclase crystallisation reduces the Eu and Sr available in the melt, resulting in apatite with an increasingly strong negative Eu anomaly and decreasing Sr content (Belousova et al., 2002; Xing et al., 2014; She et al., 2016). The Sr/Y ratio in apatite can be used as a proxy to trace fractional crystallisation of plagioclase, as the Y content of the melt increases with differentiation (Belousova et al., 2002; He et al., 2016; O'Sullivan et al., 2020). Apatite from the mafic Critical Zone and the felsic Upper Series clearly records a trend of plagioclase fractionation, with an increasingly negative Eu anomaly and decreasing Sr/Y ratio towards the apatite from the most evolved rocks (Fig. 2.10). Intercumulus apatite, when plotted on a Sr/Y vs Eu/Eu* diagram, defines a trend parallel to that of cumulus apatite, but with higher

Sr/Y ratio. This might be explained by a higher Sr content of the melt reflecting the more primitive compositions of mafic cumulates that host intercumulus apatite.

Apatite can also be used to track the appearance of late-stage mineral phases, such as zircon and REE-bearing minerals. For apatite from the felsic rocks of the Upper Series and Pointe du Criard sill, the slight light REE (LREE) or heavy REE (HREE) depletion (Fig. 2.8; Annexe 24) might be a consequence of the co-crystallisation of accessory phases (i.e., monazite, allanite, epidote; Chu et al., 2009) or zircon (Fujimaki, 1986), respectively. Indeed, accessory phases such as titanite, epidote and zircon are observed in some samples (Hounsell, 2008; Annexe 29). The wide dispersion in REE content of apatite in the felsic rocks for similar anorthite content (Fig. 2.9a) might be caused by a local depletion due to co-crystallising REE minerals cited above.

Table 2.3 – Behaviour of the trace elements that define Sept-Iles liquid line of descent and comparison with the evolution of trace element in apatite (this study in bold) with differentiation in Sept-Iles and other layered intrusions and felsic rocks

			Behaviour of trace elements			
			Increase	Increase then decrease	Decrease	Constant
Whole rock		Sept-Iles LLD[1]	K. Rb. REE+Y. Th. U. Nb	Na. Ba. Zr	Ca. Eu/Eu*. Sr. V. Mg. Ti. Mn	Pb
Apatite	**LA-ICP-MS**	**Sept-Iles Intrusive Suite[2]**	**K. Rb. REE+Y. Th. U. Nb, Mn. Pb. Na**	**Zr**	**Ca. Eu/Eu*. Sr. V. Mg**	**Ti**
Apatite	LA-ICP-MS	Sept-Iles Intrusive Suite[3]	REE+Y. Th. U. Zr			Sr. Ba
Apatite	LA-ICP-MS	Bushveld[4]	REE+Y		Sr	
Apatite	LA-ICP-MS	Panzhihua[5]	REE+Y		Sr	
Apatite	LA-ICP-MS	Felsic and mafic rocks[6]	REE+Y		Sr	
Apatite	LA-ICP-MS	Granites[7]	REE+Y		Sr	

LLD liquid line of descent; [1]Namur et al. (2011a); [2]This study; [3]Tollari et al. (2008); [4]Van Tongeren and Mathez (2012); [5]Xing et al. (2014); [6]Belousova et al. (2002); [7]Zafar et al. (2020)

The changing melt composition during fractional crystallisation also affects the partition coefficients of apatite, as they generally show an increase of 1 order of magnitude from mafic to felsic melts (Watson and Green, 1981), which is presumably related to the structure (i.e., degree of polymerisation) of the melt. Thus, the increasing concentration of incompatible trace elements in apatite may, at least in part, be caused by the increased degree of polymerisation of the felsic melt. However, partition coefficients for apatite in mafic and felsic rocks are lacking for most of the analysed trace elements except for the REE. In the case of Mn, a series of experiments conducted by Stokes et al. (2019) established that the Mn content of apatite is directly related to the degree of melt polymerisation and not fO2 (Miles et al., 2014). It implies that apatite from the felsic rocks (i.e., that crystallises from a more polymerised melt) should be richer in Mn than those from the mafic rocks. This explains the discrepancy between the increasing Mn content of apatite with differentiation (Fig. 2.9e) and the decreasing Mn concentration marked by the liquid line of descent (Fig. 2.9f). As for Mn, the constant Na increase in apatite which does not match the evolution of Na in the melt (Table 2.3), could be explained by a continuously changing partition coefficient due to an increasing degree of melt polymerisation. This is however not the only plausible explanation as coupled substitutions in apatite could also be responsible for the discrepancy with the liquid trend, and for Na in particular.

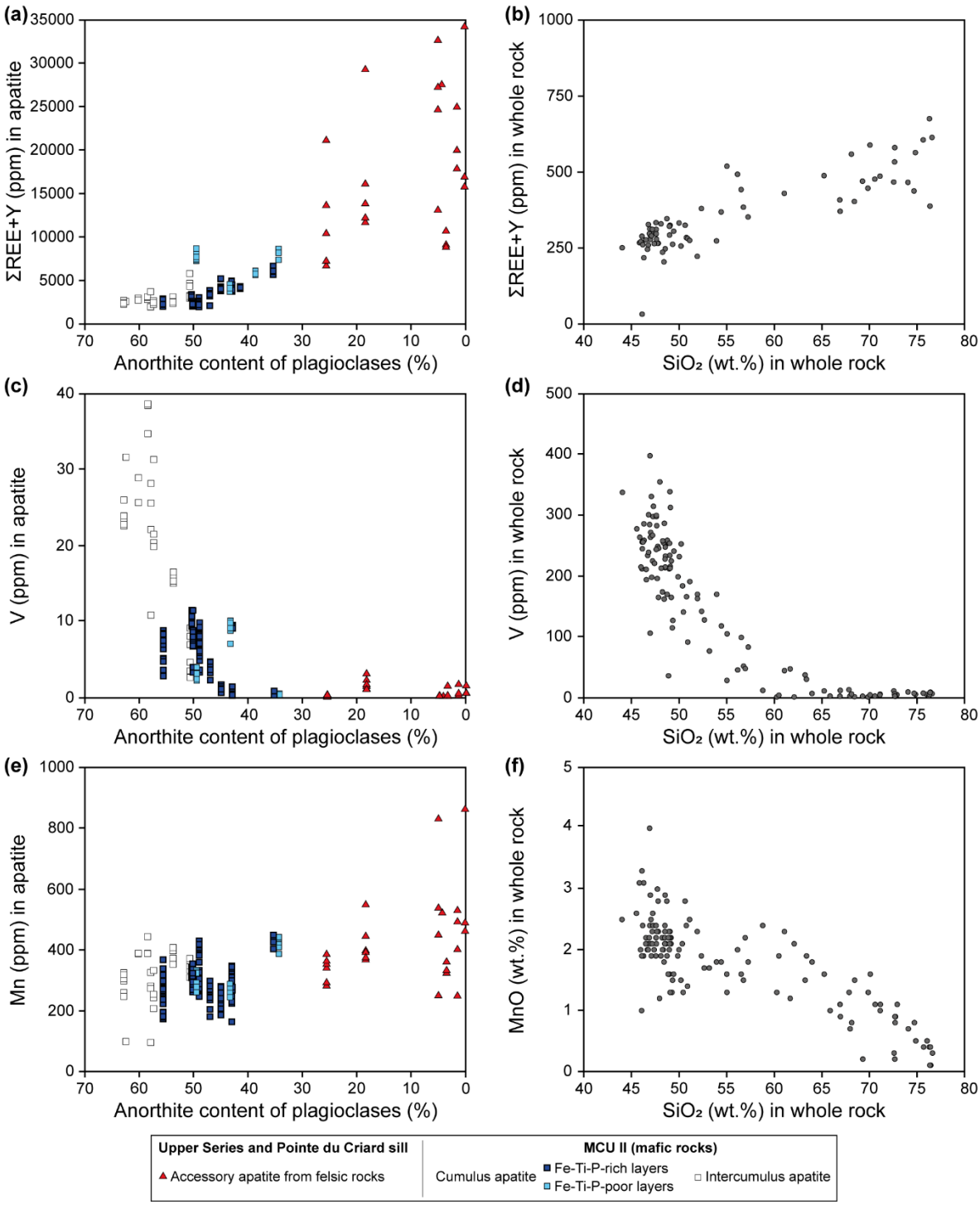

Figure 2.9 – Evolution of (a) ∑REE + Y, (c) V and (e) Mn, in intercumulus and cumulus apatite from the mafic rocks of MCU II and accessory apatite from the felsic rocks of the Upper Series and Pointe du Criard sill with anorthite content of associated plagioclase. The behaviour of these elements in apatite is compared to the evolution of (b) ∑REE + Y, (d) V and (f) MnO with SiO2 in the rocks which represent the Sept-Iles liquid line of descent (Namur et al., 2011a).

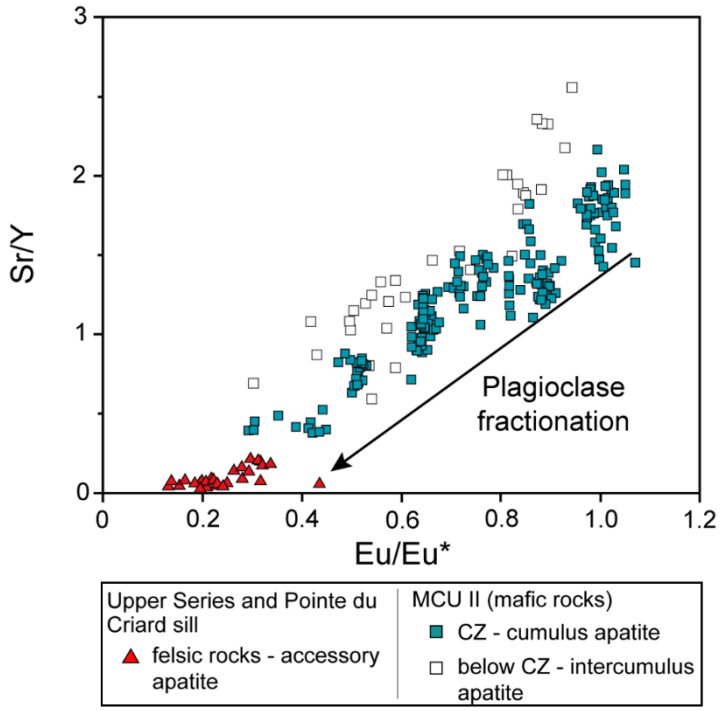

Figure 2.10 – Eu anomaly versus Sr/Y binary plot for intercumulus and cumulus apatite from the mafic rocks of MCU II and accessory apatite from the felsic rocks of the Upper Series and Pointe du Criard sill. Cumulus apatite from the mafic rocks and accessory apatite from the felsic rocks define a trend corresponding to plagioclase fractionation.

The behaviour of trace elements in apatite during fractional crystallisation is also intrinsically related to coupled substitutions. For example, the liquid line of descent shows an increase of Si and REE in the residual melt with differentiation, while Na increases then decreases (Table 2.3). Thus, the continuous increase of Na, Si and REE in apatite with progressive fractionation might be due to both melt composition and coupled substitution: to the overall increase of REE and Si in the residual melt induces the incorporation of Na into apatite via coupled substitutions. Indeed, if there is more REE in apatite, there could be more coupled substitutions with Na and Si, as they can substitute into the apatite crystal structure following the general coupled substitutions (Pan and Fleet, 2002):

$$REE^{3+} + SiO_4 = Ca^{2+} + PO_4^{3-}.$$

$$REE^{3+} + Na^{+} = 2\ Ca^{2+}.$$

2.7.2 Cotectic proportion of apatite during fractionation of ferrobasalt

The Critical Zone at the top of MCU II of Sept-Iles Intrusive Suite contains Fe–Ti–P-rich layers with anomalously high apatite content (between 7 and 36 vol%). Could this be explained by elevated cotectic proportions of apatite? The fractionation trend recorded by apatite and the liquid line of descent places constraints on the amount of apatite crystallising in the Critical Zone. Thus, in order to constrain the cotectic proportions of apatite, we modelled the global evolution of REE and Sr in the melt for variable cotectic proportions of apatite (ranging from 1 to 15 %) during fractional crystallisation of the MCU II. The model aims to constrain the behaviour of these elements (i.e., compatible or incompatible during crystallisation) while varying the amount of apatite crystallising from the melt, by comparing the composition of apatite calculated using this model with that obtained by LA-ICP-MS analyses. Although immiscibility occurred in the Critical Zone (Charlier et al., 2011; Namur et al., 2012), likely resulting in alternating Fe-rich and Si-rich layering on a cm-m scale, it is clear from the overall enrichment in REE of apatite and decrease in anorthite content of plagioclase that the bulk liquid (Fe-rich + Si-rich melts) evolves up sequence. Therefore, the Rayleigh fractional crystallisation model was calculated assuming a single bulk liquid. Details of the parameters and calculations are given in Annexe 30 to 32.

The model indicates that the cotectic proportions of cumulus apatite cannot exceed 5 to 8 % overall in the bulk liquid, and that the amount of apatite relative to plagioclase crystallising together affects the apatite composition (Table 2.3; Table 2.4; Annexe 30 to 32). In detail, the model shows that before the onset of cumulus apatite crystallisation (from F = 1 to 0.65; F: fraction of liquid remaining), the REE behave incompatibly, resulting in REE enrichment of the liquid. In contrast, Sr behaves compatibly, due to extensive plagioclase crystallisation, and the liquid becomes slightly depleted in Sr (Table 2.4). Sharper differences are observed at the onset of cumulus apatite crystallisation (F = 0.64), depending on the abundance of cotectic proportions of apatite (Table 2.4). Two kinds of behaviours can be observed. First, when low (<5 to 8 %) amounts of apatite crystallise, REE continues to behave incompatibly and Sr compatibly in the melt, resulting in increasing enrichment of REE and depletion in Sr in cumulus apatite. This behaviour matches the fractionation trends recorded by apatite in the Critical Zone (Table 2.3). Furthermore, the shape of the modelled cumulus apatite is

most similar to those of the analysed apatite in the Fe–Ti–P-poor and -rich layers of the Critical Zone (Fig. 2.11a). At F = 0.60, the patterns of the modelled apatite, calculated with 1 % and 5 to 8 % apatite, are similar to those of analysed apatite in the Fe–Ti–P-poor and -rich layers, respectively (Fig. 2.11b). This shows that smaller amounts of apatite (1 %) crystallising result in higher REE and lower Sr abundances, in agreement with the laser data. Finally, the shape of the REE patterns of the modelled melts, when there is < 5 to 8 % of apatite crystallising, is also similar to these of the parental (dolerite) melt, except for the negative Eu anomaly (Namur et al., 2011), (Fig. 2.11c). The LA-ICP-MS data of apatite was used to calculate the melt composition for the Fe–Ti–P-poor and Fe–Ti–P-rich layers and the shape of their REE patterns best matches the REE pattern for liquids calculated from the model with low (1 to 8 %) apatite (Fig. 2.11c).

In contrast, when higher cotectic proportions (10 to 15 %) of apatite are used in the model, the REE behave less incompatibly and Sr behaves incompatibly (due to less plagioclase crystallising), which does not match the stratigraphic variation of trace elements in apatite from the Critical Zone (Fig. 2.7a, 2.7d; Table 2.3). This behaviour leads to modelled cumulus apatite becoming less enriched in REE and more enriched in Sr, with increasing proportion of apatite crystallising in the model. Finally, the shape of the REE pattern of the modelled apatite changes to become a U-shape pattern, due to the preferential partitioning of MREE over LREE and HREE into apatite, upon extensive crystallisation of apatite at high cotectic proportions (Fig. 2.11b).

As an additional verification of these results, we calculated the average modal proportion of apatite for the bulk (250 m-thick) Critical Zone, using the weighted average of whole rock P_2O_5 (wt.%) on drillcore S9 (Namur et al., 2012), which crosscuts the lower 234 m of the Critical Zone, from which most of the analysed apatite were sampled from (Annexe 10). Based on these calculations presented in Annexe 33, the proportion of apatite in the Critical Zone is 5.7 wt%, which agrees with our model results (<5 to 8 % apatite). A similar low proportion of cumulus apatite is observed in mafic layered intrusions in general, such as the MCU I of Sept-Iles (5 %; Namur et al., 2012), Skaergaard (~4 %; Tegner et al., 2009) and Bushveld (~3 %; Tegner et al., 2006). Therefore, some other processes are required to accumulate larger concentrations of apatite (up to 36 vol%) and Fe-Ti oxides to form the Fe–Ti–P-rich layers of the Critical Zone of Sept-Iles and in other layered intrusions, such as crystal

settling (Tollari et al., 2008), slumping (Forien et al., 2015), or immiscibility (Charlier et al., 2011; Namur et al., 2012).

Table 2.4 – (a) Liquid and (b) apatite composition calculated using Rayleigh fractional crystallisation model.

(a) Modelled liquid composition Cotectic proportions of apatite									
Intercumulus apatite	**F**	**1**	**0.95**	**0.9**	**0.85**	**0.8**	**0.75**	**0.7**	**0.65**
0.01	Sr	511	506	497	483	464	441	415	384
	∑REE	224	234	257	296	361	465	636	929
	Eu/Eu*	0.89	0.88	0.84	0.80	0.74	0.67	0.59	0.50
Cumulus apatite	**F**	**0.64**	**0.63**	**0.62**	**0.61**	**0.6**	**0.55**	**0.5**	**0.45**
1	Sr	357	332	307	283	261	237	212	186
	∑REE	1352	1994	2981	4518	6944	11486	20590	40344
	Eu/Eu*	0.440	0.380	0.320	0.280	0.240	0.190	0.160	0.120
5	Sr	369	354	339	324	309	293	275	256
	∑REE	1246	1689	2315	3210	4501	6692	10611	18068
	Eu/Eu*	0.470	0.440	0.400	0.370	0.340	0.310	0.280	0.240
8	Sr	378	371	365	358	351	343	334	325
	∑REE	1172	1493	1919	2492	3269	4500	6533	10071
	Eu/Eu*	0.490	0.480	0.470	0.460	0.450	0.440	0.430	0.410
10	Sr	384	384	383	383	382	382	381	380
	∑REE	1126	1375	1695	2108	2648	3467	4756	6879
	Eu/Eu*	0.510	0.520	0.530	0.540	0.550	0.560	0.570	0.590
15	Sr	399	416	433	452	473	498	529	566
	∑REE	1017	1122	1246	1396	1577	1831	2194	2733
	Eu/Eu*	0.560	0.620	0.690	0.780	0.870	1.000	1.170	1.410
(b) Modelled apatite composition Cotectic proportions of apatite									
Intercumulus apatite	**F**	**1**	**0.95**	**0.9**	**0.85**	**0.8**	**0.75**	**0.7**	**0.65**
0.01	Sr	1124	1114	1094	1063	1022	971	912	845
	∑REE	1120	1172	1286	1483	1805	2326	3184	4655
	Eu/Eu*	0.52	0.51	0.49	0.47	0.43	0.39	0.34	0.29
Cumulus apatite	**F**	**0.64**	**0.63**	**0.62**	**0.61**	**0.6**	**0.55**	**0.5**	**0.45**
1	Sr	786	730	675	623	574	521	466	409
	∑REE	6768	9974	14898	22562	34651	57259	102524	200605
	Eu/Eu*	0.25	0.22	0.19	0.16	0.14	0.11	0.09	0.07
5	Sr	812	778	745	712	680	644	605	562
	∑REE	6217	8394	11458	15815	22079	32653	51452	86996
	Eu/Eu*	0.27	0.25	0.24	0.22	0.20	0.18	0.16	0.14
8	Sr	831	817	802	788	773	755	736	714
	∑REE	5835	7381	9426	12153	15826	21597	31045	47310
	Eu/Eu*	0.29	0.28	0.28	0.27	0.26	0.26	0.25	0.24
10	Sr	845	844	843	842	841	840	839	837
	∑REE	5593	6777	8282	10211	12706	16456	22293	31783
	Eu/Eu*	0.30	0.30	0.31	0.31	0.32	0.33	0.33	0.34
15	Sr	879	915	953	995	1040	1095	1163	1246
	∑REE	5034	5481	6011	6643	7401	8450	9935	12099
	Eu/Eu*	0.33	0.36	0.40	0.45	0.51	0.58	0.69	0.82

2.7.3 Chemical differences between Fe–Ti–P-poor and Fe–Ti–P-rich layers

In this section, we explore the process(es) which might be responsible for the formation of the Fe–Ti–P-rich layers in the Critical Zone. To do this, we measured and compared the trace element chemistry of apatite and plagioclase from pairs of alternating Fe–Ti–P-poor and Fe–Ti–P-rich layers, recognisable in our samples by the abundance of apatite (<0.1 vol% and between 8 and 30 vol%, respectively) and Fe–Ti oxides (<10 vol% and up to 60 vol%, respectively; Fig. 2.12). Apatite and plagioclase from Fe–Ti–P-poor layers are systematically enriched in REE + Y, As, Rb, K, Na and Th, leading to a stronger negative Eu anomaly in apatite, whereas those from the Fe–Ti–P-rich layers are enriched in Pb, Mn, Mg, Nb, and Ti (±Sr).

As shown in Section 6.2.1., apatite from Sept-Iles layered intrusion did not encounter any subsolidus process (i.e., subsolidus reequilibration and metamorphism) that could have modified their composition. Below, the possible causes of the chemical differences between apatite from the Fe–Ti–P-poor and Fe–Ti–P-rich layers, such as the reaction of apatite with trapped liquid, the amount of apatite crystallising, and an immiscibility process, are discussed.

2.7.3.1 Reaction with trapped liquid

First, we consider that the higher REE content of apatite and plagioclase from the Fe–Ti–P-poor layers might be due to reaction of apatite and plagioclase with trapped liquid, which could be in a higher amount in Fe–Ti–P-poor layers than in Fe–Ti–P-rich layers. Indeed, a reaction of early formed apatite with trapped interstitial liquid should increase the amount of REE (i.e., incompatible elements) into apatite by an amount which is proportional to the relative proportion of trapped liquid and apatite (Cawthorn, 1994, 2013). The effect of the reaction with trapped liquid is most important when the amount of apatite is small (<5 %) and the amount of trapped liquid high (>20 %; Namur and Humphreys, 2018). In addition, a REE-rich zonation can develop over a previously crystallised apatite grain, as the REE amount increases in the trapped liquid with time (Xing and Wang, 2017). The trapped liquid also has an effect on the crystallisation of the other minerals, and can result in REE-

rich plagioclase and clinopyroxene overgrowths, as was documented in the Skaergaard layered intrusion (Humphreys,2009; Namur and Humphreys, 2018).

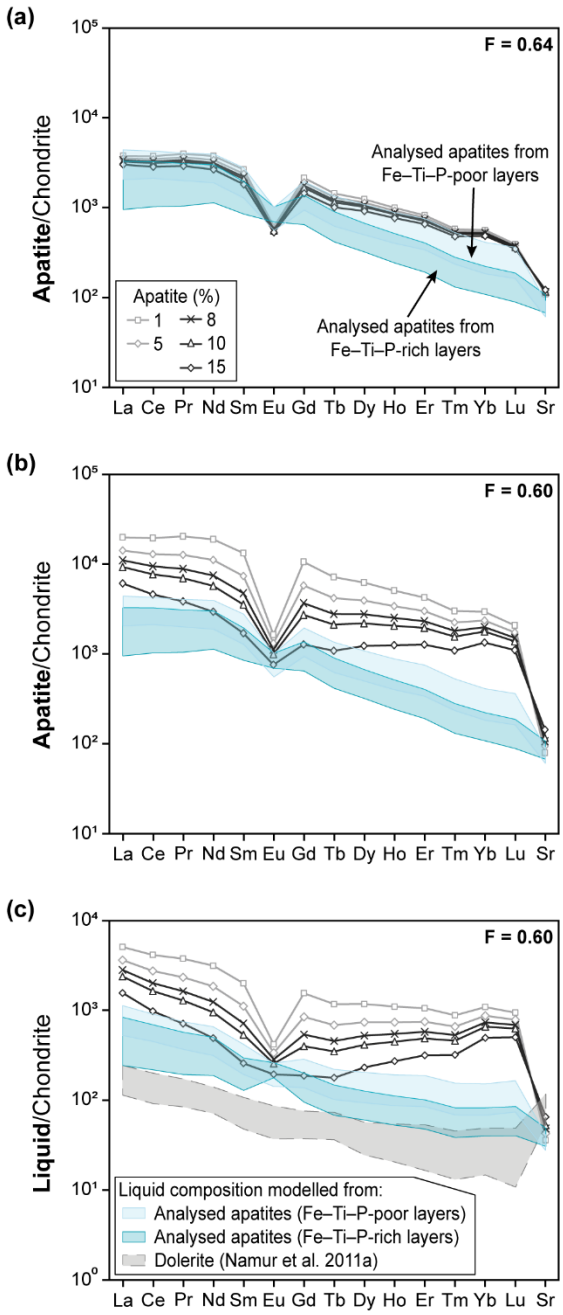

Figure 2.11 – Results of the Rayleigh fractional crystallisation model for different apatite cotectic proportions. Modelled composition of cumulus apatite is compared to the actual composition of apatite from Fe–Ti–P-poor and -rich layers at (a) F = 0.64 (onset of cumulus apatite crystallisation) and (b) F = 0.60 (onset of liquid immiscibility). (c) Liquid modelled composition obtained for different cotectic proportions of apatite is compared to liquid composition calculated from apatite analyses in Fe–Ti–P-poor and -rich layers, and to the mafic rocks used to constrain Sept-Iles liquid line of descent (Namur et al., 2011a), at F = 0.60. Chondrite values for normalisation are from McDonough and Sun (1995).

However, in the Sept-Iles Critical Zone, the fraction of intercumulus liquid is low (<3.5 %; Namur and Charlier, 2012), which should limit the effect of reaction of apatite with trapped liquid even in layers containing low proportions of apatite. No core to rim zonation is visible in transmitted light microscopy (i.e., lack of oscillatory zoning) in plagioclase from both Fe–Ti–P-poor and -rich layers, nor do apatite and plagioclase display any chemical overgrowth using core to rim LA-ICP-MS analyses (Annexe 22). Although the absence of zonation could be explained by re-equilibration of apatite and plagioclase with the surrounding minerals, this is deemed very unlikely, as diffusion is slower in plagioclase than apatite (Cherniak, 2000, 2003). Thus, plagioclase should still record REE enrichment at the rim even if this zonation was not preserved in apatite. Additionally, the trace element content of apatite fully enclosed within different host phases is similar (Fig. 2.6; see Section 6.2.1.), which provides evidence that apatite did not re-equilibrate with its surrounding mineral.

It should also be noted that apatite from Fe–Ti–P-poor layers are small (50 to 200 lm) and it thus remains plausible that their high content of REE is due to a complete reaction with, or crystallisation from, trapped liquid despite the absence of zonation. However, as the plagioclase from Fe–Ti–P-poor layer are also enriched in REE compared to those from Fe–Ti–P-rich layers, it remains unlikely that high REE content of apatite from Fe–Ti–P-poor layer might be explained by its crystallisation from trapped liquid alone.

All these observations suggest that it is highly improbable that the petrological and chemical difference between the Fe–Ti–P-poor and Fe–Ti–P-rich layers was the result of reaction with, or crystallisation from, trapped interstitial liquid. Thus, other processes must be responsible for the difference between Fe–Ti–P-poor and Fe–Ti–P-rich layers.

2.7.3.2 Silicate liquid immiscibility

Apatite from the Fe–Ti–P-rich layer hosts relatively large, rounded, dark and light melt inclusions, which are the most abundant towards the base of the Critical Zone (see Section 2.4 on Apatite petrography). Both kinds of inclusions are also observed in apatite from the Fe–Ti–P-poor layers, but they are smaller, scarcer, and mostly light (see Section 2.4 on Apatite petrography). However, the paucity of inclusions in apatite from the Fe–Ti–P-poor layers may be due a sampling problem (i.e., the small amount and size of apatite). Charlier et al. (2011) and Namur et al. (2012) demonstrated

these melt inclusions are likely the result of silicate liquid immiscibility, because the MCU II liquid line of descent enters the two-liquid field (see Fig. 11 in Namur et al., 2012). The authors suggest this immiscibility process responsible for the crystallisation of melanocratic, Fe–Ti–P-rich layers in alternation with Fe–Ti–P-poor, leucocratic layers. Although minerals crystallising from two immiscible melts are supposed to have similar chemistry, this is not always the case. For the Skaergaard Intrusion, Humphreys (2011) noted that plagioclase rims crystallising from an Fe-rich immiscible melt have higher anorthite content than those that crystallised from Si-rich melt. This disequilibrium crystallisation possibly means that both melts lost physical contact probably due to the difference in density between Fe-rich and Si-rich melts (Namur et al., 2012).

In order to evaluate if the chemical difference in apatite and plagioclase compositions between Fe–Ti–P-rich and -poor layers could be due to liquid immiscibility, the trace element concentrations of apatite and plagioclase from Fe–Ti–P-rich layers (crystallised from the Fe-rich melt) is divided by the concentrations of the same minerals from the corresponding Fe–Ti–P-poor layers (crystallised from the Si-rich melt). These are compared (Fig. 2.12) to those obtained from a series of experiments on the partitioning of trace elements during the immiscibility of gabbroic and granitic melts (Schmidt et al., 2006) and Fe-rich and Si-rich melts (Veksler and Charlier, 2015). These experiments show that the REE, along with Ba, Sr, Mn, Th, U, Sc, Ti and V, tend to partition into the Fe-rich (gabbroic) melt, whereas Rb, K, Na, and As are preferentially partitioned into the Si-rich (granitic) melt. A similar approach was used by Coint et al. (2020) and showed that pyroxene crystallising from a Fe-rich immiscible melt in enriched in trace elements compared to pyroxene from the Si-rich melt.

For apatite, many of the elements enriched in the Fe–Ti–P-rich and Fe–Ti–P-poor layers are in agreement with the experiments, with the exception of REE + Y, Sc, Th and U. These elements are enriched in apatite from Fe–Ti–P-poor layers, which may correspond to Si-rich melt, whereas they would be expected to be concentrated into the Fe-rich melt (Fig. 2.12a). For the plagioclase data, several elements are not in agreement with experimental data on immiscible melts (Fig. 2.12b). Ba, REE + Y, Th, Zr and V are concentrated in Fe–Ti–P-poor layers instead of within the Fe-rich melt, and Al is enriched in Fe–Ti–P-rich layers instead of in the Si-rich melt. However, our comparison of the relative enrichment of trace elements in apatite from Fe–Ti–P-rich and Fe–Ti–P-poor layers to

liquid–liquid partition coefficients is rather simplistic. Several factors could modify the relative trace element enrichment of apatite from the Fe–Ti–P-poor layers compared to the Fe–Ti–P-rich layers, such as: (1) variation of the partition coefficients due to the difference in polymerisation; and/or (2) abundance of apatite crystallising from each immiscible layer.

Regarding the effect of polymerisation of the melt on the partition coefficients, REE partition coefficients between apatite and a felsic melt are higher (i.e., between 8 and 38; Watson and Green, 1981) than that between apatite and a mafic melt (i.e., between 2.2 and 6.8; Charlier et al., 2005). The SiO2 content of Fe-rich and Si-rich melts produced by immiscibility in the Critical Zone has been obtained from melts inclusions in apatite by Charlier et al. (2011). Si-rich melts contain ca. 68 wt% SiO2 and are thus much more polymerised than the Fe-rich melt, that contain between 38 and 53 wt% SiO2. This difference in SiO2 content and polymerisation must have an effect on some apatite partition coefficients, which possibly justifies the higher REE concentrations measured in apatite from the Si-rich immiscible melt (i.e., Fe–Ti–P-poor layers), even if it should contain less REE than the conjugate Fe-rich melt (Fig. 2.12; Schmidt et al., 2006; Veksler and Charlier, 2015). Partition coefficients for the other trace elements are not well constrained.

This effect might be combined with the abundance of apatite that crystallises. According to several studies, such as Tollari et al. (2006), Schmidt et al. (2006), or Hou et al. (2017; 2018), the Fe-rich melt concentrates P at the expense of the Si-rich melt, which can explain the greater abundance of apatite observed in the Fe–Ti–P-rich (8 to 36 vol%) compared to the Fe–Ti–P-poor layers (<1 vol%). If immiscibility takes place, the segregation of the melt into a Si-rich and a Fe-rich melt could cause a local variation of the cotectic proportions of apatite based on the repartition of P between the 2 immiscible melts. The 2 melts remain in thermodynamic equilibrium and should therefore crystallise minerals with the same composition, though in different proportions (Charlier and Grove, 2012). However, it is clear from Fig. 2.11 that when a low proportion of apatite crystallises (i.e., < 1 vol%), REE behave highly incompatibly and the apatite are therefore enriched in REE. When more apatite crystallises (5 to 8 %), REE behave less incompatibly and apatite are thus less enriched in those trace elements. This appears to agree with the differences observed in apatite between the pairs of Fe–Ti–P-poor and Fe–Ti–P-rich layers.

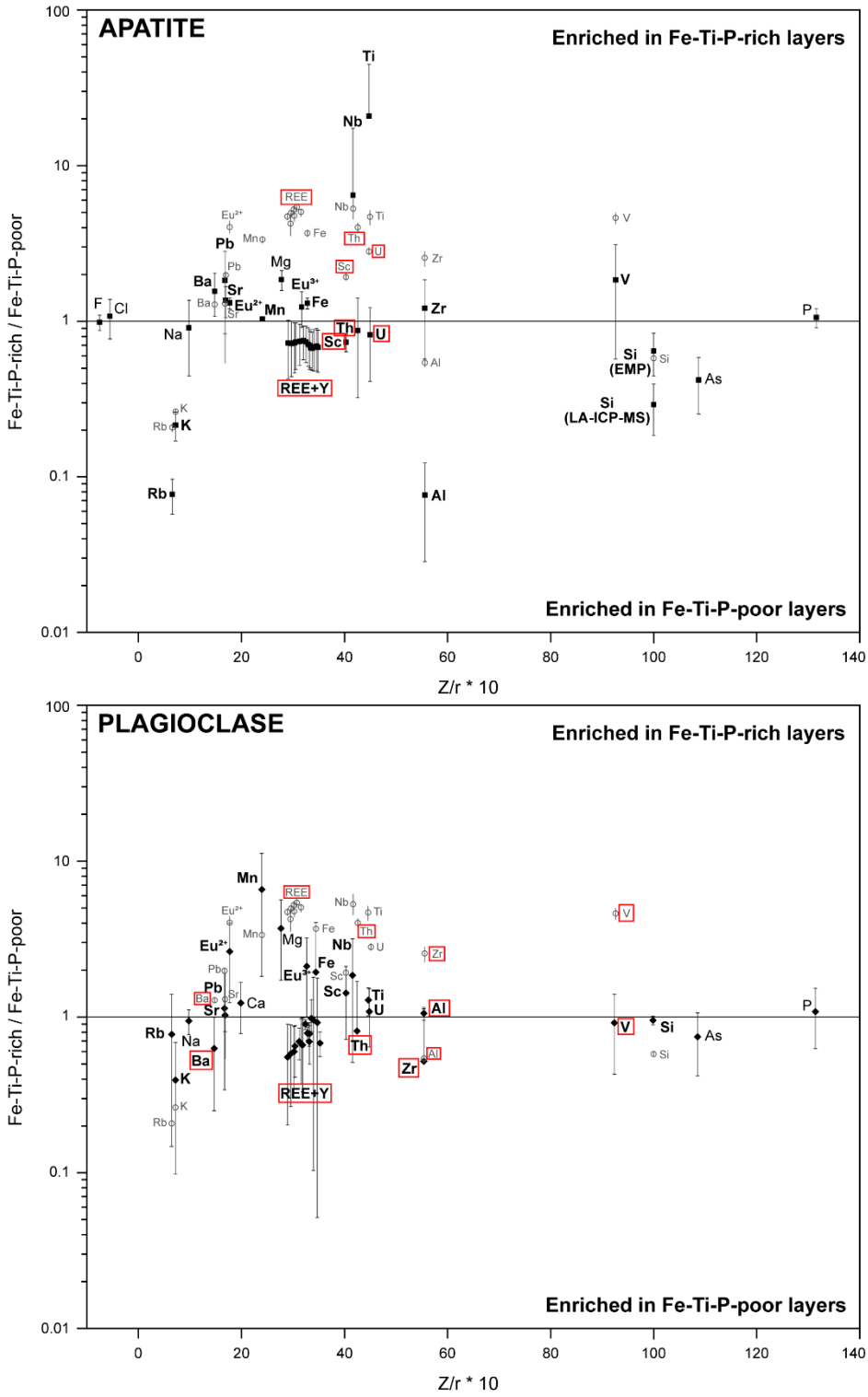

Figure 2.12 – Trace element concentration of (a) apatite and (b) plagioclase from Fe–Ti–P-rich layers divided by the concentration of associated samples from Fe–Ti–P-poor layers, and compared to the experimental data (grey; liquid–liquid) from Veksler and Charlier (2015). Elements > 1 are enriched in the Fe–Ti–P-rich layers (Fe-rich melt), and those < 1 are concentrated in Fe–Ti–P-poor layers (Si-rich melt).

Therefore, the apatite chemistry suggests that the formation of Fe–Ti–P-poor and Fe–Ti–P-rich layers is likely the result of immiscibility, resulting in the crystallisation of lower cotectic proportions of apatite in Fe–Ti–P-poor layers (<1 vol%) than in the adjacent Fe–Ti–P-rich layers (5 to 8 vol%). As no more than 5 to 8 % apatite could have crystallised in the Fe-rich melt (i.e., resulting in the formation of Fe–Ti–P-rich layers), another process is required to concentrate up to 36 vol% apatite in these layers.

2.7.4 Formation of layering in the Critical Zone by successive immiscibility stages

Tollari et al. (2008) first proposed a model to explain the crystallisation of Fe–Ti–P accumulation in the Critical Zone, whereby the decreasing amount of apatite and oxides towards the top of the Critical Zone was the result of crystal settling and compaction from an evolved magma. At the time of apatite saturation, the denser Fe–Ti oxides sank, along with apatite, to form massive oxide (<50 m thick) followed by a massive nelsonite layer (10 m thick) at the base of the Critical Zone. The residual liquid was expelled by compaction from which disseminated oxide and apatite later crystallised. This model accounts for the diminishing proportions of apatite and Fe–Ti oxides in Fe–Ti–P-rich layers towards the top of the Critical Zone, but does not explain the intercalation of Fe–Ti–P-poor layers, which were not studied in the work of Tollari et al. (2008). Indeed, if it is considered that Fe–Ti–P-poor and Fe–Ti–P-rich layers were formed by simple crystal settling of dense minerals and floatation of plagioclase, it would be expected that apatite and plagioclase from both types of layers have a similar composition over such a short, dm- to m-scale, distance. Due to the difference in apatite and plagioclase compositions described above, this is an unlikely mechanism to form Fe–Ti–P-poor and Fe–Ti–P-rich layers. It also remains unlikely that the alternation of Fe–Ti–P-poor and Fe–Ti–P-rich layers was caused by slumping of incompletely consolidated crystal slurries during seismic episodes, as is suggested for the Bushveld layered intrusion (Maier et al., 2013; Forien et al., 2015), as they occur at a much smaller scale.

Our new apatite and plagioclase trace element data support the model introduced for the Critical Zone by Charlier et al. (2011), which invokes repeated episodes of immiscibility of Fe-rich and Si-rich silicate liquids. A similar model has been proposed for the Bushveld eastern limb (Fischer et al., 2016). As a consequence of the dome-like shape of the immiscibility binodal curve, if a liquid exsolves

into 2 conjugate immiscible melts, each melt would then exsolve its conjugate with decreasing temperature even if both melts were initially physically segregated (Fig. 2.13a). Thus, for a given starting melt composition, both liquids will keep differentiating with decreasing temperature through repeated small-scale immiscibility events (Fig. 2.13a). This is in agreement with the compositional evolution of apatite from the Critical Zone as a whole, which matches the Sept-Iles liquid line of descent (see Section 7.1), as well as the decreasing abundance of apatite and Fe-Ti oxides towards the top. When an immiscibility episode occurs (Fig. 2.13b), the melt droplets are sorted due to density and viscosity contrasts (Philpotts, 1982; Charlier and Grove, 2012; Namur et al., 2015): the denser, less viscous, Fe-rich melt is responsible for the crystallisation of a Fe–Ti–P-rich layer at the bottom, while the Si-rich melt forms an overlying Fe–Ti–P-poor layer, with both conjugates crystallising different proportions of the same minerals (Fig. 2.13b). However, as we demonstrated that no more than 5 to 8 % of apatite can crystallise from the Fe-rich melt, crystal settling and compaction might be responsible for the accumulation of up to 36 vol% apatite at the scale of Fe–Ti–P-rich layers (Fig. 2.13c). The repetition of successive immiscibility episodes and the differentiation of the conjugate melts could produce the observed alternation of Fe–Ti–P-poor and Fe–Ti–P-rich layers in the Critical Zone and decreasing abundance of apatite in the Fe–Ti–P-rich layers towards its top.

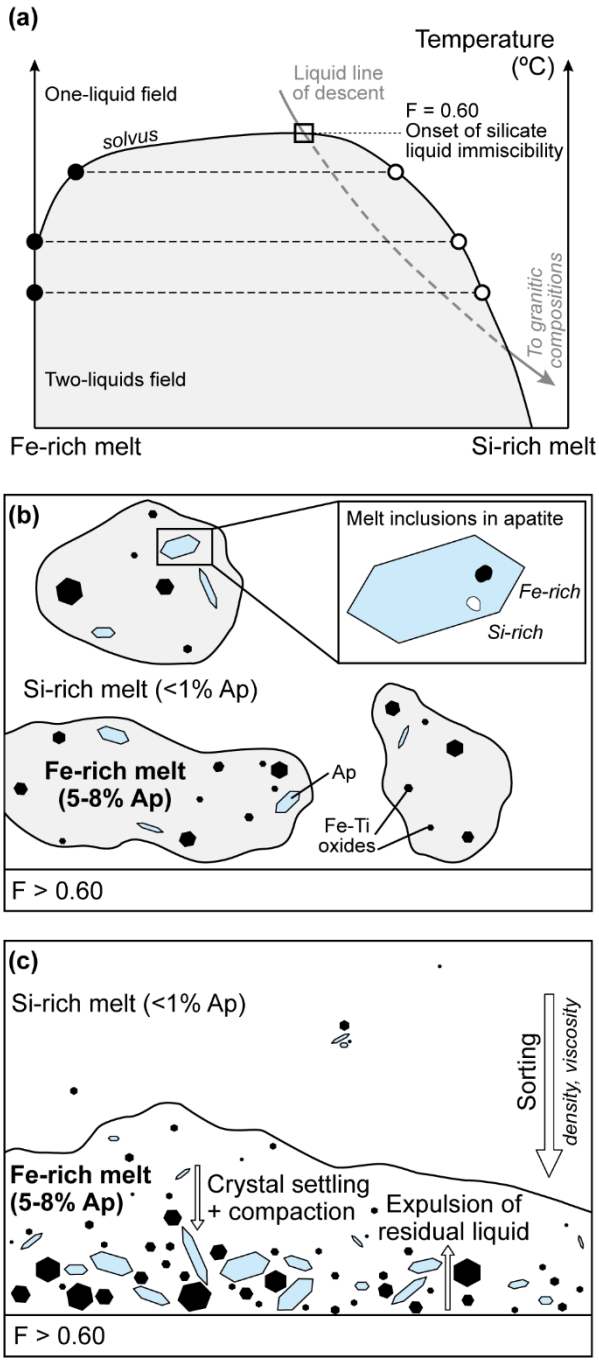

Figure 2.13 – Schematic illustrations for the formation of Fe–Ti–P-poor and -rich layers in the MCU II Critical Zone of Sept-Iles layered intrusion. (a) The Sept-Iles liquid reaches the immiscibility binodal curve and starts to exsolve in two conjugate, Fe-rich and Si-rich, melts at F = 0.60 (modified from Charlier et al., 2011, Charlier and Grove, 2012; Namur et al., 2012); (b) The two conjugate melts crystallise different cotectic proportions of apatite and Fe-Ti oxides. Melt inclusions in apatite from both Fe–Ti–P-rich and Fe–Ti–P-poor layers record this immiscibility process (Charlier et al., 2011); (c) Melt droplets are sorted by density. The denser and less viscous Fe-rich melt droplets coalesce at the bottom and form a Fe–Ti–P-rich layer. Crystal settling and compaction are thus responsible for the accumulation of up to 36 vol% apatite in Fe-rich layers (Tollari et al., 2008) where cotectic proportions of apatite initially do not exceed 5 to 8 %.

2.7.5 Implications for provenance discrimination: new apatite discrimination diagrams

In addition to using apatite as a petrogenetic indicator of igneous processes in layered intrusions, we propose a series of new provenance discrimination diagrams (Figs. 2.14, 2.15 and 2.16), to be used successively, that are capable to distinguish apatite that formed from the different parts of the Sept-Iles Intrusive Suite: (1) mafic vs felsic; (2) cumulus vs intercumulus for mafic rocks; and (3) Fe–Ti–P-rich vs Fe–Ti–P-poor layers for cumulus apatite of mafic layered intrusions. The proposed elements and ratios are based on our improved petrogenetic understanding of the processes that control trace elements in apatite at Sept-Iles. Ongoing work will test the robustness of these diagrams with larger datasets from mafic and felsic environments.

Distinguishing apatite from the different parts of a mafic layered intrusion, based on their trace element content, is of particular interest for mineral exploration, as cumulus apatite from evolved mafic melts may be associated with Fe–Ti–P mineralisation (i.e., Critical Zone; Charlier et al., 2011; Namur et al., 2012). It should be noted that in other layered intrusions, intercumulus apatite can be associated with Fe-Ti-V or Ni-Cu-PGE mineralisation that formed from more primitive mafic melts (Bushveld, Boudreau and Kruger, 1990; Stillwater, Boudreau and McCallum, 1989; Sudbury, Warner et al., 1998). However, this kind of mineralisation is missing from the lower portion of Sept-Iles layered intrusion.

2.7.5.1 Step 1: Distinguish mafic from felsic part of the intrusion

Some binary discrimination diagrams separate apatite from granites and mafic rocks using Sr, Sr/Y or the Eu anomaly combined to another element (Belousova et al., 2002; Chu et al., 2009; O'Sullivan et al., 2020). However, those existing diagrams do not allow to clearly separate apatite from the mafic and felsic parts of the Sept-Iles layered intrusion as they do not plot in the defined fields. Apatite from the mafic and felsic parts of the Sept-Iles layered intrusion display distinct chemical compositions, the most significant differences concerning ∑REE + Y, the Eu anomaly and Sr. The amount of ∑REE + Y is higher in apatite from the evolved felsic part than in those from the mafic part (MCU II) due to differentiation (see Section 7.1). In addition, apatite from the felsic rocks has a stronger negative Eu anomaly and is depleted in Sr compared to apatite from the mafic portion

(Fig. 2.7c and 2.7d, respectively) due to extensive crystallisation of plagioclase. The proposed ternary discrimination diagram for apatite uses ∑REE + Y, the Eu anomaly and Sr/Y ratio, and efficiently discriminates apatite from the mafic and felsic parts of Sept-Iles layered intrusion (Fig. 2.14).

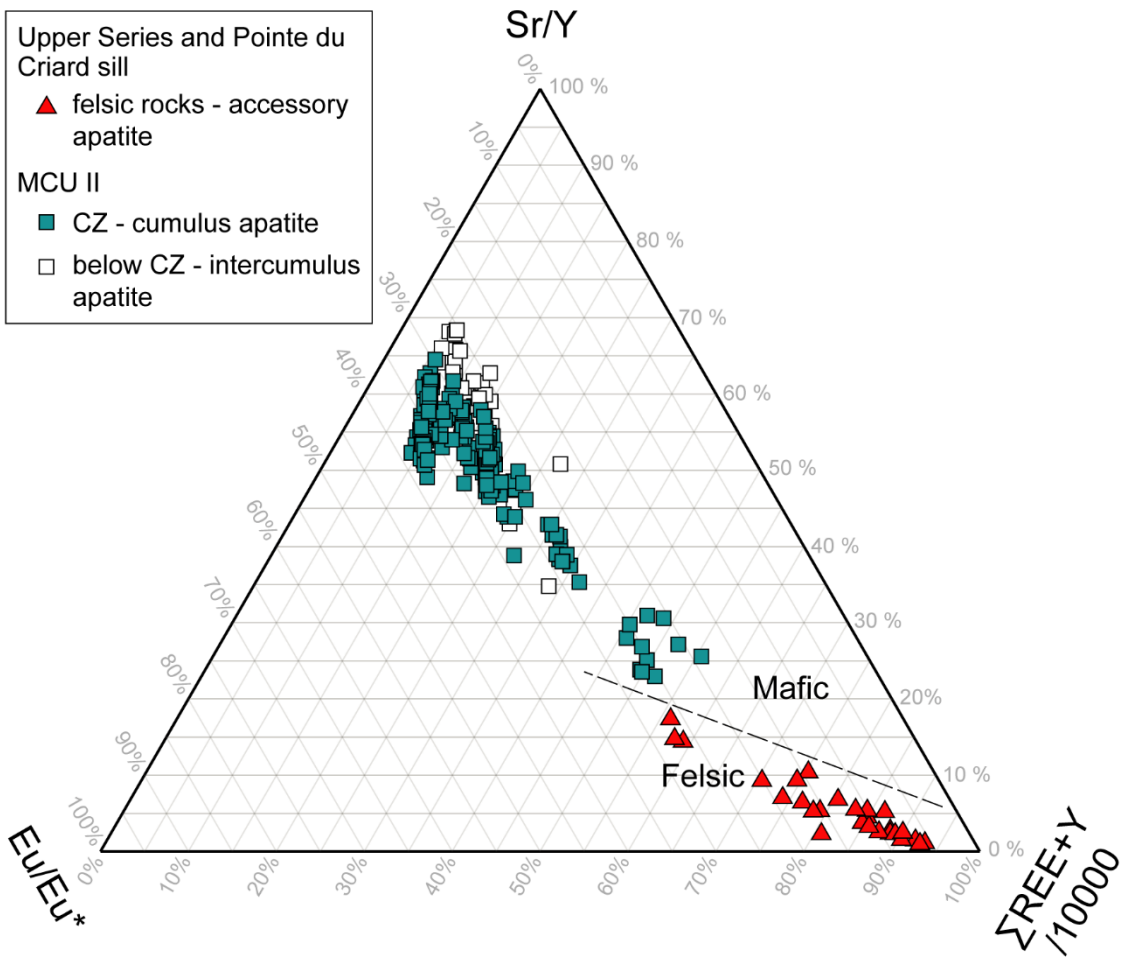

Figure 2.14 – Proposed ternary discrimination diagram to separate mafic and felsic apatite in Sept-Iles layered intrusion (n = 240 analyses).

2.7.5.2 Step 2: Distinguish cumulus and intercumulus apatite in the mafic part of intrusion

In the mafic part (MCU II) of Sept-Iles layered intrusion, intercumulus and cumulus apatite have distinctly different volatile (Fig. 2.4) and trace element contents (Fig. 2.7; Table 2.1). The first diagram is based on volatile content of apatite, determined by EMPA, whereby a binary diagram of the Cl/F ratio as a function of F (wt.%) allows the efficient discrimination of cumulus and intercumulus apatite (Fig. 2.15a), whereby cumulus apatite has a higher F and lower Cl content than intercumulus apatite,

which leads to a lower Cl/F ratio (<0.05; Table 2.1). The lower Cl content of cumulus apatite may be due to several processes, such as (1) the exsolution and escape of a fluid phase, (2) the change of partition coefficients between intercumulus and cumulus apatite (i.e., crystallisation environment), or, most probably, (3) the higher Cl content of the trapped liquid. As Cl partitions more easily than F into a fluid phase (Aiuppa et al., 2009), the exsolution and escape of a fluid phase during fractionation will affect the volatile content of apatite, as described in the Bushveld (Boudreau and Kruger, 1990) and Stillwater (Boudreau and McCallum, 1989) complexes. Thus, fluid exsolution and escape during the crystallisation of the more evolved part of the mafic melt, when apatite finally crystallises on the cotectic in the Critical zone, would lead to apatite containing more F and less Cl. On the other hand, Pedersen et al. (2021) attribute a lower Cl content of cumulus apatite to a change in the crystallisation environment between intercumulus and cumulus apatite, which is due to a higher partition of F relative to Cl in basaltic melts (Mathez and Webster, 2005; McCubbin et al., 2015). Lastly, Cl behaves as an incompatible element until the onset of cumulus apatite crystallisation, similar to Th. Thus, it becomes more concentrated in trapped liquid pockets, leading to a higher Cl concentration in intercumulus apatite.

The second proposed diagram is based on the trace element content (Lu, Th and V) of apatite determined by LA-ICP-MS. The multielement diagram (Fig. 2.8) shows that the slope between Lu and Th is steeper for intercumulus apatite (higher Th/Lu ratio), and that intercumulus apatite also contains more V than cumulus apatite. The binary plot of Th/Lu as a function of V (ppm) defines distinct fields for cumulus and intercumulus apatite (Fig. 2.15b). Th and Lu are incompatible elements in plagioclase, clinopyroxene and olivine, with Th being more incompatible than Lu (see model for Lu). As a result, even though Th and Lu both increase in the residual melt, there is an even more pronounced increase of Th. This difference in incompatibility, along with the low amount of intercumulus apatite, explains the high Th/Lu ratio of intercumulus apatite. On the other hand, we suggest that the lower Th/Lu ratio of cumulus apatite may be due to several reasons, including: (1) a higher amount of apatite crystallising, which ‘‘dilutes” the Lu and Th (see Section 2.7.2); and/or (2) a lower amount of interstitial liquid in the Critical Zone because of its expulsion (Namur and Charlier, 2012). In addition, the higher amount of V of intercumulus apatite could be due to a crystallisation

from a less evolved magma (higher anorthite content of plagioclase, see Fig. 2.2a; Fig. 2.9c, 2.9d), therefore richer in compatible elements.

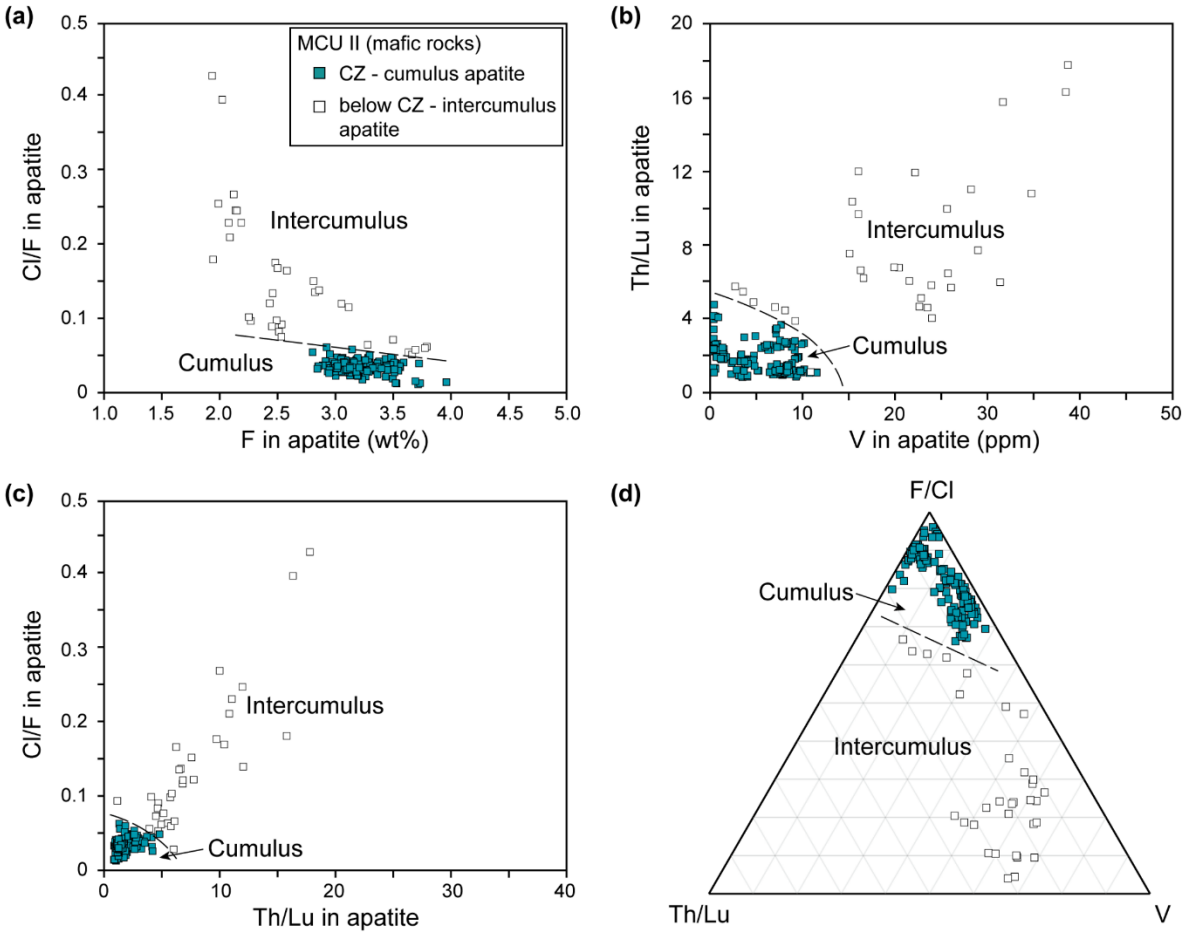

Figure 2.15 – New discrimination diagrams to distinguish cumulus from intercumulus apatite in Sept-Iles mafic layered intrusion, based on (a) apatite volatile (F and Cl) content determined by EMPA (n = 191 analyses); and (b) apatite trace element content (Th, Lu and V) determined by LA-ICP-MS (n = 213 analyses). (c) and (d) discrimination diagrams combine data obtained by EMPA and LA-ICP-MS.

When both EMPA and LA-ICP-MS analyses are available, two more discrimination diagrams can be proposed to distinguish cumulus from intercumulus apatite (Fig. 2.15c, d). The first one is a binary diagram based on the Cl/F and Th/Lu ratios, which proves to be very efficient to distinguish both types of apatite, with very minor overlapping compared to F (Fig. 2.15a) and V (Fig. 2.15b). The positive correlation of the Cl/F and Th/Lu ratios confirms that Th, Lu and Cl are behaving as incompatible elements, and are thus concentrated in the residual melt. The Cl/F ratio is useful to investigate the processes responsible for the chemical variations between cumulus and intercumulus apatite (i.e., trapped liquid, incompatibility). However, the F/Cl ratio is more convenient to use in a ternary discrimination diagram, combining all of these elements, as it allows to define more clearly the cumulus and intercumulus fields, such as that shown on Fig. 2.15d.

2.7.5.3 Step 3: Identifying cumulus apatite from mineralised Fe–Ti–P layers of the intrusion

The objective of the third discrimination step is to try to distinguish cumulus apatite from the Fe–Ti–P-rich layers from cumulus apatite from the nearby Fe–Ti–P-poor layers within the Critical Zone. Even though some elements are enriched, or depleted, in apatite from Fe–Ti–P-rich layers compared to apatite from Fe–Ti–P-poor layers (see Section 2.6.2.2), the overall differentiation trend is superimposed over these variations and hinders the creation of conclusive discrimination diagrams. The elements showing the larger variations between the Fe–Ti–P-rich and the Fe–Ti–P-poor layers, namely ∑REE + Y, Sr and Eu/Eu*, were chosen in order to minimise the effect of differentiation. Two binary (Fig. 2.16a, b) and one ternary (Fig. 2.16c) discrimination diagrams were constructed. The majority of the mineralised and unmineralised samples define two distinct fields, apart from one sample from Fe–Ti–P-rich layer which plots into the Fe–Ti–P-poor field on each diagram. This is due to the fact that this Fe–Ti–P-rich layer crystallised near the top of the Critical Zone from the most evolved magma. Future work is ongoing to test if it is possible to distinguish mineralised from unmineralised parts of mafic intrusions.

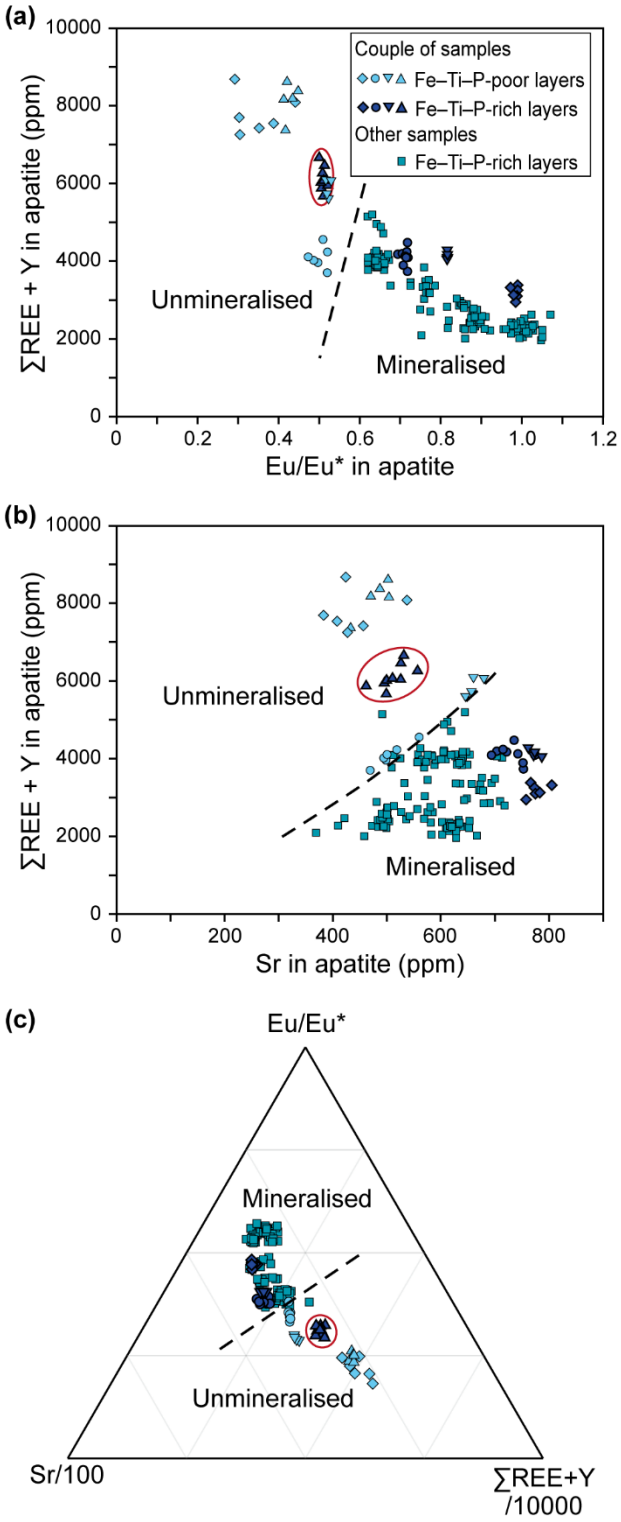

Figure 2.16 – New discrimination diagrams to separate cumulus apatite from Fe–Ti–P-rich (mineralised) layers and apatite from Fe–Ti–P-poor (unmineralised) layers in Sept-Iles Critical Zone (MCU II). Fields with a red outline indicate a sample from the stratigraphically highest Fe–Ti–P-rich layer whose composition overlaps with the field defined by apatite from Fe–Ti–P-poor layers. (For interpretation of the references to colour in this figure legend, the reader is referred to the web version of this article.)

2.8 Conclusions

This study demonstrates that the trace element content of cumulus apatite records the changing melt composition of the fractionating ferrobasalt at Sept-Iles, from the mafic Critical Zone at the top of the MCU II to the felsic Upper Series. Indeed, the behaviour of most trace elements in apatite is in accordance with the evolution of Sept-Iles liquid line of descent, with an increase of REE + Y, Th, U, K, Pb and Rb, and a decrease in Sr, V and Mg in apatite with progressive fractionation. In addition, the increasingly negative Eu anomaly and Sr/Y ratio towards the apatite from the most evolved rocks defines a trend of plagioclase fractionation.

The Critical Zone of Sept-Iles layered intrusion is composed of an alternation of Fe–Ti–P-poor (<1 vol% apatite) and Fe–Ti–P-rich (7 to 36 vol% apatite) layers on a dm to m-scale. The compositional difference between apatite and plagioclase from Fe–Ti–P-poor and Fe–Ti–P-rich layers is explained by repeated episodes of immiscibility between Fe-rich and Si-rich silicate liquids. The Si-rich liquid formed the Fe–Ti–P-poor layers, with apatite and plagioclase being enriched in REE + Y, As, Rb, K, Na and Th. The Fe-rich liquid formed the Fe–Ti–P-rich layers, in which apatite and plagioclase are enriched in Pb, Mn, Mg, Nb and Ti (±Sr). The difference of apatite abundance between Fe–Ti–P-poor and Fe–Ti–P-rich layers is a direct consequence of the immiscibility. The Si-rich liquid corresponds to cotectic proportions of 1 % of apatite, while the cotectic proportions of apatite crystallising from the Fe-rich liquid reaches 5 to 8 %. Thus, the elevated proportion of apatite (up to 36 vol%) in the Fe–Ti–P-rich layers might be due to crystal settling and accumulation of apatite.

This study also proposes new provenance discrimination diagrams that are based on apatite trace element content and on understanding of how trace elements are incorporated into apatite during magma differentiation. It is now possible to successively distinguish: (1) apatite from the mafic and the felsic part of the intrusion, using REE + Y, Sr/Y and the Eu anomaly; (2) cumulus and intercumulus apatite in the mafic part of the intrusion, using F, Cl and/or Th and Lu; and (3) cumulus apatite from mineralised parts (i.e., Fe–Ti–P-rich layers) of the intrusion, using REE + Y, Sr and the Eu anomaly. Although there are some limitations to these diagrams, they lay the foundation for the development of apatite as an indicator mineral for magmatic Fe-Ti-P mineralisation. The diagrams will be tested and further developed in future work, using a larger dataset from mafic and felsic environments.

Acknowledgements

This project was supported financially by the NSERC Discovery Grant (RGPIN-2015-05924) and Canada Research Chair of S. Dare. We thank S.-J. Barnes for providing additional samples from the Sept-Iles Critical Zone. We also thank M. Choquette (Laboratoire de Microanalyse, Laval University, Quebec City), and A. Lavoie and D. Savard (LabMaTer, University of Quebec in Chicoutimi) for their assistance with EMPA and LA-ICP-MS analyses, respectively. Discussion with A. Boudreau about the volatile content of apatite helped improve an earlier version of this manuscript. M.A.K. acknowledges support from Fonds de Recherche du Québec – Nature and technologies (merit scholarship program for foreign students, PBEEE, grant 319772).

References

Aiuppa, A., Baker, D.R., Webster, J.D., 2009. Halogens in volcanic systems. Chem. Geol. **263**, 1–18.

Andersson, S.S., Wagner, T., Jonsson, E., Fusswinkel, T., Whitehouse, M.J., 2019. Apatite as a tracer of the source, chemistry and evolution of ore-forming fluids: The case of the Olserum-Djupedal REE-phosphate mineralisation, SE Sweden. Geochim. Cosmochim. Acta **255**, 163–187.

Belousova, E.A., Griffin, W.L., O'Reilly, S.Y., Fisher, N.I., 2002. Apatite as an indicator mineral for mineral exploration: trace-element compositions and their relationship to host rock type. J. Geochem. Explor. **76**, 45–69.

Boudreau, A.E., Kruger, F.J., 1990. Variation in the composition of apatite through the Merensky cyclic unit in the western Bushveld complex. Econ. Geol. **85**, 737–745.

Boudreau, A.E., Love, C., Prendergast, M.D., 1995. Halogen geochemistry of the Great Dyke, Zimbabwe. Contrib. Miner. Petrol. **122**, 289–300.

Boudreau, A.E., McCallum, I.S., 1989. Investigations of the Stillwater Complex: Part V. Apatites as indicators of evolving fluid composition. Contrib. Miner. Petrol. **102**, 138–153.

Boudreau, A.E., Mathez, E.A., McCallum, I.S., 1986. Halogen geochemistry of the Stillwater and Bushveld complexes: evidence for transport of the platinumgroup elements by Cl-Rich fluids. J. Petrol. **27**, 967–986.

Brown, G.M., Peckett, A., 1977. Fluorapatites from the Skaergaard intrusion, East Greenland. Mineral. Mag. **41**, 227–232.

Cawthorn, R.G., 1994. Formation of chlor- and fluor-apatite in layered intrusions. Mineral. Mag. **58**, 299–306.

Cawthorn, R.G., 2013. Rare earth element abundances in apatite in the Bushveld Complex—A consequence of the trapped liquid shift effect. Geology **41**, 603– 606.

Charlier, B., Grove, T.L., 2012. Experiments on liquid immiscibility along tholeiitic liquid lines of descent. Contrib. Miner. Petrol. **164**, 27–44.

Charlier, B., Vander, A.J., Duchesne, J.-C., 2005. Geochemistry of cumulates from the Bjerkreim-Sokndal layered intrusion (S. Norway) Part II. REE and the trapped liquid fraction. Lithos **83**, 255–276.

Charlier, B., Sakoma, E., Sauvé, M., Stanaway, K., Vander, A.J., Duchesne, J.-C., 2008. The Grader layered intrusion (Havre-Saint-Pierre Anorthosite, Quebec) and genesis of nelsonite and other Fe–Ti–P ores. Lithos **101**, 359–378.

Charlier, B., Namur, O., Toplis, M.J., Schiano, P., Cluzel, N., Higgins, M.D., Vander, A.J., 2011. Large-scale silicate liquid immiscibility during differentiation of tholeiitic basalt to granite and the origin of the Daly gap. Geology **39**, 907–910.

Chen, W.T., Zhou, M.-F., Zhao, T.-P., 2013. Differentiation of nelsonitic magmas in the formation of the ~1.74 Ga Damiao Fe–Ti–P ore deposit, North China. Contrib. Miner. Petrol. **165**, 1341–1362.

Cherniak, D.J., 2000. Rare earth element diffusion in apatite. Geochim. Cosmochim. Acta **64**, 3871–3885.

Cherniak, D.J., 2003. REE diffusion in feldspar. Chem. Geol. **193**, 25–41.

Chu, M.-F., Wang, K.-L., Griffin, W.L., Chung, S.-L., O'Reilly, S.Y., Pearson, N.J., Iizuka, Y., 2009. Apatite composition: tracing petrogenetic processes in Transhimalayan Granitoids. J. Petrol. **50**, 1829–1855.

Cimon, J., 1998. Le Complexe de Sept-Îles: I- L'Unité à apatite de Rivière des Rapides, Complexe de Sept-Îles; localisation stratigraphique et facteurs à l'origine de sa formation. ET 97-05. Ministère de l'Énergie et des Ressources du Québec, p. 44.

Coint, N., Keiding, J.K., Ihlen, P.M., 2020. Evidence for silicate-liquid immiscibility in monzonites and petrogenesis of associated Fe–Ti–P-rich rocks: Example from the Raftsund Intrusion, Lofoten, Northern Norway. J. Petrol. **61**, egaa045.

Davidson, A., 1995. A review of the Grenville orogen in its North American type area. J. Austral. Geol. Geophys. **16**, 3–24.

Eales, H.V., Cawthorn, R.G., 1996. The Bushveld Complex. In: Cawthorn, R.G. (Ed.), Layered Intrusions. Elsevier, Amsterdam, pp. 181–229.

Fischer, L.A., Yuan, Q., 2016. Fe-Ti-V-(P) resources in the upper zone of the Bushveld Complex, South Africa. Pap. Proc. R. Soc. Tas. **150**, 15–22.

Fischer, L.A., Wang, M., Charlier, B., Namur, O., Roberts, R.J., Veksler, I.V., Cawthorn, R.G., Holtz, F., 2016. Immiscible iron-and silica-rich liquids in the Upper Zone of the Bushveld Complex. Earth Planet. Sci. Lett. **443**, 108–117.

Forien, M., Tremblay, J., Barnes, S.-J., Burgisser, A., Pagé, P., 2015. The Role of Viscous Particle Segregation in Forming Chromite Layers from Slumped Crystal Slurries: Insights from Analogue Experiments. J. Petrol. **56**, 2425–2444.

Fujimaki, H., 1986. Partition coefficients of Hf, Zr, and REE between zircon, apatite, and liquid. Contrib. Miner. Petrol. **94**, 42–45.

Goldoff, B., Webster, J.D., Harlov, D.E., 2012. Characterization of fluor-chlorapatites by electron probe microanalysis with a focus on time-dependent intensity variation of halogens. Am. Mineral. **97**, 1103–1115.

He, H.-L., Yu, S.-Y., Song, X.-Y., Du, Z.-S., Dai, Z.-H., Zhou, T., Xie, W., 2016. Origin of nelsonite and Fe–Ti oxides ore of the Damiao anorthosite complex, NE China: Evidence from trace element geochemistry of apatite, plagioclase, magnetite and ilmenite. Ore Geol. Rev. **79**, 367–381.

Higgins, M.D., 1990. A three-component composite dyke and its associated intrusion, the Pointe du Criard, Quebec, Canada. In: Parker, A., Rickwood, P., Tucker, D. (Eds.), Mafic Dykes and Emplacement Mechanism. Balkema, Rotterdam, pp. 63–68.

Higgins, M.D., 1991. The origin of laminated and massive anorthosite, Sept Iles layered intrusion, Quebec, Canada. Contrib. Miner. Petrol. **106**, 340–354.

Higgins, M.D., 2005. A new interpretation of the structure of the Sept Iles Intrusive suite, Canada. Lithos **83**, 199–213.

Higgins, M.D., Doig, R., 1981. The Sept Iles anorthosite complex: field relationships, geochronology, and petrology. Can. J. Earth Sci. **18**, 561–573.

Higgins, M.D., Doig, R., 1986. Geochemical constraints on the differentiation processes that were active in the Sept Iles complex. Can. J. Earth Sci. **23**, 670–681.

Higgins, M.D., van Breemen, O., 1998. The Age of the Sept Iles Layered Mafic Intrusion, Canada: Implications for the Late Neoproterozoic/Cambrian History of Southeastern Canada. J. Geol. **106**, 421–432.

Hill, R.I., Campbell, I.H., Davies, G., Griffiths, R.W., 1992. Mantle plumes and continental tectonics. Science **256**, 186–193.

Holness, M.B., Namur, O., Cawthorn, R.G., 2013. Disequilibrium Dihedral Angles in Layered Intrusions: a Microstructural Record of Fractionation. J. Petrol. **54**, 2067–2093.

Hou, T., Charlier, B., Namur, O., Schütte, P., Schwarz-Schampera, U., Zhang, Z., Holtz, F., 2017. Experimental study of liquid immiscibility in the Kiruna-type Vergenoeg iron–fluorine deposit, South Africa. Geochim. Cosmochim. Acta **203**, 303–322.

Hou, T., Charlier, B., Holtz, F., Veksler, I.V., Zhang, Z., Thomas, R., Namur, O., 2018. Immiscible hydrous Fe–Ca–P melt and the origin of iron oxide-apatite ore deposits. Nat. Commun. **9**, 1415.

Hounsell, V., 2008. Origine des roches felsiques de la Série Supérieure de la Suite Intrusive de Sept-Îles. Québec. M.Sc. Université du Québec à Chicoutimi.

Hu, L., Li, Y.-K., Wu, Z.-J., Bai, Y., Wang, A.-J., 2019. Two metasomatic events recorded in apatite from the ore-hosting dolomite marble and implications for genesis of the giant Bayan Obo REE deposit, Inner Mongolia, Northern China. J. Asian Earth Sci. **172**, 56–65.

Hughes, J.M., Rakovan, J.F., 2015. Structurally Robust, Chemically Diverse: Apatite and Apatite Supergroup Minerals. Elements **11**, 165–170.

Humphreys, M.C.S., 2009. Chemical evolution of intercumulus liquid, as recorded in plagioclase overgrowth rims from the Skaergaard intrusion. J. Petrol. **50**, 127–145.

Humphreys, M.C.S., 2011. Silicate liquid immiscibility within the crystal mush: evidence from ti in plagioclase from the Skaergaard Intrusion. J. Petrol. **52**, 147–174.

Irvine, T.N., 1982. Terminology for layered intrusions. J. Petrol. **23**, 127–162.

Jakobsen, J.K., Veksler, I.V., Tegner, C., Brooks, C.K., 2005. Immiscible iron- and silica-rich melts in basalt petrogenesis documented in the Skaergaard intrusion. Geology **33**, 885–888.

Jia, F., Zhang, C., Liu, H., Meng, X., Kong, Z., 2020. In situ major and trace element compositions of apatite from the Yangla skarn Cu deposit, southwest China: Implications for petrogenesis and mineralization. Ore Geol. Rev. **127**, 103360.

Keevil, H.A., Namur, O., Holness, M.B., 2020. Microstructures and late-stage magmatic processes in layered mafic intrusions: symplectites from the Sept-Iles intrusion, Quebec, Canada. J. Petrol. **61**, egaa071.

Konecke, B.A., Fiege, A., Simon, A.C., Linsler, S., Holtz, F., 2019. An experimental calibration of a sulfur-in apatite oxybarometer for mafic systems. Geochim. Cosmochim. Acta **265**, 242–258.

Kumarapeli, P.S., Saull, V.A., 1966. The St Lawrence valley system: a north American equivalent to the East African rift valley system. Can. J. Earth Sci. **3**, 639–658.

Loncarevic, B.D., Feininger, T., Lefebvre, D., 1990. The Sept-Îles layered mafic intrusion: geophysical expression. Can. J. Earth Sci. **27**, 201–512.

Longerich, H.P., Jackson, S.E., Günther, D., 1996. Laser Ablation Inductively Coupled Plasma Mass Spectrometric Transient Signal Data Acquisition and Analyte Concentration Calculation. J. Anal. Atomic Spect. **11**, 899–904.

Maciag, B.J., Brenan, J.M., 2020. Speciation of arsenic and antimony in basaltic magmas. Geochim. Cosmochim. Acta **276**, 198–218.

Maier, W.D., Barnes, S.-J., Groves, D.I., 2013. The Bushveld Complex, South Africa: formation of platinum–palladium, chrome- and vanadium-rich layers via hydrodynamic sorting of a mobilized cumulate slurry in a large, relatively slowly cooling, subsiding magma chamber. Miner. Deposita **48**, 1–56.

Mao, M., Rukhlov, A.S., Rowins, S.M., Spence, J., Coogan, L.A., 2016. Apatite trace element compositions: A robust new tool for mineral exploration. Econ. Geol. **111**, 1187–1222.

Mathez, E.A., Webster, J.D., 2005. Partitioning behavior of chlorine and fluorine in the system apatite-silicate melt-fluid. Geochim. Cosmochim. Acta **69**, 1275–1286.

McCubbin, F.M., Vander Kaaden, K.E., Tartese, R., Boyce, J.W., Mikhail, S., Whitson, E.S., Bell, A.S., Anand, M., Franchi, I.A., Wang, J.H., Hauri, E.H., 2015. Experimental investigation of F, Cl, and OH partitioning between apatite and Fe-rich basaltic melt at 1.0–1.2 GPa and 950–1000 degrees C. American Mineralogist **100**, 1790–1802.

McDonough, W.F., Sun, S.-S., 1995. The composition of the Earth. Chem. Geol. **120**, 223–253.

Mercer, C.N., Watts, K.E., Gross, J., 2020. Apatite trace element geochemistry and cathodoluminescent textures—A comparison between regional magmatism and the Pea Ridge IOAREE and Boss IOCG deposits, southeastern Missouri iron metallogenic province, USA. Ore Geol. Rev. **116**, 103129.

Méric, J., 2011. Caractérisation géochimique des magnétites de la zone critique de l'intrusion magmatique de Sept-Îles (Québec, Canada) et intégration à une base de données utilisant la signature géochimique des oxydes de fer comme outil d'exploration. M.Sc. Université du Québec à Chicoutimi.

Meurer, W.P., Boudreau, A.E., 1996. An evaluation of models of apatite compositional variability using apatite from the Middle Banded series of the Stillwater Complex, Montana. Contrib. Miner. Petrol. **125**, 225–236.

Miles, A.J., Graham, C.M., Hawkesworth, C.J., Gillespie, M.R., Hinton, R.W., 2013. Evidence for distinct stages of magma history recorded by the compositions of accessory apatite and zircon. Contrib. Miner. Petrol. **166**, 1–19.

Miles, A.J., Graham, C.M., Hawkesworth, C.J., Gillespie, M.R., Hinton, R.W., Bromiley, G.D., 2014. Apatite: A new redox proxy for silicic magmas?. Geochim. Cosmochim. Acta **132**, 101–119.

Morton, A., Yaxley, G., 2007. Detrital apatite geochemistry and its application in provenance studies. Geol. Soc. Am. Spec. Paper **420**, 319–344.

Nabil, H., 2003. Genèse des dépôts de Fe-Ti-P associés aux intrusions litées (exemples: l'intrusion mafique de Sept-Iles, au Québec; Complexe de Duluth aux États-Unis). Ph.D. Université du Québec à Chicoutimi.

Namur, O., Charlier, B., 2012. Efficiency of compaction and compositional convection during mafic crystal mush solidification: the Sept Iles layered intrusion, Canada. Contrib. Miner. Petrol. **163**, 1049–1068.

Namur, O., Charlier, B., Pirard, C., Hermann, J., Liégeois, J.-P., Vander, A.J., 2011b. Anorthosite formation by plagioclase flotation in ferrobasalt and implications for the lunar crust. Geochim. Cosmochim. Acta **75**, 4998–5018.

Namur, O., Charlier, B., Holness, M.B., 2012. Dual origin of Fe–Ti–P gabbros by immiscibility and fractional crystallization of evolved tholeiitic basalts in the Sept Iles layered intrusion. Lithos **154**, 100–114.

Namur, O., Higgins, M.D., Vander Auwera, J., 2015. The Sept Iles Intrusive Suite, Quebec, Canada. In: Charlier, B., Namur, O., Latypov, R., Tegner, C. (Eds.), Layered Intrusions. Springer, pp. 465–515.

Namur, O., Humphreys, M.C.S., 2018. Trace element constraints on the differentiation and crystal mush solidification in the Skaergaard Intrusion, Greenland. J. Petrol. **59**, 387–418.

Namur, O., Charlier, B., Toplis, M.J., Higgins, M.D., Liégeois, J.-P., Vander, A.J., 2010. Crystallization sequence and magma chamber processes in the ferrobasaltic Sept Iles Layered Intrusion, Canada. J. Petrol. **51**, 1203–1236.

Namur, O., Charlier, B., Toplis, M.J., Higgins, M.D., Hounsell, V., Liégeois, J.-P., Vander, A.J., 2011a. Differentiation of Tholeiitic Basalt to A-Type Granite in the Sept Iles Layered Intrusion, Canada. J. Petrol. **52**, 487–539.

Nielsen, T.F.D., Andersen, J.C.Ø., Holness, M.B., Keiding, J.K., Rudashevsky, N.S., Salmonsen, L.P., Tegner, C., Veksler, I.V., 2015. The Skaergaard PGE and Gold Deposit: the Result of in situ Fractionation, Sulphide Saturation, and Magma Chamber-scale Precious Metal Redistribution by Immiscible Fe-rich Melt. J. Petrol. **56**, 1643–1676.

O'Sullivan, G., Chew, D., Kenny, G., Henrichs, I., Mulligan, D., 2020. The trace element composition of apatite and its application to detrital provenance studies. Earth Sci. Rev. **201**, 103044.

Paiement, J.-P., Gagne, J., Duplessis, C., Rousseau, G., Gagnon, G., Dagbert M., 2013. Pre-Feasability Study Mine Arnaud Inc. Sept-Iles Deposit, Québec; Final Report, Technical Report NI 43-101, p. 377.

Pan, Y., Fleet, M.E., 2002. Compositions of the apatite-group minerals: substitution mechanisms and controlling factors. Rev. Mineral. Geochem. **48**, 13–49.

Paton, C., Hellstrom, J.C., Paul, B., Woodhead, J., Hergt, J., 2011. Iolite: freeware for the visualisation and processing of mass spectrometric data. J. Anal. At. Spectrom **26**, 2508–2518.

Pedersen, J.M., Ulrich, T., Whitehouse, M.J., Kent, A.J.R., Tegner, C., 2021. The volatile and trace element composition of apatite in the Skaergaard intrusion, East Greenland. Contrib. Miner. Petrol. **176**, 106.

Philpotts, A.R., 1982. Compositions of immiscible liquids in volcanic rocks. Contrib. Miner. Petrol. **80**, 201–218.

Piccoli, P.M., Candela, P., 2002. Apatite in Igneous Systems. Rev. Mineral. Geochem. **48**, 255–292.

Prowatke, S., Klemme, S., 2006. Trace element partitioning between apatite and silicate melts. Geochim. Cosmochim. Acta **70**, 4513–4527.

Ripley, E.M., Severson, M.J., Hauck, S.A., 1998. Evidence for Sulfide and Fe-Ti-P-Rich Liquid Immiscibility in the Duluth Complex, Minnesota. Econ. Geol. **93**, 1052–1062.

Rivers, T., 2008. Assembly and preservation of lower, mid, and upper orogenic crust in the Grenville Province: Implications for the evolution of large hot longduration orogens. Precambrian Res. **167**, 237–259.

Sadove, G., Konecke, B.A., Fiege, A., Simon, A.C., 2019. Structurally bound S^{2-}, S^{1-}, S^{4+}, S^{6+} in terrestrial apatite: The redox evolution of hydrothermal fluids at the Phillips mine, New York, USA. Ore Geol. Rev. **107**, 1084–1096.

Schisa, P.B.A., Djon, L., Tchalikian, A., Corkery, J., 2015. The Lac Des Iles Palladium Deposit, Ontario, Canada. Part II. Halogen variations in apatite. Mineralium Deposita **50**, 339–355.

Schmidt, M.W., Connolly, J.A.D., Günther, D., Bogaerts, M., 2006. Element partitioning: the role of melt structure and composition. Science **312**, 1646–1650.

Shannon, R.D., 1976. Revised effective ionic radii and systematic studies of interatomic distances in halides and chalcogenides. Acta Crystallogr. **A 32**, 751–767.

She, Y.-W., Song, X.-Y., Yu, S.-Y., Chen, L.-M., Zheng, W.-Q., 2016. Apatite geochemistry of the Taihe layered intrusion, SW China: Implications for the magmatic differentiation and the origin of apatite-rich Fe-Ti oxide ores. Ore Geol. Rev. **78**, 151–165.

Stokes, T.N., Bromiley, G.D., Potts, N.J., Saunders, K.E., Miles, A.J., EIMF, 2019. The effect of melt composition and oxygen fugacity on manganese partitioning between apatite and silicate melt. Chem. Geol. **506**, 162–174.

Stormer, J.C., Pierson, M.L., Tacker, R.C., 1993. Variation of F and Cl X-ray intensity due to anisotropic diffusion in apatite during electron microprobe analysis. Am. Mineral. **78**, 641–648.

Tegner, C., Cawthorn, R.G., Kruger, F.J., 2006. Cyclicity in the main and upper zones of the bushveld complex, South Africa: Crystallization from a Zoned Magma Sheet. J. Petrol. **47**, 2257–2279.

Tegner, C., Thy, P., Holness, M.B., Jakobsen, J.K., Lesher, C.E., 2009. Differentiation and Compaction in the Skaergaard Intrusion. J. Petrol. **50**, 813–840.

Tollari, N., Toplis, M.J., Barnes, S.-J., 2006. Predicting phosphate saturation in silicate magmas: An experimental study of the effects of melt composition and temperature. Geochim. Cosmochim. Acta **70**, 1518–1536.

Tollari, N., Barnes, S.-J., Cox, R.A., Nabil, H., 2008. Trace element concentrations in apatites from the Sept-Îles Intrusive Suite, Canada — Implications for the genesis of nelsonites. Chem. Geol. **252**, 180–190.

Toplis, M.J., Dingwell, D.B., 1996. The variable influence of P_2O_5 on the viscosityof melts of differing alkali/aluminium ratio: implications for the structural role of phosphorus in silicate melts. Geochim. Cosmochim. Acta **60**, 4107–4121.

Van Tongeren, J.A., Mathez, E.A., 2012. Large-scale liquid immiscibility at the top ofthe Bushveld Complex, South Africa. Geology **40**, 491–494.

Veksler, I.V., Charlier, B., 2015. Silicate liquid immiscibility in layered intrusions. In: Charlier, B., Namur, O., Latypov, R., Tegner, C. (Eds.), Layered intrusions. Springer, Dordrecht, the Netherlands, pp. 229–258.

Wang, K., Wang, C.Y., Ren, Z.-Y., 2018. Apatite-hosted melt inclusions from the Panzhihua gabbroic-layered intrusion associated with a giant Fe–Ti oxide deposit in SW China: insights for magma unmixing within a crystal mush. Contrib. Miner. Petrol. **173**, 59.

Warner, S., Martin, R.F., Abdel-Rahman, A.-F.-M., Doig, R., 1998. Apatite as a monitor of fractionation, degassing, and metamorphism in the Sudbury Igneous Complex, Ontario. Can. Mineral. **36**, 981–999.

Watson, E.B., Green, T.H., 1981. Apatite/liquid partition coefficients for the rare earth elements and strontium. Earth Planet. Sci. Lett. **56**, 105–421.

Webster, J.D., Piccoli, P.M., 2015. Magmatic apatite: A powerful, yet deceptive, mineral. Elements **11**, 177–182.

Xing, C.-M., Wang, C.Y., 2017. Cathodoluminescence images and trace element compositions of fluorapatite from the Hongge layered intrusion in SW China: A record of prolonged crystallization and overprinted fluid metasomatism. Am. Mineral. **102**, 1390–1401.

Xing, C.-M., Wang, C.Y., Li, C., 2014. Trace element compositions of apatite from the middle zone of the Panzhihua layered intrusion, SW China: Insights into the differentiation of a P- and Si-rich melt. Lithos **2014**, 188–202.

Zafar, T., Rehman, H.U., Mahar, M.A., Alam, M., Oyebamiji, A., U. R. S., Leng, C.-B., 2020. A critical review on petrogenetic, metallogenic and geodynamic implications of granitic rocks exposed in north and east China: New insights from apatite geochemistry. J. Geodyn. **136**, 101723.

Zhang, X., Guo, F., Zhang, B., Zhao, L., Wu, Y., Wang, G., Alemayehu, M., 2020. Magmatic evolution and post-crystallization hydrothermal activity in the early Cretaceous Pingtan intrusive complex, SE China: records from apatite geochemistry. Contrib. Miner. Petrol. **175**, 35.

Zhou, M.-F., Robinson, P.T., Lesher, C.M., Keays, R.R., Zhang, C.-J., Malpas, J., 2005. Geochemistry, Petrogenesis and Metallogenesis of the Panzhihua Gabbroic Layered Intrusion and Associated Fe–Ti–V Oxide Deposits, Sichuan Province, SW China. J. Petrol. **46**, 2253–2280.

CHAPITRE 3

APATITE CHEMISTRY AS A PETROGENETIC INDICATOR FOR MAFIC LAYERED INTRUSIONS

Marie A. Kieffer[a], Sarah A.S. Dare[a]*, Olivier Namur[b], Eduardo T. Mansur[c]

[a]Department of Applied Sciences, University of Quebec in Chicoutimi (UQAC), 555 Boulevard de l'Université, Chicoutimi, G7H 2B1, QC, Canada

*Canada Research Chair in Geochemistry Applied to Ore Deposits

[b]Department of Earth and Environmental Sciences, KU Leuven, 3000 Leuven, Belgium

[c]Geological Survey of Norway, PO Box 6315 Torgarden, Trondheim, 7491, Norway

Journal of Petrology (accepté, en révision)

Résumé

Les intrusions mafiques litées constituent un laboratoire naturel pour l'investigation des processus pétrogénétiques en utilisant les variations en éléments traces des apatites. Bien que ces intrusions soient associées à des provinces ignées, un grand nombre d'autres paramètres peut affecter la chimie du magma primaire (e.g., composition de la source, pression, température, fugacité d'oxygène), pouvant être suivi par de la contamination crustale. Cette étude utilise un jeu de données complet d'analyses d'apatite cumulus et intercumulus provenant de plusieurs intrusions mafiques litées pour démontrer l'utilité de l'apatite en tant qu'indicateur pétrogénétique. Le jeu de données (constitué à la fois de nouvelles analyses et d'analyses compilées depuis la littérature) comprend des analyses à la microsonde électronique et au LA-ICP-MS, ainsi que des analyses in situ du Sr réalisées au LA-MC-ICP-MS, dans des apatites provenant d'intrusions litées bien documentées (Sept-Iles, Skaergaard, Bushveld, Panzhihua) et du Complexe Igné de Sudbury. Pour la première fois, nous démontrons que les valeurs élevées de $(La/Nd)_N$, Th, U, Pb, As et $(^{87}Sr/^{86}Sr)_{initial}$ sont corrélées avec la contamination crustale. Un ratio $(Gd/Yb)_N$ élevé indique la fusion partielle d'une source suffisamment profonde pour retenir le Yb dans le grenat. Nous confirmons également qu'une augmentation de l'anomalie négative en Eu et la diminution du ratio Sr/Y traduisent la cristallisation fractionnée de plagioclase, tandis qu'un ratio Sr/Y élevé indique une saturation en apatite précoce et/ou un retard de la cristallisation de plagioclase. Le retour à une composition plus primitive suite à une recharge de magma provoque un enrichissement en Sr, V, Mg et un ratio Sr/Y plus élevé, ainsi que des concentrations plus faibles en ETR+Y, As et Na dans l'apatite. Enfin, nous démontrons que la signature de l'apatite permet d'identifier les intrusions mafiques des intrusions felsiques en utilisant son contenu en ETR et Sr et son anomalie en Eu. Il est également possible d'indentifier les parties les plus primitives (intercumulus) et évoluées (cumulus) d'une intrusion mafique litée en utilisant le contenu en Lu, Th, V et volatils (F/Cl) des apatites. Identifier un système magmatique mafique à partir de l'apatite détritique dans les tills peut se révéler utile pour les études de provenance et l'exploration minérale.

Mots-clefs : apatite; LA-ICP-MS; intrusions mafiques litées; éléments traces; indicateur pétrogénétique

Abstract

Mafic layered intrusions constitute a natural laboratory to investigate petrogenetic processes using trace element variations in apatite chemistry. Although these intrusions are related to large igneous provinces, there is a wide range of parameters that can affect the chemistry of the primary melt (i.e., composition of the source, pressure, temperature, oxygen fugacity), followed by possible crustal contamination. In this study, we use a comprehensive dataset of analyses of cumulus and intercumulus apatite from a variety of mafic layered intrusions to demonstrate the use of apatite as a powerful petrogenetic indicator. The dataset (determined in this study and compiled from the literature) comprises electron microprobe and LA-ICP-MS analyses, as well as in-situ LA-MC-ICP-MS analyses of Sr isotopes in apatite from well documented layered intrusions (Sept-Iles, Skaergaard, Bushveld, Panzhihua) and the Sudbury Igneous Complex. For the first time, we show that high values of $(La/Nd)_N$, Th, U, Pb, As, and $(^{87}Sr/^{86}Sr)_{initial}$ in apatite are related to contamination with continental crust. An elevated $(Gd/Yb)_N$ ratio indicates melting of a mantle source deep enough to retain Yb in garnet. We also confirm that increasingly negative Eu anomaly and decreasing Sr/Y ratio in apatite are indicators of fractional crystallisation of plagioclase, and that high Sr/Y is indicative of early saturation of apatite and/or delayed crystallisation of plagioclase. The reversal to more primitive compositions caused by magma mixing is expressed by higher Sr, V, Mg and Sr/Y ratio, and lower REE+Y, As and Na concentrations in apatite following magma replenishment. Lastly, we show that apatite signature can efficiently identify a mafic from a felsic intrusion using its REE and Sr content coupled to its Eu anomaly. It is also possible to further identify the more primitive (intercumulus) and more evolved (cumulus) parts of a mafic layered intrusion, using its Lu, Th, V and volatile (F/Cl) content. Identifying a mafic magmatic system using detrital apatite in till will prove useful for provenance and mineral exploration studies.

Keywords: apatite; LA-ICP-MS; mafic layered intrusions; trace elements; petrogenetic indicator

3.1 Introduction

Apatite is a widespread accessory mineral in most igneous, metamorphic, sedimentary and hydrothermal rocks (Piccoli & Candela, 2002; Webster & Piccoli 2015), including a variety of ore deposits of magmatic and hydrothermal origin (Zhou *et al.*, 2005; Tollari *et al.*, 2008; Mao *et al.*, 2016). Apatite can incorporate a wide variety of trace elements (Pan & Fleet, 2002), which can now be readily determined by laser ablation inductively coupled plasma mass spectrometry (LA-ICP-MS; Kieffer *et al.*, 2023). The variation in trace element content of apatite is closely related to its geological environment of formation (O'Sullivan *et al.*, 2020), which had led to a growing interest in developing apatite as a petrogenetic indicator (e.g., Belousova *et al.*, 2002; Chen *et al.*, 2013; Andersson *et al.*, 2019; Zhang *et al.*, 2020; Pedersen *et al.*, 2021; Kieffer *et al.*, 2023) and as an indicator mineral for mineral exploration of hydrothermal ore deposits (Mao *et al.*, 2016; Hu *et al.*, 2019). For example, in mafic layered intrusions, cumulus apatite is considered as a robust petrogenetic indicator because it typically crystallises from an evolved magma in the upper parts of the intrusions, which may host abundant cumulus apatite in Fe–Ti–P mineralisation (e.g., Critical Zone of Sept-Iles Intrusive Suite; Tollari *et al.*, 2008; Paiement *et al.*, 2013; Bushveld Upper Zone; Fischer & Yuan, 2016). As such, its trace element content can record the composition of the starting magma and any subsequent magmatic processes, such as fractional crystallisation (Tollari *et al.*, 2008; Pedersen *et al.*, 2021; Kieffer *et al.*, 2023), new magma injection (Xing *et al.*, 2014), or silicate liquid immiscibility (Kieffer *et al.*, 2023). On the other hand, intercumulus apatite is associated with more primitive magma in the lower parts of the intrusions, at the same stratigraphic level as Fe–Ti–V (Zhou *et al.*, 2005), Ni–Cu-PGE (Boudreau *et al.*, 1986) or chromite (Boudreau *et al.*, 1986) mineralisation. As intercumulus apatite crystallises from trapped, interstitial liquid, its trace element composition depends on the relative proportions of trapped liquid and cumulus phases, and hence cannot be used to trace magma evolution (Pedersen *et al.*, 2021; Kieffer *et al.*, 2023).

Mafic layered intrusions mainly crystallise from mantle-derived magmas and exhibit a prominent layering (Wager & Brown, 1968; see review in Namur *et al.*, 2015). This definition encompasses a group of intrusions that, although sharing common features, also have differences in terms of magma composition and evolution (see review in Smith & Maier, 2021). Most mafic layered intrusions are

related to large igneous province (LIP) magmatism (i.e., mantle plume), such as the Bushveld Magmatic Province, South Africa (Hatton, 1995) and Emeishan LIP, China (Zhou *et al.*, 2005; Pang *et al.*, 2010; Shellnutt, 2014). The LIP magmas typically consist of mantle-derived melts produced by high degree of partial melting (> 10 % for tholeiite and picrite, but up to 60 % for komatiite; Arndt & Lesher, 2004) and typically formed in a restricted timescale (< 5 Ma; White & McKenzie, 1995; Kamenetsky *et al.*, 2012; Ernst, 2014). However, there is a wide range of parameters that can affect the chemistry of the magma, and thus the chemistry of the minerals that crystallise (i.e., depth and degree of partial melting of the source, amount of crustal contamination and type of contaminant, the timing of crystallisation of apatite, and the magma fO_2 conditions). For example, the parental magma composition of mafic layered intrusions ranges from picrite (e.g., Emeishan; Zhou *et al.*, 2013) to ferrobasalt (e.g., Sept-Iles, Namur *et al.*, 2010; Skaergaard; Jakobsen *et al.*, 2010), with their primary melts having different depth and/or degree of partial melting and oxygen fugacity (fO_2; Zhou *et al.*, 2005). These magmas can have minor (< 1 %; Stewart & DePaolo, 1990) to important (20 to 30 %; Eales & Costin, 2012) amounts of crustal contamination, of dominantly silicic or carbonaceous material (Ganino *et al.*, 2013; Tang *et al.*, 2021, 2023), upon their emplacement in the crust. Isotopes of Sr in whole rock are commonly used to trace contamination, as contamination of a mantle-derived magma with crustal material should increase its $(^{87}Sr/^{86}Sr)_{initial}$ (DePaolo & Wasserburg, 1979; DePaolo, 1981). Also, apatite saturation can occur at different degrees of melt evolution in mafic layered intrusions (Table 3.1; Toplis & Carroll, 1995; McBirney, 1996; Tegner *et al.*, 2006; Pang *et al.*, 2009; Namur *et al.*, 2010; Luan *et al.*, 2014; She *et al.*, 2014). The crystallisation history of each intrusion depends on the parental magma characteristics and its intensive conditions of differentiation (i.e., fO_2, pressure), which can later be modified by magma contamination. Given that the trace element composition of apatite has the potential to unravel and record magmatic processes, the differences in parental magma composition, amount of contamination, and/or timing of apatite saturation among mafic layered intrusions should also be recorded by apatite chemistry, and further improve the use of this mineral as a petrogenetic indicator. However, this has yet to be demonstrated as most previous studies focus on using apatite chemistry to trace magma dynamics of a single intrusion (e.g., fractional crystallisation, immiscibility; Xing *et al.*, 2014, Pedersen *et al.*, 2021, Kieffer

et al., 2023). Whole rock composition is commonly used to trace fractional crystallisation (e.g., Namur *et al.*, 2010) or crustal contamination (e.g., Barnes *et al.*, 2014). Silicate minerals are commonly used to trace some of the processes listed above, using both major elements (e.g., anorthite content of plagioclase, forsterite content of olivine, Mg# in clinopyroxene; Namur *et al.*, 2010), and more recently some of the trace elements (e.g., Sr, K or Eu in plagioclase, Cr, Mn, REE, Ni, V, Ti, Sc or Co in clinopyroxene, orthopyroxene or olivine; Godel *et al.*, 2011; Tanner *et al.*, 2014) to trace fractional crystallisation. Although clinopyroxene, orthopyroxene and olivine can be used to calculate melt composition (e.g., Godel *et al.*, 2011; Bédard 2014), they can be susceptible to reaction with trapped liquid (e.g., Godel *et al.*, 2011; Yang *et al.*, 2019). As a whole, the REE and incompatible elements (e.g., Sr, U, Th, Pb) are crucial for tracking many other processes, such as melt composition, crustal contamination or depth of partial melting. The partitioning of those elements into plagioclase, olivine and orthopyroxene is limited. Moreover, silicate minerals are subject to alteration and modification of their primary composition. Apatite is, however, more resistant to alteration and can incorporate a wide variety of trace elements (Pan & Fleet 2002). These characteristics suggest that apatite might be a reliable recorder of a wider variety of processes. Being able to identify these processes through apatite alone is critical for certain cases where this information, usually provided by the mineral assemblage (i.e., plagioclase, olivine), whole rock or isotopes analyses, is lacking, or in cases where the silicates are completely altered or metamorphosed. This is essential in anorthosite massifs that commonly host massive oxide-apatite mineralisation in which no silicates occur (e.g., Grant 2020), or in the secondary environment (e.g., detrital apatite in tills), in order to better interpret or fingerprint their origin.

In this contribution, we have selected a variety of well-studied mafic intrusions to cover several of the parameters described above that can affect the magma composition (i.e., magma composition, depth and degree of partial melting of the source, amount of crustal contamination and type of contaminant the timing of crystallisation of apatite, and the magma fO_2 conditions), in order to investigate their control on apatite chemistry. As these varying parameters are well-documented in the selected intrusions, comparison of apatite composition relative to constrained parameters should allow us to improve the use of apatite as a petrogenetic indicator in mafic intrusions. We focus on six

intrusions (Table 3.1) that best express this variability among mantle-plume related intrusions, namely the Skaergaard intrusion (Greenland), Sept-Iles Intrusive Suite (Quebec, Canada), Bushveld Complex (South Africa), Hongge, Taihe and Panzhihua (Emaishen, China) layered intrusions. For comparison, we also studied apatite from the Sudbury Igneous Complex (Canada), which is the result of a meteorite impact that flash-melted the continental crust (Dressler *et al.*, 1987; Therriault *et al.*, 2002; Zieg & Marsh, 2005; Lightfoot, 2016). We provide electron microprobe analyses (EMPA) and LA-ICP-MS analyses of cumulus and intercumulus apatite from Sept-Iles Intrusive Suite (MCU I and III), Bushveld Complex and Sudbury Igneous Complex. Our new data is supplemented by data from the literature, which includes analyses from Skaergaard intrusion and 3 intrusions from Emeishan LIP (Hongge, Taihe and Panzhihua), as well as the MCU II of Sept-Iles Intrusive Suite, the Bushveld Complex and Sudbury Igneous Complex. New in situ analyses of Sr isotopes in apatite (Sept-Iles, Bushveld, Sudbury) are compared to those from plagioclase or whole rock (literature data) and are used to confirm that some of the observed trace element variations in apatite are related to crustal contamination. We show that the chemistry of cumulus apatite from mafic intrusions records crustal contamination and magma mixing. Furthermore, it gives insights about the depth of partial melting of the source of the primary melt. The timing of crystallisation of apatite also has an influence on its chemistry. Finally, we test a series of discrimination diagrams proposed from the Sept Iles study (Kieffer *et al.*, 2023) and show that they can efficiently separate apatite from felsic and mafic rocks from a variety of intrusions, which is useful for provenance studies using detrital grains, including apatite as an indicator mineral for exploration.

Table 3.1 – Characteristics of selected mafic layered intrusions. *Amp* amphibole; *Ap* apatite; *Cpx* clinopyroxene; *Cr* chromite; *Ilm* ilmenite; *LS* Layered Series; *MCU* megacyclic unit; *Mt* magnetite; *MZ* Main Zone; *NR* North Range; *Ol* olivine; *Opx* orthopyroxene; *Pl* plagioclase; *Qz* quartz; *SR* South Range; *UZ* Upper Zone

Intrusion	**Sept-Iles**[1]	**Skaergaard**[2]	**Bushveld**[3]	**Hongge**[4]	**Taihe**[5]	**Panzhihua**[6]	**Sudbury**[7]
Location	Canada	Greenland	South Africa	China	China	China	Canada
Age	564 ± 4 Ma	55.59 ± 0.13 Ma	2060 to 2055 Ma	ca. 260 Ma	ca. 260 Ma	ca. 260 Ma	1850 Ma
Parental magma	Ferrobasalt	Ferrobasalt	Si-rich komatiite (high-Mg andesite)	Picrite	Picrite	Picrite	Andesitic (Upper crust)
Estimated proportion of magma contamination	< 2 %	< 1 %	20–40 %	8-15 %	10 %	20-25 %	100 %
Type of contaminant	Grenville country rocks (*silicic*)	Gneissic country rocks (*silicic*)	Crust (*silicic*)	Schist, metasandstones (*silicic*)	Marble (*calcareous*)	Dolomitic limestone, marble (*calcareous*)	*NR* Granites *SR* Metased. (*silicic*)
Average $Sr_{initial}$[8]	*MCU I* 0.70386[a] *MCU II* 0.70415[a]	*LS* 0.70431[a] 0.70438[b]	*UZ* 0.70779[b] 0.70737[a]	*UZ* 0.70593[b]	*MZ+UZ* 0.70509[b]	*MZ* 0.70444[b]	*NR-MU* 0.70670[b] *SR-MU* 0.70675[b]
Dominant mafic minerals	Ol, Cpx	Ol, Cpx	Opx	Ol, Cpx	Ol, Cpx	Ol, Cpx	Opx
Dominant oxide type	Mt + Ilm	Mt + Ilm	Mt	Mt	Mt + Ilm	Mt	Mt
Oxygen fugacity	FMQ	FMQ+0 to +0.5	FMQ	FMQ+1 to +1.5	High	FMQ+1 to +1.5	FMQ
Crystallisation sequence	Ol+Pl → Mt+Ilm → Cpx → **Ap**	Ol+Pl → Cpx → Mt+Ilm → **Ap**	Ol → Chr → Opx → Pl → Cpx → Mt → Ilm → **Ap**	Ol → Mt+Ilm → Cpx → Pl → **Ap**	Ol+Cpx → Mt → Ilm → Pl → **Ap**	Ol+Cpx → Mt → Ilm → Pl → **Ap**	Opx → Pl → Cpx → Amp → Mt+Ilm → **Ap** → Qz
Composition of silicate minerals at the time of:							
Fe–Ti oxides saturation	*MCU I / MCU II*		*in UZ*				
Plagioclase (An)	61 / –	53	61	53	78	69	55
Olivine (Fo)	66 / –	56	–	74	68	71	–
Clinopyroxene (Mg#)	– / –	65	67	80	77	79	37
Apatite saturation							
Plagioclase (An)[9]							
Olivine (Fo)	51 / 52	39	49	(53)	(ca. 52)	53	55
Clinopyroxene (Mg#)	60 / 57 71 / 71	31 44	34 57	– ca. 72	ca. 68 ca. 76	65 76	– 37
Mineralisation associated with:							
Cumulus apatite	Fe-Ti-P (CZ)	–	Fe-Ti-P (UZc)	–	–	–	–
Intercumulus apatite	–	PGE-Au ± Cu (MZ)	PGE-Ni-Cu (CZ) Cr (CZ) Fe-Ti-V (UZa)	Fe-Ti-V (MZ, UZl) PGE-Ni-Cu (LZ_l, MZ_V)	Fe-Ti-V (LZ)	Fe-Ti-V (LZ)	Ni, Cu, PGE (contact sublayer)

Ap apatite; Amp amphibole; Bt biotite; Chr chromite; Cpx clinopyroxene; Ilm ilmenite; Mt magnetite; Ol olivine; Opx orthopyroxene; Pl plagioclase; Qz quartz

[1] Higgins & van Breemen (1998); Tollari *et al.* (2008); Namur *et al.* (2010, 2012); Paiement *et al.* (2013)

[2] Leeman & Dasch (1978); McBirney (1989, 1996); Stewart & DePaolo (1990); Andersen *et al.* (1998); McBirney & Creaser (2003); Jakobsen *et al.* (2010); Hagen-Peter *et al.* (2019); Keays &Tegner (2015); Thy *et al.* (2016); Hamilton & Brooks (2004)
[3] Boudreau *et al.* (1986); Kruger (1994); Harmer & Armstrong (2000); Maier *et al.* (2000); Cawthorn *et al.* (2002, 2005); Barnes *et al.* (2004, 2010); Harris *et al.* (2005); Tegner *et al.* (2006); Eales & Costin (2012); Yang *et al.* (2019); Solovova *et al.* (2021); Von Gruenewaldt (1993); Scoates *et al.* (2021)
[4] Zhong *et al.* (2002); Pang *et al.* (2010); Zhou *et al.* (2013); Luan *et al.* (2014); Shellnutt (2014); Tang *et al.* (2021, 2023)
[5] Shellnutt (2014); Tang *et al.* (2021, 2023); Zhou *et al.* (2013); She *et al.* (2014, 2016)
[6] Zhou *et al.* (2005, 2013); Pang *et al.* (2008, 2009); Zhang *et al.* (2009); Ganino *et al.* (2013); Shellnutt (2014); Tang *et al.* (2021, 2023)
[7] Gasparrini & Naldrett (1972); Krogh *et al.* (1984); Dickin *et al.* (1999); Therriault *et al.* (2002); Lightfoot & Zotov (2005); Mungall *et al.* (2005); Zieg & Marsh (2005); Ames & Farrow (2007); Lavrenchuk *et al.* (2010); Keays & Lightfoot (2020)
[8] Determined in plagioclase (a) or whole rock (b)
[9] Note that data plotted in Figure 5 indicates an earlier onset of apatite crystallisation (An_{63}) than that indicated from the literature (in brackets) for the Hongge and Taihe layered intrusions.

3.2 Diversity of mafic layered intrusions studied

The variability of key parameters resulting in the diversity of compositions of the mafic layered intrusions studied in this contribution is summarised in Table 3.1. Parental magmas of the considered mafic layered intrusions have a composition ranging from picrite to ferrobasalt, whose primary melts originated from a high degree of partial melting at various depths in the mantle (Table 3.1). The primary magma of Skaergaard was generated by the melting of a slightly depleted, anhydrous mantle, extracted at a shallower depth than a picritic melt (2 to 2.2 GPa; Tegner *et al.*, 1998). It evolved to a high-Ti ferrobasaltic parental magma due to abundant olivine fractionation prior to its final emplacement (Jakobsen *et al.*, 2010). The parental magma of Sept-Iles is also a ferrobasalt (Namur *et al.*, 2010). The source and parental magma composition of the Bushveld Complex is more complex, and its different units are commonly considered to have different parental magmas. The primary magma of the Bushveld Complex is considered to be a komatiite contaminated by the upper crust (B-1 magma of the Lower and Upper Zones) or the lower crust (B-2 and B-3 magmas of the Critical and Main Zones; Barnes *et al.*, 2010; Eales & Costin, 2012; Wilson, 2012; Maier *et al.*, 2016; Mansur & Barnes, 2020; Solovova *et al.*, 2021). Crustal contamination with a carbonate (dolomite) country rocks of the Transvaal Supergroup has also been identified in the northern limb (Ashwal *et al.*, 2005). In contrast, the Fe-Ti-rich picritic primary melts of Hongge, Taihe and Panzhihua intrusions of the Emeishan LIP originated from melting of a deep and fertile mantle source (Zhou *et al.*, 2013). They were contaminated by a siliceous (Hongge) or carbonaceous (Taihe, Panzhihua) crustal component upon their emplacement (Ganino *et al.*, 2013; Tang *et al.*, 2021, 2023), although carbonate assimilation is considered negligible by other studies (e.g., Yu *et al.*, 2015). In the extreme example of Sudbury Igneous Complex, the andesitic parental magma corresponds to the flash melting of predominantly upper crust (Mungall *et al.*, 2004; McNamara *et al.*, 2017; Keays & Lightfoot, 2020), induced by the impact of a high-velocity meteorite (Dressler *et al.*, 1987; Therriault *et al.*, 2002; Lightfoot & Zotov, 2005; Zieg & Marsh 2005; Lightfoot, 2016). All of the considered intrusions/igneous complexes might record silicate liquid immiscibility as Fe- and Si-rich melt inclusions in apatite (Skaergaard, Jakobsen *et al.*, 2005; Sept-Iles, Charlier *et al.*, 2011, Namur *et al.*, 2012; Bushveld, Fisher *et al.*, 2016; Panzhihua, Wang *et al.*, 2018; Sudbury, Watts, 2014), although this is debated

(e.g., Bushveld, Tegner *et al.*, 2006). A detailed study conducted at Sept-Iles showed that cumulus apatite crystallising from Fe- and Si-rich immiscible melts have a different composition (Kieffer *et al.*, 2023). The fO_2 of most of the intrusions is determined at around FMQ (Table 3.1), with the magma forming the 3 Emeishan intrusions being unusually oxidised (up to FMQ+1.5), due to contamination, as discussed below (Pang *et al.*, 2008, 2010; Ganino *et al.*, 2013; Howarth & Prevec, 2013; She *et al.*, 2016).

In the mafic layered intrusions, the importance of crustal contamination during or following the magma emplacement within the upper crust varies (Table 3.1): it can be negligible (i.e., Sept-Iles, Skaergaard) or reach up to 20 to 30 % (i.e., Panzhihua, Bushveld). Sudbury of course represents the extreme case of a crustally-derived melt (Lightfoot & Zotov, 2005). The nature of the contaminants varies according to the geologic environment in which the mafic intrusion was emplaced: either (1) a silicic component (such as silicate-bearing intrusive or metamorphic rocks) for the case of Sept-Iles, Skaergaard, Bushveld, Hongge and Sudbury, or (2) a calcareous component (such as marbles or limestones) for the case of Taihe and Panzhihua (Table 3.1, and references therein). Contamination by a Si-bearing crustal material can modify the Si activity of the melt and perturb the order of crystallisation of silicate minerals (Frost *et al.*, 2010). If unperturbed, olivine and clinopyroxene should crystallise to the detriment of orthopyroxene, as is the case for intrusions with only minor amount of crustal contamination (< 2 %), such as Skaergaard and Sept-Iles, dominated by troctolites and gabbros. However, an increase of the Si activity would cause an early crystallisation of orthopyroxene (Frost *et al.*, 2010), as is the case for Bushveld Complex and Sudbury Igneous Complex, which are dominated by (gabbro)norites in their mafic sequence (Table 3.1). On the other hand, contamination with a Si-poor but carbonate-rich crustal component, such as marble or limestone, does not cause an increase of the Si activity in the melt, but the increase of CaO favours the crystallisation of clinopyroxene (Howarth & Prevec, 2013) and apatite (Tollari *et al.*, 2006). To summarise, orthopyroxene crystallising first indicates crustal contamination, whereas contamination is minor if clinopyroxene crystallises first.

In addition, contamination with a calcareous crustal component can increase both the oxygen fugacity and H_2O content of the melt and trigger the early crystallisation of magnetite and the late

crystallisation of plagioclase, as is proposed for Panzhihua (Ganino *et al.*, 2013; Howarth & Prevec, 2013). However, other studies on Panzhihua intrusion propose that magnetite crystallises late after extensive fractionation leading to silicate liquid immiscibility (e.g., Zhou *et al.*, 2005; Wang & Zhou, 2013). Thus, the silicate mineralogical assemblage, and order of crystallisation, can be used as a proxy for contamination by a silicic or a carbonaceous component (Table 3.1).

In each of the 7 intrusions/igneous complexes studied here, cumulus apatite appears towards the very end of the crystallisation sequence, normally after extensive crystallisation of Fe-Ti oxides (Table 3.1). Nonetheless, saturation in Fe–Ti oxides, then in apatite, does not occur at the same degree of fractionation in each of the intrusions (Namur *et al.*, 2010, and references therein; summarised in Table 3.1). Thus, Fe–Ti oxides crystallised at an advanced stage of differentiation (i.e., evolved composition of the associated silicate minerals) in the Skaergaard and Bushveld intrusions. The timing of crystallisation of oxides in the Emeishan intrusions is still debated. For example, Ganino *et al.* (2013) and Howarth & Prevec (2013) provide evidence that in the Panzhihua and Taihe intrusions, early crystallisation of Fe–Ti oxides, and especially magnetite, is attributed to an increase of fO_2 of the melt by contamination with calcareous material. However, other studies on the Emeishan intrusions propose that instead magnetite crystallises late from an immiscible silicate melt (e.g., Zhou *et al.*, 2005, Xing *et al.*, 2017, Wang & Zhou, 2013). At Skaergaard, Bushveld and Sudbury, apatite saturation occurs at an evolved stage of differentiation, whereas it occurs slightly earlier in Sept-Iles and Hongge intrusions (Table 3.1). Nonetheless, apatite crystallises even earlier in Panzhihua and Taihe intrusions (Table 3.1), triggered by possible crustal (calcareous) contamination (Ganino *et al.*, 2013; Table 3.1) that increases the CaO content of the melt and probably resulting in its saturation in P (Tollari *et al.*, 2006).

3.3 Samples

Six intrusions and 1 igneous complex were selected in this study in order to cover the variations naturally occurring among different mafic layered intrusions (Table 3.1; Annexe 34). The selected mafic intrusions were chosen because they are extensively studied and provide a framework to determine which parameters affect cumulus apatite chemistry. Apatite-bearing samples from Sept-Iles Intrusive Suite (N=22), the northern limb of the Bushveld Complex (N=9) and the North (N=3)

and South (N=2) ranges of Sudbury Igneous Complex were analysed for new geochemical data (volatiles, 31 trace elements (Annexe 34), and Sr isotopes). Results are supplemented by published data from the Sept-Iles Intrusive Suite (N=21), the Skaergaard intrusion (N=51), the eastern (N=22) and western (N=13) limbs of the Bushveld Complex, Hongge (N=6), Taihe (N=26) and Panzhihua (N=37) layered intrusions and the South (N=4) and East (N=4) ranges of Sudbury Igneous Complex. Table 3.2 summarises the source and nature of all data used in this study. More details on these intrusions can be found in Annexe 35. Lithostratigraphic columns, localising the samples, are available in Annexe 34. Intrusions are presented in order of increasing degree of crustal contamination.

Sept-Iles Intrusive Suite was chosen to study the detailed variation of apatite composition throughout a single layered intrusion formed by multiple magma injections and negligible amounts of crustal contamination (Namur *et al.*, 2010). In this study, we selected 12 samples containing cumulus (Figure 3.1a) and 3 samples hosting intercumulus apatite in MCU I, along with 7 samples containing intercumulus apatite from MCU III (Annexe 34). These samples were complemented by literature data of cumulus and intercumulus apatite from MCU II, including those from the mineralised Critical Zone (Kieffer *et al.*, 2023; Table 3.2).

The Skaergaard intrusion is widely recognised as a typical example of fractional crystallisation in a closed system (Wager & Brown, 1968), with a negligible amount of crustal contamination (Stewart & DePaolo, 1990). Data of both cumulus and intercumulus apatite are exclusively compiled from the literature (EMPA and LA-ICP-MS) and cover the LZ, MZ and UZ (Table 3.2; Annexe 34; Brown & Peckett, 1977; Sonnenthal, 1992; Pedersen *et al.*, 2021).

Table 3.2 – Summary of the samples used in this study, localisation in each intrusion and type of analyses. Italic numbers into brackets correspond to the number of individual analyses of apatite grains (this study). Lithostratigraphic columns with exact location of each sample is provided in Annexe 34.

Intrusion	Apatite type	Source	EMPA, N=	LA-ICP-MS, N=	Zone
Sept-Iles	Intercumulus	Kieffer *et al.* (2023)	6	6	MCU II
		This study	10 *(47)*	10 *(49)*	MCU I, III
	Cumulus	Kieffer *et al.* (2023)	15	15	MCU II
		This study	12 *(60)*	12 *(103)*	MCU I
Skaergaard	Intercumulus	Brown & Peckett (1977)	3	–	LZa, UZa
		Sonnenthal (1992)	12	–	UZa
		Pedersen *et al.* (2021)	11	20	LZa, LZb, LZc, MZ, UZa
	Cumulus	Brown & Peckett (1977)	2	–	UZb, UZc
		Pedersen *et al.* (2021)	5	14	UZb, UZc
Bushveld					
Northern limb	Intercumulus	This study	5 *(8)*	5 *(7)*	UZa
	Cumulus	This study	4 *(71)*	4 *(69)*	UZc
Eastern limb	Intercumulus	Boudreau *et al.* (1986)	1	–	CZ
		Willmore *et al.* (2000)	7	–	LZ, MZ, UZb
	Cumulus	Boudreau *et al.* (1986)	1	–	UZc
		Willmore *et al.* (2000)	2	–	UZc
		Van Tongeren & Mathez (2012)	11	11	UZc
Western limb	Intercumulus	Boudreau & Kruger (1990)	10	–	CZ, MZ
	Cumulus	Boudreau *et al.* (1986)	3	–	CZ
Hongge	Cumulus	Xing & Wang (2017)	6	6	UZ
Taihe	Intercumulus	She *et al.* (2016)	1	1	MZ_{I}
	Cumulus	She *et al.* (2016)	22	25	MZ_{II}, MZ_{III}, MZ_{V}, MZ_{VI}, UZ
Panzhihua	Intercumulus	Pang *et al.* (2009)	4	–	MGZ, LZ, UZ
	Cumulus	Pang *et al.* (2009)	17	–	MZb
		Xing *et al.* (2014)	16	16	MZb
Sudbury					
North Range	Intercumulus	Warner *et al.* (1998)	4	–	Contact Sublayer, LU
	Cumulus	Warner *et al.* (1998)	2	–	MU
		This study	3 *(14)*	3 *(19)*	MU
South Range	Intercumulus	Warner *et al.* (1998)	2	–	LU
	Cumulus	Warner *et al.* (1998)	2	–	MU
		This study	2 *(10)*	2 *(20)*	MU
East Range	Intercumulus	Warner *et al.* (1998)	2	–	LU
	Cumulus	Warner *et al.* (1998)	2	–	MU

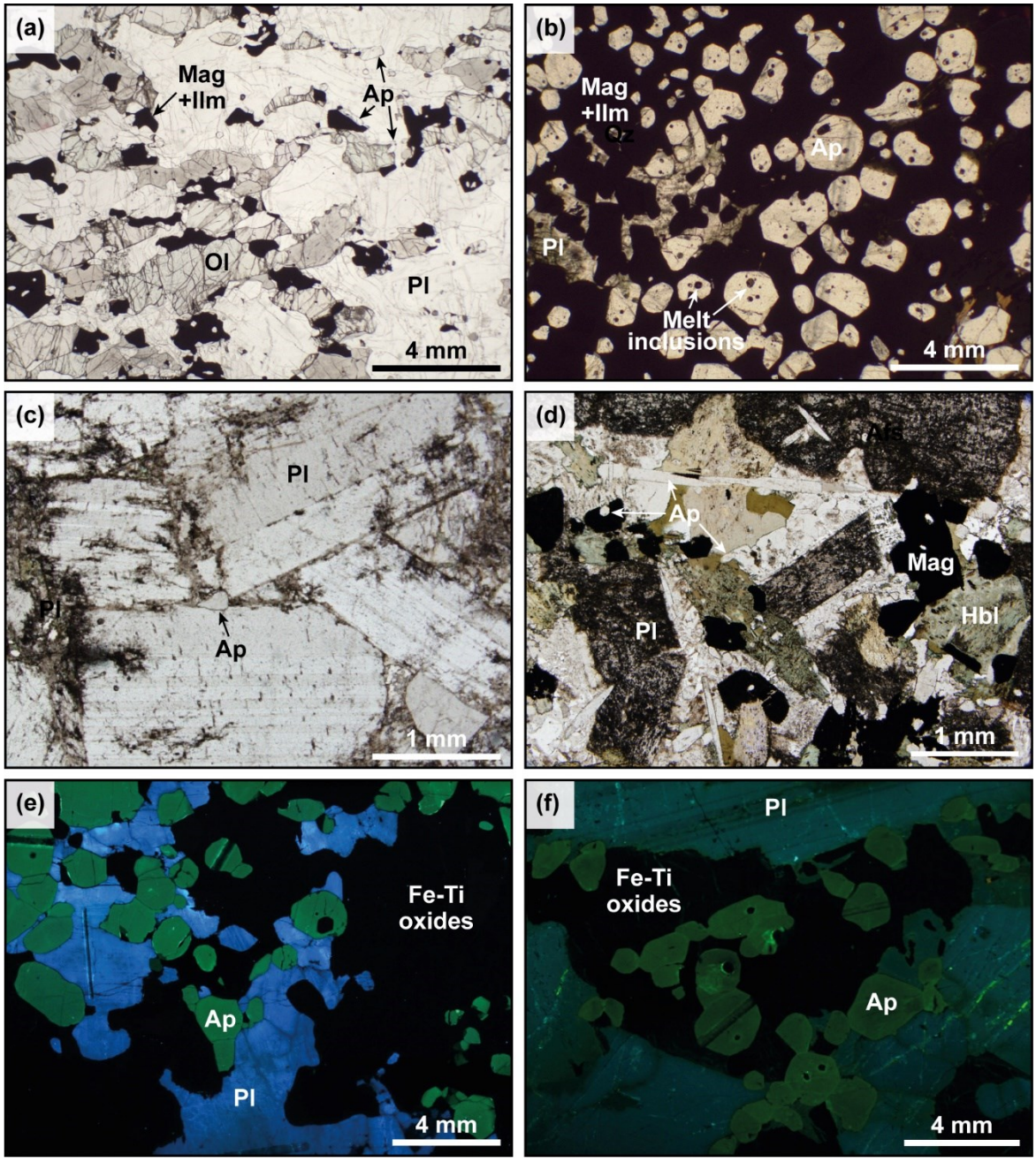

Figure 3.1 – Microphotographs (a to d) of apatite from the mafic layered intrusions studied. (a) cumulus apatite from the Fe–Ti–P unmineralised MCU I of Sept-Iles Intrusive Suite (sample 9-439.5); (b) cumulus apatite from the Fe–Ti–P mineralised nelsonite layer of the Upper Zone C of the Bushveld Complex (sample 304.72); (c) intercumulus apatite from the Upper Zone A of the Bushveld Complex (sample 1382.82) is interstitial to plagioclase crystals; and (d) cumulus apatite from the Fe–Ti–P unmineralised Main Unit (Transition Zone Gabbro) of Sudbury Igneous Complex North Range (sample 13AV-312133). Cathodoluminescence imaging (e, f) of cumulus apatite, showing the absence of altered rims of dissolution-reprecipitation due to fluid circulation. (e) cumulus apatite from Sept-Iles MCU II (sample S9-214.8); and (f) cumulus apatite from the Upper Zone of Bushveld northern limb (sample 559.16). Ap apatite, Hbl hornblende, Mag magnetite, Ilm ilmenite, Ol olivine, Pl plagioclase

The Bushveld Complex was selected because its primary komatiitic melt was significantly contaminated by the continental crust (20 to 30 %; Barnes *et al.*, 2010; Eales & Costin, 2012), and records an additional local signature depending on the host rock composition (i.e., dolomite in the northern limb; Ashwal *et al.*, 2005; Maier *et al.*, 2016). We selected 5 samples containing intercumulus apatite (Figure 3.1c) and 4 samples with cumulus apatite (Figure 3.1b) in the UZa and UZc of Bushveld northern limb, respectively (Table 3.2; Annexe 34). These samples originate from the Bellevue drillcore, whose stratigraphy and geochemistry are well-characterized by Barnes *et al.* (2004) and Ashwal *et al.* (2005). Apatite compositional data from the eastern (N=22) and western (N=13) limbs were compiled from the literature for comparison (Boudreau *et al.*, 1986; Willmore *et al.*, 2000; Van Tongeren & Mathez, 2012; Boudreau and Kruger 1990).

The Hongge Taihe and Panzhihua layered intrusions associated with the Emeishan LIP were selected as their primary melts (picrites) originated from a deep and fertile mantle source (Zhou *et al.*, 2013). The Hongge layered intrusion was contaminated with up to 15 % of metamorphic country rocks (i.e., schists and metasandstones; Tang e*t al.*, 2021). Literature data, both from EMPA and LA-ICP-MS, is available for cumulus apatite (N=6) from the UZ (Table 3.2; Annexe 34; Xing & Wang, 2017).

The Taihe layered intrusion was contaminated by up to 10 % of calcareous country rocks (Tang et al., 2021), although it is still debated. Existing apatite data, both from EMPA and LA-ICP-MS, from She *et al.* (2016) covers the MZ I (intercumulus apatite, N=1) and the MZII, III, V, VI and UZ (cumulus apatite, N=25) of Taihe layered intrusion (Table 3.2; Annexe 34).

The Panzhihua Intrusion was contaminated up to 20 % with calcareous crustal component (i.e., dolomitic limestone, marble) that triggered massive oxide crystallisation (Zhou et al., 2005; Ganino et al., 2013; Tang et al., 2021). Apatite data from the literature corresponds to intercumulus apatite from the MGZ, LZ and UZ (EMPA only, N=4; Pang *et al.*, 2009) and cumulus apatite from the MZb (EMPA and LA-ICP-MS, N=33; Table 3.2; Annexe 34; Pang *et al.*, 2009; Xing *et al.*, 2014).

The Sudbury Igneous Complex was chosen to represent a crustally-derived melt formed by partial melting of predominantly the upper crust upon a meteoritic impact (Mungall *et al.*, 2004; McNamara

et al., 2017; Keays & Lightfoot, 2020). The country rocks of the Sudbury Igneous Complex vary from granites to the North to metasediments in the South, and that their assimilation locally caused differences in the magma trace element content between the North and South ranges (Ames *et al.*, 2005; Zieg & Marsh, 2005), which can even be reflected by different arsenic content and mineralogy of the Ni-sulfide ores (Ames *et al.*, 2005; Dare *et al.*, 2010a, 2010b). In order to establish if the assimilation of different country rocks is recorded in apatite composition, we selected 3 samples containing cumulus apatite in the North Range MU (Figure 3.1d) and 2 samples from the South Range MU (Table 3.2; Annexe 34). These data are supplemented by literature data (EMPA only), including samples of the MU containing cumulus apatite (N=6) and samples from the Contact Sublayer and LU hosting intercumulus apatite (N=8) and from the North, South and East ranges (Table 3.2; Annexe 34; Warner *et al.*, 1998).

3.4 Analytical methods

Major, volatile and trace elements were determined in cumulus and intercumulus apatite from a total of 36 samples from Sept-Iles (22 samples), Bushveld (9 samples) and Sudbury (5; Table 3.2; Annexe 34) following the same analytical protocols described in Kieffer *et al.* (2023) and summarized hereafter. Major and volatile elements were determined at the Laboratoire de Microanalyse (Université Laval, Canada), using a Cameca SX100 electron micro-analyser fitted with 5 WDS detectors (wavelength dispersive spectrometers). Analytical conditions were set to a 15 kV acceleration voltage, a 10 nA beam current, and the beam was defocused to a diameter of 10 µm, in order to avoid F migration. Repeated analyses of a Durango apatite standard ensured suitable detection limits as well as good accuracy and precision. Detailed results are given as Annexe 36.

Trace elements in apatite were determined by LA-ICP-MS at LabMaTer (Université du Québec à Chicoutimi, Canada), using a Resonetics Resolution M-50 193 nm Excimer laser coupled with an Agilent 7900 ICP-MS. Apatite was analysed using a 15 to 55 µm beam, ablating lines across the grains at an ablation rate of 15 Hz, with a fluence of 5 J/cm^2, and a dwell time of 10 µm/s. Calibration was performed using the reference material NIST610, and data quality was monitored using secondary reference materials NIST612, GSD, and in-house apatite UQAC-APA. The Ca content determined by EMPA on apatite was used as the internal standard for LA-ICP-MS calibration. Data

processing was performed using the Iolite 4 software (Paton *et al.*, 2021). Three additional samples from Sept Iles MCU I (9-852, 9-514 and 9-429) were analysed at the Research School of Earth Sciences (RSES; The Australian National University) using the same analytical protocol. Detailed results are provided in Annexe 37. Although Fe was determined, the measurements of Fe^{56} and Fe^{57} are not accurate and could not be used (see Supplementary Material S4 in Kieffer *et al.*, 2023).

In situ analyses of Sr isotopes were also performed on apatite from 13 samples (Sept-Iles, Bushveld northern limb, and Sudbury North and South ranges) at the Norwegian Laboratory for Mineral and Materials Characterisation (MiMaC) at the Geological Survey of Norway (NGU). The Sr isotopes were determined by laser ablation multicollector (MC)ICP-MS using a Photon Machines Analyte excite 193 nm excimer laser equipped with a HelEx II two-volume cell coupled with a Nu Plasma 3 MC-ICP-MS. Detailed analytical protocol and results are given in Annexe 38 to 41, and a summary of the results is provided in Table 3.3.

Table 3.3 – Summary of the $(^{87}Sr/^{86}Sr)_i$ determined in cumulus apatite

Mafic layered intrusion	Unit	Sample	n =	Mean		2σ (%)	MSWD
Sept-Iles	MCU II	HN-99-50	21	0.704592	± 0.000047	0.0066	0.47
	MCU II	S9-148	24	0.704251	± 0.000053	0.0076	0.18
	MCU II	ON-07-125	17	0.704478	± 0.000086	0.012	0.51
	MCU I	9-389	6	0.704010	± 0.00012	0.016	0.34
	MCU I	9-410	19	0.703868	± 0.000052	0.0074	0.26
	MCU I	9-481	20	0.703892	± 0.000051	0.0073	0.72
	MCU I	9-505	22	0.703857	± 0.000049	0.007	0.67
	MCU I	9-538	21	0.703863	± 0.000056	0.0079	0.24
Bushveld	UZc	157.07	23	0.707490	± 0.00011	0.016	0.52
	UZc	304.72	22	0.707679	± 0.00009	0.013	0.24
	UZc	559.10	23	0.707400	± 0.00015	0.021	0.14
Sudbury North Range	MU	3AV-31213	9	0.706670	± 0.00017	0.024	0.19
Sudbury South Range	MU	01AV-466	6	0.706980	± 0.00014	0.020	0.53

3.5 Results

The volatile element content of apatite, determined by EMPA, is shown in Figure 3.2a (full data given in Annexe 36, 42). The full suite of 31 trace elements in apatite, determined by LA-ICP-MS, is displayed on a multielement diagram in which the elements are ordered according to their expected compatibility into apatite (i.e., volatiles, then increasing and decreasing compatibility from, respectively, Pb to MREE and MREE to Si) (Figure 3.3; full data given in Annexe 37). However, most analyses from the literature only have in common REE + Y, Sr, Th and U. The other trace elements were not always analysed (i.e., Rb, Ba, Mn, Zr or V) and thus limits comparisons within the whole dataset (Annexe 42).

3.5.1 Variation in volatile elements

The volatile composition of apatite was determined on 210 individual apatite grains from 21 samples containing cumulus apatite and 15 samples with intercumulus apatite originating from Sept-Iles, Bushveld (northern limb), and Sudbury (Table 3.2; Figure 3.2a; Annexe 42). These results are compared with published volatile content of cumulus apatite from 106 samples, and intercumulus apatite from 63 samples, originating from Skaergaard, Bushveld (eastern and western limbs), Hongge, Taihe, Panzhihua and Sudbury (Table 3.2; Figure 3.2b).

As is typical for apatite from the evolved part of mafic layered intrusions (Boudreau *et al.*, 1995), all cumulus apatite is fluorapatite with F > 2.45 wt.% and Cl generally < 0.8 wt.%, but the latter varying between 0.03 and 1.38 wt.%. In the F-Cl-OH ternary space, cumulus apatite generally contains > 70 % mole fraction of F and < 10 % and < 30 % moles fractions of Cl and OH, respectively (Figure 3.2). Although the cumulus apatite volatile mole fractions are homogeneous and in a restricted range within a single intrusion, there is clearly a variation in composition among the different mafic layered intrusions (Figure 3.2). The most prominent variation concerns the Cl mole fraction. It is the lowest (1 to 6 % mole fraction Cl) for Sept-Iles, Skaergaard, Hongge, Taihe and Panzhihua. The Cl mole fraction of cumulus apatite from Sept-Iles MCU I is slightly lower than that of MCU II (< 2 and < 5 % mole fractions, respectively). However, apatite contains between 5 and 13 % mole fractions of Cl for Sudbury, with the samples from the North Range having systematically higher Cl values than these from the South Range. Cumulus apatite from the Bushveld Complex reaches 7 to 20 % mole fractions

of Cl, with the higher values obtained in cumulus apatite from the northern limb. Calc-silicate xenoliths are found close to the cumulus apatite from northern limb and represent the remnants of dolomite xenoliths (Barnes *et al.*, 2004). It is possible that dissolution of the dolomite may have locally increased the Cl of the magma, because the Cl content is much higher in apatite from the northern limb compared to those from the eastern and western limbs (Figure 3.2).

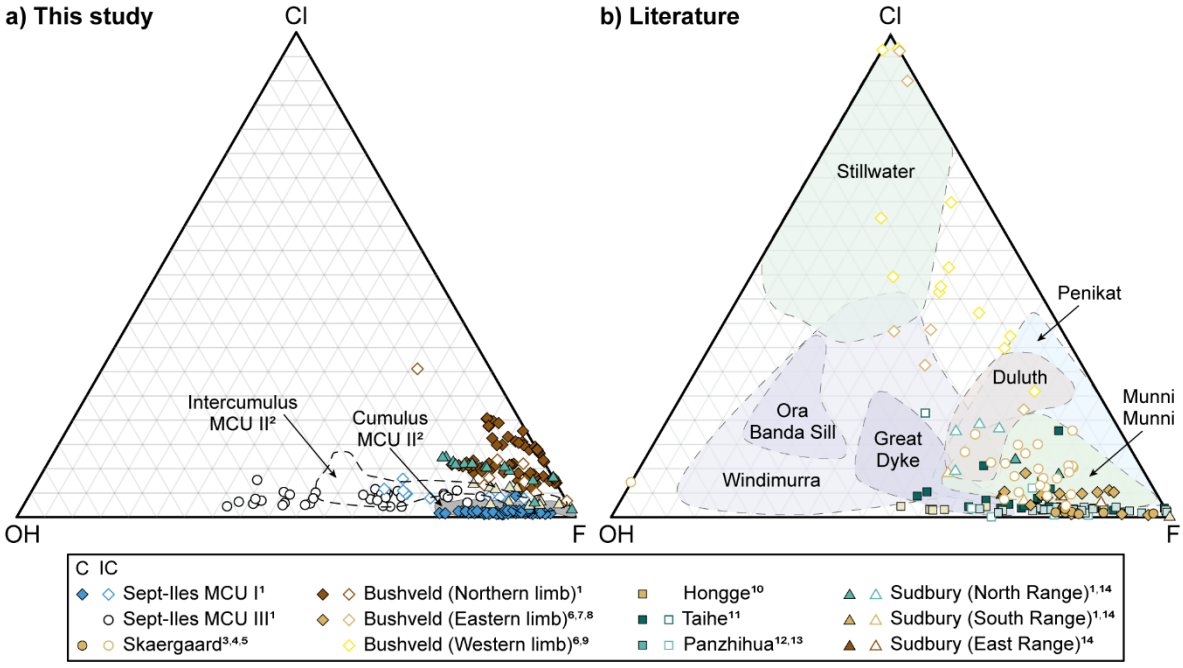

Figure 3.2 – Variation of OH-F-Cl mole fraction in apatite as a function of cumulus or intercumulus origin in several mafic layered intrusions. F, Cl and OH mole fractions were calculated according to the approach of Piccoli & Candela (2002). (a) New analyses with fields shown from Sept-Iles MCU II (from Kieffer *et al.*, 2023), and (b) compilation data, including fields for intercumulus apatite from mafic/ultramafic intrusions (modified from Boudreau *et al.*, 1995). C cumulus (filled symbols), IC intercumulus (open symbols).

Source of data: [1]this study; [2]Kieffer *et al.* (2023); [3]Brown & Peckett (1977); [4]Sonnenthal (1992); [5]Pedersen *et al.* (2021); [6]Boudreau *et al.* (1986); [7]Willmore *et al.* (2000); [8]Van Tongeren & Mathez (2012); [9]Boudreau & Kruger (1990); [10]Xing & Wang (2017); [11]She *et al.* (2016); [12]Pang *et al.* (2009); [13]Xing *et al.* (2014); [14]Warner *et al.* (1998)

Cumulus and intercumulus apatite have distinct volatile compositions: overall, intercumulus apatite from the more primitive parts of the intrusions contains less F (< 75 % mole fraction), but above all more Cl (5 to 96 % mole fractions) and/or OH (25 to 100 % moles fractions) than cumulus apatite from the more evolved parts of the intrusions (Figure 3.2). This difference can be observed not only at the scale of a single mafic layered intrusion, such as in the Skaergaard (Brown & Peckett, 1977; Pedersen *et al.*, 2021), Sept-Iles (this study; Kieffer *et al.*, 2023) and Bushveld (Boudreau *et al.*, 1986) intrusions, but also for most of the mafic layered intrusions shown in Figure 3.2. Several processes might explain the lower Cl content of cumulus apatite, such as (1) the exsolution and escape of a Cl-rich fluid phase (Bushveld; Boudreau & Kruger, 1990), (2) different F and Cl exchange coefficients at the time of intercumulus and cumulus apatite crystallisation (Skaergaard; Pedersen *et al.*, 2021), or (3) Cl behaves as an incompatible element and can only be concentrated in interstitial liquid pockets from which crystallises intercumulus apatite (i.e., Sept-Iles; Kieffer *et al.*, 2023). Some intercumulus apatite are even richer in Cl, notably just below the major PGE zones in the lower parts of Bushveld and Stillwater intrusions, and this has been interpreted as the result of the circulation of Cl-rich metasomatic fluids (Boudreau & McCallum, 1990; Boudreau *et al.*, 1986, 1995).

3.5.2 Trace element variation in apatite

In order to compare the trace element patterns from each mafic intrusion, apatite data was plotted on the multielement diagrams shown in Figure 3.3. This allows to distinguish which element or ratio vary among the different intrusions (section 3.5.2.1.) or within a single intrusion (Sept-Iles intrusive Suite; section 3.5.2.2.) Trace element composition of apatite was determined on 267 individual apatite grains from 21 samples of cumulus apatite and 15 samples of intercumulus apatite from Sept-Iles, Bushveld (northern limb), and Sudbury (Table 3.2; Annexe 37). New data are compared with previously published data of cumulus and intercumulus apatite (87 and 27 samples, respectively; average of analyses for each sample) from Skaergaard, Bushveld (eastern and western limbs), Hongge, Taihe, Panzhihua and Sudbury (Table 3.2).

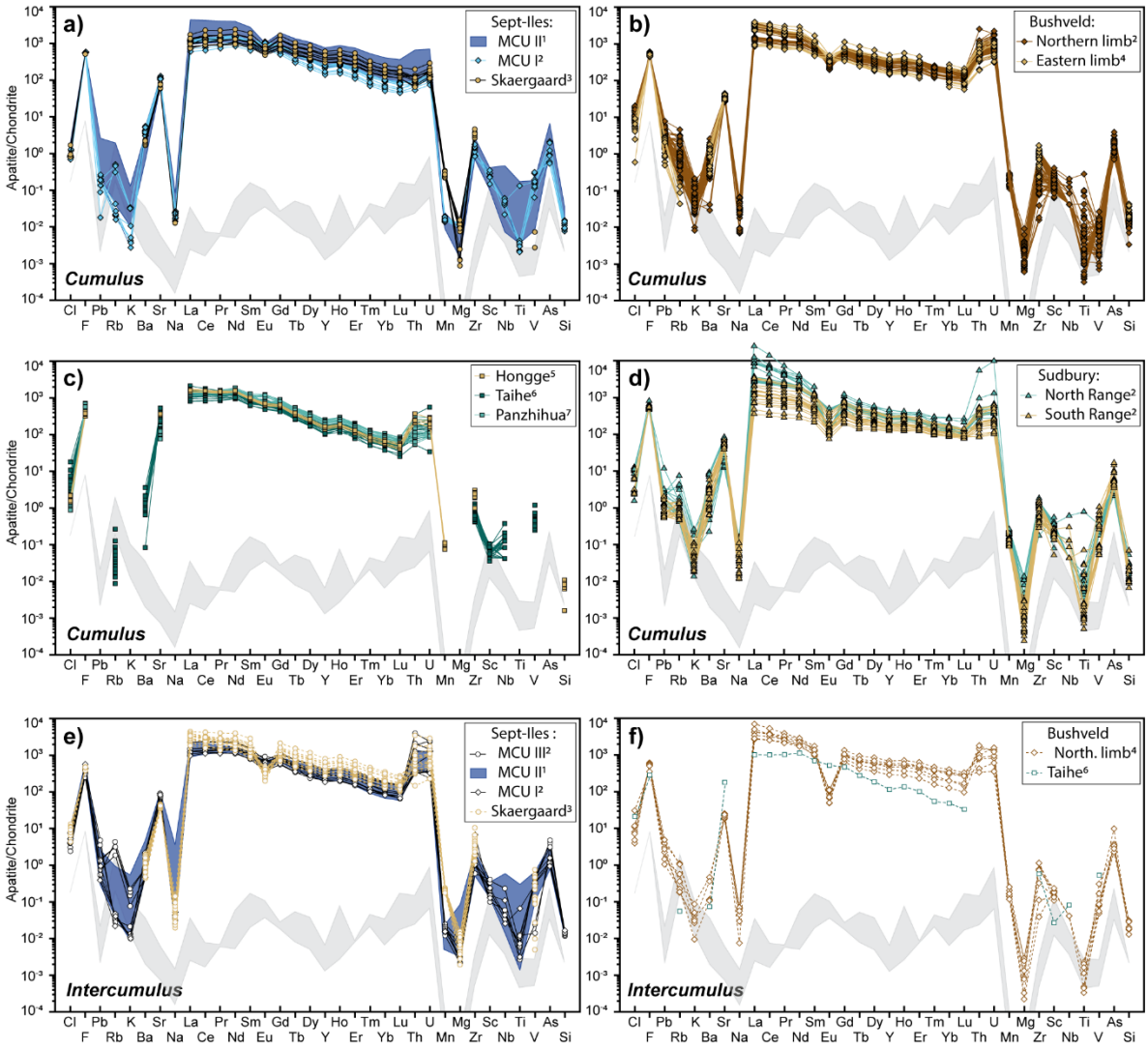

Figure 3.3 – Multielement diagrams of cumulus apatite from the mafic intrusions of (a) Sept-Iles and Skaergaard and, (b) Bushveld northern and eastern limbs, (c) Panzhihua, Hongge and Taihe layered intrusions, and (d) Sudbury North and South ranges, and for intercumulus apatite from (e) Sept-Iles and (f) Skaergaard, Bushveld northern limb and Taihe. The grey field corresponds to lower limits of detection determined with a 15 µm beam (top line) and 55 µm beam (bottom line) on the apatite reference material (UQAC-APA). Cl, F and Si detection limits are from electron microprobe analyses.

Source of data: [1]Kieffer *et al.* (2023); [2]This study; [3]Pedersen *et al.* (2021); [4]Van Tongeren & Mathez (2012); [5]Xing & Wang (2017); [6]She *et al.* (2016); [7]Xing *et al.* (2014)

3.5.2.1 Variations among mafic layered intrusions

Cumulus apatite from all layered intrusions share overall similar REE patterns with equivalent LREE enrichment (Figure 3.3a to 3.3d). However, when comparing the $(La/Nd)_N$ and $(Gd/Yb)_N$ ratios, which reflect the slope of the LREE and HREE, respectively, on the multielement diagram, several groups can be distinguished (Figure 3.4a): (1) group 1, with a $(La/Nd)_N$ ratio around 1 and the most elevated $(Gd/Yb)_N$ ratio (>7 to 13; Sept-Iles MCU I, Hongge, Taihe and Panzhihua); (2) group 2, with a $(La/Nd)_N$ ratio around 1 and the $(Gd/Yb)_N$ ratio between 4 and 7 (Sept-Iles MCU II and Skaergaard); and (3) group 3, with $(La/Nd)_N$ ratio > 1 and $(Gd/Yb)_N$ ratio < 6 (Bushveld and Sudbury). In addition, cumulus apatite crystals from the 3 groups have different Eu anomalies (Eu/Eu*). The Eu anomaly is slightly negative in apatite from Hongge, Taihe and Panzhihua, Sept-Iles MCU II and Skaergaard (Figure 3.3a and 3.3c), whereas the negative Eu anomaly is far more pronounced in the case of Sudbury and Bushveld (Figure 3.3d and 3.3b).

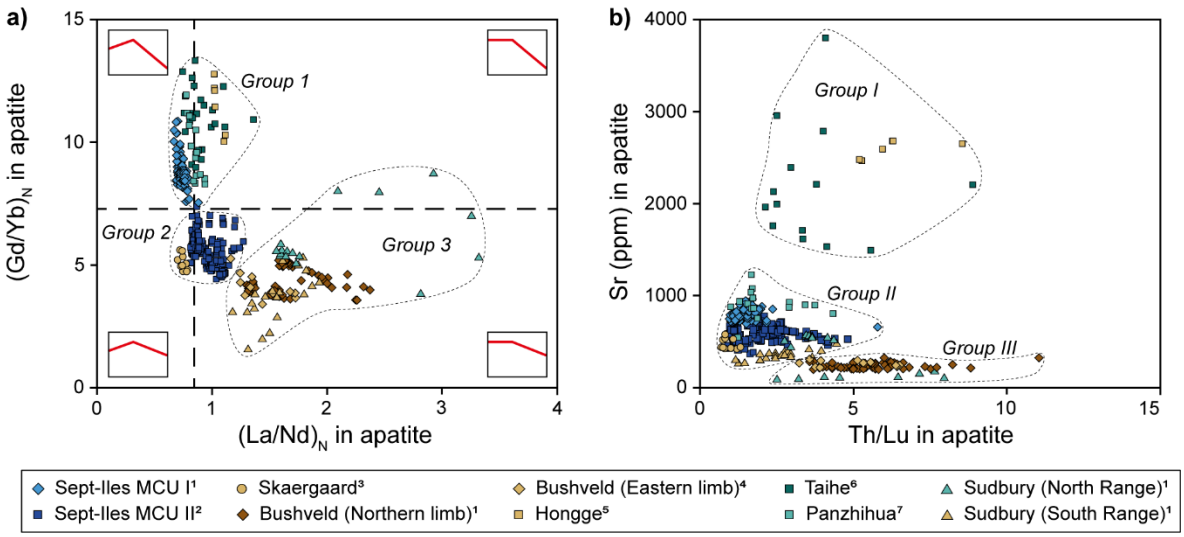

Figure 3.4 – Binary plots highlighting the key variations observed on the multielement diagrams among cumulus apatite from different mafic layered intrusions. (a) LREE $(La/Nd)_N$ and HREE $(Gd/Yb)_N$ ratios in cumulus apatite illustrating the variation of the REE slope; (b) Sr content of apatite against the slope between Th and Lu (Th/Lu) on the multielement diagram. Note that the 3 groups do not always include the same samples between a) and b).

Source of LA-ICP-MS data: [1]This study; [2]Kieffer *et al.* (2023); [3]Pedersen *et al.* (2021); [4]Van Tongeren & Mathez (2012); [5]Xing & Wang (2017); [6]She *et al.* (2016); [7]Xing *et al.* (2014)

The Th, U and Sr concentrations in apatite also vary among the different intrusions (Annexe 42). The abundances of Th and U in apatite are comparable in all the mafic layered intrusions (2.2 to 6.93 ppm and 0.8 to 2.0, respectively; Figure 3.3a, 3.3c and 3.3d), with the exception of Bushveld, in which Th and U concentrations are significantly higher (ca. 16 and 6 ppm, respectively; Figure 3.3b). Cumulus apatite from Sudbury North Range is also enriched in Th (10.5 ppm) and U (3 ppm) compared to that of the South Range of Sudbury (6 ppm Th and 1.8 ppm U). In contrast, the Sr content of apatite is the lowest in Bushveld (219 to 269 ppm) and Sudbury North Range and the highest in Hongge (2662 ppm), Taihe (1760 ppm) and Panzhihua (901 ppm) intrusions, with intermediate values for Sept-Iles (602 to 802 ppm) and Skaergaard (441 ppm). The Th concentration in apatite can also be expressed relative to the HREE concentration by using the Th/Lu ratio, which reflects the slope between Lu and Th on the multielement diagram, i.e., an enrichment of Th (and U) relative to Lu (Figure 3.4b). When compared to the Sr abundance in apatite, 3 groups can be distinguished (Figure 3.4b), that are not defined by the same samples as in Figure 3.4a: (1) apatite from group I is defined by systematically high Sr concentrations but variable Th/Lu ratio (Hongge, Taihe); (2) group II has intermediate Sr concentration and Th/Lu < 5 (Sept-Iles, Skaergaard, Panzhihua, Sudbury South Range); and (3) apatite from group III has the lowest Sr contents and highest Th/Lu < 10 (Bushveld and Sudbury North Range).

Given that the timing of saturation in apatite with respect to the degree of fractional crystallisation can vary in each mafic layered intrusion (Table 3.1), it is of the utmost importance to compare apatite compositions to a given benchmark, common to all intrusions, such as the anorthite content of plagioclase (Figure 3.5; Annexe 43). This helps tracing fractionation, as well as to evaluate which trace elements might be affected by the characteristics of mafic layered intrusions, such as the degree of magma evolution.

In general, the REE+Y, Sr, Th and U content of cumulus apatite can differ among the mafic layered intrusions at the same anorthite content of associated plagioclase. Although the elements can show the same behaviour during fractional crystallisation, different magma compositions can cause these differences in concentration at the same degree of magma evolution. In Sept-Iles MCU II, there is an increase in REE+Y with decreasing An content, but the Eu concentration increases less than that of

REE+Y. As a consequence, the Eu anomaly becomes increasingly negative with increasing fractionation (Kieffer *et al.*, 2023). Cumulus apatite from Skaergaard, possibly Bushveld, and Sudbury also show an increase in REE+Y with decreasing An content of associated plagioclase (Figure 3.5a, 5b). However, the REE+Y content of cumulus apatite from Taihe and Panzhihua is nearly constant (ca. 3000 ppm), with only a slight increase with decreasing anorthite content. The absolute Eu content of apatite from Skaergaard (ca. 35.1 ppm), Hongge, Taihe and Panzhihua (36.7 to 44.6 ppm) is within the range of that of Sept-Iles apatite (ca. 42.7 to 56.3 ppm), but the Eu content of apatite from Bushveld (15.1 to 22.2 ppm) and Sudbury (8.7 to 24.5 ppm) is lower than that in apatite from the four previously cited intrusions. A lower Eu concentration combined with an increasing REE+Y concentration causes the development of an increasingly negative Eu anomaly. Thus, the negative Eu anomaly is more pronounced in Bushveld and Sudbury cumulus apatite than that of Sept-Iles, Skaergaard, Taihe and Panzhihua, at the same anorthite content of associated plagioclase (Figure 3.3b, 3.3c; Figure 3.5c, 3.5d; Annexe 42 and 43).

In addition, the Sr concentration in apatite appears to decrease with decreasing anorthite content of associated plagioclase. This is most visible in the case of Sept-Iles MCU II (Figure 3.5e) and can be attributed to the extensive crystallisation of plagioclase (Belousova *et al.*, 2002; Tollari *et al.*, 2008; Xing *et al.*, 2014; She *et al.*, 2016; Kieffer *et al.*, 2023). Bushveld and Panzhihua cumulus apatite seem to define an evolution for Sr (Figure 3.5f) similar to that of cumulus apatite from Sept-Iles MCU II, but additional data would be required to confirm it in the other layered intrusions. Moreover, clear fractionation trends would probably be more developed in closed systems (i.e., Sept-Iles CZ, Bushveld UZ or Sudbury) rather than in open systems in which multiple magma injections (i.e., intrusions from Emeishan) cause numerous reversals to more primitive compositions.

The REE+Y, Th and U behave incompatibly and their contents in apatite increases, whereas the An content of plagioclase decreases, during fractional crystallisation (Kieffer *et al.*, 2023). However, whenever a different content of these incompatible elements is measured in apatite at a similar degree of melt evolution (i.e., same anorthite content of associated plagioclase), it implies different magma composition. The Th and U concentration in apatite are similar for all mafic intrusions at the

same anorthite content, except for Bushveld and Sudbury that have higher Th and U concentrations in apatite (Annexe 43).

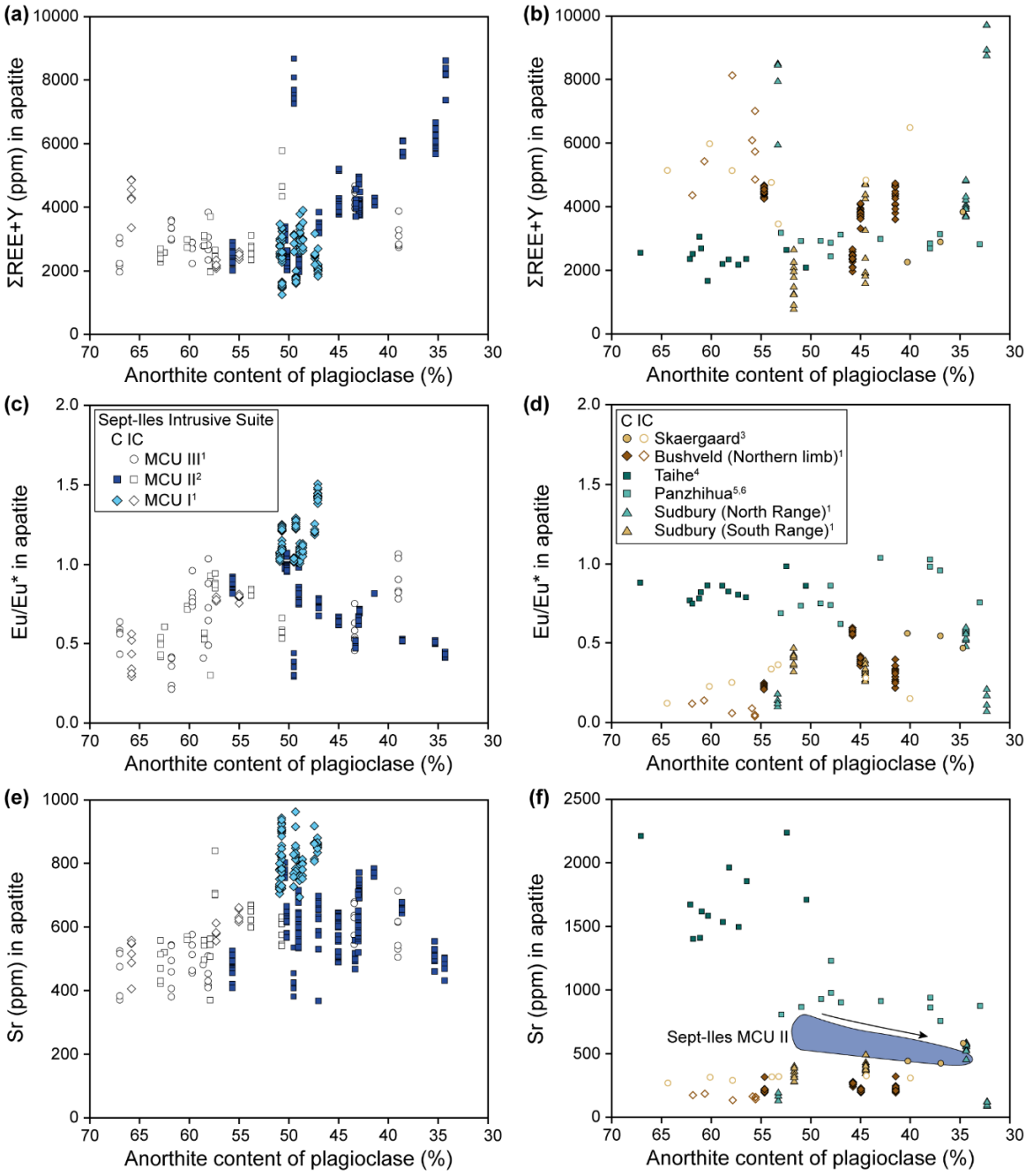

Figure 3.5 – Evolution of (a, b) REE+Y, (c, d) Eu anomaly and (e, f) Sr in cumulus (C) and intercumulus (IC) apatite from Sept-Iles Intrusive Suite (left column) and other mafic layered intrusions (right column) with anorthite content of associated plagioclase as a proxy for fractional crystallisation. Hongge intrusion and Bushveld eastern limb are not displayed for lack of corresponding plagioclase data.

Source of data: [1]This study; [2]Kieffer *et al.* (2023); [3]Pedersen *et al.* (2021); [4]She *et al.* (2016); [5]Pang *et al.* (2009); [6]Xing *et al.* (2014)

Our dataset shows that other trace elements in apatite also vary between mafic layered intrusions. However, these elements were not systematically available in the literature data, limiting the efficacity of the comparison. Thus, based on our new data, the elements that have the potential to vary significantly among mafic layered intrusions are Pb, Rb, As, Mg and V (Figure 3.3a to 3.3d). Indeed, apatite from Bushveld and Sudbury contains more Pb (1.87 to 4.88 ppm, and 4.9 to 7.52 ppm, respectively) and Rb (1.64 to 2.33 ppm, and up to 1.61 ppm, respectively) than those from Sept-Iles (0.06 to 0.85 ppm). Apatite from the Sudbury South Range is unusually enriched in As (10 ppm) compared to apatite from Sudbury North Range (4.86 ppm), Sept-Iles (1.70 to 3.57 ppm) and Bushveld (3.55 ppm). The Mg content of apatite is lower in Bushveld (139 ppm) and Sudbury South Range (41 ppm) than that in Sept-Iles (420 to 672 ppm) and Sudbury North Range (241 ppm). Skaergaard and Bushveld apatite also have less V (0.27 and 0.55 ppm, respectively) than those from Sept-Iles (5.51 to 8.83 ppm) and Sudbury South (9.76 ppm) and North (18.64 ppm) ranges. At the same anorthite content of associated plagioclase, there is more As and Na in Sudbury North Range, more Pb and Rb in Bushveld northern limb and Sudbury South Range, and more V in Taihe and Sudbury cumulus apatite. Fractional crystallisation might be responsible for an increase of Pb, Rb and As, and a decrease of V and Mg in cumulus apatite, as these elements behave incompatibly and compatibly, respectively, during crystallisation (Kieffer *et al.*, 2023). However, as the observed relative enrichments occur at the same anorthite content of associated plagioclase, they are more likely to be inherent to differences in magma composition rather than to fractional crystallisation alone. Changes in the partition coefficients of these trace elements could also lead to the crystallisation of apatite with different compositions. Finally, the K, Mn, Nb, Sc, Ti and Zr content of apatite is comparable among mafic layered intrusion and does not seem to vary with the anorthite content of associated plagioclase (Annexe 42, 43). The Mn content of Sept-Iles liquid line of descent remains constant at the time of cumulus apatite crystallisation (Namur *et al.*, 2011), which explains the lack of Mn variation in cumulus apatite. On the other hand, K, Nb, Sc, Ti and Zr, are rather incompatible into apatite and explains why small variations are not seen. However, bigger variations, such as between mafic and felsic melts, would be measurable (see Kieffer *et al.*, 2023).

Intercumulus apatite from Sept-Iles, Skaergaard and Bushveld mafic layered intrusions share similar features that allow to distinguish them from cumulus apatite. Their V, Th and U contents are generally higher than those of the corresponding cumulus apatite and they display a pronounced negative Eu anomaly. The REE+Y contents of intercumulus apatite are also typically higher than that in cumulus apatite (i.e., Skaergaard, Bushveld), but this is not always the case (i.e., Sept-Iles; Figure 3.3a, 3.3b, 3.3e and 3.3f). The Th/Lu ratio is generally higher in intercumulus apatite than in cumulus apatite (Th/Lu > 5), with the exception of Bushveld where cumulus and intercumulus apatite have similar Th/Lu (Annexe 42).

3.5.2.2 Variation within a single intrusion: Sept-Iles

Our complete detailed study of Sept-Iles Intrusive Suite reveals that cumulus apatite, associated with 2 different megacyclic units (MCU) within a single magmatic system, have distinct trace element contents and behaviours (Annexe 36, 37 and 42). On the multielement diagram (Figure 3.3a), cumulus apatite from MCU I has lower concentrations in elements that are highly incompatible during crystallisation (REE+Y, Pb, Th, U, Zr, Na, K and As) and a higher content in more compatible elements, such as Sr, Mg, V and Ba, than cumulus apatite from MCU II (Figure 3.3a). The Eu anomaly is also flat to slightly positive in cumulus apatite from MCU I, whereas it is negative in cumulus apatite from MCU II (Figure 3.3a). Concentrations in Mn, Sc, Nb and Ti are similar in cumulus apatite from both units. In addition, the REE+Y normalised pattern of cumulus apatite from MCU I is slightly depleted in LREE relative to MREE (i.e., a positive LREE slope and low $(La/Nd)_N$ ratio; Figure 3.4a) and depleted in HREE (i.e., a strongly negative HREE slope and high $(Gd/Yb)_N$ ratio; Figure 3.4a), compared to those from MCU II, which have a flatter LREE pattern (higher $(La/Nd)_N$ ratio) accompanied by a moderately negative HREE slope (lower $(Gd/Yb)_N$ ratio; Figure 3.4a). These differences observed on the multielement diagram between cumulus apatite from MCU I and MCU II are also observed for any given anorthite content of associated plagioclase (Figure 3.6; Annexe 43). However, the REE+Y are in equivalent abundance in cumulus apatite from MCU I and MCU II at the same anorthite content.

In addition, the trends of trace element concentration in cumulus apatite evolve differently with stratigraphic height in MCU I and MCU II (Figure 3.5; Annexe 44). In MCU II, the trends correspond

to increasing fractional crystallisation with decreasing stratigraphic height (Kieffer *et al.*, 2023). In contrast, for most trace elements in MCU I, there is a marked change in the trend between –2500 and –2450 m: REE+Y (including Eu; Figure 3.6a) and Na contents of cumulus apatite first increase towards -2500 m but then decrease upwards towards the top of MCU I. The Th and U content (Figure 3.6b), as well as $(La/Nd)_N$ ratio, decrease overall in MCU I but increase systematically in MCU II. In contrast, the Eu anomaly in apatite is increasingly positive in MCU I whereas it is increasingly negative in MCU II up sequence (Figure 3.6c). The Sr content (Figure 3.6d) and $(Gd/Yb)_N$ ratio of apatite also continually increase in MCU I but decrease in MCU II. The V and Mg content of cumulus apatite from MCU I at first decreases and then increases with height, whereas they continually decrease up sequence in MCU II (Figure 3.6e and 6f). Despite some differences in abundance in As, Ba, K, Mn, Nb, Rb, Sc and Ti between cumulus apatite from MCU I and MCU II, their concentrations remain constant with stratigraphic height. The Pb content of apatite remains constant in MCU I but its concentration increases in cumulus apatite from MCU II. Such differences in trace element content and evolution between the two MCU of a single mafic layered intrusion might be directly related to different magma evolution, as indicated by Namur *et al.* (2012). Indeed, magma replenishment and mixing would lead to an increase of compatible elements, such as Sr, V or Mg, that should otherwise be decreasing in the melt with increasing fractional crystallisation (Kieffer *et al.*, 2023).

Finally, intercumulus apatite from MCU I, MCU II and MCU III share similar characteristics and their multielement patterns closely overlap (Figure 3.3e): they all have higher Th, U and V concentrations than cumulus apatite.

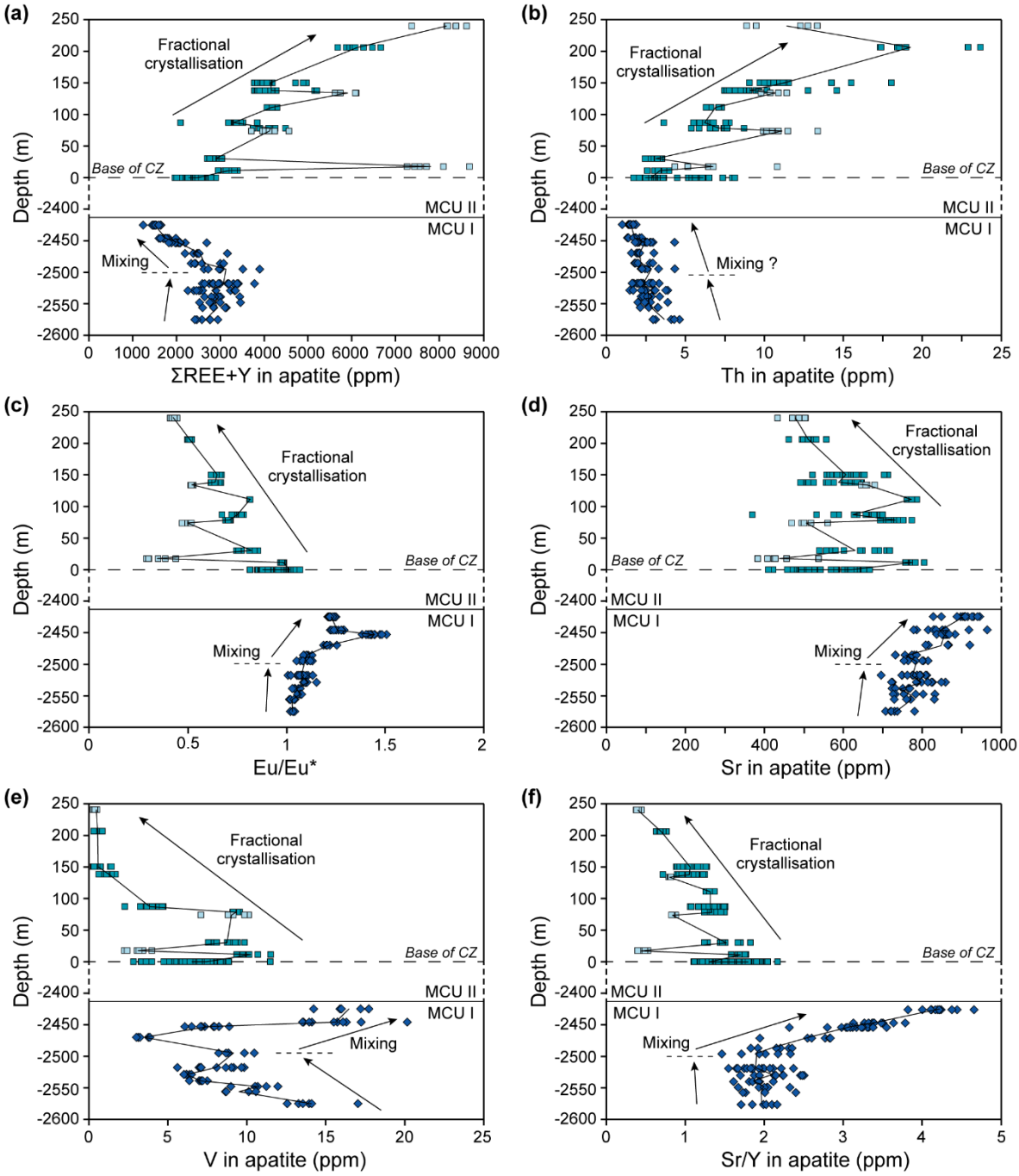

Figure 3.6 – Variation of selected trace elements in apatite with stratigraphic depths within MCU I and MCU II of Sept-Iles mafic layered intrusion. Data of MCU I is from this study, and data of MCU II is from Kieffer *et al.* (2023). In MCU II, the dark symbols correspond to apatite from Fe–Ti–P-rich layers whereas the light symbols refer to apatite from Fe–Ti–P-poor layers. Difference is interpreted in Kieffer *et al.* (2023).

3.5.3 Strontium isotopes

Strontium isotopes were measured in 233 individual cumulus apatite grains from a total of 13 samples from Sept-Iles MCU II (n = 3), Sept-Iles MCU I (n = 5), the Upper Zone C of Bushveld northern limb (n = 3), and 2 samples from the Main Unit of Sudbury (1 each from North and South ranges). Summary of the results is given in Table 3.3. The results obtained on apatite grains agree with initial Sr ($^{87}Sr/^{86}Sr)_i$ results from whole rock and/or plagioclase that were previously published either on the same sample or from the same zone of the intrusion (Annexe 42). Our apatite data can thus be compared to the ($^{87}Sr/^{86}Sr)_i$ determined on whole rock or plagioclase in other mafic layered intrusions and mafic rocks (i.e., Skaergaard, Emeishan LIP and massif-type anorthosite) with respect to the Bulk Earth Sr evolution shown in Figure 3.7. The ($^{87}Sr/^{86}Sr)_i$ is quite homogeneous within a single intrusion, whereas it varies among mafic layered intrusions where parameters, such as crustal contamination (DePaolo & Wasserburg, 1979; DePaolo, 1981) and/or mantle source, can affect the initial Sr ($^{87}Sr/^{86}Sr)_i$ values.

Olivine- and clinopyroxene-bearing intrusions (i.e., Sept-Iles, Skaergaard, Hongge, Taihe and Panzhihua) record the lowest ($^{87}Sr/^{86}Sr)_i$ values (0.70382 to 0.70553) and follow closely the Bulk Earth Sr evolution with time, with the exception of Hongge intrusion which has higher ($^{87}Sr/^{86}Sr)_i$ values (0.70450 to 0.70757; Figure 3.7). Within the Sept-Iles Intrusive Suite, cumulus apatite from MCU I has slightly lower ($^{87}Sr/^{86}Sr)_i$ values (0.703857 to 0.704010) than apatite from MCU II (0.704251 to 0.704592), confirming a slightly different magma composition or degree of crustal contamination for these 2 megacyclic units (Namur *et al.*, 2010).

As noted by Ashwal (1993) for massif-type anorthosite suites, orthopyroxene-bearing intrusions tend to have much higher ($^{87}Sr/^{86}Sr)_i$ values than those from olivine- and clinopyroxene-bearing intrusions of the same age and same location. This is explained by orthopyroxene-bearing intrusions having a more crustal signature than olivine- and clinopyroxene-bearing intrusions (Ashwal, 1993). In a similar way, the orthopyroxene-bearing intrusions of Bushveld and Sudbury have the highest ($^{87}Sr/^{86}Sr)_i$ values of all, of 0.70749, and 0.70667 to 0.70698, respectively, relative to Bulk Earth Sr evolution line (Figure 3.7).

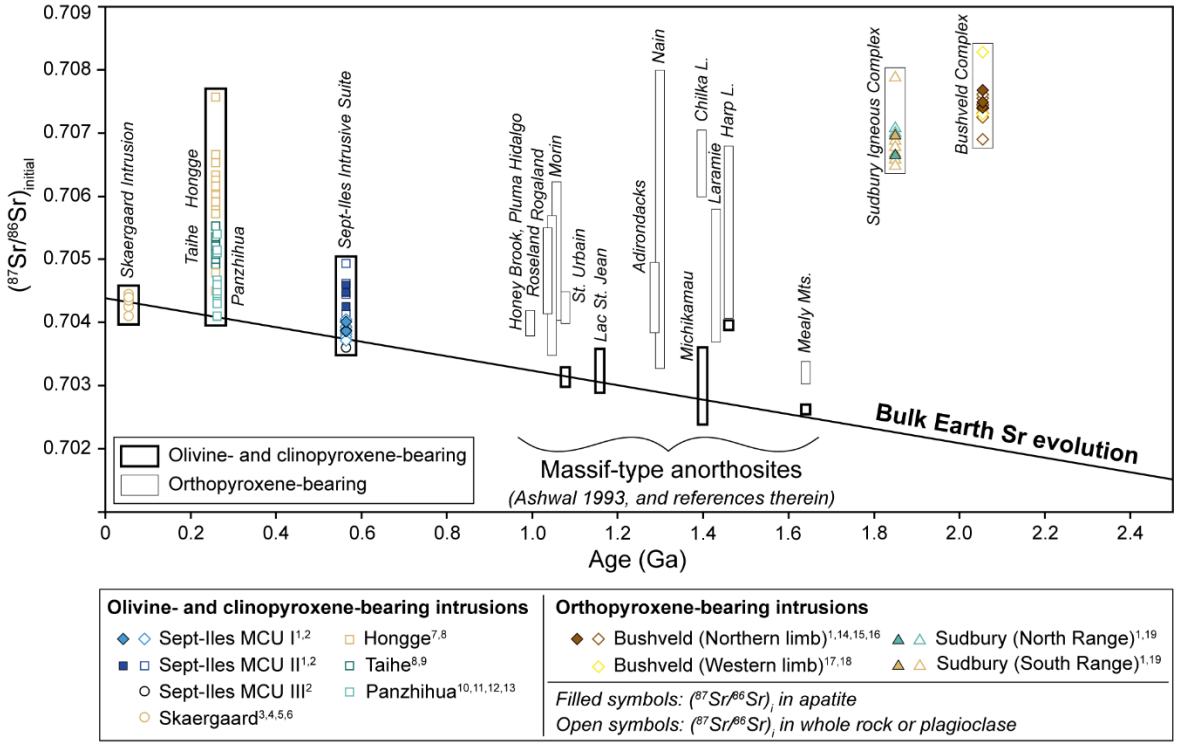

Figure 3.7 – $(^{87}Sr/^{86}Sr)_i$ of mafic layered intrusions with respect to the Bulk Earth evolution through time (DePaolo & Wasserburg, 1976). Initial Sr ratio of massif-type anorthosite is displayed for comparison (modified from Ashwal, 1993). Olivine- and clinopyroxene-bearing mafic rocks plot close to the Bulk Earth evolution while orthopyroxene-bearing mafic rocks have higher $(^{87}Sr/^{86}Sr)_i$ values.

Source of data: [1]This study; [2]Namur *et al.* (2010); [3]Leeman & Dasch (1978); [4]Stewart & DePaolo (1990); [5]McBirney & Creaser (2003); [6]Hagen-Peter *et al.* (2019); [7]Luan *et al.* (2014); [8]Tang *et al.* (2021); [9]She *et al.* (2014); [10]Zhang *et al.* (2009); [11]Howarth & Prevec (2013); [12]Hou *et al.* (2013); [13]Song *et al.* (2013); [14]Mangwegape *et al.* (2016); [15]Karykowski *et al.* (2017); [16]Huthman *et al.* (2017); [17]Kruger *et al.* (1987); [18]Kruger (1994); [19]Dickin *et al.* (1999)

3.6 Discussion

In order to develop apatite as a petrogenetic indicator for crustal contamination, depth of partial melting, fractional crystallisation and magma mixing, it is necessary to prove that sub-solidus re-equilibration and fluid metasomatism have negligible effect on apatite composition. Indeed, fluid alteration and metasomatism is common is cumulates of mafic layered intrusions, and may change the primary composition of apatite (Harlov *et al.*, 2005; Xing and Wang, 2017). Kieffer *et al.* (2023) compared trace element compositions of apatite enclosed in different minerals in samples from the CZ of Sept-Iles Intrusive Suite, to investigate whether any sub-solidus re-equilibration between apatite and host had occurred. They did not observe chemical zonation across apatite grains.

Furthermore, the composition of the apatite grains enclosed in each of the different minerals is very similar. Similarly, our new analyses from cumulus apatite from MCU I and from the UZc of Bushveld Complex, show that the difference in composition is also negligible for apatite hosted in, or adjacent to the different minerals. Furthermore, the laser ablation lines across the apatite grains reveal no significant chemical zonation between the core and the rims of apatite. Moreover, high-resolution trace element mapping of massive nelsonite from the MCU II of Sept-Iles also revealed no chemical zonation of apatite in spite of late-hydrothermal veins cross-cutting the grains (Savard *et al.*, 2023). Cathodoluminescence imaging can provide evidence of fluid alteration (Bouzari *et al.*, 2016). However, cathodoluminescence imaging of our Sept-Iles, Bushveld and Sudbury samples do no show any evidence of dissolution or reprecipitation textures (Figure 3.1e, 3.1f). Thus, subsolidus re-equilibration, as well as fluid metasomatism, do not appear to be an important factor in controlling apatite compositions in our samples. We believe that the large variation among the different samples of cumulus apatite within a single intrusion, as well as among the different intrusions, can be used to trace magmatic processes.

In this section, we discuss some of the processes that could have varied the trace element content of cumulus apatite among the different mafic magmatic systems, such as: (1) crustal contamination; (2) depth of partial melting, (3) fractional crystallisation of plagioclase, (4) magma mixing, and (5) fO_2. Although apatite preserves silicate liquid immiscibility, this process is not discussed as it would require analyses of apatite crystallising from both Fe- and Si-rich melt portions of each intrusion, as was performed in Sept-Iles MCU II (Kieffer *et al.*, 2023), and this level of detail is not available in the literature. Finally, we test the apatite discrimination diagrams proposed in Kieffer *et al.* (2023) on our compilation of apatite data from mafic layered intrusions and show that they can be used to identify mafic rocks that could be associated with Fe-Ti-P-V (cumulus apatite) or PGE-Ni-Cu (intercumulus apatite) mineralisation in mafic layered intrusions.

3.6.1 Cumulus apatite as a petrogenetic indicator in mafic layered intrusions

3.6.1.1 $(La/Nd)_N$, Th, U, Pb, Rb, As and $(^{87}Sr/^{86}Sr)_i$ in apatite as tracers of crustal contamination

The parental melt of the mafic layered intrusions studied underwent variable degrees of crustal contamination that is used to assess whether apatite can independently record this process. In this section, we show that cumulus apatite composition reflects and preserve chemical indicators of the magma from which it crystallises from. Apatite from the most contaminated intrusions (orthopyroxene-bearing) is enriched in Th, U, Pb, Rb, As, and has higher $(La/Nd)_N$ and $(^{87}Sr/^{86}Sr)_i$ compared to the less contaminated intrusions (olivine- and clinopyroxene-bearing; Figure 3.8). Several proxies are used to decipher crustal contamination of mafic-ultramafic magmas, such as trace elements concentrations, isotopic composition, or mineralogical assemblages. Highly incompatible elements concentrated in the crust (i.e., La, Th, U, or Pb; DePaolo, 1981) can be incorporated in a magma upon contamination with a crustal component, leading to an abnormal increase in these elements. In whole rock analyses, elevated ratios of incompatible (La, Ce, Th, Zr) to less incompatible (HREE, Ti, Nb) elements are indicators of crustal contamination (Pearce & Peate, 1995; Sproule *et al.*, 2002; Barnes *et al.*, 2007). Terrestrial reservoirs also have a specific O, Sr, Nd and Hf isotopic signature. Comparison of the isotopic signature of the mafic layered intrusions with those of the reservoirs and country rocks provides good estimations of the occurrence of contamination, as well as of the proportion and nature of the contaminants (Ganino *et al.*, 2013; Tang *et al.*, 2021). For example, contamination of a mantle-derived magma with crustal material should increase its $(^{87}Sr/^{86}Sr)_i$ (i.e., Bushveld, Hongge; Table 3.1; DePaolo & Wasserburg, 1979; DePaolo, 1981; Tang *et al.*, 2021; Kiglapait Intrusion, Fourny *et al.*, 2019).

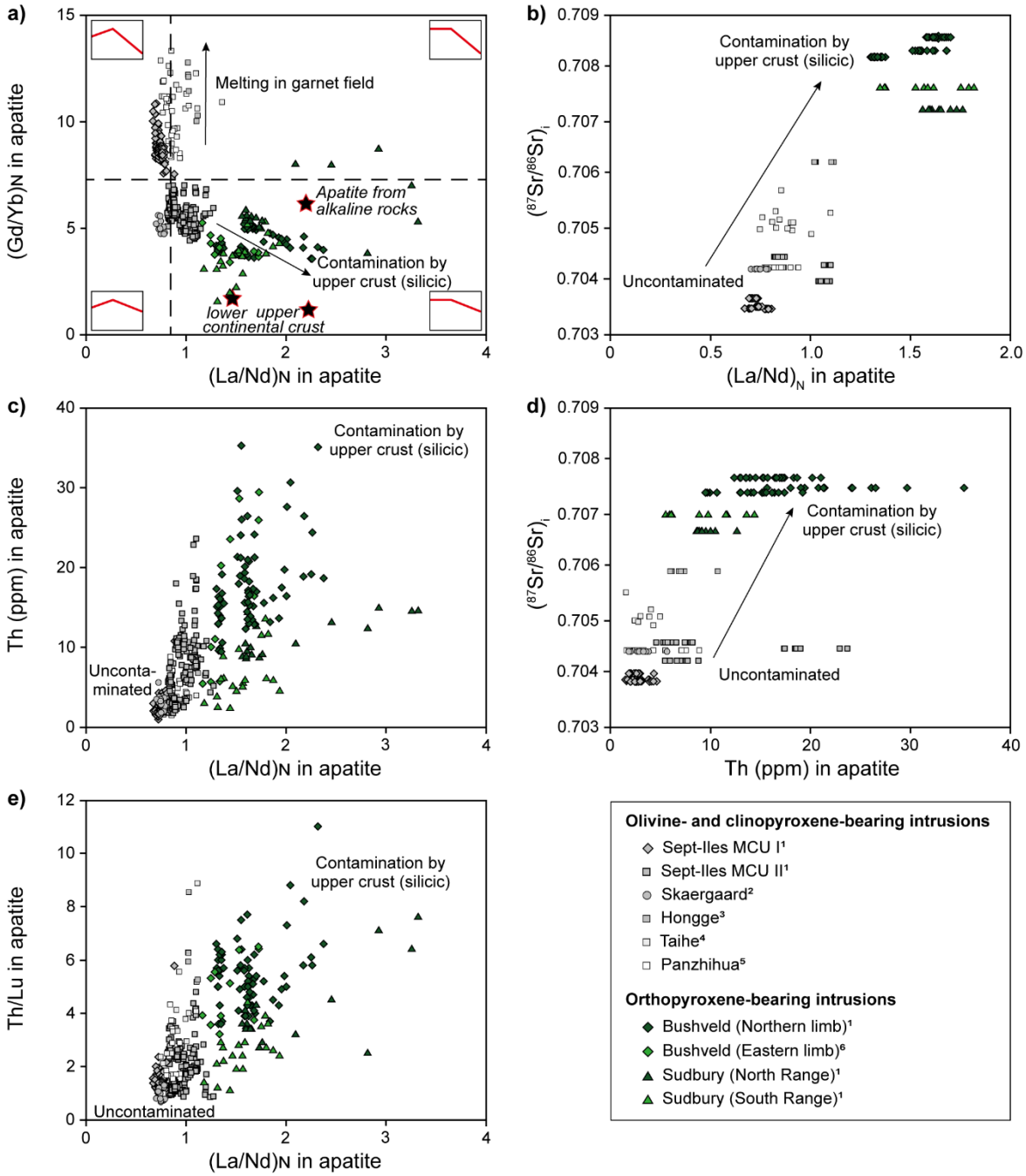

Figure 3.8 – Cumulus apatite from olivine- and clinopyroxene-bearing and orthopyroxene-bearing intrusions show evidence of crustal contamination and depth of partial melting using (a) $(La/Nd)_N$ and $(Gd/Yb)_N$ ratios; evidence of crustal contamination is shown using (b) $(^{87}Sr/^{86}Sr)_i$ as a function of $(La/Nd)_N$, (c) Th as a function of $(La/Nd)_N$, (d) $(^{87}Sr/^{86}Sr)_i$ as a function of Th, and (e) Th/Lu as a function of $(La/Nd)_N$. Values for lower and upper continental crust is from Rudnick & Gao (2014). Value for apatite from alkaline rocks is from Li *et al.* (2023).

Source of data: [1]This study; [2]Leeman & Dasch (1978), Stewart & DePaolo (1990), McBirney & Creaser (2003), Hagen-Peter *et al.* (2019), Pedersen *et al.* (2021); [3]Luan *et al.* (2014), Xing & Wang (2017), Tang *et al.* (2021); [4]She *et al.* (2014, 2016), Tang *et al.* (2021); [5]Zhang *et al.* (2009), Howarth & Prevec (2013), Hou *et al.* (2013), Xing *et al.* (2014), Song *et al.* (2013), Tang *et al.* (2021); [6]Van Tongeren & Mathez (2012)

The contamination of a mafic melt with Si-bearing crustal material increases the Si activity of the melt and allows the crystallisation of orthopyroxene before clinopyroxene (Frost *et al.*, 2010). Thus, the presence of orthopyroxene as a cotectic mineral crystallising from a mafic-ultramafic melt is typically deemed to be the result of contamination with a Si-bearing material (Frost *et al.*, 2010). This is confirmed by the actual amount of contamination calculated for these layered intrusions by previous studies. Intrusions in which contamination with a Si-bearing crustal contaminant is negligible (i.e., Sept-Iles, Skaergaard, Taihe, Panzhihua) or < 15 % (Hongge) are olivine- and clinopyroxene bearing (i.e., clinopyroxene crystallises first), whereas those with more than 20 % of crustal contamination (i.e., Bushveld) and 100% crustal melt (Sudbury) are orthopyroxene-bearing intrusions (i.e, orthopyroxene crystallises first; Table 3.1). Other mafic intrusions containing orthopyroxene as the main mafic phase also show high degree of crustal contamination (i.e., intrusions from Rogaland, Norway; Tegner *et al.*, 2005) that support our findings. However, the use of orthopyroxene alone as a proxy for contamination might not be appropriate if the presence of orthopyroxene is due to the composition of the primary melt (i.e., issued from a pyroxene-rich mantle source).

Our new results for cumulus apatite shows that the $(La/Nd)_N$ is positively correlated with the initial Sr isotope content of apatite, which confirms a relationship between La enrichment and crustal contamination (Figure 3.8b). Indeed, cumulus apatite from olivine- and clinopyroxene-bearing intrusions, with lower degrees of crustal contamination, have much lower $(La/Nd)_N$ and $(^{87}Sr/^{86}Sr)_i$ than those from orthopyroxene-bearing, contaminated intrusions. A similar La increase with $(^{87}Sr/^{86}Sr)_i$ is observed in increasingly crust-contaminated metavolcanic rocks (Gołuchowska *et al.*, 2022). Trace elements that are commonly used to trace crustal contamination, such as Th (DePaolo 1981), are also positively correlated with the $(La/Nd)_N$ and $(^{87}Sr/^{86}Sr)_i$ ratios of cumulus apatite (Figure 3.8c and 3.8d, respectively). For example, at the Bushveld Complex, cumulus apatite with higher $(La/Nd)_N$ and $(^{87}Sr/^{86}Sr)_i$ ratios also displays higher Th concentrations, due to contamination by an upper crustal material (Barnes *et al.*, 2010).

We demonstrate that processes such as fractional crystallisation, degree of partial melting or changes in the cotectic assemblage are not responsible for $(La/Nd)_N$ variations among mafic layered intrusions. Firstly, the REE patterns of cumulus apatite from the MCU II of Sept-Iles are parallel,

regardless of the degree of evolution of the melt, and that the overall enrichment in all the REE with decreasing anorthite content of associated plagioclase is thus an indicator of melt evolution (Kieffer *et al.*, 2023). As the REE patterns are all parallel, there is thus negligible change in the $(La/Nd)_N$ ratio with fractional crystallisation (variation of $(La/Nd)_N$ ratio between 0.9 and 1.1; Figure 3.4a) in cumulus apatite from Sept-Iles MCU II. As such, we interpret changes in this ratio between the different mafic intrusions to reflect the degree of crustal contamination. In addition, the variation of the $(La/Nd)_N$ ratio of cumulus apatite from mafic layered intrusions is not significantly affected by the degree of partial melting. Although low degrees of partial melting will also lead to enrichment in LREE and high $(La/Nd)_N$ ratios (as shown by apatite from alkaline magmas in Figure 3.8a), all of the studied mafic intrusions correspond to large volumes of magma associated with LIP, resulting from much higher degrees of partial melting. We also show that a change in the cotectic assemblage does not cause variations in $(La/Nd)_N$ ratio of cumulus apatite. As saturation in apatite always occurs after the crystallisation of pyroxene, but before zircon (Table 3.1, and references therein), the amount of LREE remaining in the melt after pyroxene crystallisation (clinopyroxene vs. orthopyroxene) might affect the LREE content of apatite. However, Lissenberg & MacLeod (2016) showed that as the REE partition coefficients between apatite and silicate melt are > 1, the REE pattern of apatite directly reflects the REE pattern of the melt. A significant fractionation of LREE from MREE in the melt is thus not caused by fractional crystallisation of olivine, clinopyroxene or plagioclase. Using the example of Sept-Iles, we modelled the effect of the crystallisation of various amounts of orthopyroxene (0, 20, 25, 30 or 35 %) on the chemistry of cumulus apatite, and compared the $(La/Nd)_N$ ratios to this obtained for the original cotectic proportions of clinopyroxene (20 %; Namur *et al.*, 2010). The results show that the effect of the orthopyroxene cotectic proportion on the $(La/Nd)_N$ ratio is negligible (Annexe 45). Thus, we can confirm that the crystallisation of orthopyroxene instead of clinopyroxene does not affect the LREE content of the co-crystallising apatite, and by extension cannot shift its $(La/Nd)_N$ ratio. The high $(La/Nd)_N$ ratio observed in cumulus apatite is therefore not due to a change in the cumulus assemblage but rather to contamination with a crustal Si-rich component that directly affects the LREE content of the melt. Apatite from uncontaminated intrusions (i.e., olivine- and -clinopyroxene-bearing) have $(La/Nd)_N$ between 0.7 and 1.2, whereas these from intrusions contaminated with a Si-

rich crustal component (i.e., orthopyroxene-bearing) have higher $(La/Nd)_N$ ratios (> 1.2, and up to 6.5; Figure 3.8a).

In order to express the increase in Th relative to the HREE, which are least affected by crustal contamination, we use the Th/Lu ratio (Figure 3.8e). Although Th and Lu also increase with fractional crystallisation (Kieffer *et al.*, 2023), the Th/Lu ratio only shows minor variation with fractional crystallisation. Indeed, in Sept-Iles MCU II, Th/Lu of cumulus varies between 1 and 4, which is a minor variation compared to that observed in contaminated intrusions (Figure 3.8e). Cumulus apatite from mafic layered intrusions in which contamination by a Si-bearing component is negligible have a very low and restricted range of Th/Lu values (most varies from 0.5 to 4). In contrast, cumulus apatite from orthopyroxene-bearing, contaminated, mafic layered intrusions, display scattered and higher Th/Lu values (from 1 to 11; Figure 3.8e).

Other incompatible elements, such as U, Pb, Rb or As, which can substitute into apatite, are enriched in silicic rocks from the upper crust (Rudnick & Gao, 2014). Cumulus apatite from the most contaminated intrusions (i.e., Bushveld and Sudbury) are also enriched in these elements compared to the other intrusions, and most are positively correlated (i.e., Th and U; Annexe 42). In addition, the higher As content in cumulus apatite from the Sudbury South Range compared to that from the North Range closely reflects the differences previously observed in the Ni-Cu sulfide ores, with those from the South Range being significantly richer in As (comprising As-minerals such as sulfarsenides: irarsite, hollingworthite, or PGE-Ni-rich cobaltite) than Ni-Cu sulphide ores from the North Range (Ames *et al.*, 2005; Mungall *et al.*, 2005, Dare *et al.*, 2010a, 2010b, 2011). Finally, the Cl content of cumulus apatite from the Bushveld northern limb is higher than that of the western and eastern limbs (Figure 3.2). This might be explained by contamination with sedimentary (dolomite) country rocks of the Transvaal Supergroup (Ashwal *et al.*, 2005). Indeed, Zhu *et al.* (2023) showed that contamination with evaporite can increase the Cl content of apatite.

3.6.1.2 $(Gd/Yb)_N$ as an indicator of depth of partial melting

The greater inferred melting depths for the parental picritic melts of the Emeishan (Hongge, Taihe and Panzhihua) layered intrusions (Zhou *et al.*, 2013) compared to the shallower depths of melting for the melts of Skaergaard (2 to 2.2 GPa; Tegner *et al.*, 1998), Bushveld (< 2.5 GPa; Solovova *et*

al., 2021) and Sudbury (upper crustal depths; Mungall *et al.*, 2004) is used to assess whether apatite can record the depth of partial melting of its parental magma. The REE content of whole rock is typically used to determine if the mantle was melted in the garnet stability field. As garnet retains HREE and Y, elevated La/Yb and Sr/Y ratios are indicative of deep partial melting (Moyen and Martin, 2012). Cumulus apatite from Hongge, Taihe and Panzhihua show HREE-depleted patterns (Figure 3.3a and 3.3c) that yield higher $(Gd/Yb)_N$ ratios (Figure 3.8a) than those of cumulus apatite from most of the other mafic layered intrusions, indicating the ratios of cumulus apatite reflect the depth of partial melting of the primary melt. In the case of Sept-Iles, its parental magma was determined to be a ferrobasalt (Namur *et al.*, 2010), but the depth of partial melting has not yet been constrained. Given that the proposed parental melt for Sept-Iles is close in composition to that of Skaergaard (Jakobsen *et al.*, 2010), and that cumulus apatite from Skaergaard and Sept-Iles MCU II have a similar composition (Figure 3.3a; Annexe 42), including the $(Gd/Yb)_N$ ratio (Figure 3.8a), we suggest that both parental magmas originated from a shallow depth. However, the unusually high $(Gd/Yb)_N$ ratio of cumulus apatite from Sept-Iles MCU I, different to that from MCU II and more similar to apatite from Emeishan layered intrusions, may have resulted from a slightly deeper magma source, deeper in the plume head, during the earlier stages of magma production of the layered intrusion.

Alternatively, crystallisation of amphibole can significantly modify the HREE content of intermediate to mafic rocks (Liou & Guo, 2019; Laurent *et al.*, 2020; Nathwani *et al.*, 2020). Thus, a relative depletion of HREE in apatite might also be obtained by co-crystallisation of amphibole during fractional crystallisation. To better quantify the consequence of amphibole crystallisation on apatite $(Gd/Yb)_N$ ratios, we modelled the effect of the crystallisation of various amounts of amphibole (0, 5, 10 and 15 %), co-crystallising with the cotectic assemblage of olivine, plagioclase, clinopyroxene, Fe-Ti oxides and apatite, on the chemistry of cumulus apatite. Our results clearly show that it has a negligible effect on the $(Gd/Yb)_N$ ratio (Annexe 45 and 46). Similarly, the amount of orthopyroxene crystallising, due to crustal contamination, has no significant effect on the $(Gd/Yb)_N$ ratio of apatite (Annexe 45 and 46). Given that the partition coefficients for HREE are < 1 in clinopyroxene, orthopyroxene and amphibole (McKenzie & O'Nions 1991; Dunn & Senn 1994; Charlier *et al.*, 2005), only a mineral with partition coefficients > 1 for the HREE, such as garnet or zircon which are not

cotectic minerals in evolved mafic melts, can sufficiently affect the $(Gd/Yb)_N$ ratio in cumulus apatite. Thus, the $(Gd/Yb)_N$ ratio of cumulus apatite from evolved mafic melts is an indicator of the depth of partial melting of the parental melt.

3.6.1.3 The Eu anomaly and Sr/Y ratio in cumulus apatite as indicators of fractional crystallisation

The different timing of apatite saturation regarding the degree of fractional crystallisation among mafic layered intrusions is used to assess the variations of apatite composition with the saturation in other minerals. In this study, we use the Eu anomaly and Sr/Y ratio in cumulus apatite to compare the timing of crystallisation of apatite relative to that of plagioclase, that varies among the mafic intrusions studied. It is well known that extensive fractional crystallisation of plagioclase causes an increasingly negative Eu anomaly and a decreasing Sr content in apatite (mafic layered intrusions: Tollari *et al.*, 2008; Xing *et al.*, 2014; She *et al.*, 2016; Kieffer *et al.*, 2023; anorthosites: Chen *et al.*, 2013; He *et al.*, 2016; both mafic and felsic rocks: Belousova *et al.*, 2002; O'Sullivan *et al.*, 2020; volcanic rocks: Jennings *et al.*, 2011; Nathwani *et al.*, 2020), whereas the Y content in apatite increases with differentiation (Belousova *et al.*, 2002; Jennings *et al.*, 2011; He *et al.*, 2016; O'Sullivan *et al.*, 2020; Kieffer *et al.*, 2023). The Sr content decrease in apatite reflects the evolution of the melt composition (e.g., Jennings *et al.*, 2011; Namur *et al.*, 2011). In contrast, the Sr content of plagioclase increases with fractional crystallisation, which is probably due to the increase of the Sr partition coefficient (D_{Sr}) in plagioclase with decreasing anorthite content, as shown in the experiments of Vander Auwera *et al.* (2000). On the other hand, Eu is redox sensitive and its partitioning into both plagioclase and apatite is affected by fO_2 (Bromiley, 2021). The depth of melting might have an effect on Y (i.e., Y retained in garnet at depth) and the Sr/Y ratio. However, Gd is not affected by the depth of melting, and the Sr/Gd shows the same trend as Sr/Y (Figure 3.9a to 3.9d). All mineral phases with partition coefficients for Sr and Eu > 1 will affect Sr and Eu, respectively. In mafic layered intrusions, it mainly corresponds to plagioclase. However, amphibole might also affect the Sr/Y ratio. For example, suppression of plagioclase crystallisation (leading to enrichment in Sr and Eu) and crystallisation of amphibole (leading to depletion in Y) in hydrous arc melts will increase the Sr/Y ratio of apatite (Nathwani *et al.*, 2020). Therefore, we modelled the effect of amphibole crystallisation on

the Sr/Y ratio in cumulus apatite for the cotectic assemblage at Sept-Iles. We show that although it increases with a small amount with amphibole crystallising (e.g., 0, 5, 10 and 15 % amphibole) due to an increase in Sr from less plagioclase crystallising (see Annexe 46), the overall trend of Sr/Y decreasing with fractional crystallisation is not changed. Thus, we deem that the Sr/Y ratio can be used with confidence as a proxy to trace fractional crystallisation, in particular the timing of apatite saturation relative to plagioclase crystallisation, using apatite alone. This is most important in cases where the anorthite content of associated plagioclase is not available (or too altered) or cannot be used as a benchmark due to changes in H_2O content of the melt (Howarth *et al.*, 2013).

Cumulus apatite from Sept-Iles MCU I and MCU II are aligned along a similar positive trend of Sr/Y versus Eu/Eu* (Figure 3.9a), although they evolve in opposite directions (see section 3.6.1.4.). Cumulus apatite from the other mafic layered intrusions, except those from the Emeishan intrusions, globally follows the same trend as that defined by Sept-Iles cumulus apatite from MCU II (Figure 3.9b). The trends for cumulus apatite from the Skaergaard intrusion and Bushveld northern and eastern limbs start at lower Eu/Eu* values (Figure 3.9b), which can be explained by cumulus apatite appearing relatively late in the magma crystallisation history compared to Sept-Iles (i.e., more evolved composition of silicate minerals; Table 3.1; Figure 3.5). The trends for cumulus apatite from Sudbury North and South ranges also start at a lower Eu/Eu*, and with slightly higher Sr/Y ratio than Sept-Iles (Figure 3.9). This might also be explained by cumulus apatite crystallising late from an evolved melt that is thus enriched in REE+Y (Figure 3.5b) and contains less Sr and Eu due to extensive, prior plagioclase crystallisation.

Cumulus apatite from Hongge and Taihe shows a significantly high Sr/Y ratio that sharply decreases from 18 to 6, and from 12 to 9, respectively, with respect to the decrease of the Eu anomaly, but with little variation (1 to 0.8) of the Eu anomaly (Figure 3.9b). Cumulus apatite from Hongge and Taihe are significantly enriched in Sr and Eu (Figure 3.5f; Annexe 42) and are the only apatite to have crystallised earlier at high anorthite content of associated plagioclase (An_{65-53}; Figure 3.5f) from a more primitive melt enriched in Sr (Sr/Y above 5; Figure 3.5b). Cumulus apatite from Panzhihua has lower Sr, but similar Eu content (Figure 3.9b, 3.9e), as it crystallised later (An_{53}; Figure 3.5f) but its Sr content is still higher (Sr/Y between 2 and 4; Figure 3.9b) than this of cumulus apatite

from all other mafic intrusions (Sr/Y below 2; Figure 3.9b) covering a similar range of anorthite contents. We attribute the significantly higher Sr content (and Sr/Y ratios) of cumulus apatite from Emeishan melts to the crystallisation of apatite from a more Sr- and Eu-rich magma with a less extensive history of plagioclase crystallisation (Table 3.1). Previous work on the Emeishan intrusions have proposed that the suppression of plagioclase crystallisation is due to an increase of fO_2 and H_2O content of the melt from possible assimilation of host rocks carbonates (Howarth & Prevec, 2013) or fluids (Zhou *et al.*, 2005). However, the addition of H_2O affects the anorthite content of plagioclase (i.e., more calcic; Howarth & Prevec, 2013), and makes it difficult to compare the anorthite content of plagioclase from Emeishan hydrous melts to those of dryer systems. A delayed crystallisation of plagioclase results in Sr remaining constant or even increasing in the melt, from which apatite crystallises, which causes a higher Sr/Y ratio in cumulus apatite from Hongge and Taihe intrusions and decreases with fractional crystallisation, at which time cumulus apatite from Panzihua intrusion has lower Sr/Y ratios (Figure 3.9b).

The Eu anomaly in apatite is mainly affected by plagioclase crystallisation (Kieffer *et al.*, 2023; Bromiley, 2021), but the amount of Eu incorporated into plagioclase also depends on the fO_2 of the system. Indeed, in oxidising conditions, the more abundant Eu^{3+} will partition less easily into plagioclase, and more easily into apatite (Xing *et al.*, 2014; She *et al.*, 2016) Thus, the suppression of plagioclase crystallisation due to hydrous conditions (Tang *et al.*, 2021, 2023), as well as highly oxidising conditions (Tang *et al.*, 2023) might explain the why the Eu anomaly varies less in apatite from the Emeishan intrusions than in the others (Figure 3.9b) should also affect the Eu anomaly in apatite.

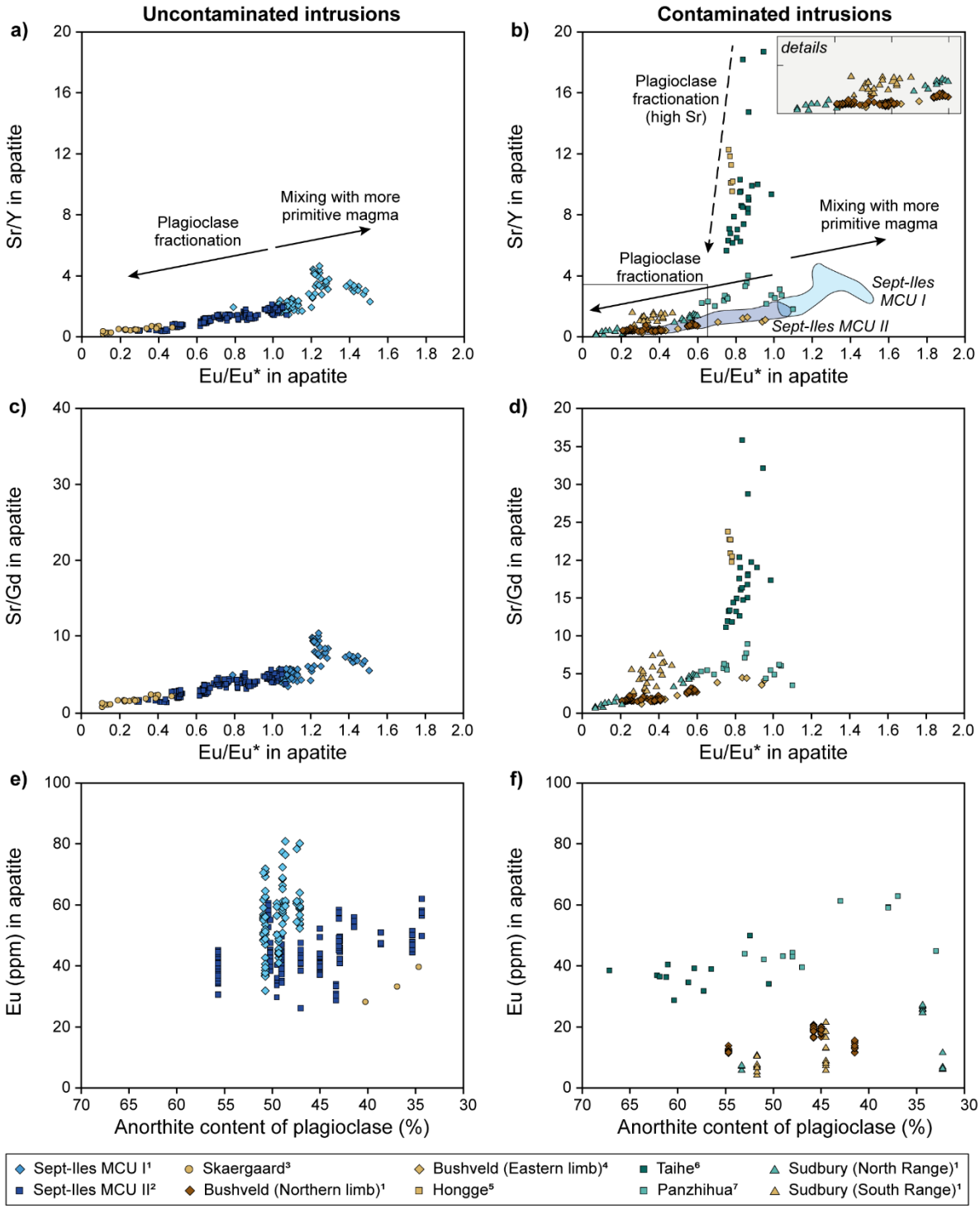

Figure 3.9 – Eu anomaly versus (a, b) Sr/Y and (c,d) G/Y binary plot, and (e ,f) Eu (ppm) as a function of the anorthite content of associated plagioclase for cumulus apatite from (left column) Sept-Iles Intrusive Suite and Skaergaard, and (right column) other mafic layered intrusions. Cumulus apatite define a trend corresponding to plagioclase fractionation.

Source of data: [1]This study; [2]Kieffer *et al.* (2023); [3]Pedersen *et al.* (2021); [4]Van Tongeren & Mathez (2012); [5]Xing & Wang (2017); [6]She *et al.* (2016); [7]Xing *et al.* (2014)

3.6.1.4 Effect of magma replenishment

In the Sept-Iles Intrusive Suite, the different behaviour of trace elements in cumulus apatite up sequence in MCU I and MCU II is used to discuss evidence for magma replenishment during the crystallisation of MCU I. Cumulus apatite from MCU I starts to follow the same compositional trends as in MCU II, but the trend reverses half way up, at around –2500 m (Figure 3.6; Annexe 44). Such a reversal to more primitive compositions (i.e., higher Sr, V, Mg and Sr/Y, and lower REE+Y, As or Na) is probably due to the mixing of the resident magma from the top of MCU I with an injection of a more primitive melt that changed the composition of the hybrid melt from which apatite continued to crystallise (i.e., enriched in compatible elements such as Sr, V or Mg, and depleted in incompatible elements such as REE+Y, As or Na), and marks the base of the MCU II (Namur *et al.*, 2010). A similar decrease in REE and increase in Sr caused by magma mixing was also described in the Panzhihua Intrusion (Xing *et al.*, 2014). However, at the same anorthite content, cumulus apatite from MCU II still has higher concentrations in Pb, Th, U, Zr, Na, K and As than those from MCU I (Figure 3.5; Annexe 43). The MCU I and MCU II have different magmatic histories (Namur *et al.*, 2010, 2012; Charlier *et al.*, 2011): MCU I crystallised in a closed system from a single differentiating batch of magma, whereas a minimum of 7 magma replenishments and mixing occurred during the crystallisation of MCU II. However, it is only at the top of MCU II, where the last batch of magma was allowed to differentiate in a closed system, that cumulus apatite started to crystallise from a hybrid melt unusually enriched in incompatible trace elements (Namur *et al.*, 2010). Thus, the effect of differentiation and magma mixing following a replenishment best explains the compositional differences observed between MCU I and MCU II cumulus apatite. If the magmas that mixed towards the top of MCU I were from the same source, there should be no variation in $(La/Nd)_N$ and $(Gd/Yb)_N$ ratios in cumulus apatite, as they are only minimally affected by fractional crystallisation. As such, there is no variation in $(La/Nd)_N$ in cumulus apatite from MCU I at around –2500 m, where mixing starts. However, the $(Gd/Yb)_N$ ratio increases sharply with mixing (Annexe 44). This indicates that there might be a slight difference in the source that affects only HREE. The best hypothesis would be that the source of the new magma is deeper, allowing to preferentially retain Yb in garnet, and shifts the $(Gd/Yb)_N$ ratio to higher values.

3.6.1.5 Apatite as an indicator of oxygen fugacity ?

The restricted range of fO_2 conditions in the mafic layered intrusions studied indicates that Eu and Ce anomalies in apatite are not reliable to estimate the fO_2 conditions of mafic intrusions. Several studies propose to use the Mn content (Miles *et al.*, 2014), or the Eu or Ce anomalies in apatite as indicators of oxygen fugacity in felsic (Cao *et al.*, 2012; Qian *et al.*, 2019; Zafar *et al.*, 2020) and in mafic (Tang *et al.*, 2023) intrusions. However, recent studies have demonstrated instead that the Mn content of apatite is related to the melt structure (i.e., polymerisation increase the partition coefficient of Mn into apatite) rather than to its fO_2 (Stokes *et al.*, 2019). Europium is redox sensitive and its partitioning into plagioclase and apatite depends on fO_2. The partition coefficient of Eu between apatite and the mafic melt is indeed much higher in oxidising conditions (i.e., FMQ+1.5; Charlier *et al.*, 2008; Miloski *et al.*, in press). However, a thorough review by Bromiley (2021) shows that the Eu anomaly in apatite is not reliable due to plagioclase crystallisation and the REE variations in apatite. In addition, the control of fO_2 on REE behaviour in apatite is not fully understood (Bromiley, 2021). Our dataset of apatite analyses from mafic intrusions, with limited fO_2 variation (from FMQ to FMQ+1.5), confirms that the Eu anomaly does not vary with fO_2 because the primary control on the large variation of Eu anomaly in apatite is due to plagioclase crystallisation (Figure 3.9), which can vary significantly for similar fO_2 conditions.

For Ce, Ce^{3+} is more compatible in apatite than Ce^{4+} and, in typical magmatic conditions, Ce^{3+} should be incorporated into apatite similarly as the other REE and cause no Ce anomaly. However, a negative Ce anomaly in apatite would be the result of more oxidising conditions but its variations are small compared to Eu (Bromiley, 2021). Cumulus apatite from our dataset do not display any significant Ce anomaly, as most are slightly positive (1 to 1.10), and some are slightly negative (0.90 to 1). The Ce anomalies are uncorrelated with the fO_2 of the host intrusion, as anomalies can be both slightly positive and negative in a single intrusion.

3.6.2 Apatite as a provenance indicator

Intercumulus and cumulus apatite occurring in mafic layered intrusions can be associated with PGE-Ni-Cu or Fe-Ti-V-P mineralisation (Table 3.1). There is growing interest in developing minerals, such as apatite, as a provenance indicators or indicator mineral for mineral exploration. As is the case

for magnetite (e.g., Dare *et al.*, 2014, Nadoll *et al.*, 2014), scheelite (e.g., Miranda *et al.*, in press) and chalcopyrite (e.g., Caraballo *et al.*, 2022), the trace element content of apatite holds a reliable record of its geological environment of formation (e.g., Belousova *et al.* 2002; Abdullin *et al.* 2016; O'Sullivan *et al.*, 2020; this study). As such, the presence and chemistry of detrital apatite from the secondary environment (e.g., tills, river sediments) has been successfully tested to identify an ore signature around known porphyry deposits (Kelley *et al.*, 2011; Rukhlov *et al.*, 2016). The work of Mao *et al.* (2016) also demonstrates that apatite from different types of mineralising systems (e.g., porphyries, skarns, orogenic) have a distinct signature, although apatite data from mafic layered intrusions were not considered in their discrimination diagrams. Intercumulus apatite is scarce but ubiquitous in the more primitive parts of mafic layered intrusions that might contain mineralisation in PGE, Ni, Cu (i.e., Skaergaard, Keays & Tegner, 2015; Hongge, Zhong *et al.*, 2002; Bushveld, Boudreau & Kruger, 1990; Sudbury, Warner *et al.*, 1998; Table 3.1), or Fe-Ti-V (i.e., Hongge, Luan *et al.*, 2014; Taihe, She *et al.*, 2014; Panzhihua, Zhou *et al.*, 2005; Table 3.1). On the other hand, cumulus apatite that crystallised from an evolved mafic melt, towards the top of the intrusion, may be associated with Fe-Ti-P mineralisation (i.e., Sept-Iles Critical Zone of MCU II, Tollari *et al.*, 2008, Kieffer *et al.*, 2023; Bushveld UZc, Von Gruenewaldt, 1993; Table 3.1). Thus, being able to identify apatite from mafic layered intrusions, and to further identify apatite from the more primitive (intercumulus) and more evolved (cumulus) parts of the intrusion is of interest for mineral exploration and sedimentary studies.

A series of apatite discrimination diagrams, detailed in Annexe 47, have been proposed by Kieffer *et al.* (2023), based on the Sept-Iles Intrusive Suite, to distinguish successively: (1) apatite in mafic rocks from those from felsic rocks (using the ternary diagram of REE+Y, Sr and Eu anomaly in apatite; Figure 3.10a), (2) cumulus from intercumulus apatite in mafic rocks (using Cl/F, Th/Lu and V; Figure 3.10b), and (3) cumulus apatite from Fe–Ti–P mineralised and unmineralised layers (using REE+Y, Sr and Eu anomaly in apatite; Figure 3.10c). We tested the robustness of these diagrams by applying them to our larger apatite dataset, from this study and from the literature, of cumulus and intercumulus apatite from the various mafic layered intrusions discussed in this contribution (Table 3.1). In general, the discrimination diagrams successfully separate apatite crystallising from mafic and felsic melts, and to identify cumulus from intercumulus apatite (Figure 3.10a, 3.10b; full details are provided in

Annexe 47). Being able to identify a mafic magmatic system using detrital apatite in till, as well as which part of the intrusion, is a good starting point for provenance and mineral exploration studies. However, the use of the diagram to distinguish apatite from Fe–Ti–P mineralised rocks from those of unmineralised host rocks is less successful (Figure 3.10c), due to the large, natural variation in magma composition (e.g., differentiation, crustal contamination, depth of partial melting). Due to such complexity, future work should be undertaken with a larger apatite composition database, and with analyses including the trace elements suggested in our study. For instance, approaches using partial least square-discriminant analysis (Caraballo *et al.*, 2022) or supervised machine learning (Qiu *et al.*, in press; Caraballo *et al.*, in press) could help to improve the classification of apatite. Nevertheless, the diagrams presented in this contribution show that apatite records the geological environment in which it formed.

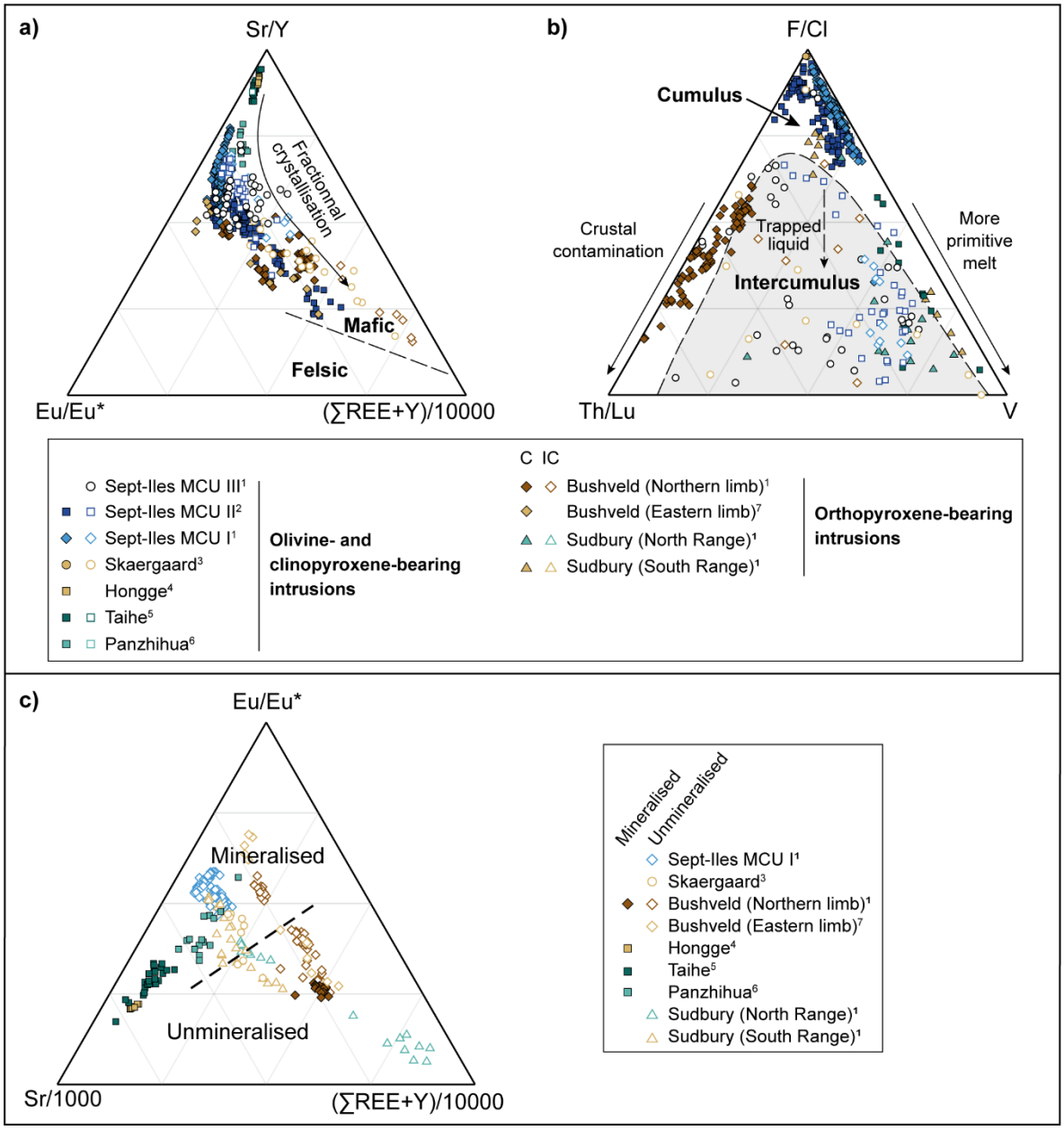

Figure 3.10 –Data from mafic layered intrusions displayed in the discrimination diagrams that combine EMPA and LA-ICP-MS data, from Kieffer et al. (2023), to separate (a) mafic and felsic apatite, (b) cumulus from intercumulus apatite, and (c) cumulus apatite from Fe–Ti–P mineralised (Min.) and unmineralised (Unmin.) layers in mafic intrusions.

Source of data: [1]This study; [2]Kieffer *et al.* (2023); [3]Pedersen *et al.* (2021); [4]Xing & Wang (2017); [5]She *et al.* (2016); [6]Xing *et al.* (2014); [7]Van Tongeren & Mathez (2012)

3.7 Conclusions

In this study, we demonstrated that cumulus apatite chemistry has the ability to record petrogenetic processes in mafic layered intrusions. Identifying these processes using apatite chemistry by itself is critical for certain cases where other petrogenetic information is lacking (i.e., absence, or extensive alteration or metamorphism of silicates; detrital apatite grains recovered from the sedimentary environment during provenance/exploration studies). Cumulus apatite from mafic intrusions contaminated by a silicic component (i.e., orthopyroxene-bearing intrusions, such as the Bushveld Complex or Sudbury Igneous Complex) is enriched in LREE, Th, U and As, and has a higher $(^{87}Sr/^{86}Sr)_i$ than those from uncontaminated intrusions or intrusions contaminated by a carbonaceous component (i.e., olivine- and clinopyroxene-bearing intrusions), such as Sept-Iles Intrusive Suite or Skaergaard intrusion, or Taihe and Panzhihua intrusions. The $(Gd/Yb)_N$ ratio of cumulus apatite is also an indicator of the depth of partial melting of the parental melt, with higher $(Gd/Yb)_N$ ratio being correlated with greater depth of partial melting. An increasingly negative Eu anomaly and decreasing Sr/Y ratio in cumulus apatite are indicator of the timing of apatite crystallisation relative to fractional crystallisation of plagioclase, whereby a high Sr/Y ratio suggests early saturation of apatite. Our study shows that cumulus apatite chemistry is sensitive to magma mixing as it records reversal to more primitive melt compositions (i.e., higher Sr, V, Mg and Sr/Y ratio, and lower REE+Y, As and Na concentration in apatite). Finally, we show that it is possible to distinguish apatite crystallising from felsic or mafic melts. The discrimination of intercumulus from intercumulus apatite, and of cumulus apatite from Fe–Ti–P mineralised or unmineralised host intrusions is perturbed by the superimposition of the effect of crustal contamination and differentiation, respectively. Thus, our study demonstrates that apatite is a powerful petrogenetic indicator in mafic layered intrusions. Apatite can further be used to identify the most evolved and primitive part of a mafic intrusion. This will prove useful for provenance and mineral exploration studies using detrital apatite in till, as the most evolved part might host abundant cumulus apatite in Fe–Ti–P mineralisation, and the most primitive part hosts intercumulus apatite at the same stratigraphic level as Fe–Ti–V, Ni–Cu-PGE, or chromite mineralisation.

Acknowledgements

The authors thank S.-J. Barnes for providing samples from the Bellevue drillhole in Bushveld northern limb and for comments that improved an earlier version of the manuscript, and D. Ames for samples from Sudbury Igneous Complex. They also thank M. Choquette (Laboratoire de Microanalyse, Laval University, Quebec City), and A. Lavoie and D. Savard (LabMaTer, University of Quebec in Chicoutimi) for their assistance with EMPA and LA-ICP-MS analyses, respectively, as well as H. Legros (Ministère des Ressources Naturelles et de la Faune, University of Quebec in Chicoutimi) for providing cathodoluminescence imaging of some of our samples.

Funding

This work was supported by the Natural Sciences and Engineering Research Council of Canada Discovery Grant [grant number RGPIN-2015-05924 to S.A.S.D.], the Canada Research Chair of S.A.S.D., and the Fonds de Recherche du Québec – Nature and Technologies, Programme de Bourses d'Excellence pour Étudiants Étrangers [grant number 319772 to M.A.K.].

References

Abdullin, F., Solé, J., Solari, L., Shchepetilnikova, V., Meneses-Rocha, J. J., Pavlinova, N. & Rodríguez-Trejo, A. (2016). Single-grain apatite geochemistry of Permian–Triassic granitoids and Mesozoic and Eocene sandstones from Chiapas, southeast Mexico: implications for sediment provenance. *International Geology Review* **58**, 1132-1157.

Ames, D. E., Davidson, A., Buckle, J. I. & Card, K. D. (2005). *Geology, Sudbury bedrock compilation, Ontario, Open File 4570*. Geological Survey of Canada.

Ames, D. E., Golightly, J. P., Lightfoot, P. C. & Gibson, H. L. (2002). Vitric compositions in the Onaping Formation and their relationship to the Sudbury Igneous Complex, Sudbury Structure. *Economic Geology* **97**, 1541-1562.

Andersen, J. C. O., Rasmussen, H., Nielsen, T. F. D. & Ronsbo, J. G. (1998). The triple group and the Platinova gold and palladium reefs in the Skaergaard intrusion: Stratigraphic and petrographic relations. *Economic Geology* **93**, 488-509.

Andersson, S. S., Wagner, T., Jonsson, E., Fusswinkel, T. & Whitehouse, M. J. (2019). Apatite as a tracer of the source, chemistry and evolution of ore-forming fluids: The case of the Olserum-Djupedal REE-phosphate mineralisation, SE Sweden. *Geochimica et Cosmichimica Acta* **255**, 163-187.

Arndt, N. & Lesher, C. M. (2004). Komatiite. In: Elsevier (ed.) *Encyclopedia of Geology*, 260-268.

Ashwal, L. D. (1993). The temporality of anorthosites. *The Canadian Mineralogist* **48**, 711-728.

Ashwal, L. D., Webb, S. J. & Knoper, M. W. (2005). Magmatic stratigraphy in the Bushveld Northern Lobe: continuous geophysical and mineralogical data from the 2950 m Bellevue drillcore. *South African Journal of Geology* **108**, 199-232.

Barnes, S. J., Lesher, C. M. & Sproule, R. A. (2007). Geochemistry of komatiites in the Eastern Goldfields Superterrane, Western Australia and the Abitibi Greenstone Belt, Canada, and implications for the distribution of associated Ni-Cu-PGE deposits. *Applied Earth Sciences: Transactions of the Institutions of Mining and Metallurgy Section B* **116**, 167-187.

Barnes, S.-J., Maier, W. D. & Ashwal, L. D. (2004). Platinum-group element distribution in the Main Zone and Upper Zone of the Bushveld Complex, South Africa. *Chemical Geology* **208**, 293-317.

Barnes, S.-J., Maier, W. D. & Curl, E. A. (2010). Composition of the Marginal Rocks and Sills of the Rustenburg Layered Suite, Bushveld Complex, South Africa: Implications for the Formation of the Platinum-Group Element Deposits. *Economic Geology* **105**, 1491-1511.

Barnes, S. J. (2014). Trace Element Contents of Mantle-Derived Magmas Through Time. *Journal of Petrology* **62**, egab024.

Bédard, J. H. (2014). Parameterizations of calcic clinopyroxene - melt trace element partition coefficients. *Geochemistry, Geophysics, Geosystems* **15**, 303-336.

Belousova, E. A., Griffin, W. L., O'Reilly, S. Y. & Fischer, N. I. (2002). Apatite as an indicator mineral for mineral exploration: trace-element compositions and their relationship to host rock type. *Journal of Geochemical Exploration* **76**, 45-69.

Boudreau, A. E. & Kruger, F. J. (1990). Variation in the Composition of Apatite through the Merensky Cyclic Unit in the Western Bushveld Complex. *Economic Geology* **85**, 737-745.

Boudreau, A. E., Love, C. & Prendergast, M. D. (1995). Halogen geochemistry of the Great Dyke, Zimbabwe. *Contributions to Mineralogy and Petrology* **122**, 289-300.

Boudreau, A. E., Mathez, E. A. & McCallum, I. S. (1986). Halogen Geochemistry of the Stillwater and Bushveld Complexes: Evidence for Transport of the Platinum-Group Elements by Cl-Rich fluids. *Journal of Petrology* **27**, 967-986.

Boudreau, A. E. & McCallum, I. S. (1990). Low temperature alteration of REE-rich chlorapatite from the Stillwater Complex, Montana. *American Mineralogist* **75**, 687-693.

Bromiley, G. D. (2021). Do concentrations of Mn, Eu and Ce in apatite reliably record oxygen fugacity in magmas? *Lithos* **384-385**, 105900.

Brown, G. M. & Peckett, A. (1977). Fluorapatites from the Skaergaard intrusion, East Greenland. *Mineralogical Magazine* **41**, 227-232.

Cao, M., Li, G., Qin, K., Seitmuratova, E. Y. & Liu, Y. (2012). Major and trace element characteristics of apatites in granitoids from central Kazakhstan: implications for petrogenesis and mineralization. *Resource Geology* **62**, 63-83.

Caraballo, E., Dare, S. A. S. & Beaudouin, G. (2022). Variation of trace elements in chalcopyrite from worldwide Ni-Cu sulfide and Reef-type PGE deposits: implications for mineral exploration. *Mineralium Deposita* **57**, 1-29.

Caraballo, E., Beaudoin, G. & Dare, S. A. S. (in press). Trace element composition of chalcopyrite as a tool for deposit type discrimination: a machine learning approach. *Journal of Geochemical Exploration*.

Cawthorn, R. G., Barnes, S. J., Ballhaus, C. & Malitch, K. N. (2005). Platinum-group element, chromium, and vanadium deposits in mafic and ultramafic rocks. *Economic Geology* **100th Anniversary Volume**, 215-249.

Cawthorn, R. G., Lee, C. A., Schouwstra, R. P. & Mellowship, P. (2002). Relations between PGE and PGM in the Bushveld complex. *The Canadian Mineralogist* **40**, 311-328.

Charlier, B., Namur, O., Toplis, M. J., Schiano, P., Cluzel, N., Higgins, M. D. & Auwera, J. V. (2011). Large-scale silicate liquid immiscibility during differentiation of tholeiitic basalt to granite and the origin of the Daly gap. *Geology* **39**, 907-910.

Charlier, B., Sakoma, E., Sauvé, M., Stanaway, K., Vander Auwera, J. & Duchesne, J.-C. (2008). The Grader layered intrusion (Havre-Saint-Pierre Anorthosite, Quebec) and genesis of nelsonite and other Fe–Ti–P ores. *Lithos* **101**, 359-378.

Charlier, B., Vander Auwera, J. & Duchesne, J.-C. (2005). Geochemistry of cumulates from the Bjerkreim–Sokndal layered intrusion (S. Norway) Part II. REE and the trapped liquid fraction. *Lithos* **83**, 255-276.

Chen, W. T., Zhou, M.-F. & Zhao, T.-P. (2013). Differentiation of nelsonitic magmas in the formation of the ~1.74 Ga Damiao Fe–Ti–P ore deposit, North China. *Contributions to Mineralogy and Petrology* **165**, 1341-1362.

Dare, S. A. S., Barnes, S.-J. & Prichard, H. M. (2010). The distribution of platinum group elements (PGE) and other chalcophile elements among sulfides from Creighton Ni-Cu-PGE sulfide deposit, Sudbury, Canada, and the origin of palladium in pentlandite. *Mineralium Deposita* **45**, 765-793.

Dare, S. A. S., Barnes, S.-J., Prichard, H. M. & Fisher, P. C. (2010). The timing and formation of platinum-group minerals from the Creighton Ni-Cu-platinum-group element sulfide deposit, Sudbury, Canada: Early crystallization of PGE-rich sulfarsenides. *Economic Geology* **105**, 1071-1096.

Dare, S. A. S., Barnes, S.-J., Prichard, H. M. & Fisher, P. C. (2011). Chalcophile and platinum-group element (PGE) concentrations in the sulphide minerals from the McCreedy East deposit, Sudbury, Canada, and the origin of PGE in pyrite. *Mineralium Deposita* **46**, 381-407.

Dare, S. A. S., Barnes, S.-J., Beaudoin, G., Méric, J., Boutroy, E. & Potvin-Doucet, C. (2014). Trace elements in magnetite as petrogenetic indicators. *Mineralium Deposita* **49**, 785-796.

DePaolo, D. J. (1981). Trace element and isotopic effects of combined wallrock assimilation and fractional crystallization. *Earth and Planetary Science Letters* **53**, 189-202.

DePaolo, D. J. & Wasserburg, G. J. (1976). Inferences about magma sources and mantle structure from variations of $^{143}Nd/^{144}Nd$. *Geophysical Research Letters* **3**, 743-746.

DePaolo, D. J. & Wasserburg, G. J. (1979). Petrogenetic mixing models and Nd^Sr isotopic patterns. *Geochimica et Cosmichimica Acta* **43**, 615-625.

Dickin, A. P., Nguyen, T. & Crocket, J. H. (1999). Isotopic evidence for a single impact melting origin of the Sudbury Igneous Complex. In: Dressler, B. O. & Sharpton, V. L. (eds.) *Large meteorite impacts and planetary evolution II: Geological Society of America Special Paper 339*, 361-371.

Dressler, B. O., Morrison, G. G., Peredery, W. V. & Rao, B. V. (1987). The Sudbury Structure, Ontario, Canada—a review. In: Pohl, J. (ed.) *Research in Terrestrial Impact Structures*, 39-68.

Dunn, T. & Sen, C. (1994). Mineral/matrix partition coefficients for orthopyroxene, plagioclase, and olivine in basaltic to andesitic systems: A combined analytical and experimental study. *Geochimica et Cosmichimica Acta* **58**, 717-733.

Eales, H. V. & Costin, G. (2012). Crustally contaminated komatiite: primary source of the chromitites and Marginal, Lower, and Critical Zone magmas in a staging chamber beneath the Bushveld Complex. *Economic Geology* **107**, 645-665.

Ernst, R. E. (2014). *Large Igneous Provinces*: Cambridge University Press.

Fischer, L. A., Wang, M., Charlier, B., Namur, O., Roberts, R. J., Veksler, I. V., Cawthorn, R. G. & Holtz, F. (2016). Immiscible iron-and silica-rich liquids in the Upper Zone of the Bushveld Complex. *Earth and Planetary Science Letters* **443**, 108-117.

Fischer, L. A. & Yuan, Q. (2016). Fe-Ti-V-(P) resources in the Upper Zone of the Bushveld Complex, South Africa. *Papers and Proceedings of the Royal Society of Tasmania* **150**, 15-22.

Fourny, A., Weis, D. & Scoates, J. S. (2019). Isotopic and Trace Element Geochemistry of the Kiglapait Intrusion, Labrador: Deciphering the Mantle Source, Crustal Contributions and Processes Preserved in Mafic Layered Intrusions. *Journal of Petrology* **60**, 553-590.

Frost, C. D., Frost, B. R., Lindsley, D. H., Chamberlain, K. R., Swapp, S. M. & Scoates, J. S. (2010). Geochemical and isotopic evolution of the anorthositic plutons of the Laramie anorthosite complex: Explanations for variations in silica activity and oxygen fugacity of massif anorthosites. *The Canadian Mineralogist* **48**, 925-946.

Ganino, C., Harris, C., Arndt, N. T. & Prevec, S. A. (2013). Assimilation of carbonate country rock by the parent magma of the Panzhihua Fe-Ti-V deposit (SW China): Evidence from stable isotopes. *Geoscience Frontiers* **4**, 547-554.

Grant, M. (2020). Formation of magmatic Fe-Ti-V-P deposits within the Lac St. Jean area Saguenay, Québec, Canada: Insights from trace element composition of Fe-oxides and apatite. Department of Earth Sciences. Ottawa: University of Ottawa, 359.

Hagen-Peter, G., Tegner, C. & Lesher, C. (2019). Strontium isotope systematics for plagioclase of the Skaergaard intrusion (East Greenland): A window to crustal assimilation, differentiation, and magma dynamics. *Geology* **47**, 313-316.

Harlov, D. E., Richard, W. & F., H.-J. (2005). An experimental study of dissolution-reprecipitation in fluorapatite: fluid infiltration and the formation of monazite. *Contributions to Mineralogy and Petrology* **150**, 268-286.

Harmer, R. E. & Armstrong, R. A. (2000). Duration of the Bushveld Complex (seno lato) magmatism: constraints from new SHRIMP zircon chronology. *Workshop on the Bushveld Complex*. Gethane Lodge, Burgersfort, South Africa.

Harris, C., Pronost, J.J.M., Ashwal, L.D. & Cawthorn, R.G. (2005). Oxgyen and hydrogen isotope stratigraphy of the Rustenburg Layered Suite, Bushveld Complex: constraints on crustal contamination. *Journal of Petology* **45**, 579-601.

Hatton, C. J. (1995). Mantle plume origin for the Bushveld and Vantersdorp magmatic provinces. *Journal of African Earth Sciences* **21**, 571-577.

He, H.-L., Yu, S.-Y., Song, X.-Y., Du, Z.-S., Dai, Z.-H., Zhou, T. & Xie, W. (2016). Origin of nelsonite and Fe–Ti oxides ore of the Damiao anorthosite complex, NE China: Evidence from trace element geochemistry of apatite, plagioclase, magnetite and ilmenite. *Ore Geology Reviews* **79**, 367-381.

Hou, T., Zhang, Z. C., Encarnacion, J., Santosh, M. & Sun, Y. L. (2013). The role of recycled oceanic crust in magmatism and metallogeny: Os-Sr-Nd isotopes, U-Pb

geochronology and geochemistry of picritic dykes in the Panzhihua giant Fe-Ti oxide deposit, central Emeishan large igneous province, SW China. *Contributions to Mineralogy and Petrology* **165**, 805-822.

Howarth, G. H. & Prevec, S. A. (2013). Hydration vs. oxidation: Modelling implications for Fe-Ti oxide crystallisation in mafic intrusions, with specific reference to the Panzhihua intrusion, SW China. *Geoscience Frontiers* **4**, 555-569.

Hu, S., Zeng, Z., Fang, X., Qi, H., Yin, X., Chen, Z., Li, X. & Zhu, B. (2019). Geochemical Study of Detrital Apatite in Sediment from the Southern Okinawa Trough: New Insights into Sediment Provenance. *Minerals* **9**.

Huthman, F. M., Kinnaird, J. A., Yudovskaya, M. A. & Elburg, M. A. (2017). The Sr isotopic stratigraphy of the far northern Bushveld Complex. *South African Journal of Geology* **120**, 499-510.

Jakobsen, J. K., Tegner, C., Brooks, C. K., Kent, A. J. R., Lesher, C. E., Nielsen, T. F. D. & Wiedenbeck, M. (2010). Parental magma of the Skaergaard intrusion: constraints from melt

inclusions in primitive troctolite blocks and FG-1 dykes. *Contributions to Mineralogy and Petrology* **159**, 61-79.

Jakobsen, J. K., Veksler, I. V., Tegner, C. & Brooks, C. K. (2005). Immiscible iron- and silica-rich melts in basalt petrogenesis documented in the Skaergaard intrusion. *Geology* **33**, 885-888.

Jennings, E. S., Marschall, H. R., Hawkesworth, C. J. & Storey, C. D. (2011). Characterization of magma from inclusions in zircon: Apatite and biotite work well, feldspar less so. *Geology* **39**, 863-866.

Kamenetsky, V. S., Chun, S.-L., Kamenetsky, M. & Kuzmin, D. V. (2012). Picrites from the Emeishan Large Igneous Province, SW China: a Compositional Continuum in Primitive Magmas and their Respective Mantle Sources. *Journal of Petrology* **53**, 2095-2113.

Karykowski, B. T., Yang, S.-H., Maier, W. D., Lahaye, Y., Lissenberg, C. J. & O'Brien, H. (2017). In situ Sr Isotope Compositions of Plagioclase from a Complete Stratigraphic Profile of the Bushveld Complex, South Africa: Evidence for Extensive Magma Mixing and Percolation. *Journal of Petrology* **58**, 2285-2308.

Keays, R. R. & Lightfoot, P. C. (2020). Mafic intrusions in the footwall of the Sudbury Igneous Complex: Origin of the Sudbury impact melt sheet and its associated ore deposits. *Ore Geology Reviews* **120**, 103435.

Keays, R. R. & Tegner, C. (2015). Magma Chamber Processes in the Formation of the Low-sulphide Magmatic Au–PGE Mineralization of the Platinova Reef in the Skaergaard Intrusion, East Greenland. *Journal of Petrology* **56**, 2319-2340.

Kelley, K. D., Eppinger, R. G., Lang, J., Smith, M. D. & Fey, D. L. (2011). Porphyry Cu indicator minerals in till as an exploration tool: example from the giant Pebble porphyry Cu-Au-Mo deposit, Alaska, USA. *Geochemistry: Exploration, Environment, Analysis* **11**, 321-334.

Kieffer, M. A., Dare, S. A. S. & Namur, O. (2023). The use of trace elements in apatite to trace differentiation of a ferrobasaltic melt in the Sept-Iles Intrusive Suite, Quebec, Canada: Implications for provenance discrimination. *Geochimica et Cosmichimica Acta* **342**, 169-197.

Krogh, T. E., Davis, D. W. & Corfu, F. (1984). Precise U-Pb zircon and baddeleyite ages for the Sudbury area. In The Geology and Ore Deposits of the Sudbury Structure. In: Pye, E. G., Naldrett, A. J. & P.E., G. (eds.) *The Geology and Ore Deposits of the Sudbury Structure, Ontario Geological Survey, Specifications* Sudbury, 431-446.

Kruger, F. J. (1994). The Sr-isotopic stratigraphy of the western Bushveld Complex. *South African Journal of Geology* **97**, 393-398.

Kruger, F. J., Cawthorn, R. G. & Walsh, K. (1987). Strontium isotopic evidence against magma addition in the Upper Zone of the Bushveld Complex. *Earth and Planetary Science Letters* **84**, 51-58.

Laurent, O., Björnsen, J., Wotzlaw, J.-F., Bretscher, S., Pimenta Silva, M. & Moyen, J.-F. (2020). Earth's earliest granitoids are crystal-rich magma reservoirs tapped by silicic eruptions. *Nature Geoscience* **13**.

Leeman, W. P. & Dasch, E. J. (1978). Strontium, lead, and oxygen isotopic investigation of the Skaergaard Intrusion, East Greenland. *Earth and Planetary Science Letters* **41**, 47-59.

Li, W., Costa, F., Oppenheimer, C. & Nagashima, K. (2023). Volatile and trace element partitioning between apatite and alkaline melts. *Contributions to Mineralogy and Petrology* **178**.

Lightfoot, P. C. (2016). *Nickel sulfide ores and impact melts: Origin of the Sudbury Igneous Complex*: Elsevier.

Lightfoot, P. C. & Zotov, I. A. (2005). Geology and geochemistry of the Sudbury Igneous Complex, Ontario, Canada: origin of nickel sulfide mineralization associated with an impact-generated melt sheet. *Geology of Ore Deposits* **47**, 349-381.

Liou, P. & Guo, J. (2019). Generation of Archaean TTG Gneisses Through Amphibole-Dominated Fractionation. *Journal of Geophysical Research: Solid Earth* **124**, 3605-3619.

Lissenberg, C. J. & MacLeod, C. J. (2016). A Reactive Porous Flow Control on Mid-ocean Ridge Magmatic Evolution. *Journal of Petrology* **57**, 2195-2220.

Luan, Y., Song, X.-Y., Chen, L.-M., Zheng, W.-Q., Zhang, X.-Q., Yu, S.-Y., She, Y.-W., Tian, X.-L. & Ran, Q.-Y. (2014). Key factors controlling the accumulation of the Fe–Ti oxides in the Hongge layered intrusion in the Emeishan Large Igneous Province, SW China. *Ore Geology Reviews* **57**, 518-538.

Maier, W. D., Arndt, N. T. & Curl, E. A. (2000). Progressive crustal contamination of the Bushveld Complex: evidence from Nd isotopic analyses of the cumulate rocks. *Contributions to Mineralogy and Petrology* **140**, 316-327.

Maier, W. D., Barnes, S.-J. & Karykowski, B. T. (2016). A chilled margin of komatiite and Mg-rich basaltic andesite in the western Bushveld Complex, South Africa. *Contributions to Mineralogy and Petrology* **171**, 1-22.

Mangewape, M., Roelofse, F., Mock, T. & Carlson, R. W. (2016). The Sr-isotopic stratigraphy of the Northern Limb of the Bushveld Complex, South Africa. *Journal of African Earth Sciences* **113**, 95-100.

Mansur, E. T. & Barnes, S.-J. (2020). Concentrations of Te, As, Bi, Sb and Se in the Marginal Zone of the Bushveld Complex: Evidence for crustal contamination and the nature of the magma that formed the Merensky Reef. *Lithos* **358**, 105407.

Mao, M., Rukhlov, A. S., Rowins, S. M., Spence, J. & Coogan, L. A. (2016). Apatite Trace Element Compositions: A Robust New Tool for Mineral Exploration. *Economic Geology* **111**, 1187-1222.

McBirney, A. R. (1989). The Skaergaard Layered Series: I. Structure and average compositions. *Journal of Petrology* **30**, 363-397.

McBirney, A. R. (1996). The Skaergaard intrusion. In: Cawthorn, R. G. (ed.) *Layered Intrusions*: Elsevier Science B.V., 147-180.

McBirney, A. R. & Creaser, R. A. (2003). The Skaergaard Layered Series, Part VII: Sr and Nd Isotopes. *Journal of Petrology* **44**, 757-771.

McKenzie, D. & O'Nions, R. K. (1991). Partial melt distributions from inversion of rare Earth element concentrations. *Journal of Petrology* **32**, 1021-1081.

McNamara, G. S., Lesher, C. M. & Kamber, B. S. (2017). New Feldspar Lead Isotope and Trace Element Evidence from the Sudbury Igneous Complex Indicate a Complex Origin of Associated Ni-Cu-PGE Mineralization Involving Underlying Country Rocks. *Economic Geology* **112**, 569-590.

Miles, A. J., Graham, C. M., Hawkesworth, C. J., Gillespie, M. R., Hinton, R. W. & Bromiley, G. D. (2014). Apatite: A new redox proxy for silicic magmas? *Geochimica et Cosmochimica Acta* **132**, 101-119.

Miloski, P., Dare, S. A. S., Morisset, C. E., Davis, J. S., Perrot, M. & Savard, S. (in press). Petrogenesis of Fe-Ti-P mineralization associated with Proterozoic anorthosite massifs at Lac à l'Orignal, Quebec, Canada: insights from oxide and apatite trace-element geochemistry. *Mineralium Deposita*.

Miranda, A. C. R., Beaudoin, G., Rottier, B., Pasava, J., Bohdalek, P. & Malec, J. (in press). Trace Element Signatures in Scheelite Associated with Various Deposit Types: A Tool for Mineral Targeting. *Journal of Geochemical Exploration*.

Moyen, J.-F. & Martin, H. (2012). Forty Years of TTG Research. *Lithos* **148**, 312-336.

Mungall, J. E., Ames, D. E. & Hanley, J. J. (2004). Geochemical evidence from the Sudbury Structure for crustal redistribution by large bolide impacts. *Nature* **429**, 546-548.

Mungall, J. E., Andrews, D. R. A., Cabri, L. J., Sylvester, P. J. & Tubrett, M. (2005). Partitioning of Cu, Ni, Au, and platinum-group elements between monosulfide solid solution and sulfide melt under controlled oxygen and sulfur fugacities. *Geochimica et Cosmichimica Acta* **69**, 4349-4360.

Nadoll, P., Angerer, T., Mauk, J. L., French, D. & Walshe, J. (2014). The chemistry of hydrothermal magnetite: A review. *Ore Geology Reviews* **61**, 1-32.

Namur, O., Abily, B., Boudreau, A. E., Blanchette, F., Bush, J. W. M., Ceuleneer, G., Charlier, B., Donaldson, C. H., Duchesne, J.-C., Higgins, M. D., Morata, D., Nielsen, T. F. D., O'Driscoll, B., Pang, K. N., Peacock, T., Spandler, C. J., Toramaru, A. & Veksler, I. V. (2015). Igneous Layering in Basaltic Magma Chambers. In: Charlier, B., Namur, O., Latypov, R. & Tegner, C. (eds.) *Layered Intrusions*. Dordrecht: Springer Geology.

Namur, O., Charlier, B., Toplis, M. J., Higgins, M. D., Liégeois, J.-P. & Vander Auwera, J. (2010). Crystallization Sequence and Magma Chamber Processes in the Ferrobasaltic Sept Iles Layered Intrusion, Canada. *Journal of Petrology* **51**, 1203-1236.

Namur, O., Charlier, B. & Holness, M. B. (2012). Dual origin of Fe–Ti–P gabbros by immiscibility and fractional crystallization of evolved tholeiitic basalts in the Sept Iles layered intrusion. *Lithos* **154**, 100-114.

Nathwani, C. L., Loader, M. A., Wilkinson, J. J., Buret, Y., Sievwright, R. H. & Hollings, P. (2020). Multi-stage arc magma evolution recorded by apatite in volcanic rocks. *Geology* **48**, 323-327.

O'Sullivan, G., Chew, D., Kenny, G., Henrichs, I. & Mulligan, D. (2020). The trace element composition of apatite and its application to detrital provenance studies. *Earth-Science Reviews* **201**, 103044.

Paiement, J.-P., Gagne, J., Duplessis, C., Rousseau, G., Gagnon, G. & M., D. (2013). Pre-Feasability Study Mine Arnaud Inc. Sept-Iles Deposit, Québec; Final Report, Technical Report NI 43-101. 377.

Pan, Y. & Fleet, M. E. (2002). Compositions of the Apatite-Group Minerals: Substitution Mechanisms and Controlling Factors. *Reviews in Mineralogy and Geochemistry* **48**, 13-49.

Pang, K.-N., Li, C., Zhou, M.-F. & Ripley, E. M. (2009). Mineral compositional constraints on petrogenesis and oxide ore genesis of the Panzhihua layered gabbroic intrusion, SW China. *Lithos* **110**, 199-214.

Pang, K.-N., Zhou, M.-F., Lindsley, D. H., Zhao, D. & Malpas, J. (2008). Origin of Fe^Ti Oxide Ores in Mafic Intrusions: Evidence from the Panzhihua Intrusion, SW China. *Journal of Petrology* **49**, 295-313.

Pang, K.-N., Zhou, M.-F., Qi, L., Shellnutt, G., Wang, C. Y. & Zhao, D. (2010). Flood basalt-related Fe–Ti oxide deposits in the Emeishan large igneous province, SW China. *Lithos* **119**, 123-136.

Paton, C., Hellstrom, J. C., Paul, B., Woodhead, J. & Hergt, J. (2011). Iolite: freeware for the visualisation and processing of mass spectrometric data. *Journal of Analytical Atomic Spectrometry* **26**, 2508-2518.

Pearce, J. A. & Peate, D. W. (1995). Tectonic implications of the composition of volcanic arc magmas. *Annual Review of Earth and Planetary Sciences* **23**, 251-285.

Pêcher, A., Arndt, N., Jean, A., Bauville, A., Ganino, C. & Athurion, C. (2013). Structure of the Panzhihua intrusion and its Fe-Ti-V. deposit, China. *Geoscience Frontiers* **4**, 571-581.

Pedersen, J. M., Ulrich, T., Whitehouse, M. J., Kent, A. J. R. & Tegner, C. (2021). The volatile and trace element composition of apatite in the Skaergaard intrusion, East Greenland. *Contributions to Mineralogy and Petrology* **176**, 102.

Piccoli, P. M. & Candela, P. A. (2002). Apatite in Igneous Systems. *Reviews in Mineralogy and Geochemistry* **48**, 255-292.

Qian, L., Wang, Y., Xie, J. & Sun, W. (2019). The Late Mesozoic granodiorite and polymetallic mineralization in southern Anhui Province, China: A perspective from apatite geochemistry. *Solid Earth Sciences* **4**, 178-189.

Qiu, K.-F., Zhou, T., Chew, D., Hou, Z.-L., Müller, A., Yu, H.-C., Lee, R. G., Chen, H. & Deng, J. (in press). Apatite trace element composition as an indicator of ore deposit types: a machine learning approach. *American Mineralogist*.

Rudnick, R. L. & Gao, S. (2014). Composition of the Continental Crust. In: Turekian, H. & Holland, K. (eds.) *Treatise on Geochemistry*. Oxford: Elsevier, 1-51.Rukhlov, A. S., Plouffe, A., Ferbey, T., Mao, M. & Spence, J. (2016). Application of trace-element compositions of detrital apatite to explore for porphyry deposits in central
British Columbia. In: Mines, B. C. M. o. E. a. (ed.) Geological Fieldwork 2015, British Columbia Geological Survey Paper 2016-1, 145-179.

Savard, D., Dare, S. A. S., Bédard, L. P. & Barnes, S.-J. (2023). A New Mapping Protocol for Laser Ablation (with Fast-Funnel) Coupled to a Time-of-Flight Mass Spectrometer (LA-FF-ICP-ToF-MS) for the Rapid, Simultaneous Quantification of Multiple Minerals. *Geostandards and Geoanalytical Research* **47**, 243-265.

She, Y.-W., Song, X.-Y., Yu, S.-Y., Chen, L.-M. & Zheng, W.-Q. (2016). Apatite geochemistry of the Taihe layered intrusion, SW China: Implications for the magmatic differentiation and the origin of apatite-rich Fe-Ti oxide ores. *Ore Geology Reviews* **78**, 151-165.

She, Y.-W., Yu, S.-Y., Song, X.-Y., Chen, L.-M., Zheng, W.-Q. & Luan, Y. (2014). The formation of P-rich Fe–Ti oxide ore layers in the Taihe layered intrusion, SW China: Implications for magma-plumbing system process. *Ore Geology Reviews* **57**, 539-559.

Shellnutt, J. G. (2014). The Emeishan large igneous province: A synthesis. *Geoscience Frontiers* **5**, 369-394.

Smith, W.D. & Maier, W.D. (2021). The geotectonic setting, age and mineral deposit inventory of global layered intrusions. *Earth-Science Reviews* **220**, 103736.

Solovova, I. P., Yudovskaya, M. A., Kinnaird, J. A., Wilson, A. H. & Zinovieva, N. G. (2021). A siliceous komatiitic source of Bushveld magmas revealed by primary melt inclusions in olivine. *Lithos* **388-389**, 106094.

Song, X.-Y., Qi, H.-W., Hu, R.-Z., Chen, L.-M., Yu, S.-Y. & Zhang, J.-F. (2013). Formation of thick stratiform Fe-Ti oxide layers in layered intrusion and frequent replenishment of fractionated mafic magma: Evidence from the Panzhihua intrusion, SW China. *Geochemistry, Geophysics, Geosystems* **14**, 712-732.

Sonnenthal, E. L. (1992). Geochemistry of dendritic anorthosites and associated pegmatites in the Skaergaard Intrusion, East Greenland: Evidence for metasomatism by a chlorite-rich fluid. *Journal of Volcanology and Geothermal Research* **52**, 209-230.

Sproule, R. A., Lesher, C., Ayer, J., Thurston, P. & Herzberg, C. (2002). Spatial and temporal variations in the geochemistry of komatiites and komatiitic basalts in the Abitibi greenstone belt. *Precambrian Research* **115**, 153-186.

Stewart, B. W. & DePaolo, D. J. (1990). Isotopic studies of processes in mafic magma chambers: II. The Skaergaard Intrusion, East Greenland. *Contributions to Mineralogy and Petrology* **104**, 125-141.

Stokes, T. N., Bromiley, G. D., Potts, N. J., Saunders, K. E. & Miles, A. J. (2019). The effect of melt composition and oxygen fugacity on manganese partitioning between apatite and silicate melt. *Chemical Geology* **506**, 162-174.

Tang, Q., Li, C., Ripley, E. M., Bao, J., Su, T. & Xu, S. (2021). Sr-Nd-Hf-O isotope constraints on crustal contamination and mantle source variation of three Fe-Ti-V oxide ore deposits in the Emeishan large igneous province. *Geochimica et Cosmichimica Acta* **292**, 364-381.

Tanner, D., Mavrogenes, J. A., Arculus, R. J. & Jenner, F. E. (2014). Trace Element Stratigraphy of the Bellevue Core, Northern Bushveld: Multiple Magma Injections Obscured by Diffusive Processes. *Journal of Petrology* **55**, 859-882.

Tegner, C., Cawthorn, R. G. & Kruger, F. J. (2006). Cyclicity in the Main and Upper Zones of the Bushveld Complex, South Africa: Crystallization from a Zoned Magma Sheet. *Journal of Petrology* **47**, 2257-2279.

Tegner, C., Lesher, C. E., Larson, L. M. & Watt, W. S. (1998). Evidence fromthe rare-earth element record of mantle melting for cooling of the Tertiary Iceland plume. *Nature* **395**, 591-594.

Tegner, C., WIlson, J. R. & Robins, B. (2005). Crustal assimilation in basalt and jotunite: Constraints from layered intrusions. *Lithos* **83**, 299-316.

Therriault, A. M., Fowler, A. D. & Grieve, R. A. F. (2002). The Sudbury Igneous Complex: A Differenciated Impact Melt Sheet. *Economic Geology* **97**, 1521-1540.

Thy, P., Lesher, C. E. & Tegner, C. (2009). The Skaergaard liquid line of descent revisited. *Contributions to Mineralogy and Petrology* **157**, 735-747.

Tollari, N., Toplis, M.J. & Barnes, S.-J. (2006). Predicting phosphate saturation in silicate magmas: An experimental study of the effects of melt composition and temperature. *Geochimica et Cosmochimica Acta* **70**, 1518–1536.

Tollari, N., Barnes, S., Cox, R. & Nabil, H. (2008). Trace element concentrations in apatites from the Sept-Îles Intrusive Suite, Canada — Implications for the genesis of nelsonites. *Chemical Geology* **252**, 180-190.

Toplis, M. J. & Carroll, M. R. (1995). An Experimental Study of the Influence of Oxygen Fugacity on Fe-Ti Oxide Stability, Phase Relations, and Mineral—Melt Equilibria in Ferro-Basaltic Systems. *Journal of Petrology* **36**, 1137-1170.

Toplis, M. J., Dingwell, D. B. & Libourel, G. (1994). The effect of phosphorus on the iron redox ratio, viscosity, and density of an evolved ferrobasalt. *Contributions to Mineralogy and Petrology* **117**, 293-204.

Vander Auwera, J., Longhi, J. & Duchesne, J. C. (2000). The effect of pressure on D_{Sr} (plag/melt) and D_{Cr} (opx/melt): implications for anorthosite petrogenesis. *Earth and Planetary Science Letters* **178**, 303-314.

Van Tongeren, J. A. & Mathez, E. A. (2012). Large-scale liquid immiscibility at the top of the Bushveld Complex, South Africa. *Geology* **40**, 491-494.

Von Gruenewaldt, G. (1993). Ilmenite-Apatite Enrichments in the Upper Zone of the Bushveld Complex: A Major Titanium-Rock Phosphate Resource. *International Geology Review* **35**, 987-1000.

Wager, L. R. & Brown, G. M. (1968). *Layered Igneous Rocks*: Oliver and Boyd.

Wang, K., Wang, C. Y. & Ren, Z.-Y. (2018). Apatite-hosted melt inclusions from the Panzhihua gabbroic-layered intrusion associated with a giant Fe–Ti oxide deposit in SW China: insights for magma unmixing within a crystal mush. *Contributions to Mineralogy and Petrology* **173**, 59.

Wang, C. Y. & Zhou, M.-F. (2013). New textural and mineralogical constraints on the origin of the Hongge Fe-Ti-V oxide deposit, SW China. *Mineralium Deposita* **48**, 787-798.

Warner, S., Martin, R. F., Abdel-Rahman, A.-F. M. & Doig, R. (1998). Apatite as a monitor of fractionation, degassing, and metamorphism in the Sudbury Igneous Complex, Ontario. *The Canadian Mineralogist* **36**, 981-999.

Watts, K. M. (2014). A melt inclusion study of the Sudbury Igneous Complex (Ontario, Canada): Evidence for two-liquid immiscibility and constraints on trace elements distribution. Halifax, Nouvelle-Ecosse: Saint Mary's University, 129.

Webster, J. D. & Piccoli, P. M. (2015). Magmatic Apatite: A Powerful, Yet Deceptive, Mineral. *Elements* **11**, 177-182.

White, R. S. & McKenzie, D. (1995). Mantle plumes and flood basalts. *Journal of Geophysical Research: Solid Earth* **100**, 17543-17585.

Willmore, C. C., Boudreau, A. E. & Kruger, F. J. (2000). The Halogen Geochemistry of the Bushveld Complex, Republic of South Africa: Implications for Chalcophile Element Distribution in the Lower and Critical Zones. *Journal of Petrology* **41**, 1517-1539.

Wilson, A. H. (2012). A chill sequence to the Bushveld Complex: insight into the first stage of emplacement and implications for the parental magmas. *Journal of Petrology* **53**, 1123-1162.

Xing, C.-M., Wang, C. Y. & Li, C. (2014). Trace element compositions of apatite from the middle zone of the Panzhihua layered intrusion, SW China: Insights into the differentiation of a P- and Si-rich melt. *Lithos* **204**, 188-202.

Xing, C.-M. & Wang, C. Y. (2017). Cathodoluminescence images and trace element compositions of fluorapatite from the Hongge layered intrusion in SW China: A record of prolonged crystallization and overprinted fluid metasomatism. *American Mineralogist* **102**, 1390-1401.

Xing, C.-M., Wang, C. Y. & Tan, W. (2017). Disequilibrium growth of olivine in mafic magmas revealed by phosphorus zoning patterns of olivine from mafic–ultramafic intrusions. *Earth and Planetary Science Letters* **479**, 108-119.

Yang, S.-H., Maier, W. D., Godel, B., Barnes, S.-J., Hanski, E. & O'Brien, H. (2019). Parental magma composition of the Main Zone of the Bushveld Complex: Evidence from in situ LA-ICP-MS trace element analysis of silicate minerals in the cumulate rocks. *Journal of Petrology* **60**, 359-392.

Yu, S.-Y., Song, X.-Y., Ripley, E. M., Li, C., Chen, L.-M., She, Y.-W. & Luan, Y. (2015). Integrated O–Sr–Nd isotope constraints on the evolution of four important Fe–Ti oxide ore-bearing mafic–ultramafic intrusions in the Emeishan large igneous province, SW China. *Chemical Geology* **401**, 28-42.

Zafar, T., Rehman, H. U., Mahar, M. A., Alam, M., Oyebamiji, A., Rehman, S. U. & Leng, C.-B. (2020). A critical review on petrogenetic, metallogenic and geodynamic implications of granitic rocks exposed in north and east China: New insights from apatite geochemistry. *Journal of Geodynamics* **136**, 101723.

Zhang, X., Guo, F., Zhang, B., Zhao, L., Wu, Y., Wang, G. & Alemayehu, M. (2020). Magmatic evolution and post-crystallization hydrothermal activity in the early Cretaceous Pingtan intrusive complex, SE China: records from apatite geochemistry. *Contributions to Mineralogy and Petrology* **175**.

Zhang, Z. C., Mao, J. W., Saunders, A. D., Y., A., Li, Y. & Zhao, L. (2009). Petrogenetic modeling of three mafic-ultramafic layered intrusions in the Emeishan large igneous province, SW China, based on isotopic and bulk geochemical constraints. *Lithos* **113**, 369-392.

Zhong, H., Zhou, X. H., Zhou, M.-F., Sun, M. & Liu, B.-G. (2002). Platinum-group element geochemistry of the Hongge Fe-V-Ti deposit in the Pan-Xi area, southwestern China. *Mineralium Deposita* **37**, 226-239.

Zhou, M.-F., Chen, W. T., Wang, C. Y., Prevec, S. A., Liu, P. P. & Howarth, G. H. (2013). Two stages of immiscible liquid separation in the formation of Panzhihua-type Fe-Ti-V oxide deposits, SW China. *Geoscience Frontiers* **4**, 481-502.

Zhou, M.-F., Robinson, P. T., Lesher, C. M., Keays, R. R., Zhang, C.-J. & Malpas, J. (2005). Geochemistry, Petrogenesis and Metallogenesis of the Panzhihua Gabbroic Layered Intrusion and Associated Fe–Ti–V Oxide Deposits, Sichuan Province, SW China. *Journal of Petrology* **46**, 2253-2280.

Zhu, Q., Xie, G., Cook, N. J. & Ciobanu, C. L. (2023). Fingerprinting involvement of evaporites in magmatic-hydrothermal processes from the Jinshandian Fe skarn deposit, eastern China, using apatite geochemistry. *Lithos* **442-443**, 107076.

Zieg, M. J. & Marsh, B. D. (2005). The Sudbury Igneous Complex: Viscous emulsion differentiation of a superheated impact melt sheet. *Geological Society of America Bulletin* **117**.

CHAPITRE 4

DISCRIMINATION OF APATITE FROM I-, S- AND A-TYPE GRANITES USING TRACE ELEMENTS: IMPLICATIONS FOR MINERAL EXPLORATION AND PROVENANCE STUDIES

Marie A. Kieffer[1], Sarah A.S. Dare[1]*, Marylou Gendron[1,2]

[1]Department of Applied Sciences, University of Quebec in Chicoutimi (UQAC), 555 Boulevard de l'Université, Chicoutimi, G7H 2B1, QC, Canada

*Canada Research Chair in Geochemistry Applied to Ore Deposits

[2]Explo-logik Inc., Quebec, Canada

Chemical Geology (soumis au journal le 19 septembre 2023)

Résumé

L'apatite enregistre son environnement géologique de formation grâce à sa capacité à incorporer un grand nombre d'éléments traces. De ce fait, il y a un intérêt croissant pour développer l'apatite en tant que minéral indicateur pour les études de provenance et l'exploration minérale à partir de grains détritiques retrouvés dans l'environnement secondaire. En ce qui concerne l'exploration, des travaux récents se concentrent sur le type de gisement (e.g., porphyre, skarn, ioron-oxide copper gold) et la fertilité de l'intrusion hôte, plutôt que sur l'indentification de la nature de l'intrusion hôte. Dans cette contribution, nous compilons pour la première fois un jeu de données d'analyses d'apatites provenant de granites de type I, S et A, peralumineux à métalumineux, à l'échelle mondiale. Nous proposons un nouveau schéma de classification pour identifier les apatites des granites de type I, S et A parmi celles provenant d'autres roches intrusives (e.g., intrusions mafiques, carbonatites), en utilisant une suite complète d'éléments traces analysées à l'ablation laser ICP-MS. Ceci est réalisé en 4 étapes : (1) l'utilisation de Sr/Y en fonction des ETR légers permet d'identifier les apatites provenant des intrusions mafiques et felsiques; (2) les apatites des intrusions mafiques sont exclues grâce au diagramme ternaire ETR+Y – Sr/Y – Eu/Eu*, pour ne garder que celles provenant des intrusions felsiques; (3) une fois que les apatites sont identifiées comme provenant d'une source felsique, les apatites archéennes de TTG (Tonalite-Trondhjémite-Granodiorite) sont discriminées en utilisant le diagramme $log(La/Yb)_N$ en fonction de Yb_N; enfin, (4) parmi les apatites post-archéennes, les apatites des intrusions felsiques peuvent être classifiée comme provenant de granites de type I, S et A grâce à leur contenu en Mn et V et à leur ratio $(La/Nd)_N$. Comme les granites de type I, S et A peuvent être hôtes de différents types de minéralisations, il est primordial d'identifier le type d'intrusion (e.g., mafique, felsique, autre) avant d'évaluer sa fertilité. Cette étude démontre que l'apatite a toutes les qualités requises pour idendifier sa roche source grâce à sa chimie.

Mots-clef : apatite; éléments traces; LA-ICP-MS; minéral indicateur; provenance; types de granites

Abstract

Apatite has the ability to fingerprint its geological environment of formation due to the fact that it can incorporate a variety of trace elements. As such, there is a growing interest in developing it as an indicator mineral for mineral exploration and provenance studies in secondary environments using detrital grains. For exploration, recent studies focus directly on the deposit type (e.g., porphyry, skarn, iron-oxide copper gold deposits) and the fertility of the host intrusion rather than identifying the type of host intrusion. In this contribution, we compiled for the first time a global dataset of apatite analyses for I-, S- and A-type granites, ranging from peraluminous to metaluminous, from worldwide intrusions. We propose a novel classification scheme to identify apatite from I-, S- and A-type granites among apatite from other intrusive rocks (e.g., mafic intrusions, carbonatites) using a full suite of trace elements determined by laser ablation ICP-MS. This is achieved in 4 steps: (1) the use of Sr/Y vs. LREE identifies apatite coming from a mafic or felsic intrusion; (2) apatite from mafic intrusions is excluded using the REE+Y, Sr/Y and Eu/Eu* ternary diagram, to keep only those from felsic intrusions. In some cases, apatite from I-type granite is misclassified as it plots in the mafic field but an additional ternary diagram, using the As, $(Gd/Yb)_N$ and Pb+Th+U, ensures apatite is correctly classified as felsic; (3) once apatite is identified as coming from a felsic source, Archean apatite from TTG (Tonalite-Trondhjemite-Granodiorite) is discriminated from post-Archean apatite using the $log(La/Yb)_N$ vs. Yb_N diagram; and finally, (4) among the post-Archean intrusions, the origin of felsic apatite can be classified as I-, S- and A-type using Mn, V and $(La/Nd)_N$ ratio. As I-, S- and A-type granites can host different types of mineralisation, it is of utmost importance to identify the rock type (e.g., mafic, felsic, other) prior to evaluating the fertility of a given intrusion. This study demonstrates that apatite has all the abilities to be used as an indicator mineral to fingerprint its host rock.

Keywords: apatite; granite types; indicator mineral; LA-ICP-MS; provenance; trace elements

Graphical astract

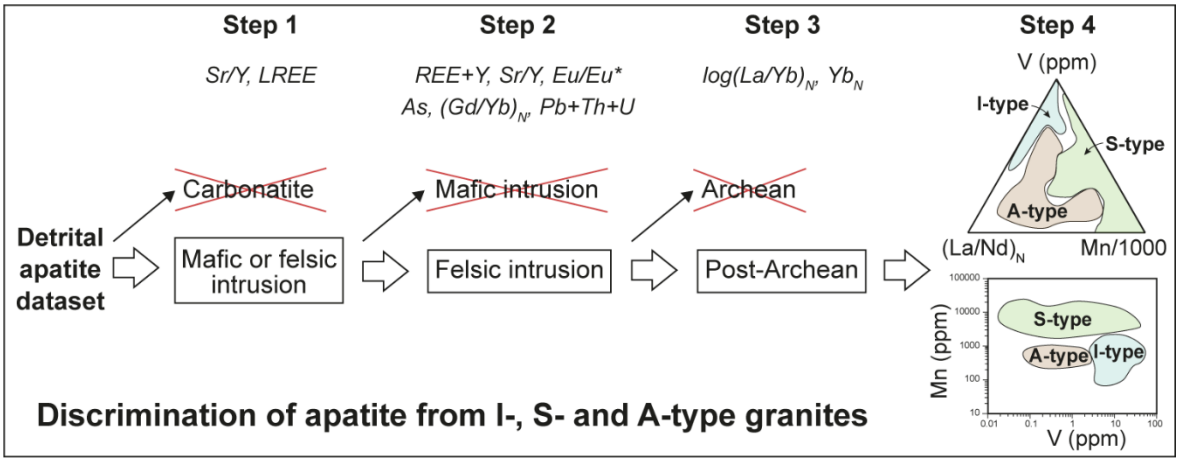

4.1 Introduction

Apatite is sensitive to its geological environment of formation (Belousova *et al.* 2002; O'Sullivan *et al.* 2020) and can incorporate a variety of trace elements (Pan and Fleet 2002), that are now readily determined by laser ablation ICP-MS (Kieffer *et al.* 2023), which thus makes it a powerful petrogenetic indicator. For example, apatite can record magmatic processes in felsic intrusions (e.g., Hsieh *et al.* 2008; Chu *et al.* 2009; Qu *et al.* 2019; Yang *et al.* 2020; Zhang *et al.* 2020; Cao *et al.* 2023) as well as in mafic intrusions (e.g., Tollari *et al.* 2008; Chen *et al.* 2013; Pedersen *et al.* 2021; Kieffer *et al.* 2023; accepted). There is also a growing interest in using apatite as a provenance indicator mineral for sedimentary studies (e.g., Belousova *et al.* 2002; Abdullin *et al.* 2016; O'Sullivan *et al.* 2020) and for mineral exploration of ore deposits using detrital grains from the secondary environment (e.g., glacial or river sediments; Mao *et al.* 2016; Zhou *et al.* 2023), similar to other indicator minerals (e.g., magnetite, Dare *et al.* 2014, Nadoll *et al.* 2014; scheelite, Miranda *et al.* in press; and chalcopyrite, Caraballo *et al.* 2022).

Granitoids and granite-related rocks represent the majority of the upper continental crust (Frost *et al.* 2001) and can host different types of mineralisation (Blevin and Chappell 1995), according to different magma compositions and tectonic settings. Their different petrogenesis led to the establishment of more than 20 classifications (e.g., Chappell and White 1974; Pearce *et al.* 1984; Barbarin 1990, 1999; Frost *et al.* 2001; Bonin *et al.* 2020). A commonly accepted classification is that based on granite petrogenesis (i.e., magma source) defined by Chappell and White (1974) for I- and S-type granites, with the recognition and addition of A-type granites by Loiselle and Wones (1979). The 3 types of granites have variable aluminium saturation index (ASI), defined as molar $Al_2O_3/(Na_2O+K_2O+CaO)$ by Shand (1927). Although other classifications exist (e.g., based on tectonic setting, Pearce *et al.* 1984), and that it might be more efficient to use a more descriptive classification (Bonin *et al.* 2020), the aim of this contribution is not to review nor discuss the existing classifications of granitic rocks, but rather to provide a framework for the apatite data that are presented in this paper, to evaluate if apatite from different granite types are compositionally distinct. I-type granites derive from the partial melting of a meta-igneous source material (Chappell and White 1974), that is probably dacitic to andesitic crust formed beneath magmatic arcs (Clemens *et al.* 2011),

or fractionate from mantle-derived mafic melts (Castro 2020). The aluminium saturation index of I-type granites is variable. Whereas most I-type granites are metaluminous (Al-undersaturated), some can also have an excess in Al and are thus peraluminous (Chappell and White 1992). I-type granites also contain high Sr, CaO and Na_2O concentrations (Chappell and White 1992). The S-type granites, on the other hand, originate by partial melting of metasedimentary protoliths in metamorphic terranes linked to collisional settings (i.e., Al-rich metasedimentary rocks; Chappell and White 1974, 2001). The vast majority of S-type granites are peraluminous, with lower Sr, CaO and Na_2O concentrations than I-type granites (Chappell and White 1992). Lastly, the 'A' of A-type granites stands for its formation in an anorogenic setting (Loiselle and Wones 1979; Eby 1990) that ranges from a within-plate to a plate boundary setting (Bonin 2007). Frost and Frost (2011) suggests that the term 'A-type' should be replaced by 'ferroan' granites due to a specific magma chemistry that can be obtained in various geological settings. A-type granites are typically peralkaline (Frost and Frost 2011, and references therein) with the magma source likely corresponding to a mantle-derived melt with an alkaline affinity (Bonin 2007). Such A-type granites contain high Fe/(Fe+Mg), K_2O and incompatible trace elements (e.g., REE, Zr, Nb, Ta), with lower concentrations of compatible elements (e.g., Sr, V) (Loiselle and Wones 1979). However, A-type granites can also be metaluminous or peraluminous. The example of A-type granites (metaluminous and ferroan) overlying the mafic layered intrusion of the Sept-Iles Intrusive Suite, Canada, represents the end product of extreme fractional crystallisation of a mantle-sourced ferrobasaltic melt with negligible crustal contamination (Namur *et al.* 2011) associated to within plate magmatism (Hill *et al.* 1992).

The different I-, S-, and A-type granites are associated with different types of magmatic-hydrothermal mineral deposits. I-type granites can be related to porphyry Cu-Mo±Au or Pb-Zn-Ag hydrothermal veins (e.g., Li *et al.* 2017; Bouzari *et al.* 2018; Duan *et al.* 2019; Gao *et al.* 2020; Xing *et al.* 2020; Yang *et al.* 2020). Porphyry deposits are generally associated with I-type granites of the magnetite series, whose source can be located in the upper mantle or lower crust (Ishihara 1977). Hydrothermal mineralisation is rather related to I-type granites of the ilmenite series, that have a lower oxygen fugacity than those of the magnetite series due to interaction with carbon-bearing materials (e.g., metamorphic or sedimentary rocks; Ishihara 1977). On the other hand, S-type granites are

generally related to Sn-, W-, Pb-, Zn-bearing skarns (Blevin and Chappell 1995; Cao *et al.* 2012; Zhang *et al.* 2023) or Sn-bearing greisen and hydrothermal veins (Liu *et al.* 2020; Roda-Robles *et al.* 2022 and references therein) mineralisation. Finally, W-Sn greisens or skarns (Li *et al.* 2018; Jiang *et al.* 2008) and REE mineralisation (Dostal *et al.* 2014) can be associated with A-type granites. A large number of apatite studies focus on the study of mineral deposits associated with granitoids. In particular, those works aim to identify fertile from barren intrusions of I- and S-type granites (e.g. Li *et al.* 2017; Azabakht *et al.* 2018; Bouzari *et al.* 2018; Qian *et al.* 2019; Gao *et al.* 2020; Zafar *et al.* 2020), or to distinguish different types of mineralisation (e.g., porphyry Cu, skarn W; Duan *et al.* 2019; Gao *et al.* 2020; Mao *et al.* 2016; Tan *et al.* 2023; Zhang *et al.* 2023) based on the trace element content of apatite. However, all those studies are performed at a local, deposit scale, and none of them aim to identify the host granitic rocks using apatite composition.

Granitoids commonly contain apatite as an accessory mineral (< 1 vol.%; Piccoli and Candela 2002; Webster and Piccoli 2015), and a few studies show the potential to discriminate apatite from different granite types using its chemical composition. According to the compilation of apatite studies on granites, the granitic host-rock of apatite is generally classified into I-, S- and A-type granites (see Table 4.1 and Table 4.2, and references therein). It has been shown that apatite from Archean and post-Archean granitoids (Antoine *et al.* 2020; Bruand *et al.* 2020), from I- and S-type granites (Sha and Chappell 1999; Laurent *et al.* 2017), or from I- and A-type granites (Wang *et al.* 2018) have a different trace element concentrations. However, these studies only compare 2 of the 3 granite types and were typically done on a restricted locality and from a restricted dataset (i.e., few samples and/or number of analysed trace elements). For example, the only existing study that compares apatite composition from the 3 types of granites (Richard 2019) is limited to apatite from 2 batholiths from the Oslo rift (Norway) compared to analyses of apatite from I-, S- and A-type compiled from 4 publications, and only considers REE+Y and Mn in the discrimination diagrams. As such, all existing discrimination diagrams might not work on a larger scale, using a worldwide dataset of apatite from I-, S-, and A-type granites.

Table 4.1 – Summary of the samples used in this study and source of additional information and description of samples. *AMCG* Anorthosite-Mangerite-Charnockite-Granite; *LIP* Large Igneous Province. [a]Data from Kieffer *et al.* (2023)

	Localities	Rock type	Sample name	References
I-type granite				
Metaluminous	Guichon Creek, Chataway variety (Canada)	Granodiorite	MH-03-115, MH-03-119	D'Angelo *et al.* (2017)
	Tuolumne, Sawmill Canyon, Cathedral Peak (U.S.A.)	Granite, granodiorite	TS11A, TS31B	Solgadi and Sawyer (2008); Solgadi (2010)
	Bemboka Granodiorite, Lachlan Fold Belt (Australia)	Granodiorite	AB103	Blevin and Chappell (1995)
	Illapel plutonic suite, Coastal batholith (Chile)	Granodiorite	ILL-08-74A, ILL-08-104A	Higgins (2017); Parada *et al.* (1999)
Peraluminous	Vredenburg Pluton, Western Cape Suite (South Africa)	Granite	VL1, VL2	Scheepers (1995)
I-type granite: mafic				
Metaluminous	Jindabyne Tonalite, Tuross Head Tonalite, Lachlan Fold Belt (Australia)	Tonalite	KB22, MG16	Griffin *et al.* (1978); Chappell and White (1992)
S-type granite				
Peraluminous	Wulumna (Australia)	Granite	SL-48, SL-62	Lavaure and Sawyer (2011); Lavaure (2012)
	Dalgety Granodiorite, Lachlan Fold Belt (Australia)	Granodiorite	BB9	Chappell (1984)
	Jillamatong Granodiorite, Lachlan Fold Belt (Australia)	Granodiorite	KB32	Hine *et al.* (1978); Chappell (1984)
	Peninsula pluton, Western Cape Suite (South Africa)	Granite	PG24B BB-11	Farina *et al.* (2012); Villaros *et al.* (2009)
	Margeride Granite, French Massif Central (France)	Biotite granite with cordierite	FMC-18, FMC-21	Moyen *et al.* (2017); Antonelli *et al.* (2023)
	Bougès Granite, French Massif Central (France)	Biotite leucogranite	FMC-25	
	Laubies Granite, French Massif Central (France)	Two-mica–cordierite leucogranite	FMC-26	
A-type granite				
Metaluminous	Chicoutimi Mangerite, Saguenay–Lac-St-Jean (AMCG) (Canada)	Mangerite	19SDLI-04B, -04C	Higgins and Van Breemen (1996)
	La Baie Granite, Saguenay–Lac-St-Jean (AMCG) (Canada)	Granite	19SDLI-03A, -03B	Higgins and Van Breemen (1996)
	Lac Labrecque Granite, Saguenay–Lac-St-Jean (AMCG) (Canada)	Granite	19SDLI-08	Higgins and Van Breemen (1996)
	St Ambroise Pluton, Saguenay–Lac-St-Jean (AMCG) (Canada)	Syenite – monzonite	19SDLI-05, -06	Higgins and Van Breemen (1996)
	Pointe du Criard sill, Sept-Iles Intrusive Suite (LIP) (Canada)	Granite Syenite	VH-03-11[a] VH-03-08 [a], VH-03-09 [a]	Hounsell (2006); Namur *et al.* (2011)
	Upper Series, Sept-Iles Intrusive Suite (LIP) (Canada)	Granite Syenite Monzonite	VH-03-22 [a], VH-03-35 [a] VH-03-37 [a], VH-03-48 [a] VH-03-42 [a]	Hounsell (2006); Namur *et al.* (2011)

Table 4.2 – Summary of compiled apatite data from mafic and felsic rocks. References in bold indicate the availability of LA-ICP-MS data, that may be associated with EMPA data, whereas other reference only refer to EMPA data. N number of samples, n number of analyses. The database of apatite from felsic rocks is provided in Annexe 50.

	Localities	References
MAFIC ROCKS		
Large Igneous Provinces *(N = 155, n = 1191)*	Bushveld Complex[1,2]; Hongge[3]; Panzhihua[4]; Skaergaard[5]; Sept-Iles Intrusive Suite[2,6,7]; Taihe[8]; Bijigou[9]	[1]**Van Tongeren and Mathez (2012)**; [2]**Kieffer *et al.* (accepted)**; [3]**Xing and Wang (2017)**; [4]**Xing *et al.* (2014)**; [5]**Pedersen *et al.* (2021)**; [6]**Tollari *et al.* (2008)**; [7]**Kieffer *et al.* (2023)**; [8]**She *et al.* (2016)**; [9]**Wang and Wang (2020)**
AMCG suites *(N = 144, n = 1044)*	Bjerkreim-Sokndal[10,11,12]; Damiao[13,14]; Fedorivka[15]; Grader[16]; Lac à Paul[17,18]; Lac à l'Orignal[17,19]; Lac Perron[17]; Saint-Charles-de-Bourget[20]	[10]**Charlier *et al.* (2005)**; [11]**Ihlen *et al.* (2014)**; [12]**Decrée *et al.* (2022)**; [13]**Chen *et al.* (2013)**; [14]**He *et al.* (2016)**; [15]**Duchesne *et al.* (2006)**; [16]**Charlier *et al.* (2008)**; [17]**Grant (2020)**; [18]**Chartier-Montreuil *et al.* (2017)**; [19]**Miloski *et al.* (2023)**; [20]**Desormiers (2015)**
FELSIC ROCKS		
I-type granite	*(EMPA: N = 113, n = 1448; LA-ICP-MS : N = 89, n = 1355)*	
Metaluminous	Tuolumne[21]; Mount Isa Inlier[22]; Western Cape Suite[23]; Nanling mountains[24]; Central Kazakhstan[25]; Matok Pluton[26]; New Brunswick[27]; Guichon Creek, Takomkane, Granite Mountain[28]; Jiuhuashan[29]; Tongling[30]; Luanshuan[31,32]; Great Xing'an Range[33]; Kukaazi[34]; Huojihe[35]	[21]Piccoli and Candela (1994); [22]**Belousova *et al.* (2001)**; [23]**Spicer (2001)**; [24]**Hsieh *et al.* (2008)**; [25]**Cao *et al.* (2012)**; [26]**Laurent *et al.* (2017)**; [27]**Azadbakht *et al.* (2018)**; [28]**Bouzari *et al.* (2018)**; [29]Wang *et al.* (2018); [30]**Xie *et al.* (2018)**; [31]**Du *et al.* (2019)**; [32]**Yang *et al.* (2020)**; [33]**Qu *et al.* (2019)**; [34]**Zafar *et al.* (2020)**; [35]**Xing *et al.* (2020)**; [36]Broska *et al.* (2004); [37]Broska *et al.* (2005); [38]**Chu *et al.* (2009)**; [39]**Duan *et al.* (2019)**; [40]**Zhang *et al.* (2020)**; [41]**Qian *et al.* (2019)**; [42]Szopa (2013)
Peraluminous	Tuolumne[21]; Western Carpathians[36,37]; Gangdese Batholith[38]; Nanling Mountains[23]; Agtokai[25]; New Brunswick[27]; Guichon Creek, Takomkane[28]; Luanshuan[31,32]; Zhuxiling[38]; Great Xing'an Range[33]; Jiuhuashan[29]; Huojihe[35]; Luanshuan[31]; Pingtan[40];	
I-type granite: mafic	*(EMPA : N = 49, n = 958; LA-ICP-MS : N = 23, n = 195)*	
Metaluminous	Gangdese Batholith[38]; Southern Anhui Province[41]	
Peraluminous	Gangdese Batholith[38]; Western Tatra Mountains[42]	
S-type granite	*(EMPA : N = 73, n = 1131; LA-ICP-MS : N = 30, n = 175)*	
Metaluminous	Strzegom-Sobotka Massif[43]; Wushan[38]	[43]Birski *et al.* (2019); [44]Broska and Petrik (2008); [45]Miles *et al.* (2013); [46]Jiao *et al.* (2015); [47]Liu *et al.* (2020); [48]**Roda-Robles *et al.* (2022)**; [49]Zhang *et al.* (2023)
Peraluminous	Western Cape Suite[23]; Western Carpathians[36,44]; Nanling Mountains[23]; Northern magmatic belt[38]; Criffell pluton[45]; Darongshan[46]; New Brunswick[27]; Malay Peninsula[47]; Central Iberian Zone[48]; Zhuxi[49]	
A-type granite	*(EMPA : N = 32, n = 302; LA-ICP-MS : N = 48, n = 421)*	
Metaluminous	Haiyang massif[50]; Jiuhuashan[29]; Drammen batholith, Finnemarka batholith[51]; Xiangshan complex[52];	[50]**Li *et al.* (2014)**; [51]**Richard (2019)**; [52]**Yu *et al.* (2019)**; [53]**Quan *et al.* (2023)**; [54]**Yang *et al.* (2023)**; [55]Abdel-Karim *et al.* (2021)
Peraluminous	Western Carpathians[36]; Haiyang massif[47]; Jiuhuashan[29]; Drammen batholith, Finnemarka batholith[51]; Xiangshan complex[52]; Huanren pluton[53]; Huangmeijan[54]	
Peralkaline	Western Cape Suite[23]; Maladob ring complex[55]	

In this study, we use a global dataset of newly acquired and previously published apatite analyses from a worldwide variety of granites to 1) test the range of applicability and the limits of the existing discrimination diagrams and 2) develop new and improved discrimination diagrams to better identify apatite of I-, S- and A-type granites from a large, worldwide dataset of apatite compositions. The aim is to be able to use these diagrams for detrital apatite grains for provenance studies and mineral exploration. We chose to apply a petrogenetic (e.g., Dare *et al.* 2014; Kieffer *et al.* 2023) rather than a statistical approach (e.g., Mao *et al.* 2016; Deng *et al.* 2023; Tan *et al.* 2023) to explore our datasets, because 1) interpretation of trace element data is directly supported by the geological information of each sample (e.g., mineralogy); 2) all data is readily viewed on a single multielement diagram that allow to identify key elements or ratio, useful for discrimination; and 3) as shown in section 4.3, the dataset is heterogeneous in terms of number of samples per granite type (e.g., I-type is over-sampled compared to S-, and especially A-type), and of number of analysed trace elements (e.g., a few studies consider few other trace elements than REE+Y and Sr).

As detrital apatite can be of any origin, we first show that apatite from felsic rocks has a distinct composition from apatite originating from mafic intrusions or carbonatites. Then, we show that apatite signature from Archean (Tonalite-Trondhjemite-Granodiorite) and post-Archean granitoids (I-, S- and A-type granites) is systematically distinct at a global scale, and demonstrate that apatite from the 3 types of granites can also be identified. Thus, analysing a large suite of trace elements (REE+Y, Sr, As, Mn, V, Pb, Th, and U), and applying the proposed workflow, demonstrates a great potential to fingerprint the host rock of detrital apatite in unexplored, covered terrains.

4.2 Analytical methods

Major and volatile elements were determined in apatite from 24 samples of I-, S- and A-type granites, following the same analytical protocol described in Kieffer *et al.* (2023). Analyses were performed using a Cameca SX100 electron micro-analyser (EMPA) fitted with 5 WDS detectors (wavelength dispersive spectrometers) at the Laboratoire de Microanalyse (Université Laval, Canada). The analytical conditions recommended to limit the diffusion of volatiles (F, Cl) are a 15 kV acceleration voltage, a 10 nA beam current, and a defocused beam of 10 µm diameter. Repeated

analyses of a Durango apatite reference material ensured suitable detection limits, analytical accuracy and precision. F, Cl and OH mole fractions were calculated using the method of Piccoli and Candela (2002), and the correction described by Kieffer *et al.* (2023) when applicable. Detailed results are provided in Annexe 48 and displayed on Figure 4.1. For most samples, S is below detection limits. As analytical conditions are key to ensure the proper measurement of F and Cl (Stormer *et al.* 1993), only the analyses performed under analytical conditions close to the ones described above were compiled from the literature. This criterion of compilation aims to provide a basis for comparison of our newly acquired dataset with this from the literature.

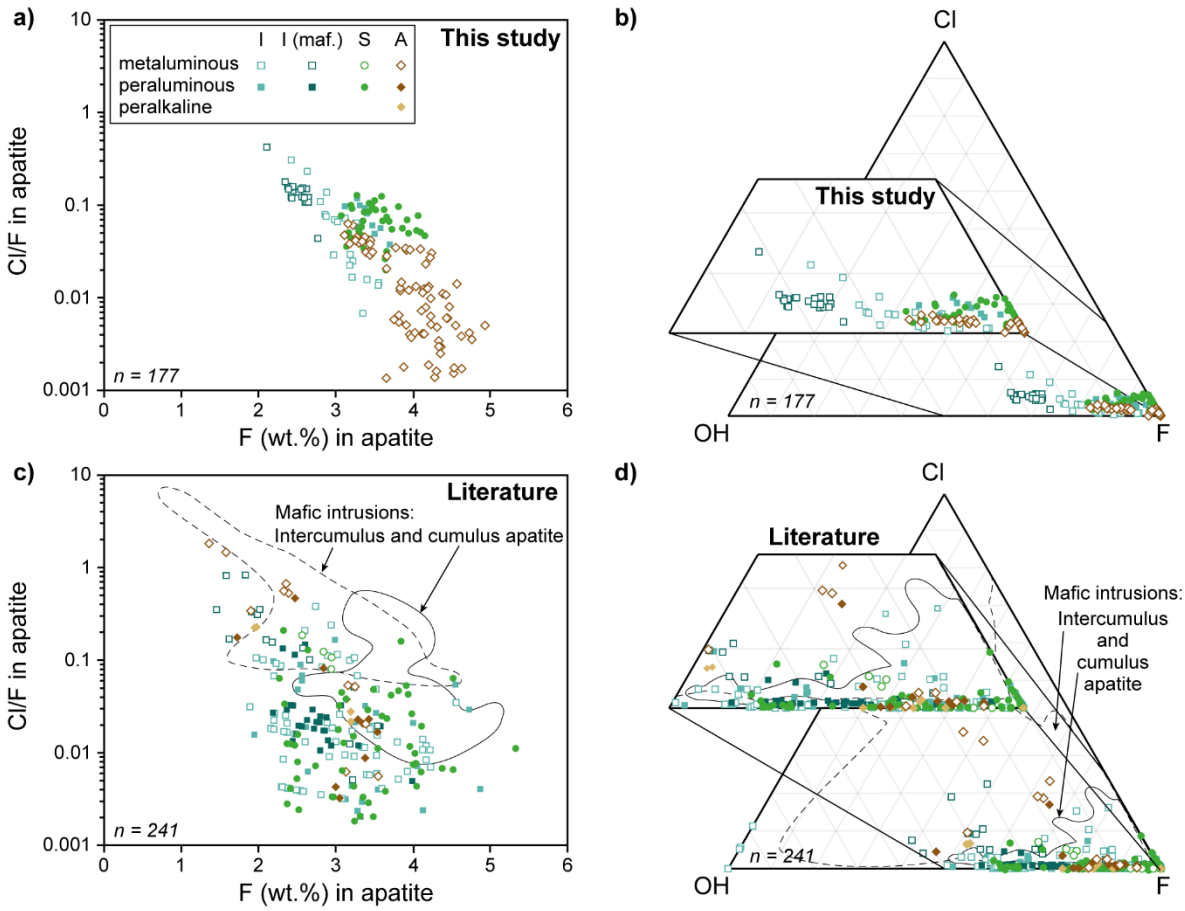

Figure 4.1 – Volatile content of apatite from various types of granites (from this study (a, b) and literature compilation (c, d)). Volatile contents are compared in the Cl/F vs. F (wt.%) binary diagram (a, c) and in the F-Cl-OH ternary space (b, d) in which the F, Cl and OH mole fractions in apatite were calculated following the approach of Piccoli and Candela (2002). The fields for intercumulus and cumulus apatite are drawn after Kieffer *et al.* (accepted) and references therein (c, d), with additional intercumulus apatite from and Boudreau *et al.* 1995 (d). *n* number of analyses

Trace elements were determined in apatite from 36 samples of I-, S- and A-type granites by laser ablation inductively coupled plasma mass spectrometer (LA-ICP-MS) following the analytical protocol of Kieffer *et al.* (2023). Sixteen of the 36 new samples were analysed by Gendron (2021) as part of an honour's thesis co-supervised by M. Kieffer and S. Dare. The system used at LabMaTer (University of Quebec in Chicoutimi, Canada) is a Resonetics Resolution M-50 193 nm Excimer laser coupled with an Agilent 7900 ICP-MS. Lines were ablated across apatite grains with a 15 to 55 µm beam, at an ablation rate of 15 Hz, a fluence of 5 J/cm^2, and a dwell time of 10 µm/s. The certified reference material NIST610 was used to perform calibration, whereas secondary reference materials NIST612, GSD, and in-house apatite UQAC-APA were used for monitoring data quality. The Ca content of apatite, as determined by EMPA, was used as the internal standard for the quantification of the LA-ICP-MS results. The Ca content of was set to 395000 ppm, which corresponds to the stoichiometric content of Ca in apatite, for the 12 samples that were not analysed by EMPA. Suitable detection limits, accuracy and precision were obtained by repeated analyses of reference materials. Data processing was performed using the Iolite 4 software (Paton *et al.* 2011). Detailed results are given in Annexe 49. The full suite of measured trace element concentration is presented on the multielement diagram specifically designed for apatite by Kieffer *et al.* (2023), on Figure 4.2, along with the LA-ICP-MS analyses compiled from the literature (compilation available in Annexe 50).

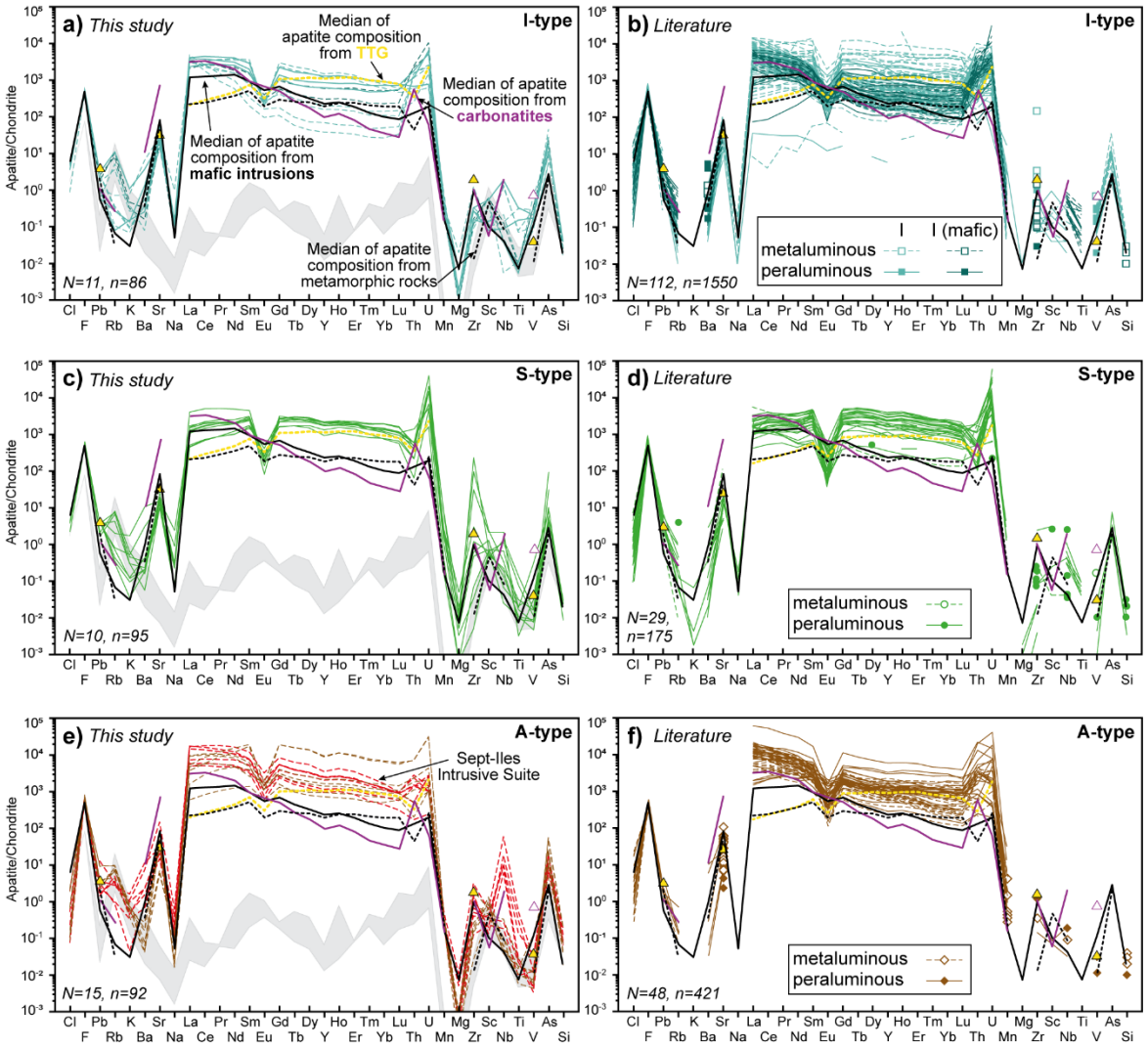

Figure 4.2 – Multielement diagrams of apatite from (a, b) I-type, (c, d) S-type, and (e, f) A-type granite (chondrite values for normalisation are from McDonough and Sun 1995), in which elements are ordered according to their expected compatibility into apatite (Kieffer *et al.* 2023). Data from this study is displayed in the diagrams of the left column (a, c, and e) and those compiled from the literature on the right column (b, d and f) to show that our new data is representative of each granite type. The grey field corresponds to lower limits of detection determined with a 15 µm beam (top line) and 55 µm beam (bottom line) on the apatite reference material (UQAC-APA). Cl, F and Si are determined by EMPA. Apatite from I-type granites are the most represented (b), whereas less studies have been conducted on apatite from A-type (f) and S-type (d) granites, and in which less trace elements have been analysed. *N* number of samples; *n* number of analyses. *TTG* Tonalite-Trondhjemite-Granodiorite. Composition of apatite from mafic intrusions is averaged from the references cited in Table 2 (N = 299; n = 2235). Composition of apatite from TTG is averaged (N = 10; n = 235) from Antoine *et al.* (2020) and Bruand *et al.* (2020). Composition of apatite from carbonatites is averaged (N = 128; n = 883) from: Belousova *et al.* (2002); Brassinnes *et al.* (2005); Chen and Simonetti (2013); Mao *et al.* (2016); Chakhmouradian *et al.* (2017); Deng *et al.* (2017); Doroshkevich *et al.* (2017); Wang *et al.* (2019). Composition of apatite from metamorphic rocks is averaged (N = 49; n = 587) from: Bea *et al.* (1994); Bea and Montero (1999); Nutman (2007); El Korh *et al.* (2009); Henrichs *et al.* (2018)

4.3 Sample and sources of apatite data

Apatite trace element data used in this study consists of newly acquired data (N = 37, n = 273; this study) and a compilation dataset (N = 190, n = 2146; compiled from 35 publications) originating from I-, S- and A-type granites from a wide range of geographical locations, as summarised in Table 4.1 and Table 4.2, respectively. The samples are classified by granite type (i.e., I-, S- and A-) and further subdivided according to its aluminium saturation index (i.e., metaluminous, peraluminous, or peralkaline). I-type granites that contain less than 70 wt.% SiO_2 are referred to as I-type mafic (Sha and Chappell 1999). Additional apatite data from mafic intrusions and carbonatites are also compiled from the literature in order to improve the discrimination of apatite from granites.

Most apatite data from this study comprise volatile as well as trace elements analysed on polished thin sections. However, data from the literature is more heterogeneous, as I-type granites are more commonly represented than S-type granite and A-type granites being particularly scarce (note that peralkaline A-type trace element data is non-existent). Additionally, most studies focused on volatile elements in apatite, and where trace elements are analysed by LA-ICP-MS, only a restricted number of them were considered (i.e., REE, Sr, Th, U; see Table 4.3 and Annexe 50) compared to the full suite of trace elements analysed in this study.

Table 4.3 – Frequency the trace elements analysed in apatite from I-, S- and A-type granites that is reported in the literature compiled in this study

	Frequency of each trace element that is reported (%)[1]															
	Pb	Rb	K	Ba	**Sr**	Na	**REE+Y**[2]	**Th**	**U**	**Mn**	Mg	Zr	Sc	Nb	Ti	**V**	**As**
Number of publications: 24	88	54	4	58	92	17	99	92	92	42	17	67	21	50	8	50	13
Total number of samples: 190	68	33	2	40	79	7	97	85	83	55	17	40	9	30	14	30	11
I-type granite samples (112)	79	37	0	42	77	8	97	94	94	53	25	47	9	33	18	44	15
S-type granite samples (30)	80	50	13	77	67	13	96	80	87	23	13	57	20	47	20	20	13
A-type granite (48)	38	13	0	13	94	0	99	69	54	81	0	13	4	13	0	4	0

[1]elements highlighted in bold are critical for discrimination, as presented in this study

[2]in 2 studies, Tb, Y, Ho or Tm are not analysed.

4.3.1 I-type granites

Apatite was analysed in 7 samples of metaluminous and 2 samples of peraluminous I-type granites (EMPA: n = 29; LA-ICP-MS: n = 69), in addition to 2 samples from metaluminous mafic I-type (Table 4.1; EMPA: n = 17; LA-ICP-MS: n = 17). Samples of metaluminous I-type granites originate from the Chataway subfacies of the Guichon Creek batholith (Canada; D'Angelo *et al.* 2017), the Tuolumne Intrusive Suite of the Sierra Nevada batholith (U.S.A.; Solgadi and Sawyer 2008), the Bega batholith of the Lachlan Fold Belt (Australia; Blevin and Chappell 1995), and the Illapel plutonic suite of the Coastal Batholith of central Chile (Parada *et al.* 1999; Higgins 2017). The two samples of metaluminous mafic I-type are tonalite originating from the Jindabyne suite of the Kosciusko batholith and from the Moruya batholith, both within the Lachlan Fold Belt (Australia; Griffin *et al.* 1978; Chappell and White 1992). The two I-type samples from the Vredenburg Pluton within the Western Cape Suite (South Africa) are peraluminous granite (Scheepers 1995).

Apatite from I-type granites have drawn considerable attention recently, given their association with porphyry mineral deposits (e.g., Bouzari *et al.* 2018; Qian *et al.* 2019; Gao *et al.* 2020; Xing *et al.* 2020). Thus, a large amount of apatite data is available in the literature, both from EMPA (N = 113, n = 1448) and LA-ICP-MS (N = 89, n = 1355) analyses, compared to apatite from S- and A-type granites (Table 4.2, and references therein). Literature data covers apatite compositions from metaluminous and peraluminous I-type granites from a wide range of arc localities, such as the USA, Australia, South Africa, Canada, and China. In addition, 3 studies report apatite compositions from metaluminous and peraluminous mafic I-type granites (EMPA: N = 49, n = 958; LA-ICP-MS: N = 23, n = 195) from China and Poland (Table 4.2).

4.3.2 S-type granites

Apatite was analysed in a total of 10 samples of peraluminous S-type granites (EMPA: n = 37; LA-ICP-MS: n = 95), originating from Australia (Wulumna pluton and Lachlan Fold Belt), South Africa (Western Cape Suite), and the French Massif Central (Table 4.1). The Wulumna granite corresponds to a heterogeneous pluton that emplaced within its metasedimentary source rocks (Lavaure and Sawyer 2011). The Dalgety and Jillamatong granodiorites are part of the larger Berridale and Kosciusko batholiths (Chappell 1984; Hine *et al.* 1978) within the Lachlan Fold Belt. The Peninsula

pluton is the southernmost of the 4 major S-type plutons of the Cape Granite Suite, which shows a compositional variation from leucogranite to granodiorite (Stevens *et al.* 2007; Villaros *et al.* 2009; Farina *et al.* 2012). The samples from the French Massif Central (Table 4.1) correspond to peraluminous leucogranites (Bougès and Laubies granite) and strongly porphyritic peraluminous granite (Margeride granite; Moyen *et al.* 2017; Antonelli *et al.* 2023).

Apatite from S-type granites has been much less studied than apatite from I-type granites in the literature. Most available data concerns peraluminous S-type granites (EMPA: N = 60, n = 1070; LA-ICP-MS: N = 29; n = 152) from South Africa, Europe, China, and Canada (see Table 2 and references therein), but Birski *et al.* (2019) and Chu *et al.* (2009) also report some apatite composition from metaluminous S-type granites (EMPA: N = 13, n = 61; LA-ICP-MS: N = 1; n = 23). However, even fewer studies report trace element content of apatite from S-type granites. For example, although close to 1000 analyses of volatile elements were performed on apatite from 73 samples, only 175 analyses of trace elements from 30 samples by LA-ICP-MS were found in the literature (Table 4.2).

4.3.3 A-type granites

Apatite was analysed in 15 samples of metaluminous A-type granite (EMPA: n = 89; LA-ICP-MS: n = 67). Seven granite samples originate from 4 plutons of the Saguenay–Lac-St-Jean region (Quebec, Canada; Table 4.1; EMPA: n = 69; LA-ICP-MS: n = 65), that are associated with the anorthosite-mangerite-charnockite-granite (AMCG) magmatism in the Central Grenville Province (Higgins and van Breemen 1996). The mafic component of AMCG suites is mostly thought to originate from a mantle-derived melt, with variable contamination with continental crust, that were underplated at the bottom of the crust from which crystal mushes of plagioclases were emplaced into the mid-crust to form anorthosite massifs (Emslie *et al.* 1994; Ashwal and Bybee 2017). The contemporaneous felsic components (mangerite-charnockite-granite: MCG) are considered to have formed from melting of the lower predominantly mafic crust due to the underplating of hot mafic magma (Emslie *et al.* 1994; Ashwal and Bybee 2017). In some cases, extreme fractional crystallisation of these mafic melts could also have formed the MCG suites (Zhang *et al.* 2007).

Another 8 granite samples originate from the Upper Series and Pointe du Criard Sill of the Sept-Iles Intrusive Suite (Quebec, Canada; Table 4.1). These granitoids represent the felsic end of the

extreme fractional crystallisation of a ferrobasaltic melt, from which previously crystallised 4.8 to 5.2 km of mafic cumulates (Namur *et al.* 2011). Although apatite from these samples were investigated by Kieffer *et al.* (2023), to trace fractional crystallisation, they are classified as 'new data' as they were analysed under the same analytical protocol by the same author (EMPA: n = 20; LA-ICP-MS: n = 27). Additional data for metaluminous and peraluminous A-type granites was compiled from published articles (Table 4.2; EMPA: N = 22, n = 259; LA-ICP-MS: N = 45, n = 409). Samples mostly originate from China (Haiyang massif, Jiuhuashan, Xiangshan complex, Huangmeijan), but also from Norway, South Africa and Egypt (see Table 2 and references therein). Peralkaline A-type granites are scarce and have not drawn any particular interest so far, explaining why few analyses of apatite are available in the literature (Table 4.2; EMPA: N = 10, n = 43). This, combined with the lack of trace elements in the published analyses, explains why apatite from peralkaline A-type granites are not displayed on the diagrams using trace elements that will be presented further.

4.3.4 Compilation of apatite data from mafic intrusions, carbonatites, and Archean TTG

Trace element data for apatite from mafic intrusions (layered intrusions in large igneous provinces and AMCG suites) and carbonatite were also compiled from the literature in order to try to distinguish apatite from felsic intrusions from the other intrusions. Indeed, as apatite can originate from a wide range of rocks, it is necessary to ensure that the apatite host rock is felsic prior to further classification into I-, S- or A-type granites. For this reason, although both apatite crystallising as a cumulus phase and from the interstitial liquid (i.e., intercumulus apatite) were compiled in mafic layered intrusions and AMCG suites, they will further be referred to as 'apatite from mafic intrusions'. However, Kieffer *et al.* (2023; accepted) proposed discrimination diagrams to separate apatite from mafic intrusions into cumulus and intercumulus apatite.

Apatite trace element data from a total of 163 samples originate from mafic layered intrusions in large igneous provinces (Table 4.2), such as the Bushveld Complex (South Africa), Sept-Iles Intrusive Suite (Quebec, Canada), Skaergaard (Greenland), Hongge, Panzhihua and Bijigou intrusions in China (LA-ICP-MS: n = 1301, compiled from 9 publications), and from AMCG suites in Norway, Canada, Ukraine and China (N = 144, n = 1044, compiled from 11 publications). Trace element

composition of apatite from carbonatites in Russia, China and Canada was compiled from 128 samples (n = 883) from 8 publications. Trace element composition of apatite from Archean granitoids (Tonalite-Trondhjemite-Granodiorite suites; TTG) in Canada and Russia was compiled from 2 publications (N = 10; n = 235).

4.4 Apatite chemistry

4.4.1 Minor differences in volatile composition of apatite

Apatite from all types of granites, from both this study and the literature, is fluorapatite, with a F concentration comprising between 2 and 5 wt.% and Cl concentration lower than 1 wt.% (Figure 4.1; detailed results for new analyses are provided in Annexe 48). There is only minor variation in F content and Cl/F ratio in apatite from I-, S- and A-type granites. Our new apatite from A-type granite data have a slightly higher F content and lower F/Cl ratio than apatite from I- and S-types (Figure 4.1a). At the same F content (between 3 and 4 wt.%), apatite from S-type granite have a higher Cl/F ratio than apatite from I-type granite (Figure 4.1a). The 3 types of granites can also be roughly separated in the F-Cl-OH ternary space (Figure 4.1b). All apatite composition is clustered close to the F endmember, with apatite from S-type granites having higher mole fractions of Cl than this from I- and A-type granites. On the other hand, apatite from I-type granites has lower F and higher OH and Cl mole fractions than apatite from S-type granites (Figure 4.1b).

Although the distinction between apatite from I-, S- and A-type granites is subtle using our new EMPA data, the difference between the 3 groups is not as marked considering EMPA analyses from the literature (Figure 4.1c, 4.1d). This scattering of data may be caused by a possible volatile diffusion during EMPA analyses (Stormer *et al.* 1993). Although we carefully compiled analyses performed under analytical conditions similar to the ones performed in this study, small differences in protocol, and from one study to the other, might explain why the literature dataset is less consistent than the one we acquired for this study. In addition, the volatile content of apatite from felsic intrusions is similar to that of apatite (both intercumulus and cumulus) from mafic intrusions (Figure 4.1c, 4.1d). Thus, the datasets displayed on Figure 4.1 shows that volatile concentrations in apatite cannot readily

discriminate apatite from I-, S- and A-type granite nor to distinguish apatite crystallising from felsic and mafic melts.

4.4.2 Distinctive apatite trace element concentrations

The dataset of new analyses of apatite from the 3 groups of granites, displayed in the multielement diagram (Figure 4.2), is representative of the 3 groups of granites in general. This is because their patterns are similar to those of the larger dataset from the literature, although the availability of trace element other than REE, Sr, Pb, Th and U is scarcer in the literature. The multielement diagram allows us to review the full suite of data available for apatite from I-, S- and A-type granites. It shows that apatite from the 3 types of granites have contrasting features and highlights which elements vary the most, which will later help to define the most efficient discriminating ratios.

Although there are no 'key' elements that allow to separate apatite from the 3 types of granite directly, a combination of different features is applied, as 2 types of granites often share similar characteristics. For instance, apatite from S-type granite is enriched in Mn and in U (i.e., strongly positive slope between Th and U) with respect to apatite from I- and A-type granites, but there is more V in apatite from I- than A-type granite. In addition, the LREE slope of apatite from I-type granite is generally negative (i.e., enriched in LREE; Figure 4.2a, 4.2b) whereas it is mostly flat to slightly positive for apatite from A- and S-type granite (i.e., depleted in LREE; Figure 4.2c to 4.2f). Lastly, apatite from A-type granites is more enriched in LREE but contains less Na and As than apatite from S-type granites. Thus, visualising the full datasets on the multielement diagram reveals ratios that have the potential to discriminate apatite from the 3 types of granites. These ratios illustrate the LREE enrichment (e.g., La/Sm, La/Nd, or Sm/Nd), or combine elements that are enriched in apatite from one type of granite relative to the other (e.g., Th/U or Mn/Th).

All apatite from I-, S- and A-type granites are post-Archean and have a different composition to that of Archean apatite from tonalite-trondhjemite-granodiorite (TTG) suites (Figure 4.2). Apatite from TTG is LREE-depleted but enriched in HREE compared to post-Archean apatite. The median of the composition of apatite from mafic intrusions (see references provided in Table 4.2) is also plotted in Figure 4.2 and shows key differences compared to apatite in I-, S- and A-type granites (Figure 4.2). As a whole, apatite crystallising from all types of felsic melts is enriched in REE and other incompatible

elements (i.e., Rb, K, Na, Pb, Th, U and As), depleted in Sr, and shows a stronger negative Eu anomaly with respect to apatite crystallising from mafic melts (Figure 4.2). Apatite from I-type granite contains more V than apatite from the mafic intrusions (Figure 4.2a, 4.2b), but apatite from S- and A-type granites contain less V than this of mafic intrusions (Figure 4.2c to 4.2f). Although the slope of the LREE patterns is generally similar between apatite from mafic and felsic rocks, with exception of apatite from S-type granites, the HREE slope of apatite from mafic intrusions is steeper than that of apatite from I- and S-type granites. The REE pattern of apatite from mafic intrusions and A-type granites from Sept-Iles Intrusive Suite have the same shape, but with the latter being 10 times enriched in REE (Figure 4.2e). Apatite from carbonatites have a strongly fractionated REE pattern that is distinct than that of apatite from all 3 granite types and from mafic intrusions, as well as systematically higher Sr content (Figure 4.2).

4.5 Discussion: apatite as a provenance indicator of intrusive rocks

This section proposes successive steps to classify apatite using its chemistry, starting from a database of apatite compositions from carbonatites and mafic and felsic intrusions, the latter ranging from Archean to post-Archean granites. The aim is to efficiently classify post-Archean granitoids into I-, S- and A-type granites. First, we propose a series of diagrams to identify apatite from felsic intrusions from apatite from other intrusions (mafic and carbonatites). Then, using an existing discrimination diagram, we show that apatite from felsic rocks can further be screened into apatite from Archean and post-Archean granites. We test and improve existing discrimination diagrams to separate the post-Archean dataset into apatite originating from I-, S- and A-type granite. In a final step, we finally propose new discrimination diagrams based on the best-working elements, identified on the existing discrimination diagrams and the multielement diagrams (Figure 4.2), that include new trace elements that are not commonly analysed in the literature.

4.5.1 How to identify apatite from felsic intrusions from other sources?

Apatite from bedrock and detrital grains can be of various origins (Belousova *et al.* 2002; Mao *et al.* 2016; O'Sullivan *et al.* 2020). Thus, before attempting the classification of apatite from I-, S- and A-type granites, the first step is to ensure that this apatite has indeed crystallised from a felsic rather than a mafic, carbonatite or alkaline melts. The diagram proposed by O'Sullivan *et al.* (2020) proposes

to classify apatite, based on its Sr/Y ratio and LREE (sum of La to Nd, in ppm) content, from a variety of sources: alkali-rich igneous rocks, mafic igneous rocks, S-type granitoids, mafic and felsic I-type granitoids, metamorphic rocks, and ultramafic rocks including carbonatites, lherzolites and pyroxenites (Figure 4.3). The majority of our dataset of apatite from mafic intrusions plots well in the mafic I-type / mafic igneous rocks field (IM), with only a few samples plotting in the metamorphic field (HM, LM; Figure 4.3a). However, according to the literature, our compilation of apatite from mafic samples did not undergo metamorphism nor hydrothermal alteration. In addition, all analyses of apatite from carbonatites compiled from the literature plot correctly in the field of carbonatites (Figure 4.3a), with the exception of 3 outliers, demonstrating the robustness of O'Sullivan *et al.* (2020) diagram. In contrast, more than a half of apatite from our felsic dataset, both new and compiled, is misclassified (Figure 4.3b). Half of the dataset for both apatite from I-type and S-type granite plot in the high-grade metamorphic field (HM), whereas the other half plots correctly in its corresponding field (IM and S, respectively). Finally, as the diagram does not include a field for apatite from A-type granite, the corresponding analyses (metaluminous A-type) are scattered between the mafic I-type granitoids and mafic igneous rocks (IM), high-grade metamorphic (HM), and S-type granitoids (S) fields (Figure 4.3b). The sample that plots in the 'ALK' field corresponds to a peraluminous A-type granitoid of the Drammen batholith (Richard 2019). At last, apatite from Archean granitoids (TTG suites) plot all in the field of low- to medium-grade metamorphic rocks (Figure 4.3b). Although the compiled TTG samples correspond to orthogneisses (Antoine *et al.* 2020) and metamorphosed TTG (Bruand *et al.* 2020), according to the authors the apatite is magmatic, rather than metamorphic, in origin. Plus, apatite from TTG has a signature distinct from this of apatite from metamorphic rocks (Figure 4.2), the latter being depleted in REE and showing a flat REE pattern with only a slight LREE enrichment.

Therefore, the O'Sullivan *et al.* (2020) diagram is a good first approximation to distinguish the majority of apatite from mafic and felsic intrusions from the other rocks, but the discrimination between apatite from mafic and felsic intrusions, as well as within the felsic intrusions, could be improved (Figure 4.3). There is indeed an overlap between the fields of apatite from mafic and felsic intrusions, that is also observed within the widely used discrimination diagrams of Belousova *et al.* (2002) (Figure

4.4). However, clear differences between apatite from mafic and felsic intrusions are observed on the multielement diagrams (Figure 4.2), but some key elements (e.g., As, Pb, Th, U) or REE ratios (e.g., $(Gd/Yb)_N$) are not used in O'Sullivan *et al.* (2020) and Belousova *et al.* (2002) diagrams.

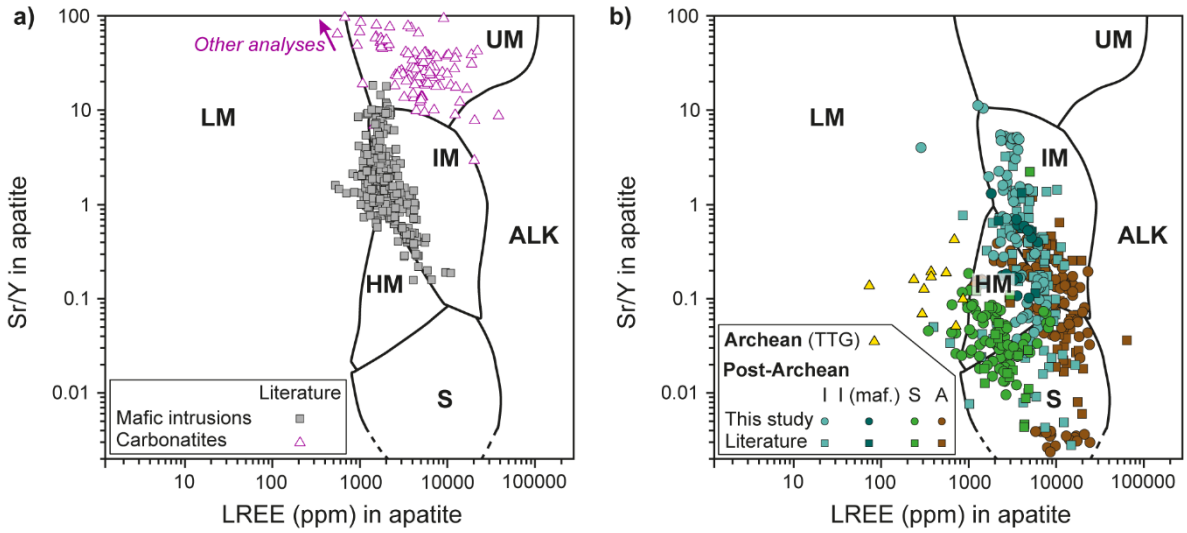

Figure 4.3 – Datasets of apatite from (a) mafic rocks and carbonatites and (b) felsic rocks (I-, S- and A-type granites) plotted in the discrimination diagram developed by O'Sullivan *et al.* (2020). ∑LREE corresponds to the sum of LREE from La to Nd. *TTG* Tonalite-Trondhjemite-Granodiorite; *ALK* alkali-rich igneous rocks; *IM* mafic I-type granitoids and mafic igneous rocks; *LM* low- and medium-grade metamorphic and metasomatic; *HM* partial-melts/leucosomes/high-grade metamorphic; *S* S-type granitoids and high aluminium saturation index (ASI) 'felsic' I-types; *UM* ultramafic rocks including carbonatites, lherzolites and pyroxenites. Composition of apatite from carbonatites is compiled from: Belousova *et al.* (2002); Brassinnes *et al.* (2005); Chen and Simonetti (2013); Mao *et al.* (2016); Chakhmouradian *et al.* (2017); Deng *et al.* (2017); Doroshkevich *et al.* (2017); Wang *et al.* (2019). Source of analyses of apatite from mafic and felsic intrusions are provided in Table 2.

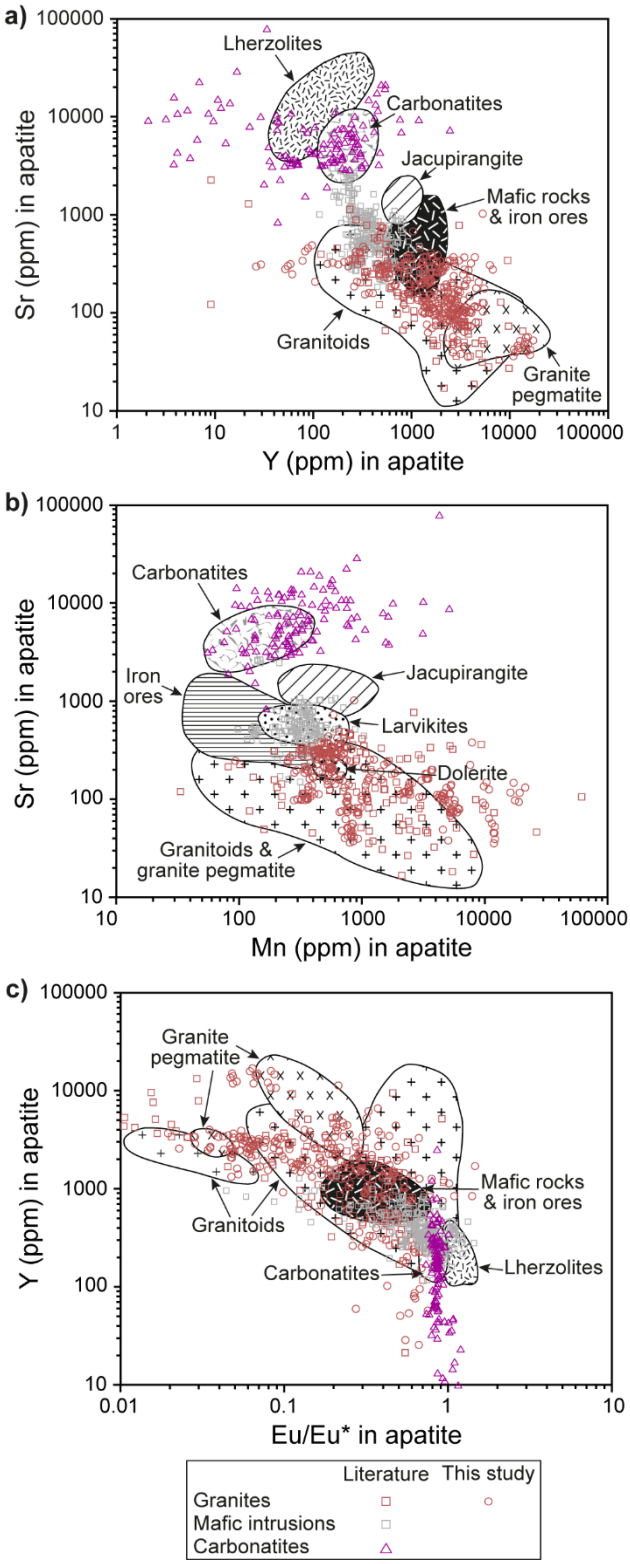

Figure 4.4 – Apatite from felsic intrusions (this study and the literature) and from mafic intrusions and carbonatites (literature) displayed in the (a) Sr vs. Y, (b) Sr vs. Mn, and (c) Y vs. Eu/Eu* discrimination diagrams of Belousova et al. (2002). Apatite from felsic intrusions is plotted regardless of its origin (I-, S- or A-type), are there is no distinction between granite types on the diagrams.

Recently, Kieffer *et al.* (2023) proposed a ternary diagram of (∑REE+Y)/10000, Sr/Y and Eu anomaly (Figure 4.5) to discriminate apatite crystallising from mafic and felsic melts, based on co-genetic mafic and felsic rocks of the Sept-Iles Intrusive Suite. This diagram efficiently identifies apatite crystallising from mafic melts, as all apatite from mafic intrusions compiled from the literature from layered intrusions and anorthosite suites plot in the corresponding mafic field, without exception (Figure 4.5a). This is due to relatively high Sr/Y ratios and low Eu negative anomaly compared to apatite from felsic rocks, that have lower Sr/Y rations a more pronounced negative Eu anomaly due to extensive crystallisation of plagioclase (Kieffer *et al.* 2023; accepted). In addition, when displayed in the ternary space, apatite from carbonatites defines a new field that is distinct from the mafic one (Figure 4.5a), and in which no apatite from felsic intrusions plots (Figure 4.5b, 4.5c). However, although most apatite from Archean TTG plot in the felsic field, this ternary diagram is less efficient to classify correctly apatite from post-Archean felsic intrusions (Figure 4.5b, 4.5c). Considering the new data from this study, all apatite from S- and A-type granites, except 2 analyses, are correctly classified as felsic in origin, but 63% of apatite from I-type granites plot in the mafic field (Figure 4.5b). Similarly, all apatite from S-type granites from the literature dataset are in the felsic field, and most apatite from A-type granites are also well classified (Figure 4.5c). Again, apatite from I-type granite from the literature compilation is scattered in both the felsic (70% of the data) and mafic field (30%; Figure 4.5c). The high Sr/Y ratios and small Eu anomaly of those apatite from I-type granite plotting in the mafic field might relate to the hydrous nature of arc melts. A high water pressure suppresses plagioclase but facilitates amphibole crystallisation, leading to a Sr enrichment and Y depletion of the melt, respectively, that is characteristic of fertile arc magmas (Rohrlach and Loucks 2005). This fertile signature is also identified in apatite, along with a slightly negative Eu anomaly, attributed to the suppression of plagioclase crystallisation (Nathwani *et al.* 2020; Zhou *et al.* 2022). Thus, we propose a series of additional diagrams to help separate apatite from felsic intrusions that were wrongly classified in the mafic field, from apatite that originated from mafic intrusions (Figure 4.6), using trace elements that are not affected by plagioclase suppression. Several alternatives using different trace elements are proposed, because these diagrams use trace elements that are not systematically analysed in the available literature.

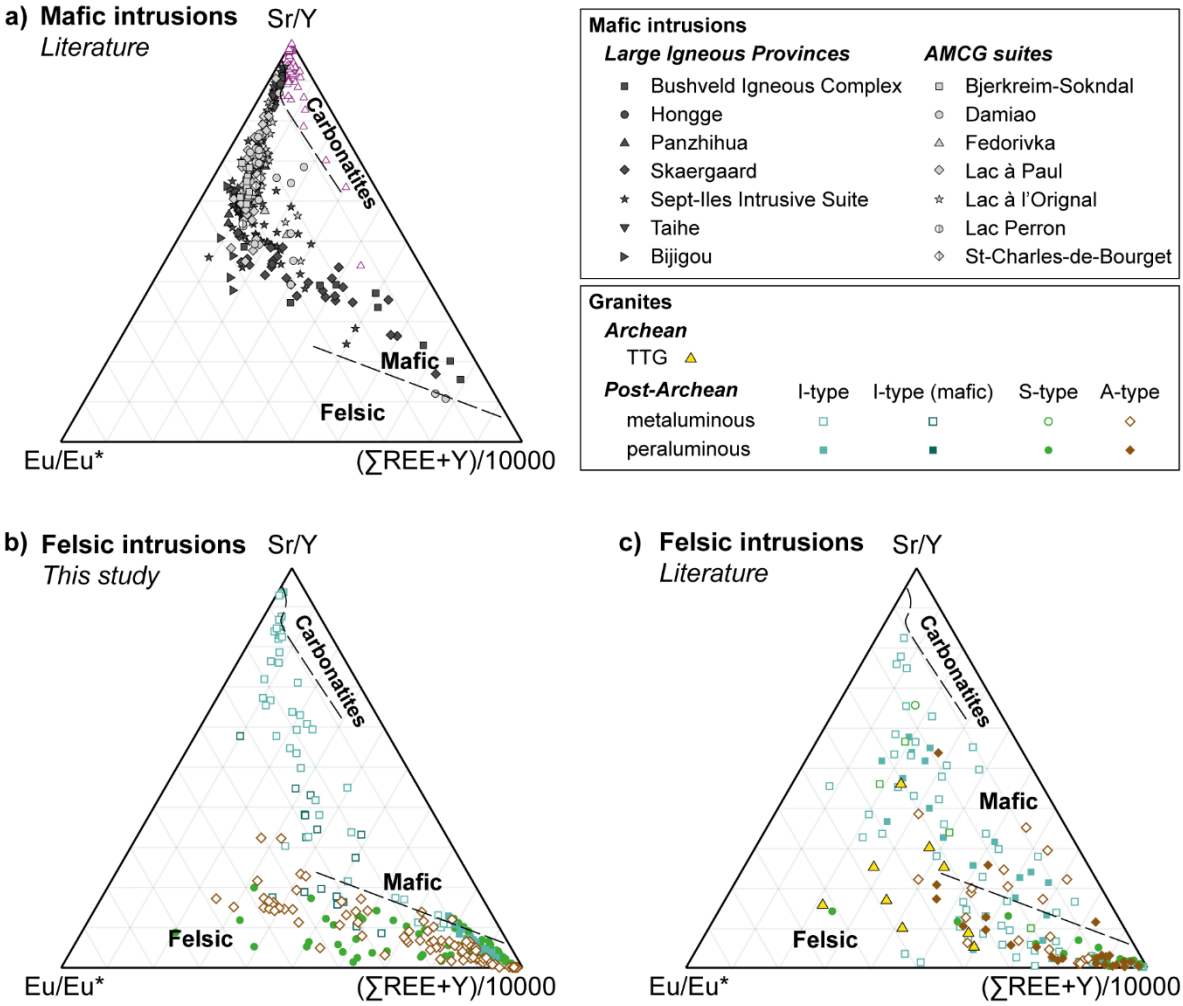

Figure 4.5 – Datasets of apatite from mafic intrusions (a) and felsic intrusions (I-, S- and A-type granites) acquired in this study (b) and compiled from the literature (c), displayed in the ternary discrimination diagram developed by Kieffer et al. (2023) to separate apatite crystallising from a mafic and a felsic melt. Addition of apatite data from carbonatites (see source of data in caption of Figure 4.3) allows to define a new, specific field, distinct from the mafic and felsic fields.

The first binary diagram uses Mn and the sum of Pb, Th and U (Figure 4.6a). Most apatite from felsic intrusions has higher concentrations in Mn, Pb, Th and U than this from mafic intrusions, although there is an overlap between the felsic and mafic fields at intermediate Mn, Pb, Th and U concentrations. As Mn is dependent on melt composition, especially the degree of polymerisation, i.e., its SiO_2 content (Chu *et al.* 2009; Stokes *et al.* 2019), higher Mn concentrations are expected in apatite crystallising from more evolved, felsic melt, compared to that crystallising from mafic melts. This has been shown in the Sept-Iles Intrusive Suite, where the liquid line of descent shows that Mn

decreases with fractional crystallisation from mafic to felsic melts, but the Mn content of apatite is higher in apatite from the felsic rocks than that from the mafic rocks (Kieffer *et al.* 2023). In addition, Pb, Th, U and As behave incompatibly during differentiation and should also be enriched in apatite crystallising from felsic melts (Kieffer *et al.* 2023). Apatite from mafic and felsic intrusions also display distinct HREE slopes on the multielement diagrams (Figure 4.2), which can be quantified by $(Gd/Yb)_N$ ratios. Therefore a binary diagram of As and $(Gd/Yb)_N$ ratio can also separate most apatite from felsic and mafic intrusions, with very little overlap (Figure 4.6b) compared to the previous diagram (Figure 4.6a), with apatite from felsic intrusions having higher As content and lower $(Gd/Yb)_N$ ratio than this from mafic intrusions. The most efficient diagram is thus a ternary using a combination of As, $(Gd/Yb)_N$ and the sum of Pb, Th and U (Figure 4.6c). Here, apatite from the felsic intrusions plots close to the Pb+Th+U endmember, with a trail towards the As endmember, whereas apatite from the mafic intrusions is scattered towards the $(Gd/Yb)_N$ pole. A final binary diagram illustrates the behaviour of As and Mg in apatite, that behave incompatibly and compatibly, respectively, during differentiation (Figure 4.6d). Although these elements can isolate the misclassified apatite from felsic intrusions from those from mafic intrusions, almost half of the well classified apatite from felsic intrusions plot in the mafic part. Thus, this diagram is not robust enough to be used.

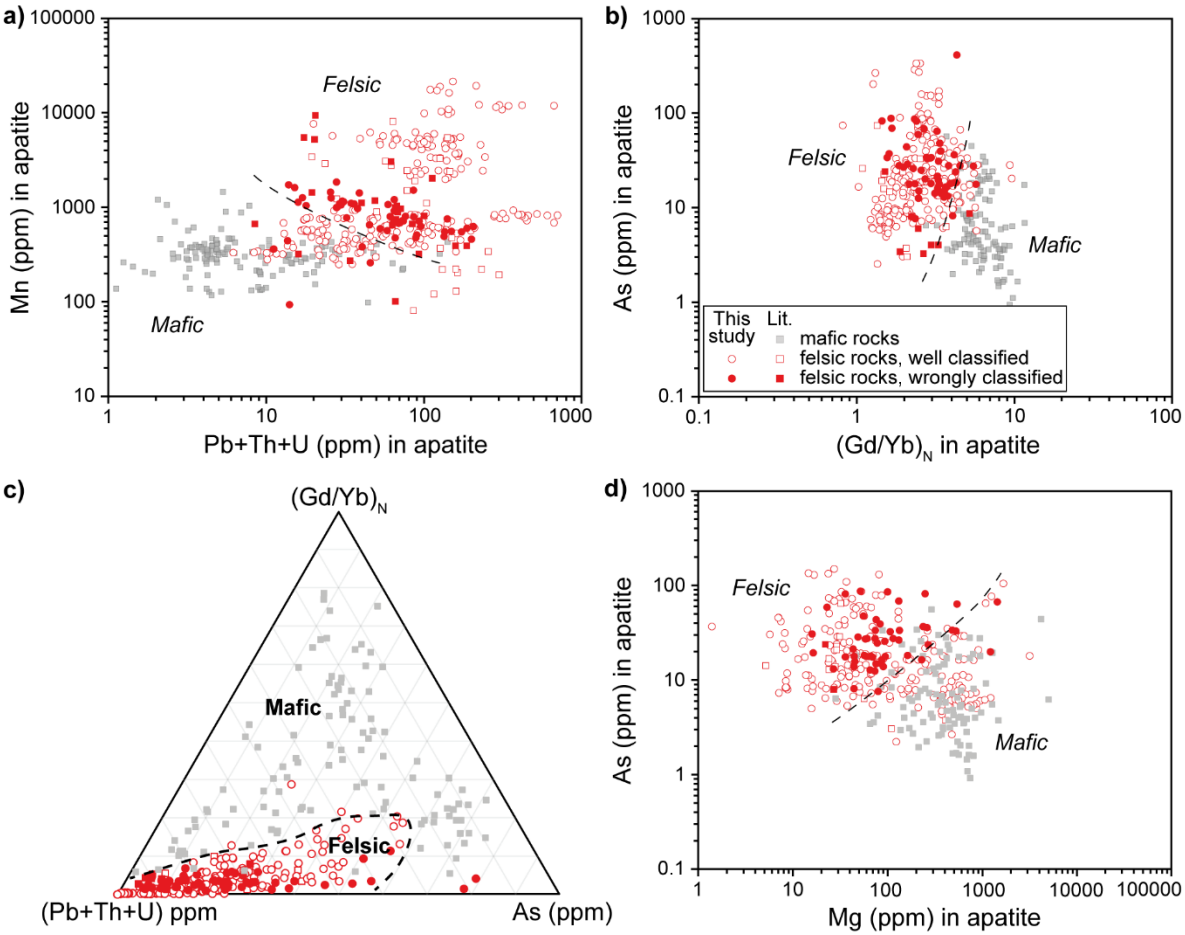

Figure 4.6 – Proposed discrimination diagrams to separate apatite from felsic and mafic intrusions, using (a) Mn vs. Pb+Th+U; (b) As vs. the HREE ratio $(Gd/Yb)_N$; (c) As, $(Gd/Yb)_N$ and Pb+Th+U; and (d) As vs. Mg. In (a), (b) and (d), the dashed line separates apatite from felsic intrusions (mainly I-type) that were wrongly classified as mafic from 'real' mafic. In (c), the dashed line isolates all analyses of apatite from felsic rocks from those of mafic rocks.

4.5.2 Apatite in felsic intrusions: Archean and post-Archean apatite have different compositions

There is a clear compositional change in whole rock composition between Archean and Proterozoic granitic rocks (Hansen *et al.* 2002; Moyen and Martin 2012). Proterozoic granitic rocks are enriched in K_2O, MREE and HREE, with only a slight LREE enrichment (i.e., high Yb_N and low $(La/Yb)_N$), have a low Sr/Y ratio, and display a negative Eu anomaly, compared to Archean TTG (Moyen *et al.* 2012). This difference is also recorded in apatite chemistry, which led to the definition of discrimination diagrams by Antoine *et al.* (2020) and Bruand *et al.* (2020) (Figure 4.7). The diagram using $\log(La/Yb)_N$ as a function of Yb_N in apatite (Figure 4.7a, 4.7c) clearly separates apatite from

Archean and post-Archean granites (Antoine *et al.* 2020). Apatite from the datasets of post-Archean felsic intrusions produced in this study (Figure 4.7a) and compiled from the literature (Figure 4.7c) is also correctly classified as post-Archean on their diagram. The same diagram also allows to classify apatite that originated from metaluminous or peraluminous post-Archean granitoids. Regarding the dataset from this study (Figure 4.7a), apatite from peraluminous S-type granite plots in the corresponding field. Similarly, all analyses of apatite from metaluminous I-type granite are in the 'metaluminous granitoids' field. However, apatite from peraluminous I-type granite is misclassified as metaluminous granitoids by this diagram. Finally, although some apatite from metaluminous A-type granite plot in the 'metaluminous' field, most analyses are shifted to the right of this field due to higher Yb_N ratios (Figure 4.7a). The same results, although more scattered, are observed with the literature dataset (Figure 4.7c).

The ternary diagram developed by Bruand *et al.* (2020) also succeeds to separate apatite from Archean and post-Archean granitoids from this study (Figure 4.7b) and the literature (Figure 4.7d) datasets, using Y, the sum of LREE (defined as La to Gd) and Sr in apatite. In this diagram, the fields are also defined to classify post-Archean apatite into I-type and S-type to peraluminous granitoids. All apatite from peraluminous S-type granites from this study and the literature plot in its dedicated field (Figure 4.7b, Figure 4.7d). Apatite from I-type granite is evenly spread within the I-type and the S-type/peraluminous granite fields, irrespective of its actual aluminium saturation index (i.e., metaluminous or peraluminous; Figure 4.7b, 4.7d). Analyses of apatite from peraluminous and metaluminous A-type granites are scattered within the I- and S-type fields, along the 10Y-∑LREE side of the ternary diagram, as no specific field was defined for this category of apatite (Figure 4.7b, 4.7d).

Thus, the discrimination diagrams defined by Antoine *et al.* (2020) and Bruand *et al.* (2020) prove to be highly effective to categorise felsic apatite into Archean or post-Archean granitoids. However, our comprehensive dataset of apatite from I-, S- and A-type granites demonstrates that the combination of trace elements used in these existing diagrams are not sufficient to further discriminate apatite from these 3 categories of granites accurately. Other diagrams, specific to the classification of apatite into I-, S- and A-type, will thus be discussed in the following section.

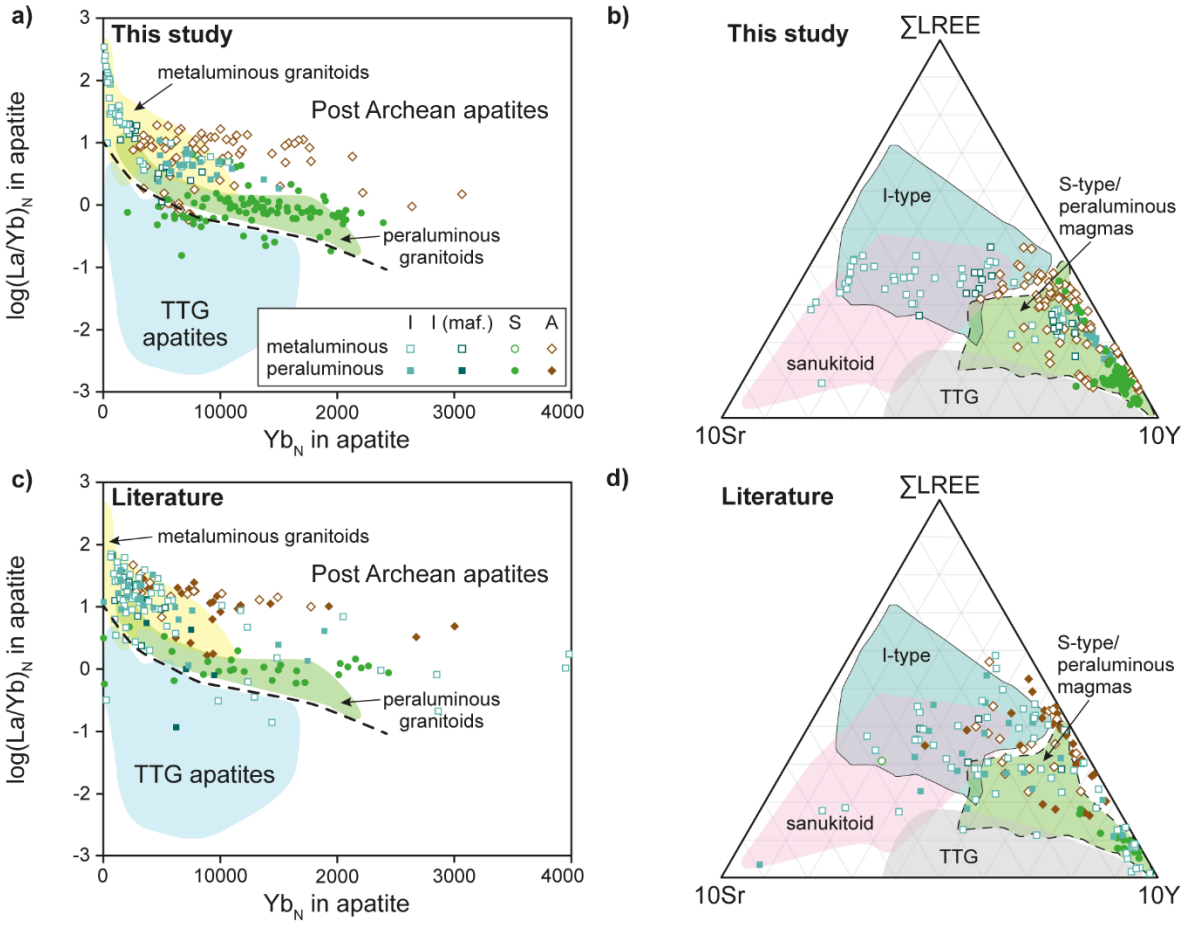

Figure 4.7 – Datasets of apatite from post-Archean felsic rocks from this study (a-b), and the literature (c-d) displayed in the Archean (TTG) vs. post-Archean apatite discrimination diagrams developed by Antoine et al. (2020) in (a) and (c) and by Bruand et al. (2020) in (b) and (d). In (b) and (d), ∑LREE corresponds to the sum of LREE from La to Gd. TTG Tonalite-Trondhjemite-Granodiorite.

4.5.3 Identifying apatite from I-, S- and A-type granites using their distinct chemical signature

The methodology presented in the following part of the discussion can be achieved only if the previous steps described in sections 4.5.1 and 4.5.2 have been resolved successfully using the appropriate diagrams: (1) to ensure that the analysed apatite originate from a felsic source rock (see section 4.5.1 and Figure 4.3, 4.5 and 4.6); and (2) confirm that the felsic apatite originated from a post-Archean granitoid (see section 4.5.2 and Figure 4.7).

The multielement diagrams show that apatite from the 3 types of granites have distinctive signatures (Figure 4.2). The different REE abundance and ratios in apatite from I-, S- and A-type

granite may be explained by the timing of saturation of the melt in apatite relative to the crystallisation of other REE-bearing accessory minerals (Richard 2019). Indeed, in I-type magmas, the higher proportion of Ca in the melt causes apatite to crystallise earlier than that in S-type magmas, in which monazite crystallises before apatite (Chappell 1999; Sha and Chappell 1999). Thus, the suppression of monazite crystallisation in I-type melts may explain the relative LREE enrichment in apatite (Figure 4.2a, 4.2b). On the other hand, the presence of monazite in S-type granitic melts causes a LREE depletion in apatite from S-type granites (Sha and Chappell 1999; Figure 4.2c, 4.2d). The MREE and HREE depletions are more pronounced in apatite from I- than S-type granite (Figure 4.2a to 4.2d). This may be due to the crystallisation of titanite in I-type melts and its absence in S-type melts (Chappell et White 1992). Indeed, titanite has a strong preference to partition MREE over LREE and HREE from the melt (Smith *et al.* 2009; Padilla and Gualda 2016). Crystallisation of HREE-bearing minerals will in turn affect the HREE budget in apatite. Zircon and xenotime typically crystallise in S-type melts, whereas zircon and hornblende crystallise from I-type melts (Chappell and White 1974, 1992, 2001). However, hornblende crystallises in greater abundances in I-type granites (Chappell et White 1992; Clemens *et al.* 2011), which might cause a relative HREE depletion in apatite from I-type granite compared to those from S-type granite (Figure 4.2a to 4.2d). In addition, if the TiO_2 content of the melt is low, Ti can be incorporated into biotite rather than in titanite, and the REE would go into a separate accessory phase, such as allanite (Hine *et al.* 1978). This might in turn cause a LREE depletion in apatite, as is observed for some apatite from metaluminous I-type granite (Figure 4.2).

Similar to I-type granites, the presence of titanite, and of zircon and amphibole, in A-type granites (Bonin 2007) may also be responsible for the relative depletion in MREE and HREE, respectively (Figure 4.2e, 4.2f). However, LREE in apatite exhibit a different behavior between peraluminous and metaluminous A-type (Figure 4.2e, 4.2f). Apatite from metaluminous A-type granite (e.g., from Sept-Iles Intrusive Suite, Figure 4.2e, and all sample from the literature, Figure 4.2f) show no LREE depletion, which may be caused by the absence of other LREE-bearing minerals. On the other hand, some apatite from metaluminous A-type granites from our study (i.e., associated to AMCG suites) and apatite from peraluminous granite (see Table 4.2 for location of the samples) display a LREE

depletion that might have been caused by the crystallisation of a LREE-bearing phase, such as monazite.

This section aims to test and propose discrimination diagrams that efficiently classify apatite that originate from felsic intrusions into I-, S- and A-type granite. It is based on the key elements and ratios observed on the multielement diagrams, which are linked to the magma composition and accessory mineralogy. One may argue that this has already been proposed by some authors, and for the first time by Sha and Chappell (1999). We acknowledge the work that has previously been published and build on and improve it, using additional apatite data and importantly a full suite of trace elements. Thus, in our approach, we first review the existing discrimination diagrams designed for apatite from felsic intrusions. The majority of these diagrams was mostly conceived using apatite data from only 2 types of granites at a time (e.g., I- and S-types, Sha and Chappell 1999, Laurent *et al.* 2017; I- and A-types, Wang *et al.* 2018), and/or focus on a specific locality (e.g., Spicer 2001). Thus, for the first time this study uses a broader dataset including analyses of apatite from I-, S- and A-type granites from all around the world (Table 4.1, Table 4.2) in order to: (1) test the efficiency of the existing diagrams; (2) when possible, define fields for apatite from all 3 types of granites in existing diagrams; and (3) based on a combination of best-working discriminating trace elements identified from the multi-element diagram, propose new discrimination diagrams that effectively separate apatite from I-, S- and A-type granites.

4.5.3.1 Robustness of existing discrimination diagrams tested with a broader dataset

Several authors propose discrimination diagrams using trace elements in apatite to identify apatite from I-, S- or A-type granites (Sha and Chappell 1999; Spicer 2001; Zhu *et al.* 2004; Hsieh *et al.* 2008; Laurent *et al.* 2017; Wang et al. 2018; Richard et al. 2019). All of these diagrams were tested with our comprehensive datasets (both new and compiled), but this section will only discuss the most relevant diagrams.

The 2 apatite diagrams proposed by Laurent *et al.* (2017) indicate if the felsic magma was likely to be ‘mantle-derived’ or ‘crust-derived’, and thus formed I- or S-type granites, respectively (Figure 4.8a to 4.8d). Apatite from ‘crust-derived’, S-type granites, are enriched in Y and depleted in Ce compared to apatite from ‘mantle-derived’, I-type granites (Figure 4.8a). The datasets presented in

this study show similar features (Figure 4.2a to 4.2d), with the majority of apatite from I- and S-type granites plotting in the relevant fields defined by Laurent et al. (2017) (Figure 4.8a). The second diagram uses the Th/U and La/Sm ratios, with both of them being lower in apatite from S-type granites compared to those from I-type granite (Figure 4.8b). Again, our datasets fall in the corresponding fields, with an overlap at intermediate La/Sm values (Figure 4.8b). The lower Th/U and La/Sm ratios in apatite from S-type granites is due to a higher U content and a depletion in LREE, respectively (Figure 4.2a to 4.2d). When plotted in the 2 previous diagrams, apatite from A-type granite fall mostly into the 'mantle-derived', I-type granite field (Figure 4.8c, 4.8d), with a spread towards higher Y and Ce concentrations (Figure 4.8c) and lower (La/Sm) ratios (Figure 4.8d). Indeed, apatite from I- and A-type granites show roughly similar multielement patterns, with apatite from A-type being enriched overall in REE (Figure 4.2a, 4.2b, 4.2e, 4.2f). These shared characteristics might be inherited from the magma source, as the A-type granites studied in this contribution can be considered 'mantle-derived' (Eby 1990; Bonin 2007). For example, A-type granite from the Sept-Iles Intrusive Suite represent extreme differentiation of 'true' mantle-derived ferrobasaltic melt (Namur *et al.* 2011). However, A-type metaluminous granites associated with AMCG suites are considered to form by melting of lower crust (i.e., dominantly igneous) induced from underplating of hot basaltic magma, that forms the anorthosite massif, at the base of the crust (Emslie *et al.* 1994; Ashwal and Bybee 2017). Thus, the diagrams proposed by Laurent *et al.* (2017) can be applied to separate apatite from 'crust-derived' (i.e., S-type granite) from apatite from 'mantle-derived' origin (not only I-type, but also metaluminous and peraluminous A-type granites). Therefore, discrimination needs to be improved to separate the 3 granite types using apatite.

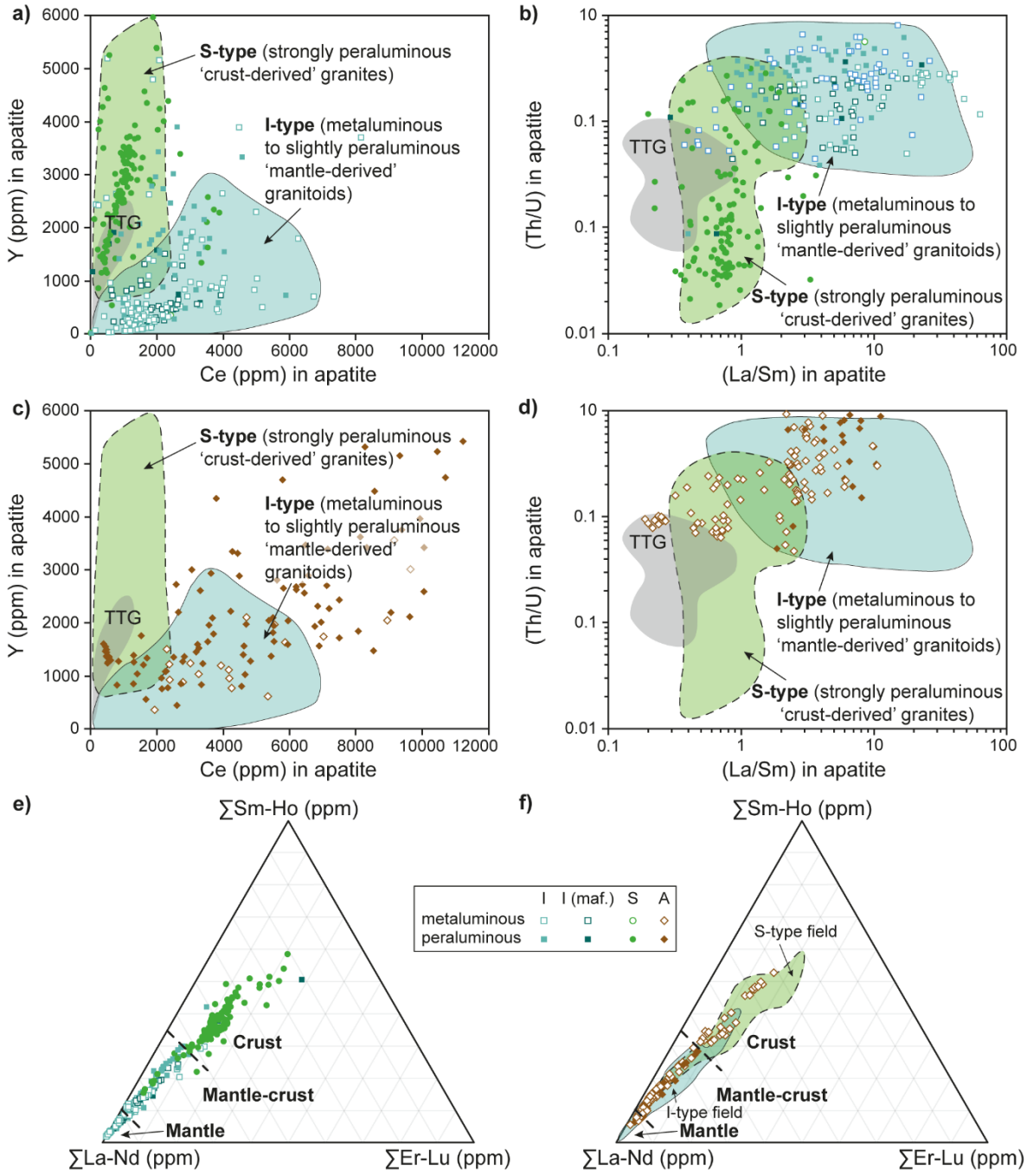

Figure 4.8 – Apatite from I- and S-type granites (a), (b), (e) and A-type granites (c), (d), (f) from both this study and the literature displayed in the binary diagrams of (a to d) Laurent et al. (2017) and ternary diagram (e, f) of Zhu et al. (2004). These diagrams give insights on the type of granite, and thus potential magma source. The diagrams of Laurent et al. (2017) discriminate apatite from I- and S-type granites using Y vs. Ce (a), (c) and (Th/U) vs (La/Sm) (b), (d), whereas the diagram of Zhu et al. (2004) is based on the sum of LREE, MREE and HREE to estimate granite origin.

The same distinction (i.e., S- vs. I- and A-type) can be made using the ternary diagram of Zhu *et al.* (2004) (Figure 4.8e, 4.8f). The REE content of apatite defines if the granitic melt it crystallised from has a 'purely mantellic' (more LREE, i.e., ∑La-Nd, than MREE and HREE) or crustal (more MREE, i.e., ∑Sm-Ho, than LREE and HREE) origin, or is a combination of both (Zhu *et al.* 2004). As expected, apatite from S-type granite is most exclusively restricted to the crust compositional range (Figure 4.8e). It is not surprising, as it is widely accepted that the source of S-type granites corresponds to the partial melting of Al-rich metasedimentary rocks (Chappell and White 1974, 2001). On the other hand, Clemens *et al.* (2011) showed that I-type felsic magmas probably correspond to melts of the igneous crust beneath magmatic arcs (i.e., mostly dacite to andesite), which causes a mixed signature between the mantle and the crust. This would explain the REE signature of apatite from I-granite, that spreads between the mantle- and mantle-crustal field (Figure 4.8e). Lastly, apatite from A-type granite display a wider scatter, between the purely mantellic and purely crustal endmembers (Figure 4.8f). Apatite from peraluminous A-type granites plot closer to the mantle field, whereas those from the felsic part of the Sept-Iles Intrusive Suite (metaluminous) fall within the mantle field. This is because this felsic melt represents extreme fractional crystallisation of a ferrobasaltic melt sourced from the mantle, with negligible crustal contamination (Namur *et al.* 2011). Thus, the diagram of Zhu *et al.* (2004) allows to estimate the influence of the crust and/or the mantle on the magma composition, but does not allow to discriminate apatite from the 3 types of granites.

Richard (2019) is the only study that attempts to discriminate apatite from I-, S- and A-type granites. This study proposed a binary diagram (Figure 4.9a) based on the Eu anomaly (Eu*), defined as the square root of ($Sm_N \times Gd_N$), divided by Eu_N, in which apatite from I-type granite have the lowest Eu*, whereas apatite from S- and A-type granite has higher Eu*. However, apatite from S-type granite have lower Eu_N than that of A-type granite. Similarly, the datasets from our study shows that apatite from I- and S-type granites have similar Eu_N abundances, with the Eu* being overall more pronounced in apatite from peraluminous I- and S-type granites. On the other hand, apatite from A-type granite display similar Eu* than those from S-type granite, but with higher Eu_N values (Figure 4.9a), which is due to the overall REE enrichment compared to apatite from the other types of granites (Figure 4.2e, 4.2f). In that respect, the Eu* vs. Eu_N diagram roughly isolates apatite from I-, S- and A-type granites,

with an overlap of the 3 categories at intermediate Eu* and Eu_N values. However, apatite from peraluminous I-type and S-type granites display similar Eu* and Eu_N values and cannot be separated (Figure 4.9a).

The MREE (Sm/Nd) vs. Eu in apatite diagram of Hsieh *et al.* (2008) was initially designed to display the results of apatite compositions in I- and S-type granites only. In this diagram, the higher (Sm/Nd) ratio in apatite from S-type granite compared to that of I-type granite is attributed to the early crystallisation of monazite (Hsieh *et al.* 2008). The addition of the datasets from this study and our literature compilation shows that this diagram also has the potential to separate apatite from all 3 types of granites (Figure 4.9b). Apatite from I-type granites have lower Sm/Nd ratio, which is likely a result of titanite fractionation, whereas the higher (Sm/Nd) ratio of apatite from S-type granite might be due to monazite crystallisation, as suggested by Hsieh *et al.* (2008). In addition, apatite from A-type granite have higher Eu concentrations than those from both I- and S-type granites, due to their overall higher REE abundances (Figure 4.2). Although these features allow the broad separation of apatite from I-, S- and A-type granites, there is again an overlap between the 3 categories at intermediate Sm/Nd and Eu values, and especially between apatite from peraluminous I- and S-type granites (Figure 4.9b).

Finally, the datasets of apatite from this study and our compilation were displayed on the Mn vs. Na diagram of Sha and Chappell (1999), that was originally used to separate apatite from mafic I-type granites from those of felsic I- and S-type in the Lachlan Fold Belt (Figure 4.9c). The higher Mn content in apatite from the felsic I-type and S-type granites was attributed to higher aluminium saturation index, as well as lower oxygen fugacity. However, it has been demonstrated that the degree of polymerisation of the melt, rather than its oxygen fugacity, affects Mn partitioning into apatite (Stokes *et al.* 2019). Using our datasets, the Mn vs. Na binary diagram shows that apatite from S-type granites do have higher Mn concentrations than those from I-type, with the exception of 2 samples from Wulumna. Although the degree of polymerisation of the melt affects the Mn partitioning into apatite, we infer that a higher Mn concentration in the source rocks (i.e., metasediments) might also lead to higher Mn concentrations into apatite. The addition of apatite from A-type granite shows that its Mn and Na contents is similar to this of apatite from I-type granite (Figure

4.9c). Thus, although the Mn vs. Na diagram allows to identify apatite from S- and I-type granites, it does not allow to discriminate apatite from A-type granites. Although apatite from S-type granite can also have higher Na concentrations, this is not a constant feature, and it does not allow to separate them from apatite of I- and A-type granite (Figure 4.9c).

As a conclusion to this section of the discussion, the display of the datasets from this study in existing diagrams show that there is a potential to use them as they are designed, although the majority was originally designed for 2 types of granites. For example, apatite from S-type granites can be distinguished from those of I- and A-type granite, for the most part, using Sha and Chappell (1999), Zhu *et al.* (2004), or Laurent *et al.* (2017) diagrams. The 3 categories of granites can be roughly isolated using the diagrams of Richard (2019) and Hsieh et al. (2008), with peraluminous I- and S-type often plotting in the same field. However, all these diagrams do not offer a systematic classification, as there is always an overlap between apatite compositions, which leaves room for their improvement.

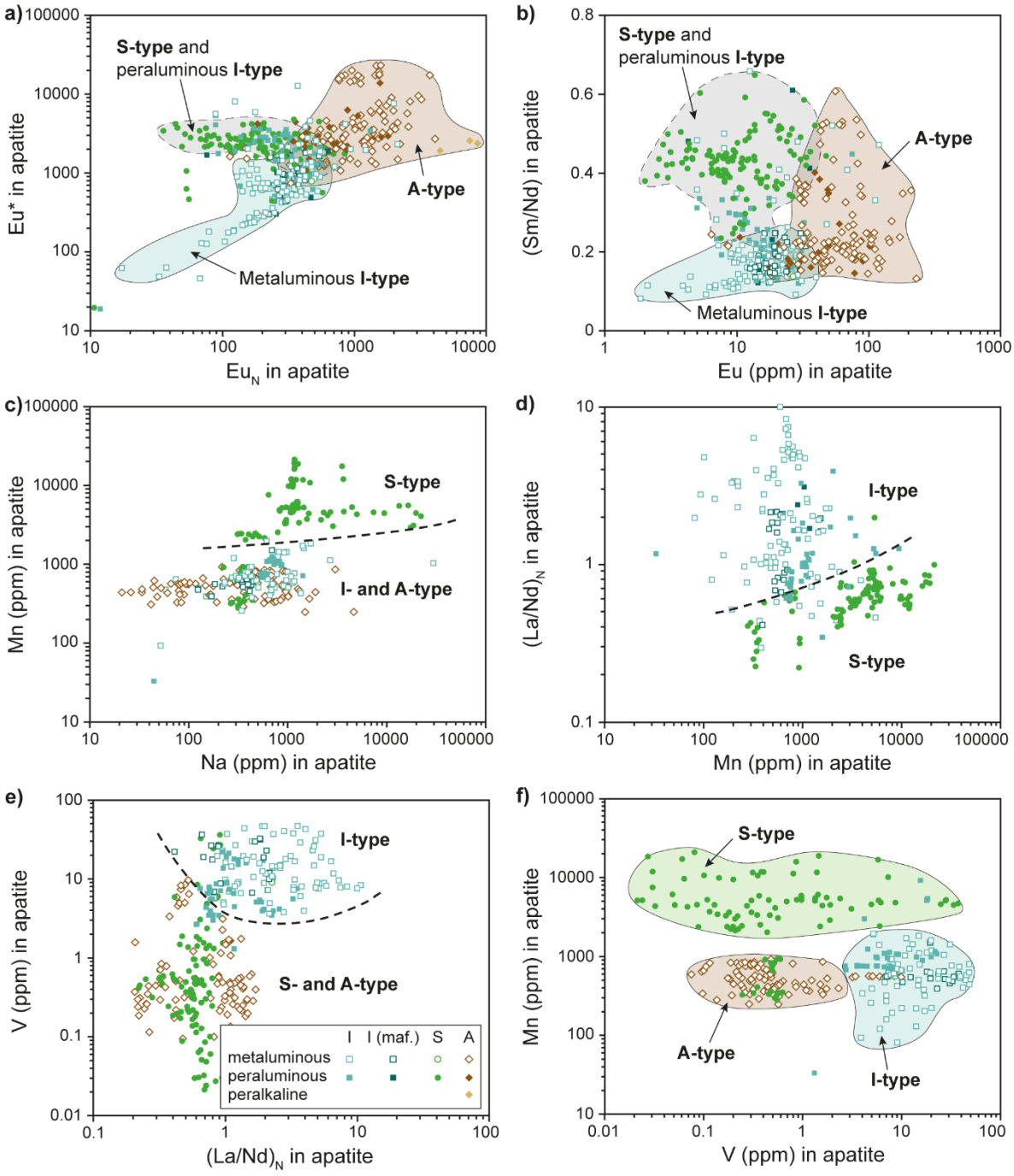

Figure 4.9 – Apatite from both this study and the literature datasets plotted in existing discrimination diagrams using (a) the Eu anomaly (Eu*), defined as the square root of (Sm_N*Gd_N), vs. Eu_N (Richard 2019); (b) (Sm/Nd) vs. Eu in apatite (Hsieh *et al.* 2008); and (c) Mn vs. Na (Sha and Chappell 1999). No fields were drawn by the authors on these diagrams. Therefore, all the fields visible here are drawn from this study. Proposed new binary discrimination diagrams (this study) to separate apatite from (d) peraluminous I- and S-type granites, using Mn and $(La/Nd)_N$; (e) I-type and S- and A-types, using V and $(La/Nd)_N$; and (f) the 3 types of granites, using Mn and V.

4.5.3.2 Proposed discrimination diagrams using new trace elements

In order to better discriminate all apatite from I- and S-type granites, which in previous studies peraluminous I-type were indistinguishable from peraluminous S-type (Richard 2019, Figure 4.9a; Hsieh *et al*. 2008, Figure 4.9b), we propose the following diagram using Mn and $(La/Nd)_N$ in apatite (Figure 4.9d). On the multielement diagram (Figure 4.2a to 4.2d), apatite from S-type granite have a positive LREE slope, whereas that from I-type granite (both peraluminous and metaluminous) have a negative LREE slope. This leads to low and high LREE ratio $(La/Nd)_N$ in apatite from S- and I-type granites, respectively, with most apatite from S-type granite also having higher Mn concentrations, as noted by Sha and Chappell (1999) (Figure 4.9d).

In addition, we propose a series of new discrimination diagrams based on a combination of the best discriminating elements identified on the existing discrimination diagrams presented earlier (Figure 4.8; Figure 4.9a to 4.9c), as well as the observations made from the multielement diagrams (Figure 4.2). The diagram using the V content in apatite as a function of the $(La/Nd)_N$ ratio in apatite (Figure 4.9e) shows that apatite from all I-type granites, regardless of their aluminium saturation index, can be isolated from those of S- and A-type granites due to their generally higher LREE ratios, but most importantly higher V content. This is consistent with whole rock analyses, as I-type granites contain more V than S-type granites, and A-type granites containing only minor amounts of V (Whalen *et al.* 1987; Chappell and White 1992). Once apatite from I-type granites have been identified using the V vs. $(La/Nd)_N$ diagram (Figure 4.9e), several geochemical signatures can be used to separate apatite from S- and A-type granites, such as their REE, As, Na, Mn or Sr abundances (Figure 4.10). These figures show that apatite from A-type granites are indeed generally enriched in REE+Y, As and Th, and depleted in Sr, Mn and Na compared to those from S-type granites.

However, the combination of V and Mn (Figure 4.9f), or of V, Mn and $(La/Nd)_N$ (Figure 4.11) can directly separate apatite from the I-, S- and A-type granites. Indeed, it has been shown in the previous diagrams (Figure 4.9, 4.10) and by the multielement diagrams (Figure 4.2) that apatite from S-type granite contain more Mn than those from I- and A-type granites, and that apatite from I-type granite can be separated from those of A-type due to their higher V content, leading to the definition of the V vs. Mn diagram (Figure 4.9f). The other diagram also uses Mn and V, but with the addition of the

$(La/Nd)_N$ ratio as a third discriminant parameter (Figure 4.11). In this diagram, apatite from I-type granites is clustered close to the V endmember. Apatite from S-type granites are scattered along the Mn and V trend, but clustered closer to the Mn endmember. Finally, apatite from A-type granites are closer to the $(La/Nd)_N$ endmember but with a dispersion towards the Mn and V endmembers (Figure 4.11).

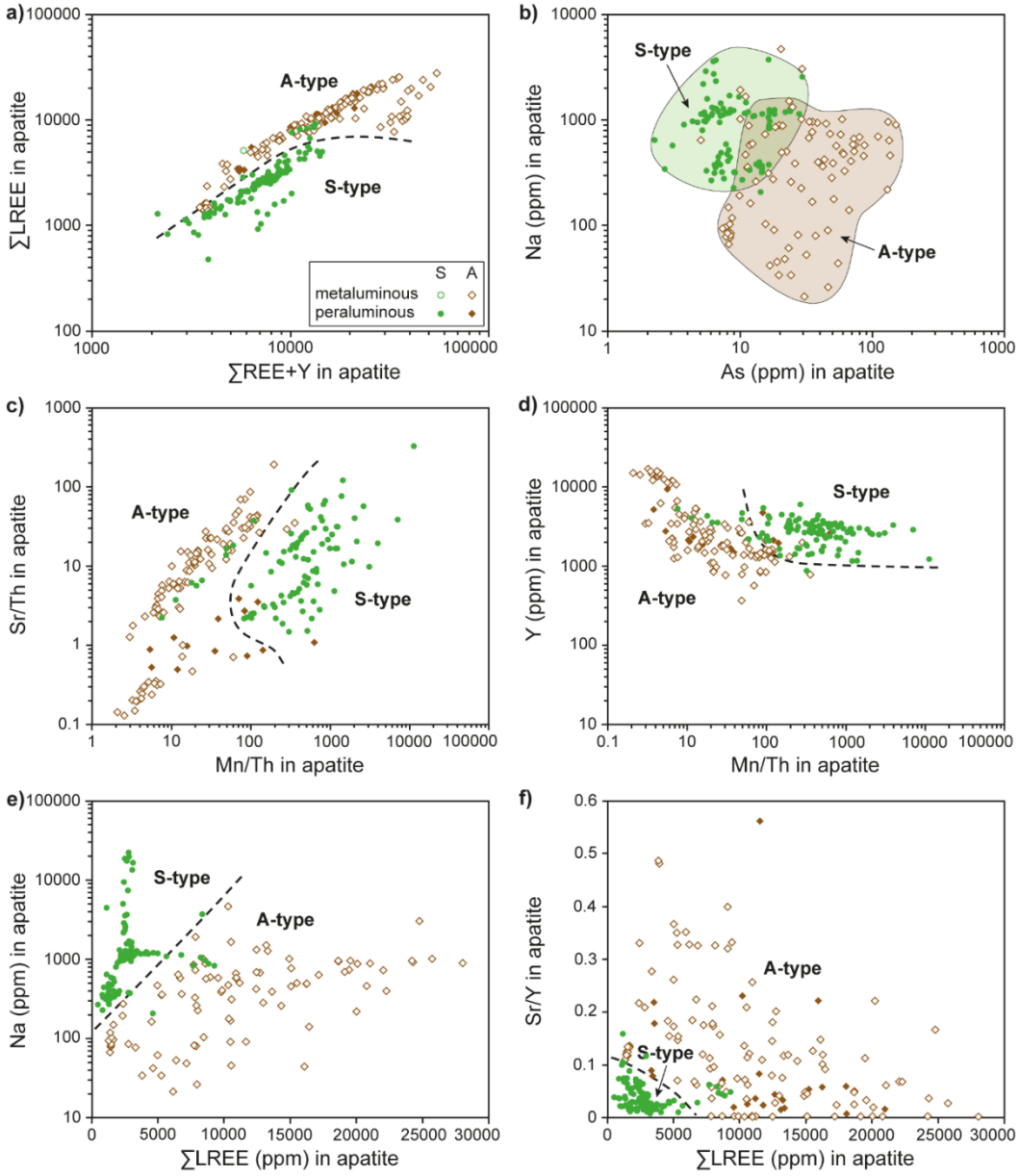

Figure 4.10 – Proposed new discrimination diagrams to separate apatite from S- and A-type granites, identified using the V vs. $(La/Nd)_N$ diagram of Figure 4.8e, using: (a) ∑LREE vs. ∑REE+Y in apatite; (b) As vs. Na; (c) Sr/Th vs. Mn/Th; (d) Y vs. Mn/Th; (e) Na vs. ∑LREE; and (f) Sr/Y vs. ∑LREE. Note that most analyses displayed on these diagrams originate from this study, as few analyses of trace elements, apart from REE, were available in the literature.

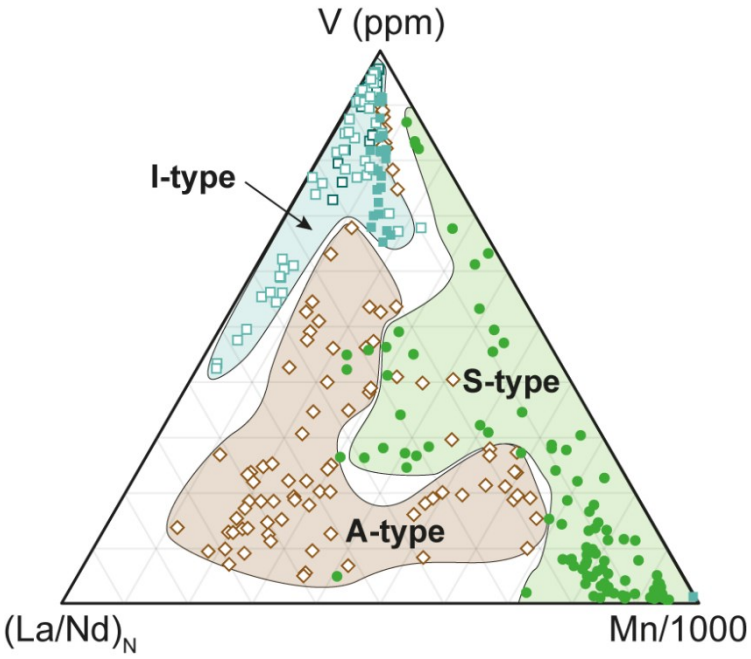

Figure 4.11 – Proposed new ternary discrimination diagram to separate apatite from I-, S- and A-type granites, using Mn, V and $(La/Nd)_N$. This diagram is designed using apatite analyses from this study, as both V and Mn are rarely available simultaneously in the literature.

4.5.4 Application of the discrimination diagrams for the provenance of igneous apatite

In this section, we propose an idealised work-flow (Figure 4.12) to illustrate the steps required to identify apatite from I-, S- or A-type granites from apatite of other origins. For this purpose, we use the trace element data published by Yang *et al.* (2018) for apatite from metaluminous I-type and peraluminous S-type granites from the arc-related, Mesozoic Xihuashan and Shuikoushan plutons in China, respectively. This data was not used in the previous sections to test the discrimination diagrams already published in the literature, nor to create the discrimination diagrams proposed due to the lack of some trace elements (i.e., Mn, As, Mg) in their dataset. However, the apatite data of Yang *et al.* (2018) allows us to test the workflow proposed in this study to identify apatite from I-, S- and A-type granites (Figure 4.13) and to illustrate the limits of missing discriminant elements when using the discrimination diagrams. Indeed, our compilation shows that the availability of data for apatite from I-type granite exceeds the number of analyses available for apatite from S- and A-type granites. Moreover, additional data is required to further test the robustness of the existing and newly proposed discrimination diagrams. Thus, we encourage researchers to analyse apatite from S- and

A- type granites (in particular peralkaline type) in order to enlarge the apatite dataset. Most importantly, the entire suite of trace elements required to apply the discrimination diagrams proposed in this contribution (i.e., REE, Y, Mn, Na, As, Sr, Pb, Th, U and V) should be analysed, as emphasised by the example given below, although other trace elements might also be useful (e.g., Cu, W, Sn).

Step 1: Identifying apatite from mafic or felsic intrusions from other types of rocks

The first step aims to filter all apatite that does not originate from a mafic or felsic intrusive host rock (i.e., alkaline, carbonatite, metamorphic). The recommended discrimination diagram was developed by O'Sullivan *et al.* (2020) and uses Sr/Y vs. LREE in apatite (Figure 4.12). We have demonstrated that apatite from mafic or felsic intrusions plots within the IM, HM or S field. However, the diagram requires improving as some apatite from granite plots in the HM field (i.e., high-grade metamorphic; see Figure 4.3b), and apatite from TTG plot in the LM field (i.e., low-grade metamorphic; see Figure 4.3b). All apatite from I- and S-type granite from Yang *et al.* (2018) dataset plot within the IM, HM and S fields, and thus originate from a mafic or a felsic intrusion. All apatite from I-type granite of Yang *et al.* (2018) plots in its corresponding field (IM; Figure 4.13a). Most of the apatite from S-type granite is in the 'S-type granitoids' whereas some of them plot in the 'high-grade metamorphic' field (HM; Figure 4.13a).

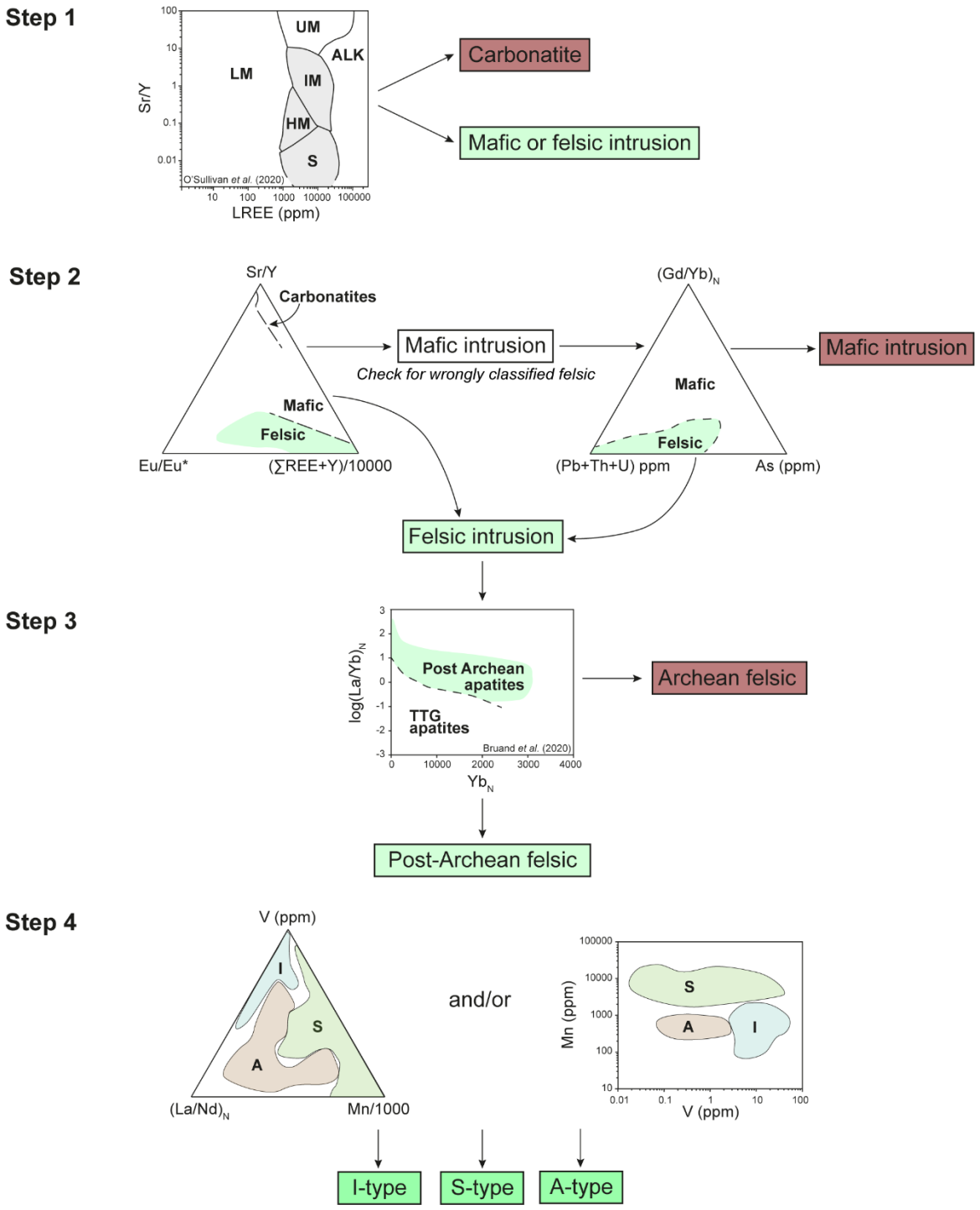

Figure 4.12 – Recommended work-flow to identify apatite from I-, S- and A-type granite. Only the output data framed in green should be used to proceed to the next discrimination step. Diagram used in step 1 is from O'Sullivan *et al.* (2020), the first diagram of step 2 is modified from Kieffer *et al.* (2023), and the diagram proposed in step 3 is from Bruand *et al.* (2020). At step 4, if Mn is not analysed, it is recommended to use the discrimination diagrams showed on Figure 8e and 8f, then those from Figure 9. Note that apatite from mafic intrusions can be used to identify the more primitive and evolved parts of the intrusion by using the diagrams proposed by Kieffer *et al.* (2023; accepted).

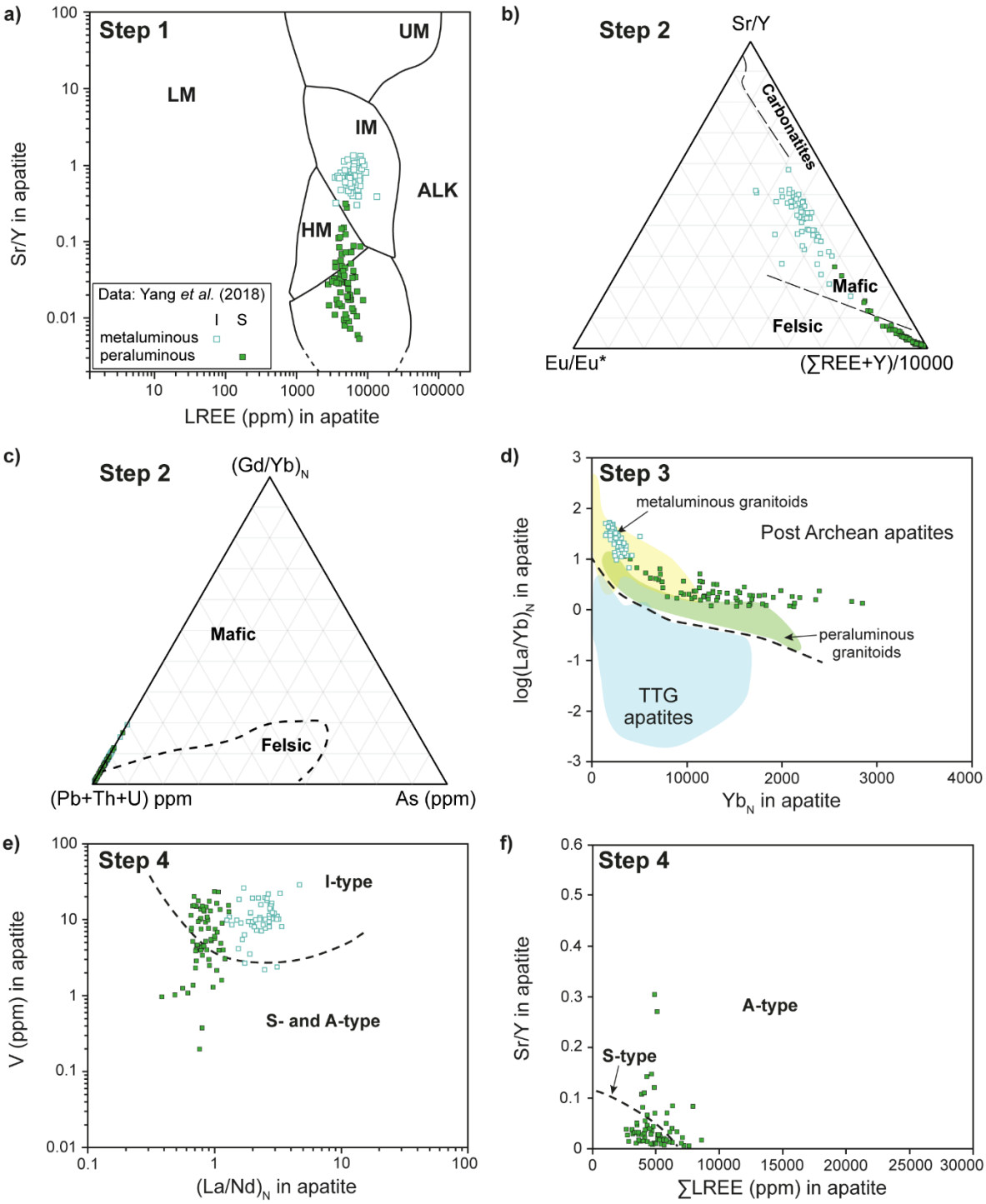

Figure 4.13 – Example of application of the discrimination diagrams for the provenance of igneous apatite, using the data of Yang *et al.* (2018) for apatite from I- and S-type granites. In step 2 (c), As is not analysed. Note that the recommended discrimination diagrams (Step 4, as illustrated on Figure 12) to classify apatite from I-, S- and A-type granites, cannot be tested using Yang *et al.* (2018) data due to the absence of Mn in the dataset.

Step 2: Identifying apatite from mafic and felsic intrusions

Two ternary diagrams are proposed to discriminate apatite from mafic and felsic intrusions. The first contains elements that are commonly analysed (REE+Y, Sr/Y and Eu/Eu*). However, apatite from some felsic intrusions (in particular, I-type granites) can be misclassified as mafic in this diagram due to their high Sr/Y ratios. The second diagram, using trace element less commonly analysed (e.g., As) is more efficient at classifying all apatite from felsic intrusions (Figure 4.12). Indeed, the first discrimination diagram (Figure 4.13b) allows the identification of apatite that plots into the felsic field from those in the mafic field and confirms that apatite does not originate from carbonatite. Most apatite from S-type granite of Yang *et al.* (2018) plots in the felsic field, whereas all apatite from I-type granite plots in the mafic field. At this step, it is required to plot all the data that is in the mafic field into the second discrimination diagram that uses As, $(Gd/Yb)_N$ and (Pb+Th+U) (Figure 4.12; Figure 4.13c). This will ensure that the apatite really originated from a mafic intrusion, or if it corresponds to an apatite from a felsic rock that was wrongly classified as 'mafic'. Unfortunately, As was not analysed in apatite by Yang *et al.* (2018), and this does not allow to use the discrimination diagram to full advantage (Figure 4.13c). However, Yang *et al.* (2018) data plots in the correct range of (Pb+Th+U) for felsic intrusions (Figure 4.13c), but As is required in order to be certain that it really plots in the felsic field. The data could be plotted in the binary discrimination diagrams proposed in Figure 4.6 as an alternative, but Mn and Mg were not analysed by Yang *et al.* (2018). This example shows the limitation of incomplete apatite datasets when using some of the newly proposed discrimination diagrams, as the most efficient diagrams require certain trace elements (As, Mn, V, Mg) that are not commonly available in the literature – but should be included in future studies on apatite. However, as we know that this apatite is from granitic rock (Yang *et al.* 2018), we will continue with the following steps nonetheless. Note that apatite originating from mafic intrusions can further be used to identify the more primitive and the more evolved parts of the intrusion by applying the diagrams proposed by Kieffer *et al.* (2023, accepted).

Step 3: Identifying apatite from Archean and post-Archean felsic intrusions

At this step, we recommend the use of Bruand et al. (2020) binary discrimination diagram that uses $log(La/Yb)_N$ as a function of Yb_N in apatite (Figure 4.12). In this diagram, all apatite analyses from Yang *et al.* (2018) plot in the post-Archean field, which is consistent with the geological context presented in their study (Figure 4.13d).

Step 4: Identifying apatite from post-Archean I-, S- or A-type granites

The recommended discrimination diagrams use Mn, V and $(La/Nd)_N$ or Mn as a function of V as they allow a clear distinction of apatite from the 3 types of granites (Figure 4.12). However, as Mn is not available in Yang *et al.* (2018) dataset, we test the alternative diagrams. First, the V vs. $(La/Nd)_N$ diagram (i.e., one axis of the ternary diagram) should isolate apatite from I-type granite from apatite from both S- and A-type granites (Figure 4.12). In this diagram, Yang *et al.* (2018) apatite from I-type granite plots into the I-type field (Figure 4.13e). However, 66% of apatite from S-type granite also plot in the I-type field. Thus, this example shows that due to the limited availability of data for apatite from S-type granites, the definition of the limit between the I-type (higher V) and S- and A-type field (lower V) is not optimal using this diagram, but when combined with Mn (in the Mn, V, $(La/Nd)_N$ ternary diagram; Figure 4.11), the discrimination is optimal. The use of the diagrams with Mn as the main discriminator would have provided easier classification, but this element was missing.

Apatite that plots in the S- and A-type field of Figure 4.13d should then be separated using the LREE vs. REE+Y, and/or Sr/Y vs. LREE binary discrimination diagram (Figure 4.13f). To test these diagrams, we only plotted the apatite identified as originating from S-type granites by Yang *et al.* (2018) (i.e., even apatite that plot in the 'I-type' field on Figure 4.13e). The majority of apatite (but not all) falls within the S-type field, as expected. However, as suggested earlier, additional data for apatite from S- and A-type should allow a better definition of the limit between the S- and A-type fields. So ideally, the original workflow (Figure 4.12) should be used with a full suite of key elements, as the alternatives (Figure 4.13f, 4.13e) are not robust enough.

4.5.5 Relevance for mineral exploration

It has been demonstrated by some authors (e.g., Belousova et al. 2002; Abdullin *et al.* 2016; O'Sullivan *et al.* 2020), and emphasised in this contribution, that the trace element content of apatite holds a reliable record of its geological environment of formation. This has been recently shown to be the case for other minerals, such as magnetite (e.g., Dare *et al.* 2014, Nadoll *et al.* 2014), scheelite (e.g., Miranda *et al.* in press) or chalcopyrite (Caraballo *et al.* 2022). Felsic intrusions are commonly associated with a variety of mineral deposits (Blevin and Chappell 1995), such as porphyry Cu-Mo, Sn-, W-, Pb-, Zn-bearing skarns, W-Sn greisens or hydrothermal veins (e.g., Blevin and Chappell 1995; Bouzari *et al.* 2018; Li *et al.* 2018; Liu *et al.* 2020). Mafic intrusions can also be host of Fe-Ti-P, Fe-Ti-V, or Ni-Cu-PGE or chromite mineralisation (Boudreau and Kruger 1990; Warner *et al.* 1998; Ma *et al.* 2003; Charlier *et al.* 2011). At a local scale, it has already been shown by some workers that apatite has the potential to indicate fertility of felsic intrusions (I- and S-type granites) for hosting mineral deposits, as apatite chemistry can distinguish fertile from barren felsic intrusions (e.g., Li *et al.* 2017; Azabakht *et al.* 2018; Bouzari *et al.* 2018; Qian *et al.* 2019; Gao *et al.* 2020; Zafar *et al.* 2020). Apatite from fertile intrusions, hosting different types of mineralisation (e.g., porphyry Cu, skarn W), show distinctive chemical signatures (e.g., Duan *et al.* 2019; Gao *et al.* 2020; Mao *et al.* 2016; Tan *et al.* 2023; Zhang *et al.* 2023). Exploration for porphyry deposits using the presence (Kelley et al. 2011) and chemistry (Rukhlov et al. 2016) of detrital apatite in the secondary environment (e.g., glacial tills or river sediments) has already been successfully tested around known porphyry deposits to identify an ore signature. This confirms the interest and potential of apatite as an indicator mineral for exploration.

Thus, being able to fingerprint the host rock of detrital apatite in unexplored, covered terrains (e.g., with glacial sediments) could provide an additional tool to help evaluate the prospectivity of a larger area. For example, this study shows that apatite could be used at first to determine which kind of rock type is overlain by glacial sediments (e.g., mafic or felsic intrusions), and more specifically identify I-, S- or A-type granite among the felsic intrusions, thus revealing information on the tectonic environment in which these granites formed and hence what kind of mineralisation could be present.

4.6 Conclusions and future work

This study combines new and compiled analyses of apatite from felsic intrusions (both Archean and post-Archean) and compares them to apatite from mafic intrusions. It shows that apatite from I-, S- and A-type granites can be identified within this dataset of apatite from various origins, given their distinct chemical compositions. The first discrimination step (1) separates apatite from mafic and felsic intrusions from those from other rock types, such as carbonatites, alkaline rocks and low-grade metamorphic rocks, using O'Sullivan *et al.* (2020) diagram. Then, (2) apatite crystallising from mafic and felsic melt are distinguished using their Sr/Y and REE+Y contents. Apatite from mafic intrusions has higher Sr/Y ratio, whereas apatite from felsic rocks has more REE+Y and a stronger Eu negative anomaly. Apatite whose composition plots as mafic (in particular I-type) need to be further screened to ensure that they are not those of felsic origin that were misclassified. (3) Once the felsic apatite has been identified, the diagrams of Antoine *et al.* (2020) and Bruand *et al.* (2020) separate Archean (TTG) from post-Archean apatite. Indeed, Archean apatite have a distinct REE pattern (i.e., depletion in LREE but enrichment in MREE and HREE) that allows easy identification. At last (4), apatites from I-, S- and A-type granites are identified within the post-Archean granitoid dataset. Although several diagrams have been proposed in the literature, this study shows that the discrimination fields often overlap. We thus propose new discrimination diagrams that are based on the knowledge of the best-performing discrimination elements used in the existing diagrams, and on our new and compiled analyses of apatite datasets. The key diagrams involve V, Mn and the $(La/Nd)_N$ ratio in apatite. Apatite from most I-type granites have higher V content and $(La/Nd)_N$ ratio than those of apatite from S- and A-type granites. However, apatite from S-type granite has 10 times more Mn than apatite from A-type granites. As apatite from I-type granites can be easily distinguished, we propose additional binary diagrams specifically to separate apatite from S- and A-type granites.

This study builds on the previously published research work by various authors, which mainly focused on apatite from I-type granites. We showed that additional data (including REE, Y, Mn, Na, As, Sr, Pb, Th, U and V) is required to test the robustness of the newly proposed discrimination diagrams, with an emphasis on apatite from S- and A-type granites. To conclude, this study brings a new perspective to the application of apatite chemistry for provenance and mineral exploration.

Exploration using the secondary environment has become critical in areas covered by glacial or river sediments. Knowing that detrital apatite chemistry can fingerprint the type of intrusions (I-, S- or A-type granite or mafic) present in unexplored, covered terrains, will help to evaluate the prospectivity of a larger area.

Acknowledgements

This project was supported financially by the Natural Sciences and Engineering Research Council of Canada Discovery Grant (grant number RGPIN-2015-05924) and the Canada Research Chair of Geochemistry Applied to Ore deposits (grant number CRC-2017-0286) of Sarah A.S. Dare. Marie A. Kieffer acknowledges support from Fonds de Recherche du Québec – Nature and Technologies, Programme de Bourses d'Excellence pour Étudiants Étrangers [grant number 319772; merit scholarship program for foreign students].

Marylou Gendron analysed 16 samples as part of her honour's thesis (Gendron 2021), under the co-supervision of Marie A. Kieffer and Sarah A.S. Dare. Jean-François Moyen (Laboratoire Magmas et Volcans, Université de Lyon, France) is warmly thanked for his comments prior to the writing of this contribution, and for his assistance in finding additional granite samples. The authors thank Vojtěch Janoušek (Czech Geological Survey, Prague, Czech Republic) and Gary Stevens (Department of Earth Sciences, University of Stellenbosch, Matieland, South Africa) for providing samples of granites from, respectively, the French Massif Central (S-type) and the Western Cape Suite (S- and I-type) investigated here. Michael D. Higgins and Edward W. Sawyer (University of Quebec in Chicoutimi, Canada) are also thanked for providing additional samples of I-type granites from Guichon Creek and Illapel plutonic suite, and of I-type granite from Tuolumne and S-type granites from Wulumna, respectively. We thank Marc Choquette (Laboratoire de Microanalyse, Laval University, Quebec City), and Audrey Lavoie and Dany Savard (LabMaTer, University of Quebec in Chicoutimi) for their assistance with conducting EMPA and LA-ICP-MS analyses, respectively.

References

Abdel-Karim, A.-A., Azer, M., Sami, M., 2021. Petrogenesis and tectonic implications of the Maladob ring complex in the South Eastern Desert, Egypt: new insights from mineral chemistry and whole-rock geochemistry. International Journal of Earth Sciences **110**, 53-80. doi.org/10.1007/s00531-020-01937-2.

Abdullin, F., Solé, J., Solari, L., Shchepetilnikova, V., Meneses-Rocha, J.J., Pavlinova, N., Rodríguez-Trejo, A., 2016. Single-grain apatite geochemistry of Permian–Triassic granitoids and Mesozoic and Eocene sandstones from Chiapas, southeast Mexico: implications for sediment provenance. International Geology Review **58**(9), 1132-1157. doi.org/10.1080/00206814.2016.1150212.

Antoine, C., Bruand, E., Guitreau, M., Devidal, J.-L., 2020. Understanding Preservation of Primary Signatures in Apatite by Comparing Matrix and Zircon-Hosted Crystals From the Eoarchean Acasta Gneiss Complex (Canada). Geochemistry, Geophysics, Geosystems **21**, e2020GC008923. doi.org/10.1029/2020GC008923.

Antonelli, M.A., Yakymchuk, C., Schauble, E.A., Foden, J., Janoušek, V., Moyen, J.F., Hoffmann, J., Moynier, F., Bachmann, O., 2023. Granite petrogenesis and the $\delta^{44}Ca$ of continental crust. Earth and Planetary Science Letters **608**, 118080. doi.org/10.1016/j.epsl.2023.118080.

Ashwal, L.D., Bybee, G.M., 2017. Crustal evolution and the temporality of anorthosites. Earth Science Reviews **173**, 307-330. doi.org/10.1016/j.earscirev.2017.09.002.

Azadbakht, Z., Lentz, D.R., McFarlane, C.R.M., 2018. Apatite Chemical Compositions from Acadian-Related Granitoids of New Brunswick, Canada: Implications for Petrogenesis and Metallogenesis. Minerals **8**, 598. doi.org/10.3390/min8120598.

Barbarin, B., 1990. Granitoids: Main petrogenetic classifications in relation to origin and tectonic setting. Geological Journal **25**(3-4), 227-238. doi.org/10.1002/gj.3350250306.

Barbarin, B., 1999. A review of the relationships between granitoid types, their origins and their geodynamic environments. Lithos **46**(3), 605-626. doi.org/10.1016/s0024-4937(98)00085-1.

Bea, F., Pereira, M.D., Stroh, A., 1994. Mineral/leucosome trace-element partitioning in a peraluminous migmatite (a laser ablation-ICP-MS study). Chemical Geology **117**, 291-312. doi.org/10.1016/0009-2541(94)90133-3.

Bea, F., Montero, P., 1999. Behavior of accessory phases and redistribution of Zr, REE, Y, Th, and U during metamorphism and partial melting of metapelites in the lower crust: An example from the Kinzigite Formation of Ivrea-Verbano, NW Italy. Geochimica et Cosmochimica Acta **63**(7-8), 1133-1153. doi.org/10.1016/S0016-7037(98)00292-0.

Belousova, E.A., Walters, S., Griffin, W.L., O'Reilly, S.Y., 2001. Trace-element signatures of apatites in granitoids from the Mt Isa Inlier, northwestern Queensland. Australian Journal of Earth Sciences **48**(4), 603-619. doi.org/10.1046/j.1440-0952.2001.00879.x.

Belousova, E.A., Griffin, W.L., O'Reilly, S.Y., Fischer, N.I., 2002. Apatite as an indicator mineral for mineral exploration: trace-element compositions and their relationship to host rock type. Journal of Geochemical Exploration **76**, 45-69. doi.org/https://doi.org/10.1016/S0375-6742(02)00204-2.

Birski, Ł., Słaby, E., Domańska-Siuda, J., 2019. Origin and evolution of volatiles in the Central Europe late Variscan granitoids, using the example of the Strzegom-Sobótka Massif, SW Poland. Mineralogy and Petrology **113**, 119-134. doi.org/10.1007/s00710-018-0615-6.

Blevin, P.L., Chappell, B.W., 1995. Chemistry, Origin, and Evolution of Mineralized Granites in the Lachlan Fold Belt, Australia: The Metallogeny of I- and S-Type Granites. Economic Geology **90**, 1604-1619. doi.org/10.2113/gsecongeo.90.6.1604.

Bonin, B., 2007. A-type granites and related rocks: Evolution of a concept, problems and prospects. Lithos **97**, 1-29. doi.org/10.1016/j.lithos.2006.12.007.

Bonin, B., Janoušek, V., Moyen, J.-F., 2020. Chemical variation, modal composition and classification of granitoids, in: Janoušek, V., Bonin, B., Collins, W.J., Farina, F., Bowden, P. (Eds.), Post-Archean Granitic Rocks: Contrasting Petrogenetic Processes and Tectonic Environments. Geological Society of London Special Publications **491**, pp. 9-51.

Boudreau, A.E., Kruger, F.J., 1990. Variation in the Composition of Apatite through the Merensky Cyclic Unit in the Western Bushveld Complex. Economic Geology **85**, 737-745. doi.org/10.2113/gsecongeo.85.4.737.

Boudreau, A.E., Love, C., Prendergast, M.D., 1995. Halogen geochemistry of the Great Dyke, Zimbabwe. Contributions to Mineralogy and Petrology **122**, 289-300. doi.org/10.1007/s004100050128.

Bouzari, F., Hart, C.J.R., Bissig, T., Lesage, G., 2018. Mineralogical and Geochemical Characteristics of Porphyry-Fertile Plutons: Guichon Creek, Takomkane and Granite Mountain Batholiths, south-central British Columbia (NTS 092I, P, 093A, B). Geoscience BC Report 2018-17 412, 36p.

Brassinnes, S., Balaganskaya, E., Demaiffe, D., 2005. Magmatic evolution of the differentiated ultramafic, alkaline and carbonatite intrusion of Vuoriyarvi (Kola Peninsula, Russia). A LA-ICP-MS study of apatite. Lithos **85**, 76-92. doi.org/10.1016/j.lithos.2005.03.017.

Broska, I., Williams, C.T., Uher, P., Konečný, P., Leichmann, J., 2004. The geochemistry of phosphorus in different granite suites of the Western Carpathians, Slovakia: the role of apatite and P-bearing feldspar. Chemical Geology **205**, 1-15. doi.org/10.1016/j.chemgeo.2003.09.004.

Broska, I., Williams, C.T., Janák, M., Nagy, J., 2005. Alteration and breakdown of xenotime-(Y) and monazite-(Ce) in granitic rocks of the Western Carpathians, Slovakia. Lithos **82**, 71-83. doi.org/10.1016/j.lithos.2004.12.007.

Broska, I., Petrík, I., 2008. Genesis and stability of accessory phosphates in silicic magmatic rocks: a Western Carpathian case study. Mineralogia **39**(1-2), 53-65. doi.org/10.2478/v10002-008-0004-6.

Bruand, E., Fowler, M., Storey, C., Laurent, O., Antoine, C., Guitreau, M., Heilimo, E., Nebel, O., 2020. Accessory mineral constraints on crustal evolution : elemental fingerprints for magma discrimination. Geochemical Perspectives Letters **13**, 7-12. doi.org/10.7185/geochemlet.2006.

Cao, M., Li, G., Qin, K., Seitmuratova, E.Y., Liu, Y., 2012. Major and trace element characteristics of apatites in granitoids from central Kazakhstan: implications for petrogenesis and mineralization. Resource Geology **62**, 63-83. doi.org/10.1111/j.1751-3928.2011.00180.x.

Caraballo, E., Dare, S.A.S., Beaudouin, G., 2022. Variation of trace elements in chalcopyrite from worldwide Ni-Cu sulfide and Reef-type PGE deposits: implications for mineral exploration. Mineralium Deposita **57**(8), 1-29. doi.org/10.1007/s00126-021-01091-y.

Castro, A., 2020. The dual origin of I-type granites: the contribution from experiments, in: Janoušek, V., Bonin, B., Collins, W.J., F., F., Bowden, P. (Eds.), Post-Archean Granitic Rocks: Contrasting Petrogenetic Processes and Tectonic Environments. Geological Society of London Special Publications **491**, pp. 101-145.

Chakhmouradian, A.R., Reguir, E.P., Zaitsev, A.N., Couëslan, C., Xu, C., Kynický, J., Mumin, A.H., Yang, P., 2017. Apatite in carbonatitic rocks: Compositional variation, zoning, element partitioning and petrogenetic significance. Lithos **274-275**, 188-213. doi.org/10.1016/j.lithos.2016.12.037.

Chappell, B.W., 1984. Source Rocks of I- and S-Type Granites in the Lachlan Fold Belt, Southeastern Australia. Philosophical Transactions of the Royal Society of London. Series A, Mathematical and Physical Sciences **310**, 693-707. doi.org/10.1098/rsta.1984.0015.

Chappell, B.W., 1999. Aluminium saturation in I- and S-type granites and the characterization of fractionated haplogranites. Lithos **46**, 535-551. doi.org/10.1016/S0024-4937(98)00086-3.

Chappell, B.W., White, A.J.R., 1974. Two Contrasting Granite Types. Pacific Geology **8**, 173-174.

Chappell, B.W., White, A.J.R., 1992. I- and S-type granites in the Lachlan Fold Belt. Transactions of the Royal Society of Edinburgh: Earth Sciences **83**, 1-26. doi.org/10.1017/S0263593300007720.

Chappell, B.W., White, A.J.R., 2001. Two contrasting granite types: 25 years later. Australian Journal of Earth Sciences **48**(4), 489-499. doi.org/10.1046/j.1440-0952.2001.00882.x.

Charlier, B., Vander Auwera, J., Duchesne, J.-C., 2005. Geochemistry of cumulates from the Bjerkreim–Sokndal layered intrusion (S. Norway) Part II. REE and the trapped liquid fraction. Lithos **83**, 255-276. doi.org/10.1016/j.lithos.2005.03.005.

Charlier, B., Sakoma, E., Sauvé, M., Stanaway, K., Vander Auwera, J., Duchesne, J.-C., 2008. The Grader layered intrusion (Havre-Saint-Pierre Anorthosite, Quebec) and genesis of nelsonite and other Fe–Ti–P ores. Lithos **101**(3-4), 359-378. doi.org/10.1016/j.lithos.2007.08.004.

Charlier, B., Namur, O., Toplis, M.J., Schiano, P., Cluzel, N., Higgins, M.D., Auwera, J.V., 2011. Large-scale silicate liquid immiscibility during differentiation of tholeiitic basalt to granite and the origin of the Daly gap. Geology **39**(10), 907-910. doi.org/https://doi.org/10.1130/g32091.1.

Chartier-Montreuil, W., Dare, S.A.S., Barnes, S.-J., Stevenson, R., 2017. Characterisation of rare earth elements in apatite from the Lac à Paul P-Ti deposit, Saguenay-Lac St. Jean, in: Wavrant, L.-M., Sappin, A.-A., Beland, C.M.J., Chartier-Montreuil, W., Fleury, F., Zhao, P., Beaudoin, G., Barnes, S.-J., Cheng, L.Z., Chouteau, M., Constantin, M., Dare, S., Dupuis, C., Stevenson, R., Williams-Jones, A.E. (Eds.), Projet Terres Rares au Québec: Rapport final, par le Réseau DIVEX pour le Ministère de l'Energie et Ressources naturelles. Quebec, pp. 25-41.

Chen, W., Simonetti, A., 2013. In-situ determination of major and trace elements in calcite and apatite, and U–Pb ages of apatite from the Oka carbonatite complex: Insights into a complex crystallization history. Chemical Geology **353**, 151-172. doi.org/10.1016/j.chemgeo.2012.04.022.

Chu, M.-F., Wang, K.-L., Griffin, W.L., Chung, S.-L., O'Reilly, S.Y., Pearson, N.J., Iizuka, Y., 2009. Apatite Composition: Tracing Petrogenetic processes in Transhimalayan Granitoids. Journal of Petrology **50**(10), 1829-1855. doi.org/10.1093/petrology/egp054.

Clemens, J.D., Stevens, G., Farina, F., 2011. The enigmatic sources of I-type granites: The peritectic connexion. Lithos **126**, 174-181. doi.org/10.1016/j.lithos.2011.07.004.

D'Angelo, M., Alfaro, M., Hollings, P., Byrne, K., Piercey, S., Creaser, R.A., 2017. Petrogenesis and Magmatic Evolution of the Guichon Creek Batholith: Highland Valley Porphyry Cu ± (Mo) District, South-Central British Columbia. Economic Geology **112**, 1857-1888. doi.org/10.5382/econgeo.2017.4532.

Dare, S.A.S., Barnes, S.-J., Beaudoin, G., Méric, J., Boutroy, E., Potvin-Doucet, C., 2014. Trace elements in magnetite as petrogenetic indicators. Mineralium Deposita **49**(7), 785-796. doi.org/10.1007/s00126-014-0529-0.

Decrée, S., Coint, N., Debaille, V., Hagen-Peter, G., Leduc, T., Schiellerup, H., 2022. The potential for REEs in igneous-related apatite deposits in Europe, in: Smelror, M., Hanghøj, K., Schiellerup, H. (Eds.), The Green Stone Age: Exploration and Exploitation of Minerals for Green Technologies. Geological Society, London, Special Publications. doi.org/10.1144/SP526-2021-175.

Deng, M., Xu, C., Song, W., Tang, H., Liu, Y., Zhang, Q., Zhou, Y., Feng, M., Wei, C., 2017. REE mineralization in the Bayan Obo deposit, China: Evidence from mineral paragenesis. Ore Geology Reviews **91**, 100-109. doi.org/10.1016/j.oregeorev.2017.10.018.

Desormiers, M., 2015. In-situ determination of volatile and trace elements in apatite [Ca5(PO4)3(F, Cl, OH)] from Fe-Ti-P deposits by electron microprobe and laser ablation ICP-MS. University of Ottawa, Ottawa, Ontario, p. 40.

Doroshkevich, A.G., Veksler, I.V., Klemd, R., Khromova, E.A., Izbrodin, I.A., 2017. Trace-element composition of minerals and rocks in the Belaya Zima carbonatite complex (Russia): Implications for the mechanisms of magma evolution and carbonatite formation. Lithos 284-**285**, 91-108. doi.org/10.1016/j.lithos.2017.04.003.

Dostal, J., Kontak, D.J.K., S.M., 2014. The early Jurassic Bokan Mountain peralkaline granitic complex (southeastern Alaska): geochemistry, petrogenesis and rare-metal mineralization. Lithos **202-203**, 395-412. doi.org/10.1016/j.lithos.2014.06.005.

Du, J., Wang, G., Jia, L., 2019. In situ major and trace element compositions of apatites from Luanchuan ore cluster: Implications for porphyry Mo mineralization. Ore Geology Reviews **115**, 103174. doi.org/10.1016/j.oregeorev.2019.103174.

Duan, X.-X., Chen, B., Sun, K.-K., Wang, Z.-Q., Yan, X., Zhang, Z., 2019. Accessory mineral chemistry as a monitor of petrogenetic and metallogenetic processes: A comparative study of zircon and apatite from Wushan Cu- and Zhuxiling W(Mo)-mineralization-related granitoids. Ore Geology Reviews **111**, 102940. doi.org/10.1016/j.oregeorev.2019.102940.

Duchesne, J.C., Shumlyanskyy, L., Charlier, B., 2006. The Fedorivka layered intrusion (Korosten Pluton, Ukraine): An example of highly differentiated ferrobasaltic evolution. Lithos **89**(3-4), 353-376. doi.org/10.1016/j.lithos.2006.01.003.

El Korh, A., Schmidt, S.T., Ulianov, A., Potel, S., 2007. Trace Element Partitioning in HP-LT Metamorphic Assemblages during Subduction-related Metamorphism, Ile de Groix, France: a Detailed LA-ICPMS Study. Journal of Petrology **50**(6), 1107-1148. doi.org/0.1093/petrology/egp03.

Emslie, R.F., Hamilton, M.A., Thériault, R.J., 1994. Petrogenesis of a Mid-Proterozoic Anorthosite-Mangerite-Charnockite-Granite (AMCG) Complex: Isotopic and Chemical Evidence from the Nain Plutonic Suite. The Journal of Geology **102**(5), 539-558. doi.org/10.1086/629697.

Eby, G.N., 1990. The A-type granitoids: A review of their occurrence and chemical characteristics and speculations on their petrogenesis. Lithos **26**(1-2), 115-134. doi.org/10.1016/0024-4937(90)90043-Z.

Farina, F., Stevens, G., Villaros, A., 2012. Multi-batch, incremental assembly of a dynamic magma chamber: the case of the Peninsula pluton granite (Cape Granite Suite, South Africa). Mineralogy and Petrology **106**, 193-216. doi.org/10.1007/s00710-012-0224-8.

Frost, C.D., Frost, B.R., 2011. On Ferroan (A-type) Granitoids: their Compositional Variability and Modes of Origin. Journal of Petrology **52**, 39-53. doi.org/10.1093/petrology/egq070.

Frost, B.R., Barnes, C.G., Collins, W.J., Arculus, R.J., Ellis, D.J., Frost, C.D., 2001. A Geochemical Classification for Granitic Rocks. Journal of Petrology **42**(11), 2033-2048. doi.org/10.1093/petrology/42.11.2033.

Gao, X., Yang, L., Wang, C., He, W., Bao, X., Zhang, S., 2020. Halogens and trace elements of apatite from Late Mesozoic and Cenozoic porphyry Cu-Mo-Au deposits in SE Tibet, China: Constraints on magmatic fertility and granitoid petrogenesis. Journal of Asian Earth Sciences **203**, 104552. doi.org/10.1016/j.jseaes.2020.104552.

Gendron, M., 2021. Les éléments traces dans l'apatite des granites de type I, S et A : implication pour l'exploration minérale. Université du Québec à Chicoutimi, Chicoutimi, Quebec, p. 44.

Grant, M., 2020. Formation of magmatic Fe-Ti-V-P deposits within the Lac St. Jean area Saguenay, Québec, Canada: Insights from trace element composition of Fe-oxides and apatite, Department of Earth Sciences. University of Ottawa, Ottawa, p. 359.

Griffin, T.J., White, A.J.R., Chappell, B.W., 1978. The Moruya Batholith and geochemical contrasts between the Moruya and Jindabyne suites. Journal of the Geological Society of Australia **25**(3-4), 235-247. doi.org/10.1080/00167617808729030.

Hansen, J., Skjerlie, K.P., Pedersen, R.B., De La Rosa, J., 2002. Crustal melting in the lower parts of island arcs: An example from the Bremanger Granitoid complex, west Norwegian Caledonides. Contributions to Mineralogy and Petrology **143**(3), 316-335. doi.org/10.1007/s00410-001-0342-5.

He, H.-L., Yu, S.-Y., Song, X.-Y., Du, Z.-S., Dai, Z.-H., Zhou, T., Xie, W., 2016. Origin of nelsonite and Fe–Ti oxides ore of the Damiao anorthosite complex, NE China: Evidence from trace element geochemistry of apatite, plagioclase, magnetite and ilmenite. Ore Geology Reviews **79**, 367-381. doi.org/10.1016/j.oregeorev.2016.05.028.

Henrichs, I.A., O'Sullivan, G., Chew, D., M., Mark, C., Babechuk, M.G., McKenna, C., Emo, R., 2018. The trace element and U-Pb systematics of metamorphic apatite. Chemical Geology **483**, 218-238. doi.org/10.1016/j.chemgeo.2017.12.031.

Higgins, M.D., 2017. Quantitative investigation of felsic rock textures using cathodoluminescence images and other techniques. Lithos **277**, 259-268. doi.org/10.1016/j.lithos.2016.05.006.

Higgins, M.D., van Breemen, O., 1996. Three generations of anorthosite-mangerite-charnockite-granite (AMCG) magmatism, contact metamorphism and tectonism in the Saguenay-Lac-Saint-Jean region of the Grenville Province, Canada. Precambrian Research 79(3-4), 327-**346**. doi.org/10.1016/0301-9268(95)00102-6.

Hine, E., Williams, I.S., Chappell, B.W., White, A.J.R., 1978. Contrasts between I- and S-type granitoids of the Kosciusko Batholith. Journal of the Geological Society of Australia **25**, 219-234. doi.org/10.1080/00167617808729029.

Hounsell, V., 2006. Origine des roches felsiques de la Série Supérieure de la Suite Intrusive de Sept-Îles, Québec, Département des Sciences de Appliquées. Université du Québec à Chicoutimi, Chicoutimi, Québec, Canada, p. 203.

Hsieh, P.-S., Chen, C.-H., Yang, H.-J., Lee, C.-Y., 2008. Petrogenesis of the Nanling Mountains granites from South China: Constraints from systematic apatite geochemistry and whole-rock geochemical and Sr–Nd isotope compositions. Journal of Asian Earth Sciences **33**, 428-451. doi.org/10.1016/j.jseaes.2008.02.002.

Ihlen, P.M., Schiellerup, H., Gautneb, H., Skår, Ø., 2014. Characterization of apatite resources in Norway and their REE potential — A review. Ore Geology Reviews **58**, 126-147. doi.org/10.1016/j.oregeorev.2013.11.003.

Ishihara, S., 1977. The Magnetite-series and Ilmenite Series Granitic Rocks. Mining Geology **27**(145), 293-305. doi.org/10.11456/shigenchishitsu1951.27.293.

Jiang, S.Y., Zhao, K.D., Jiang, Y.H., Dai, B.Z., 2008. Characteristics and genesis of Mesozoic A-type granites and associated mineral deposits in the southern Hunan and northern Guangxi Provinces along the Shi-Hang belt, South China. Geological Journal of China Universities **14**(4), 496-509.

Jiao, S.-J., Li, X.-H., Huang, H.-Q., Deng, X.-G., 2015. Metasedimentary melting in the formation of charnockite: Petrological and zircon U-Pb-Hf-O isotope evidence from the Darongshan S-type granitic complex in southern China. Lithos **239**, 217-233. doi.org/10.1016/j.lithos.2015.10.004.

Kelley, K.D., Eppinger, R.G., Lang, J., Smith, M.D., Fey, D.L., 2011. Porphyry Cu indicator minerals in till as an exploration tool: example from the giant Pebble porphyry Cu-Au-Mo deposit, Alaska, USA. Geochemistry: Exploration, Environment, Analysis **11**, 321-334. doi.org/10.1144/1467-7873/10-IM-041.

Kieffer, M.A., Dare, S.A.S., Namur, O., 2023. The use of trace elements in apatite to trace differentiation of a ferrobasaltic melt in the Sept-Iles Intrusive Suite, Quebec, Canada: Implications for provenance discrimination. Geochimica et Cosmochimica Acta **342**, 169-197. doi.org/10.1016/j.gca.2022.12.016.

Kieffer, M.A., Dare, S.A.S., Namur, O., Mansur, E.T. (accepted). Apatite chemistry as a petrogenetic indicator for mafic layered intrusions. Journal of Petrology.

Laurent, O., Zeh, A., Gerdes, A., Villaros, A., Gros, K., Słaby, E., 2017. How do granitoid magmas mix with each other? Insights from textures, trace element and Sr–Nd isotopic composition of apatite and titanite from the Matok pluton (South Africa). Contributions to Mineralogy and Petrology **172**, 80. doi.org/10.1007/s00410-017-1398-1.

Lavaure, S., Sawyer, E.W., 2011. Source of biotite in the Wuluma Pluton: Replacement of ferromagnesian phases and disaggregation of enclaves and schlieren. Lithos **125**, 757-780. doi.org/10.1016/j.lithos.2011.04.005.

Lavaure, S., 2012. Origine des enrichissements en biotite dans les granites de type S: évidences pétrogéochimiques et pétrogénétiques du granite de Wulumna, Australie, Département des Sciences Appliquées. Université du Québec à Chicoutimi, Chicoutimi, Québec, Canada, p. 273.

Li, H., Ling, M.-X., Ding, X., Zhang, H., Li, C.-Y., Liu, D.-Y., Sun, W.-D., 2014. The geochemical characteristics of Haiyang A-type granite complex in Shandong, eastern China. Lithos 200-**201**, 142-156. doi.org/10.1016/j.lithos.2014.04.014.

Li, C.-Y., Hao, X.-L., Liu, J.-Q., Ling, M.-X., Ding, X., Zhang, H., Sun, W.-D., 2017. The formation of Luoboling porphyry Cu–Mo deposit: Constraints from zircon and apatite. Lithos **272-273**, 291-300. doi.org/10.1016/j.lithos.2016.12.003.

Li, H., Palinkaš, L.A., Watanabe, K., Xi, X.-S., 2018. Petrogenesis of Jurassic A-type granites associated with Cu-Mo and W-Sn deposits in the central Nanling region, South China: Relation to mantle upwelling and intra-continental extension. Ore Geology Reviews **92**, 449-462. doi.org/10.1016/j.oregeorev.2017.11.029.

Liu, L., Hu, R.-Z., Zhong, H., Yang, J.-H., Kang, L.-F., Zhang, X.-C., Fu, Y.-Z., Mao, W., Tang, Y.-W., 2020. Petrogenesis of multistage S-type granites from the Malay Peninsula in the Southeast Asian tin belt and their relationship to Tethyan evolution. Gondwana Research **84**, 20-37. doi.org/10.1016/j.gr.2020.02.013.

Loiselle, M.C., Wones, D.R., 1979. Characteristics of Anorogenic Granites. Geological Society of America, Abstracts with Programs **11**, 468.

Ma, Y., Ji, X.T., Li, J.C., Huang, M., Kan, Z.Z., 2003. Mineral Resources of the Panzhihua Region. Sichuan Science and Technology Press, Chengdu.

Mao, M., Rukhlov, A.S., Rowins, S.M., Spence, J., Coogan, L.A., 2016. Apatite Trace Element Compositions: A Robust New Tool for Mineral Exploration. Economic Geology **111**(5), 1187-1222. doi.org/10.2113/econgeo.111.5.1187.

McDonough, W.F., Sun, S.-s., 1995. The composition of Earth. Chemical Geology **120**(3-4), 223-253. doi.org/10.1016/0009-2541(94)00140-4.

Miles, A.J., Graham, C.M., Hawkesworth, C.J., Gillespie, M.R., Hinton, R.W., 2013. Evidence for distinct stages of magma history recorded by the compositions of accessory apatite and zircon. Contributions to Mineralogy and Petrology **166**, 1-19. doi.org/10.1007/s00410-013-0862-9.

Miloski, P., Dare, S. A. S., Morisset, C. E., Davis, J. S., Perrot, M. & Savard, S. (in press). Petrogenesis of Fe-Ti-P mineralization associated with Proterozoic anorthosite massifs at Lac à l'Orignal, Quebec, Canada: insights from oxide and apatite trace-element geochemistry. Mineralium Deposita.

Miranda, A.C.R., Beaudoin, G., Rottier, B., Pašava, J., Bohdálek, P., Malec, J., in press. Trace Element Signatures in Scheelite Associated with Various Deposit Types: A Tool for Mineral Targeting. Journal of Geochemical Exploration. doi.org/10.2139/ssrn.4470997.

Moyen, J.-F., Martin, H., 2012. Forty years of TTG research. Lithos 148, 312-336. doi.org/10.1016/j.lithos.2012.06.010.

Moyen, J.-F., Laurent, O., Chelle-Michou, C., Couzinié, S., Vanderhaeghe, O., Zeh, A., Villaros, A., Gardien, V., 2017. Collision vs. subduction-related magmatism: Two contrasting ways of granite formation and implications for crustal growth. Lithos **277**, 154-177. doi.org/10.1016/j.lithos.2016.09.018.

Nadoll, P., Angerer, T., Mauk, J.L., French, D., Walshe, J., 2014. The chemistry of hydrothermal magnetite: A review. Ore Geology Reviews **61**, 1-32. doi.org/10.1016/j.oregeorev.2013.12.013.

Nathwani, C.L., Loader, M.A., Wilkinson, J.J., Buret, Y., Sievwright, R.H., Hollings, P., 2020. Multi-stage arc magma evolution recorded by apatite in volcanic rocks. Geology **48**(4), 323-327. doi.org/10.1130/G46998.1.

Namur, O., Charlier, B., Toplis, M.J., Higgins, M.D., Hounsell, V., Liegeois, J.P., Vander Auwera, J., 2011. Differentiation of Tholeiitic Basalt to A-Type Granite in the Sept Iles Layered Intrusion, Canada. Journal of Petrology 52(3), 487-539. doi.org/10.1093/petrology/egq088.

Nutman, A.P., 2007. Apatite recrystallisation during prograde metamorphism, Cooma, southeast Australia: implications for using an apatite – graphite association as a biotracer in ancient metasedimentary rocks. Australian Journal of Earth Sciences 58(8), 1023-1032. doi.org/10.1080/0812009070148832.

O'Sullivan, G., Chew, D., Kenny, G., Henrichs, I., Mulligan, D., 2020. The trace element composition of apatite and its application to detrital provenance studies. Earth-Science Reviews 201, 103044. doi.org/10.1016/j.earscirev.2019.103044.

Padilla, A.J., Gualda, G.A.R., 2016. Crystal-melt elemental partitioning in silicic magmatic systems: An example from the Peach Spring Tuff high-silica rhyolite, Southwest USA. Chemical Geology 440(15), 326-344. doi.org/10.1016/j.chemgeo.2016.07.004.

Pan, Y., Fleet, M.E., 2002. Compositions of the Apatite-Group Minerals: Substitution Mechanisms and Controlling Factors. Reviews in Mineralogy and Geochemistry 48(1), 13-49. doi.org/10.2138/rmg.2002.48.2.

Parada, M.A., Nystrom, J.O., Levi, B., 1999. Multiple sources for the Coastal Batholith of central Chile (31-34 degrees S): geochemical and Sr-Nd isotopic evidence and tectonic implications. Lithos 46(3), 505-521. doi.org/10.1016/S0024-4937(98)00080-2.

Paton, C., Hellstrom, J.C., Paul, B., Woodhead, J., Hergt, J., 2011. Iolite: freeware for the visualisation and processing of mass spectrometric data. Journal of Analytical Atomic Spectrometry 26, 2508-2518. doi.org/10.1039/C1JA10172B.

Pearce, J.A., Harris, N., Tindle, A.G., 1984. Trace Element Discrimination Diagrams for the Tectonic Interpretation of Granitic Rocks. Journal of Petrology 25, 956-983. doi.org/10.1093/petrology/25.4.956.

Pedersen, J.M., Ulrich, T., Whitehouse, M.J., Kent, A.J.R., Tegner, C., 2021. The volatile and trace element composition of apatite in the Skaergaard intrusion, East Greenland. Contributions to Mineralogy and Petrology 176, 102. doi.org/10.1007/s00410-021-01861-x.

Piccoli, P., Candela, P., 1994. Apatite in felsic rocks: A model for the estimation of initial halogen concentrations in the Bishop Tuff (Long Valley) and Tuolumne Intrusive Suite (Sierra Nevada Batholith) magmas. American Journal of Science 294(1), 92-135. doi.org/10.2475/ajs.294.1.92.

Piccoli, P.M., Candela, P.A., 2002. Apatite in Igneous Systems. Reviews in Mineralogy and Geochemistry 48(1), 255-292. doi.org/10.2138/rmg.2002.48.6.

Qian, L., Wang, Y., Xie, J., Sun, W., 2019. The Late Mesozoic granodiorite and polymetallic mineralization in southern Anhui Province, China: A perspective from apatite geochemistry. Solid Earth Sciences 4, 178-189. doi.org/10.1016/j.sesci.2019.11.006.

Qu, P., Li, N.-B., Niu, H.-C., Yang, W.-B., Shan, Q., Zhang, Z.-Y., 2019. Zircon and apatite as tools to monitor the evolution of fractionated I-type granites from the central Great Xing'an Range, NE China. Lithos 348-349, 105207. doi.org/10.1016/j.lithos.2019.105207.

Quan, Y.-K., Mu, M.-S., Yang, D.-B., Yan, X.-Y., Wang, A.-Q., Hao, L.-R., Wang, F., 2023. Geochronology and in-situ apatite geochemistry of late Paleoproterozoic A-type granites in the Jiao-Liao-Ji Belt, North China Craton: Implications for petrogenesis and tectonic evolution. Geochemistry (in press). doi.org/10.1016/j.chemer.2023.126009.

Richard, B.J., 2019. Tracing magmatic processes in plutonic environments: Insight from apatite and rift-related granites, Department of Geology and Environmental Earth Science. Faculty of Miami University, Miami, p. 79.

Roda-Robles, E., Gil-Crespo, P.P., Pesquera, A., Lima, A., Garate-Olave, I., Merino-Martínez, E., Cardoso-Fernandes, J., Errandonea-Martin, J., 2022. Compositional Variations in Apatite and Petrogenetic Significance: Examples from Peraluminous Granites and Related Pegmatites and Hydrothermal Veins from the Central Iberian Zone (Spain and Portugal). Minerals 12, 1401. doi.org/10.3390/min12111401.

Rohrlach, B.D., Loucks, R.R., 2015. Multi-million-year cyclic ramp-up of volatiles in a lower crustal magma reservoir trapped below the Tampakan copper-gold deposit by Mio-Pliocene crustal compression in the Southern Philippines, in: Porter, T.M. (Ed.) Super porphyry copper and gold deposits - a global perspective. PGC Publishing, 2, pp. 369-407.

Rukhlov, A.S., Plouffe, A., Ferbey, T., Mao, M., Spence, J., 2016. Application of trace-element compositions of detrital apatite to explore for porphyry deposits in central British Columbia, in: British Columbia Ministry of Energy and Mines (Ed.) Geological Fieldwork 2015, British Columbia Geological Survey Paper 2016-1. pp. 145-179.

Sha, L.-K., Chappell, B.W., 1999. Apatite chemical composition, determined by electron microprobe and laser-ablation inductively coupled plasma mass spectrometry, as a probe into granite petrogenesis. Geochimica et Cosmochimica Acta 63(22), 3861-3881. doi.org/10.1016/S0016-7037(99)00210-0.

Shand, S.J., 1927. The Eruptive Rocks. Van Nostrand, D., New-York. 360p.

She, Y.-W., Song, X.-Y., Yu, S.-Y., Chen, L.-M., Zheng, W.-Q., 2016. Apatite geochemistry of the Taihe layered intrusion, SW China: Implications for the magmatic differentiation and the origin of apatite-rich Fe-Ti oxide ores. Ore Geology Reviews 78, 151-165. doi.org/10.1016/j.oregeorev.2016.04.004.

Smith, M.P., Storey, C.D., Jeffries, T.E., Ryan, C., 2009. In situ U–Pb and trace element analysis of accessory minerals in the Kiruna district, Norrbotten, Sweden: new constraints on the timing and origin of mineralization. Journal of Petrology 50(11), 2063-2094. doi.org/10.1093/petrology/egp069.

Solgadi, F., Sawyer, E.W., 2008. Formation of Igneous Layering in Granodiorite by Gravity Flow: a Field, Microstructure and Geochemical Study of the Tuolumne Intrusive Suite at Sawmill Canyon, California. Journal of Petrology 49(11), 2009-2042. doi.org/10.1093/petrology/egn056.

Solgadi, F., 2010. Origine et développement de litages dans des roches de composition granitique, Département des Sciences Appliquées. Université du Québec à Chicoutimi, Chicoutimi, Québec, Canada, p. 486.

Spicer, E.M., 2001. Apatite, allanite, titanite and monazite characteristics in S-, I- and A-type Cape Granites, Department of Geology. University of Stellenbosch, p. 215.

Stevens, G., Villaros, A., Moyen, J.-F., 2007. Selective peritectic garnet entrainment as the origin of geochemical diversity in S-type granites. Geology 35(1), 9-12. doi.org/10.1130/G22959A.1.

Stokes, T.N., Bromiley, G.D., Potts, N.J., Saunders, K.E., Miles, A.J., 2019. The effect of melt composition and oxygen fugacity on manganese partitioning between apatite and silicate melt. Chemical Geology 506, 162-174. doi.org/10.1016/j.chemgeo.2018.12.015.

Stormer, J.C., Pierson, M.L., Tacker, R.C., 1993. Variation of F and Cl X-ray intensity due to anisotropic diffusion in apatite during electron microprobe analysis. American Mineralogist 78(5-6), 641-648.

Szopa, K., Gawęda, A., Müller, A., Sikorska, M., 2013. The petrogenesis of granitoid rocks unusually rich in apatite in the Western Tatra Mts. (S-Poland, Western Carpathians). Mineralogy and Petrology 107, 609-627. doi.org/10.1007/s00710-012-0262-2.

Tan, H.M.R., Huang, X.-W., Meng, Y.-M., Xie, H., Qi, L., 2023. Multivariate statistical analysis of trace elements in apatite: Discrimination of apatite with different origins. Ore Geology Reviews 153, 105269. doi.org/10.1016/j.oregeorev.2022.105269.

Tollari, N., Barnes, S., Cox, R., Nabil, H., 2008. Trace element concentrations in apatites from the Sept-Îles Intrusive Suite, Canada — Implications for the genesis of nelsonites. Chemical Geology 252(3-4), 180-190. doi.org/10.1016/j.chemgeo.2008.02.016.

Van Tongeren, J.A., Mathez, E.A., 2012. Large-scale liquid immiscibility at the top of the Bushveld Complex, South Africa. Geology 40(6), 491-494. doi.org/10.1130/g32980.1.

Villaros, A., Stevens, G., Buick, I.S., 2009. Tracking S-type granite from source to emplacement: clues from garnet in the Cape Granite Suite. Lithos 112(3-4), 217-235. doi.org/10.1016/j.lithos.2009.02.011.

Wang, M., Wang, C.Y., 2020. Crystal Size Distributions and Trace Element Compositions of the Fluorapatite from the Bijigou Fe–Ti Oxide-Bearing Layered Intrusion, Central China: Insights for the Expulsion Processes of Interstitial Liquid from Crystal Mush. Journal of Petrology 61(7), egaa069. doi.org/10.1093/petrology/egaa069.

Wang, L.-X., Ma, C.-Q., Zhang, C., Zhu, Y.-X., Marks, M.A.W., 2018. Halogen geochemistry of I- and A-type granites from Jiuhuashan region (South China): Insights into the elevated fluorine in A-type granite. Chemical Geology 478, 164-182. doi.org/10.1016/j.chemgeo.2017.09.033.

Wang, C., Liu, J., Zhang, H., Zhang, X., Zhang, D., Xi, Z., Wang, Z., 2019. Geochronology and mineralogy of the Weishan carbonatite in Shandong province, eastern China. Geoscience Frontiers 10, 769-785. doi.org/10.1016/j.gsf.2018.07.00.

Warner, S., Martin, R.F., Abdel-Rahman, A.-F.M., Doig, R., 1998. Apatite as a monitor of fractionation, degassing, and metamorphism in the Sudbury Igneous Complex, Ontario. The Canadian Mineralogist 36, 981-999.

Webster, J.D., Piccoli, P.M., 2015. Magmatic Apatite: A Powerful, Yet Deceptive, Mineral. Elements 11(3), 177-182. doi.org/10.2113/gselements.11.3.177.

Whalen, J.B., Currie, K.L., Chappell, B.W., 1987. A-type granites: geochemical characteristics, discrimination and petrogenesis. Contributions to Mineralogy and Petrology 95, 407-419. doi.org/10.1007/BF00402202.

Xie, J., Wang, Y., Li, Q., Yan, J., Sun, W., 2018. Petrogenesis and metallogenic implications of Late Mesozoic intrusive rocks in the Tongling region, eastern China: a case study and perspective review. International Geology Review 60, 1361-1380. doi.org/10.1080/00206814.2017.1386130.

Xing, C.-M., Wang, C.Y., 2017. Cathodoluminescence images and trace element compositions of fluorapatite from the Hongge layered intrusion in SW China: A record of prolonged crystallization and overprinted fluid metasomatism. American Mineralogist 102(7), 1390-1401. doi.org/10.2138/am-2017-6028.

Xing, C.-M., Wang, C.Y., Li, C., 2014. Trace element compositions of apatite from the middle zone of the Panzhihua layered intrusion, SW China: Insights into the differentiation of a P- and Si-rich melt. Lithos 204, 188-202. doi.org/10.1016/j.lithos.2014.02.009.

Xing, K., Shu, Q., Lentz, D.R., Wang, F., 2020. Zircon and apatite geochemical constraints on the formation of the Huojihe porphyry Mo deposit in the Lesser Xing'an Range, NE China. American Mineralogist 105(3), 382-396. doi.org/10.2138/am-2020-7226.

Yang, F., Santosh, M., Glorie, S., Xue, F., Zhang, S., Zhang, X., 2020. Apatite geochronology and chemistry of Luanchuan granitoids in the East Qinling Orogen, China: Implications for petrogenesis, metallogenesis and exploration. Lithos 378-379, 105797. doi.org/10.1016/j.lithos.2020.105797.

Yang, X., Liu, Q., Du, G., Qi, H., 2023. Petrogenesis and tectonic significance of Late Mesozoic A-type granite from the Huangmeijian intrusion in the Luzong volcanic basin, eastern China: Constraints from geochronology and geochemistry. Geochemistry (in press), 125977. doi.org/10.1016/j.chemer.2023.125977.

Yu, Z.-Q., Chen, W.-F., Chen, P.-R., Wang, K.-X., Fang, Q.-C., Tang, X.-S., Ling, H.-F., 2019. Chemical composition and Sr isotopes of apatite in the Xiangshan A-type volcanic-intrusive complex, Southeast China: New insight into petrogenesis. Journal of Asian Earth Sciences 172, 66-82. doi.org/10.1016/j.jseaes.2018.08.019.

Zafar, T., Rehman, H.U., Mahar, M.A., Alam, M., Oyebamiji, A., Rehman, S.U., Leng, C.-B., 2020. A critical review on petrogenetic, metallogenic and geodynamic implications of granitic rocks exposed in north and east China: New insights from apatite geochemistry. Journal of Geodynamics 136, 101723. doi.org/10.1016/j.jog.2020.101723.

Zhang, S.-H., Liu, S.-W., Zhao, Y., Yang, J.H., Song, B., Liu, X.-M., 2007. The 1.75–1.68 Ga anorthosite-mangerite-alkali granitoid-rapakivi granite suite from the northern North China Craton: Magmatism related to a Paleoproterozoic orogen. Precambrian Research 155, 287-312. doi.org/10.1016/j.precamres.2007.02.008.

Zhang, X., Guo, F., Zhang, B., Zhao, L., Wu, Y., Wang, G., Alemayehu, M., 2020. Magmatic evolution and post-crystallization hydrothermal activity in the early Cretaceous Pingtan intrusive complex, SE China: records from apatite geochemistry. Contributions to Mineralogy and Petrology 175, 35. doi.org/10.1007/s00410-020-1675-2.

Zhang, X.-N., Pan, J.-Y., Lehmann, B., Li, J.-X., Yin, S., Ouyang, Y.-P., Zhang, Y., Zhong, F.-J., Fu, J.-L., Wu, B., 2023. Geochemical composition of apatite from the Zhuxi tungsten granite and the Zhenzhushan granite porphyry in the Jiangnan porphyry-skarn tungsten belt, China. Geochemistry (in press). doi.org/10.1016/j.chemer.2023.126010.

Zhou, R.-J., Wen, G., Li, J.-W., Cao, K., Wei, K.-T., Cai, H.-A., Shang, S.-C., Sun, Y.L., Fan, L., Li, B.-C., Dai, X.-K., 2022. Petrogenesis and metal fertility of Yinzu pluton in the Daye district, eastern China: Insights from whole-rock and mineral (zircon, apatite and amphibolite) geochemistry. Lithos 432-433, 106898. doi.org/10.1016/j.lithos.2022.106898.

Zhou, T., Cai, Y.-W., An, M.-G., Zhou, F., Zhi, C.-L., Sun, X.-C., Tamer, M., 2023. Visual Interpretation of Machine Learning: Genetical Classification of Apatite from Various Ore Sources. Minerals 13(4), 491. doi.org/10.3390/min13040491.

Zhu, X.Q., Wang, Z.G., Huang, Y., Wang, H.L., 2004. REE content and distribution in apatite and its geological tracing significance. Chinese Rare Earths 25, 41.

CHAPITRE 5

SYNTHÈSE

5.1 Introduction

Ce chapitre synthétise les conclusions de ce projet de doctorat et leur intégration dans l'effort de recherche actuel. La première partie se concentre sur l'utilisation de l'apatite en tant qu'indicateur pétrogénétique. La seconde partie met l'emphase sur le développement de l'apatite comme minéral indicateur pour les études de provenance sédimentaires et l'exploration minérale. Enfin, la troisième et dernière partie suggère de futurs axes de recherche basés sur des questions soulevées par ces travaux de recherche et leurs conclusions.

5.2 Développement de l'apatite en tant qu'indicateur pétrogénétique

La première partie de ce projet de doctorat s'est concentrée sur l'investigation des processus qui font varier la composition chimique des apatites. Pour ce faire, l'élaboration d'un nouveau diagramme multiéléments a permis de faciliter l'identification des éléments et des ratios utiles pour tracer les processus pétrogénétiques, mais aussi pour discriminer les types de roches (voir section suivante). Les résultats des travaux ont établi que, dans une seule intrusion mafique litée étudiée dans son entièreté (i.e., la Suite Intrusive de Sept-Iles), les variations chimiques de l'apatite cristallisant en phase cumulus peuvent être attribués à différents processus, chacun causant une signature distincte. La différenciation cause un enrichissement en ETR+Y, Th, U, K, Pb et Rb, et un appauvrissement en Sr, Ba, V et Mg dans les apatites. Le processus d'immiscibilité de liquides silicatés engendre la cristallisation d'apatite en proportions cotectiques variables dans les niveaux pauvres (1 %) et riches (5 à 8 %) en Fe-Ti-P, qui s'accompagne d'une composition chimique différente. Les apatites des niveaux pauvres en Fe-Ti-P sont en effet enrichies en ETR+Y, As, Rb, K, Na and Th par rapport à celles de niveaux riches en Fe-Ti-P, qui sont enrichies en Pb, Mn, Mg, Nb et Ti. La recharge de magma engendre quant à elle une diminution de la concentration en éléments compatibles (e.g., ETR+Y, As et Na) et une augmentation de celle en éléments incompatibles (e.g., Sr, V et Mg) dans les apatites. L'ensemble de ces processus avaient été documentés en utilisant d'autres supports que l'apatite, telles que des analyses de type roche totale, le contenu en anorthite des plagioclases ou en forstérite de l'olivine, le Mg# du pyroxène, ou la présence d'inclusions de magma (Namur *et al.* 2010, 2011a, 2011b, 2012; Charlier *et al.* 2011).

Ces travaux étudient également les variations de la chimie de l'apatite entre différentes intrusions mafiques. À notre connaissance, il s'agit des premiers travaux combinant les analyses d'éléments traces dans les apatites des intrusions mafiques litées disponibles dans la littérature à l'échelle mondiale qui explorent l'effet de différents processus sur la composition des apatites (e.g., degré de contamination crustale). À partir de cette compilation et de nouvelles analyses d'apatites, les travaux démontrent que les paramètres qui diffèrent entre les intrusions affectent également le contenu en éléments traces des apatites. Notamment, la contamination crustale se traduit par des concentrations plus importantes en Th, U, Pb et As, ainsi que par des ratios $(La/Nd)_N$ plus élevés dans l'apatite. L'effet de la contamination crustale sur la signature des apatites est appuyé par des analyses isotopiques du Sr dans l'apatite ($(^{87}Sr/^{86}Sr)_{initial}$). Ces analyses sont communément réalisées sur des plagioclases ou en roche totale, mais les résultats obtenus avec l'apatite sont similaires, ce qui prouve que les analyses in situ des isotopes du Sr dans l'apatite sont robustes. La profondeur de fusion partielle du magma parental engendre des ratios $(Gd/Yb)_N$ élevés dans l'apatite, en raison de la rétention de Yb dans la source par le grenat. De nouveaux diagrammes utilisant les éléments mentionnés ci-dessus sont proposés afin de définir les variations causées par la contamination crustale et la profondeur de fusion partielle du magma parental. Ces diagrammes sont supportés par des modélisations de cristallisation fractionnée testant l'effet de la co-cristallisation de différents minéraux (e.g., amphibole, clino et orthopyroxène) sur ces variations.

L'étude de Boudreau *et al.* (1986) a identifié que les apatites cristallisant sur la cotectique (cumulus) et à partir du liquide interstitiel (intercumulus) ont un contenu en éléments volatiles différents (i.e., riches en F et en Cl, respectivement). Les résultats de ces travaux de doctorat montrent que, dans la Suite Intrusive de Sept-Iles, ces deux types d'apatite ont également une signature en éléments traces distincte (e.g., apatite intercumulus enrichie en V et avec un ratio Th/Lu plus élevé que les apatites cumulus), ce qui a permis de définir des diagrammes de discrimination. Leur test avec la compilation générée pour la contribution présentée au chapitre 3 montre que ces nouveaux diagrammes sont généralisables pour les apatites provenant d'autres intrusions mafiques litées.

La contribution majeure de ce premier volet du projet de doctorat est que l'apatite constitue un indicateur fiable des processus magmatiques, au même titre que d'autres indicateurs communément utilisés (e.g., *liquid line of descent* obtenue à partir des analyses de type roche totale, contenu en anorthite des plagioclases ou en forstérite de l'olivine, Mg# du pyroxène, isotopes du Sr dans la roche ou dans les plagioclases). Cette contribution est particulièrement importante, car elle montre que l'apatite est un indicateur indépendant, notamment dans les cas où il n'y a pas de silicates dans la roche, comme dans des minéralisations en oxides de fer et apatite (communes dans les suites AMCG; Grant 2020), ou si les silicates sont altérés (e.g., métamorphisme, hydrothermalisme).

Le projet prouve également qu'il est possible de séparer les apatites provenant de différents types de granites suivant leur contenu en éléments traces (ETR+Y, Sr, As, Pb, Th, U, Mn et V). La classification des granites est en effet un sujet très discuté, et il est possible que certaines classifications parviennent à un meilleur résultat que d'autres. La compilation d'analyses d'apatites dans les granites de type I, S et A bâtie durant ces travaux est la plus aboutie à ce jour, à notre connaissance. Elle est complétée par de nouvelles analyses comportant l'ensemble des éléments traces présentés sur le nouveau diagramme multiéléments. Les résultats confirment que des critères chimiques permettant d'identifier les granites de type I, S et A sont aussi reflétés par la composition de l'apatite. En revanche, les minéraux accessoires exercent également un fort contrôle sur sa signature (e.g., la cristallisation de titanite ou de monazite cause un appauvrissement en ETR moyens et lourds, et en ETR légers, respectivement), le type de minéral accessoire étant contrôlé par la chimie du magma. Par exemple, la titanite est associée aux granites de type I (Chappell et White 1992), tandis que la monazite est associée à ceux que type S (Sha et Chappell 1999).

5.3 Développement de l'apatite en tant que minéral indicateur pour les études de provenance et l'exploration

Une autre contribution majeure de ce projet de doctorat utilise le schéma de classification général des apatites introduit à la section précédente. Ce schéma peut être appliqué non seulement dans une étude de provenance sédimentaire, comme proposé par O'Sullivan *et al.* (2020), mais également dans un contexte d'exploration minérale en environnement secondaire (e.g., terrains recouverts par

des sédiments glaciaires). En effet, les apatites cumulus ou intercumulus des intrusions mafiques litées peuvent être associées à des minéralisations (Fe-Ti-P ou Fe-Ti-V, et Ni-Cu-EGP-Cr, respectivement; Boudreau et Kruger 1990; Warner *et al.* 1998; Ma *et al.* 2003; Charlier *et al.* 2011). Ces travaux ont montré que les apatites cumulus et intercumulus ont une signature distincte, mais également qu'il existe une différence entre la composition des apatites cumulus associées à des minéralisations en Fe-Ti-P et celles qui ne le sont pas. En revanche, bien que distinguable à petite échelle, l'effet de la différenciation magmatique masque cette différence à plus grande échelle. Quant aux apatites des intrusions felsiques, elles peuvent être associées à différents types de minéralisations, comme des porphyres à Cu, Mo, Au (type I; Blevin et Chappell 1995; Bouzari *et al.* 2018), des skarns à Sn, W, Pb ou Zn (type S; Blevin et Chappell 1995; Cao *et al.* 2012), ou encore des greisens ou des skarns à W-Sn et des minéralisations en ETR (type A; Dostal *et al.* 2014; Jiang *et al.* 2008; Li *et al.* 2018). Bien que plusieurs auteurs aient proposé une approche similaire (e.g., Mao *et al.* 2016, Deng *et al.* 2023, Tan *et al.* 2023), ces travaux n'incluaient pas les apatites des intrusions mafiques litées, et regroupaient les granites de type I, S et A dans une seule catégorie. Les diagrammes de discrimination existants sont donc améliorés et de nouveaux sont proposés, en utilisant des éléments traces qui ne sont pas analysés systématiquement. Les travaux aboutissent à un schéma de classification général pour identifier les apatites provenant des parties inférieures (intercumulus) et supérieures (cumulus) des intrusions mafiques, et des intrusions felsiques (granites de type I, S et A), auxquelles peuvent être associés différents types de minéralisation. Cette étude complète donc celles existantes et contribue à orienter l'exploration, la chimie des apatites détritiques pouvant aider à évaluer la prospectivité de terrains couverts par des sédiments glaciaires ou alluviaux.

5.4 Conclusion et travaux futurs

Les travaux réalisés contribuent à développer l'apatite non seulement en tant qu'indicateur pétrogénétique, mais aussi en tant que minéral indicateur pour les études de provenance et l'exploration minérale. Ils soulèvent également plusieurs points qui nécessiterait de futures investigations, telles que :

- Tester la classification proposée pour les apatites de granites de type I, S et A en y apportant de nouvelles données, incluant les éléments traces présentés sur le nouveau diagramme multiéléments. Les apatites des granites de type I étant sur-échantillonnées, l'emphase devrait être mise sur les apatites des granites de type S, et tout particulièrement sur celles des granites de type A peralcalins. Les apatites de porphyres d'affinité alcaline pourraient également être incluses, car les analyses compilées à ce jour portent exclusivement sur des porphyres dont l'affinité est calco-alcaline.
- Explorer d'autres pistes de classifications pour les apatites des granites, telles qu'une classification plus 'descriptive' (e.g., Bonin *et al.* 2020).
- Raffiner le schéma de classification proposé en y ajoutant des données d'apatites provenant d'autres roches (e.g., roches alcalines; distinguer la signature des apatites des TTG de celle des roches métamorphiques). Il serait également intéressant de combiner l'approche pétrogénétique utilisée ici à une approche statistique.
- À petite échelle, plusieurs études ont montré que les apatites provenant d'intrusions felsiques fertiles et stériles ont une signature différente. Il serait intéressant de tester si cette différence est généralisable à grande échelle. Cela permettrait de raffiner le schéma de classification en précisant si chaque type de granite présente un potentiel pour les minéralisations.
- L'apatite est un minéral qui permet l'utilisation de plusieurs systèmes isotopiques. Il serait intéressant de coupler plusieurs systèmes isotopiques (Sr, Nd), afin de mieux contraindre la contribution de la contamination crustale sur la composition des apatites, notamment dans les granites. Le développement des datations Lu-Hf et U-Pb *in situ* dans l'apatite permettrait de mieux contraindre les âges des minéralisations directement (Glorie *et al.* 2023).
- Explorer les effets du métamorphisme et de l'altération par les fluides (hydrothermaux, magmatiques contemporains à la cristallisation de l'apatite, deutéritiques) sur la chimie des apatites.
- Les apatites investiguées dans ces travaux sont exclusivement magmatiques (i.e., elles cristallisent à partir d'un fluide magmatique). Or, il existe également des apatites d'origine hydrothermale (e.g., cristallisant à partir d'un fluide hydrothermal), comme par exemple dans

des carbonatites (e.g., Chakhmouradian *et al.* 2017), des gisements de type porphyre, skarn ou orogénique (e.g., Mao *et al.* 2016), ou des sulfures massifs volcanogènes (Genna et Gaboury 2015). Les diagrammes de discrimination proposés par Mao *et al.* (2016) combinent les apatites d'origine magmatique et hydrothermale pour définir un même champ (e.g., champ de composition pour les porphyres). Récemment, Tan *et al.* (2023) montrent via l'apprentissage machine que d'une façon générale, les apatites d'origine magmatique et hydrothermale semblent avoir une signature différente. Utiliser une approche pétrogénétique telle que celle utilisée dans ces travaux, et par Dare *et al.* (2014) sur la magnétite, permettrait de comprendre quels éléments sont caractéristiques des apatites cristallisant à partir des 2 types de fluides, car cela a des implications au niveau des processus minéralisateurs dans les gisements.

Références

Blevin, P.L., et Chappell, B.W. 1995. Chemistry, Origin, and Evolution of Mineralized Granites in the Lachlan Fold Belt, Australia: The Metallogeny of I- and S-Type Granites. Economic Geology **90**: 1604-1619. doi: 10.2113/gsecongeo.90.6.1604.

Bonin, B., Janoušek, V., et Moyen, J.-F. 2020. Chemical variation, modal composition and classification of granitoids. Dans Post-Archean Granitic Rocks: Contrasting Petrogenetic Processes and Tectonic Environments. Sous la direction de V. Janoušek, Bonin, B., Collins, W.J., Farina, F., Bowden, P. Geological Society of London Special Publications **491**. pp. 9-51.

Boudreau, A.E., et Kruger, F.J. 1990. Variation in the Composition of Apatite through the Merensky Cyclic Unit in the Western Bushveld Complex. Economic Geology **85**: 737-745. doi: 10.2113/gsecongeo.85.4.737.

Boudreau, A.E., Mathez, E.A., et McCallum, I.S. 1986. Halogen Geochemistry of the Stillwater and Bushveld Complexes: Evidence for Transport of the Platinum-Group Elements by Cl-Rich fluids. Journal of Petrology **27**(4): 967-986. doi: https://doi.org/10.1093/petrology/27.4.967.

Bouzari, F., Hart, C.J.R., Bissig, T., et Lesage, G. 2018. Mineralogical and Geochemical Characteristics of Porphyry-Fertile Plutons: Guichon Creek, Takomkane and Granite Mountain Batholiths, south-central British Columbia (NTS 092I, P, 093A, B). Geoscience BC Report 2018-17 412: 36p.

Cao, M., Li, G., Qin, K., Seitmuratova, E.Y., et Liu, Y. 2012. Major and trace element characteristics of apatites in granitoids from central Kazakhstan: implications for petrogenesis and mineralization. Resource Geology **62**: 63-83. doi: 10.1111/j.1751-3928.2011.00180.x.

Chakhmouradian, A.R., Reguir, E.P., Zaitsev, A.N., Couëslan, C., Xu, C., Kynický, J., Mumin, A.H., et Yang, P. 2017. Apatite in carbonatitic rocks: Compositional variation, zoning, element partitioning and petrogenetic significance. Lithos **274-275**: 188-213. doi: 10.1016/j.lithos.2016.12.037.

Chappell, B.W., et White, A.J.R. 1992. I- and S-type granites in the Lachlan Fold Belt. Transactions of the Royal Society of Edinburgh: Earth Sciences **83**: 1-26. doi: 10.1017/S0263593300007720.

Charlier, B., Namur, O., Toplis, M.J., Schiano, P., Cluzel, N., Higgins, M.D., et Auwera, J.V. 2011. Large-scale silicate liquid immiscibility during differentiation of tholeiitic basalt to granite and the origin of the Daly gap. Geology **39**(10): 907-910. doi: https://doi.org/10.1130/g32091.1.

Dare, S.A.S., Barnes, S.-J., Beaudoin, G., Méric, J., Boutroy, E., et Potvin-Doucet, C. 2014. Trace elements in magnetite as petrogenetic indicators. Mineralium Deposita **49**(7): 785-796. doi: 10.1007/s00126-014-0529-0.

Qiu, K.-F., Zhou, T., Chew, D., Hou, Z.-L., Müller, A., Yu, H.-C., Lee, R.G., Chen, H., et Deng, J. in press. Apatite trace element composition as an indicator of ore deposit types: a machine learning approach. American Mineralogist. doi: 10.2138/am-2022-8805.

Dostal, J., et Kontak, D.J.K., S.M. 2014. The early Jurassic Bokan Mountain peralkaline granitic complex (southeastern Alaska): geochemistry, petrogenesis and rare-metal mineralization. Lithos **202-203**: 395-412. doi: 10.1016/j.lithos.2014.06.005.

Genna, D., et Gaboury, D. 2015. Deciphering the Hydrothermal Evolution of a VMS System by LA-ICP-MS Using Trace Elements in Pyrite: An Example from the Bracemac-McLeod Deposits, Abitibi, Canada, and Implications for Exploration. Economic Geology **110**: 2087-2108. doi: 10.2113/econgeo.110.8.2087.

Glorie, S., Hand, M., Mulder, J., Simpson, A., Emo, R.B., Kamber, B., Fernie, N., Nixon, A., et Gilbert, S. 2023. Robust laser ablation Lu–Hf dating of apatite: an empirical evaluation. Geological Society, London, Special Publications **537**. doi: 10.1144/SP537-2022-205

Grant, M. 2020. Formation of magmatic Fe-Ti-V-P deposits within the Lac St. Jean area Saguenay, Québec, Canada: Insights from trace element composition of Fe-oxides and apatite, Department of Earth Sciences, University of Ottawa, Ottawa.

Jiang, S.Y., Zhao, K.D., Jiang, Y.H., et Dai, B.Z. 2008. Characteristics and genesis of Mesozoic A-type granites and associated mineral deposits in the southern Hunan and northern Guangxi Provinces along the Shi-Hang belt, South China. Geological Journal of China Universities **14**(4): 496-509.

Li, H., Palinkaš, L.A., Watanabe, K., et Xi, X.-S. 2018. Petrogenesis of Jurassic A-type granites associated with Cu-Mo and W-Sn deposits in the central Nanling region, South China: Relation to mantle upwelling and intra-continental extension. Ore Geology Reviews **92**: 449-462. doi: 10.1016/j.oregeorev.2017.11.029.

Ma, Y., Ji, X.T., Li, J.C., Huang, M., et Kan, Z.Z. 2003. Mineral Resources of the Panzhihua Region. Sichuan Science and Technology Press, Chengdu.

Mao, M., Rukhlov, A.S., Rowins, S.M., Spence, J., et Coogan, L.A. 2016. Apatite Trace Element Compositions: A Robust New Tool for Mineral Exploration. Economic Geology **111**(5): 1187-1222. doi: 10.2113/econgeo.111.5.1187.

Namur, O., Charlier, B., Toplis, M.J., Higgins, M.D., Liégeois, J.-P., et Vander Auwera, J. 2010. Crystallization Sequence and Magma Chamber Processes in the Ferrobasaltic Sept Iles Layered Intrusion, Canada. Journal of Petrology **51**(6): 1203-1236. doi: 10.1093/petrology/egq016.

Namur, O., Charlier, B., Pirard, C., Hermann, J., Liégeois, J.-P., et Vander Auwera, J. 2011. Anorthosite formation by plagioclase flotation in ferrobasalt and implications for the lunar crust. Geochimica et Cosmochimica Acta **75**(17): 4998-5018. doi: 10.1016/j.gca.2011.06.013.

Namur, O., Charlier, B., Toplis, M.J., Higgins, M.D., Hounsell, V., Liegeois, J.P., et Vander Auwera, J. 2011. Differentiation of Tholeiitic Basalt to A-Type Granite in the Sept Iles Layered Intrusion, Canada. Journal of Petrology **52**(3): 487-539. doi: 10.1093/petrology/egq088.

Namur, O., Charlier, B., et Holness, M.B. 2012. Dual origin of Fe–Ti–P gabbros by immiscibility and fractional crystallization of evolved tholeiitic basalts in the Sept Iles layered intrusion. Lithos **154**: 100-114. doi: 10.1016/j.lithos.2012.06.034.

O'Sullivan, G., Chew, D., Kenny, G., Henrichs, I., et Mulligan, D. 2020. The trace element composition of apatite and its application to detrital provenance studies. Earth-Science Reviews **201**: 103044. doi: 10.1016/j.earscirev.2019.103044.

Sha, L.-K., et Chappell, B.W. 1999. Apatite chemical composition, determined by electron microprobe and laser-ablation inductively coupled plasma mass spectrometry, as a probe into granite petrogenesis. Geochimica et Cosmichimica Acta **63**(22): 3861-3881. doi: 10.1016/S0016-7037(99)00210-0.

Tan, H.M.R., Huang, X.-W., Meng, Y.-M., Xie, H., et Qi, L. 2023. Multivariate statistical analysis of trace elements in apatite: Discrimination of apatite with different origins. Ore Geology Reviews **153**: 105269. doi: 10.1016/j.oregeorev.2022.105269.

Warner, S., Martin, R.F., Abdel-Rahman, A.-F.M., et Doig, R. 1998. Apatite as a monitor of fractionation, degassing, and metamorphism in the Sudbury Igneous Complex, Ontario. The Canadian Mineralogist **36**: 981-999.

ANNEXES

ANNEXE 1 – PDAC-SEG Student Mineral Colloquium 2021

Affiche et communication orale présentées lors du congrès PDAC-SEG Student Mineral Colloquium (Toronto, Canada), du 8 au 11 mars 2021.

Résumé soumis :

Trace elements in apatite in layered intrusions: insights into magmatic processes and application to mineral exploration

M Kieffer[*1], S Dare[1]
[1]Department of Applied Sciences, Université du Québec à Chicoutimi (UQAC), Chicoutimi, Quebec, Canada
*marie.kieffer1@uqac.ca

Apatite is a weathering-resistant mineral that can be found in most igneous, sedimentary, metamorphic and hydrothermal rocks. Numerous studies have shown that apatite chemistry can be used as a provenance indicator for several kinds of rocks and/or mineral deposits, as well as providing information on magmatic processes. In igneous rocks, the chemistry of apatite primarily depends on magma composition, but may be further modified by processes during and/or after their crystallization. Even if these processes are known, it has not yet been determined if their influence on apatite chemistry is significant, nor if they could hinder or help the use of apatite as an indicator mineral for exploration purposes. This study uses LA-ICP-MS analyses (LabMaTer, UQAC) to obtain the full suite of trace elements of apatite from Sept-Iles (Quebec) and Bushveld (South Africa) layered intrusions, as well as Sept-Iles granites (most differentiated part of the intrusion). Our results show that the chemistry of apatite from mafic layered intrusions reflects magmatic differentiation and gives insights into the nature of the intrusions' magma. We show that the content of several incompatible elements (i.e. bulk D; including rare earth elements) increases during differentiation in apatite. In particular, a clear trend can be observed from the layered intrusion to the evolved granite of Sept-Iles. Apatites crystallizing from trapped liquid (intercumulus) display a different signature than those formed as a cumulus phase. Also, elements such as U, Th or Pb in apatite can reflect crustal contamination of the host intrusions. Even if apatite is already widely used as a provenance and petrogenetic indicator, apatite from mafic layered intrusions have not been taken into account by previous studies. However, mafic layered intrusions contain significant phosphorus, iron, titanium and vanadium resources, and possibly rare earth elements (hosted in apatite). Improving our understanding of apatite chemistry from layered intrusions will enlargen their use as a provenance indicator.

ANNEXE 2 – Goldschmidt 2021

Présentation orale lors du congrès Goldschmidt (Lyon, France), du 4 au 9 juillet 2021.

Résumé soumis :

Goldschmidt 2021 Abstract
https://doi.org/10.7185/gold2021.5453

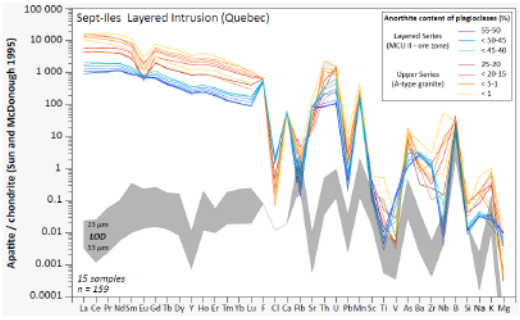

Developing apatite as an indicator mineral for exploration: insights from layered intrusions

MARIE A. KIEFFER[1] AND SARAH A. S. DARE[2]

[1]University of Quebec in Chicoutimi
[2]Universite du Quebec a Chicoutimi (UQAC)
Presenting Author: marie.kieffer1@uqac.ca

Apatite is a weathering-resistant mineral that occurs in most igneous, sedimentary, metamorphic and hydrothermal rocks. Trace element chemistry in apatite is typically used for tracking magmatic processes [1] and as a provenance indicator for sedimentary studies [2]. Other studies also show the potential of apatite as an indicator mineral for mineral exploration [3, 4]. However, these studies mainly focus on felsic rocks and hydrothermal deposits. Apatite from mafic layered intrusions – which are important hosts of Fe-Ti-V-P resources – have not been included in previous discrimination diagrams. Additionally, several processes may influence the trace element composition of apatite during and/or after its crystallisation (e.g., subsolidus reequilibration). It is not yet known if their influence on apatite chemistry is significant, nor if they could hinder or help the use of apatite as an indicator mineral for exploration purposes. This study uses a petrogenetic approach to improve our understanding of apatite chemistry from layered intrusions, thus enlarging its use as a provenance indicator. Microprobe (Laval University) and LA-ICP-MS analyses (LabMaTer, UQAC) are used to obtain, respectively, the volatile content and full suite of trace elements of apatites from mafic layered intrusions (e.g. Sept-Iles, Quebec; Bushveld, South Africa), as well as granites (Sept-Iles granites, as the most differentiated part of the intrusion, and others). These new data are also compared to a compilation of apatites from other mafic and felsic rocks. Our results show that apatite from mafic layered intrusions display a distinct signature from apatite in felsic rocks (e.g. lower REE, V or Mg, and higher Th, U or As), as a result of protracted fractional crystallisation (Fig. 1). Apatites from the mineralised (oxide-apatite) parts of layered intrusions are chemically different (e.g. more Mn) to apatite from unmineralised mafic parts. In addition, elements such as U, Th or Pb in apatite can reflect crustal contamination of the host intrusions.

[1] Tollari *et al.* (2008), *Chemical Geology* **252** (3-4), 180-190. [2] O'Sullivan *et al.* (2020), *Earth-Science Reviews* **201**, 103044. [3] Belousova *et al.* (2002), *Journal of Geochemical Exploration* **76**, 45-69. [4] Mao *et al.* (2016), *Economic Geology* **111** (5), 1187-1222.

ANNEXE 3 – 16th biennial meeting SGA 2022

Présentation orale lors du 16th biennial meeting SGA 2022 (Rotorua, Nouvelle-Zélande), du 28 au 31 mars 2022.

Résumé soumis :

Trace elements in apatite record differentiation processes in Sept-Iles mafic layered intrusion

Marie A. Kieffer, Sarah A.S. Dare*
Department of Applied Sciences, University of Quebec in Chicoutimi (UQAC), Chicoutimi, QC, Canada
**Canada Research Chair in Geochemistry Applied to Ore Deposits*

Olivier Namur
Department of Earth and Environmental Sciences, KU Leuven, Heverlee, Belgium

Apatite is a weathering-resistant mineral that occurs in most igneous, sedimentary, metamorphic and hydrothermal rocks. Trace element chemistry in apatite is typically used to track magmatic processes, as a provenance indicator for sedimentary studies, and has the potential as an indicator mineral for mineral exploration. Although several processes may influence the trace element content of apatite during and/or after its crystallisation (such as reaction with trapped liquid, subsolidus reequilibration), it is not yet known if their influence on apatite chemistry is significant. To better constrain these processes, we have determined the chemical composition of apatite (by electron microprobe and LA-ICP-MS) throughout the whole sequence of the mafic layered intrusion of Sept Iles (Québec, Canada) where the process of differentiation (fractional crystallization, magma mixing, contamination and immiscibility) are well-constrained based on whole rock, mineral chemistry (e.g. plagioclase, olivine, pyroxenes and iron-oxides) and Sr isotopes. Apatite occurs as a cumulus phase at the top of each megacyclic unit, but only one of those is mineralized (Critical Zone, up to 27% vol. apatite) with evidence for liquid immiscibility (e.g. Fe-rich and Si-rich silicate melts). In this study, we demonstrate that apatite in the Sept-Iles layered intrusion not only records the bulk fractional crystallization (increase of Th, U, Ba and REE) but that the crystallization of apatite, when in a sufficient amount, may also fractionate the REE content of the melt, affecting subsequent apatite REE patterns. Furthermore, apatite can indicate magma contamination using Pb, Th and U. Intercumulus apatite is distinguished from cumulus apatite using different elements, such as a higher Cl or V content. Improving our understanding of apatite chemistry from layered intrusions – which are important hosts of Fe-Ti-V-P resources – enlarges its use as an indicator mineral for exploration purposes.

ANNEXE 4 – Québec Mines+Énergie 2022, Défi de la recherche en géosciences

Affiche et communication orale présentées au Défi de la recherche en géosciences, lors du congrès Québec Mines+Énergie 2022 (Québec, Canada), du 21 au 24 novembre 2022.

Résumé soumis :

Les apatites des intrusions mafiques litées : de l'enregistrement des processus magmatiques … à leur utilisation pour l'exploration de minéralisations en Fe-Ti-P

Marie Kieffer (DSA, UQAC), Sarah Dare (DSA, UQAC) et Olivier Namur (KU Leuven)

L'apatite est un minéral résistant à l'altération et commun dans la majorité des roches ignées, sédimentaires, métamorphiques et hydrothermales. Sa chimie est communément utilisée afin de tracer des processus magmatiques, mais aussi comme indicateur de provenance pour des études sédimentaires. L'apatite a également le potentiel pour être employée en tant que minéral indicateur pour l'exploration car sa signature chimique semble varier selon les types de gisements desquels elle provient. Toutefois, les apatites des intrusions mafiques litées, hôtes d'importantes ressources en Fe-Ti-V-P, ne sont à ce jour pas prises en compte dans les diagrammes de discrimination. Cette étude applique donc une approche pétrogénétique visant à améliorer notre compréhension des variations chimiques de l'apatite dans les intrusions mafiques litées, afin de développer leur utilisation comme indicateur de provenance et pour l'exploration.

La Suite Intrusive de Sept-Iles (Québec, Canada) comporte l'une des plus volumineuses intrusions mafiques litées au monde. Elle constitue un laboratoire naturel pour étudier la différenciation d'un magma ferrobasaltique ayant produit un magma felsique par cristallisation fractionnée extrême. L'immiscibilité a joué un rôle prépondérant dans la formation de l'horizon minéralisé en Fe-Ti-P au sommet de la séquence mafique (Zone Critique). La composition chimique détaillée des apatites provenant de la Série Litée mafique et de la Série Supérieure felsique a été déterminée par des analyses à la microsonde et au LA-ICP-MS (31 éléments; LabMaTer, UQAC). Les résultats montrent que les apatites cumulus enregistrent les changements compositionnels du magma ferrobasaltique lors de son fractionnement, depuis les roches mafiques vers les roches felsiques (enrichissement en éléments de terres rares, Th, U, K, Pb, et appauvrissement en Sr, Ba, V et Mg, dans les apatites). De plus, les différences chimiques entre les apatites des niveaux riches et pauvres en Fe-Ti-P de la Zone Critique sont attribuées à la répartition des éléments traces entre deux liquides silicatés immiscibles riches en Fe et en Si, ainsi qu'aux différentes proportions cotectiques d'apatite qui cristallisent à partir de ces liquides (calculées à 5 à 8 % et 1 %, respectivement). L'abondance d'apatite (7 à 36 vol.%) dans les niveaux riches en Fe-Ti-P est alors expliquée par le tri et l'accumulation des cristaux. Enfin, la meilleure compréhension de la chimie des apatites à Sept-Iles a permis de proposer une nouvelle série de diagrammes de discrimination (mafique vs. felsique, cumulus vs. Intercumulus), prouvant le potentiel de l'apatite comme minéral indicateur pour l'exploration de minéralisations en Fe-Ti-P associées aux intrusions mafiques litées.

DSA : Département des Sciences Appliquées (Canada)

UQAC : Université du Québec à Chicoutimi (Canada)

KU Leuven : Katholieke Universiteit Leuven (Belgique)

ANNEXE 5 – GAC-MAC Sudbury 2023

Présentation orale lors du congrès GAC-MAC Sudbury 2023 (Sudbury, Canada), du 24 au 27 mai 2023. Ne pouvant être présente, ma directrice de thèse Sarah Dare a présenté mes travaux de recherche.

Résumé soumis :

Trace elements in apatite record differentiation processes in Sept-Iles mafic layered intrusion: implications for mineral exploration of Fe-Ti-P mineralisation

Kieffer, M.A.[1], Dare, S.A.S.[1] and Namur, O.[2]

[1]Department of Applied Sciences, University of Quebec in Chicoutimi (UQAC), 555 Boulevard de l'Université, Chicoutimi G7H 2B1, QC, Canada, marie.kieffer1@uqac.ca
[2]Department of Earth and Environmental Sciences, KU Leuven, 3000 Leuven, Belgium

---

Apatite is a weathering-resistant mineral that can be found in most igneous, sedimentary, metamorphic and hydrothermal rocks. Its chemistry is commonly used to trace magmatic processes [1], but also as a provenance indicator for sedimentary studies [2]. As its chemical composition varies according to deposit type, apatite also has the potential to be used as an indicator mineral for exploration. However, apatite from mafic layered intrusions, which are host to Fe-Ti-V-P resources, are not yet taken into account by existing discrimination diagrams. Our study uses a petrogenetic approach aiming to better understand chemical variations of apatite within mafic layered intrusions, and develop the use of apatite as a provenance indicator and as an indicator mineral for exploration [3].

Sept-Iles Intrusive Suite (Quebec, Canada) is one of the world's most voluminous mafic layered intrusions. It represents a natural laboratory to study the differentiation of a ferrobasaltic melt that evolved to a felsic magma by extreme fractional crystallisation [4]. Immiscibility [5] played an important role in the formation of the Fe-Ti-P mineralisation at the top of the mafic sequence of Megacyclic Unit II (Critical Zone). Detailed chemical composition of apatite from the mafic Layered Series and from the felsic Upper Series was determined by electron microprobe analyses and LA-ICP-MS (31 trace elements; LabMaTer, UQAC). Results show that cumulus apatite records the compositional variations of the ferrobasaltic magma during its fractionation from the mafic towards the felsic rocks (enrichment in rare earth elements, Th, U, K, Pb, and depletion in Sr, Ba, V and Mg, in apatite; Figure 1. Chemical differences between apatite from the Fe-Ti-P-rich and -poor layers of the Critical Zone is attributed to the partitioning of trace elements between two immiscible silicate melts, as well as to the different cotectic proportions of apatite that crystallises from these melts (calculated at 5 to 8 % and 1 %, respectively; Figure 2). The abundance of apatite (7 to 36 vol.%) in Fe-Ti-P-rich layers is explained by sorting and crystal settling. A better understanding of Sept-Iles apatite chemical composition allowed us to propose new discrimination diagrams (mafic vs. felsic, cumulus vs. intercumulus: [3]), which prove the potential of apatite as an indicator mineral for the exploration of Fe-Ti-P mineralisation associated with mafic layered intrusions.

References:

[1] Pedersen J.M. et al. (2021) Contrib. to Mineral. Petrol. 176: 102

[2] O'Sullivan G. et al. (2020) Earth Sci Rev. 201: 103044

[3] Kieffer M. A. et al. (2023) Geochim. Cosmochim. Acta 342: 169-197

[4] Namur O. et al. (2011) J Petrol 52: 487-539

[5] Charlier B. et al. (2011) Geology 39: 907-910

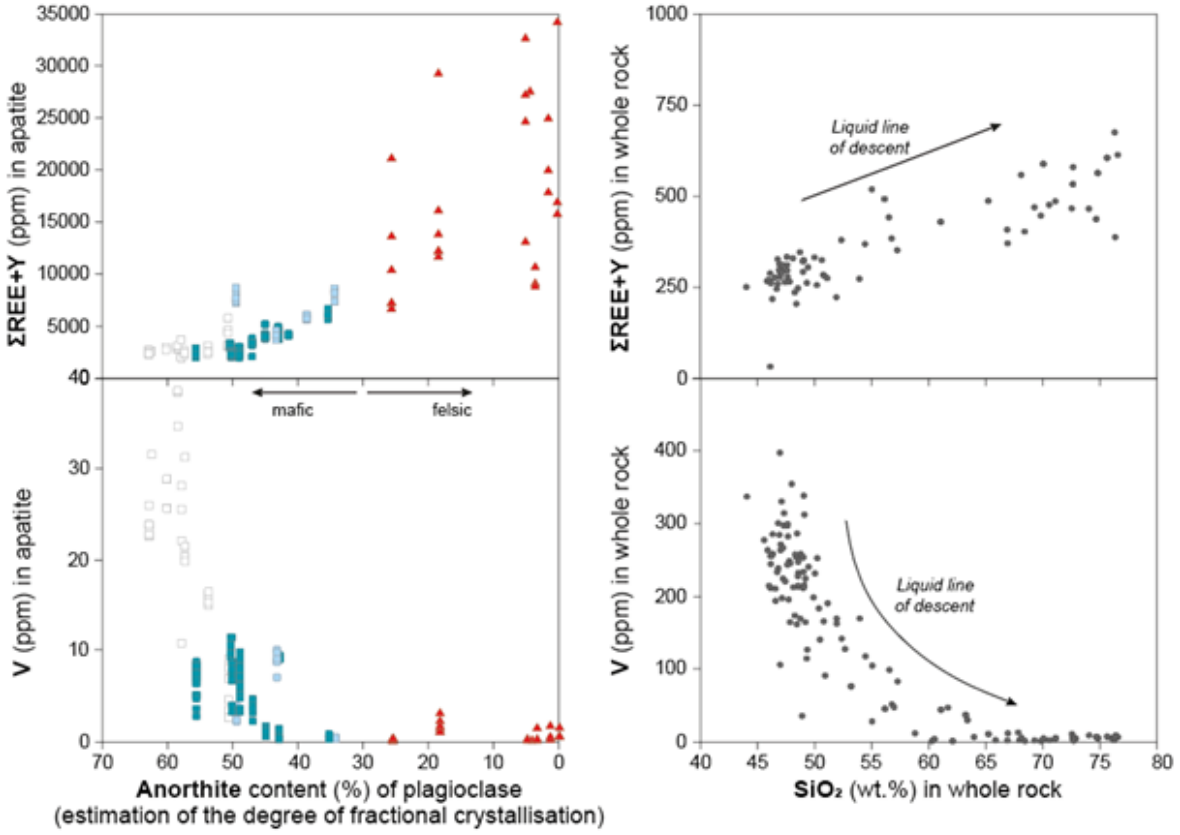

Figure 1: Evolution of REE and V in intercumulus and cumulus apatite from the mafic rocks of MCU II and accessory apatite from the felsic rocks (Upper Series and Pointe du Criard sill) with anorthite content of associated plagioclase (left). They record the same same evolutionary trends as the Sept-Iles liquid line of descent determined by Namur et al. (2011).

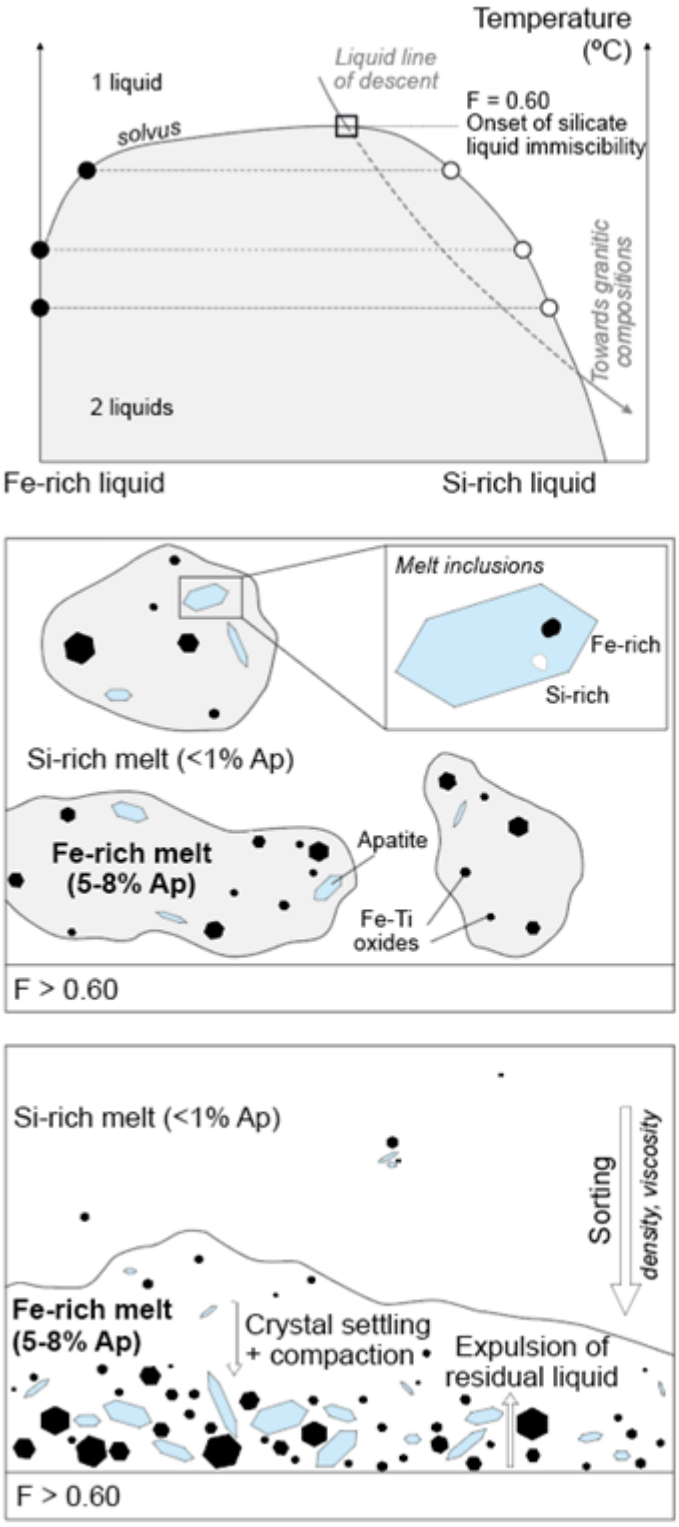

Figure 2: Proposed modelled for the formation of Fe-Ti-P-rich and -poor layers based on apatite trace element composition

ANNEXE 6 – Wager & Brown Layered Intrusions Workshop IV

Présentation orale lors du congrès Wager & Brown Layered Intrusions Workshop IV (Cardiff, Pays de Galles, Royaume-Uni), du 30 juin au 2 juillet 2023.

Résumé soumis :

Apatite chemistry as a petrogenetic indicator for mafic layered intrusions

Kieffer, M.A.[1], Dare, S.A.S.[2], Namur, O.[3], and Mansur, E.T.[4]

[1]Department of Applied Sciences, University of Quebec in Chicoutimi (UQAC), 555 Boulevard de l'Université, Chicoutimi, G7H 2B1, QC, Canada. marie.kieffer1@uqac.ca
[2]Canada Research Chair in Geochemistry Applied to Ore Deposits, Department of Applied Sciences, University of Quebec in Chicoutimi (UQAC), 555 Boulevard de l'Université, Chicoutimi, G7H 2B1, QC, Canada.
[3]Department of Earth and Environmental Sciences, KU Leuven, 3000 Leuven, Belgium
[4]Geological Survey of Norway, PO Box 6315 Torgarden, Trondheim, 7491, Norway

---

Apatite is a weathering-resistant mineral that can be found in most igneous, sedimentary, metamorphic and hydrothermal rocks, and in a wide range of magmatic-hydrothermal deposits [1]. In mafic layered intrusions, apatite is present either as a cumulus phase, which can form Fe-Ti-P mineralisation in the more evolved parts of some intrusions [2], or as an intercumulus (i.e., interstitial) phase in the more primitive portions that can be associated with Fe-Ti-V or Ni-Cu-PGE [7] mineralisation. Apatite can incorporate a wide variety of trace elements that are closely related to its geological environment of formation. Thus, its volatile and trace element chemistry is commonly used as a petrogenetic indicator [3,4], but also as a provenance indicator for sedimentary studies [9] with potential for using apatite as an indicator mineral for exploration [5]. There is a limited amount of apatite trace element data available in the literature for mafic layered intrusions, and the full suite of trace elements is not systematically analysed. In this study, we investigate the variation in trace elements in apatite from different mafic intrusions and identify the key parameters controlling significant and systematic variations.

Mafic layered intrusions constitute a natural laboratory to investigate petrogenetic processes using trace element variations in apatite chemistry. In general, these intrusions are related to large igneous provinces [14,15], whereby the mantle-derived melts are produced by high degrees of partial melting [16], producing picritic, tholeiitic and komatiitic primary melts. However, there is a wide range of parameters that can affect the chemistry of the magma, such as composition of the primary melt (i.e., depth of partial melting, oxygen fugacity), or the amount of crustal contamination, by a silicic or carbonaceous material, upon magma emplacement in the upper crust [17,18]. Apatite saturation occurs at different degrees of melt evolution [19,20,21,22], with the crystallisation history of the intrusion depending on the parental magma characteristics and its intensive conditions of differentiation.

In this study, we use a comprehensive dataset of analyses of cumulus and intercumulus apatite from a variety of mafic layered intrusions (i.e., Skaergaard intrusion, Greenland; Sept-Iles Intrusive Suite, Canada; Bushveld Complex, South Africa; Hongge, Taihe and Panzhihua intrusions, China) and the differentiated impact melt sheet of Sudbury Igneous Complex (Canada) to show that apatite chemistry is a petrogenetic indicator of differences in the depth of partial melting, magma contamination with a silicic component, fractional crystallisation of plagioclase, and magma mixing. The dataset (determined in this study and from the literature) comprises electron microprobe (EMPA) for the volatile elements, laser ablation inductively coupled plasma mass spectrometry (LA-ICP-MS) analyses for a full suite of trace elements, along with in-situ analyses of Sr isotopes in apatite by LA-multicollector-ICP-MS). For the first time, we show that high $(La/Nd)_N$, Th, U, Pb, As, and $(^{87}Sr/^{86}Sr)_{initial}$ in apatite are related to crustal contamination with silicic crust, as recorded by cumulus apatite from Bushveld and Sudbury (Figure 1). An elevated $(Gd/Yb)_N$ ratio indicates melting of a source deep enough to retain Yb in garnet, as shown by the Emeishan intrusions of Hongge, Taihe and Panzhihua, related to picritic parental melts (Figure 1a). We also confirm that increasingly negative Eu anomalies and decreasing Sr/Y ratios in apatite are indicators of the fractional crystallisation of plagioclase, and that high Sr/Y is indicative of early apatite saturation (Figure 2). The reversal to more primitive compositions caused by magma mixing is also recorded in apatite from Sept-Iles, with higher Sr, V, Mg and Sr/Y ratio, and lower REE+Y, As and Na concentration in apatite following magma replenishment.

References:

[1] Mao M et al. (2016) Econ Geol 111:1187-1122

[2] Tollari N. et al. (2008) Chem Geol 252:180-190

[3] Belousova EA et al. (2002) J Geochem Explor 76:45-69

[4] Pedersen JM et al. (2021) Contrib Miner Petrol 176:106

[5] O'Sullivan G et al. (2020) Earth Sci Rev 201:103044

Figure 1 Cumulus apatite from olivine- and clinopyroxene-bearing (grey) and orthopyroxene-bearing (green) intrusions show (a) evidence of crustal contamination and depth of partial melting, using $(La/Nd)_N$ and $(Gd/Yb)_N$ ratios, and (b) evidence of crustal contamination, using $(^{87}Sr/^{86}Sr)_i$ as a function of $(La/Nd)_N$.

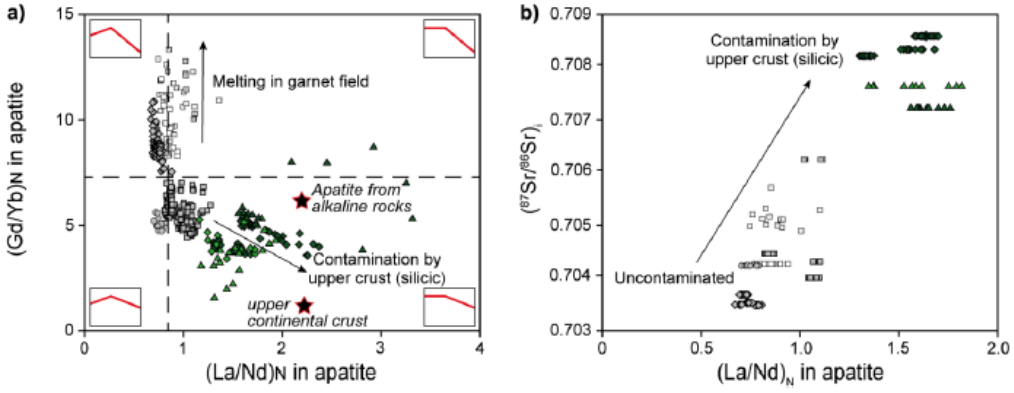

Figure 2 Eu anomaly versus Sr/Y binary plot for cumulus apatite from (a) Sept-Iles Intrusive Suite and Skaergaard (b) other mafic layered intrusions. Cumulus apatite define a trend corresponding to plagioclase fractionation.

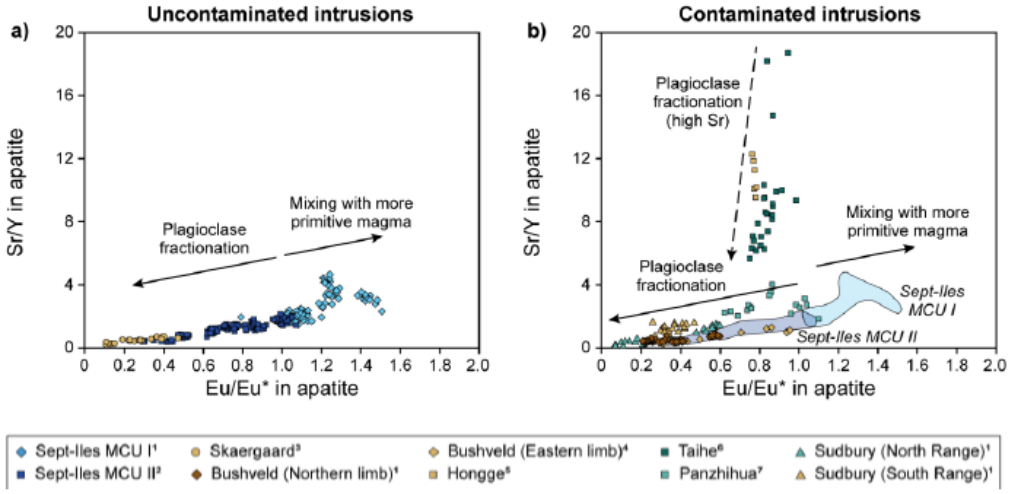

ANNEXE 7 – 14th International Platinum Symposium 2023

Affiche présentée lors du congrès 14th International Platinum Symposium (Cardiff, Royaume-Uni), du 4 au 7 juin 2023.

Résumé soumis :

Trace elements in apatite record differentiation processes in Sept-Iles mafic layered intrusion: implications for mineral exploration of Fe-Ti-P mineralisation

Kieffer, M.A.[1], Dare, S.A.S.[1], Namur, O.[2]

[1]Department of Applied Sciences, University of Quebec in Chicoutimi (UQAC), 555 Boulevard de l'Université, Chicoutimi G7H 2B1, QC, Canada, marie.kieffer1@uqac.ca
[2]Department of Earth and Environmental Sciences, KU Leuven, 3000 Leuven, Belgium

---

Apatite is a weathering-resistant mineral that can be found in most igneous, sedimentary, metamorphic and hydrothermal rocks. Its chemistry is commonly used to trace magmatic processes [1], but also as a provenance indicator for sedimentary studies [2]. As its chemical composition varies according to deposit type, apatite also has the potential to be used as an indicator mineral for exploration. However, apatite from mafic layered intrusions, which are host to Fe-Ti-V-P resources, are not yet taken into account by existing discrimination diagrams. Our study uses a petrogenetic approach aiming to better understand chemical variations of apatite within mafic layered intrusions, and develop the use of apatite as a provenance indicator and as an indicator mineral for exploration [3].

Sept-Iles Intrusive Suite (Quebec, Canada) is one of the world's most voluminous mafic layered intrusions. It represents a natural laboratory to study the differentiation of a ferrobasaltic melt that evolved to a felsic magma by extreme fractional crystallisation [4]. Immiscibility between Si- and Fe-rich silicate melts [5] played an important role in the formation of the Fe-Ti-P mineralisation at the top of the mafic sequence of Megacyclic Unit II (Critical Zone). Detailed chemical composition of apatite from the mafic Layered Series and from the felsic Upper Series was determined by electron microprobe analyses and LA-ICP-MS (31 trace elements; LabMaTer, UQAC). Results show that cumulus apatite records the compositional variations of the ferrobasaltic magma during its fractionation from the mafic towards the felsic rocks (enrichment in rare earth elements, Th, U, K, Pb, and depletion in Sr, Ba, V and Mg, in apatite; Figure 1). Chemical differences between apatite from the Fe-Ti-P-rich and -poor layers of the Critical Zone is attributed to the partitioning of trace elements between two immiscible silicate melts, as well as to the different cotectic proportions of apatite that crystallise from these melts (calculated at 5 to 8 % and 1 %, respectively; Figure 2). The abundance of apatite (7 to 36 vol.%) in Fe-Ti-P-rich layers is explained by sorting and crystal settling. A better understanding of Sept-Iles apatite chemical composition allowed us to propose new discrimination diagrams [3] to separate (1) apatite crystallising from mafic and felsic melts, using REE+Y, Sr/Y, and the Eu anomaly in apatite; and (2) cumulus from intercumulus apatite, using volatile elements (Cl/F vs. F) or trace elements (Th/Lu vs. V) in apatite from mafic rocks (Figure 3). These diagrams prove the potential of apatite as an indicator mineral for the exploration of Fe-Ti-P mineralisation associated with mafic layered intrusions.

References:

[1] Pedersen J.M. et al. (2021) Contrib. to Mineral. Petrol. 176: 102
[2] O'Sullivan G. et al. (2020) Earth Sci Rev. 201: 103044
[3] Kieffer M. A. et al. (2023) Geochim. Cosmochim. Acta 342: 169-197
[4] Namur O. et al. (2011) J Petrol 52: 487-539
[5] Charlier B. et al. (2011) Geology 39: 907-910

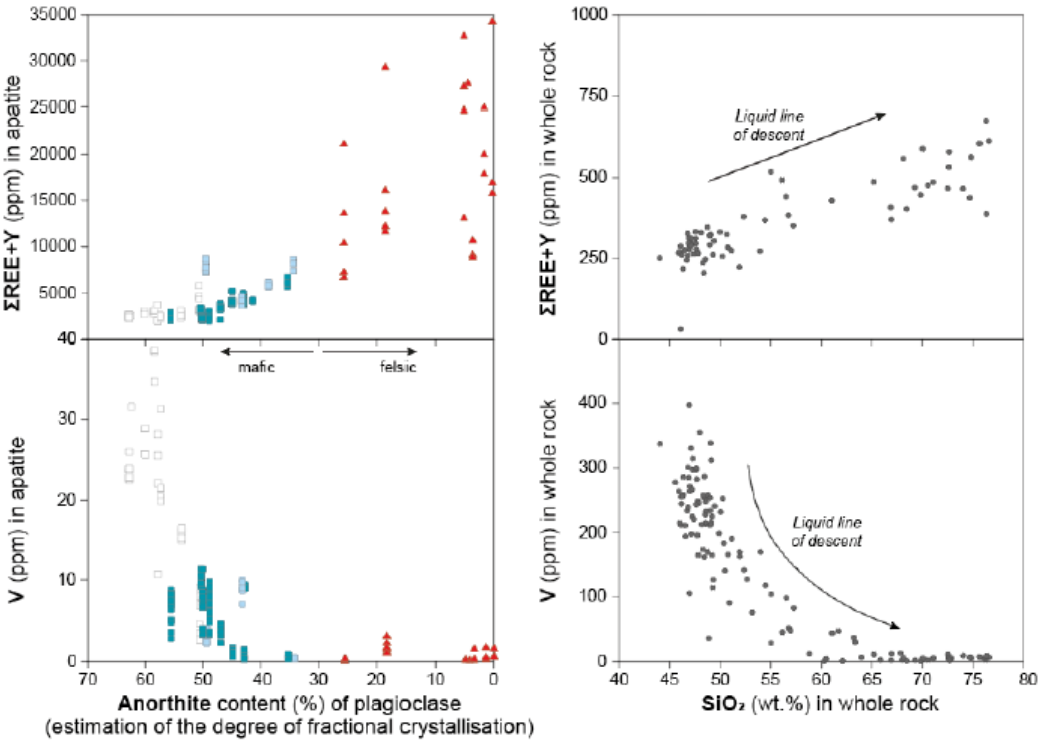

Figure 1: Evolution of REE and V in intercumulus (open squares) and cumulus apatite (solid squares) from the mafic rocks of MCU II and accessory apatite (red triangles) from the felsic rocks (Upper Series and Pointe du Criard sill) with anorthite content of associated plagioclase (left; [3]). They record the same same evolutionary trends as the Sept-Iles liquid line of descent determined by Namur et al. [4].

ANNEXE 8 – 14th International Platinum Symposium 2023

Communication orale lors du congrès 14th International Platinum Symposium (Cardiff, Royaume-Uni), du 4 au 7 juin 2023

Résumé soumis :

Apatite chemistry as a petrogenetic indicator for mafic layered intrusions

Kieffer, M.A.[1], Dare, S.A.S.[2], Namur, O.[3], and Mansur, E.T.[4]

[1]Department of Applied Sciences, University of Quebec in Chicoutimi (UQAC), 555 Boulevard de l'Université, Chicoutimi, G7H 2B1, QC, Canada. marie.kieffer1@uqac.ca
[2]Canada Research Chair in Geochemistry Applied to Ore Deposits, Department of Applied Sciences, University of Quebec in Chicoutimi (UQAC), 555 Boulevard de l'Université, Chicoutimi, G7H 2B1, QC, Canada.
[3]Department of Earth and Environmental Sciences, KU Leuven, 3000 Leuven, Belgium
[4]Geological Survey of Norway, PO Box 6315 Torgarden, Trondheim, 7491, Norway

---

Apatite is a weathering-resistant mineral that can be found in most igneous, sedimentary, metamorphic and hydrothermal rocks, and in a wide range of magmatic-hydrothermal deposits [1]. In mafic layered intrusions, apatite is present either as a cumulus phase, which can form Fe-Ti-P mineralisation in the more evolved parts of some intrusions [2], or as an intercumulus (i.e., interstitial) phase in the more primitive portions that can be associated with Fe-Ti-V or Ni-Cu-PGE [7] mineralisation. Apatite can incorporate a wide variety of trace elements that are closely related to its geological environment of formation. Thus, its volatile and trace element chemistry is commonly used as a petrogenetic indicator [3,4], but also as a provenance indicator for sedimentary studies [9] with potential for using apatite as an indicator mineral for exploration [5]. There is a limited amount of apatite trace element data available in the literature for mafic layered intrusions, and the full suite of trace elements is not systematically analysed. In this study, we investigate the variation in trace elements in apatite from different mafic intrusions and identify the key parameters controlling significant and systematic variations.

Mafic layered intrusions constitute a natural laboratory to investigate petrogenetic processes using trace element variations in apatite chemistry. In general, these intrusions are related to large igneous provinces [14,15], whereby the mantle-derived melts are produced by high degrees of partial melting [16], producing picritic, tholeiitic and komatiitic primary melts. However, there is a wide range of parameters that can affect the chemistry of the magma, such as composition of the primary melt (i.e., depth of partial melting, oxygen fugacity), or the amount of crustal contamination, by a silicic or carbonaceous material, upon magma emplacement in the upper crust [17,18]. Apatite saturation occurs at different degrees of melt evolution [19,20,21,22], with the crystallisation history of the intrusion depending on the parental magma characteristics and its intensive conditions of differentiation.

In this study, we use a comprehensive dataset of analyses of cumulus and intercumulus apatite from a variety of mafic layered intrusions (i.e., Skaergaard intrusion, Greenland; Sept-Iles Intrusive Suite, Canada; Bushveld Complex, South Africa; Hongge, Taihe and Panzhihua intrusions, China) and the differentiated impact melt sheet of Sudbury Igneous Complex (Canada) to show that apatite chemistry is a petrogenetic indicator of differences in the depth of partial melting, magma contamination with a silicic component, fractional crystallisation of plagioclase, and magma mixing. The dataset (determined in this study and from the literature) comprises electron microprobe (EMPA) for the volatile elements, laser ablation inductively coupled plasma mass spectrometry (LA-ICP-MS) analyses for a full suite of trace elements, along with in-situ analyses of Sr isotopes in apatite by LA-multicollector-ICP-MS). For the first time, we show that high $(La/Nd)_N$, Th, U, Pb, As, and $(^{87}Sr/^{86}Sr)_{initial}$ in apatite are related to crustal contamination with silicic crust, as recorded by cumulus apatite from Bushveld and Sudbury (Figure 1). An elevated $(Gd/Yb)_N$ ratio indicates melting of a source deep enough to retain Yb in garnet, as shown by the Emeishan intrusions of Hongge, Taihe and Panzhihua, related to picritic parental melts (Figure 1a). We also confirm that increasingly negative Eu anomalies and decreasing Sr/Y ratios in apatite are indicators of the fractional crystallisation of plagioclase, and that high Sr/Y is indicative of early apatite saturation (Figure 2). The reversal to more primitive compositions caused by magma mixing is also recorded in apatite from Sept-Iles, with higher Sr, V, Mg and Sr/Y ratio, and lower REE+Y, As and Na concentration in apatite following magma replenishment.

References:

[1] Mao M et al. (2016) Econ Geol 111:1187-1122

[2] Tollari N. et al. (2008) Chem Geol 252:180-190

[3] Belousova EA et al. (2002) J Geochem Explor 76:45-69

[4] Pedersen JM et al. (2021) Contrib Miner Petrol 176:106

[5] O'Sullivan G et al. (2020) Earth Sci Rev 201:103044

Figure 1 Cumulus apatite from olivine- and clinopyroxene-bearing (grey) and orthopyroxene-bearing (green) intrusions show (a) evidence of crustal contamination and depth of partial melting, using $(La/Nd)_N$ and $(Gd/Yb)_N$ ratios, and (b) evidence of crustal contamination, using $(^{87}Sr/^{86}Sr)_i$ as a function of $(La/Nd)_N$.

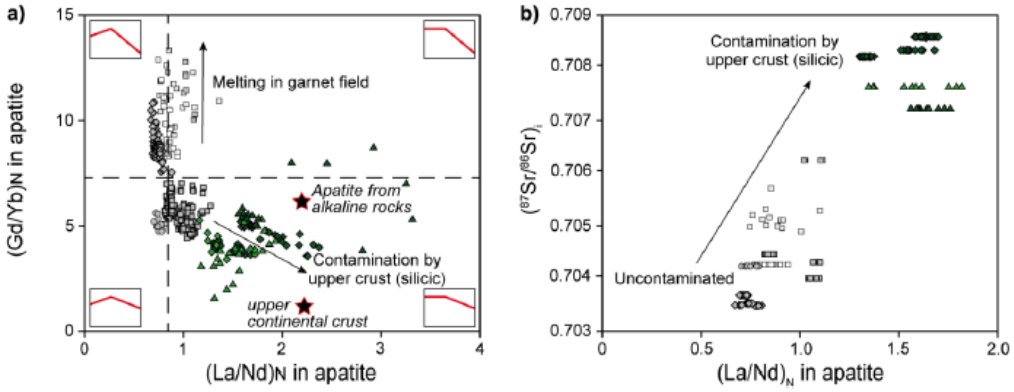

Figure 2 Eu anomaly versus Sr/Y binary plot for cumulus apatite from (a) Sept-Iles Intrusive Suite and Skaergaard (b) other mafic layered intrusions. Cumulus apatite define a trend corresponding to plagioclase fractionation.

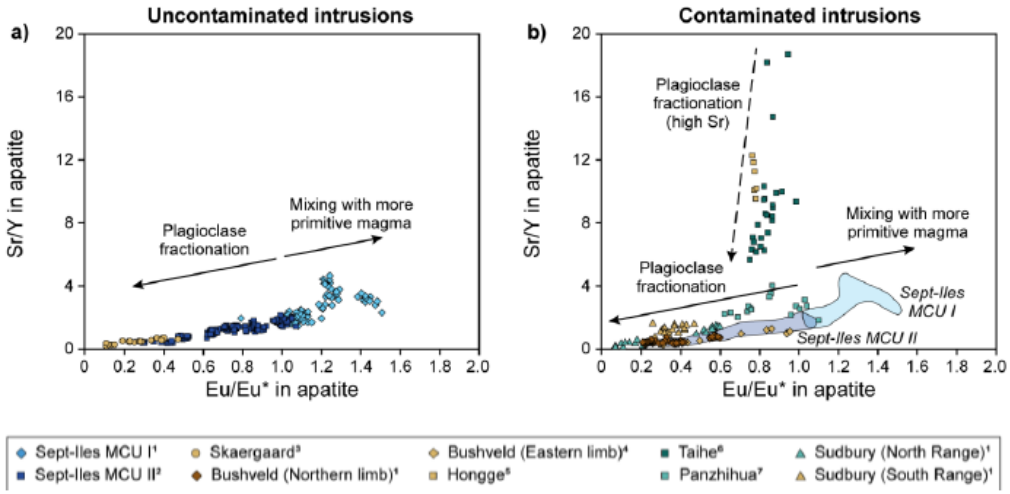

ANNEXE 9 – Québec Mines+Énergie 2023, Défi de la recherche en géosciences

Affiche et communication orale présentées au Défi de la recherche en géosciences, lors du congrès Québec Mines+Énergie 2023 (Québec, Canada), du 20 au 23 novembre 2023.

Résumé soumis :

Apatite, exploration minérale et études de provenance:
Identification de la signature des apatites dans les granites de type I, A et S

Marie Kieffer (DSA, UQAC), Sarah Dare (DSA, UQAC) et Marylou Gendron (UQAC; Explo-logik Inc.)

La chimie de l'apatite est communément utilisée afin de tracer son environnement géologique de formation. Il y a donc un intérêt croissant pour développer les apatites détritiques en tant que minéral indicateur pour l'exploration minérale et les études de provenance dans les environnements secondaires (e.g., terrains recouverts par des sédiments glaciaires). En revanche, les études existantes portent directement sur la signature des apatites de différents types de gisements (e.g., porphyre, skarn) et sur la fertilité des intrusions hôtes. Or, avant d'identifier un type de gisement, il est primordial identifier la nature de l'intrusion hôte (e.g., mafique ou felsique) et son environnement tectonique, car cela permet d'orienter l'exploration et d'évaluer la prospectivité d'un secteur à grande échelle. Par exemple, les intrusions mafiques peuvent être associées à des ressources en Fe-Ti-V-P et/ou Ni-Cu-EGP-Cr, tandis plusieurs types de gisements et substances (e.g., Cu, Mo, W, Sn) peuvent être associés aux intrusions felsiques, dépendamment du type de granite (I, S ou A).

Cette étude est la première à créer une base de données d'analyses d'apatites provenant de granites de type I, S et A à l'échelle mondiale. Cette base de données est constituée de nouvelles analyses réalisées au LA-ICP-MS (LabMaTer, UQAC; n = 273), incluant des granites de type A du Saguenay–Lac-St-Jean, et d'une compilation depuis la littérature (n = 2146). Elle permet d'élaborer un nouveau schéma de classification pour identifier les apatites des différents types de granites (I, S et A) de celles provenant d'autres roches (e.g., mafiques, carbonatites). La classification est conçue en suivant une approche pétrogénétique en 4 étapes : (1) les apatites des intrusions mafiques et felsiques sont isolées de celles provenant d'autres intrusions en utilisant le ratio Sr/Y et les ETR légers; (2) les apatites des intrusions mafiques sont exclues selon leur contenu en ETR+Y, Sr/Y et Eu/Eu*, et au besoin As, $(Gd/Yb)_N$ et Pb+Th+U; (3) les apatites post-archéennes sont séparées de celles archéennes grâce au diagramme $log(La/Yb)_N$ vs. Yb_N; enfin, (4) parmi les apatites provenant d'intrusions felsiques post-archéennes, leur contenu en Mn, V et $(La/Nd)_N$ permet d'identifier les apatites provenant des granites de type I, S et A, auxquels sont associés différents types de minéralisations. Cette étude démontre que l'apatite a toutes les qualités requises pour être utilisée en tant que minéral indicateur pour l'exploration et les études de provenance sédimentaires, afin d'évaluer la prospectivité d'un terrain recouvert par des sédiments glaciaires, particulièrement au Québec.

DSA : Département des Sciences Appliquées (Canada)

UQAC : Université du Québec à Chicoutimi (Canada)

ANNEXE 23

Variation of trace elements in apatite with stratigraphic depth within the Sept-Iles layered intrusion plotted against the concentration of trace elements in apatites from the mafic rocks of MCU II and from the felsic rocks of the Upper Series (US) and Pointe du Criard sill (PdC). Each data point corresponds to an apatite analyse. Black lines link the average composition of each sample

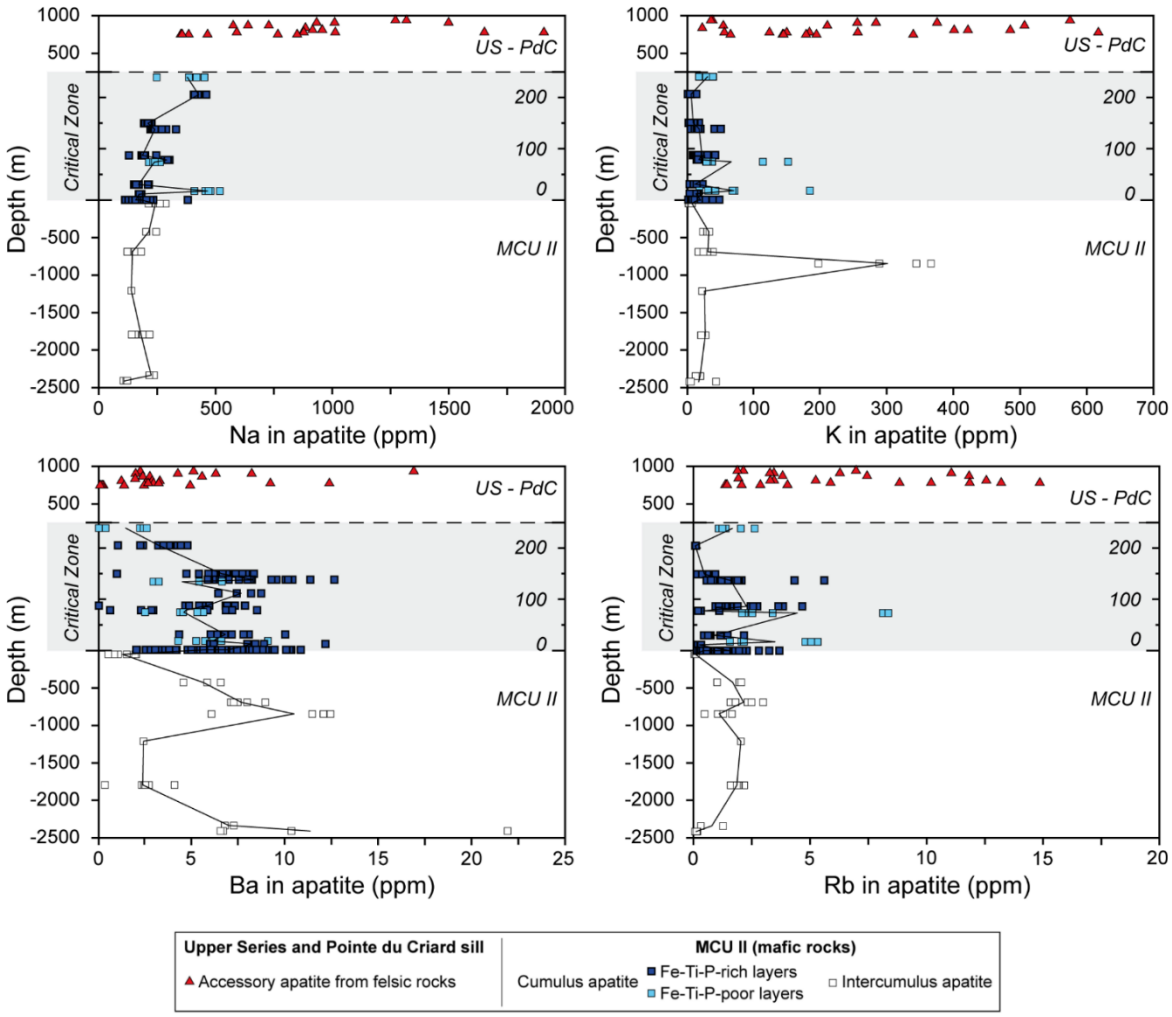

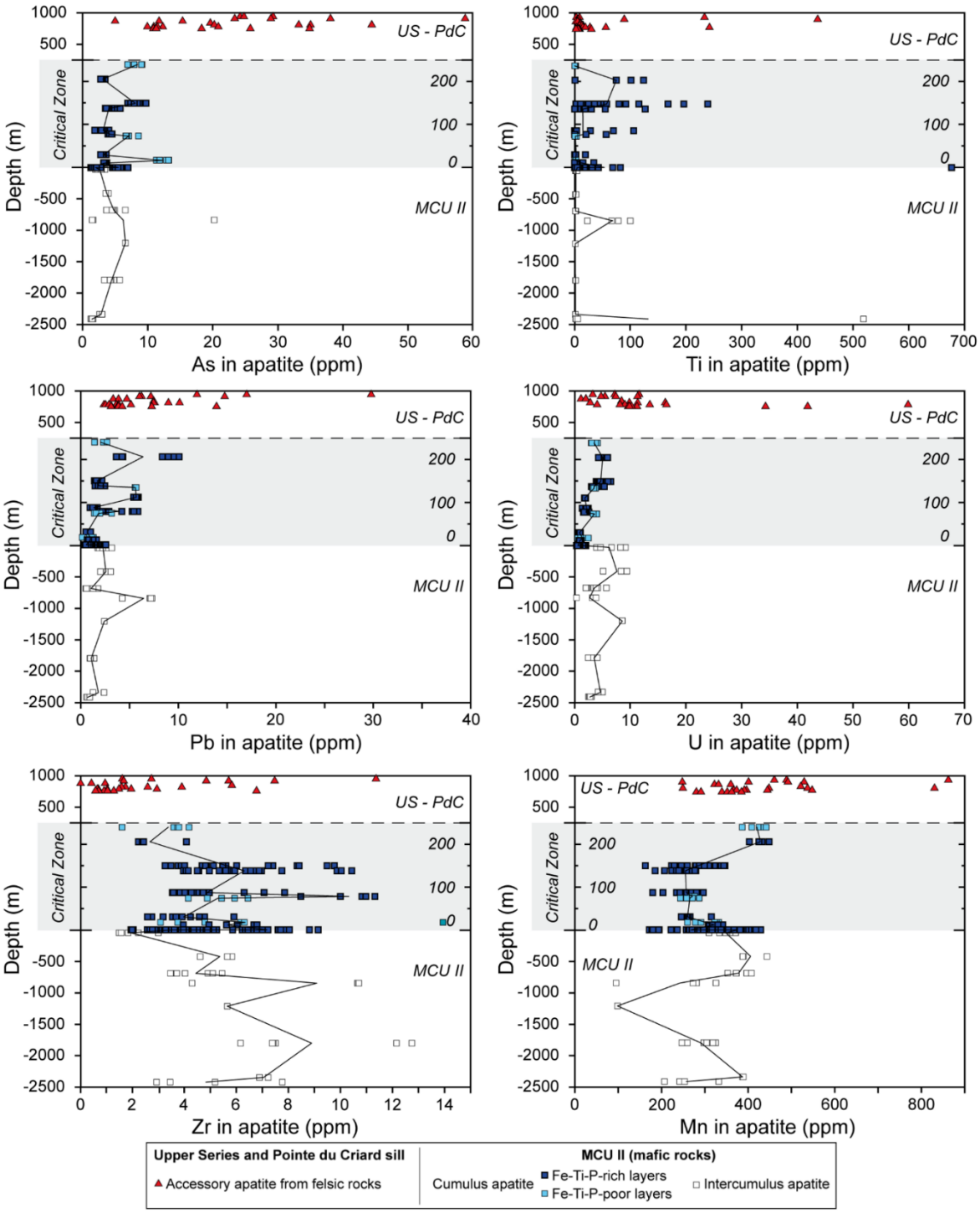
US - PdC
Critical Zone
MCU II
Depth (m)
As in apatite (ppm)
Ti in apatite (ppm)
Pb in apatite (ppm)
U in apatite (ppm)
Zr in apatite (ppm)
Mn in apatite (ppm)
Upper Series and Pointe du Criard sill
Accessory apatite from felsic rocks
MCU II (mafic rocks)
Cumulus apatite
Fe-Ti-P-rich layers
Fe-Ti-P-poor layers
Intercumulus apatite

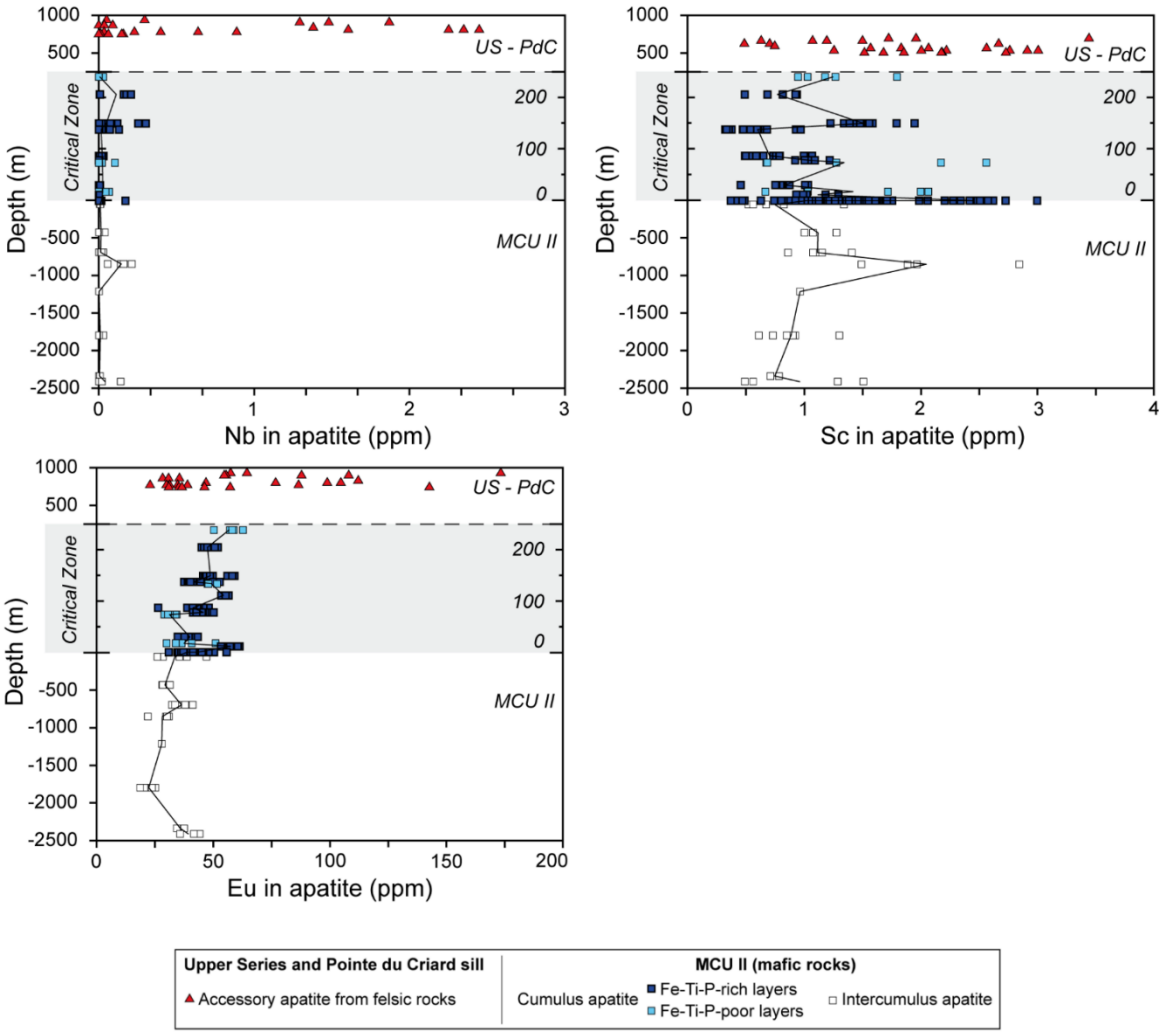
Depth (m)
Nb in apatite (ppm)
Sc in apatite (ppm)
Eu in apatite (ppm)
US - PdC
Critical Zone
MCU II
200
100
0
Upper Series and Pointe du Criard sill
Accessory apatite from felsic rocks
MCU II (mafic rocks)
Cumulus apatite
Fe-Ti-P-rich layers
Fe-Ti-P-poor layers
Intercumulus apatite

ANNEXE 24

Detailed multielement diagrams for: (a) intercumulus apatite from MCU II, (b) cumulus apatite from MCU II (Critical Zone), and (c) apatite from the felsic rocks of the Upper Series and Pointe du Criard sill. Each line corresponds to the average of analyses for a given sample. The grey field corresponds to lower limits of detection determined with a 15 µm beam (top) and 55 µm beam (bottom).

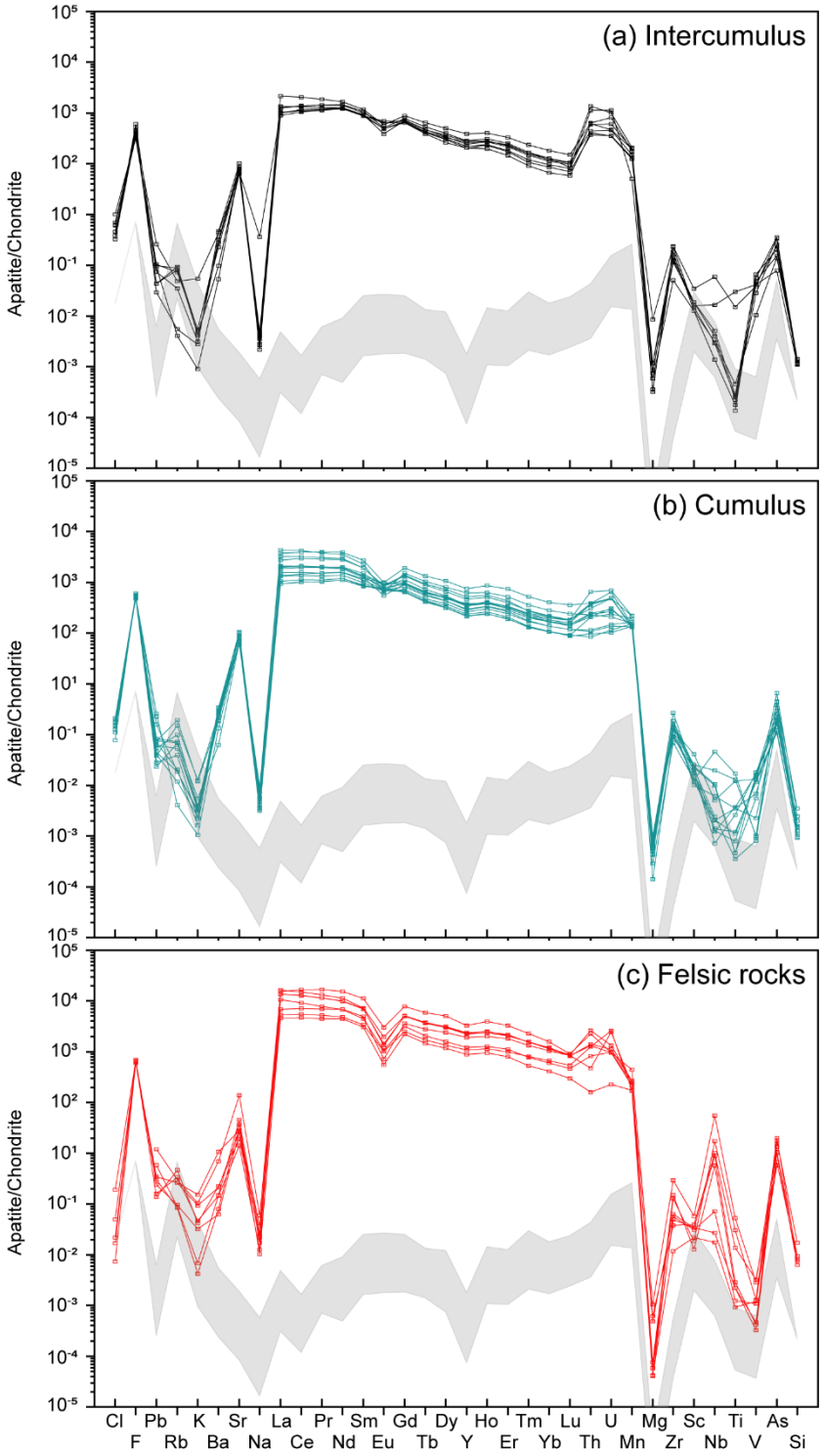

ANNEXE 25

Detailed multielement diagrams for: (a) cumulus apatite from MCU II (Critical Zone), and (b) apatite from the felsic rocks of the Upper Series and Pointe du Criard sill. Each line corresponds to the average of analyses for a given sample. Colors correspond to the anorthite content of plagioclases of each sample (see inset for detailed values). The grey field corresponds to lower limits of detection determined with a 15 µm beam (top) and 55 µm beam (bottom).

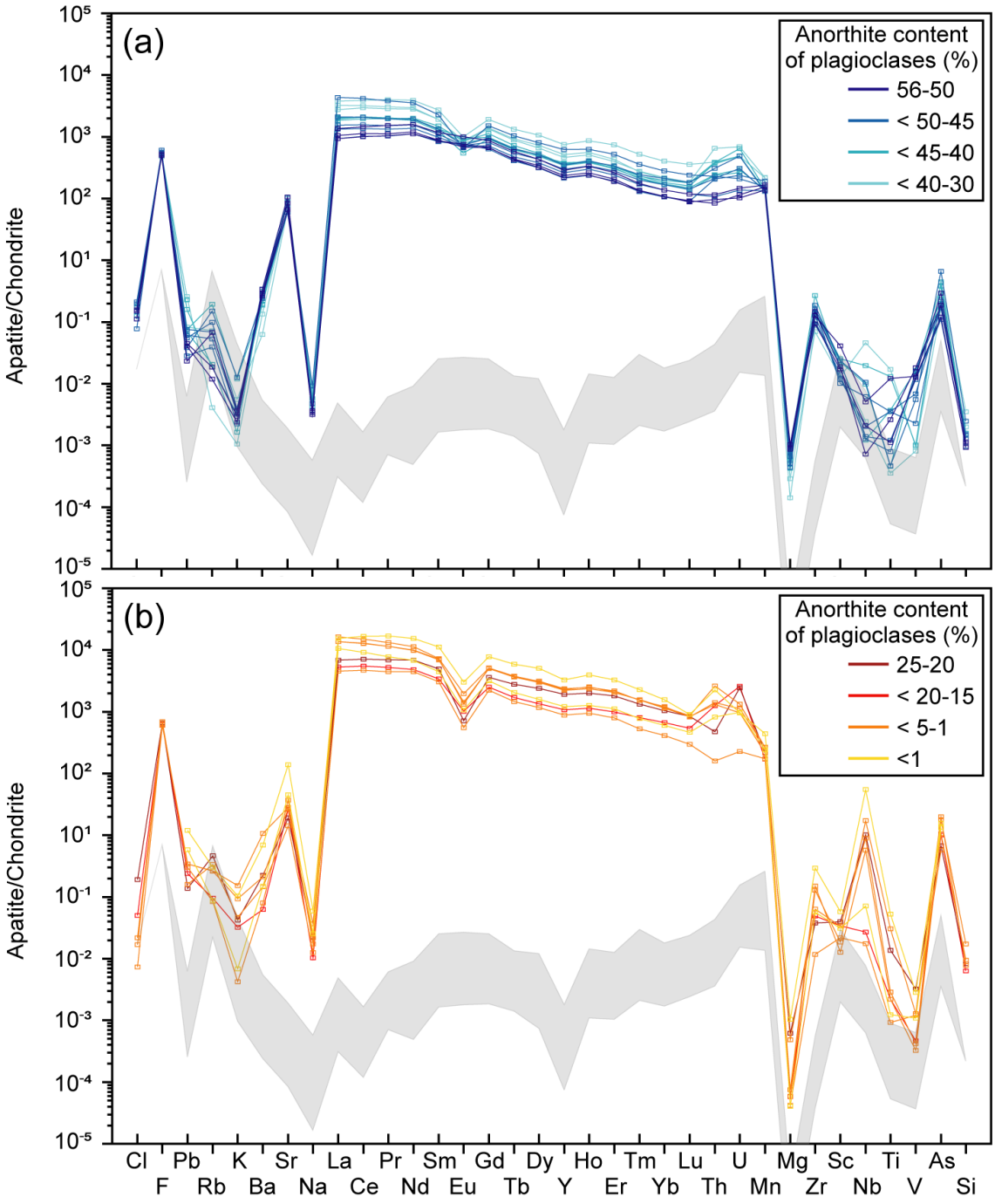

ANNEXE 26

Multielement diagram comparing the analyses of apatite from the Fe–Ti–P-rich, melanocratic layers of Tollari et al. (2008) (n=12 samples) to the field defined for cumulus apatite of the Critical Zone (this study).

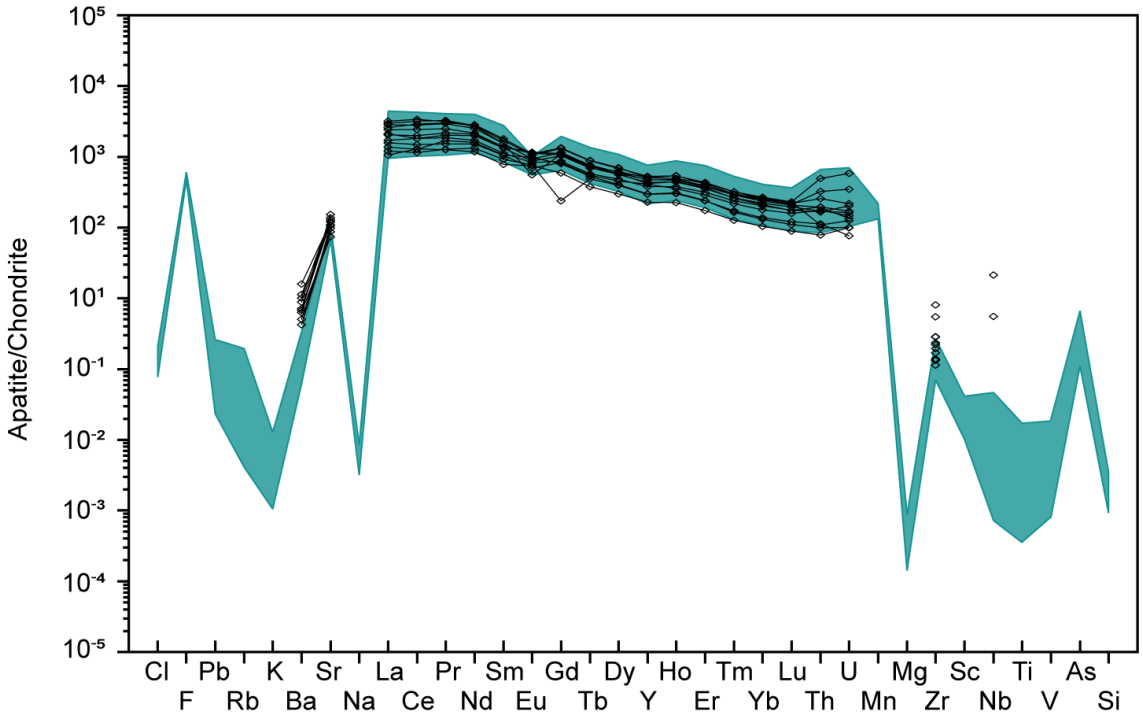

ANNEXE 27

Multielement diagrams for plagioclase in spatially associated Fe–Ti–P-rich (red) and -poor (blue) layers. Each field contains the plagioclase analyses for a sample. Note that HREE (hatched area) are close to or below the detection limit indicated by a grey dashed line.

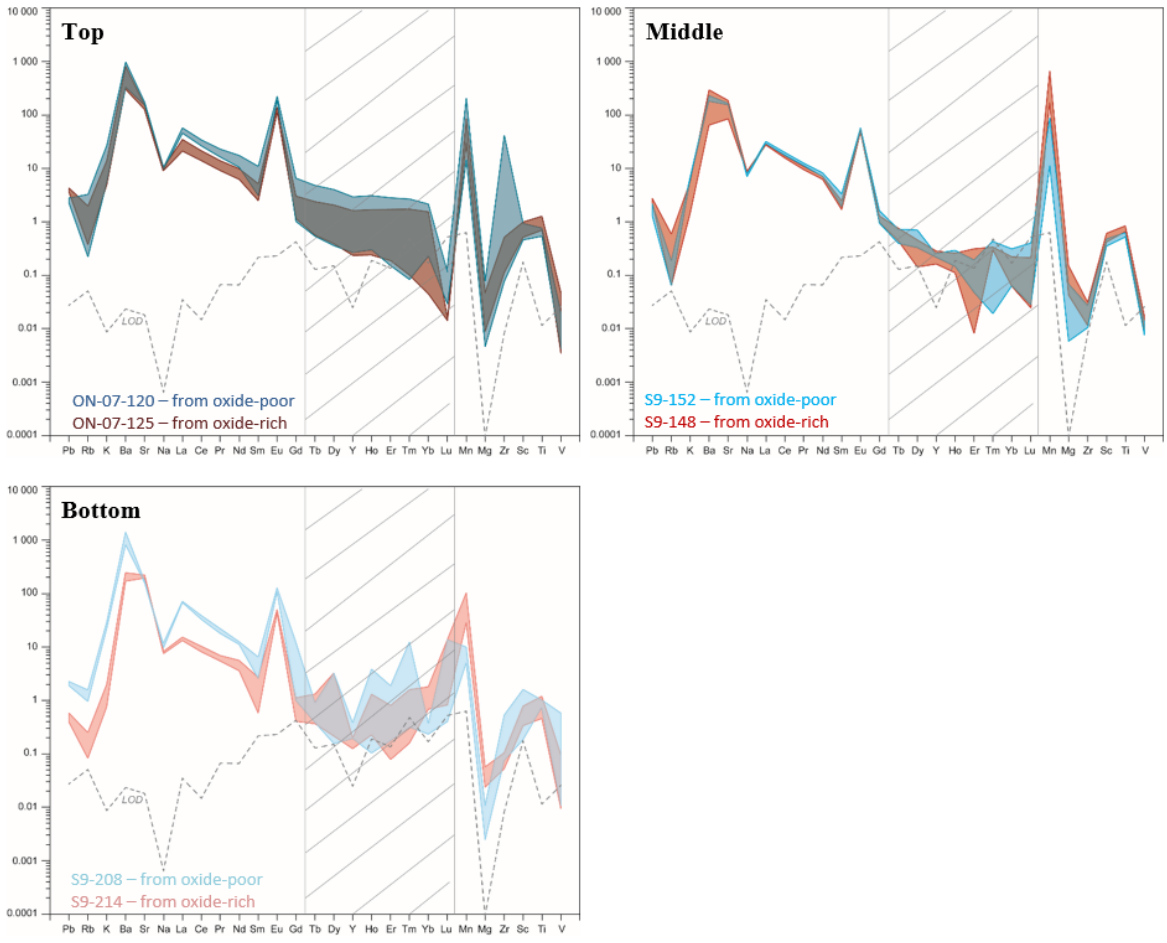

ANNEXE 28

Trace element content of apatite plotted against the anorthite content of associated plagioclases (left column; this study). Each data point corresponds to an apatite analyse. Liquid lines of descent for whole rocks of the Sept-Iles layered intrusion (data from Namur et al., 2011, see article for details) are shown in the right column.

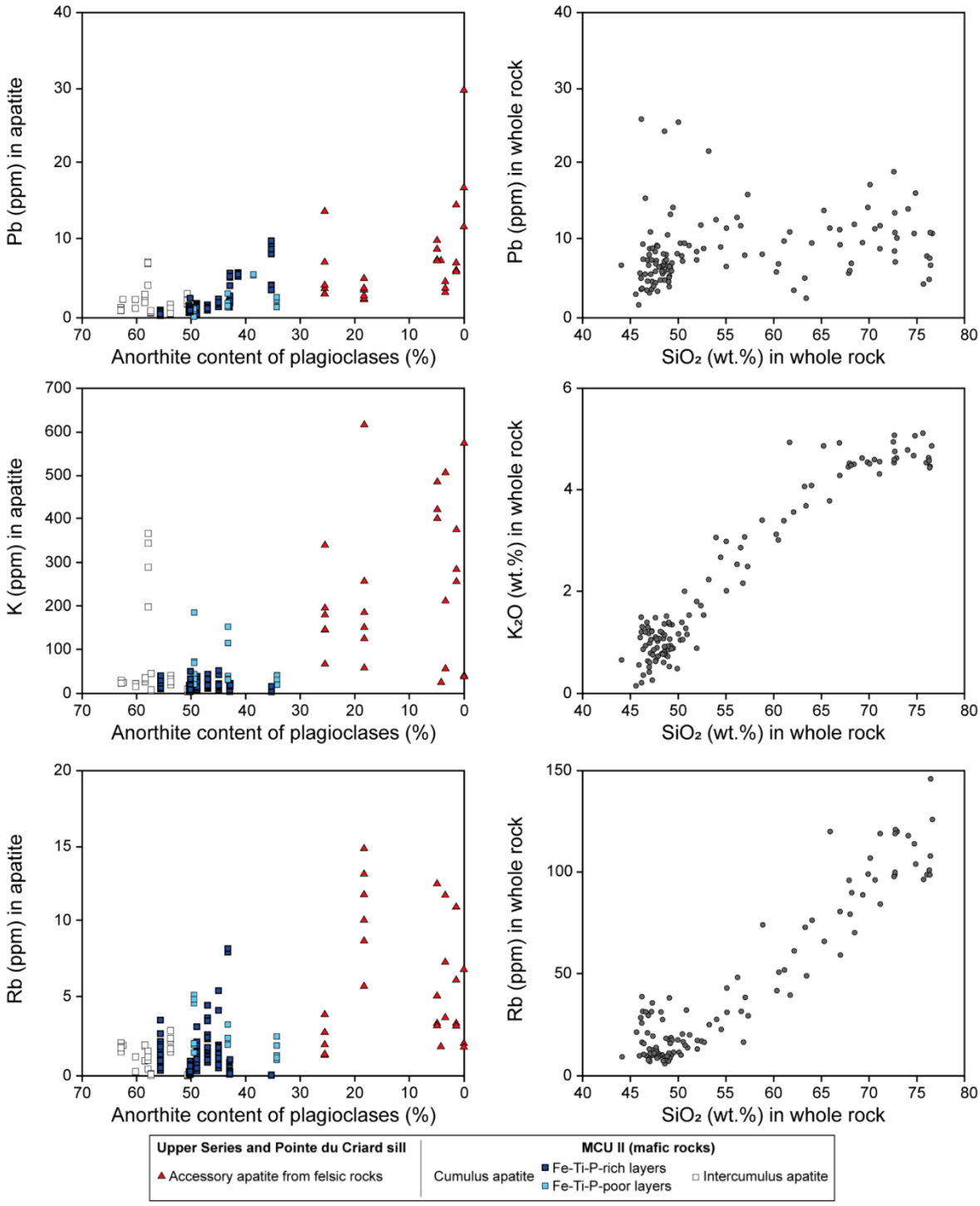

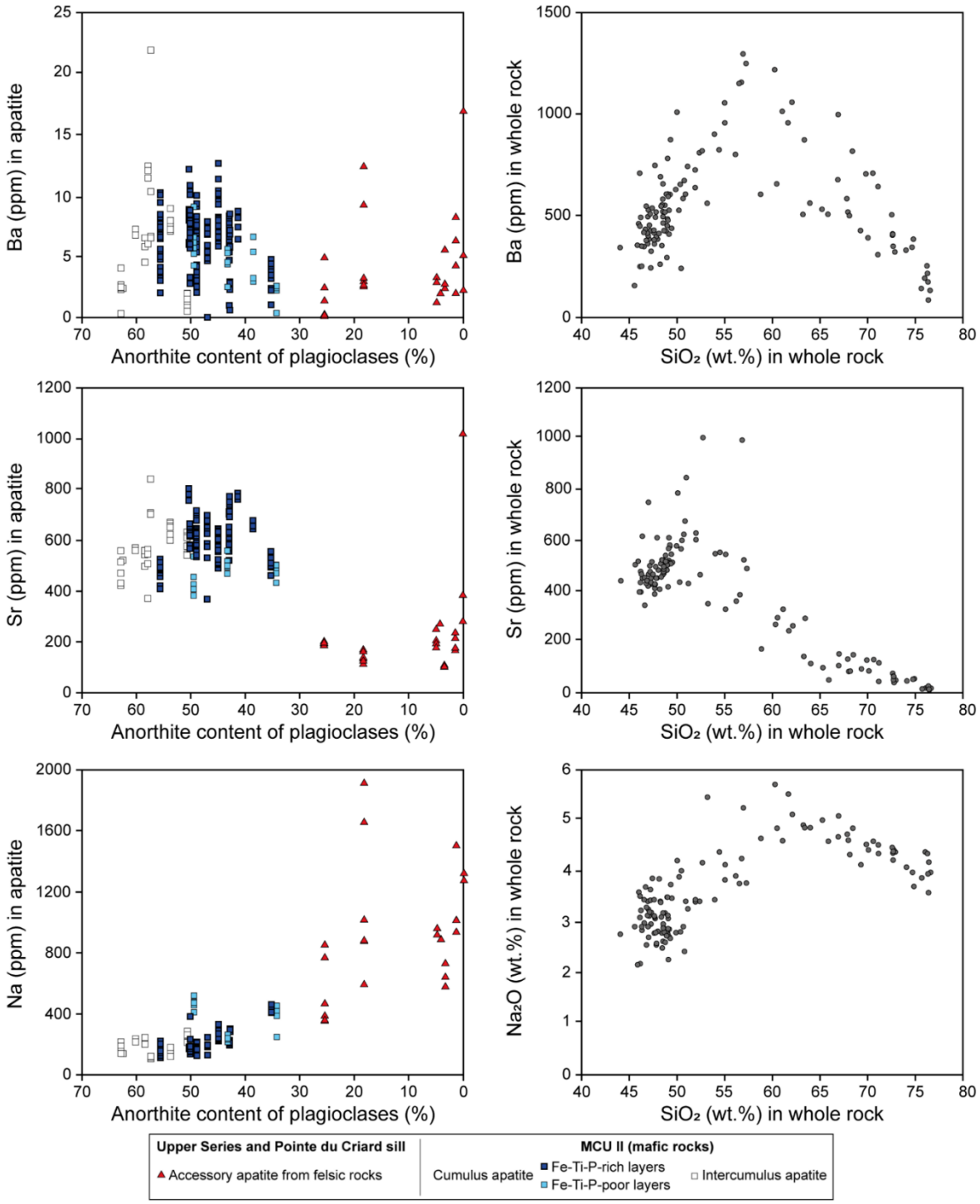
Ba (ppm) in apatite
Anorthite content of plagioclases (%)
Ba (ppm) in whole rock
SiO₂ (wt.%) in whole rock
Sr (ppm) in apatite
Anorthite content of plagioclases (%)
Sr (ppm) in whole rock
SiO₂ (wt.%) in whole rock
Na (ppm) in apatite
Anorthite content of plagioclases (%)
Na₂O (wt.%) in whole rock
SiO₂ (wt.%) in whole rock
Upper Series and Pointe du Criard sill
Accessory apatite from felsic rocks
MCU II (mafic rocks)
Cumulus apatite
Fe-Ti-P-rich layers
Fe-Ti-P-poor layers
Intercumulus apatite

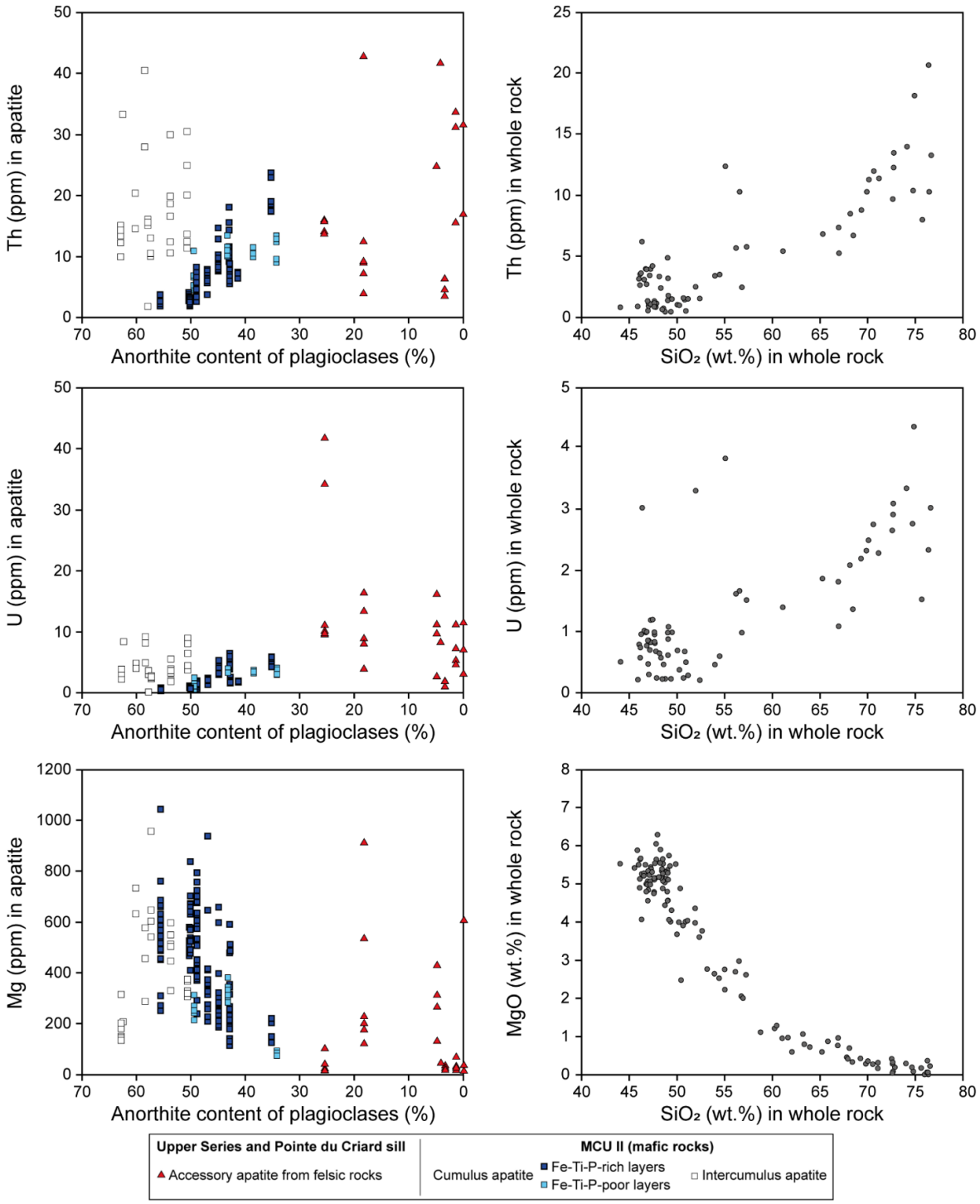
Th (ppm) in apatite
Anorthite content of plagioclases (%)
Th (ppm) in whole rock
SiO₂ (wt.%) in whole rock
U (ppm) in apatite
Anorthite content of plagioclases (%)
U (ppm) in whole rock
SiO₂ (wt.%) in whole rock
Mg (ppm) in apatite
Anorthite content of plagioclases (%)
MgO (wt.%) in whole rock
SiO₂ (wt.%) in whole rock
Upper Series and Pointe du Criard sill
Accessory apatite from felsic rocks
MCU II (mafic rocks)
Cumulus apatite
Fe-Ti-P-rich layers
Fe-Ti-P-poor layers
Intercumulus apatite

ANNEXE 29

Microphotographs in polarised light (a and c) and in cross nicols (b and d) of LREE- (titanite, epidote) and HREE-bearing (zircon) accessory phases in the felsic rocks of the Upper Series and Pointe du Criard sill. (a and b) idiomorphic titanite crystal enclosed in an other tinanite crystal; (c and d) apatite, magmatic epidote, titanite and zircon enclosed in a biotite longitudinal section. *Afs* alkali feldspar, *Amp* amphibole, *Ap* apatite, *Bt* biotite, *Ep* epidote, *Ilm* ilmenite, *Mag* magnetite, *Qz* quartz, *Ttn* titanite, *Zrn* zircon.

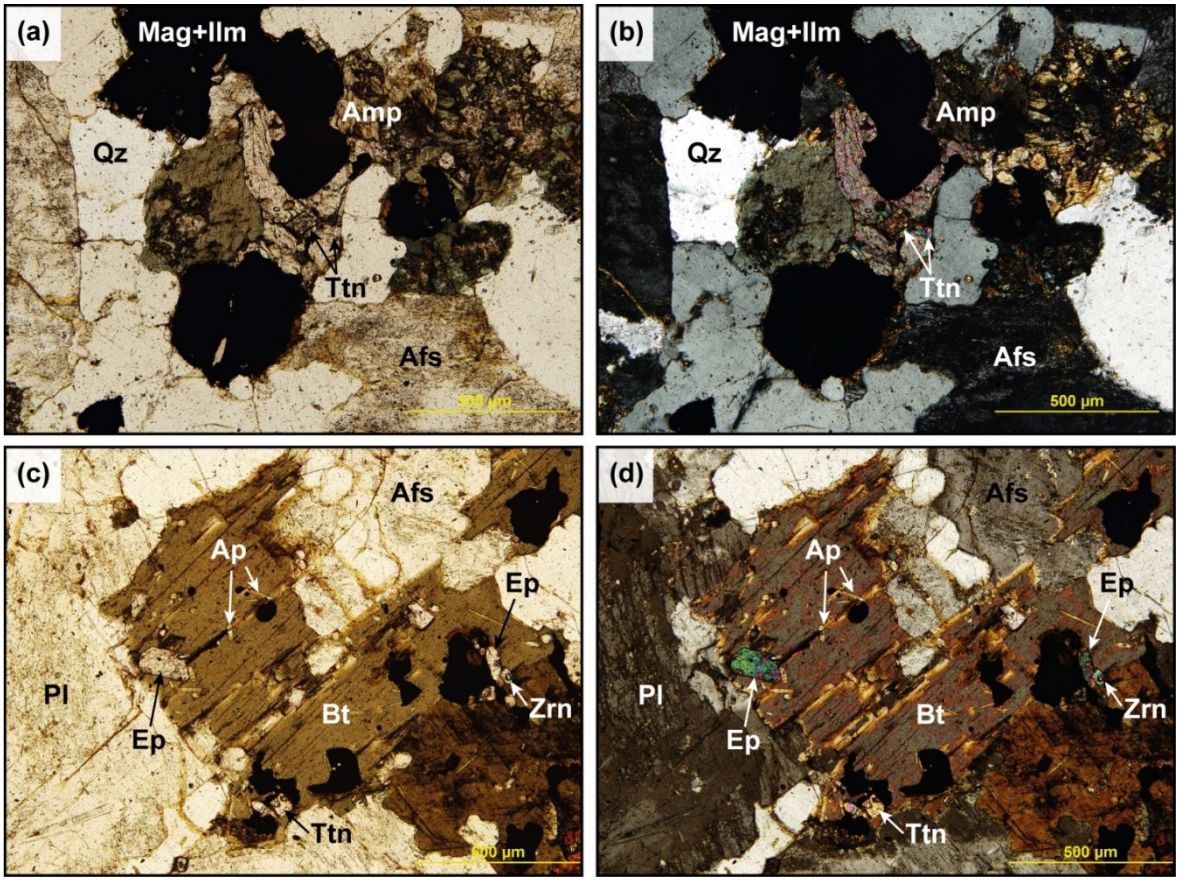

ANNEXE 34

Lithostratigraphic columns showing the location of the samples containing cumulus (filled symbols) and intercumulus (open symbols) in each studied mafic intrusion. Ap apatite; Aug augite; Ilm ilmenite; Mt magnetite; Ol olivine; Pl plagioclase; Wo wollastonite

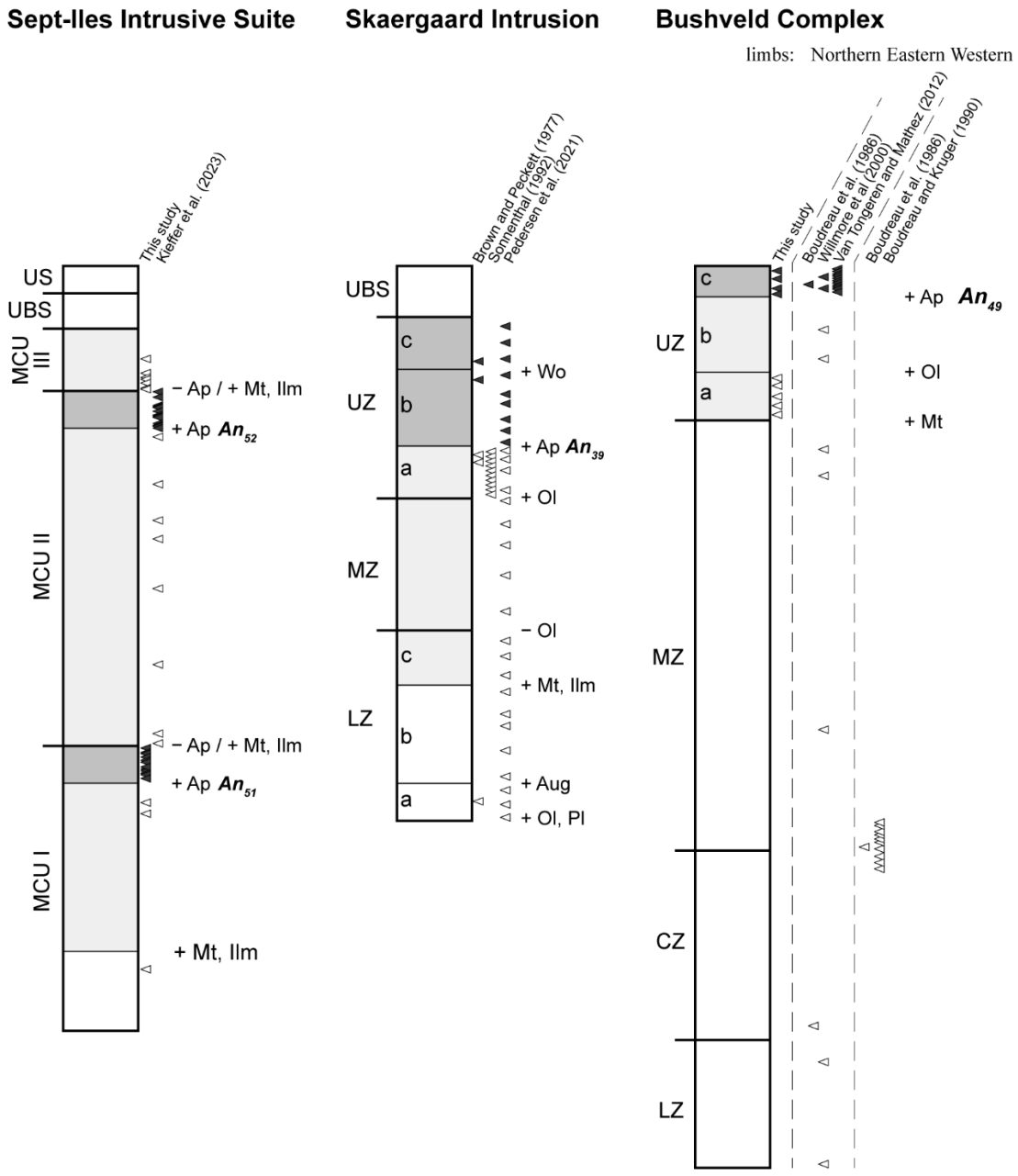

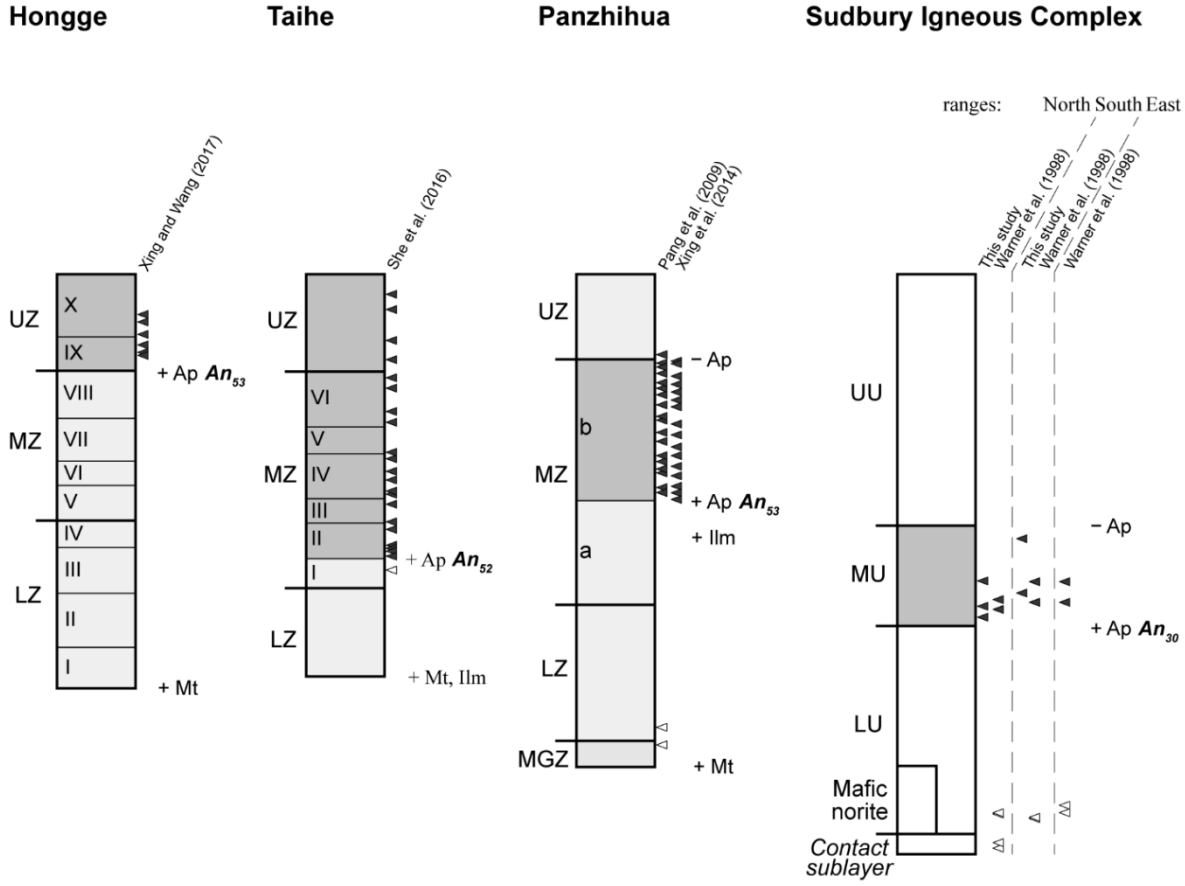
Hongge
Taihe
Panzhihua
Sudbury Igneous Complex
Xing and Wang (2017)
She et al. (2016)
Pang et al. (2009)
Xing et al. (2014)
ranges:
North South East
This study
Warner et al. (1998)
UZ
MZ
LZ
MGZ
UU
MU
LU
X
IX
VIII
VII
VI
V
IV
III
II
I
a
b
+ Ap An53
+ Ap An52
+ Ap An30
− Ap
+ Ilm
+ Mt
+ Mt, Ilm
Mafic norite
Contact sublayer

ANNEXE 35

Geological context for the 7 mafic intrusions studied

Sept-Iles Intrusive Suite

The 564 ± 4 Ma Sept-Iles Intrusive Suite (Quebec, Canada; Higgins & van Breemen, 1998) formed during the initial stages of opening of the Iapetus Ocean (Kumarapeli & Saull, 1966) accompanied by the activity of a mantle plume (Hill *et al.*, 1992). The 4.7 km-thick Layered Series (LS) of the Sept-Iles Intrusive Suite comprises 3 mafic megacyclic units (MCU), overlain by an anorthositic Upper Border Series (UBS) and a felsic Upper Series (US) that correspond to the felsic end of the differentiation of the LS (Namur *et al.*, 2010, 2011). The amount of crustal contamination, determined by Sr isotopes on whole rock and plagioclase, is negligible (< 2 %; Namur *et al.*, 2010). Each MCU of the LS corresponds to a new influx of parental magma, which mixed with the resident magma, and is formed of troctolite, Fe–Ti oxide-bearing troctolite and layered (olivine)gabbro (Namur et al., 2010). Fe–Ti oxides crystallised as a cumulus phase throughout most of the intrusion, whereas saturation in apatite only occurred at the top of both MCU I (constant abundance of 4 to 8 vol.% apatite; Namur *et al.*, 2012) and MCU II (decrease from 30 to 3 vol.% apatite; Tollari *et al.*, 2008; Namur *et al.*, 2012; Kieffer *et al.*, 2023) from an evolved ferrobasaltic magma (Namur et al., 2010). However, only the top of MCU II, named the Critical Zone, is mineralised in Fe–Ti oxides and apatite (measured + indicated resources estimated at 482 Mt at 4.18 % P2O5; Cimon, 1998; Paiement *et al.*, 2013). Namur et al. (2010) determined that at the onset of cumulus apatite crystallisation in the Critical Zone, the magma was unusually enriched in incompatible trace elements due to at least 7 cycles of magma differentiation and mixing with more primitive magma (i.e., crystallisation in an open system), which finally triggered immiscibility (Charlier *et al.*, 2011; Namur *et al.*, 2012). In contrast, the whole of MCU I crystallised in a closed system from a single differentiating batch of magma, that did not lead to such high concentrations of incompatible trace elements, or to immiscibility (Namur *et al.*, 2012).

Skaergaard intrusion

The Skaergaard intrusion (Greenland) was emplaced at 55.59 ± 0.13 Ma (Hamilton & Brooks 2004) at the interface between the gneiss basement and the continental flood basalts generated by the North Atlantic breakup, and originates from the former Iceland mantle plume (Momme *et al.*, 2006; Jakobsen *et al.*, 2010). The Skaergaard intrusion is widely recognised as a typical example of fractional crystallisation in a closed system (Wager & Brown 1968), with a negligible amount of crustal contamination (Stewart & DePaolo, 1990). Indeed, after the rapid filling of the magmatic chamber by several pulses of magma (Holness *et al.*, 2015; Annen *et al.*, 2022), the system remained closed and gabbroic rocks crystallised simultaneously from the floor (Layered Series, LS), the roof (Upper Border Series, UBS), and the walls (Marginal Border Series) of the magma chamber. The LS of Skaergaard intrusion is subdivided according to the cumulus assemblage (Wager & Deer, 1939; Wager & Brown, 1968). It consists of a Lower Zone (LZ) containing olivine and plagioclase (LZa), then augite (LZb) and Fe–Ti oxides (LZc), and a Main Zone (MZ) defined by the temporary disappearance of olivine. The Upper Zone (UZ) is marked by the reappearance of olivine (UZa), apatite (UZb; decrease from 10 to 2 vol.%; Pedersen *et al.*, 2021), and ferrobustamite (now inverted to hedenbergite; UZc). The UBS presents the same crystallisation sequence as the LS, from the roof downwards.

Bushveld Complex

The Bushveld Complex (South Africa) was emplaced over a ~5 Ma interval from 2060 to 2055 Ma (Scoates *et al.*, 2021) in the Kaapvaal Craton, and is generally accepted that it is the product of a mantle plume (Hatton, 1995; Fiorentini *et al.*, 2020). The 350 km-diameter and 6.5 km thick Rustenburg Layered Suite (RLS) of the Bushveld Complex is the most voluminous mafic layered intrusion on Earth. The RLS is subdivided into northern, eastern and western limbs that display a similar stratigraphy (Hall, 1932; Cawthorn & Walraven, 1998; Webb *et al.*, 2011). The RLS is in turn subdivided into 5 zones according to the cumulus assemblage (Figure ESM1; Hall, 1932): The noritic Marginal Zone, the ultramafic Lower Zone (LZ) formed of peridotite and pyroxenite, the Critical Zone

(CZ) consisting of cyclic units of chromitite, pyroxenite and norite, the gabbronoritic Main Zone (MZ), and the Upper Zone (UZ). The base of the UZ is defined by the appearance of magnetite (UZa), followed by olivine (UZb) and apatite (UZc) and consists of cyclic layers of magnetitite, gabbronorite and anorthosite overlain by diorite. The UZc contains 2 to 9 vol.% apatite and a thin horizon of nelsonite (up to 30 vol.% apatite; Figure 1b) that is considered mineralised in P (Ashwal *et al.*, 2005; Barnes et al., 2004; Yuan et al., 2017). The RLS crystallised from multiple magma injections and is considered an open system (Cawthorn & Walraven, 1998).

Hongge layered intrusion

The Hongge, Taihe and Panzhihua layered intrusions (China) were formed at around 260 Ma (Zhou et al., 2005) as part of the Emeishan Large Igneous Province (ELIP; Shellnutt, 2014, and references therein). The 1.5 km-thick Hongge layered intrusion is part of a small magma plumbing system (Zhong *et al.*, 2002), in which several replenishments are recorded by mineral chemistry (Luan *et al.*, 2014). Its magma has been contaminated with up to 15 % of metamorphic country rocks (i.e., schists and metasandstones; Tang *et al.*, 2021, 2023). The intrusion is divided into a Lower Zone (LZ) of hornblende- and biotiteolivine-bearing clinopyroxenite, a Main Zone (MZ) of clinopyroxenite hosting massive and disseminated Fe–Ti–V oxide layers, and an Upper Zone of apatite- and magnetite-bearing gabbro (Figure ESM1; Wang & Zhou 2013; Luan *et al.*, 2014). Each zone is further subdivided into cycles based upon the mineral crystallisation sequence. Fe–Ti–V oxides are cumulus phases in the whole intrusion whereas apatite only joins the cumulus assemblage at the base of the UZ (5 to 7 vol.% apatite; Luan *et al.*, 2014).

Taihe layered intrusion

The 1.2 km-thick Taihe layered intrusion (China) was formed in a complex magma plumbing system (She *et al.*, 2014). Its parental magma was contaminated with up to 10 % of calcareous country rocks (Tang *et al.*, 2021, 2023). The Taihe layered intrusion is subdivided in 3 zones (She *et al.*, 2014). The Lower Zone (LZ) is composed of olivine clinopyroxenite, gabbro and massive Fe–Ti–V oxides towards the top. The Main Zone (MZ), comprising magnetite clinopyroxenite, magnetite-apatite clinopyroxenite, and apatite-bearing gabbro, is divided into six rhythmic units according to varying mineral proportions. The Upper Zone (UZ) is exclusively formed of apatite-bearing gabbro (Figure ESM1; She *et al.*, 2014). Similar to the Hongge layered intrusion, Fe–Ti–V oxides constitute a cumulus phase throughout the whole intrusion, whereas cumulus apatite starts to crystallise in cycle II of the MZ (6 to 12 % apatite; She *et al.*, 2014, 2016).

Panzhihua Intrusion

The Panzhihua Intrusion (China) is 2 km-thick intrusion that hosts a giant Fe–Ti–V oxide deposit (Ma et al., 2003). It is proposed that the intrusion represents a magma conduit system (i.e., open system; Song et al., 2013; Pêcher *et al.*, 2013). It has been proposed that the parental magma was contaminated with up to 20 % with calcareous crustal component (i.e., dolomitic limestone, marble) that triggered massive oxide crystallisation (Ganino *et al.*, 2013; Tang *et al.*, 2021, 2023). However, other studies suggest that contamination with carbonate material is negligible (Yu *et al.*, 2005), and that introduction of fluids from country rocks might have resulted in the formation of an immiscible oxide melt from which the oxides crystallised (Zhou *et al.*, 2005, 2013). The Panzhihua Intrusion is divided into 4 zones that do not reflect variations of the cumulus mineralogy (Ma *et al.*, 2001; Zhou *et al.*, 2005). Rather, these zones were defined by mining geologists according to internal structures and the extent of Fe–Ti–V oxide mineralisation (Zhou *et al.*, 2005). The Marginal Zone (MGZ) represents the chilled base of the intrusion and is a microgabbro with abundant marble xenoliths. The Lower Zone (LZ) is formed of layered melagabbro intercalated with layers of massive oxidesores. The Main Zone (MZ) corresponds to layered gabbro that may contain Fe–Ti–V oxide-rich layers (MZa), with apatite (up to 5 vol.%; Pang *et al.*, 2008; Zhou *et al.*, 2005) appearing as a cumulus phase in MZb, whereas the Upper Zone (UZ) is constituted of unmineralized gabbro (Figure ESM1; Ma *et al.*, 2001; Zhou *et al.*, 2005). Fe–Ti–V oxides exist as a cumulus phase in the entirety of Panzhihua intrusion, but apatite is a cumulus phase in the MZb only (Zhou *et al.*, 2005; Pang *et al.*, 2008).

Sudbury Igneous Complex

The Sudbury Igneous Complex (Canada) is a differentiated, meteorite impact melt-sheet, and best known as one of the world's largest Ni–Cu–PGE mining camps, hosting over 90 deposits (Ames & Farrow, 2007). It is subdivided into North, South and East ranges, that are composed of 5 units (Figure ESM1; Lightfoot *et al.*, 1997; Ames *et al.*, 2002; Lightfoot & Zotov, 2005; Lavrenchuk *et al.*, 2010). At the base, the Contact Sublayer is composed of gabbronoritic breccias in embayments hosting the Ni-Cu mineralisation. This is overlain by the Lower Unit (LU) which is a mafic norite in the North Range only and a felsic norite in the South Range. The Middle Unit is composed of quartz gabbro, otherwise named Transition Zone Gabbro (TZG), and a granophyric Upper Unit (UU). Cumulus apatite (0.5 to 7 vol.%) and Fe–Ti oxides only occur in the TZG (Gasparrini & Naldrett, 1972; Warner *et al.*, 1998). The country rocks of the Sudbury Igneous Complex vary from granites to the North to metasediments in the South, and that their assimilation locally caused differences in the magma trace element content between the North and South ranges (Ames *et al.*, 2005; Zieg & Marsh, 2005), which can even be reflected by different arsenic content and mineralogy of the Ni-sulfide ores (Ames *et al.*, 2005; Dare *et al.*, 2010a, 2010b).

References cited:

Ames, D. E. & Farrow, C. E. G. (2007). Metallogeny of the Sudbury mining camp, Ontario. In: W.D., G. (ed.) Mineral deposits of Canada: A Synthesis of Major Deposit Types, District Metallogeny, the Evolution of Geological Provinces, and Exploration Methods: Geological Association of Canada, Mineral Deposits Division, Special Publication 5, 329-350.

Ames, D. E., Golightly, J. P., Lightfoot, P. C. & Gibson, H. L. (2002). Vitric compositions in the Onaping Formation and their relationship to the Sudbury Igneous Complex, Sudbury Structure. *Economic Geology* **97**, 1541-1562.

Ames, D.E., Davidson, A., Buckle, J.I., Card, K.D. (2005). Geology, Sudbury bedrock compilation, Ontario, Open File 4570, Geological Survey of Canada.

Annen, C., Latypov, R., Chistyakova, S., Cruden, A. R. & Nielsen, T. F. D. (2022). Catastrophic growth of totally molten magma chambers in months to years. *Science Advances* **8**, eabq0394.

Ashwal, L. D., Webb, S. J. & Knoper, M. W. (2005). Magmatic stratigraphy in the Bushveld Northern Lobe: continuous geophysical and mineralogical data from the 2950 m Bellevue drillcore. *South African Journal of Geology* **108**, 199-232.

Barnes, S.-J., Maier, W. D. & Ashwal, L. D. (2004). Platinum-group element distribution in the Main Zone and Upper Zone of the Bushveld Complex, South Africa. *Chemical Geology* **208**, 293-317.

Cawthorn, R. G. & Walraven, F. (1998). Emplacement and Crystallization Time for the Bushveld Complex. *Journal of Petrology* **39**, 1669-1687.

Charlier, B., Namur, O., Toplis, M. J., Schiano, P., Cluzel, N., Higgins, M. D. & Auwera, J. V. (2011). Large-scale silicate liquid immiscibility during differentiation of tholeiitic basalt to granite and the origin of the Daly gap. *Geology* **39**, 907-910.

Cimon, J. (1988). Le Complexe de Sept-Îles: I- L'Unité à apatite de Rivière des Rapides, Complexe de Sept-Îles; localisation stratigraphique et facteurs à l'origine de sa formation. ET 97-05.: Ministère de l'Énergie et des Ressources du Québec, p.44.

Dare, S. A. S., Barnes, S.-J. & Prichard, H. M. (2010). The distribution of platinum group elements (PGE) and other chalcophile elements among sulfides from Creighton Ni-Cu-PGE sulfide deposit, Sudbury, Canada, and the origin of palladium in pentlandite. *Mineralium Deposita* **45**, 765-793.

Dare, S. A. S., Barnes, S.-J., Prichard, H. M. & Fisher, P. C. (2010). The timing and formation of platinum-group minerals from the Creighton Ni-Cu-platinum-group element sulfide deposit, Sudbury, Canada: Early crystallization of PGE-rich sulfarsenides. *Economic Geology* **105**, 1071-1096.

Fiorentini, M. L., O'Neill, C., Giuliani, A., Choi, E., Maas, R., Pirajno, F. & Foley, S. (2020). Bushveld superplume drove Proterozoic magmatism and metallogenesis in Australia. *Scientific Reports* **10**, 19729.

Ganino, C., Harris, C., Arndt, N. T. & Prevec, S. A. (2013). Assimilation of carbonate country rock by the parent magma of the Panzhihua Fe-Ti-V deposit (SW China): Evidence from stable isotopes. *Geoscience Frontiers* **4**, 547-554.

Gasparrini, E. & Naldrett, A. J. (1972). Magnetite and Ilmenite in the Sudbury Nickel Irruptive. **Economic Geology 67**, 605-621.

Hall, A. L. (1932). The Bushveld Igneous Complex of the central Transvaal. *Union of South Africa Geological Survey Memoir* **28**, 560.

Hamilton, M. A. & Brooks, C. K. (2004). A precise U–Pb age for the Skaergaard intrusion. Goldschmidt 2004 Abstract. *Geochimica et Cosmichimica Acta* **68**, A587.

Hatton, C. J. (1995). Mantle plume origin for the Bushveld and Vantersdorp magmatic provinces. *Journal of African Earth Sciences* **21**, 571-577.

Higgins, M. D. & van Breemen, O. (1998). The Age of the Sept Iles Layered Mafic Intrusion, Canada: Implications for the Late Neoproterozoic/Cambrian History of Southeastern Canada. *The Journal of Geology* **106**, 421-431.

Hill, R. I., Campbell, I. H., Davies, G. & Griffiths, R. W. (1992). Mantle plumes and continental tectonics. *Science* **256**, 186-193.

Holness, M. B., Tegner, C., Namur, O. & Pilbeam, L. (2015). The Earliest History of the Skaergaard Magma Chamber: a Textural and Geochemical Study of the Cambridge Drill Core. *Journal of Petrology* **56**, 1199-1227.

Jakobsen, J. K., Tegner, C., Brooks, C. K., Kent, A. J. R., Lesher, C. E., Nielsen, T. F. D. & Wiedenbeck, M. (2010). Parental magma of the Skaergaard intrusion: constraints from melt inclusions in primitive troctolite blocks and FG-1 dykes. *Contributions to Mineralogy and Petrology* **159**, 61-79.

Kieffer, M. A., Dare, S. A. S. & Namur, O. (2023). The use of trace elements in apatite to trace differentiation of a ferrobasaltic melt in the Sept-Iles Intrusive Suite, Quebec, Canada: Implications for provenance discrimination. *Geochimica et Cosmichimica Acta* **342**, 169-197.

Kumarapeli, P. S. & Saull, V. A. (1966). The St. Lawrence Valley system : a north American equivalent of the east African rift system. *Canadian Journal of Earth Sciences* **3**, 639-657.

Lavrenchuk, A., Latypov, R. & Lightfoot, P. C. (2010). The Sudbury Igneous Complex, Canada: Numerical Modeling Confirms Fractionation of a Single Parental Magma: Ontario Geological Survey, Miscellaneous Release-Data.

Lightfoot, P. C., Keays, R. R., Morrison, G. G., Bite, A. & Farrell, K. P. (1997). Geochemical relationships in the Sudbury igneous complex; origin of the main mass and offset dikes. *Economic Geology* **92**, 289-307.

Lightfoot, P. C. & Zotov, I. A. (2005). Geology and geochemistry of the Sudbury Igneous Complex, Ontario, Canada: origin of nickel sulfide mineralization associated with an impact-generated melt sheet. *Geology of Ore Deposits* **47**, 349-381.

Luan, Y., Song, X.-Y., Chen, L.-M., Zheng, W.-Q., Zhang, X.-Q., Yu, S.-Y., She, Y.-W., Tian, X.-L. & Ran, Q.-Y. (2014). Key factors controlling the accumulation of the Fe–Ti oxides in the Hongge layered intrusion in the Emeishan Large Igneous Province, SW China. *Ore Geology Reviews* **57**, 518-538.

Ma, Y., Ji, X. T., Li, J. C., Huang, M. & Kan, Z. Z. (2003). Mineral Resources of the Panzhihua Region: Sichuan Science and Technology Press, Chengdu.

Ma, Y., Liu, J. F., Wang, H. F., Mao, Y. S., Ji, X. T., Wang, D. K. & Yan, Z. Z. (2001). Geology of the Panzhihua Region: Sichuan Science and Technology Press, Chengdu.

Momme, P., Tegner, C., Brooks, C. K. & Keays, R. R. (2006). wo melting regimes during Paleogene flood basalt generation in East Greenland: combined REE and PGE modeling. *Contributions to Mineralogy and Petrology* **151**, 88-100.

Namur, O., Charlier, B., Toplis, M. J., Higgins, M. D., Hounsell, V., Liegeois, J. P. & Vander Auwera, J. (2011). Differentiation of Tholeiitic Basalt to A-Type Granite in the Sept Iles Layered Intrusion, Canada. *Journal of Petrology* **52**, 487-539.

Namur, O., Charlier, B., Toplis, M. J., Higgins, M. D., Liégeois, J.-P. & Vander Auwera, J. (2010). Crystallization Sequence and Magma Chamber Processes in the Ferrobasaltic Sept Iles Layered Intrusion, Canada. *Journal of Petrology* **51**, 1203-1236.

Namur, O., Charlier, B. & Holness, M. B. (2012). Dual origin of Fe–Ti–P gabbros by immiscibility and fractional crystallization of evolved tholeiitic basalts in the Sept Iles layered intrusion. *Lithos* **154**, 100-114.

Paiement, J.-P., Gagne, J., Duplessis, C., Rousseau, G., Gagnon, G. & M., D. (2013). Pre-Feasability Study Mine Arnaud Inc. Sept-Iles Deposit, Québec; Final Report, Technical Report NI 43-101. 377.

Pang, K.-N., Zhou, M.-F., Lindsley, D. H., Zhao, D. & Malpas, J. (2008). Origin of Fe^Ti Oxide Ores in Mafic Intrusions: Evidence from the Panzhihua Intrusion, SW China. *Journal of Petrology* **49**, 295-313.

Pêcher, A., Arndt, N., Jean, A., Bauville, A., Ganino, C. & Athurion, C. (2013). Structure of the Panzhihua intrusion and its Fe-Ti-V. deposit, China. *Geoscience Frontiers* **4**, 571-581.

Pedersen, J. M., Ulrich, T., Whitehouse, M. J., Kent, A. J. R. & Tegner, C. (2021). The volatile and trace element composition of apatite in the Skaergaard intrusion, East Greenland. *Contributions to Mineralogy and Petrology* **176**, 102.

Scoates, J. S., Wall, C. J., Friedman, R. M., Weis, D., Mathez, E. A. & Van Tongeren, J. A. (2021). Dating the Bushveld Complex: Timing of Crystallization, Duration of Magmatism, and Cooling of the World's Largest Layered Intrusion and Related Rocks. *Journal of Petrology* **62**, egaa107.

She, Y.-W., Yu, S.-Y., Song, X.-Y., Chen, L.-M., Zheng, W.-Q. & Luan, Y. (2014). The formation of P-rich Fe–Ti oxide ore layers in the Taihe layered intrusion, SW China: Implications for magma-plumbing system process. *Ore Geology Reviews* **57**, 539-559.

She, Y.-W., Song, X.-Y., Yu, S.-Y., Chen, L.-M. & Zheng, W.-Q. (2016). Apatite geochemistry of the Taihe layered intrusion, SW China: Implications for the magmatic differentiation and the origin of apatite-rich Fe-Ti oxide ores. *Ore Geology Reviews* **78**, 151-165.

Shellnutt, J. G. (2014). The Emeishan large igneous province: A synthesis. *Geoscience Frontiers* **5**, 369-394.

Song, X.-Y., Qi, H.-W., Hu, R.-Z., Chen, L.-M., Yu, S.-Y. & Zhang, J.-F. (2013). Formation of thick stratiform Fe-Ti oxide layers in layered intrusion and frequent replenishment of fractionated mafic magma: Evidence from the Panzhihua intrusion, SW China. *Geochemistry, Geophysics, Geosystems* **14**, 712-732.

Stewart, B. W. & DePaolo, D. J. (1990). Isotopic studies of processes in mafic magma chambers: II. The Skaergaard Intrusion, East Greenland. *Contributions to Mineralogy and Petrology* **104**, 125-141.

Tang, Q., Li, C., Ripley, E. M., Bao, J., Su, T. & Xu, S. (2021). Sr-Nd-Hf-O isotope constraints on crustal contamination and mantle source variation of three Fe-Ti-V oxide ore deposits in the Emeishan large igneous province. *Geochimica et Cosmichimica Acta* **292**, 364-381.

Tang, Q., Chusi, L., Liu, C., Xue, S., Xu, S., Zhang, Y., Li, Z., Bao, J. & Song, H. (2023). Contrasting magmatic controls on the genesis of Fe-Ti-V oxide deposits in the Emeishan large igneous province using apatite Sr-Nd isotopes and apatite-zircon trace elements. *Mineralium Deposita* **58**, 1279-1296.

Tollari, N., Barnes, S., Cox, R. & Nabil, H. (2008). Trace element concentrations in apatites from the Sept-Îles Intrusive Suite, Canada — Implications for the genesis of nelsonites. *Chemical Geology* **252**, 180-190.

Wager, L. R. & Brown, G. M. (1968). Layered Igneous Rocks: Oliver and Boyd.

Wager, L. R. & Deer, W. A. (1939). Geological investigations in East Greenland, Part III. The petrology of the Skaergaard Intrusion, Kangerdlugssuaq, East Greenland. *Meddr Grønland* **105**, 352.

Warner, S., Martin, R. F., Abdel-Rahman, A.-F. M. & Doig, R. (1998). Apatite as a monitor of fractionation, degassing, and metamorphism in the Sudbury Igneous Complex, Ontario. *The Canadian Mineralogist* **36**, 981-999.

Webb, S., Ashwal, L. D. & Cawthorn, R. G. (2011). Continuity between eastern and western Bushveld Complex, South Africa, confirmed by xenoliths from kimberlite. *Contributions to Mineralogy and Petrology* **162**, 101-107.

Yu, S.-Y., Song, X.-Y., Ripley, E. M., Li, C., Chen, L.-M., She, Y.-W. & Luan, Y. (2015). Integrated O–Sr–Nd isotope constraints on the evolution of four important Fe–Ti oxide ore-bearing mafic–ultramafic intrusions in the Emeishan large igneous province, SW China. Chemical Geology 401, 28-42.

Yuan, Q., Namur, O., Fischer, L. A., Roberts, R. J., Lü, X. & Charlier, B. (2017). Pulses of Plagioclase-laden Magmas and Stratigraphic Evolution in the Upper Zone of the Bushveld Complex, South Africa. *Journal of Petrology* **58**, 1619-1643.

Zhong, H., Zhou, X. H., Zhou, M.-F., Sun, M. & Liu, B.-G. (2002). Platinum-group element geochemistry of the Hongge Fe-V-Ti deposit in the Pan-Xi area, southwestern China. *Mineralium Deposita* **37**, 226-239.

Zhou, M.-F., Chen, W. T., Wang, C. Y., Prevec, S. A., Liu, P. P. & Howarth, G. H. (2013). Two stages of immiscible liquid separation in the formation of Panzhihua-type Fe-Ti-V oxide deposits, SW China. *Geoscience Frontiers* **4**, 481-502.

Zhou, M.-F., Robinson, P. T., Lesher, C. M., Keays, R. R., Zhang, C.-J. & Malpas, J. (2005). Geochemistry, Petrogenesis and Metallogenesis of the Panzhihua Gabbroic Layered Intrusion and Associated Fe–Ti–V Oxide Deposits, Sichuan Province, SW China. *Journal of Petrology* **46**, 2253-2280.

Zieg, M. J. & Marsh, B. D. (2005). The Sudbury Igneous Complex: Viscous emulsion differentiation of a superheated impact melt sheet. *Geological Society of America Bulletin* **117**.

ANNEXE 43

Evolution of trace elements in cumulus and intercumulus apatite from Sept-Iles (left column) and other mafic layered intrusions (right column) with anorthite content of associated plagioclase. Source of data: [1]This study; [2]Kieffer *et al.* (2023); [3]Pedersen *et al.* (2021); [4]She *et al.* (2016); [5]Pang *et al.* (2009); [6]Xing *et al.* (2014).

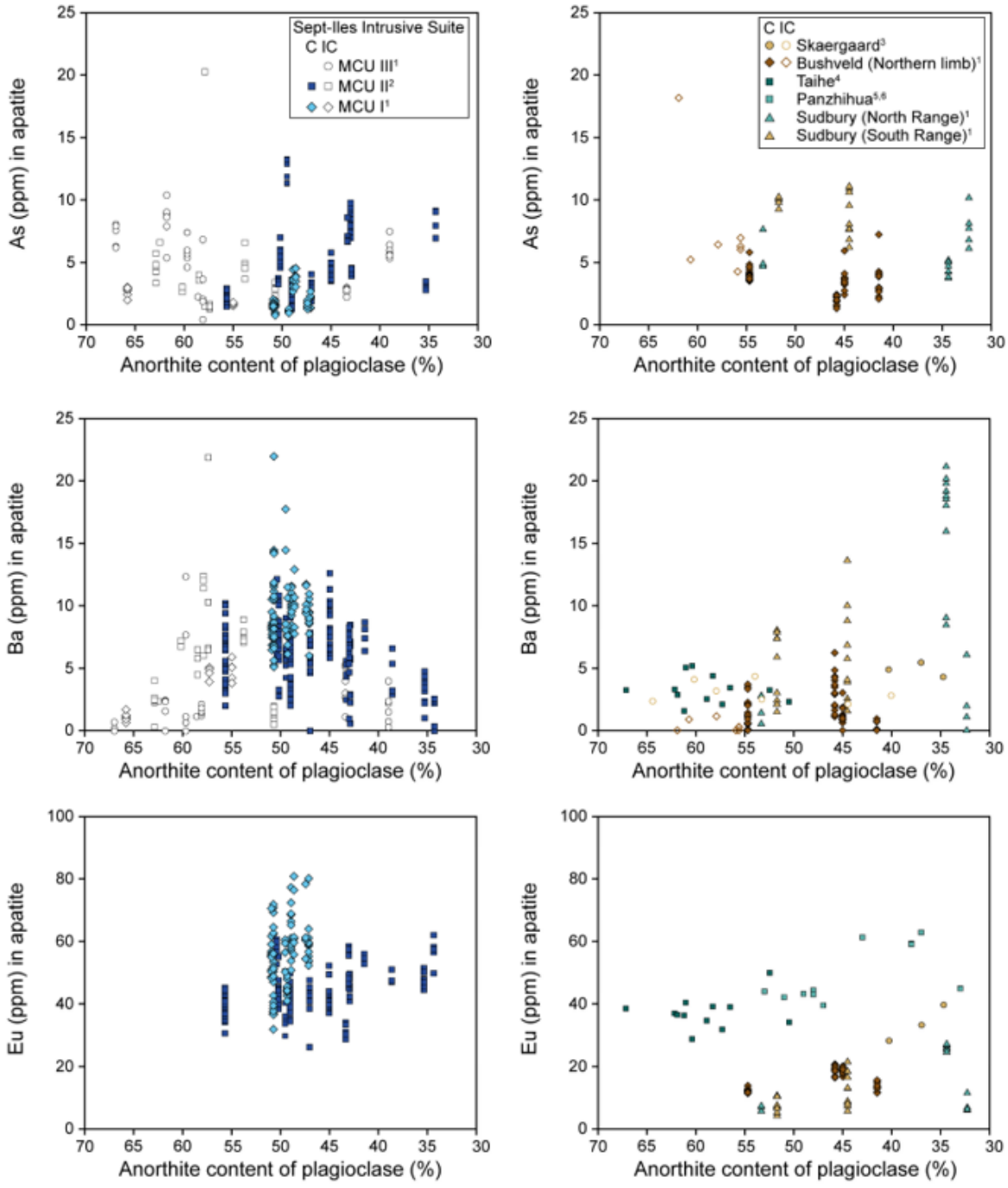

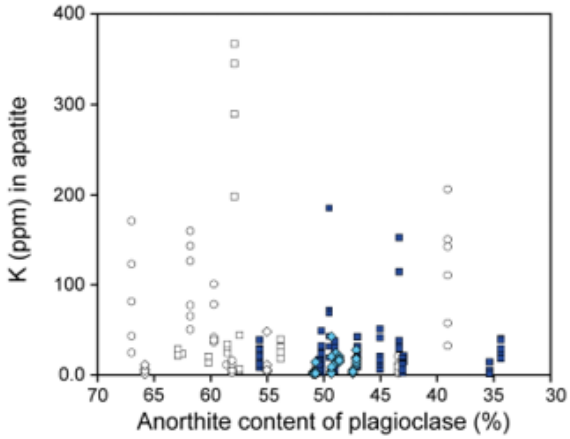
K (ppm) in apatite
400
300
200
100
0.0
70
65
60
55
50
45
40
35
30
Anorthite content of plagioclase (%)

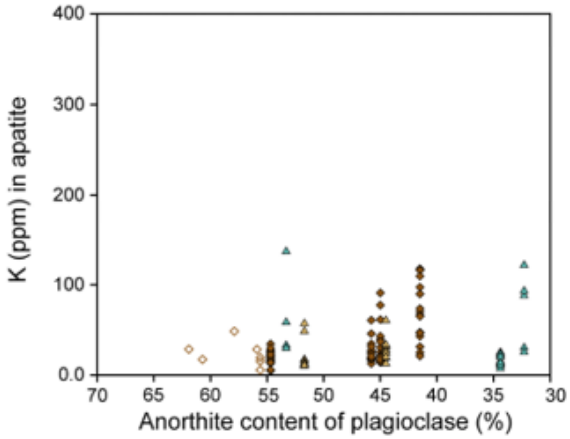
K (ppm) in apatite
400
300
200
100
0.0
70
65
60
55
50
45
40
35
30
Anorthite content of plagioclase (%)

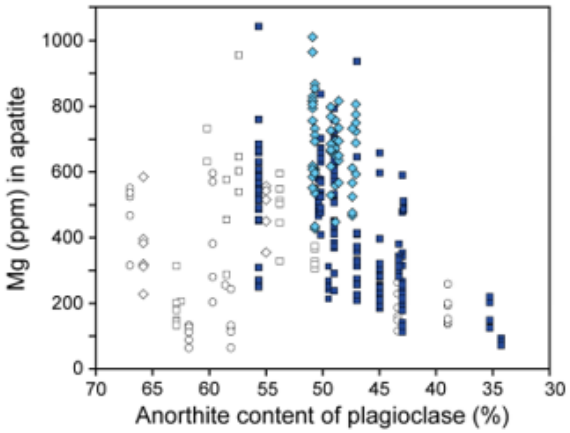
Mg (ppm) in apatite
1000
800
600
400
200
0
70
65
60
55
50
45
40
35
30
Anorthite content of plagioclase (%)

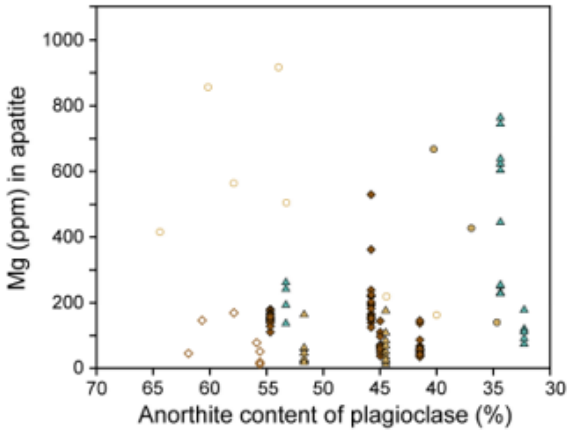
Mg (ppm) in apatite
1000
800
600
400
200
0
70
65
60
55
50
45
40
35
30
Anorthite content of plagioclase (%)

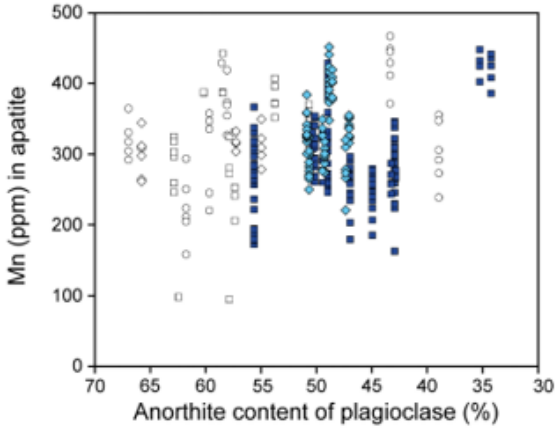
Mn (ppm) in apatite
500
400
300
200
100
0
70
65
60
55
50
45
40
35
30
Anorthite content of plagioclase (%)

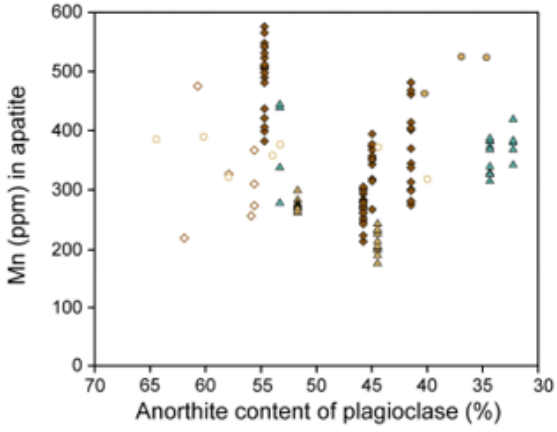
Mn (ppm) in apatite
600
500
400
300
200
100
0
70
65
60
55
50
45
40
35
30
Anorthite content of plagioclase (%)

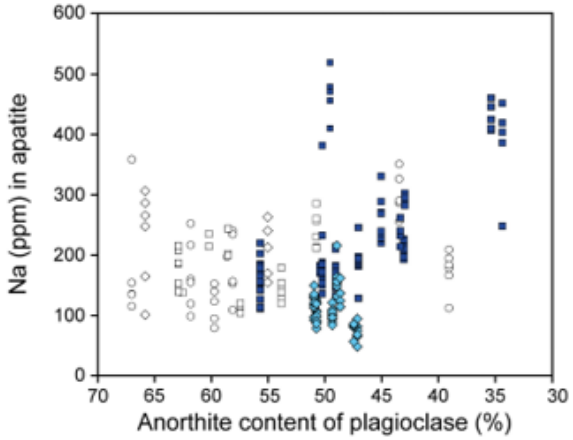
Na (ppm) in apatite
Anorthite content of plagioclase (%)

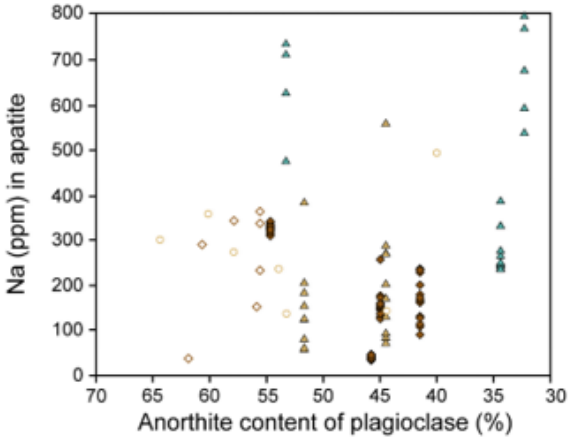
Na (ppm) in apatite
Anorthite content of plagioclase (%)

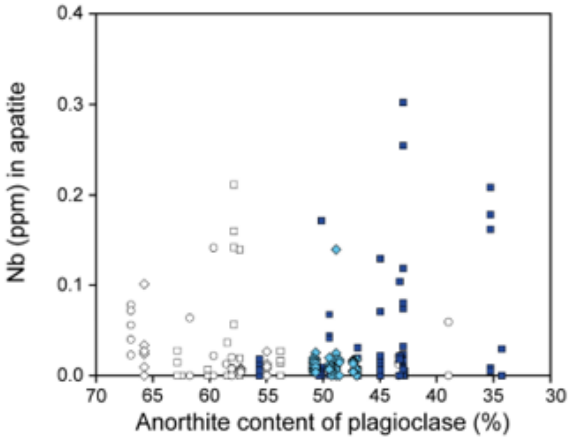
Nb (ppm) in apatite
Anorthite content of plagioclase (%)

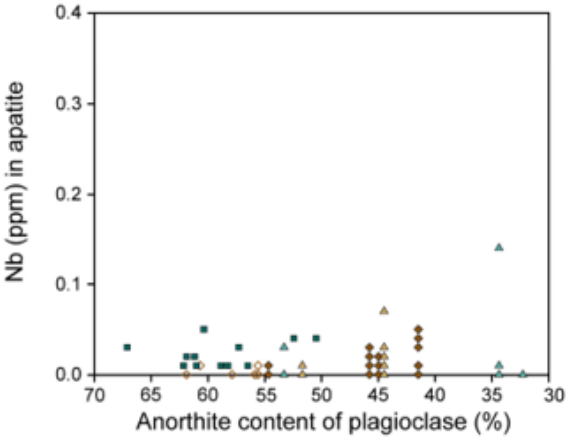
Nb (ppm) in apatite
Anorthite content of plagioclase (%)

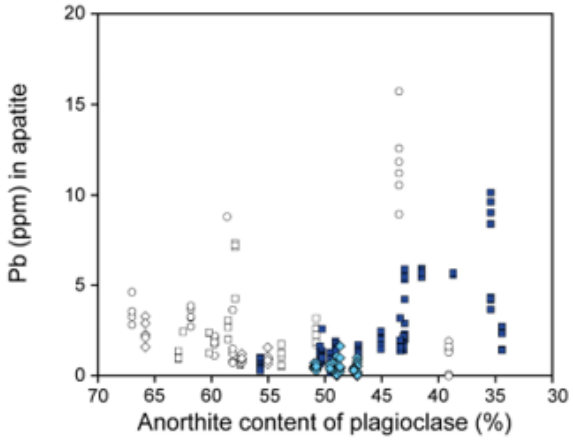
Pb (ppm) in apatite
Anorthite content of plagioclase (%)

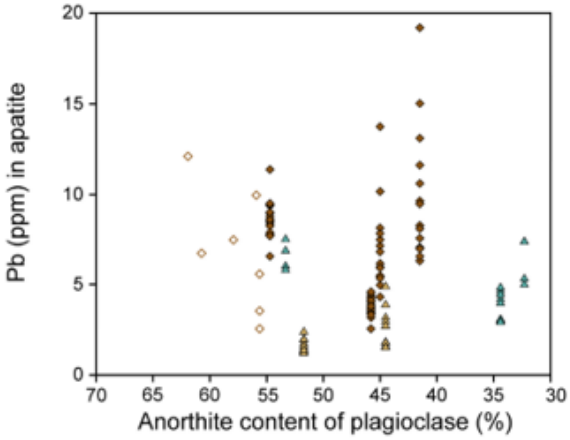
Pb (ppm) in apatite
Anorthite content of plagioclase (%)

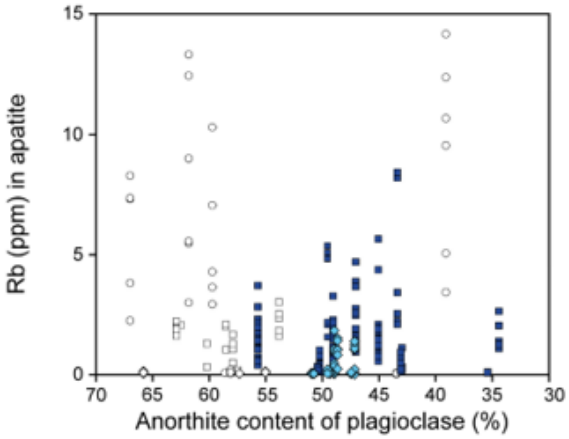
Rb (ppm) in apatite
Anorthite content of plagioclase (%)

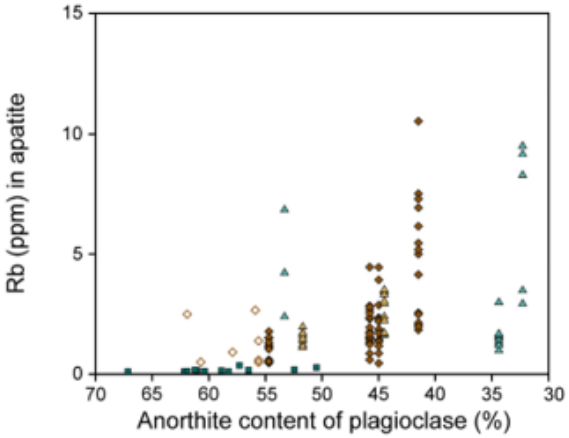
Rb (ppm) in apatite
Anorthite content of plagioclase (%)

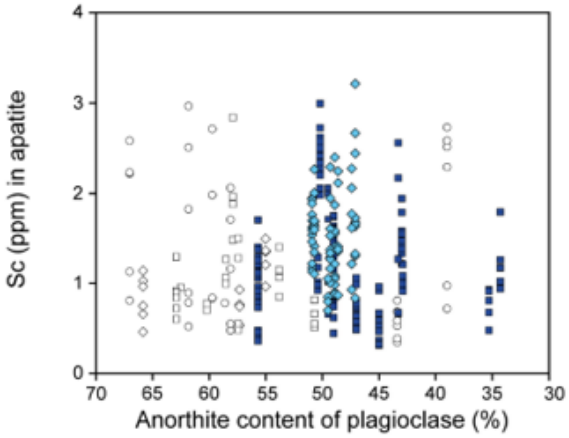
Sc (ppm) in apatite
Anorthite content of plagioclase (%)

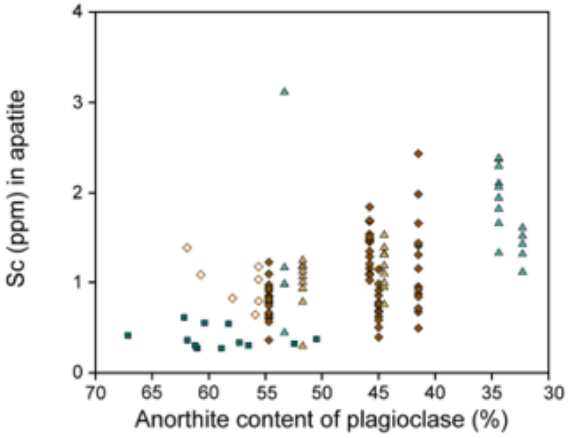
Sc (ppm) in apatite
Anorthite content of plagioclase (%)

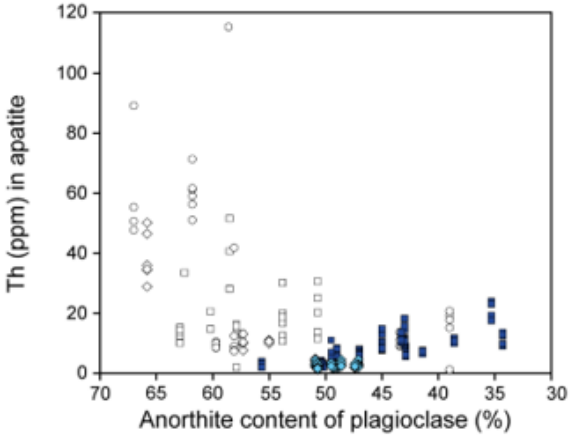
Th (ppm) in apatite
Anorthite content of plagioclase (%)

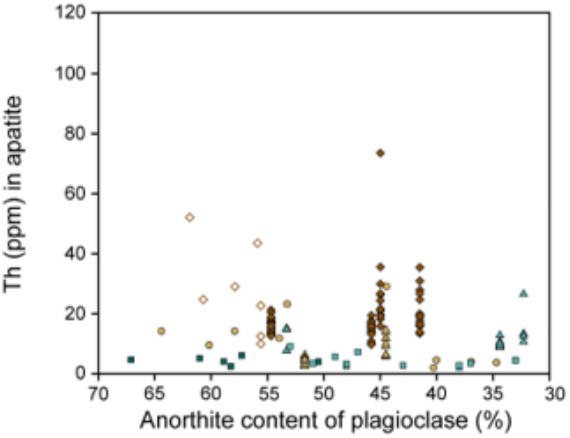
Th (ppm) in apatite
Anorthite content of plagioclase (%)

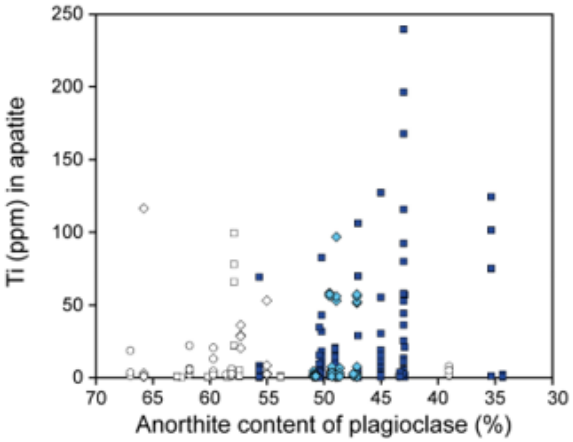
Ti (ppm) in apatite
250
200
150
100
50
0
70 65 60 55 50 45 40 35 30
Anorthite content of plagioclase (%)

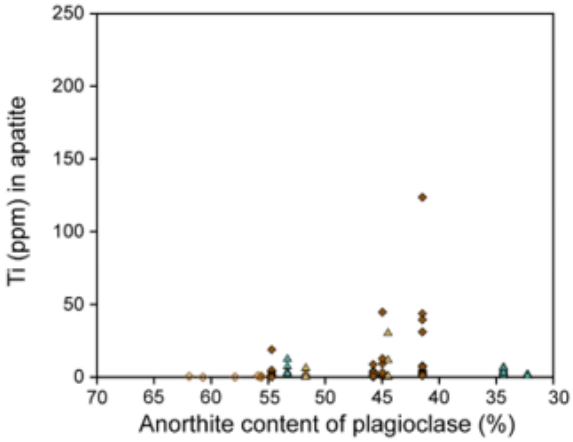
Ti (ppm) in apatite
250
200
150
100
50
0
70 65 60 55 50 45 40 35 30
Anorthite content of plagioclase (%)

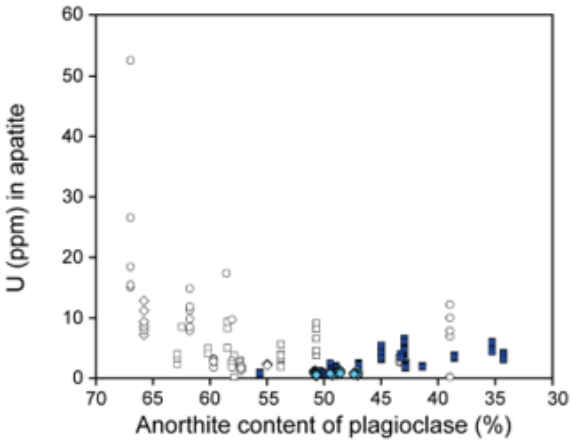
U (ppm) in apatite
60
50
40
30
20
10
0
70 65 60 55 50 45 40 35 30
Anorthite content of plagioclase (%)

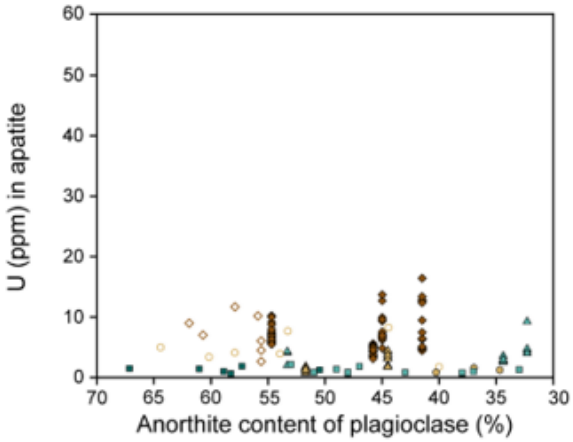
U (ppm) in apatite
60
50
40
30
20
10
0
70 65 60 55 50 45 40 35 30
Anorthite content of plagioclase (%)

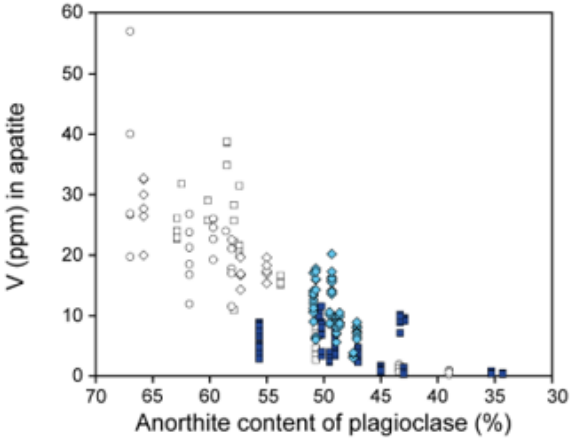
V (ppm) in apatite
60
50
40
30
20
10
0
70 65 60 55 50 45 40 35 30
Anorthite content of plagioclase (%)

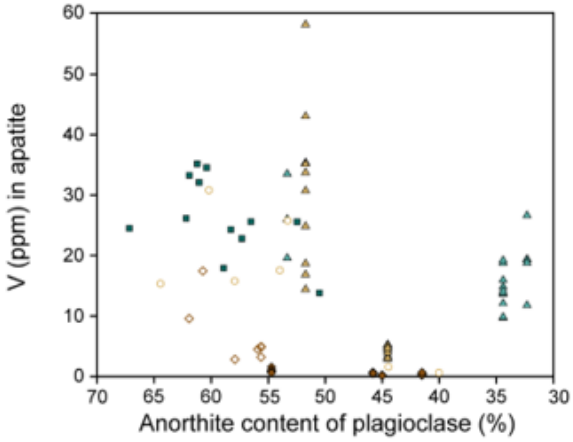
V (ppm) in apatite
60
50
40
30
20
10
0
70 65 60 55 50 45 40 35 30
Anorthite content of plagioclase (%)

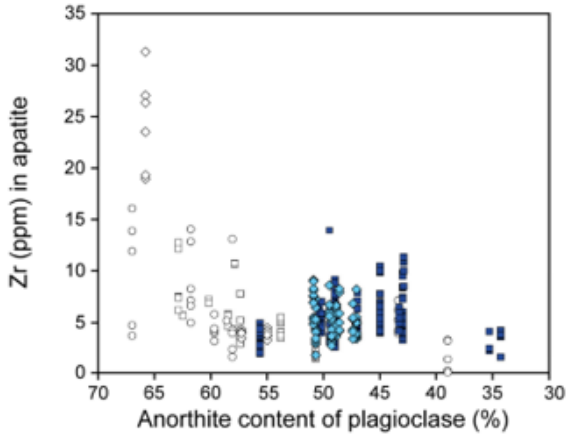
Zr (ppm) in apatite
Anorthite content of plagioclase (%)

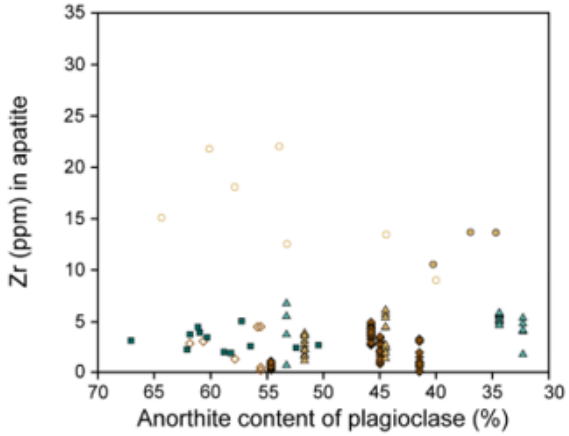
Zr (ppm) in apatite
Anorthite content of plagioclase (%)

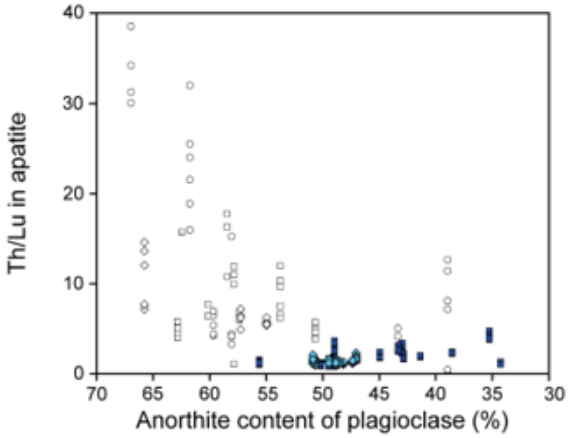
Th/Lu in apatite
Anorthite content of plagioclase (%)

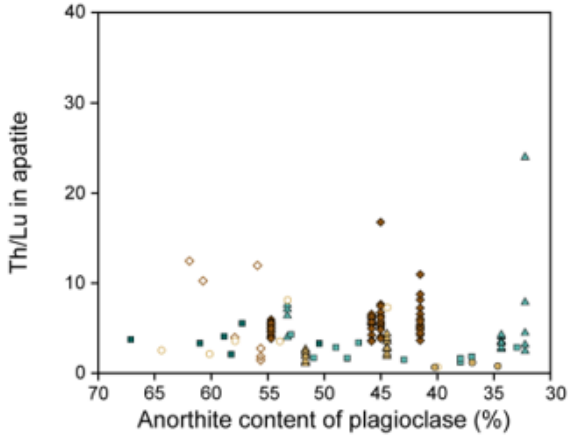
Th/Lu in apatite
Anorthite content of plagioclase (%)

ANNEXE 44

Variation of trace elements in cumulus apatite with stratigraphic depth within the MCU I (this study) and MCU II (Kieffer *et al.*, 2023) of Sept-Iles Intrusive Suite. In MCUII, cumulus apatite (dark squares) is from Fe–Ti–P-rich layers, and cumulus apatite (pale squares) are from Fe–Ti–P-poor layers, crystallysing from 2 silicate immiscible melts (Fe- and Si-rich, respectively; data from Kieffer *et al.*, 2023). Each data point corresponds to an apatite analysis. Black lines link the average composition of each sample.

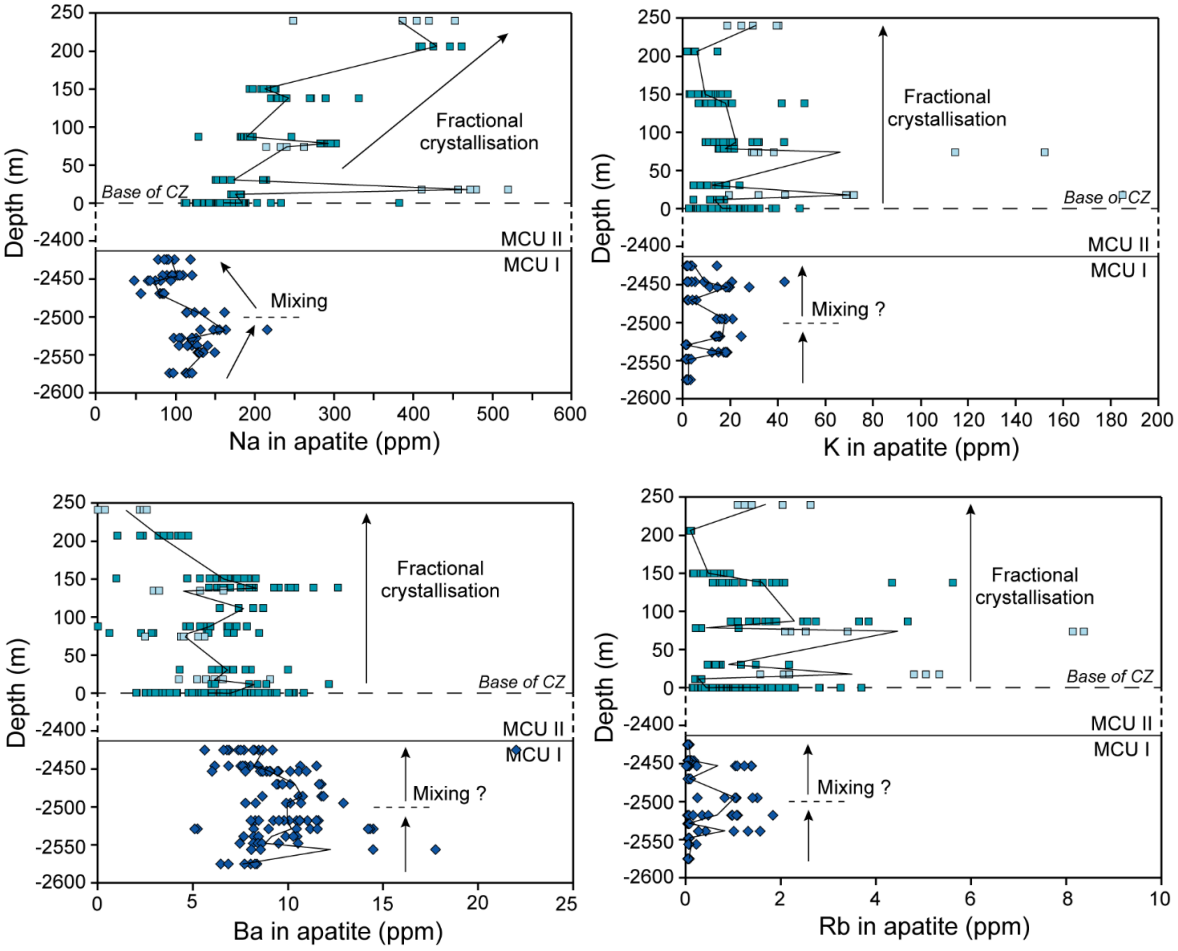

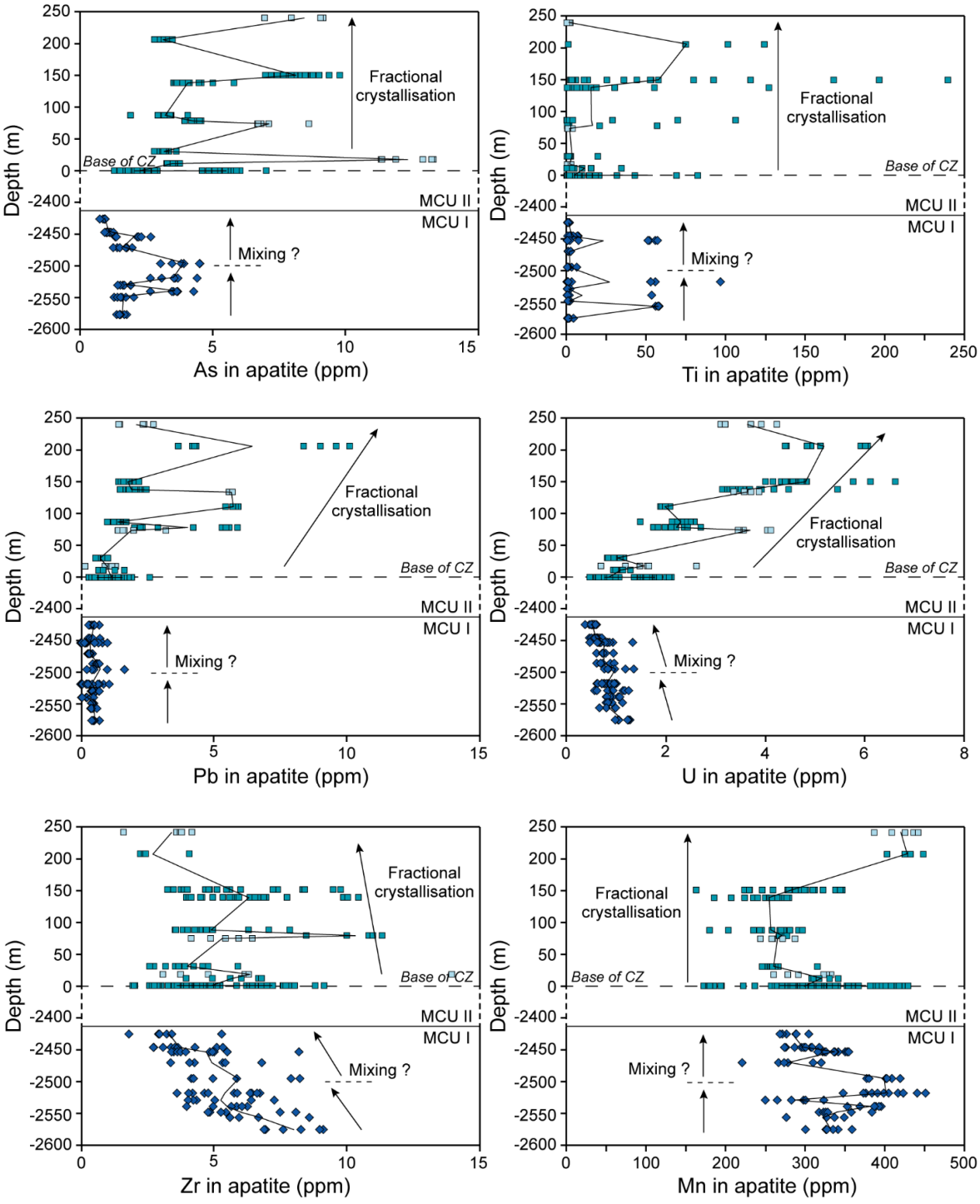
Depth (m)
As in apatite (ppm)
Ti in apatite (ppm)
Pb in apatite (ppm)
U in apatite (ppm)
Zr in apatite (ppm)
Mn in apatite (ppm)
Fractional crystallisation
Base of CZ
MCU II
MCU I
Mixing ?

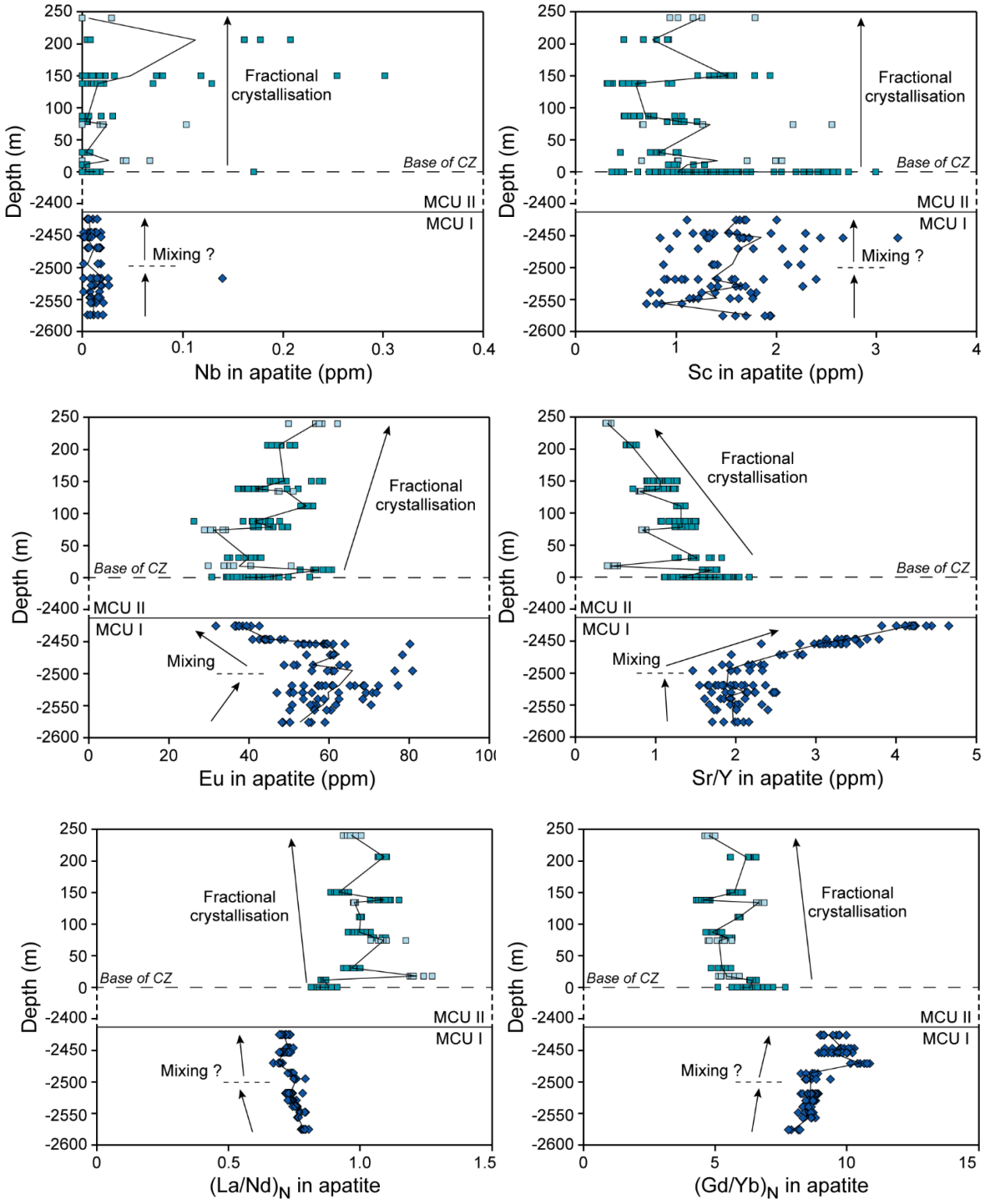
Depth (m)
Fractional crystallisation
Base of CZ
MCU II
MCU I
Mixing ?
Nb in apatite (ppm)
Sc in apatite (ppm)
Mixing
Eu in apatite (ppm)
Sr/Y in apatite (ppm)
(La/Nd)N in apatite
(Gd/Yb)N in apatite

ANNEXE 47

The use of apatite as a provenance indicator (Chapitre 3)

A series of apatite discrimination diagrams have been proposed by Kieffer *et al.* (2023) as follows, based on the Sept-Iles Intrusive Suite, to distinguish successively: (1) apatite in mafic rocks from those from felsic rocks, (2) cumulus from intercumulus apatite in mafic rocks and (3) cumulus apatite from Fe–Ti–P mineralised and unmineralised layers,:

Step 1: Distinguish apatite crystallising from a mafic or a felsic melt. When plotted in the ternary diagram to separate mafic from felsic apatite, based on the REE+Y, Sr and Eu anomaly in apatite, all cumulus and intercumulus apatite from all of the mafic layered intrusions plot in the mafic field, towards the Sr/Y pole, without exception (Figure 46-1.a). This is because during differentiation: (1) Sr/Y decreases, with Sr decreasing and Y increasing; (2) Eu* becomes increasingly negative; and (3) REE+Y increases. The Sr and Y content of apatite from the mafic intrusions are thus respectively higher and lower than apatite from the felsic intrusions (Kieffer *et al.*, 2023). The Sr/Y ratio has been proposed by Belousova *et al.* (2002) as a first discrimination step to separate ultramafic rocks and carbonatites from more felsic rocks. O'Sullivan *et al.* (2020) also used the Sr/Y ratio of apatite to discriminate ultramafic, mafic intrusions from granitoids and S-type granitoids. Further work in ongoing to test the robustness of this ternary mafic vs. felsic diagram with a larger dataset of apatite from granites.

Step 2: Distinguish cumulus from intercumulus apatite. The first diagram to discriminate cumulus from intercumulus apatite is based on the volatile content of apatite from mafic intrusions, as determined by EMPA (Figure 46-1.b). Intercumulus apatite have a higher Cl/F ratio than cumulus apatite due to a higher Cl content. Several processes might explain the lower Cl content of cumulus apatite, such as (1) the exsolution and escape of a Cl-rich fluid phase (i.e., Bushveld; Boudreau & Kruger 1990), (2) different F and Cl partition coefficients at the time of intercumulus and cumulus apatite crystallisation (i.e., Skaergaard; Pedersen *et al.* 2021), or (3) as Cl behaves as an incompatible element until the onset of cumulus apatite crystallisation, it can only be concentrated in interstitial liquid pockets from which crystallises intercumulus apatite (i.e., Sept-Iles; Kieffer *et al.* 2023). Some intercumulus apatite are even richer in Cl due to the circulation of Cl-rich metasomatic fluids, notably just below the major PGE zones in the lower parts of Bushveld and Stillwater intrusions (Boudreau & McCallum 1990; Boudreau *et al.*, 1986, 1995). Cumulus and intercumulus apatite from the majority of layered intrusions plot in their dedicated fields. However, Bushveld and Sudbury cumulus apatite have unusually high Cl/F ratios that places them in the intercumulus field (Figure 46-1.b). The high Cl/F ratio is due the high Cl content of cumulus apatite (Annexe 35), which, in the case of Bushveld, could be explained by the anomalous enrichment in Cl of the magma (Willmore *et al.*, 2002). As only apatite from the Northern limb appears to be Cl-rich, it is thus probable that this Cl enrichment is caused by a different contamination signature between the Northern limb (dolomite; Ashwal *et al.*, 2005) and the Eastern and Western limbs, rather to linked to the parental magma composition. The diagram relying solely on volatile elements allows to efficiently distinguish cumulus and intercumulus apatite, but has limited use if the magma was unusually due to contamination(i.e., Bushveld, Sudbury).

The second binary diagram proposed by Kieffer *et al.* (2023) involves trace elements (Th/Lu as a function of V). Although Th and Lu in apatite are available for most of the compiled data, V is rarely analysed, which limits testing of this diagram with literature data. Instead, we have replaced V by REE+Y which are more commonly analysed, in Figure 46-1.c (Th/Lu vs. REE+Y). Overall, cumulus apatite has lower Th/Lu ratio than intercumulus apatite, again with the exception of Bushveld and Sudbury (Figure 46-1.c). Cumulus apatite from these highly-contaminated intrusions have higher Th/Lu ratios, due to higher Th concentrations, which make them plot into the intercumulus field. This implies that the influence of crustal contamination hinders the proper use of the discrimination diagram.

If both volatile and trace elements are available, it is possible to test the diagrams based on Cl, F, Th, Lu and V. The first one is a binary diagram based on Cl/F as a function of Th/Lu (Figure 46-1.d).

As expected, all apatite plot in their dedicated fields except for Bushveld and Sudbury, for the reasons detailed above. The second diagram is a ternary diagram involving F/Cl, Th/Lu and V (Figure 46-1.e) to better distinguish cumulus from intercumulus apatite. Although Th/Lu is an indicator of contamination for cumulus apatite, it is also an indicator of intercumulus apatite, as Th is enriched in trapped liquid. Vanadium is compatible during crystallisation and is thus an indicator of a less evolved magma from which intercumulus apatite crystallises (Kieffer *et al.*, 2023). Analyses that can be plotted in this diagram are restricted to our new analyses and those from Pedersen *et al.* (2021) for Skaergaard apatite. This diagram shows that cumulus apatite from Sept-Iles and Skaergaard have a high F/Cl ratio. Again, cumulus apatite from Bushveld is distinguishable as it has high Th/Lu ratio (due to contamination) and low V content (as apatite crystallised late after extensive magnetite crystallisation, from an evolved melt). Cumulus apatite from Taihe and Sudbury (North Range) have intermediate Th/Lu and high V values (Figure 46-1.e), with both plotting in the intercumulus field, that might be due to their contaminated nature. However, the high V content of cumulus apatite from Taihe might also be due to its crystallisation from a more primitive melt. Indeed, in this intrusion, apatite crystallises early very shortly after oxides crystallise. It is also the case in Hongge and Panzhihua, but no V data is available in apatite from these intrusions to test this hypothesis. Intercumulus apatite is scattered in the middle of the diagram, regardless of its provenance (Figure 46-1.e). Among all proposed diagrams, this ternary diagram using V (to track the primitive signature of intercumulus apatite) is the most efficient to discriminate cumulus and intercumulus apatite, even if cumulus apatite composition is affected by crustal contamination.

Step 3: Distinguish cumulus apatite associated with Fe–Ti–P mineralised and unmineralised rocks. Finally, we plotted our dataset of cumulus apatite from mafic intrusions into the diagrams proposed by Kieffer *et al.* (2023) to separate apatite from Fe–Ti–P mineralised samples (oxide-apatite-rich) from the oxide-apatite-poor layers (unmineralised) of the Critical Zone (MCU II) of Sept-Iles (Figure 46-2). Note that the difference in composition was triggered by silicate liquid immiscibility (Kieffer *et al.*, 2023). Kieffer *et al.* (2023) showed that even if the diagrams mostly work for MCU II, the effect of the differentiation trend superimposed on the chemical characteristics of apatite from mineralised and unmineralised layers does not allow to efficiently separate them. We observed the same results with our dataset (Figure 46-2). All of the unmineralised samples from Sept-Iles MCU I, containing 6 to 8 vol.% cumulus apatite, plot in the mineralised field in the 3 diagrams. Samples from Skaergaard and Sudbury are not related to any Fe–Ti–P mineralisation, and therefore mostly plot in the unmineralised field in all discrimination diagrams. However, some samples do not behave as expected, probably due to several overprinting processes, such as differentiation or crustal contamination. In detail, all cumulus apatite from Hongge, Taihe and Panzhihua are considered mineralised in Fe–Ti–V (but not Fe-Ti-P) and plot in the Fe–Ti–P mineralised field in all 3 diagrams. One sample from Bushveld Northern limb is mineralised (i.e., nelsonite), but it does not plot in the mineralised field in any of the 3 diagrams. Other samples that are not mineralised plot in the mineralised field in 2 of 3 the diagrams. Therefore, the use of these diagrams is not recommended to identify mineralisation in Fe–Ti–P from unmineralised samples from mafic layered intrusions.

In general, discrimination diagrams work to separate apatite crystallising from felsic and mafic melt, and to identify cumulus from intercumulus apatite (Figure 46-1), but the effect of crustal contamination on apatite chemistry might perturb the use of these diagrams (Figure 46-2). Due to such complexity, future work should be undertaken with a larger apatite composition database, and with analyses including the trace elements suggested in our study. For instance, approaches using partial least square-discriminant analysis (Caraballo *et al.*, 2022) or supervised machine learning (Qiu *et al.*, 2023) could help to improve the classification of apatite. Nevertheless, the diagrams presented in this contribution provide interesting information about the petrogenesis of mafic layered intrusions.

References cited:

Ashwal, L. D., Webb, S. J. & Knoper, M. W. (2005). Magmatic stratigraphy in the Bushveld Northern Lobe: continuous geophysical and mineralogical data from the 2950 m Bellevue drillcore. *South African Journal of Geology* **108**, 199-232.

Belousova, E. A., Griffin, W. L., O'Reilly, S. Y. & Fischer, N. I. (2002). Apatite as an indicator mineral for mineral exploration: trace-element compositions and their relationship to host rock type. *Journal of Geochemical Exploration* **76**, 45-69.

Boudreau, A. E. & Kruger, F. J. (1990). Variation in the Composition of Apatite through the Merensky Cyclic Unit in the Western Bushveld Complex. *Economic Geology* **85**, 737-745.

Boudreau, A. E. & McCallum, I. S. (1990). Low temperature alteration of REE-rich chlorapatite from the Stillwater Complex, Montana. *American Mineralogist* **75**, 687-693.

Boudreau, A. E., Mathez, E. A. & McCallum, I. S. (1986). Halogen Geochemistry of the Stillwater and Bushveld Complexes: Evidence for Transport of the Platinum-Group Elements by Cl-Rich fluids. *Journal of Petrology* **27**, 967-986.

Boudreau, A. E., Love, C. & Prendergast, M. D. (1995). Halogen geochemistry of the Great Dyke, Zimbabwe. *Contributions to Mineralogy and Petrology* **122**, 289-300.

Caraballo, E., Dare, S. A. S. & Beaudouin, G. (2022). Variation of trace elements in chalcopyrite from worldwide Ni-Cu sulfide and Reef-type PGE deposits: implications for mineral exploration. *Mineralium Deposita* **57**, 1-29.

Kieffer, M. A., Dare, S. A. S. & Namur, O. (2023). The use of trace elements in apatite to trace differentiation of a ferrobasaltic melt in the Sept-Iles Intrusive Suite, Quebec, Canada: Implications for provenance discrimination. *Geochimica et Cosmichimica Acta* **342**, 169-197.

O'Sullivan, G., Chew, D., Kenny, G., Henrichs, I. & Mulligan, D. (2020). The trace element composition of apatite and its application to detrital provenance studies. *Earth-Science Reviews* **201**, 103044.

Pedersen, J. M., Ulrich, T., Whitehouse, M. J., Kent, A. J. R. & Tegner, C. (2021). The volatile and trace element composition of apatite in the Skaergaard intrusion, East Greenland. *Contributions to Mineralogy and Petrology* **176**, 102.

Qiu, K.-F., Zhou, T., Chew, D., Hou, Z.-L., Müller, A., Yu, H.-C., Lee, R. G., Chen, H. & Deng, J. (2023). Apatite trace element composition as an indicator of ore deposit types: a machine learning approach. *American Mineralogist*.

Willmore, C. C., Boudreau, A. E., Spivack, A. & Kruger, F. J. (2002). Halogens of Bushveld Complex, South Africa: δ^{37}Cl and Cl/F evidence for hydration melting of the osurce region in a back-arc setting. *Chemical Geology* **182**, 503-511.

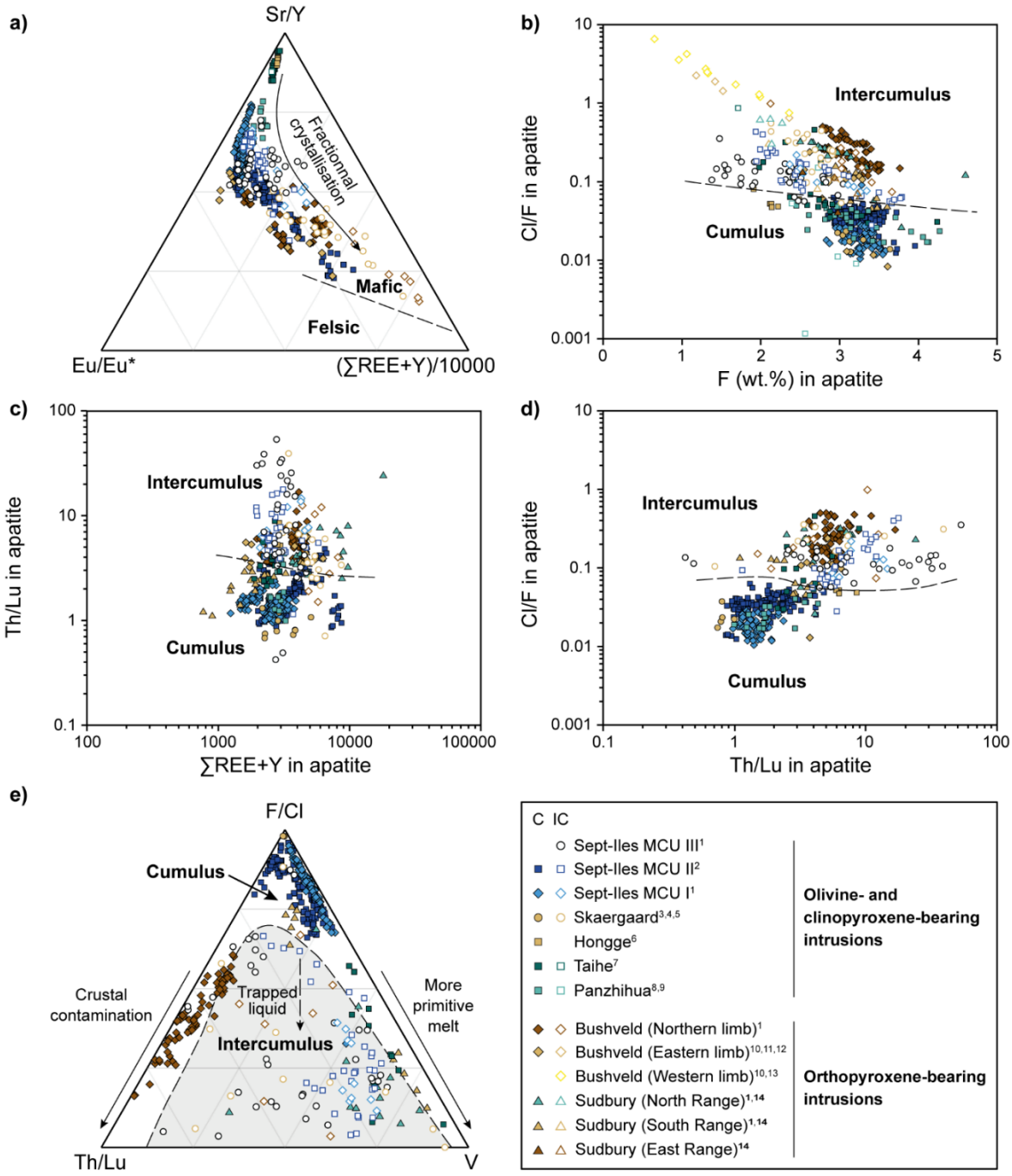

Figure 46-1 – Data from mafic layered intrusions displayed in the discrimination diagrams from Kieffer et al. (2023). (a) Ternary discrimination diagram to separate apatite from mafic and felsic melts (Kieffer *et al.*, 2023). Binary and ternary discrimination diagrams to distinguish cumulus from intercumulus apatite, based on (b) the volatile content determined by EMPA, the (c) trace element content determined by LA-ICP-MS. (d) and (e) discrimination diagrams combine data obtained by EMPA and LA-ICP-MS (modified from Kieffer *et al.*, 2023). Note that apatite from Hongge and Panzhihua are not displayed on (e) due to the lack of V data. Source of data: [1]this study; [2]Kieffer *et al.* (2023); [3]Brown and Peckett (1977); [4]Sonnenthal (1992); [5]Pedersen *et al.* (2021); [6]Xing and Wang (2017); [7]She *et al.* (2016); [8]Pang *et al.* (2009); [9]Xing *et al.* (2014); [10]Boudreau *et al.* (1986); [11]Willmore *et al.* (2000); [12]Van Tongeren and Mathez (2012); [13]Boudreau and Kruger (1990); [14]Warner *et al.* (1998)

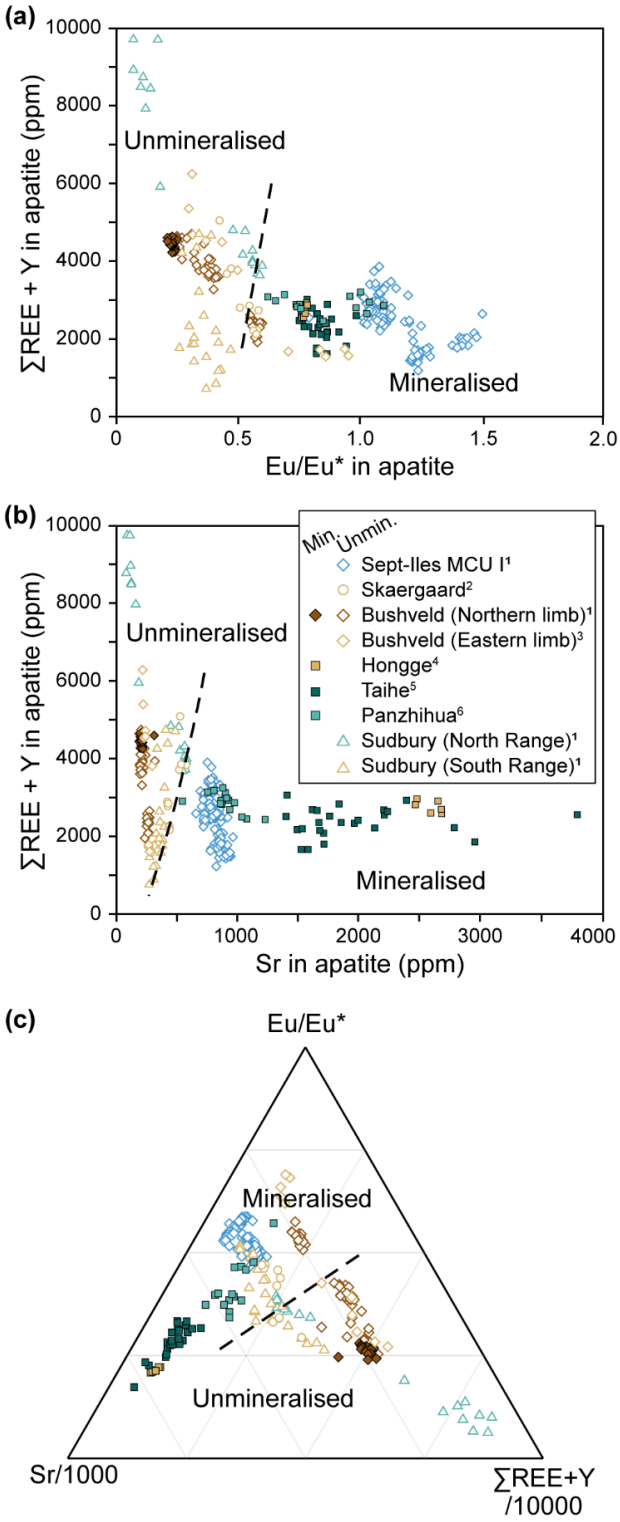

Figure 46-1 – Data from mafic layered intrusions displayed in the discrimination diagrams from Kieffer et al. (2023), to separate apatite from Fe–Ti–P mineralised (Min.) and unmineralised (Unmin.) layers. Source of data: [1]this study; [2]Pedersen et al. (2021); [3]Van Tongeren and Mathez (2012); [4]Xing and Wang (2017); [5]She *et al.* (2016); [6]Xing *et al.* (2014)